ШЕСТОЙ МОСКОВСКИЙ СИМПОЗИУМ ПО СОЛНЕЧНОЙ СИСТЕМЕ

THE SIXTH MOSCOW SOLAR SYSTEM SYMPOSIUM

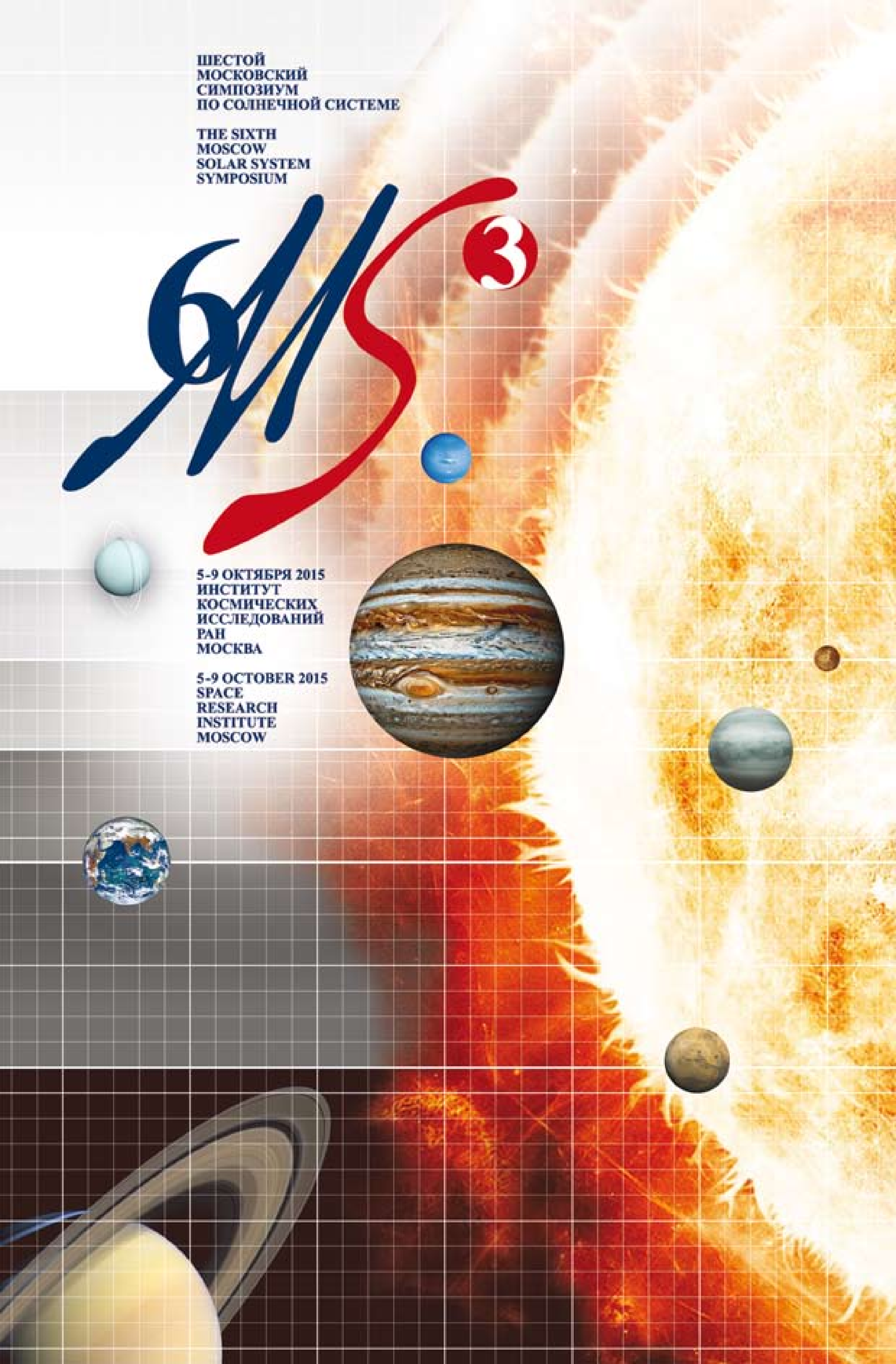

5-9 ОКТЯБРЯ 2015
ИНСТИТУТ
КОСМИЧЕСКИХ
ИССЛЕДОВАНИЙ
РАН
МОСКВА

5-9 OCTOBER 2015
SPACE
RESEARCH
INSTITUTE
MOSCOW

6M-S³ SCIENTIFIC PROGRAM

	5 october 2015		
	session 1: MOON **convener: Igor MITROFANOV**		**10.00-19.00**
6MS3-MN-01	**James HEAD and L.WILSON**	Generation, Ascent and Eruption of Magma on the Moon: New Insights Into Source Depths, Magma Supply, Intrusions and Effusive/Explosive Eruptions	10.00-10.20
6MS3-MN-02	**Mikhail KRESLAVSKY et al**	Morphometric peculiarities of small impact craters in the lunar polar areas	10.20-10.40
6MS3-MN-03	**Gennady KOCHEMASOV**	Coupling principal tectonic features of some planets and their satellites: Earth-Moon, Mars-Phobos, Pluto-Charon	10.40-11.00
6MS3-MN-04	**Natalia KOZLOVA et al**	Revision of estimates of absolute age of small lunar craters (quantitative analysis of crater morphology for determination of their degree of degradation)	11.00-11.20
6MS3-MN-05	**Dmitri SKULACHEV**	Grain-to-Grain Contacts and Lunar Regolith Thermal Conductivity	11.20-11.40
	coffee-break		**11.40-12.00**
6MS3-MN-06	**Ekaterina KRONROD et al**	Temperature distribution and uranium content in the lunar crust and in the lunar mantle	12.00-12.20
6MS3-MN-07	**Svetlana PUGACHEVA and Vladislav SHEVCHENKO**	Morphology of the Moon areas with anomalously high content of thorium	12.20-12.40
6MS3-MN-08	**Alexander BASILEVSKY et al**	Geologic characteristics of the Lunokhod 1 and Yutu rover landing sites, NW Mare Imbrium of the Moon	12.40-13.00
	lunch		**13.00-14.00**
6MS3-MN-09	**Carle PIETERS and James HEAD**	M3's Top-Ten Target Issues [in the next phase of exploration]	14.00-14.20
6MS3-MN-10	**Anton SANIN on behalf of LEND team**	Water maps of the polar Moon: LEND data after 6 years on the lunar orbit	14.20-14.40
6MS3-MN-11	**James FASTOOK and James HEAD**	Cold-based Glaciation on Mercury: Accumulation and Flow of Ice in Permanently Shadowed Circum-Polar Crater Interiors	14.40-15.00
6MS3-MN-12	**Ariel DEUTSCH et al**	Mapping areas of shadow in Mercury's north polar region to constrain the extent of stable thermal environments for ice deposits	15.00-15.20
6MS3-MN-13	**Maxim LITVAK**	Volatiles in Lunar Polar Regolith	15.20-15.40
6MS3-MN-14	**Ross POTTER and James HEAD**	Basin formation on Mercury and the Moon - the same or different? Insights from numerical modeling	15.40-16.00
	coffee-break		**16.00-16.20**
6MS3-MN-15	**Vladislav TRETYAKOV**	Lunar robotic missions, as precursors for manned lunar flights	16.20-16.40

6MS3-MN-16	**Simone DELL'AGNELLO et al**	New Generation Laser Retroreflectors for the Moon, Mars, Phobos and Deimos	16.40-17.00
6MS3-MN-17	**Alexander GUSEV et al**	Dynamics of the inner solid and outer liquid cores of the Moon for ChangE-4/5, Luna-25/26, ILOM projects	17.00-17.20
6MS3-MN-18	**Lukas HOFER et al**	Development of the gas chromatograph – mass spectrometer to investigate volatile species in the lunar soil for the Luna-Resurs mission	17.20-17.40
6MS3-MN-19	**Alexey BEREZHNOY et al**	Properties of crater Boguslawski in application to planned Lunar Infrared Spectrometer (LIS) measurements	17.40-18.00
6MS3-MN-20	**Vladimir GROMOV and Alexander KOSOV**	The Objectives of the Radioscience Experiment in Luna-Resource and Luna-Glob Space Projects	18.00-18.20
6MS3-MN-21	**Berengere HOUDOU on behalf of Roscosmos/ ESA cooperation**	Perspectives and plans of ESA/Roscosmos cooperation on robotic lunar missions	18.20-18.40
6MS3-MN-22	**Igor MITROFANOV**	Moon is our seventh continent: will it ever be inhabited?	18.40-19.00
	POSTER SESSION (all sessions)		**19.00-20.00**

	6 october 2015		
	session 2: GIANT PLANETS AND THEIR MOONS **convener: Mikhail IVANOV**		**10.00-11.40**
6MS3-GP-01	**Anna DUNAEVA et al**	Physical and thermal constraints on the models of partially differentiated Titan	10.00-10.20
6MS3-GP-02	**Mikhail PODZOLKO et al**	Radiation hazard for different scenarios of space missions to Jupiter's moons	10.20-10.40
6MS3-GP-03	**Alex EKONOMOV et al**	Scientific ballooning on Jupiter and other outer planets	10.40-11.00
6MS3-GP-04	**Sergey BULAT et al**	Life in the subglacial Antarctic Lake Vostok: First Results with Borehole-Frozen Lake Water	11.00-11.20
6MS3-GP-05	**Vera DOROFEEVA**	Studies of comets and problems of cosmochemistry	11.20-11.40
	coffee-break		**11.40-12.00**
	session 3. SOLAR SYSTEM SMALL BODIES **convener: Mikhail IVANOV**		**12.00-17.40**
6MS3-SB-01	**Alexander BAZILEVSKIY et al**	NavCam observations of the nucleus of comet 67P/Churyumov-Gerasimenko	12.00-12.20
6MS3-SB-02	**Oleksandr POTASHKO and E. SHNYUKOV.**	Geology irregularities of the comet 67P	12.20-12.40
6MS3-SB-03	**Leonid KSANFOMALITY et al**	On comparison of the nuclei of comets 67P/CG and 1P/Halley	12.40-13.00
	lunch		**13.00-14.00**
6MS3-SB-04	**Yuri SKOROV et al**	Cometary dust within the near-nucleus environment. Application to 67P/Churyumov-Gerasimenko	14.00-14.20
6MS3-SB-05	**Peter WURZ et al**	Volatiles in the Coma of comet Churyumov-Gerasimenko	14.20-14.40
6MS3-SB-06	**Vladimir BUSAREV et al**	Spectral signs of cometary activity on primitive asteroids (145) Adeona, (704) Interamnia, (779) Nina, and (1474) Beira	14.40-15.00
6MS3-SB-07	**Evgenij ZUBKO et al**	Characteristics of dust in Comet C/1995 O1 (Hale-Bopp) inferred with polarimetry	15.00-15.20
6MS3-SB-08	**Vacheslav EMEL'YANENKO**	Asteroids near the Sun	15.20-15.40
6MS3-SB-09	**Vladislav SIDORENKO et al**	Rotational Dynamics of Cometary Nuclei and Related Physics	15.40-16.00
	coffee-break		**16.00-16.20**
6MS3-SB-10	**Sergei IPATOV**	Origin of orbits of secondaries in discovered trans-Neptunian binaries	16.20-16.40
6MS3-SB-11	**Anton ERMAKOV et al**	Constraints on Ceres' internal structure from the Dawn shape and gravity data	16.40-17.00
6MS3-SB-12	**Sergey VOROPAEV**	Ceres Structure and some Tips for the Study of gravitational Potential by the Dawn Mission	17.00-17.20
6MS3-SB-13	**Gennady KOCHEMASOV**	Principles of the wave planetology manifesting in the Pluto-Charon system, Ceres, and the Moon	17.20-17.40

	7 october 2015		
	session 4: DUST AND DUSTY PLASMA IN SPACE **convener: Alexander ZAKHAROV**		**10.00-13.00**
6MS3-DP-01	**Andrey RUSOL and Mikhail MAROV**	Gas-Dust Protoplanetary Disc: Modeling Primordial Dusty Clusters Evolution	10.00-10.25
6MS3-DP-02	**Vladislav IZMODENOV et al**	Modeling of the insterstellar dust in the interplanetary medium	10.25-10.50
6MS3-DP-03	**Tamas GOMBOSI et al**	Negatively Charged Nano-grains at 67P/ Churyumov-Gerasimenko	10.50-11.15
6MS3-DP-04	**Alexey BEREZHNOY and J. BOROVIČKA**	Molecular bands in the spectra of the Benešov bolide	11.15-11.40
	coffee-break		11.40-12.00
6MS3-DP-05	**Yangxiaoyi LU and Vladislav SHEVCHENKO**	Study lunar soil and dust with Chang'E-3 mission data	12.00-12.20
6MS3-DP-06	**Sergey POPEL, Barbara ATAMANIUK, Lev ZELENYI**	Electric fields and dust particle rise near the lunar terminator	12.20-12.40
6MS3-DP-07	**Sergey POPEL et al**	Meteoroid impacts and dust particle release from the lunar surface	12.40-13.00
	lunch		13.00-14.00
	session 5: VENUS **convener: Ludmila ZASOVA**		14:00-18:00
6MS3- VN -01	**Håkan SVEDHEM**	Eight and a half years at Venus - The successes of Venus Express /***invited talk***/	14.00-14.20
6MS3- VN -02	**Vladimir KRASNOPOLSKY**	Modeling of Chemical Composition in the Venus Lower and Middle Atmospheres /***invited talk***/	14.20-14.40
6MS3- VN -03	**Denis BELYAEV et al**	Chemistry of Venus' mesosphere as measured by SPICAV/SOIR on-board Venus Express	14.40-15.00
6MS3- VN -04	**Ludmila ZASOVA et al**	Influence of the surface topography in Venus atmosphere	15.00-15.20
6MS3- VN -05	**Sanjay S. LIMAYE**	Some Questions About Venus Atmosphere	15.20-15.40
6MS3- VN -06	**Nikolay IGNATIEV et al**	Upper cloud haze on the night side of Venus	15.40-16.00
	coffee-break		**16.00-16.20**
6MS3- VN -07	**Alexander BASILEVSKY et al**	Past and present volcanism of Venus /***invited talk***/	16.20-16.40
6MS3- VN -08	**Mikhail IVANOV and James HEAD**	Venus: Main regimes of resurfacing	16.40-17.00
6MS3- VN -09	**Evgeniya GUSEVA**	The rift zones of Venus: rift valleys and belts of graben	17.00-17.20
6MS3- VN -10	**Michael BONDARENKO and Anatoly GAVRIK**	On Non-Meteoric Origin of Layers below V1 in Venusian Ionosphere	17.20-17.40
DISCUSSION			**17.40-18.00**
	POSTER SESSION (all sessions)		**18.00-19.00**

	8 october 2015		
	session 6: MARS **convener: Oleg KORABLEV**		**10.00-18.00**
	session 6.1: MARS SURFACE AND GEOLOGY **conveners: James HEAD, Oleg KORABLEV**		**10.00-11.30**
6MS3-MS-01	**Thomas DUXBURY et al**	Resurrecting the Mariner 1969 images of Mars using the MOLA global digital terrain model and modern computer techniques	10.00-10.15
6MS3-MS-02	**James HEAD**	Lyot Crater, Mars: Major Amazonian-Age Impact and the Nature of Ejecta Emplacement, Ejecta Deposit Characteristics and Modification	10.15-10.30
6MS3-MS-03	**Violaine SAUTTER et al**	Mafic and felsic igneous rocks at Gale crater: a ChemCam study	10.30-10.45
6MS3-MS-04	**Maxim LITVAK on behalf of DAN science team**	DAN continues active neutron sensing on Mars: recent results from Curiosity	10.45-11.00
6MS3-MS-05	**Ashley HORAN and James HEAD**	Impact Cratering as a Cause for Rainfall Producing Valley Networks on Mars: Predictions and Tests of the Hypothesis	11.00-11.15
6MS3-MS-06	**Dmitry GOLOVIN on behalf of DAN science team**	Unusual spot on the crater Gale: DAN requests Curiosity to make U-turn	11.15-11.30
	session 6.2: TERRESTRIAL ANALOGS **conveners: James HEAD, Jessica FLAHAUT**		**11.30-12.45**
6MS3-MS-07	**Alexander KOZYREV on behalf of DAN team**	Field tests for Mars exploration in the Yakutia	11.30-11.45
	coffee-break		**11.45-12.00**
6MS3-MS-08	**Marina DIAZ MICHELENA and R. KILIAN**	Magnetic on ground surveys on the orogenic crust of the Patagonian Andes. Implication for planetary exploration	12.00-12.15
6MS3-MS-09	**Nikita DEMIDOV and V.V. LUKIN**	Lessons learned in Antarctica for international exploration of Moon and Mars	12.15-12.30
6MS3-MS-10	**Jessica FLAHAUT et al**	Combined VNIR and Raman spectroscopy of Mars analogue sediments from the Atacama salt flats	12.30-12.45
	session 6.3: EARLY CLIMATE AND ESCAPE **convener: Eduard DUBININ**		**12.45-15.15**
6MS3-MS-11	**James DICKSON et al**	Formation of Gullies on Mars by Water at High Obliquity: Quantitative Integration of Global Climate Models and Gully Distribution	12.45-13.00
	lunch		**13.00-14.00**
6MS3-MS-12	**Ashley HORAN and James HEAD**	The Faint Young Sun Paradox: What It Means for Earth and Mars	14.00-14.15
6MS3-MS-13	**Vladimir KRASNOPOLSKY**	Variations of the HDO/ H2O Ratio in the Martian Atmosphere and Loss of Water from Mars	14.15-14.30
6MS3-MS-14	**Anna FEDOROVA et al**	Water vapor in the middle atmosphere of Mars during the global dust storm in 2007	14.30-14.45

6MS3-MS-15	**Valery SHEMATOVICH**	Neutral escape induced by the precipitation of high-energy protons and hydrogen atoms of the solar wind origin into the Martian atmosphere	14.45-15.00
6MS3-MS-16	**Oleg VAISBERG**	Mars atmospheric losses induced by the solar wind: comparison of observations with models	15.00-15.15
	session 6.4: MISSIONS AND RESULTS		**15.15-18.00**
	conveners: Dmitrij TITOV, Hakan SVEDHEM		
6MS3-MS-17	**Dmitrij TITOV et al**	Recent science highlights of the Mars Express mission	15.15-15.35
6MS3-MS-18	**Eduard DUBININ and M. FRAENZ**	Ionosphere of Mars as seen by Mars Express	15.35-15.50
6MS3-MS-19	**Brigitte GONDET and Jean-Pierre BIBRING**	Mesopheric CO2 clouds at Mars: 7 Martian years survey by OMEGA/MEX	15.50-16.05
	coffee-break		**16.05-16.30**
6MS3-MS-20	**Alexey PANKINE**	Variability of water vapor in the Martian atmosphere in MY26-30 from PFS/LW observations	16.30-16.45
6MS3-MS-21	**Svetlana GUSLYAKOVA et al**	Long-term nadir observations of the O2 dayglow by SPICAM IR	16.45-17.00
6MS3-MS-22	**Hakan SVEDHEM et al**	ExoMars Mission	17.00-17.30
6MS3-MS-23	**Pascal ROSENBLATT and J.C. MARTY**	Using radio-navigation data of ESA's Trace Gas Orbiter (TGO) to improve the Mars' gravity seasonal variations	17.30-17.45
DISCUSSION			**17.45-18.00**

	9 october 2015		
	session 7: NEW PROJECTS AND EXPERIMENTS **convener: Oleg KORABLEV**		**10.00-15.30**
	session 7.1: LABORATORY INVESTIGATIONS AND ASTROBIOLOGY **convener: Mikhail GERASIMOV**		
6MS3-NP-1	**Christof JANSSEN et al**	Spectroscopic and Mass Spectrometric Studies on Ozone - Implications for Ozone Formation and the Origin of the Oxygen Isotopic Heterogeneity in the Solar System	10.00-10.15
6MS3-NP-2	**Dmitry SKLADNEV et al**	Nanobiotechnology for detection of extraterrestrial life	10.15-10.30
6MS3-NP-3	**Vladimir SOROKIN et al**	Phages as markers for extraterrestrial life	10.30-10.45
6MS3-NP-4	**Georgi MANAGADZE et al**	Space Factors Providing the Conditions for Abiotic Origin of the Living Matter	10.45-11.00
6MS3-NP-5	**Konstantin LUCHNIKOV et al**	A Novel Technique and Mass-Spectrometric Instrument for Extraterrestrial Microbial Life Detection via Analyses of the Elemental Composition of Martian Regolith and Permafrost/Ice Samples	11.00-11.15
6MS3-NP-6	**Georgi MANAGADZE**	Aerobiology research on Mars and the possibility of its implementation	11.15-11.30
6MS3-NP-7	**Rongqiao HE et al**	Martian magnetic field: deserve to be concerned before heading to Mars	11.30-11.45
	coffee-break		**11.45-12.00**
	session 7.2: MISSIONS AND INSTRUMENTS **convener: Hakan SVEDHEM**		
6MS3-NP-8	**Yafeng GUAN et al**	Gas Chromatograph for On-site Analysis of Organics on Mars	12.00-12.20
6MS3-NP-9	**Andrey FEDOROV**	Scientific Goals and Instruments design of the Solar Orbiter Plasma Package	12.20-12.40
6MS3-NP-10	**Daniel RODIONOV, Jorge VAGO et al**	ExoMars 2018 Surface platform science investigations	12.40-13.00
	lunch		**13.00-14.00**
6MS3- NP-11	**Marina Diaz MICHELENA**	MAG-TRACE Instrument for Exomars’18 for extended capabilities in the planetary magnetic exploration	14.00-14.15
6MS3- NP-12	**Francesca ESPOSITO et al**	MICROMED: a compact dust detector for Martian airborne dust investigation	14.15-14.30
6MS3- NP-13	**Greg KOYNASH et al**	The Wind Sensor of MeteoStation for ExoMars project	14.30-14.45
6MS3- NP-14	**Imant VINOGRADOV et al**	Adaptation of tunable diode laser absorption spectroscopy for in situ planetary studies. Application for planned missions to Moon, Mars and Venus	14.45-15.00

6MS3- NP-15	**Alexei SHAPKIN et al**	Development of a mast or robotic arm-mounted infrared AOTF spectrometer for surface Moon and Mars probes	15.00-15.15
6MS3- NP-16	**Andrey GAROV et al**	Planetary data archive: new approach to data access, exploration and collaborative research	15.15-15.30

POSTER SESSION

5 october 19.00-20.00
7 october 18.00-19.00

	MOON	
6MS3-PS-01	**Anton SANIN et al**	Short list of landing sites at Lunar poles
6MS3-PS-02	**Dmitry GOLOVIN**	Testing facility for nuclear planetology in Dubna
6MS3-PS-03	**Erica JAWIN et al**	Examining Spectral Variations in Lunar Localized Dark Mantle Deposits
6MS3-PS-04	**Le QIAO et al**	Young Lunar Mare Basalts: Definition and Analysis of their Characteristics, Distribution, Mode of Emplacement and Origin
6MS3-PS-05	**Lauren JOZWIAK et al**	The Effect of Evolving Gas Distribution on Shallow Lunar Magmatic Intrusion Density: Implications for Gravity Anomalies
6MS3-PS-06	**Mikhail IVANOV and James HEAD**	Contribution of lunar basins to materials in the Luna-Glob perspective landing sites
6MS3-PS-07	**Natalia BULATOVA**	Three-dimensional spatio-temporal technology
6MS3-PS-08	**Alexander SHIRENIN**	The concept is considered in relation to the establishment of high-precision selenodetic coordinate system during the mission “Luna-Glob, Luna-Resource”
6MS3-PS-09	**Alexandre SKALSKY et al**	The wave phenomena resulted from the solar wind-Moon interaction
6MS3-PS-10	**Natalia KOZLOVA et al**	PRoViDE: Planetary Robotics Vision Data Exploitation based on lunar archive panoramic image processing
6MS3-PS-11	**Mikhail SINITSYN**	The distribution of epithermal neutron flux in impact basins over the equatorial lunar surface
6MS3-PS-12	**Albert ABDRAKHIMOV et al**	Crater Boguslawsky: Slope hazard estimation by shadow area measurement
6MS3-PS-13	**Alexey BEREZHNOY et al**	Search for impact-produced optical flashes at the Moon along the terminator
6MS3-PS-14	**Jianguo YAN et al**	Lunar mascons high resolution density structure investigation using GRAIL gravity data
6MS3-PS-15	**Alexander KOSOV et al**	New Features of Radio Science Experiments in Russian “Luna-Glob” and “Luna-Resource” Programs
6MS3-PS-16	**Sergey PAVLOV et al**	Evaluation of miniaturized broad-band UV-VIS-NIR spectrometers for implementation in a laser-induced plasma spectrometer for planetary research
6MS3-PS-17	**Maike Brigitte NEULAND et al**	A miniature laser ablation mass spectrometer for quantitative in situ chemical composition measurements of rocks and soil on a planetary surface
6MS3-PS-18	**Oleg KHAVROSHKIN et al**	Lunar seismic noise: new astrophysics periodicity & neutrinos
6MS3-PS-19	**Michael SHPEKIN et al**	Some objectives of the study and exploration of the Moon
6MS3-PS-20	**Jinsong PING et al**	Two-Way Lunar Radio Ranging and Preliminary Result from CE-3 Mission

	GIANT PLANETS AND THEIR MOONS	
6MS3-PS-21	**Gennady KOCHEMASOV**	Hexagonal figures in Saturnian system and on Ceres
6MS3-PS-22	**Victor TEJFEL et al**	The evidences of latitudinal asymmetry of the ammonia absorption on Saturn
6MS3-PS-23	**Petr LYSENKO et al**	The study of methane-ammonia absorption on Jupiter in the visibility season of 2015
6MS3-PS-24	**Victor KRONROD and Andrei MAKALKIN**	Capture of material by the circumplanetary disks of Jupiter and Saturn due to interaction of the falling planetesimals with the gaseous medium of the disks
6MS3-PS-25	**Elena BELENKAYA**	Dynamo action beyond the magnetospheres of quickly spinning planets and heliopause
6MS3-PS-26	**Andrei MAKALKIN et al**	Formation of planetesimals: effect of particle layer interaction with surrounding gas in the protoplanetary disk and fractional particle sublimation on the water–ice evaporation front
	SOLAR SYSTEM SMALL BODIES	
6MS3-PS-27	**Maxim ZAITSEV et al**	Characterization of the complex organic compounds synthesized by laser vaporization of silicates in nitrogen-methane atmosphere: Application for the impact-induced prebiotic synthesis
6MS3-PS-28	**Fabrice CIPRIANI et al**	Definition of Environment specifications for the Asteroid Impact Mission (AIM)
	DUST AND DUSTY PLASMA IN SPACE	
6MS3-PS-29	**Sergey POPEL and A. Yu. DUBINSKII**	On formation of water molecules incorporated in near-surface lunar regolith
6MS3-PS-30	**Vladimir CHEPTSOV et al**	Long-Term Impact of Low Pressure on Bacterial Biodiversity and Activity in Soil and Sediments
6MS3-PS-31	**Evgeny LISIN and I.A. KUZNETSOV**	On the possibility of photoinduced levitation of dust particles under ground-based laboratory conditions
	VENUS	
6MS3-PS-32	**Mikhail LUGININ et al**	Retrieval of aerosol properties in the upper haze of Venus using SPICAV-IR data
6MS3-PS-33	**Anna FEDOROVA et al**	Cloud top and water vapor variations in the Venus' mesosphere from the SPICAV observations
6MS3-PS-34	**Daria EVDOKIMOVA et al**	Variations of SO2 content at the night side of Venus' mesosphere
6MS3-PS-35	**Marina PATSAEVA et al**	Dependence of longitudinal distribution of zonal wind and UV albedo at cloud top level on Venus topography from VMC camera onboard Venus Express
6MS3-PS-36	**Leonid KSANFOMALITY et al**	Possible signs of fauna and flora on Venus
6MS3-PS-37	**Anatoly GAVRIK et al**	Multi-frequency phase-coherent systems: new instrument for occultation in the project Venus-D
6MS3-PS-38	**Azariy BARENBAUM**	Formation of analogous geological structures on terrestrial planets by Galaxy's comets (I): the galactic comets and their mechanism interaction with planets
6MS3-PS-39	**Azariy BARENBAUM**	Formation of analogous geological structures on terrestrial planets by Galaxy's comets (II): factual data and their discussion

	MARS	
6MS3-PS-40	**James DICKSON et al**	Conditions and strategies for detecting ephemeral brine activity at the Mars Science Laboratory landing site, Gale Crater, Mars
6MS3-PS-41	**James DICKSON et al**	Concentrating Ice in Polar Deserts: Lessons for Mars from Punctuated Gully In-cision in the McMurdo Dry Valleys
6MS3-PS-42	**James CASSANELLI and James HEAD**	Ice Sheet Lava-loading on Late Noachian Mars: Implications for Meltwater Generation, Groundwater Recharge, and Geomorphology
6MS3-PS-43	**David K. WEISS and James W. HEAD**	Degradation State of Noachian Highland Craters: Assessing the Role of Crater-Related Ice Substrate Melting in a Cold and Icy Mars
6MS3-PS-44	**Kenneth RAMSLEY and James HEAD**	The secondary impact ejecta spike of Phobos from Stickney Crater
6MS3-PS-45	**Sergey KRASILNIKOV**	Morphometric characteristics of polygonal structure of Mars depending on surface morphology
6MS3-PS-46	**Elodie GLOESENER et al**	Modeling water vapor transport in the Martian subsurface
6MS3-PS-47	**Ruslan KUZMIN et al**	Study of the seasonal variations of the water equivalent of hydrogen amount in the subsurface regolith on Mars based on the HEND data accumulated during the five Martian years
6MS3-PS-48	**Vladimir ZHARKOV et al**	Anomalous density waves method for estimating the stresses in the crust and mantle of Mars
6MS3-PS-49	**Tamara GUDKOVA and Vladimir ZHARKOV**	Martian interior structure models: tradeoff between the density of the crust and Fe content in the mantle
	NEW PROJECTS AND EXPERIMENTS	
6MS3-PS-50	**Irek KHAMITOV et al**	Investigations of the Solar System Objects at RTT150.
6MS3-PS-51	**Alexandre SKALSKY et al**	The electromagnetic phenomena at Mars and their survey at landing platform
6MS3-PS-52	**Anastasia ZHARKOVA et al**	New cartography of Mercury: maps and globe
6MS3-PS-53	**Yuri OZOROVICH et al**	Yupiter's Moon Europa: Planetary Geoelectrical Markers and Oreols of the Liquid Ocean under the Ice on the Surface of the Yupiter's Moon Europe
6MS3-PS-54	**Oleg KHAVROSHKIN et al**	Periodicity of radioactivity source: channels of registration & physical mechanism
6MS3-PS-55	**Ilia KUZNETSOV et al**	Dust Complex onboard the ExoMars-2018 lander for investigations of Martian dust dynamic

GENERATION, ASCENT AND ERUPTION OF MAGMA ON THE MOON: NEW INSIGHTS INTO SOURCE DEPTHS, MAGMA SUPPLY, INTRUSIONS AND EFFUSIVE/EXPLOSIVE ERUPTIONS

L. Wilson[1,2], J.W. Head[2]
[1]Lancaster Environment Centre, Lancaster University, Lancaster LA1 4YQ, UK; [2]Department of Earth, Environmental and Planetary Sciences, Brown University, Providence, RI 02912 USA.
james_head@brown.edu

Introduction:

We model the ascent and eruption of lunar mare basalt magmas with new data on crustal thickness and density (GRAIL), magma properties, and surface topography, morphology and structure (Lunar Reconnaissance Orbiter).

Analysis:

GRAIL recently measured the broad spatial variation of the bulk density structure of the crust of the Moon. Comparing this with the densities of lunar basaltic and picritic magmas shows that essentially all lunar magmas were negatively buoyant everywhere within the lunar crust. Thus positive excess pressures must have been present in melts at or below the crust-mantle interface to enable them to erupt (Figure 1). The source of such excess pressures is clear: melt in any region experiencing partial melting or containing accumulated melt, behaves as though an excess pressure is present at the top of the melt column if the melt is positively buoyant relative to the host rocks and forms a continuously interconnected network. The latter means that, in partial melt regions, probably at least a few percent melting must have taken place. Petrologic evidence suggests that both mare basalts and picritic glasses may have been derived from polybaric melting of source rocks in regions extending vertically for at least a few tens of km. This is not surprising: the vertical extent of a region containing inter-connected partial melt produced by pressure-release melting is approximately inversely proportional to the acceleration due to gravity. Translating the ~25 km vertical extent of melting in a rising mantle diapir on Earth to the Moon then implies that melting could have taken place over a vertical extent of up to 150 km (Figure 1). If convection were absent, melting could have occurred throughout any region in which heat from radioisotope decay was accumulating; in the extreme this could have been most of the mantle.

The maximum excess pressure that can be reached in a magma body depends on its environment. If melt percolates upward from a partial melt zone and accumulates as a magma reservoir (Figure 1), either at the density trap at the base of the crust or at the rheological trap at the base of the elastic lithosphere, the excess pressure at the top of the magma body will exert an elastic stress on the overlying rocks. This will eventually cause them to fail in tension when the excess pressure has risen to close to twice the tensile strength of the host rocks, perhaps up to ~10 MPa, allowing a dike to propagate upward from this point (Figure 1). If partial melting occurs in a large region deep in the mantle, however, connections between melt pockets and veins may not occur until a finite amount, probably a few percent, of melting has occurred. When interconnection does occur, the excess pressure at the top of the partial melt zone will rise abruptly to a high value, again initiating a brittle fracture, i.e. a dike. That sudden excess pressure is proportional to the vertical extent of the melt zone, the difference in density between the host rocks and the melt, and the acceleration due to gravity, and could readily be ~100 MPa, vastly greater than the value needed to initiate a dike. We therefore explore excess pressures in the range ~10 to ~100 MPa.

If eruptions take place through dikes extending upward from the base of the crust, the mantle magma pressure at the point where the dike is initiated must exceed the pressure due to the weight of the magmatic liquid column (Figure 1). This means that on the nearside the excess pressure must be at least ~19 ± 9 MPa and on the farside must be ~29 ± 15 MPa. If the top of the magma body feeding an erupting dike is a little way below the base of the crust, slightly smaller excess pressures are needed because the magma is positively buoyant in the part of the dike within the upper mantle.

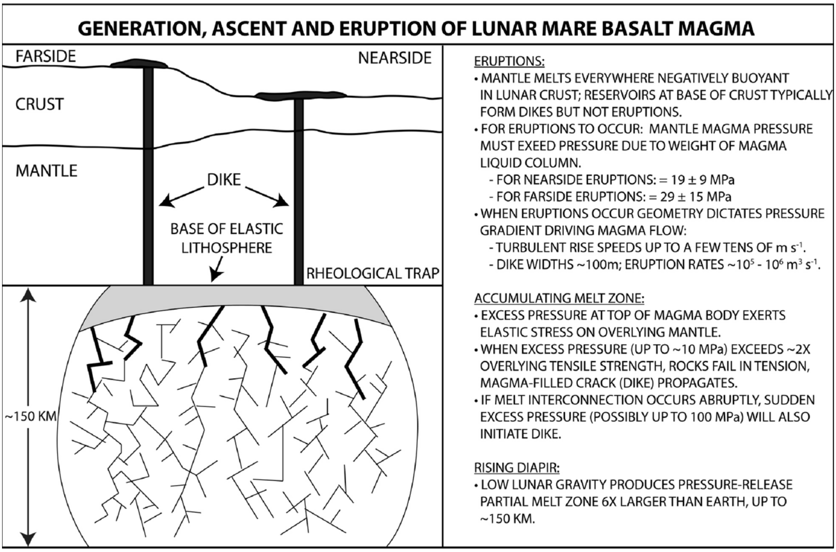

Fig. 1. Generation, ascent and eruption of lunar mare basalt magma.

Even the smallest of these excess pressures is greater than the ~10 MPa likely maximum value in a magma reservoir at the base of the crust or elastic lithosphere, but the values are easily met by the excess pressures in extensive partial melt zones deeper within the mantle. Thus magma accumulations at the base of the crust would have been able to intrude dikes part-way through the crust, but not able to feed eruptions to the surface; in order to be erupted, magma must have been extracted from deeper mantle sources, consistent with petrologic evidence.

Buoyant dikes growing upward from deep mantle sources of partial melt can disconnect from their source regions and travel though the mantle as isolated bodies of melt that encounter and penetrate the crust-mantle density boundary. They adjust their lengths and internal pressure excesses so that the stress intensity at the lower tip is zero. The potential total vertical extent of the resulting melt body depends on the vertical extent of the source region from which it grew. For small source extents, the upper tip of the resulting dike crossing the crust-mantle boundary cannot reach the surface anywhere on the Moon and therefore can only form a dike intrusion; for larger source extents, the dike can reach the surface and erupt on the nearside but still cannot reach the surface on the farside; for even larger source extents, eruptions could occur on both the nearside and the farside. The paucity of farside eruptions therefore implies a restricted range of vertical extents of partial melt source region sizes, between ~16 to ~36 km. When eruptions can occur, the available pressure in excess of what is needed to support a static magma column to the surface gives the pressure gradient driving magma flow. The resulting typical turbulent magma rise speeds are ~10 to a few tens of m s^{-1}, dike widths are of order 100 m, and eruption rates from 1-10 km long fissure vents are of order 10^5 to 10^6 m^3 s^{-1}.

Volume fluxes in lunar eruptions derived from lava flow thicknesses and surface slopes or rille lengths and depths are found to be of order 10^5 to 10^6 m^3 s^{-1} for volume-limited lava flows and $>10^4$ to 10^5 m^3 s^{-1} for sinuous rilles, with dikes widths of ~50 m. The lower end of the volume flux range for sinuous rilles corresponds to magma rise speeds approaching the limit set by the fact that excessive cooling would occur during flow up a 30 km long dike kept open by a very low excess pressure. These eruptions were thus probably fed by partial melt zones deep in the mantle. Longer eruption durations, rather than any subtle topographic slope effects, appear to be the key to the ability of these flows to erode sinuous rille channels.

Summary and Conclusions:

1) Essentially all lunar magmas were negatively buoyant everywhere within the crust.

2) Positive excess pressures of at least 20-30 MPa must have been present in mantle melts at or below the crust-mantle interface to drive magmas to the surface.

3) Such pressures are easily produced in zones of partial melting by pressure-release during mantle convection or simple heat accumulation from radio-isotopes.
4) Magma volume fluxes available from dikes forming at the tops of partial melt zones are consistent with the 10^5 to 10^6 m^3 s^{-1} volume fluxes implied by earlier analyses of surface flows.
5) Eruptions producing thermally-eroded sinuous rille channels involved somewhat smaller volume fluxes of magma where the supply rate may be limited by the rate of extraction of melt percolating through partial melt zones.

We compare these predictions with the observed geological record.

MORPHOMETRIC PECULIARITIES OF SMALL IMPACT CRATERS IN THE LUNAR POLAR AREAS

M.A. Kreslavsky[1,2], A.A. Kokhanov[1], I.P. Karachevtseva[1]
[1]Moscow State University of Geodesy and Cartography (MIIGAiK), Gorokhovskiy pereulok, 4, Moscow, 105064, Russia;
[2]University of California - Santa Cruz, 1156 High Street, Santa Cruz, CA, 95064, USA.
mkreslav@ucsc.edu

Introduction:

The polar areas of the Moon are of special interest for two major reasons. First, low temperatures, the presence of volatiles and other peculiarities open way for a set of unique and poorly studied processes that are of great scientific interest. Second, the polar areas are considered as prospective places for future landing and exploration, and their better understanding is of great practical interest.

Impact craters are widely used as probes into planetary processes. Here we report on morphometric measurements of populations of small (*D* = 100 m - 1 km) craters in the polar areas and compare them with typical non-polar highland regions. We describe peculiarities found and discuss their possible origin.

Source data:

Morphometric measurements require topographic data of adequate resolution and accuracy. There are two principally different sources of high-resolution topographic data: data from laser altimeters, in particular, LOLA onboard LRO [Smith et al., 2010], and digital terrain models (DTM) obtained through photogrammetric analysis of image pairs, in particular, LROC NAC images [Robinson et al., 2010]. On the poles, where the sun is always low, and the area of shadows is always huge, the photogrammetric DTMs cannot be of sufficient quality and are useless. On the other hand, because LRO orbit tracks cross each other near the pole, the density of LOLA ranging points here is high, and resolution of DTMs derived from LOLA data is high. At low latitudes, the gaps between LRO orbit tracks are wide, and LOLA-derived DTM have insufficient resolution. On the other hand, LROC NAC -derived DTM can be of high quality. Thus, we have to use different data sets for the polar areas (LOLA-derived DTM at 5 m per pixel sampling), and for the low-latitude comparison areas (LROC NAC DTM at 2 m per pixel sampling).

Sample sites:

We selected six sample sites, three in the polar regions: SP at the South pole, NP ant the North pole, and SA at ~88ºS 180ºE selected for its highest density of LOLA data points, and three outside the polar areas, L20 at Luna 20 landing site, 3.8ºN 56.6ºE, NC at 51.2°S 22.1°E, and F at 31.8°N 140.6°E. Since both poles are in highlands, we selected the latter three sites in typical highlands, in places with good LROC NAC DTM available. Areas of the sample sites range from 120 to 700 km^2.

Crater identification:

In each sample area we catalogued all craters in 100 m - 1 km diameter range by manual fitting circles in ArcGIS environment with CraterTools [Kneissl et al., 2011]. We used artificial image of shadowed topography generated from the same DEM as to be used for morphometric measurements to avoid misalignment and areas of bad DTM quality. The created catalogs contain crater center coordinates and diameters for ~3700 craters for all sites.

Morphometry:

Measurement of shape and depth of small craters in highlands is not straightforward due to complicated steep background topography; in many cases crater depth cannot be unambiguously defined. For massive morphometric measurements of simple bowl-shaped craters we developed special computer program that takes crater center and diameter *D* and estimates crater depth-to-diameter ratio (*d*/*D*), and a parameter α of crater shape. Parameter α is a power law exponent (between 1 and 6) providing the best fit for axially-simmetric profile of the inner half of the crater bowl. α = 1 means conical funnel-shaped crater, α = 2 means a parabolic bowl, and larger α mean more flat-floored profile. The majority of measured craters have α between 1 and 2 meaning somewhat conical bowl.

The measurement algorithm is the following. (1) Elevations within a ring with inner/outer diameters of 1.9D/2.2D are least-square-fitted by a plane, which is considered as a surrounding surface and all elevations are calculated with respect to it. (2) Position of the crater center is rectified by minimizing deflection from axial symmetry of the bowl. (3) d is calculated as average of the four DTM pixels closest to the rectified center. (4) α is estimated by least-square-fitting of the inner part of the bowl with a power-law profile. The program can work as a stand-alone code or be embedded as a tool into ArcGIS. With this program we successfully obtained d/D and α for ~ 2100 catalogued craters (measurements failed for the rest due to too complicated background topography).

Population analysis:

Small craters on highlands are in equilibrium: craters are obliterated by regolith gardening at the same rate as they are formed. This means that each population contains craters of all degradation stages and therefore for all d/D from the initial one to zero; the threshold of identification of heavily degraded craters depends on the nature of the data and is not objective, therefore statistical analysis of morphometric parameters is not straightforward. First, we excluded the most degraded craters and limited all statistical inferences by craters with $d/D > 0.05$. All such craters are reliably identifiable in our topographic data sets. We use the median of α as a measure of *a typical shape parameter*. The median is much more tolerant to outliers than the mean. We use the upper quartile Q of d/D in the population as a measure of *a typical depth-to-diameter ratio of relatively fresh craters*. We ensured that the particular choice of somewhat arbitrarily chosen threshold of $d/D = 0.05$ and percentile of 25% (quartile) for Q do not affect the results qualitatively.

Results:

The Figure shows the median α and Q for polar (stars) and non-polar (rhombs) sites. It is seen that the polar craters have somewhat higher median α, that is a little less conical shapes, however, this difference is very minor. All non-polar sites have essentially the same Q, which is consistent with identical degradation sequence of small craters. The polar crater populations have significantly lower Q. This means that <u>either the newly formed craters in the polar areas are shallower, or they initially degrade quicker</u> than their non-polar counterparts.

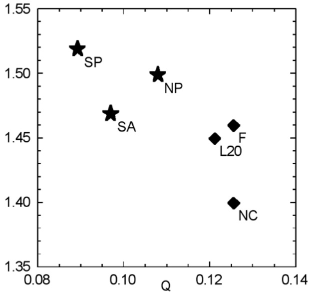

Fig. 1.

Bias analysis:

In principle, a coarser resolution of polar DTM may bias estimates of Q toward lower values, and estimates α toward higher values. Therefore our results should be taken with caution. We, however, think that the observed peculiarity of the polar crater populations is not a result of such biases, but a real phenomenon. First, there is no correlation between the density of LOLA measurements and inferred Q, which would be expected if the bias is significant. Second, for subpopulations of smaller and larger craters, the results are qualitatively the same, while for larger craters the bias is certainly absent.

Possible interpretations:

1) The regolith in the polar areas is enriched in H [e.g., Mitrofanov et al., 2010], which means the presence of volatiles (water ice or organics). Evaporation of volatiles by impact causes additional fluidization of the impact-mobilized material, the relaxation flow stops later, and the newly forming crater are shallower causing a lower Q. They also may have a flatter floor, causing a higher α, at least, initially.

2) Floors of fresh (high d/D) craters in the polar areas are usually permanently shadowed and therefore are effective volatile traps. If volatiles are sufficiently mobile, they accumulate in the traps. This causes disproportionally quick infill (decrease of d/D) of fresh deep craters, which results in a lower Q for the crater population. A somewhat similar (but much quicker) process of small crater infill with ice occurs in the polar areas of Mars [Banks et al. 2010].

3) Electrostatic charging of soil particles by solar UV radiation is known to cause dust levitation. This process can be even more active in the polar areas due to lower conductivity of the particles under lower temperatures. Permanently shadowed floors of fresh craters are traps for levitating particles (a particle landed there will never see the Sun and therefore will never fly out). Accumulation of soil particles again causes disproportionally quick

infill, which results in a lower Q.

Other explanations might involve unusual mechanical properties of materials under low temperatures.

Conclusions:

Small relatively fresh craters in the polar areas have a significantly lower depth-to-diameter ratio than their counterparts in typical non-polar highlands. We proposed several mechanisms that can explain this peculiarity, however, we do not know, which mechanism is actually responsible for it. A better understanding of surface processes on the Moon in general and in the polar areas in particular are needed to decipher this. Additional studies of small crater populations will also help.

Acknowledgements:

This work has been carried out in MIIGAiK under support of Russian Science Foundation, project 14-22-00197.

References:

Banks, M. E.et al. (2010) Crater population and resurfacing of the Martian north polar layered deposits, J. Geophys. Res. 115, E08006.
Kneissl T.et al.(2011) Map-projection-independent crater size-frequency determination in GIS environments - New software tool for ArcGIS, Planetary and Space Science, 59, 1243–1254.
Mitrofanov I. G. et al. (2010) Hydrogen Mapping of the Lunar South Pole Using the LRO Neutron Detector Experiment LEND. Science 330, 483-486.
Robinson, M. S. et al. (2010) Lunar Reconnaissance Orbiter Camera (LROC) Instrument Overview, Space Sci. Rev. 150, 81-124.
Smith, D. E. et al. (2010) The Lunar Orbiter Laser Altimeter Investigation on the Lunar Reconnaissance Orbiter Mission. Space Sci. Rev. 150, 209-241

COUPLING PRINCIPAL TECTONIC FEATURES OF SOME PLANETS AND THEIR SATELLITES: EARTH – MOON, MARS – PHOBOS, PLUTO – CHARON

G.G. Kochemasov;
IGEM of the Russian Academy of Sciences, 35 Staromonetny, 119017 Moscow
kochem.36@mail.ru

There are only three solid planet-satellite pairs in the Solar system: Earth – Moon, Mars – Phobos, Pluto – Charon. For the first two pairs tectonic analogies were shown and explained by moving them in one circumsolar orbit. As it is known from the wave planetology [3, 4, 6] - “orbits make structures”. For the third pair the same was stated as a prediction based on this fundamental rule. Global tectonic forms of wave origin appear in cosmic bodies because they move in keplerian orbits with periodically changing accelerations. Warping bodies waves have a stationary character and obeying wave harmonics lengths. Starting from the fundamental 2πR- long wave 1 making the ubiquitous tectonic dichotomy (two-face appearance) warping wave lengths descend along harmonics. Very prominent along with the wave 1 are waves 2 responsible for tectonic sectoring superimposed on the wave 1 segments. Practically all bodies have traces of shorter waves making numerous polygons (rings) often confused with impact craters.

Earth and the Moon moving in one circumsolar orbit both are distorted by wave 1, wave 2 and wave 4 features aligned along extent tectonic lines [1, 4, 5]. At Earth they are: Pacific Ocean (2πR-structure) and Indian Ocean (πR-structure) from both ends with Malay Archipelago (πR/4-structure) in the middle. At Moon they are: Procellarum Ocean (2πR) and SPA Basin (πR) from ends and Mare Orientale (πR/4) in the middle. A regular disposition is surprising. Both Oceans and Basin occur on opposite hemispheres, lying in the middle both ring structures occur in the boundary between two hemispheres and are of the same relative size. These triads stretch along lines parallel to the equator (Earth) and with the angle about 30 degrees to it (Moon) indicating at a different orientation of the rotation axes in the ancient time [2]. On the whole, one could speak about a “lunar mould” of Earth [5] (Fig. 1-3).

Another tectonic twin is the pair Mars – Phobos. Both bodies sharing one circumsolar orbit, twice as long as the Earth – Moon orbit, acquire slightly oblong ellipsoidal shape (Fig. 4, 5). Very pronounced on both so much different in size and composition bodies the deepest basins – Hellas and Stickney (sectoral πR-structures) are comparable features.

The structural unity is predicted also for the third solid body pair – Pluto – Charon (Fig. 6-10).

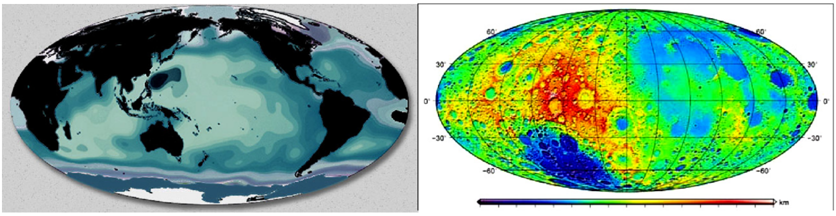

Fig. 1, 2. Earth’s oceans and lunar topography.

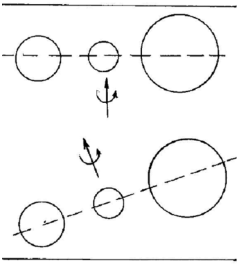

Fig. 3. Schematic sizes and relative dispositions of terrestrial (above) and lunar wave born tectonic features. Pacific Ocean and Procellarum Ocean at the right - 2πR structures. Indian Ocean and SPA Basin on the left– πR structures. Malay Archipelago and Mare Orientale at the center – πR/2 structures. Equators (axis of rotation) positions at present (Earth) and at ancient Moon.

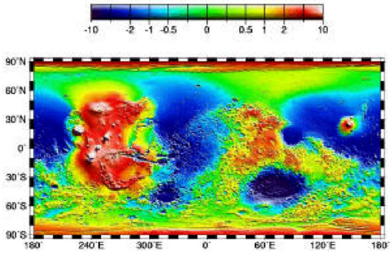

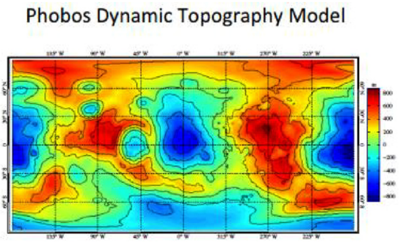

Fig. 4, 5. Mars (above) and Phobos topography [7].Global tectonic parallel.

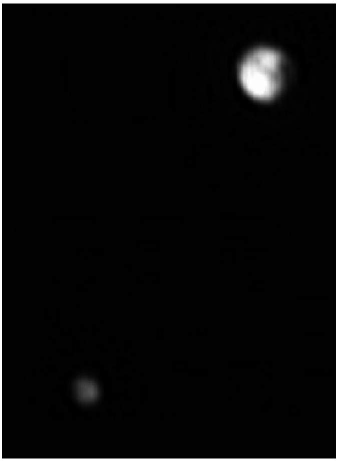

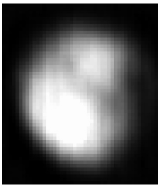

Fig. 7. Enlarged Pluto'view from Fig. 6. R= 1184 km

Fig.6. New Horizons' view of Pluto and Charon on June 6, 2015 from 46 million kms distance. 20150609_nh_pluto_charon_4x-20150606_registax. Credit NASA/JHUAPL/SwRI/Björn Jónsson

Fig. 8. Pluto and Charon. The first appearance of the predicted dichotomy of Charon (R=603.5 km). LORRI image on June 19, 2015 from about 20 million miles. North is up in this image.

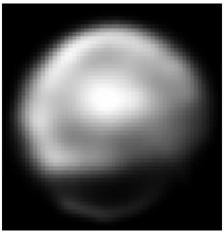

Fig. 9. Pluto, 13 June 2015.Dichotomy.

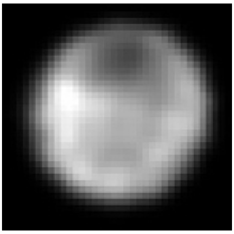

Fig.10. Charon, enlarged from Fig. 8. Dichotomy.

References:

[1] Andrews-Hanna, J.C., Besserer, J., Head III, J.W. et al. 2014b. Structure and evolution of the lunar Procellarum region as revealed by GRAIL gravity data. Nature, v. 514, #7529, 2014, 68-71, doi: 10.1038/nature 1369; **[2]** Garrick-Bethell, I., Perera, V., Nimmo, F., and Zuber, M.T. 2014. The tidal-rotational shape of the Moon and evidence for polar wander. Nature, v. 512, issue 7513, 14 Aug. 2014, 181-184; **[3]** Kochemasov G.G. Theorems of wave planetary tectonics. Geophys. Res. Abstr. 1999. V.1, №3, P.700; **[4]** Kochemasov G.G. Earth and Moon: similar structures – common origin // NCGT Journal, 2014, v. 2, # 2, 28-38; **[5]** Kochemasov G.G. A lunar "mould" of the Earth's tectonics: four terrestrial oceans and four lunar basins are derivative of one wave tectonic process // NCGT Journal, v. 3, # 1, March 2015, 29-33; **[6]** Kochemasov G.G. Ceres' two-face nature: expressive success of the wave planetology // NCGT Journal, v. 3, # 1, March 2015, 63-64; **[7]** Oberst, J., Shi, X., Elgner, S., Willner, K. 2014. Dynamic shape and down-slope directions on Phobos. The fifth Moscow Solar system symposium. Space Research Institute (IKI) -18 October 2014, Abstract 5MS3-MS-11.

Credit: NASA/Johns Hopkins University Applied Physics Laboratory/Southwest Research Institute

REVISION OF ESTIMATES OF ABSOLUTE AGE OF SMALL LUNAR CRATERS (QUANTITATIVE ANALYSIS OF CRATER MORPHOLOGY FOR DETERMINATION OF THEIR DEGREE OF DEGRADATION)

N. Kozlova[1], Yu. Rybakin[1], A. Kokhanov[1], Basilevsky A.[1,2], I. Karachevtseva[1]
[1]Moscow State University of Geodesy and Cartography, (MIIGAiK), MIIGAiK Extraterrestrial Laboratory (MExLab), Russia. natally.ko@gmail.com;
[2]Vernadsky Institute of Geochemistry and Analytical Chemistry, RAS, GEOKHI, Moscow 119991 Russia. atbas@geokhi.ru

Introduction:

We present the work on revision of earlier made estimates of absolute age of small lunar craters based on degree of their morphologic degradation and crater diameter (Basilevsky, 1974; Basilevsky, 1976). In that work was used qualitative presentation of craters' degradation degree in the form of morphologic classes of craters: from morphologically prominent and relatively deep and steep-sloped crater of class A to shallow and gentle-sloped craters of class C (Florensky and Taborko, 1972; Florensky et al., 1972). Morphologic analysis of Lunar Orbiter high-resolution images led to determination of age relations between craters of different morphologic prominence and different sizes and the resulted dependence was calibrated into absolute ages using the ages of cosmic exposure of rocks on the rims of nine craters in the Apollo landing sites.

Usage of results of that work was based on visual inspection of the craters as at that time there was no sufficient terrain models to measure crater morphometric parameters. Now we reinvestigate the same 9 plus study 6 new craters based on new LRO NAC data and modern GIS software in order to test the previous assessments.

Morphometric study of crater profiles:

We have made measurements of geometry of 15 mentioned above craters which absolute age was determined based on exposure ages of samples taken within their ejecta during Apollo 12, 14, 15, 16 missions. To obtain morphometric parameters of the selected craters we used crater profiles generated based on LRO NAC DEMs (http://lroc.sese.asu.edu/). To automatize the process of profile creation a special algorithm has been developed and implemented by means of ArcGIS 10.1.

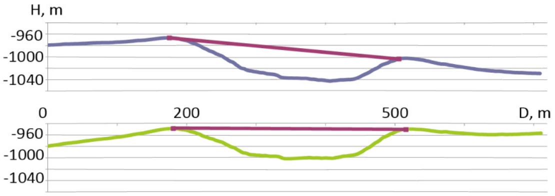

Fig. 1a. NS-profile for Cone crater (Apollo 14): upper image - original crater profile; lower image - profile corrected for the general tilt of the surrounding surface

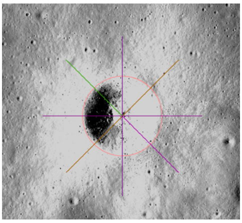

Fig. 1b. Cone crater (Apollo 14) on LRO NAC image and crater-profile lines

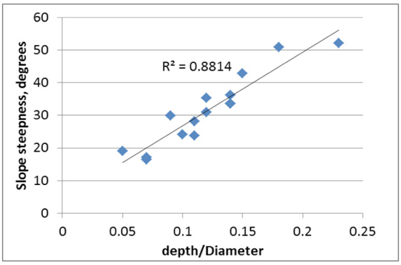

Fig. 2. Correlation of measured maximum steepness of inner slopes with depth/Diameter ratio for the selected 15 craters.

Some craters are located on the inclined terrain so their profiles look asymmetric (Fig. 1a – blue profile). In case of direct measurements such inclination of the surface strongly affects measurements of the crater depth and entirely comes into steepness of the slopes. To obtain accurate morphometric parameters we have corrected profiles for the general slope of the surrounding surface (Fig. 1a – green profile) and then measured crater depth, depth/diameter ratio, and maximum slope steepness (for both slopes). Some slopes are highly affected by new craters or slides so we excluded their steepness values from further processing. For each crater we made four profiles (NS, WE, NWSE, and SWNE, Fig. 1b) and taken into the work the average value for all parameters. Obtained values shows that the maximum steepness of inner slopes has strong correlation with depth/diameter ratio, and the coefficient of correlation for the selected craters is R^2=0.88 (Fig. 2)

Study of crater ages and degradation rate:

Figure 3 shows our preliminary results on correlation between the measured crater geometries, diameters and absolute ages. Size of the circlets is inversely proportional to maximum slope steepness measured in this study. The plot area is divided with functions which describe craters lifetime in each morphologic class (A+AB, B, BC, C) according to (Basilevsky, 1974; Basilevsky, 1976).

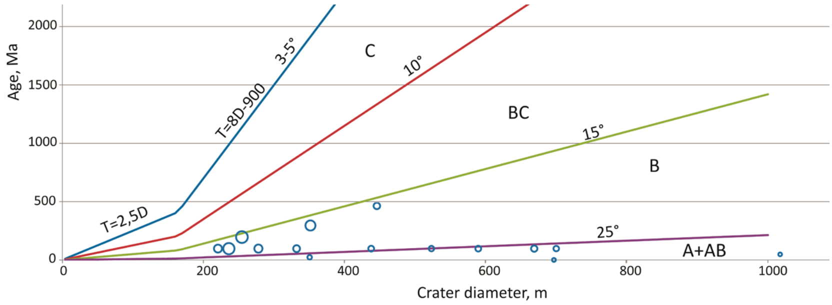

Fig. 3. Correlation between crater geometry, diameter and its absolute age.

Table 1. Morphometric parameters of the dated craters and their morphologic class

No	Apollo mission	Crater name	Max slope steepness	d/D ratio	Diameter, m	Age, Ma	Morphologic class
1	15	Elbow Crater	19.1	0.05	352.0	300	B
2	15	Dune Crater	29.8	0.09	446.3	470	B
3	12	Surveyor	16.5	0.07	254.7	200	B
4	14	Cone Crater	42.9	0.15	350.9	25	A+AB
5	16	North Ray	52.0	0.23	1018.9	50	A+AB
6	16	South Ray	50.8	0.18	697.7	2	A+AB
7	17	Camelot	35.3	0.12	701.0	100	A+AB
8	17	Steno-Apollo	33.6	0.14	590.3	100	A+AB
9	17	Emory	30.9	0.12	669.8	100	A+AB
10	17	Sherlock	36.2	0.14	523.9	100	A+AB
11	17	Powell	33.5	0.14	438.3	100	B
12	17	Powell A	28.1	0.11	332.4	100	B
13	17	Steno-Apollo A	17.1	0.07	236.1	100	B
14	17	Sherlock B	23.8	0.11	278.1	100	B
15	17	Sherlock A	24.1	0.10	220.7	100	B

The graph shows that younger craters have steeper slopes (are represented by smaller circlets) and are mostly situated under the purple line. That means that these craters can be related to A+AB morphologic class. This is in good agreement with their depth/diameter ratio which is ≥0.12. Other craters are considered to be older, have lower d/D ratio (except for Powell), more gentle slopes and appear in class B.

Obtained parameters are presented in Table 1.

Conclusion:

Our morphometric measurements, which are based on modern LRO NAC data, are in good agreement with previous studies (Basilevsky, 1974; Basilevsky, 1976), but quantitative approach will hopefully make estimation of crater ages to be more reliable.

Acknowledgments:

The work on morphometric study of craters was carried out at MIIGAiK and supported by Russian Science Foundation, project 14-22-00197. The work on revision of earlier made estimates of absolute age of small lunar craters was carried out at GEOKHI.

References:

Basilevsky A.T. Age of small lunar craters. Izvestia of Academy of Sciences (USSR), 1974, No 8, 139-142 (in Russian).

Basilevsky A.T. On the evolution rate of small lunar craters // Proc. Lunar Sci. Conf. 7th, 1976, p. 1005-1020.

Florensky K.P. et al. On the problem of the structure of lunar maria surface. Modern understanding of the Moon, 1972, 21-45 (in Russian).

Florensky K.P. and Taborko I.M. Some conclusions on the morphometry of lunar regions pictured by “Luna-12” spacecraft. In coll. “Physics of the Moon and planets”. Intern. Symposium in Kiev, 1972 (in Russian).

GRAIN-TO-GRAIN CONTACTS AND LUNAR REGOLITH THERMAL CONDUCTIVITY

D.P. Skulachev
Space Research Institute (IKI), 117997, 84/32 Profsoyuznaya Str, Moscow, Russia.
dskulach@mx.iki.rssi.ru

Lunar regolith structure is a granular material with high porosity. The pores in the regolith are filled with vacuum and occupy approximately one-half of the total volume. The regolith heat transfer possible by conduction and radiation through the pores, as well as conduction through grain-to-grain contact. In real conditions, the heat flux through the pore is much smaller than the flux through the contacts of the grains. It is known that thermal conductivity of porous materials is determined not so much by the physical properties of individual grains, but by thermal transfer resistance and number of contacts of the grains with each other. In this report, we attempt to justify the hypothesis that the presence in the contact zone even small amounts of cementing material, such as ice, can significantly change the total thermal resistance of the material.

The size distribution of the lunar regolith grains is well studied on the basis of samples taken by automatic lunar stations and manned expeditions of Apollo. The regolith grain sizes are from sub-micron to a few millimeters with an average size of about 100 microns. Dense packing of grains with such a distribution should have small porosity, while the experimentally measured porosity of the lunar regolith is sufficiently large and close to 50%. This fact suggests that the regolith grains are loosely packed and form hollow spaces. Photomicrographs of samples of regolith confirm this: large grains rarely in contact with each other, they are framed by smaller particles, between aggregations of particles are observed hollow spaces of different sizes.

In [1] authors investigated the thermal model of the regolith in the form of small glass spheres. It was shown that for mixtures of spheres of different size, the conductivity is mainly determined by the fine fraction of the mixture.

Grain regolith have a rough surface with fine irregularities and contact with each other with the ridges of roughness. Microscopic irregularities of the grains are mainly formed as a result of brittle fracture of the initial material in the process of blows of meteorites and ancient geological processes on the Moon. It is known that by brittle fracture of the rods in compression cracks and chips are formed at angles close to 45 angular degrees to force direction. It is natural to assume that the angle of inclination of slopes of the roughness is of the same value. If we assume that the microscopic irregularities in the contact zone are of submicron size, even a thin film of ice can significantly increase the overall thermal conductivity of the regolith.

Reference:

1. Huetter, E. S., N. I. Koemle, G. Kargl, and E. Kaufmann (2008), Determination of the effective thermal conductivity of granular materials under varying pressure conditions, J. Geophys. Res., 113, E12004.

TEMPERATURE DISTRIBUTION AND URANIUM CONTENT IN THE LUNAR CRUST AND IN THE LUNAR MANTLE

E.V. Kronrod, O.L. Kuskov, V.A. Kronrod
Vernadsky Institute of Geochemistry and Analytical Chemistry, 19, Kosygin Str. Moscow, Russia 119991.
e.kronrod@gmail.com

Introduction:

Selenodetic data from GRAIL imply new constraints on the thickness, density and porosity of the lunar crust. The goal of this study is to combine selenodetic data with the one-dimensional model of thermal conductivity and magma ocean model of the Moon in order to obtain the temperature distribution and uranium content in the lunar crust and lunar mantle as well as the mantle heat flow and the surface heat flow.

The model of the Moon:

The spherically symmetric model of the Moon is considered. The Moon is regarded to consist of the crust, the upper mantle with heat source intensity q_{upper} and the lower boundary at the depth of 750 km (H_b), the lower mantle with heat source intensity q_{lower} and the core with specified core radius R_{core} =350 km. The following phase composition in the mantle was assumed: Ol-Px in the upper mantle (at the depth down to 500 km) and Ol-Cpx-Gar composition in the lower mantle [1]. To calculate heat sources intensities and concentrations of uranium in the mantle, the model of magma ocean was applied. The temperature in the vicinity of the core was assumed to be sufficiently high to provide partial melting of the mantle substance.

The model of the Moon's crust:

The average characteristics of the crust (thickness, porosity, density) were defined according to [2]. Thermal conductivity was assumed to be expressed by an exponential function of porosity. In the upper layer of the crust the layer of regolith with the depth of 15 m and the temperature difference of 15°C [3] was considered. Two models of the crust were taken into consideration. The first model consists of three layers with constant physical properties in each layer. The second one contains exponential laws of porosity change [4] and the change of heat source intensities (concentration of uranium) with depth. The crust thickness varies in the range of 34-43 km.

Thermal model:

The heat transfer from the core-mantle boundary to the surface in quasi-stationary problem statement can be specified by one-dimensional steady-state thermal conductivity equation. The whole zone of heat transfer (the crust together with mantle) in our model was divided into five layers for calculation: the upper, middle and lower crust layers, upper mantle and lower mantle. In each layer (i=1-5) the heat source intensity q_i was assumed to be constant. We apply conditions of temperature and heat flow equality at the depth of boundaries between five considered layers. At the upper boundary the temperature T_0 and the heat flow J_0 were specified.

The mantle was divided into two zones with heat flow intensity q_{upper} in the upper mantle and q_{lower} in the lower mantle. The heat transfer system of equations has a unique solution when specifying bulk uranium content of the Moon (q_{bulk}) and average mass concentration of U in the crust (q_{crust}). Concentration of U in lower mantle was calculated from the balance ratio resulted from the model of magma ocean. The conversion of uranium concentration into heat source intensities was performed on the assumption of Th/U=3.7, K/U=2000 [5].

Constraints on the temperature distribution:

1. The temperature at the crust-mantle boundary obtained from the conversion of seismic velocities into temperature [6]: $T_{crust-mantle}$=400-450°C. Taking into account the uncertainty in the temperature of the seismic data, the following range of temperature values was considered $T_{crust-mantle}$ = 250-550°C.
2. The temperature gradient in the upper mantle was estimated to be dT/dH ≈1.17 °C/km [7-Кронрод и др., 2014]
3. The highest possible temperature at the depth of 1250 km is defined by the condition of closeness of the temperature at this depth with solidus temperature: T_{1250} ≈ 1600°C [6, 7].

Results:

In the range of uranium concentrations in the crust U_{crust}=80-240 ppb in case of the crust thickness of 34 km and the depth of upper-lower mantle boundary of 750 – approximately the depth of sharp seismic velocities increase [8] – the calculations were performed and the following parameters were obtained: the temperature distribution in the mantle and in the crust (fig.1), possible temperatures at the crust-mantle boundary (fig.2), temperature gradients in the mantle at the depth close to crust and heat flows from the surface of the Moon (J_{Moon}).

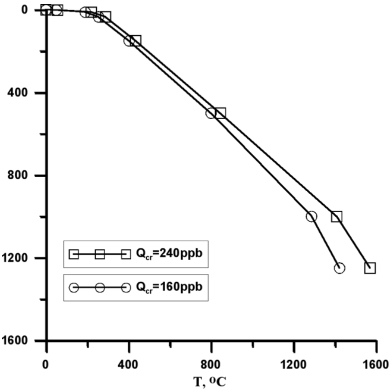

Fig. 1. The temperature distribution in the Moon from the surface to the depth of H=1250 km.

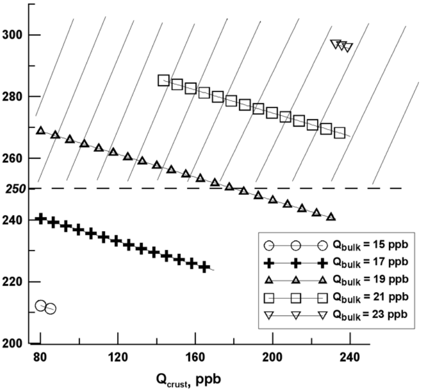

Fig. 2. The temperature at the depth of crust-mantle boundary depending on uranium content in the crust. The solution region is shown in the figure Tcr-mantle>250oC.

Conclusions:

Based on the results of the research performed the following conclusions can be made:

1. The temperature distribution, the heat source intensities (uranium concentrations) in the crust and In the mantle: of the Moon which satisfy geochemical and geophysical conditions were obtained.
2. Uranium bulk content in the Moon is 19-23 ppb in case of crust thickness of 34 km and average porosity of ~12% that is close to Earth's estimations (about ~19 ppb).
3. Uranium concentrations in the Moon's crust exceed 160 ppb.
4. The surface heat flow is 6-9 mW/m^2.

Acknowledgements:

This research was supported by Russian Academy of Sciences and by RFBR grant 15-05-02572 and 15-05-01161.

References:

[1] Kuskov O.L., V.A. Kronrod, Kronrod E.V. 2014. Thermo-chemical constraints on the interior structure and composition of the lunar mantle. *Phys. Earth Planet. Interiors.* http://dx.doi.org/10.1016/j.pepi.2014.07.011
[2] Wieczorek M.A., Neumann G.A., Nimmo F. et al. 2013. The crust of the Moon as seen by GRAIL. *Science.,* V. 339 (6120). P. 671–675.
[3] Ziethe R., Seiferlin K., Hiesinger H. 2009. Duration and extent of lunar volcanism: Comparison of 3D convection models to mare basalt ages. *Planet. Space Sci.* V. 57. P. 784–796.
[4] Han SC., Schmerr N., Neumann G., Holmes S. 2014. Global characteristics of porosity and density stratification within the lunar crust from GRAIL gravity and Lunar Orbiter Laser Altimeter topography data, *Geophysical Research Letters.* V. 41, Issue 6 P. 1882–1889. DOI: 10.1002/2014GL059378
[5] Hagermann A., Tanaka S. 2006. Ejecta deposit thickness, heat flow, and a critical ambiguity on the Moon. *Geophys. Res.* Lett. 33. L19203. doi:10.029/2006GL027030.
[6] Kuskov, O. L., Kronrod, V. A. 2009. Geochemical constraints on the model of the composition and thermal conditions of the Moon according to seismic data. *Izv. Phys. Solid Earth*, V.45, P.753–768.
[7] Kronrod V. A., Kronrod E. V., Kuskov O. L. 2014. Constraints on the Thermal Regime and Uranium Content in the Moon: Evidence from Seismic Data. *Doklady Earth Sciences.* V. 455, Part 2, pp. 485–489.
[8] Gagnepain-Beyneix J., Lognonné P., Chenet H., Lombardi D., Spohn T. 2006. A seismic model of the lunar mantle and constraints on temperature and mineralogy. *Phys. Earth and Planet Int.* V. 159, P. 140-166.

MORPHOLOGY OF THE MOON AREAS WITH ANOMALOUSLY HIGH CONTENT OF THORIUM

S.G. Pugacheva, V.V. Shevchenko,
Sternberg Astronomical Institute, MoscowStateUniversity, Universitetsky 13, Moscow 119992, Russia.
sve-pugacheva@yandex.ru

Introduction:

The article describes the morphological features of the moon areas with anomalously high content of thorium. The areas with high content of thorium are located in vicinity of Maria of the Moon visage. In the last years, the anomalously high content of thorium was found at the far side of the Moon, in the South Pole-Aitken basin, as well as in the area of Compton-Belkovich ancient impact craters (the Compton-Belkovich thorium anomaly). The areas of the thorium anomalies were discovered by the gamma spectrometer of the space probe Lunar Prospector in 1998. Thorium content in the sub-soil surface layer of the Moon is provided in the cataloguesand mapped[1, 4].

Thorium anomalies at the near side Moon.

According to lunar soil samples collected by Apollo-17 and Luna-16 expeditions all the Maria on the Moon area of volcanic origin. Age of mare basalt is evaluated starting from 3.8 up to 3.1 milliards years [2]. Photographs taken by in-orbit satellites of the Moon show the lunar Maria covered with volcanic lava, meandering lava flows, cones, domes and destroyed depressions. Traditionally, it is accepted to single out two landscapes of the Moon: highlands – bright surfaces, and Maria – dark surfaces. In 2000, the third surface type was proposed, occupying the major part of the “mare-type” surface – basaltic volcanism, which was called PKT (Procellarum KREEP Terrane). Pore spaces filled with thorium can be seen in PKT areas at the Moon surface space images. Jolliff proposed the theory of thorium anomalies formation [3]. According to his theory, on the early stage of the Moon construction, heated radioactive elements of mantle were heating and melting the mantle solid intensely, as a result of which heavy elements like ferrum and silicon were crystallizing, which formed the higher slice of the mantle. Rising to the surface of the Moon, lava was cooling down and differentiating, forming a siliciousrock with higher content of thorium. Affected by the impact of the cosmic bodies, basaltic lava was pouring out through the fissures to the Moon surface, filling depressions and other lowlands with lava.

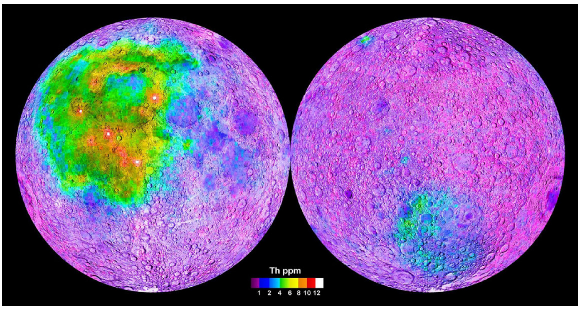

Fig.1. Thorium concentration on the Moon. The model was created with the help of computer processing of the lunar soil elemental composition measurements data by the space probe Lunar Prospector. Almost all of them are surrounded by the lunar Procellarum KREEP Terrane[NASA/GSFC/Arizona State University].

Thorium anomalies at the far side of the Moon.

There are rather less areas with high content of thorium at the far side of the Moon. High content of thorium is registered in the South Pole-Aitken basin and Mare Ingenii. As a result of detailed investigation of the Lunar Prospector space vehicle data, the new complex of the thorium anomalies has been explored in the area of large ancient Compton-Belkovich craters [4]. Initially, this area was interpreted as a surface with stones accumulation owning to material ejection when cratering due to a fall of meteorite. Gamma ray spectrometer of the Lunar Prospector space vehicle fixed high temperature of the surface in this area, as well as high concentration of the radioactive element – thorium. Subsequently, this area got the name the Compton-Belkovich thorium anomaly.

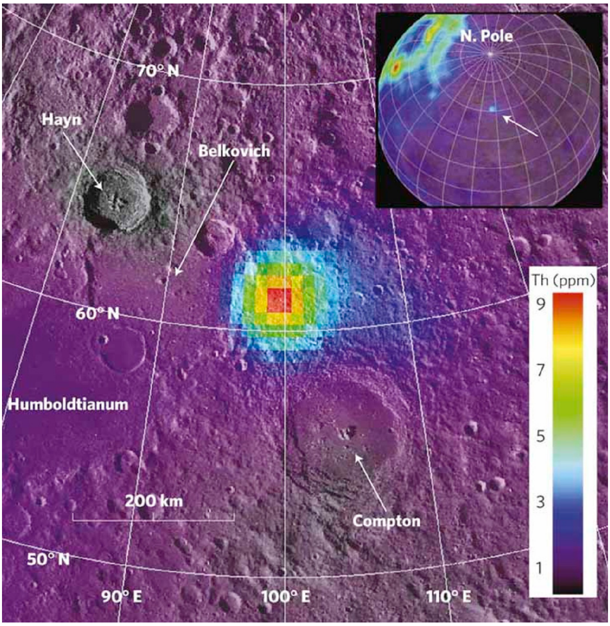

Fig.2. The Compton-Belkovich thorium anomaly [NASA, Washington University]. The thorium anomaly is located in 900 km from the major zone PKT. In the center of the image, a complex of craters from 25 to 35 km in diameter is located. Diameters of the Compton craters – 162 km, of the Belkovich crater – 214 km [5].

The Compton-Belkovich thorium anomaly is located in the north hemisphere of the Moon, the length of anomaly is 60.5^{o}N – 61.5^{o}N in latitude, 95^{o}E – 101^{o}E longitudinally, the area occupies the space of 70 km^2. The anomaly is located 2.9 km lower the zero altitude level. Thorium content in the central point of the anomaly is 10 ppm. The thickness of the crust in this area, according to the Grail data, is 20 km, the surface openness is 8%, density – 2375kg m^{-3}[6.7].

Tables with the morphological features of the thorium anomalies are provided in the report, as well as the results of the lunar ground investigations by the AMIE/SMART, Apollo 14 and Apollo 15 space vehicles.

Conclusion.

Abounding reserves of thorium on the Moon are the important natural resource. Gradually, thorium reactors succeed uranium reactors in the atomic power energetics. The thorium reactors are operating in Norway, and the experimental variants are created in India and China. Besides thorium, the metals required for the industry and innovative technologies development have been found out in the lunar regolith. These are vanadium, tantalum, niobium, cadmium, zirconium, yttrium and strontium rare earth metals. The lunar ground investigation via the space vehicles allow us to suppose that the rare earth rocks, thorium and ferric hydroxide underlie in the lunar Maria covered with volcanic lava, on the surface or shallow depth of the lunar surface.

References:

[1] Gillis, J. J., Jolliff, B. L., and Korotev, R. L. (2004) Lunar surface geochemistry: Global concentrations of Th, K, and FeO as derived from Lunar Prospector and Clementine data. *GeochimicaetCosmochimicaActa,* v. 68, p. 3791-3805. [2] Harald H., Jauman R., Newkum G. et al, Ages of mare basalts on the lunar nearside, *Journal of geophysical research, 2000,* V. 105, No. E12, p. 239-275. [3] Jolliff, B.L., Gillis J.J., Haskin L.A., Korotev R.L., and Wieczorek M.A. (2000) Major lunar crustal terranes: Surface expressions and crust-mantle origins. *Journal of Geophys. Res.,* v. 105, p. 4197-4216. [4] Lawrence D.J., Feldman W.C., Barraclough B.L., Binder A.B., Elphic R.C., Maurice S., Miller *JGR, 105,2005,* No. E8, 20, 307-20,331. [5] Jolliff B. L., Wiseman S. A., Lawrence S. J., Tran T. N., Robinson M., S., Sato H., Hawke B. R., Scholten F., Oberst J., Hiesinger H., van der Bogert C. H., Greenhagen B. T., Glotch T. D., and Paige D. A. (2011) **Nature Geoscience**, doi:10.1038/ngeo1212. [6] Jolliff B. L. (2014) Merrillite and apatite as recorders of planetary magmatic processes. **American Mineralogist** 99, 2161-2162. [7]Seddio S. M., Jolliff B. L., Korotev R. L., and Carpenter P. K. (2014) **Geochimica et CosmochimicaActa135**, 307–320.

GEOLOGIC CHARACTERISTICS OF THE LUNOKHOD 1 AND YUTU ROVER LANDING SITES, NW MARE IMBRIUM OF THE MOON

A.T. Basilevsky[1,2], A.M. Abdrakhimov[1], J.W. Head[2], C.M. Pieters[2], Wu Yunzhao[3], Xiao Long[4]
[1]Vernadsky Institute, Russian Academy of Sciences, Moscow, 119991, Russia.
atbas@geokhi.ru;
[2]Department of Earth, Environmental and Planetary Studies, Brown University, Providence RI, 02912, USA;
[3]School of Geographic and Oceanographic Sciences, Nanjing University, Nanjing, 210023, China;
[4]Planetary Science Institute, China University of Geosciences, Wuhan, 430074, China

This work is a part of a joint research project between the Vernadsky Institute, Moscow, Russia, Brown Uni-versity, Providence, RI, USA, Nanjing University, Nanjing, China and China University of Geosciences, Wuhan, China. We compared and assessed the results of measurements and observations by the Lunokhod 1 and Yutu rovers, both of which explored the northwestern part of Mare Imbrium [1-7,12] (Figure 1). Both sites are within the distinctive Eratosthenian-aged lava flow geologic unit and our comparisons showed that the geologies of these exploration sites are very similar.

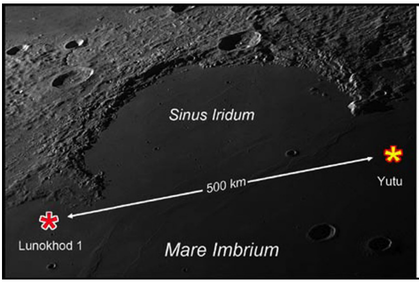

Fig. 1. Area of work of Lunokhod-1 and Yutu rover at the NW part of Mare Imbrium. Image source: http:// www.visit-the-moon.com/ sinus-iridumr13-04-05-07.

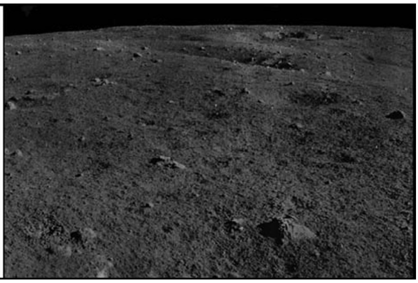

Fig. 2. Typical landscape at the Lunokhod-1 work area. Small craters and rock fragments are dominating features. Portion of Lunokhod-1 panorama L1_D09_S05_P10.

As in the majority of other areas of the Moon, the dominant landforms in these sites are small impact craters, having various degrees of morphologic prominence and states of preservation, and rock fragments, mostly asso-ciated with the rims and interiors of fresh craters (Figures 2 and 3). The shape and the degree of preservation of the observed rock fragments in these two sites are similar.

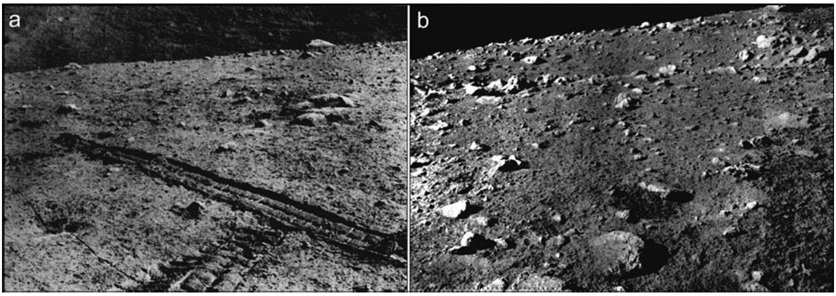

Fig. 3. a) Moderately rocky surface in the WSW part of the rim of the relatively large (D = 470 m) crater Borya. In the upper part of the image the opposite internal slope of this crater is seen. The Lunokhod track width is 20 cm. b) Rocky surface on the western internal slope of crater Borya. Parts of panoramas L1_D07_S04_P08 and L1_D06_S02_P03.

In both sites sporadic rock fragments were observed whose morphologies suggest that their source rocks had columnar jointing (Figure 4). Localization of these specific rocks on the rims of 450-470 m in diameter craters implies that the source rocks are at depths of 40-50 m.

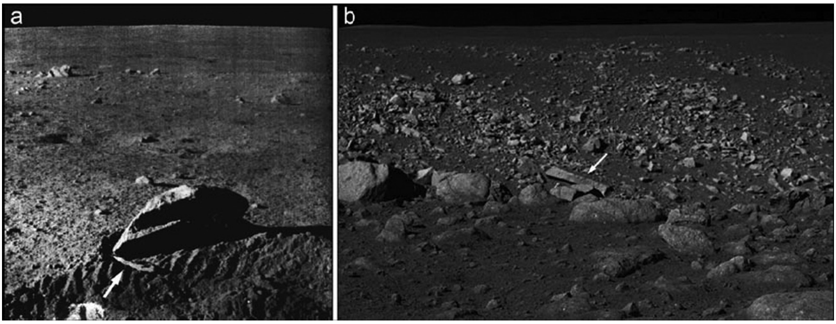

Fig. 4. Fragments of rocks whose morphology suggests a columnar jointing. Portions of Lunokhod-1 panora-ma L1_D05_S01_P01 and Yutu image ID: CE3_BMYK_PCAML-C-015_SCI_N_20140113191514_ 20140113191514_0008_A.

Regolith in the study areas is typically a few meters thick, but locally can be much thicker. The ground pene-trating radar of the Yutu rover revealed the multilayer regolith structure [10,11, 13,14], which is determined by superposition of crater ejecta. With some local variations, this type of the regolith stratigraphy should be typical of the majority of lunar mare sites. The physico-mechanical properties of the regolith in these two sites appear to be rather similar and close to values measured by PROP instrument along the Lunokhod-1 route [9]: the bearing capacity ranges from 0.04 to 1.44 kg/cm2, with a modal value ~0.45 kg/cm2, and the shear strength ranges from 0.02 to 0.1 kg/cm2, with a modal value ~0.05 kg/cm2. Both these parameters decrease by a factor of 3 to 4 with an increase of surface slope from ~2 to 12o. The chemical composition of surface materials determined by the rover instruments at these two sites differ from those derived from the remote sensing data for the Eratosthenian-aged basalts on which the two sites are located. This could be partly due to low measurement accuracies, espe-cially in the case of Lunokhod 1, but may also represent real variations in the composition of the surface materi-als compared to returned lunar samples.

Recommendations for future lunar rover missions are: 1) to use ground penetrating radar and a robotic arm, and 2) to employ radial study tactics for impact crater documentation and analysis.

Acknowledgements.

We thank Russian Academy of Sciences/Roskosmos and the five systems in the Chinese Lunar Exploration Project and National Astronomical Observatories of the Chinese Academy of Sciences (NAOC) for providing the Lunokhod 1 and Chang'E-3/Yutu data. We acknowledge NASA Lunar Reconnais-sance Orbiter (LRO) Mission, Lunar Orbiter Laser Altimeter (LOLA) Experiment Team (Grants NNX11AK29G and NNX13AO77G), and NASA Solar System Exploration Research Virtual Institute (SSERVI) grant for Evolution and Environment of Exploration Destinations under cooperative agreement number NNA14AB01A at Brown University for ATB, CMP and JWH. This research was supported by the National Natural Science Foun-dation of China (41422110). Discussions with M.I. Malenkov were very helpful.

References

[1] Abdrakhimov A.M. et al., 2014. 45th Lunar and Planetary Science Conference. Abs. #1239.
[2] Basilevsky A.T. et al., 2014. Planetary and Space Science. V. 92, 77–87.
[3] Fa W. et al., 2014. Journal of Geophysical Research. V. 119, No. E8, 1914-1935.
[4] Florensky C.P. et al., 1971. Preliminary results of geomorphological analysis of panoramas. In: Mobile
Laboratory on the Moon Lunokhod-1. A.P. Vinogradov ed. Nauka Press. Moscow. 96-115. (in Russian).
[5] Florensky C.P. et al., 1972. Geomorphological analysis of the area of Mare Imbrium explored by the automatic roving vehicle Lunokhod 1. Space Research XII. Akademie-Verlag. 107-121.
[6] Florensky C.P. et a., 1978. Geologic-morphologic studies of lunar surface. In: Mobile Laboratory on the Moon Lunokhod-1. V. 2. V.L. Barsukov ed. Nauka Press. Moscow. 102-135. (in Russian).
[7] Karachevtseva I. et al., 2013. Planetary and Space Science. V. 85, 175–187.
[8] Kocharov G.E. et al., 1971. Lunar automatic spectrometric instrument RIFMA. In:

Mobile Laboratory on the Moon Lunokhod-1. A.P. Vinogradov ed. Nauka Press. Moscow. 89-95 (in Russian).
[9] Leonovich A.K. et al., 1978. Automotive chassis of Lunokhod 1 as instrument for the lunar surface study. In: Mobile Laboratory on the Moon Lunokhod-1. V. 2. V.L. Barsukov ed. Nauka Press. Moscow. 25-43.
[10] Qiao L., et al., 2015. 46th Lunar and Planetary Science Conference. Abs. #1050.
[11] Su Y. et al., 2014. Research in Astronomy and Astrophysics. V. 14. No 12, 1623-1632.
[12] Wu Y. et al., 2015. Compositional diversity and geologic context of the northwest Imbrium region. (in preparation).
[13] Xiao L. et al., 2015.. Science. V. 347. No 6227, 1226-1229.
[14] Zhao J N. et al., Science China - Physics, Mechanics & Astronomy, 2014, 57: 569-576.

M[3]'S TOP-TEN TARGET ISSUES [IN THE NEXT PHASE OF EXPLORATION]

C.M. Pieters[1], J.W. Head[1]
[1]Dept. Earth, Environment, and Planetary Sciences, Brown Univ., Providence, RI 02912.
Carle_Pieters@brown.edu

Introduction:

The Moon Mineralogy Mapper (M[3]) was supported by NASA as a Discovery Mission of Opportunity and flown on India's Chandrayaan-1 mission to the Moon in 2008-2009 [1]. The primary objective of M[3] was to identify and map compositional properties across the Moon at high spatial resolution. M[3] is an advanced imaging spectrometer that uses a single two-dimensional detector covering the spectral range of 500-3000 nm to gather a three dimensional cube of data (two spatial and one spectral) in a 'push-broom' mode. A summary of the characteristics and operations of M[3] can be found in [2,3].

In spite of several onboard challenges, M[3] was a resounding technical and scientific success and it is appropriate to ask "What is next?" There are two parts to the answer. One relates to advancements in technology in the last decade resulting in improved spatial and spectral resolution as well as radiometric accuracy for the next imaging spectrometer. The second, briefly discussed here, relates to targeting a new set of issues that build on remarkable and diverse new data and discoveries from the last decade of lunar exploration (Kaguya, Chandrayaan-1, Chang'E, LRO, GRAIL, LADEE) with emphasis on those that can be addressed further with improved imaging spectroscopy details. Many issues are linked to surface experiments and sample return strategy.

Top Ten Target Issues (no priority assigned)

Water: The remarkable discoveries in 2008-2010 [4, 5, 6, 7] provided direct evidence for the presence of OH and H2O in three forms on the Moon: a) in the samples themselves reflecting information about the primordial lunar interior, b) pervasive surficial deposits across the Moon as H from the solar wind bonds with O on the surface, and c) predicted accumulations in the regolith of a permanently shadowed polar crater (along with other volatiles). The form, abundance, distribution, and time variation of these different species across the Moon and how they interact with one another are very poorly known.

Magnetic anomalies: Great progress has been made documenting the direct interaction of an airless silicate body (the Moon) with plasma of the space environment [8, 9, 10]. Of particular interest are the interactions that occur at locations of relatively strong magnetic anomalies that are often accompanied by mysterious high albedo markings, called 'swirls'. It has now been shown that these unusual high albedo areas are protected from solar wind H by the local magnetic field and do not form significant OH on the surface [11, 12], it is also clear that the markings are <u>not</u> the result of reduced space weathering, but are more likely an interaction of a well developed regolith with the local magnetic field [e.g., 12, 13]. The character, magnitude and local variation of the geophysical properties at these potentially useful regions are unknown.

Basin Processes: Large impact basins dominate the geology of the first 500 Myr of the Earth and the Moon's evolution. Continual upgrading and application of basin impact models with new observational data provides improved constraints on the surface and interior of the Moon. Two aspects of such basin derived processes are also directly relevant for the following three target issues about the crust below the megaregolith. First, the inner ring of basins are believed to expose crustal material directly uplifted from depth, whereas the outer basin rings more likely represent slip faults exposing upper parts of the megaregolith [e.g. 14, 15]. Second, extensive basin deposits form a major component of the megaregolith and their origin and character is a mixed sampling (breccias etc.) of the crustal column excavated by the basin impacts [e.g., 16]. Characterizing and dating materials associated with impact basins is fundamental to the early history of the Earth/Moon system and allows the compositional stratigraphy of the lunar crust and mantle to be partially constrained.

Upper crust: Pure Plagioclase from the Magma Ocean. Pure (<5% mafics) crystalline plagioclase has been identified across the Moon by its highly diagnostic absorption at 1.25 μm [17, 18, 19, 20]. The best exposure is throughout the inner ring of Orientale Basin, indicating this is a pervasive (thick) MO product.

Middle Crust: plagioclase + Mg-Spinel, olivine. Similarly, when sufficiently well exposed, the inner rings of other basins contain mafic-free plagioclase with small outcrops of Mg-spinel, olivine, and (rarely) Mg-pyroxene [21, 22, 23]. A current model thus includes these Mg-rich minerals as small local components of a plagioclase-rich lower crust.

Lower Crust/Upper mantle: plagioclase + Mg-pyroxene (Low-Ca). Nevertheless, the megaregolith (which is derived largely from basin deposits) across the Moon is dominated by plagioclase with various amounts of Mg-rich pyroxene [24, 25, 26, 27, 28]. Although still strongly feldspathic, this mixture strongly suggests the origin of the pervasive Mg-pyroxene component is below the pure plagioclase zone and the limited amounts of olivine and spinel found in the upper and middle crust.

Mantle: Regional Spinel-bearing Pyroclastics. The Apollo 17 orange and black beads, the Apollo 15 green glass, and small amounts of other pyroclastic beads identified in the lunar samples are under intense study since they are samples that are most directly tied to the character of the lunar mantle [e.g. 4, 29]. However, remote measurements have identified a regional pyroclastic deposit on the lunar nearside that contains abundant spinel (Cr or Fe-rich) [30, 31] that is clearly not in our sample collection.

Complex Crater Processes: Although much smaller than basins, complex craters with central peaks often (but not always) tap below the megaregolith and are more abundant and often more recent than basins. Their size allows integrated processes to be more easily assessed. For example, it has been documented that impact melt at such a crater is not only heterogeneous in composition, but also not well mixed spatially [e.g., 32, 33]

Volatile Mobility: Day-night cycles. An issue that has barely been addressed, largely due to lack of data, is how volatile components move across the Moon, either through random events or during diurnal cycles. These can be modeled [e.g. 34], but this issue suffers greatly from insufficient data.

Dust Mobility: Similarly, dust mobility and its drivers is of great interest for planning surface operations as well an for understanding the history of the regolith. The recent LADEE results show that the finest particles appear to have a permanent, although asymmetric, abundance at ~50-100 km, but spikes are readily detected after meteor showers [35].

Specific targets to address these issues will suggested for open discussion.

Acknowledgements. We gratefully acknowledge support provided by the NASA Solar System Exploration Research Virtual Institute (SSERVI) under grant NNA14AB01A.

References.

1. Pieters, C. M., et al. (2009a), The Moon Mineralogy Mapper (M3) on Chandrayaan-1, Current Science, 96, 500-505.
2. Green, R. O., et al. (2011), The Moon Mineralogy Mapper (M3) imaging spectrometer for lunar science: Instrument description, calibration, on-orbit measurements, science data calibration and on-orbit validation, J. Geophys. Res., 116, E00G19,
3. Boardman, J. W., et al. (2011), Measuring moonlight: An overview of the spatial properties, lunar coverage, selenolocation and related Level 1B products of the Moon Mineralogy Mapper, J. Geophys. Res., 116, E00G14, doi:10.1029/2010JE003730.
4. Saal, A. E., E. H. Hauri, M. L. Cascio, J. A. van Orman, M. C. Rutherford, and R. F. Cooper (2008), Volatile content of lunar volcanic glasses and the presence of water in the Moon’s interior, Nature, 454, 192–195, doi:10.1038/nature07047.
5. Pieters, C. M., et al. (2009b), Character and spatial distribution of OH/H2O on the surface of the Moon seen by M3 on Chandrayaan-1, Science, 326, 568-572
6. Colaprete, A., et al. (2010), Detection of water in the LCROSS ejecta Plume, Science, 330, 463-468, doi: 10.1126/science.1186986.
7. Schultz, P. H., et al. (2010), The LCROSS cratering experiment, Science, 330, 468-472, doi: 10.1126/science.1187454.
8. Barabash, S., et al. (2009), Investigation of the solar wind–Moon interaction onboard Chandrayaan−1 mission with the SARA experiment, Curr. Sci., 96(4), 526–532.
9. Wieser, M., et al. (2009), Extremely high reflection of solar wind protons as neutral hydrogen atoms from regolith in space, Planet. Space Sci., 57, 2132–2134, doi:10.1016/j.pss.2009.09.012.
10. Wieser, M., et al. (2010), First observation of a mini-magnetosphere above a lunar magnetic anomaly using energetic neutral atoms, Geophys. Res. Lett., 37, L05103, doi:10.1029/2009GL041721.
11. Kramer, G. Y., et al. (2011), M3 spectral analysis of lunar swirls and the link between optical maturation and surface hydroxyl formation at magnetic anomalies, J. Geophys. Res., 116, E00G18
12. Pieters, C. M., and I. Garrick-Bethell (2015), Hydration variations at lunar swirls, Lunar Planet. Sci. Conf., XLVI # 2120.
13. Pieters, C. M., et al. (2014), Atypical regolith processes hold the key to enigmatic lunar swirls, *Lunar Planet. Sci., XLV,* # 1408.
14. Head III, J. W. (2010), Transition from complex craters to multi-ringed basins on

terrestrial planetary bodies: Scale-dependent role of the expanding melt cavity and progressive interaction with the displaced zone, Geophys. Res. Lett., 37, L02203
15. Baker, D. M. H. and Head, J. W. (2015) Constraints on the Depths of Origin of Peak Rings on the Moon from Moon Mineralogy Mapper Data, Icarus, in press.
16. Petro, N. E., and C. M. Pieters (2008), The lunar-wide effects of basin ejecta distribution on the early megaregolith, Meteor. Planet. Sci., 43, 1517-1529, doi: 10.1111/j.1945-5100.2008tb01025.x.m
17. Ohtake, M., et al. (2009) The global distribution of pure anorthosite on the Moon, Nature, 461, 236–240.
18. Yamamoto, S., et al. (2012) Massive layer of pure anorthosite on the Moon, Geophys. Res. Lett., 39, L13201,
19. Cheek, L. C., K. L. Donaldson Hanna, C. M. Pieters, J. W. Head III, and J. L. Whitten (2013), The distribution and purity of anorthosite across the Orientale basin: New perspectives from Moon Mineralogy Mapper data, J. Geophys. Res., 118, 1-16,
20. Donaldson Hanna, K. L., et al. (2014), Global assessment of pure crystalline plagioclase across the Moon and implications for the evolution of the primary crust, J. Geophys. Res., 119, 1516-1545, doi: 10.1002/2013JE004476.
21. Pieters, C. M., et al. (2011), Mg-spinel lithology: A new rock type on the lunar farside, J. Geophys. Res., 116, E00G08,
22. Dhingra, D., et al. (2011) Compositional diversity at Theophilus Crater: Understanding the geological context of Mg-spinel bearing central peaks, Geophys. Res. Lett., 38, L11201, doi: 10.1029/2011GL047314.
23. Pieters, C. M., et al. (2014), The distribution of Mg-spinel across the Moon and constraints on crustal origin, American Mineralogist, 99, 1893-1910, doi: 10.2138/am-2014-4776.
24. Pieters, C. (1986) Noritic anorthosite is the most common highland rock type seen on the surface of the lunar nearside. Rev. Geophys. 24, 57_588.
25. Isaacson, P. J., and C. M. Pieters (2009), Northern Imbrium Noritic anomaly, J. Geophys. Res., 114, E09007,
26. Lucey, P. G., and J. T. Cahill (2009), The composition of the lunar surface relative to samples, Lunar Planet. Sci., 40, Abstract 2424.
27. Nakamura, R., et al. (2009), Ultramafic impact melt sheet beneath the South Pole–Aitken basin on the Moon, Geophys. Res. Lett., 36, L22202, doi:10.1029/2009GL040765
28. Klima, R. L., et al. (2011), New insights into lunar petrology: Distribution and composition of prominent of Low-Ca pyroxene exposures as observed by the Moon Mineralogy Mapper (M3), J. Geophys. Res., 116, E00G06, doi: 10.1029/2010JE003719.
29. Hauri, E.H., Weinreich, T., Saal, A.E., Rutherford, M.C., Van Orman, J.A., 2011. High pre-eruptive water contents preserved in lunar melt inclusions. Science333, 213–215.
30. Yamamoto, S., et al. (2013), A new type of pyroclastic deposit on the Moon containing Fe-spinel and chromite, Geophys. Res. Lett., 40, 4549–4554, doi:10.1002/grl.50784.
31. Jackson, C. R. M., et al. (2014), Visible-infrared spectral properties of iron-bearing aluminate spinel under lunar-like redox conditions, American Mineralogist, 99, 1821-1833, doi: 10.2138/am-2014-4793.
32. Dhingra, D., C. M. Pieters, J. W. Head III, and P. J. Isaacson (2013), Large mineralogically distinct impact melt feature at Copernicus crater – Evidence for retention of compositional heterogeneity, Geophys. Res. Lett., 40, doi: 10.1002/grl.50255.
33. Dhingra, D., C. M. Pieters, and J. W. Head III (2015), Multiple origins for olivine at Copernicus crater, Earth Planet. Sci. Lett., 420, 95-101, doi: 10.1016/j.epsl.2015.03.039
34. Hurley, D. M. et al. (2014) Propagation of Chang'e 3 Exhaust.
35. Horaniy, M. et al. (2015) A permanent, asymmetric dust cloud around the Moon, Nature, 522, doi:10.1038/nature14479

WATER MAPS OF THE POLAR MOON: LEND DATA AFTER 6 YEARS ON THE LUNAR ORBIT

A.B. Sanin on behalf of DAN science team
Spase Research Institute

LEND neutron mapping of the Moon is shown to allow to build up the maps of water distribution over the polar areas. The most recent results are presented based on the 6 years of the instrument operations.

COLD-BASED GLACIATION ON MERCURY: ACCUMULATION AND FLOW OF ICE IN PERMANENTLY SHADOWED CIRCUM-POLAR CRATER INTERIORS

J.L. Fastook[1], J.W. Head[2]
[1]University of Maine, Orono, ME, USA;
[2] Brown University, Providence, RI, USA.
fastook@maine.edu

Introduction:

Extensive radar [1] evidence exists for the presence of ice [2-9] in permanently shaded craters near the poles of Mercury [10,11]. Ice has been shown to be thermally stable under these conditions [12,13], and a detailed energy-balance model of the surface temperatures around and within these craters [14] suggests an annual mean temperature near 110 K in permanent shade with surface temperatures close to 400 K in sunlit regions. Here we describe the dynamic properties of the proposed ice deposits to delineate the effects of ice deformation and the potential for flow that would modify these deposits in the time interval for which they are believed to have existed.

Modeling:

We use a simple geometry, a function of only crater diameter and latitude, that allows us to define the shape of the crater walls and floor, as well as the permanently shaded volume that defines the surface of the ice deposit. Depth of the crater is determined from the d/D ratio, which Vasavada [14] gives as 1:5 for craters less than 10 km in diameter and 1:25 for craters with diameters of 100 km. Talpe et al. [15] provides various power law fits for the d/D ratio as well as for the crater-wall slope, which we use to define the crater geometry. An example based on Crater C, with a diameter of 50 km at a latitude of 87.5o is shown in Figure 1.

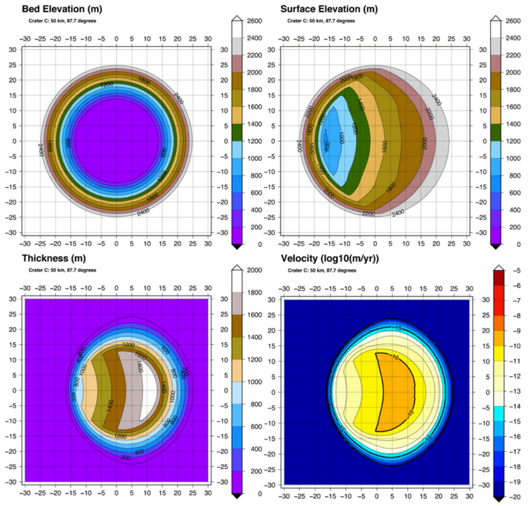

Fig. 1. Geometry based on Talpe et al. (2012) and Crater C, with 50 km diameter at latitude 87.5o.

This configuration is passed to our ice dynamics model (UMISM, the University of Maine Ice Sheet Model, a finite-element shallow-ice approximation model that has been used extensively both on Earth [16-18] and Mars [19-24], here adapted for Mercury gravity. UMISM is a thermomechanically-coupled ice sheet model, where ice properties that control deformation are functions of temperature, which itself is derived from a time-dependent solution of the energy equation.

An ablation rate of -1.0 m/yr is assumed in the sunlit areas, while minor accumulation (10^{-10} m/yr) is assumed for the ice surface [25]. With such a low accumulation rate the ice sheet surface will basically attempt to “relax” into a configuration where the driving stress is minimized and any observed velocity is a result of internal deformation and not of mass-balance driven flux.

Thermodynamics: Boundary conditions for the thermodynamic component, used to calculate the ice hardness, include mean-annual surface temperature, taken to be 110 K, and basal heat flux. Because the ice is thin (basically the crater depth) and the slope is shallow (basically the sun angle), as well as the fact that the ice is cold, modeled velocities are very low, on the order of 10^{-10} m/yr for a uniform heat flux of 50 mW/m^2. Velocity, shown in Figure 1, is highest at the base of the crater wall where thickness is greatest. Long-term deformation with this velocity distribution would result in a thinning upstream toward the crater rim and a thickening downstream toward the crater center as the profile relaxes to a minimum driving stress configuration. However, with velocities this low little deformation would take place in the billion-year time span available.

Warmer ice is exponentially softer than colder ice due to the Arrhenius relationship between the parameter in the non-linear Glen's Flow Law [26-27] relating strain rate to stress, and ice at depth is warmer than at the surface due to the insulating power of the ice. As such, the heat flux is a key parameter controlling ice deformation, and hence, ice velocity. Vasavada [14] uses an estimate for the heat flux of 20 mW/m^2 [28]. An estimate based on the height of a scarp and its implications for the depth of the brittle-ductile transition, as well as the depth of melting of the crustal-mantle transition yields a surface heat flux that ranges from 30 to 60 mW/m^2 [29], but their method is based on the assumption of 30-40 mW/m^2 originating from the mantle (which they allow could be as much as 10 mW/m^2 higher) with the rest provided by the radiogenic contribution of the crust.

Lateral Transport of Heat: An additional consideration is the lateral transport of heat from the warm sunlit surroundings of the cold shaded crater interior. A 2D solution of the steady-state heat flow equation **[*30*]** for a rectangular domain with a "cold spot" on the surface results in a depression of the isotherms below the cold spot. This depression and warping of the isotherms directs additional heat from the surroundings beneath the hot surface terrain into the center of the cooler region beneath the cold spot.

The effect of lateral heat flux is affected by the diameter of the crater, with it being most pronounced near the edges of the crater. For this reason smaller craters have much higher heat fluxes at their centers, decreasing as the crater diameter increases. Temperature isotherms are bowed down beneath the cold spot, and since heat flows perpendicularly to the isotherms, heat is preferentially focused onto the base of the cold spot. The region of enhanced lateral flux is most intense beneath the edge of the crater, where the temperature discontinuity is largest (400 to 100 K). With the smallest 10 km crater, the contributions from the edges overlap in the center, resulting in the largest flux at the center of the crater. Larger craters result in deeper penetration of the temperature anomaly, and hence steeper temperature gradients carrying more flux, but since the edges are farther apart, the synergistic contribution is less at the center of the crater and less enhanced fluxes are delivered.

Results:

To investigate the effect of the enhanced lateral heat flux, we run the ice sheet model for various crater sizes and latitudes (10 to 55 km in 5 km steps and 85 to 89.5^o in 0.5^o steps, a total of 100 model runs). Figure 2 shows the base-10 logarithm of the maximum velocity observed in each model run (a value of -10 corresponds to 10^{-10} m/yr) for the uniform flux case (left) as well as the non-uniform lateral heat transport case (center). A black star with a 'C' in it indicates the position of Crater C, shown as an example in Figure 1. Other craters with known deposits are also indicated. Since depth is determined from the d/D ratio (Talpe et al. 2012), in the uniform flux case larger craters display faster velocities, primarily due to the thicker ice that can exist in the deeper craters. A secondary effect is the surface slope, which is steeper at lower latitudes. This effect is negated by the thinner ice available at the base of the crater walls with these steeper slopes, resulting in an optimal latitude at 89^o where the velocity is maximum for a given size crater. Lowest velocities are observed in the smallest craters at the lowest latitudes for the uniform heat flux case.

Given the significantly increased heat flux that can be delivered to the base of the crater by lateral transport, we re-apply the ice sheet model with these en-

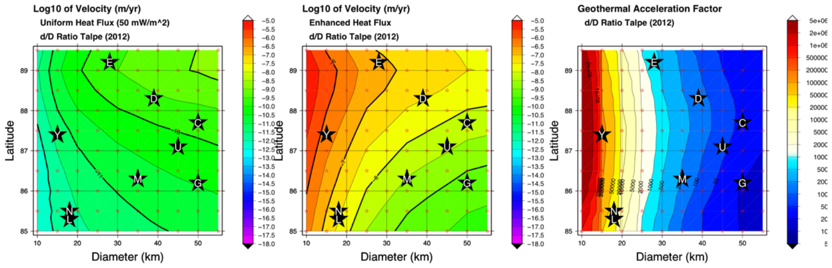

Fig. 2. Base-10 log of velocity for the uniform flux case (left), the lateral heat transport case (center), and the ratios of these (right).

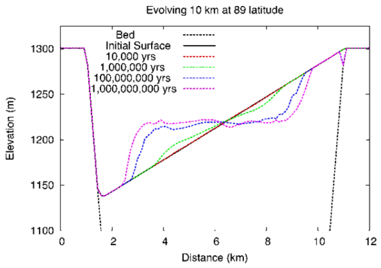

Fig. 3. Evolution of a 10 km cra-ter at 89o, showing initial surface and deforming surface at 104, 106, 108, and 109 years.

hanced fluxes instead of the uniform 50 mW/m^2. With the same set of crater sizes and latitudes, but with the enhanced lateral transport heat fluxes, we obtain a very different looking pattern of velocities, (Figure 2 center). The much greater heat fluxes result in warmer ice, which being softer and easier to deform, yields higher velocities. The relative speedup due to this softer ice (Figure 2 right) is greatest for the smallest craters at the highest latitudes, reaching in some cases six orders of magnitude, attaining velocities of 10^{-5} m/yr. Even with large craters at low latitudes, where the warming is least, an order of magnitude speedup is observed. Large craters at high latitudes, where uniform-flux velocities are a maximum, experience a hundred-fold increase in velocity with the enhanced fluxes.

The highest velocities are observed in a 10 km crater at a latitude of 89^o, and Figure 3 shows the evolution of the ice surface in such a crater over a billion years. Thinning upstream and thickening downstream results in a flattening of the surface where the velocity is a maximum.

Conclusions:

The thickest deposits with the greatest surface slope have the largest driving stresses as well as the warmest, softest ice at the bed, and hence the fastest velocities. However, accounting for the enhanced flux of heat from the surrounding hot sun-lit terrain is extremely important, offering orders of magnitude speedup over the uniform flux case, with the effect most pronounced for small craters where the greatest lateral heat flux is delivered to the centers of the craters. Even with the enhanced heat fluxes, the cold environment of the Mercury polar craters yields very small velocities and deformation is minimal on a time scale of millions of years. Even at it most rapid flow velocity, the ice surface would move only a kilometer in a hundred million years.

References:

1. J. Harmon. *Space Sci. Rev.* **132**, 307 (2007). ***2.*** M. Slade et al. *Science*, **258**, 635 (1992). ***3.*** J. Harmon, M. Slade. *Science*, **258**, 640 (1992). ***4.*** B. Butler et al. *J. Geophys. Res.*, **98**, 15003 (1993). ***5.*** J. Harmon et al. *Nature*, **369**, 213 (1994). ***6.*** J. Harmon et al. *Icarus*, **211**, 37 (2011). ***7.*** D. Lawrence et al. *Science*, **339**, 292 (2013). ***8.*** G. Neumann et al. *Science*, **339**, 296 (2013). ***9.*** N. Chabot et al. *Geology*, **42**, 1051 (2014). ***10.*** N. Chabot et al. *Geophys. Res. Lett.*, **39**, L09204 (2012). ***11.*** N. Chabot et al. *J. Geophys. Res. (Planets)*, **118**, 26 (2013). ***12.*** D. Paige et al. *Science*, **258**, 643 (1992). ***13.*** D. Paige et al. *Science*, **339**, 300 (2013). ***14.*** A. Vasavada et al. *Icarus*, **141**, 179 (1999). ***15.*** M. Talpe et al. *J. Geophys. Res. (Planets)*, **117**, E00L13 (2012). ***16.*** J. Johnson, J. Fastook. *Quatern. Int.*, **95-96**, 65 (2002). ***17.*** J. Kleman et al. *Quatern. Int.*, **95-96**, 87 (2002). ***18.*** R. Hooke, J. Fastook. *J. Glaciol.*, **53**, 646 (2007). ***19.*** J. Fastook et al. *Icarus*, **198**, 305 (2008). ***20.*** J. Fastook et al. *Icarus*, **216**, 23 (2011). ***21.*** J. Fastook et al. *Icarus*, **219**, 25 (2012). ***22.*** J. Fastook et al. *Icarus*, **228**, 54 (2013). ***23.*** J. Fastook, J. Head. *Planet. Space Sci.*, **91**, 60 (2014). ***24.*** J. Fastook, J. Head. *Planet. Space Sci.*,**106**, 82 (2015). ***25.*** J. Moses et al. *Icarus*, **137**, 197 (1999). ***26.*** J. Glen. In L. J. Tison, editor, *Physics of the Movement of Ice*, **47**, 171 (1958). ***27.*** W. Paterson, W. F. Budd. *Cold Reg. Sci. and Technol.*, **6**, 175 (1982). ***28.*** G. Schubert et al. In F. Vilas et al, editors, *Mercury*, 429 (1988). ***29.*** F. Nimmo, T. Watters. *Geophys. Res. Lett.*, **31**, L02701 (2004). ***30.*** E. Becker et al. *Finite Elements, An Introduction*. Prentice-Hall, Englewood Cliffs (1981).

MAPPING AREAS OF SHADOW IN MERCURY'S NORTH POLAR REGION TO CONSTRAIN THE EXTENT OF STABLE THERMAL ENVIRONMENTS FOR ICE DEPOSITS

A. N. Deutsch[1], N. L. Chabot[2], J. W. Head[1]
[1]Brown University, Providence, RI 02912, USA;
[2]Johns Hopkins University Applied Physics Laboratory, Laurel, MD 20723, USA;
ariel_deutsch@brown.edu

Introduction:

Through a combination of Earth-based radar observations, spacecraft data, and thermal modeling, the evidence has grown to support that the planet Mercury hosts water ice deposits in its polar regions. Radar observations reveal intriguing radar-bright materials near Mercury's poles [1], similar to radar observations of ice at the Martian polar caps and the icy outer solar system satellites. The radar-bright deposits are found predominately on crater floors and trend to poleward-facing crater walls at lower latitudes [2]. The MErcury Surface, Space ENvironment, GEochemistry, and Ranging (MESSENGER) spacecraft returned neutron spectrometer data that measured higher hydrogen concentrations in Mercury's north polar region, consistent with models for the radar-bright deposits to be composed of water ice [3]. Thermal models indicate that the permanently shadowed regions near Mercury's north pole provide thermal environments capable of hosting stable water ice deposits on geologic timescales [4]. MESSENGER laser altimeter reflectance measurements [5] and imaging of the radar-bright deposits in the shadowed polar craters [6] revealed low-reflectance surfaces that extend to the edges of shadowed areas and terminate with sharp boundaries; these low-reflectance surfaces are interpreted to be layers of organic-rich materials, formed as lag deposits, which insulate the water ice beneath. In contrast, Prokofiev crater is of special interest because laser altimeter reflectance and imaging observations have revealed a high-reflectance surface, suggesting the crater contains a widespread water ice deposit exposed at the surface [5, 6].

Here, we focus on the spatial distribution of the shadowed regions near Mercury's north pole, constraining the areas in which water ice is possible. We map shadowed regions on Mercury from 65°N to 90°N from images taken by MESSENGER's Mercury Dual Imaging System (MDIS). We compare the distribution of regions of shadow to that of Earth-based radar observations and discuss implications for radar-bright materials on Mercury.

Data Set:

During its just over four years of orbital operations, MDIS repeatedly imaged Mercury's north polar region for a large variety of imaging campaigns. In particular, the wide-angle camera (WAC) on MDIS provided images of Mercury's surface under a range of illumination conditions that expose the planet in different degrees of shadow. In this study, we utilize images that span MESSENGER's full orbital mission to identify regions of persistent shadow. In total, 16,207 WAC images taken with the 750-nm G filter (5.1-nm band width) and the 700-nm B filter (600-nm band width) were used to map areas of shadow from 65°N to the pole at 200 m/pixel (Fig. 1). Images exist for other narrow-band WAC filters, but since the other filters were always used in conjunction with filter G to provide color sets of the surface, the images from these other filters do not contain any information not captured

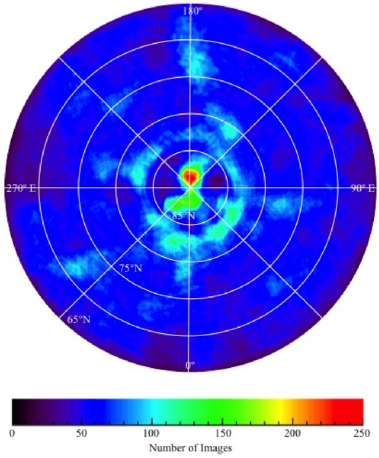

Fig. 1. Overview of the number of WAC im-ages centered at latitudes ≥65°N that were used to create the MDIS-derived persistent shadow map. On average, 50 images were used for each point on the surface in the study area. At least 9 images were used for each surface point.

by the G filter imaging. In contrast, MDIS filter B is a broadband filter and was utilized in a separate campaign to image within the shadowed regions near Mercury's pole by scattered sunlight [6]. Filter B images with exposure times greater than 2 ms contained significant saturation within the images, which led into shadowed areas of the image, and were thus not used.

Methodology:

First a photometric correction was applied to filter G images <84°N to apply more uniform surface reflectance values. By accounting for differences in viewing and lighting conditions with the photometric correction, a single threshold value could be used to divide all filter G images in this region into sunlit and shadowed terrain. Images ≥84°N had high incidence angles that were challenging for the photometric correction and surface coverage near the pole was lost if such a correction was applied. Filter B images were taken with MDIS's clear broadband filter, for which no photometric correction has been developed.

The images were then separated into areas of illumination and shadow, automated by thresholding each image based on the DN value of each individual pixel. Any area that remained in shadow in all available imagery was classified as a region of "persistent shadow." With such a robust data set (Fig. 1), regions identified as "persistent shadow" become increasingly likely to be regions of permanent shadow. For filter G images, different thresholding values were used for the images with and without the photometric correction. Filter B and G images required different thresholding values due to differences in narrowband and broadband passes.

Discussion:

Areas of Persistent Shadow. The MDIS-derived shadow map indicates that ~0.87% of the surface between 65°N to 90°N is cast in persistent shadow, similar to the ~1% that was calculated for the region 65°N to 85°N using MDIS images after just one year of orbital data [2]. We calculate that ~4.2% of the surface between 80°N to 90°N is in persistent shadow. This value is similar to the ~4.5% and ~5.6% of shadowed surface modeled for ten degrees on the Moon's north and south poles, respectively [7].

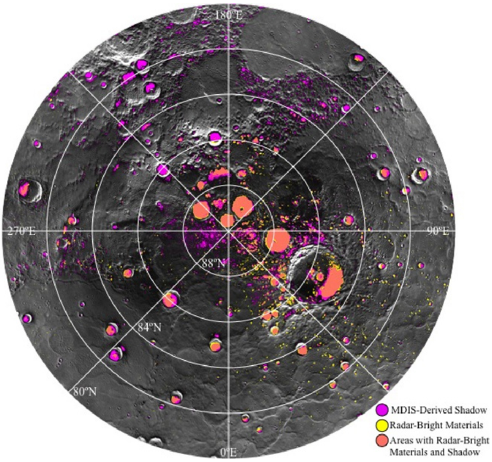

Fig. 2. Mosaic of MESSENGER images in a polar stereographic projection from 80°N to 90°N. Areas shadowed in all MDIS images are shaded in purple, regions with radar-bright materials are in yellow, and areas with both shadow and radar-bright materials are in coral.

Comparison with Radar Data. The radar data that was used as a standard of comparison was a combination of the *Harmon et al.* (2011) Figure 3b and Figure 4 radar data [1]. Figure 3b was constructed from a weighted sum algorithm of the Arecibo observations to minimize radar shadowing effects. Because this data set is geographically limited to the latitudes closest to the pole, we supplemented these data by adding the large-scale radar view provided in Figure 4 to cover the region from 80°N to 90°N.

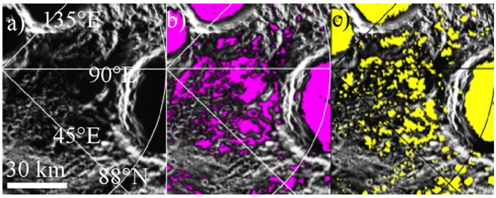

Fig. 3. a) Mosaic of MESSENGER images highlight-ing the "diffuse patch." b) Areas shadowed in all MDIS images are shaded in purple. c) Regions with radar-bright materials are in yellow.

To account for noise in the radar data, we subtracted four noise standard deviations, as was done by [1]. Subtracting four standard deviations resulted in radar-bright material covering ~0.5% of the surface from 65°N to 90°N, in general agreement with our calculation of ~0.87% of the surface in persistent shadow.

Qualitative comparisons between our shadow map and radar-bright data from [1] is shown in Figure 2. The shadow shows strong agreement in spatial distribution with Mercury's radar-bright material. In the region 80°N to 90°N, ~79% of the radar-bright deposits align with shadow. We attribute the remaining ~21% to limitations in our methodologies, as the unaligned radar-bright material is found in small craters with diameters <5 km or within 5 km of mapped shadowed terrain.

One specific region of interest is the "diffuse patch," first discussed in [8] and in more detail in [9]. This large patch of radar-bright material aligns very closely with our mapped shadow (Fig. 3). The strong radar signature here has been repeatedly observed, but never identified in a geological context due to limited coverage of this area near the pole in previous work [2]. Now with image coverage of this region, we have determined the diffuse patch to reside in very rough terrain. This example reveals a thermal environment different from crater floors where significant radar-bright material resides; such a setting could provide a different thermal environment for water ice and is worthy of future study.

In the study area at latitudes 80°N to 90°N, ~46% of the shadow contains radar-bright materials. Thus, there is a considerable number of shadowed regions that do not host radar-bright deposits, raising the question of why they do not. This finding suggests future thermal studies to investigate why certain cold-traps do not host radar-bright water ice deposits. It is also possible that certain shadowed regions are not visible to Earth-based radar observations or that they host ice deposits that are covered by thicker lag deposits that mask radar signatures. We are currently investigating these possibilities.

References:

[1] Harmon J.K. et al. (2011), *Icarus*, 211, 37-50.
[2] Chabot N.L. et al. (2013), *JGR*, 118, 26-36.
[3] Lawrence D.J. et al. (2013), *Science*, 339, 292-296.
[4] Paige D.A. et al. (2013), *Science*, 339, 300-303.
[5] Neumann G.A. et al. (2013), *Science*, 339, 296-300.
[6] Chabot N.L. et al. (2014), *Geology*, 42, 1051-1054.
[7] Mazarico E. et al. (2011), *Icarus*, 211, 1066.
[8] Harmon J.K. et al. (1994), *Nature*, 369, 213-215.
[9] Harmon J.K. et al. (2001), *Icarus*, 149, 1-15.

VOLATILES IN LUNAR POLAR REGOLITH

M.L. Litvak
Spase Research Institute

The presence of volatiles in lunar polar regolith is considered from different points of view: origin, content, composition, access, processing, in situ analysis and sample return.

BASIN FORMATION ON MERCURY AND THE MOON – THE SAME OR DIFFERENT? INSIGHTS FROM NUMERICAL MODELING

R.W.K. Potter[1,2], J.W. Head[1,2],
[1]Department of Earth, Environmental and Planetary Sciences, Brown University, Providence, RI, 02912, USA; [2]NASA Solar System Research Virtual Institute
ross_potter@brown.edu

Introduction:

Like the Moon, a number of impact basins have been recognized on Mercury [1]. These observations, however, illustrate a paucity of large basins (greater than 500 km in diameter) on Mercury compared to the Moon. Basins on Mercury appear more degraded than their lunar counterparts, implying greater modification, relaxation, and/or erosion. [1] suggested this may be due to differences in the basin-forming process between Mercury and the Moon.

In this work, therefore, numerical modeling of Mercurian basin-forming impacts is undertaken with results compared to previous modeling of lunar basin formation (e.g., [2, 3]). Mercurian impacts comparable to Caloris, the largest Mercurian basin (~1500 km diameter [4, 5]) are modeled. This will concurrently allow insight into the post-dynamic form of Caloris basin, which has been heavily modified by volcanic and tectonic processes since its formation ~3.9 Ga. One unit within Caloris, exposed in crater walls and ejecta – Low-Reflectance Material (LRM) – is of specific interest. LRM may represent the original basin floor material [6] and may have a lower crustal and/or upper mantle composition [6]. The numerical models will be able to predict the composition of Caloris' basin floor material.

Methods:

The iSALE shock physics code (e.g., [7]) was used to numerically model Caloris-sized basin-forming impacts. iSALE has been used extensively to model basin-scale impact events (e.g., [2, 3]). Simulations used both halfspace and fully spherical targets divided into a 50 km crust [8] and 350 km mantle [9] on top of a core. Semi-analytical equations of state (ANEOS) for basalt [10], dunite [11], and iron [12] were used to represent the crust, mantle and core responses to thermodynamic and compressibility changes, respectively. Impact diameters of 50-250 km were considered along with impact velocities of 15-50 km/s. Cell size was 5 km. Two thermal profiles (based on [13]) estimating target conditions at the time of Caloris' formation were used.

Results:

Figure 1 illustrates the transient (a) and final (b) craters for a Caloris-sized impact (impactor diameter 100 km, impact velocity 42 km/s). The impact excavates crustal material from the basin center creating a large central zone of (partially and completely) molten mantle material. Mantle material extends to a distance of ~800 km from the basin center. Figure 1a demonstrates that to produce a basin the size of Caloris, its transient crater will not penetrate into Mercury's sizable core. Only impacts producing basins larger than Caloris penetrated into Mercury's core. There is, however, no evidence of basins larger than Caloris on Mercury [1], suggesting that, despite its size, Mercury's core does not affect the basin-forming process. This is reflected in the numerical models, where basin formation follows that predicted by models of lunar basin formation (see discussion).

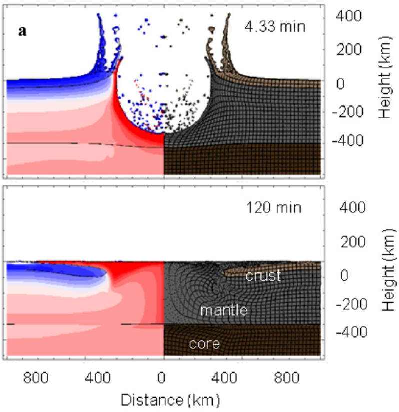

Fig. 1. A Caloris-sized impact event showing the tran-sient crater (a) and the final basin (b) structure. Left panels show temperature (blue is low, red is high); right panels show material (crust, beige; mantle, gray; core, brown). Impactor 100 km diameter, velocity 42 km/s.

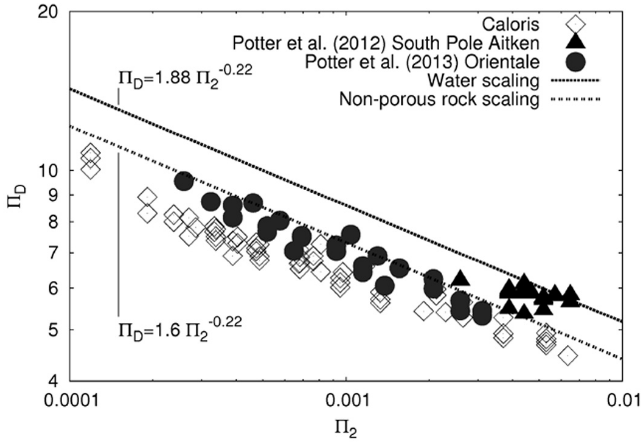

Fig. 2. Π_D as a function of Π_2. Π_D is a crater size measure defined as $D_{tc}/(M_i/\rho_t)^{1/3}$. Π_2 is a gravity-scaled impact size defined as 3.22 $g\ r_i/u^2$. D_{tc}: transient crater diameter; M_i: impactor mass; ρ_t: target density; g: surface gravity; r_i: impactor radius; u: impact velocity. Scaling laws from [15].

Discussion:

Basin formation. Pi-scaling relationships (e.g., [14]), which can be used to compare impacts of varying size, velocity, and target gravity, demonstrate that the Caloris-sized impacts are comparable to Orientale-sized impacts on to the Moon (Figure 2). These follow the scaling law for impacts into non-porous rock [15], which is expected given their relatively cool thermal gradients compared to older impacts into warmer targets (e.g., South Pole-Aitken, Moon). Excavation depth-to-diameter ratios for the Mercurian impacts (~0.12) were also comparable to those estimated for craters at a range of sizes through a variety of techniques (e.g., [2, 16, 17]). Mercurian basin-forming impacts appear to follow proportional scaling. Differences between the number and size of basins on Mercury and the Moon appears, therefore, most likely due to post-impact processes such as volcanism and tectonics.

Caloris. The numerical models suggest the floor of the Caloris basin will be primarily partially or completely molten mantle material. The LRM could, therefore, have originally had a mantle composition. The Caloris impacts produced melt volumes on the order of 10^7 km^3, agreeing with scaling estimates (e.g., [18]). This volume of material is likely to undergo differentiation [19] to form a lower density, crustal-like layer towards the surface. This could explain the discrepancy between the numerical models, which predict no crust at the basin center, and the ~20 km thick crust inferred from gravity data beneath Caloris today [8]. Other LRM-like, low albedo deposits have also been recognized around other large Mercurian impact basins [e.g., Rembrandt] and interpreted as impact melt [20]. A deep origin for the LRM also agrees with the interpretation that the LRM darkening agent is an intrinsic component of Mercury's crust and/or mantle [21]. A source depth of 30 km has been suggested [22] which further implies lower crust and, possibly, upper mantle.

References:

[1] Fassett, C. I. et al. (2012) *JGR*, 117, E00L08. [2] Potter, R. W. K. et al. (2012) *Icarus*, 220, 730-744. [3] Potter, R. W. K. et al. (2013) *JGR*, 118, 963-979. [4] Murchie, S. L. et al. (2008) *Science*, 321, 73-76. [5] Fassett, C. I et al. (2009) *EPSL*, 285, 297-308. [6] Ernst, C. M. et al. (2015) *Icarus*, 250, 413-429. [7] Collins, G. S. et al. (2004) *MAPS*, 39, 217-231. [8] Smith, D. E. et al. (2012) *Science*, 336, 214-217. [9] Hauck, S. A. et al. (2004) *EPSL*, 222, 713-728. [10] Pierazzo, E. et al. (2005) *GSA Spec. Pap.,* 384, 443-457. [11] Benz, W. et al. (1989) *Icarus*, 81, 113-131. [12] Thompson, S. L. and Lauson, H. S. (1972) Sandia Nat. Lab. Report SC-RR-71 0714. [13] Zuber, M. T. et al. (2010) *Icarus*, 209, 247-255. [14] Melosh, H. J. (1989) Impact cratering: A geologic process, New York, Oxford Univ. Press, 245 p. [15] Schmidt, R. M. and Housen, K. R. (1987) *Int. J. Imp. Eng.*, 5, 543-560. [16] Croft, S. K. (1980) *Proc. LPSC 11th*, 2347-2378. [17] Hikida, H. and Wieczorek, M. A. (2007) *Icarus*, 192, 150-166. [18] Abramov, O. et al. (2013) *Icarus*, 218, 906-916. [19] Vaughan, W. M. et al. (2013) *Icarus*, 223, 744-765. [20] Whitten J. L. and Head, J. W. (2015) *Icarus*, in press, doi:10.1016/j.icarus.2015.06.022. [21] Murchie, S. L. et al. (2015) *Icarus*, 254, 287-305. [22] Rivera-Valentin, E. G. and Barr, A. C. (2014) *EPSL*. 391, 234-242.

LUNAR ROBOTIC MISSIONS, AS PRECURSORS FOR MANNED LUNAR FLIGHTS

V.I. Tretyakov
Spase Research Institute

The goals and tasks are presented of the sequence of robotic lunar mission, as precursors for human Moon exploration.

NEW GENERATION LASER RETROREFLECTORS FOR THE MOON, MARS, PHOBOS AND DEIMOS

S. Dell'Agnello[1], G. DelleMonache, R. Vittori, A. Boni, E. Ciocci, M. Martini, G. Patrizi, M. Tibuzzi, G. Bianco, D. Currie, T. Murphy, J. J. Chandler, N. Intaglietta, L. Salvatori, C. Lops, S. Contessa, L. Porcelli, C. Mondaini, P. Tuscano, M. Maiello
[1]INFN-LNF, via E. Fermi 40, Frascati (Rome) 00044, Italy.
simone.dellagnello@lnf.infn.it

We will describe our research program (carried out in collaboration with ESA and ASI,) for lunar and other solar system mission based on innovative laser retroreflectors (including collaborations with IKI and Roscosmos):

1) The Moon as a laser-ranged test body for General Relativity

- Development and characterization of a next-generation passive LLR payloads based on the solid fused silica retroreflector technology, inheriting from Apollo, including a single, large CCR (Cube Corner Retroreflector), called "MoonLIGHT" and a microreflector payload, called "INRRI"
- Precision tests of General Relativity with MoonLIGHT CCRs, the ASI-Matera Satellite and Lunar Laser Ranging Station in Italy and a highly specialized lunar orbit tracking software (Planetary Ephemeris Program)

2) Laser retroreflectors for Mars exploration

Extension of Lunar program to Mars and its satellites

- Next generation Mars surface retroreflectors will include lightweight, passive and compact CCR array (of the INRRI type) laser-located by orbiters
- Multiple INRRIs on landers and rovers will establish a Mars Geophysical Network and define Mars Prima Meridian. INRRI will provide accurate geo-referencing of Rover exploration activity, Lidar atmospheric trace species detection; laser-communication test and diagnostics.
- Study and realization of PANDORA (Phobos AND DeimOs laser Retroreflector Array)

3) ILRS payload standards in Earth Orbits, as a reference for other solar system CCR payloads. This will includes support to Apollo and Lunokhod

4) Study of SCF_Lab upgrade to perform the precision time-of-flight laser "range correction" of the above CCRs in representative space conditions.

DYNAMICS OF THE INNER SOLID AND OUTER LIQUID CORES OF THE MOON FOR CHANGE-4/5, LUNA-25/26, ILOM PROJECTS

A. Gusev[1], H. Hanada[2], A. Kosov[3], J. Ping[4], O. Titov[5]
[1]Kazan federal University, Kazan, Russia;
[2]NAOJ, Mizusawa, Japan;
[3]IKI RAS, Moscow, Russia;
[4]NAOC CAS, Beijing, China;
[5]Geoscience Australia, Canberra, Australia.
alexander.gusev@mail.ru

Introduction

The problem of rotation of the multi-layer Moon will remain a central problem for selenodesy, selenodynamics and selenophysics. Its actuality increases with an increase of accuracy of different kind observations of the Moon. Now the laser ranging measurements of distances to the lunar reflectors achieves a millimetre level of accuracy. The LRO, GRAIL, ChangE-3/4, ILOM projects are focused on even more precision description of a gravitational field and physical librations of the Moon (with accuracy of determination of the main selenopotential coefficients up to 10^{-12}).

The orbit of the multi-layer Moon is inclined on $5{,}17^0$ to the ecliptic and regresses with an 18.6 year period. The rotation of the Moon is synchronous with the orbital motion (Cassini laws). The spin axis of the solid Moon is tilted with respect to the ecliptic and its precession is locked to the precession of the orbit (Peale, 1968). Goldreich (1967) demonstrated that a Lunar liquid core of low viscosity would not precess with the mantle. The spin axis of the lunar core is nearly normal to the ecliptic plane. If the Lunar core is locked to the mantle, then the spin axis of the core is nearly aligned with the symmetry of the core-mantle boundary.

If a spin axis of the core is slightly displaced from the configuration then the spin axis precesses about the symmetry axis with the core precessions period $P_{core} = P_{Moon}\cdot(C_m/C)\cdot(1/e_c)$, where P_{Moon} is the rotation period of the Moon, e_c is the core flattening , and (C_m/C) the ration of the polar moment of inertia of the Moon to that of the mantle. The core flattening is given by $e_c = (C_c - A_c)/C_c$, where A_c and C_c are a moments inertia of the core. If the mantle precesses faster than the core $P_m < P_c$, the core will not follow the mantle as is the today. If the precession period of the core is less than that of the mantle $P_m > P_c$ the core and mantle will precess together, with the core oscillating around the symmetry axis of the mantle. Locking occurs for core flattening larger than ratio P_{Moon}/P_{mantle}. In the limit of very small flattening, the rotation axis of the core is perpendicular to the ecliptic plane and fluid core of the Moon does not precess with the mantle (Meyer, 2011).

Our goal is to show how the milliarcsecond precision observations of lunar physical librations and lunar tides in the project ChangE-3/4-5/6, Luna-25/26 and ILOM: the optical telescopes or radio beacons on the Moon, or the long-term observations of the lunar satellite with high-precision camera and laser altimetry by differential, Inverse and Same Beam Interference (SBI) VLBI may be used for determining the parameters of liquid and rigid cores of the Moon. It is shown, that the analytical theory of physical libration of the Moon can be used as the convenient tool for carrying out of modeling of the future supervision from a lunar surface, for understanding of distinctions in lunar coordinate systems and carrying out of the approached estimations of changes in Moon dynamic characteristics.

Outer liquid and inner rigid core of the Moon

For a planet or moon with a solid inner core and a liquid outer core, there are four rotational normal modes. This numbers is reduced to two for a planet without inner core, and to one for a planet without liquid core (Dehant et al, 2003). The *Chandler Wobble* (CW), which is a motion of the rotation axis of the Moon around its dynamical figure axis due to the bulges of the Lunar body. The *Free Core Nutation* (FCN), which represents a differential rotation of the liquid core relatively the rotation of the mantle. The *Free Inner Core Nutation* (FICN), which represents a differential rotation of the rigid inner core relatively the rotation of the mantle. The *Inner Core Wobble* (ICW), which represents a differential rotation of the figure axis of the lunar inner core with respect to the rotation axis of the Moon. All type of modes are result of non-coincidence of rotation axes of mantle, outer and inner core.

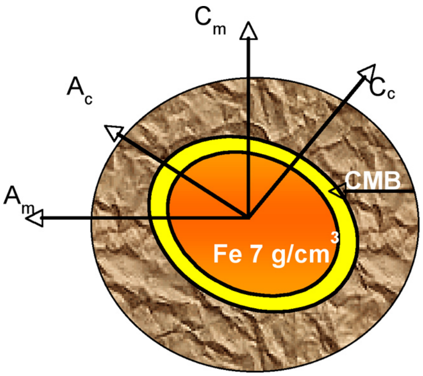

Fig. 1.

Williams et al. (2014) presented that the ratio of the polar liquid core moment to the total moment of inertia of the Moon C_c/C is $(3\div7)\cdot10^{-4}$ and CMB flattening $e_c = (2.46 \pm 1.4)\cdot10^{-4}$, which clearly demonstrates the existence of the fluid core for the Fe-FeS eutectic composition. The fluid rotation may be different from the rigid rotation. The free core rotation depend on the oblate shape, the flattening, of the outer core boundaries. Periods of FCN is 144 – 187 years for $e_c = (4.0 \div 5.17)\cdot10^{-4}$. The precession period is expected to be more 100 - 300 yrs. The inner core moment of inertia is $1.2\cdot10^{-4}$ of the full lunar moment of inertia. The three inner core modes are analogous to the mantle modes: a longitude libration, a wobble mode (ICW) and free precession (FICN). The model of normal mode calculation include periods and potential amplitudes.

The 240 km Fe inner core can be slightly oblate from spin and triaxle from tides. There are problems of relaxation for the hot lower mantle, CMB and flattening of inner core. The inner core rotation is expected to be synchronous on average, but a small variation in space would not precisely follow that of the outer core and mantle. An inner core of the Moon my be detected from its gravitational field (Williams, 2007) and/or from optical observation of the Lunar physical librations by small telescope on lunar surface (Hanada et al, 2012, ILOM project). Any non-spherical gravity field of inner core would cause a time variable gravity cos F and sin F components with the period P = 27.212 day for the coefficient C_{21} and S_{21}. Rotating the inner core gravity field into mantle frame gives small variable coefficient that depend on sin (I_m - I_{ic}). The difference I_m - I_{ic} depends on two torques: ones is between the Earth and inner core J_2 and C_{22} and second is the coupling between the inner core and the mantle (Williams et al., 2015). A non-spherical shape for the inner core and outer core boundaries can explain the discrepancy of small nonzero lunar gravity field coefficient S_{21} between LLR and GRAIL dates.

Tides on the Moon

Due to tides raised on the Earth, the Moon removed spiral at a speed of 38.08 mm/y, corresponding to an acceleration of the Moon's orbital mean longitude of – 25.82 ± 0.13 "/cent^2 (Williams, 2013). Tidal deformations of lunar surface are described by the sum of periodic terms. The maximum of **vertical tidal displacement** is characterized by amplitude about 100 mm and by anomalistic period in 27.555d (period of mean anomaly). Other significant tidel term has the period 27.212 d (period of node crossing of lunar orbit on ecliptic). Others tidal deformations of the elastic Moon with amplitudes about 10 mm are characterized by the periods in 1 and 1/2 months, and an amplitudes about millimeters are characterized by the periods: 1/3, 7 months, 1 year and 6 years. **Horizontal tidal** displacements of lunar surface are characterized by amplitudes approximately twice smaller in comparison with mentioned above. Solar tides on the Moon has amplitude 2 mm. The third harmonic gives tides with small amplitudes less than 1 mm. Polar (rotational) tide have the same order. The tidal bulge oscillates from east to west and north to south during each month. The Sun pertubes the lunar orbit causing major variations at periods of 2 weeks, 1 month, 7 months and 1 year. The argument of perigee precesses with a 6 year period and the node precesses in 18.6 years. Lunar tidal dissipation was detected at monthly and annual tidal periods (Williams et al., 2001). In the theory of tidal distortions of the Earth there is a resonance due to the flattening of the core-mantle boundary(CMB). This so-called Free Core Nutation Resonance to a 14 month retrograde free precession of the fluid core. The lunar core is much smaller than the Earth core, the rotation rate is less, the flattening of the CMB is less; the associated core precession period is 144yr in space coordinate system. For the Moon this resonance will occur at period that is slightly shorter than the sidereal periods of 27.322 days in lunar coordinate system. There is also a nearby dynamical resonance at 27.296 days that is associated with an 81 year retrograde free precession of the lunar mantle (Rambaux and Williams, 2011). Tidal periods other than 1 month are a particular interest for Love number k_2 and quality factor Q: 2 weeks, 7 months, 1 year and 6 years.

Study of influence of the Lunar two-layered core on its librations would require investigation of 1) values of dynamic and geometrical flattening of a liquid/rigid cores, as well as 2) estimation of geometrical flattening of the core-mantle boundary on the basis of solution of the Clairaut's differential equation for geometrical polar and equatorial compression under the influence of Lunar rotation and the Earth's tidal influence.

We have obtained geometrical flattening values as functions of distances from the center of the Moon and we determined the moments of inertia of the Moon's core. Description of the geophysical profile of the Moon is based on exact values of mass, radius and moment of inertia of the Moon. The given calculations coordinate with the numerical solution of Clairaut's equation published in (Zhang C. Z., 1994), being also close to estimations of parameters of geometrical and dynamic flattening at the core-mantle boundary received on the basis of LLR and GRAIL dates (Williams, 2014; 2015).

Perspectives

The new prospects for establishment of a liquid/rigid core existence and for studying its contribution in physical librations of the Moon, and also for direct studies of tidal and non-tidal "breath" of the Moon: variations of its shape, gravitational field and selenopotential coefficients will be opened. Differential radio and optical technologies have been proposed for measurements of Lunar physical librations and lunar tides. A new big size corner cubes reflectors (CCR) and a stable long-lived radio beacons would be desirable experiments on future lunar landers. Sensitivities to physical libration and tidal displacements would be enhanced by a broad geographical spread of the CCR, radio beacons, seismometers at ChangE-4/5/6, Luna-25,26,27, ILOM projects.

DEVELOPMENT OF THE GAS CHROMATOGRAPH – MASS SPECTROMETER TO INVESTIGATE VOLATILE SPECIES IN THE LUNAR SOIL FOR THE LUNA-RESURS MISSION

L. Hofer[1], P. Wurz[1], A. Buch[4], M. Cabane[2], P. Coll[3], D. Coscia[2], M. Gerasimov[5], D. Lasi[1], A. Sapgir[5], C. Szopa[2], M. Tulej[1],
[1]Physics Institute, University of Bern, Sidlerstrasse 5, 3012 Bern, Switzerland;
[2]LATMOS, Université Pierre et Marie Curie, 75252 Paris, France;
[3]LISA, Université Paris-Est Créteil, Université Denis Diderot & CNRS, 94010 Créteil, France;
[4]LGPM, Ecole Centrale Paris, 92295 Châtenay-Malabry, France;
[5]Space Research Institute, Profsoyuznaya 84/32, 117997 Moscow, Russia.
lukas.hofer@space.unibe.ch

Introduction

All lunar soil samples available on Earth originate from a restricted area at the lunar near side close to the equator. The Russian space agency Roskosmos will launch the spacecraft Luna-Resurs, which will be landing on the lunar South Pole. As part of the gas chromatographic mass spectrometric complex (GC-MS), which is dedicated to the analysis of the volatiles in the lunar soil, we combined our compact time-of-flight mass spectrometer (TOF-MS) with the advantages of chemical sample separation by gas chromatography (GC). This Neutral Gas Mass Spectrometer (NGMS) can also be operated as a standalone instrument for the analysis and monitoring of the tenuous lunar exosphere.

The Neutral Gas Mass Spectrometer

The Neutral Gas Mass Spectrometer (NGMS) is a time-of-flight type mass spectrometer (TOF-MS) [4]. Electron impact ionization is used to ionize the neutral gas. To achieve advanced performance a grid-less ion mirror (reflectron) is integrated in the ion path [3]. The ion optical design of NGMS is based on the P-BACE instrument [1].A TOF mass spectrometer allows the acquisition of complete mass spectra at once without the necessity of scanning over the mass range. These qualities are, combined with high sensitivity and a large dynamic range of up to 10^6 within 1s integration time, useful for continuous measurements as they are needed for the detection and analysis of the temporal separated species at the output of a gas chromatographic column (GC).

Experimental

A sample valve with a defined sample volume attached to it is used as an injection system to load a sample into the chromatographic column. Due to the individual interaction of each compound with the stationary phase of the gas chromatographic column, the sample is temporal separated to its components. At the GC output, NGMS is able to measure and analyse the gas chromatographic gas to its composition and molecular structure. Figure 1 shows the scheme of the GC-MS setup in the laboratory.

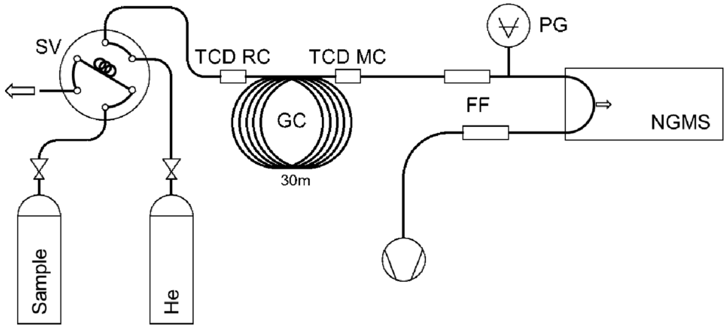

Fig. 1. Scheme of the laboratory GC-MS setup.

Laboratory prototype

The GC-MS concept was verified by performing GC-MS measurements with two different types of gas chromatographic columns and using the setup shown in Figure 1: One column is suitable for the separation of hydrocarbons and one for noble gas separation. Both gas chromatographic modules allow representative GC-MS measurements, since they are spare modules from the GC-MS instrument aboard the Phobos-Grunt mission.

Starting with relatively large sample volumes, the sample gas concentration was decreased until a detection limit for the prototype setup could be estimated. By taking into account the volume of the pyrolytic oven and assuming mean properties of the Moon's regolith, a detection limit of $2 \cdot 10^{-10}$ by mass was estimated for the detection of hydrocarbons and $2 \cdot 10^{-9}$ for noble gases [2].

Flight design

To test the GC-MS performance of the flight design of NGMS, the qualification model of the ion optical system was installed in a vacuum chamber. In contrast to the prototype setup, the gas chromatographic module, assembled with a column for noble gas separation, was placed in vacuum as well. Having both instruments together in the vacuum chamber allowed to have them as close together as possible and therefore using a transfer line as short as possible.

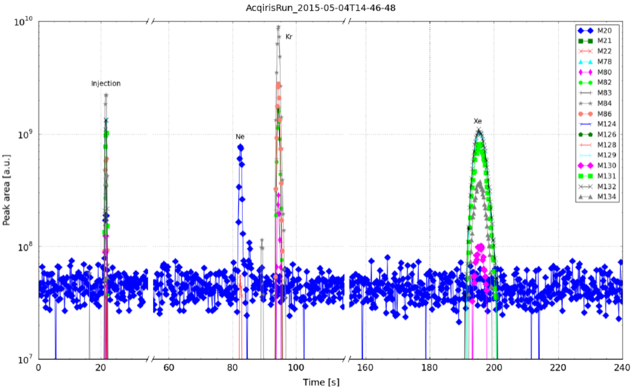

Fig. 2. Mass spectrometric data of a GC-MS measurement of noble gases, performed with the qualification model of the NGMS ion optical system.

Figure 2 shows the temporal evolution of selected mass lines belonging to noble gases, which were measured by the qualification model of the NGMS ion optical system at the columns output. Each time step corresponds to a full mass spectrum of 200ms integration time in a series of continuously recorded mass spectra. A sample gas containing each 100ppm of neon, krypton and xenon in helium was used together with a 25µl sample loop to perform this measurement. Prototype measurements showed that this sample volume might be at the detection limit of the instrument. As this figure shows clearly, the detection limit of the flight design is not yet reached. Taking into account the signal-to-noise ratios of the krypton and xenon peaks in the mass spectra, allows the estimation that the detection limit for the flight design of the NGMS ion optical system is $2 \cdot 10^{-11}$ by mass for krypton and $2 \cdot 10^{-10}$ by mass for xenon.

Summary and Conclusions:

Our compact time-of-flight neutral gas mass spectrometer (NGMS) was successfully combined with sample separation by gas chromatography. NGMS is able to record full mass spectra continuously at the gas chromatographic columns output with a dynamic range of 10^6 within 1s integration time. The GC-MS concept was successfully tested with our prototype instrument and the detection limit could be improved by one to two decades with the development of the flight design of the ion optical system.

References:

[1] D. Abplanalp, P. Wurz, L. Huber, I. Leya, E. Kopp, U. Rohner, M. Wieser, L. Kalla, and S. Barabash: A neutral gas mass spectrometer to measure the chemical composition of the stratosphere, Adv. Space Res. 44 (2009) 870–878.
[2] L. Hofer et al., Prototype of the gas chromatograph-mass spectrometer to investigate volatile species in the lunar soil for the Luna-Resurs mission, Planetary and Space Science, 111 (2015) 126-133.
[3] S. Scherer, K. Altwegg, H. Balsiger, J. Fischer, A. Jäckel, A. Korth, M. Mildner, D. Piazza, H. Rème, and P. Wurz, A novel principle for an ion mirror design in time-of-flight mass spectrometry, Int. Jou. Mass Spectr. 251 (2006) 73-81.
[4] P. Wurz, D. Abplanalp, M. Tulej, and H. Lammer, A Neutral Gas Mass Spectrometer for the Investigation of Lunar Volatiles, Planet. Sp. Science 74 (2012) 264–269.

PROPERTIES OF CRATER BOGUSLAWSKY IN APPLICATION TO PLANNED LUNAR INFRARED SPECTROMETER (LIS) MEASUREMENTS

A. Berezhnoy[1], A. Grumpe[2], N. Evdokimova[3], A. Fedorova[3,4], E. Feoktistova[1], A. Ivanov[3], Yu. Kalinnikov[5], K. Kapoor[2], O. Korablev[3], S. Mantsevich[3], A. Shapkin[3], V. Shevchenko[1], A. Stepanov[6,3], C. Wöhler[2], and LIS Team (A. Kiselev, A. Basilevsky, Yu. Skorov, D. Bisikalo, Yu. Velikodsky, L. Starukhina, U. Mall, J. Flahaut, S. Barabash, N. Bowles, J.-P. Bibring, M. Gerasimov, R. Kuzmin, Yu. Kalinnikov, A. Titov, N. Vyazovetskiy, P. Moiseev, A. Victorov, A. Bondarenko, I. Dokuchaev)

[1]Sternberg Astronomical Institute, Moscow State University, Universitetskij pr., 13, Moscow, 19991 Russia;
[2]Image Analysis Group, TU Dortmund University, Dortmund, Germany; [3] Space Research Institute, Profsoyuznaya Street, 84/32, Moscow, 117342 Russia;
[4]Moscow Institute of Physics and Technology (MIPT), 9 Institutsky dr., Dolgoprudniy, Moscow region, 141700 Russia;
[5]National Research Institute for Physicotechnical and Radio Engineering Measurements, Mendeleevo, 141570 Russia;
[6]Faculty of Physics, Moscow State University, GSP-1, Leninskiye Gory, Moscow, Russia. ber@sai.msu.ru

Introduction:

The Lunar Infrared Spectrometer (LIS) is an experiment onboard the Russian surface missions Luna-Glob (Luna 25) and Luna-Resource (Luna 27). It is a pencil-beam spectrometer to be pointed by a robotic arm of the landing module. The field of view (FOV) of the instrument of 1° is co-aligned with the FOV (45°) of a stereo TV camera. The spectral range of LIS corresponds to 1.15-3.3 μm. It is planned to study selected surface areas with LIS. The spectral selection is carried out by an acoustooptic tunable filter (AOTF), which scans the spectral range sequentially. Electrical command of the AOTF allows for selecting the spectral sampling and permits a random access if needed.

One of the most impressive results of recent Moon studies has been the discovery of water and/or hydroxyl in the surface layer. The Moon Mineralogy Mapper (M^3) spectrometer onboard Chandrayaan-1 with its spectral range of 0.42-3.0 μm [1] discovered that significant part of the lunar surface contains H_2O/OH-bearing material [2]. The M^3 results are in line with earlier lunar observations made in 1999 with the VIMS optical spectrometer of the Cassini spacecraft and are confirmed by new SIM/Deep Impact mapping spectrometer observations [3]. M^3 was the first spectrometer which carried out systematic mapping of the Moon in the IR and showed that the hydrated mineral band at about 3 μm is widely spread, especially at the polar regions [2]. The IR measurements detected H_2O and/or OH in the thin (few microns) surface layer of the Moon regolith.

The primary goal of the LIS experiment is to detect the regolith hydration at 3 μm, to identify its form from the shape of the spectrum, and to follow its changes during the day/shadow pattern. LIS will also allow for studying the mineralogical composition from mineral spectral signatures within the spectral range and will be used for identifying samples on the surface to be analyzed by other instruments. The crater Boguslawsky was selected as a primary landing site for Luna-Glob mission. For this reason we performed a detailed study of this crater.

Status of LIS development:

At present a qualification model (QM) of LIS (see Fig. 1) is passing QM tests, including thermal tests [4].

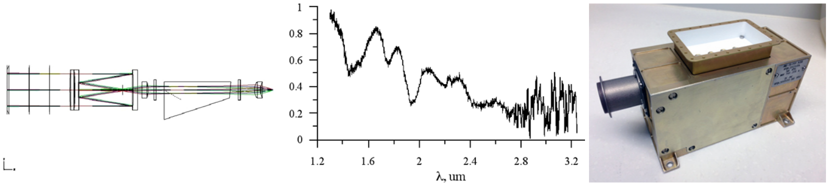

Fig. 1. LIS optical scheme (left); measured spectrum of gypsum, normalized to the source of light (middle); LIS qualification model (right).

Temperature regime and OH content in crater Boguslawsky:

The M³-based approach in [5] to estimating the lunar surface temperature tends to compensate the M³ reflectance spectra only incompletely for thermal emission in the presence of strong OH absorptions [5]. The lunar surface temperature strongly dependends on the local topography. We thus constructed a digital elevation model (DEM) of the crater Boguslawsky of high lateral resolution by combining GLD100 stereo data [6] and M³ spectral radiance data based on the method described in [7, 8]. Then the thermal equilibrium based temperature estimation method introduced in [9] was applied, where the Hapke model [10, 11] was used for describing the surface reflectance, and an iterative adaptation of the surface temperature and the thermally corrected M³ spectral reflectance was performed. For the Boguslawsky region, we estimated the surface temperature based on M³ data acquired at local lunar morning and midday time (about 82 and 223 hours after sunrise, respectively) (Fig. 2a and d). As a proxy for the OH absorption depth we used the R_{2657} / R_{2817} reflectance ratio (Fig. 2b and e).

Furthermore, we applied the two-layer model of [12], which assumes the presence of an insulating surface layer of 2 cm thickness with low thermal conductivity above a higher-conductivity second layer. In a raytracing-based approach, the direct and indirect solar flux (the latter depending on the relative orientations between surface elements inferred from the LOLA DEM [13]) and the internal thermal flux were taken into account to solve the one-dimensional time-dependent heat diffusion equation. The obtained results (Fig. 2c and f) indicate crater floor temperatures typically higher by about 10-15 K than the M³-based method. A detailed analysis of the differences between the surface temperature estimation methods will be a focus of our future work.

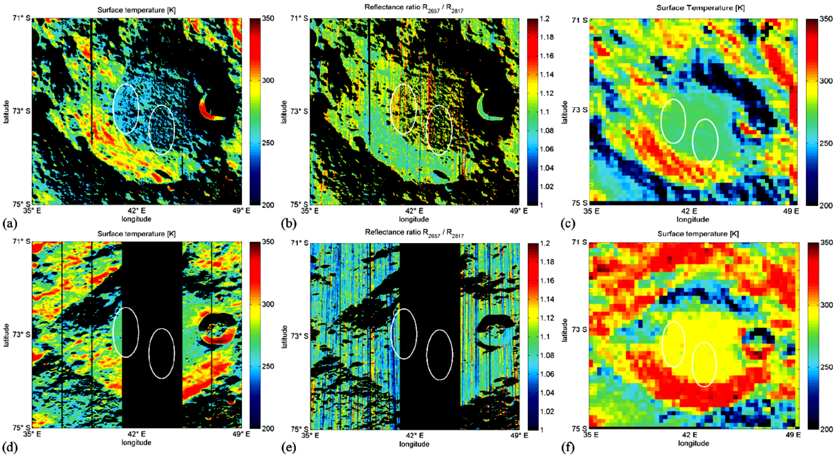

Fig. 2. (a)-(c) M³-based surface temperature estimation, OH absorption depth, raytracing-based temperature estimation under local morning illumination and (d)-(f) midday illumination. Black: missing data. Landing ellipses according to [14].

In the lunar morning, the OH absorption of the flat crater floor is stronger than that of the warmer southwestern wall inclined towards the sun (Fig. 2b). At midday, the strength of the OH absorption does not show a clear dependence on the topography and is significantly lower than the average morning level (Fig. 2e). This observation of a daytime-dependent OH absorption depth suggests an origin of the OH from the adsorption of solar wind protons by the surface material, a process e.g. proposed in [15].

References:

[1] Pieters C.M., Boardman J., Buratti B. et al. The Moon Mineralogy Mapper (M³) on Chandrayaan-1, Current Science, Vol. 96, No. 4, pp. 500-505, 2009
[2] Pieters C.M., Goswami J.N., Clark R.N. et al. Character and Spatial Distribution of OH/H_2O on the Surface of the Moon Seen by M3 on Chandrayaan 1, Science, Vol. 326, No. 5952, pp. 568-572, 2009
[3] Sunshine J.M., Farnham T.L., Feaga L.M. et al. Temporal and Spatial Variability of Lunar Hydration as Observed by the Deep Impact Spacecraft, Science, Vol. 326, No. 5952, p. 565, 2009
[4] Mantsevich S.N., Korablev O.I., Kalinnikov Yu.K., Ivanov A.Yu., Kiselev A.V. Wide-aperture TeO2 AOTF at low temperatures: Operation and survival, Ultrasonics, accepted
[5] Clark N.C., Pieters C.M., Green R.O., Boardman J.W., Petro N.E. Thermal removal from near-infrared imaging spectroscopc data of the Moon, Journal of Geophysical

Research, Vol. 116, E00G16, 2011
[6] Scholten F., Oberst J., Matz K.-D., Roatsch T., Wählisch M., Speyerer E.J., Robinson M.S. et al. GLD100: The near-global lunar 100 m raster DTM from LROC WAC stereo image data, Journal of Geophysical Research, Vol. 117, E00H17, 2012
[7] Grumpe A., Wöhler C. Recovery of Elevation from Estimated Gradient Fields Constrained by Digital Elevation Maps of Lower Lateral Resolution, ISPRS Journal of Photogrammetry and Remote Sensing, Vol. 94, pp. 37-54, 2014
[8] Grumpe A., Belkhir F., Wöhler C. Construction of lunar DEMs based on reflectance modelling. Advances in Space Research, Vol. 53, No.12, pp. 1735-1767, 2014
[9] Shkuratov Y., Kaydash V., Korokhin V., Velikodsky Y., Opanasenko N., Videen G. et al. Optical measurements of the Moon as a tool to study its surface, Planetary and Space Science, Vol. 59, pp. 1326-1371, 2011
[10] Hapke B. Bidirectional reflectance spectroscopy: 3. Correction for macroscopic roughness, Icarus, Vol. 59, No. 1, pp. 41-59, 1984
[11] Hapke B. Bidirectional reflectance spectroscopy: 5. The coherent backscatter opposition effect and anisotropic scattering, Icarus, Vol. 157, No. 2, pp. 523-534, 2002
[12] Mitchell, D.L., de Pater I. Microwave Imaging of Mercury's Thermal Emission at Wavelengths from 0.3 to 20.5 cm. Icarus, Vol. 110, pp. 2-32, 1994
[13] Smith D.E., Zuber M.T., Neumann G.A. Initial observations from the Lunar Orbiter Laser Altimeter (LOLA). Geophysical Research Letters, Vol. 27, L18204, 2010
[14] Hiesinger H., Ivanov M., Pasckert J.H., Bauch K., van der Bogert C.H. Geology of the Lunar Glob landing sites in Boguslawsky crater, Moon, LPSC XXXXV, abstract #2370, 2014
[15] McCord T.B., Taylor L.A., Combe J.-P., Kramer G., Pieters C.M., Sunshine J.M., Clark R.N. Sources and physical processes responsible for OH/H2Oin the lunar soil as revealed by the Moon Mineralogy Mapper (M^3), Journal of Geophysical Research, Vol. 116, E00G05, 2011

THE OBJECTIVES OF THE RADIOSCIENCE EXPERIMENT IN LUNA-RESOURCE AND LUNA-GLOB SPACE PROJECTS

V.D. Gromov, A.S. Kosov
IKI RAS, 84/32Profsouznaya, Moscow, Russia. vgromov@iki.rssi.ru

Introduction:

Measurements of the Doppler shift of a radio signal from a spacecraft, along with interferometric location of angular position of the radio source, achieves nowdays a very high accuracy. It permits to use them not only for orbit determinations, but also for sophisticated research of mass and gravity effects. A last decade demonstrated an impressive progress in these investigations [1-3]

It is a frequently situation when achievement of some high level of accuracy of measurements produces a break-through in science, like it was with plentiful exoplanet detections due to progress in photometric accuracy, or with determination of most fundamental parameters of Universe due to achievement by the Radioscience community of an accuracy ~10^{-6} in measurements of intensity of the Cosmic Microwave Background [4-6]. In space Doppler measurements the accuracy is approaching to 10^{-8} (better than 0.03 mm/sec).

Radioscience Measurements in Lunar Missions and Accuracy Limitation Factors:

Orbital Doppler Measurements.

Instrument uncertainties of Doppler measurements are linked with instability of local oscillators and thermal noises of radio receivers. For the ground based stations for space communications, there is an additional source of errors, fluctuations of signal delay in Earth troposphere and ionosphere. Decreasing of the ionospheric errors could be reached by increasing of the carrier frequency, particularly by a transition from X-band to Ka-band. Doppler measurements on orbit of the Moon entirely exclude the Earth environment effects. Therefore the orbiter's Ka-band receiver can measure acceleration with high accuracy. The acceleration variations are related to deviations of Luna's gravitation field. Precise measurements of Lunar gravity was made in GRAIL experiment [2, 3] using two orbiters. The accuracy of the Lander-Orbiter experiment could be better, but a coverage of the Lunar surface is more restricted.

VLBI Interferometry.

Very Long Base Interferometry is a traditional tool for precise measurements of a descent/lander probe position since the Vega mission [7, 8]. An extended VLBI network permits to measure the Lander's position with high accuracy in X-band in spite of tropospheric and ionospheric errors.

Same Beam Interferometry (SBI).

Accuracy of Radioscience measurements is enough to reveal GR deviation from Newton theory. More and more precise determination of the GR effects gives the tests for comparison of GR with other theories of gravity.

Scientific phenomena, for which investigations the Radioscience is a most fruitful tool:

Orbital and rotational movement of the Earth and the Moon.

A movement of lunar probes is determined by positions of Earth, Moon and other Solar System bodies. Precise measurements of probe velocities and positions gives information for improvement of the reference frames for the Earth and the Moon, for better lunar rotation dynamics, lunar orbit, and lunar ephemeris, incorporating the numerous Newtonian perturbations as well as the much more subtle relativistic phenomena, which are all used for spacecraft missions.

Mass distribution and possible internal movements in the Moon's interior.

A movement of orbital probe is sensitive to subsurface mass concentration. A movement of lander probe reflects rotation of the Moon's body, revealing its precession, nutation and wobbling, which are dependent on the moments of inertia of the whole Moon and the structure of its core (inner core and outer core).

General Relativity (GR) effects.

Accuracy of Radioscience measurements is enough to reveal GR deviation from Newton theory. More and more precise determination of the GR effects gives the tests for comparison of GR with other theories of gravity.

Scientific Perspectives for Lunar Radioscience Experiments:

An accuracy of acceleration measurements in the Lander-Orbiter experiment [9] coud be about 3-10 mGal, two times better than in GRAIL experiment. The area of these measurements is restricted by distance approximately equal to a value of height *H* of an orbit.

The altitude distribution of the gravity potential *V* of the Moon could be written using an expansion in harmonics:

$$V = \frac{GM}{R+H}\left[-1+\sum_{n=2}^{m}\left(\frac{R+H}{R}\right)^{-n} P_n(\lambda,\Theta)\right]$$

where *G* is the gravitational constant, *M* and *R* are the mass and the radius of the Moon, λ and θ are longitude and latitude on the Lunar surface, P_n are sums of the *n*-th degree Legendre polynomials with coefficients to be defined from measurements for the definition of the nonuniformity of the Lunar gravity field picture. The maximum degree m of the expansion is inversely proportional to the spatial resolution ΔL of the picture. To a value ΔL ~ 10 km corresponds m ~ 500. The equation demonstrates so strong damping with altitude of the high resolution details, that measurements with resolution ΔL needs an orbit with *H* ~ ΔL, which reduces a measurement area diameter to ~2*H*.

The scientific perspectives of the experiments depend on accuracy of resulting scientific values, obtained after experimental data reduction using a quantitative (digital) model of the physical phenomenon. A model is also necessary for the choice of the experiment configuration (orbit and so on) due to contradictory requirements to some configuration parameters, as was shown above. These scientific models are under development by the Radioscience Experiment Team.

References:

1. Konopliv, A. S., S. W. Asmar, et al. (2011). Icarus, 211: 401
2. Konopliv, A. S., R. S. Park, et al. (2014). Geophysical Res. Lett. 41: 1452.
3. Williams, J., A.S. Konopliv, et al. (2014). J. Geophys. Res.: Planets. 119: 1546.
4. Strukov, I., A. Kosov, et al. (1996). Examining the Big Bang and Diffuse Background Radiations. M. C. Kafatos (ed). 168: 45.
5. De Bernardis, P., P. A. R. Ade, et al. (2000). Nature. 404: 955.
6. Smoot, G. (2007). Rev. of Modern Phys. 79: 1349.
7. Sagdeev, R. Z., V. V. Kerzhanovitch, et al. (1992). Astronomy and Astrophys. 254: 387.
8. Linkin, V. M., A. S. Kosov, et al. (2009). European Planetary Science Congress 2009: 376.
9. Kosov, A. S. (2015). This simposium.

PERSPECTIVES AND PLANS OF ESA/ROSCOSMOS COOPERATION ON ROBOTIC LUNAR MISSIONS

B. Houdou,
ESA

The content of ESA/Roscosmos cooperation will be presented for future robotic missions Luna-Glob, Luna-Resourse and Lunar Polar Sample Return.

MOON IS OUR SEVENTH CONTINENT: WILL IT EVER BE INHABITED?

I.G. Mitrofanov
Spase Research Institute

The strategy of Moon exploration is considered taking into account the current knowledge on lunar resources and lunar opportunities for physics, astronomy and long-distance space flights.

PHYSICAL AND THERMAL CONSTRAINTS ON THE MODELS OF PARTIALLY DIFFERENTIATED TITAN

A.N. Dunaeva, V. Kronrod, O. Kuskov
Vernadsky Institute of Geochemistry and Analytical Chemistry, Russian Academy of Sciences, Kosygin Str., 19, 119991 Moscow, Russia.
dunaeva.an@gmail.com

Introduction:

In this paper, the models of partially differentiated Titan with outer water-ice shell, rock-ice mantle and innermost silicate core were discussed for the range of normalized moment of inertia (I/MR^2) of 0.31-0.36. It has been shown that for the predicted values of the satellite's heat fluxes of 5-7 mW/m^2 the rock-ice mantle could exist if the satellite's moment of inertia factor lies within the limits of $0.312<I/MR^2<0.348$-0.353. Beyond the scope of these constraints (for the moment of inertia and for the heat flux values) the satellite can't be described in the terms of undifferentiated model.

Problem description: The study and interpretation of the Cassini's spacecraft data have led to the new results in the assessment of the Titan's gravity field, rotation state (obliquity) and the features of surface topography. In particular, the originally measured Titan's axial moment of inertia factor (I/MR^2) was found to be 0.342 [1]. This value is intermediate between the moments of inertia of the similar space objects such as the large icy satellites of Jupiter - Ganymede ($I/MR^2 = 0.3105$) and Callisto ($I/MR^2 = 0.3549$).

Numerous theoretical models of the Ganymede and Callisto internal structure suggest that Ganymede has passed through the stage of fully differentiation with separation into outer water-ice shell, silicate mantle and central metallic Fe-FeS core [2]. Callisto, by contrast, is only partially differentiated, and consists of an extensive rock-ice area (mantle) lying between the outer water-ice shell and the inner rock-iron core [3].

Titan's moment of inertia gives no way to make a firm conclusion about its internal structure based on the analogy with the structure of Callisto and Ganymede. In addition, the value $I/MR^2 = 0.342$ was calculated assuming that Titan is in hydrostatic equilibrium. Meanwhile, the degree-three spherical harmonic coefficients in the Titan gravity field approximation [1] as well as the long wavelength topography [4] indicate that Titan deviates from the hydrostatic state that reduces, consequently, the accuracy of obtained I/MR^2 estimations. Supposedly, the uncertainty in the moment of inertia calculation caused by the non-hydrostatic effects, is about 10% [5], resulting in the scatter in the true values of I/MR^2 in the range of $0.32 <I/MR^2 <0.355$ [6].

In this paper, the models of the Titan internal structure for I/MR^2 varying from 0.31 to 0.36 were considered. This allows to take into account uncertainty in I/MR^2 experimental measurements, and also to assess the influence of the moment of inertia value on extent of satellite's differentiation.

Computer simulation and results: Within the proposed model, Titan was assumed to consist of three major structural domains: the outermost water-ice shell, intermediate rock-ice mantle and the rock-iron core. The satellite's rock-ice mantle was modeled on the assumption about the existence of the global convection in the mantle reservoir. In all calculations, the Titan's central rock-iron core was assumed to be uncompressible with predetermined density of 3.62 g/cm^3. The density of the rock-iron component in the rock-ice mantle was chosen in the range typical for the chondritic substance taking into account probable hydration of silicates – from 3.15 to 3.62 g/cm^3 [7].

The influence of Titan's moment of inertia on the extent of satellite's differentiation. The results of model calculations of the Titan internal structure for the different moment of inertia values from 0.31 to 0.36 are shown in Fig. 1. It is evident from the figure that the rock-ice mantle in Titan can exist in a wide range of the satellite's moments of inertia: from values close to 0.36 (the structure is similar to partially differentiated Callisto) to a value of 0.31 (the structure is similar to the fully differentiated Ganymede without a central Fe-FeS core). When the satellite moment of inertia increases toward the limiting values of $I/MR^2 \sim 0.4$ corresponding to entirely homogeneous body, the satellite will be totally built from the ice-rock mixture (inner rocky core and water-ice shell are nearly absent). With the decreasing of the moment of inertia (for example, as a result of satellite's structural evolution) the sizes of an inner rocky core and an outer water-ice shell are synchronously increasing, while the rock-ice mantle gradually decreasing and completely thinning out at $I/MR^2 = 0.312$. This value is the minimum moment of inertia, below which the presence of the satellite rock- ice mantle is ruled out.

Another important consequence to the performed calculations is the constraints on the thickness of Titan's water-ice shell and on the radius of its inner core, prescribed by the satellite moment of inertia (Fig. 1 and 2). Figure 1 shows that the moment of inertia determines only the maximum thickness of the H_2O-shell, while its structure and the phase composition are mainly governed by the T-P conditions in the icy crust.

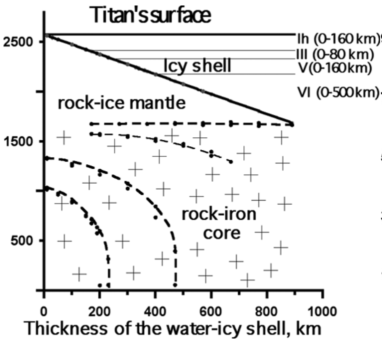

Fig. 1. Titan' internal structure with rock-ice mantle and without internal ocean. Dotted lines - the core-mantle boundary (core radius) for different values of the normalized moment of inertia I/MR2 (shown by digits).

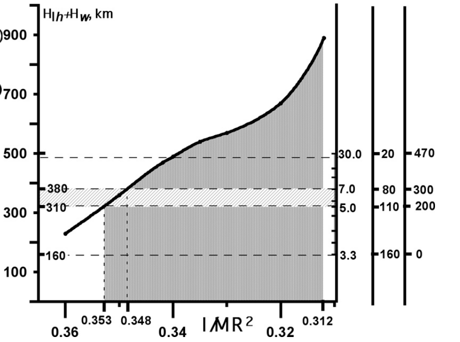

Fig. 2. The maximum permissible thickness of the Titan water-ice shell inferred from the different moments of inertia values (solid line) and the minimum permissible thickness of the H2O-shell (HIh+Hw) calculated from the Titan's heat flux values (dotted lines).
Shaded field - the Titan's features at the modern heat fluxes. Grey field - the area in which the Titan models with rock-ice mantle could exist within the constraints of the satellite's moments of inertia and the heat fluxes.

Model constraints inferred from the Titan heat flux: Long-term observations of Titan during Cassini mission lead to hypothesis of the possible existence of a deep ocean within the satellite's water-ice shell [1, 4]. It has been shown earlier [8] that the formation of such an ocean is possible if a value of heat flow through the ice crust exceed 3.3 mW/m^2. Importantly, heat flux (F) uniquely defines the depth of the ocean (H_w) and the thickness of the outer I*h*-crust (H_{Ih}). Thus, at the modern heat fluxes of 5-7 mW/m^2 [9, 10] the ice crust is 80-110 km, and the ocean depth is 200-300 km (Fig. 2). The total thickness of the outer I*h*-crust and internal ocean ($H_{Ih} + H_w$) is an important parameter to determine the stability of Titan's ice-rock mantle. The ($H_{Ih} + H_w$) value is constant for every individual value of heat flux, and remains an independent constraint on the minimum thickness of the water-ice shell permitted in the satellite. Thus, to obtain an adequate model of partially differentiated Titan, the minimum thickness of its water-ice shell determined from the heat flux values must not exceed the maximum allowable thickness of the H_2O-shell, calculated from the moment of inertia. Otherwise, the mantle's icy component will melt (in accordance with the water phase diagram), resulting in a physical inconsistent model.

In Fig. 2 the permissible maximum (from the moments of inertia) and the minimum (from heat fluxes) values of the Titan H_2O-shell were plotted. It was shown that for F=5-7 mW/m^2 the thickness of the outer water-ice shell can't be less than 310-380 km. At the same time, for the satellite's moments of inertia exceeding values of 0.348-0.353, the largest possible thickness the H_2O-shell is significantly lower (230 km at the point of 0.36). Thus, $I/MR^2 = 0.348\text{-}0.353$ corresponds to the maximum value of the Titan moment of inertia, beyond which the satellite rock-ice mantle doesn't exist.

Combining these results, the main conclusion can be formulated as: at the Titan heat flux of 5-7 mW/m^2 its undifferentiated rock-ice mantle could exist when the satellite moment of inertia is equal to $0.312<I/MR^2<0.348\text{-}0.353$. Within this I/MR^2 limits the maximum thickness of the water-ice shell can reach of about 900 km, the maximum size of the inner core does not exceed 1700 km. The thickness of the outer ice Ih-crust is H_{Ih} = 80-110 km, the depth of the internal ocean is H_w = 200-300 km.

This research was supported by the RFBR grant 15-05-02572.

References:

[1] Iess L. et al. // Science, V. 337(6093), pp. 457-459, 2012.
[2] Kuskov O.L., Kronrod V.A. // Icarus. V. 151. pp. 204–227, 2001.
[3] Kuskov O.L., Kronrod V.A. // Icarus. V. 177. pp. 550–569, 2005.
[4] Hemingway et al. // Nature, V. 500(7464), 550-552, 2013.
[5] Gao P., Stevenson D.J. // Icarus. V. 226. No. 2. pp. 1185-1191, 2013.
[6] Lefevre A. et al. // Icarus. V. 237. pp. 16-28,2014.
[7] Kronrod V.A., Kuskov O.L. // Geokhimiya, № 9, pp. 968-983, 2003.
[8] Dunaeva et al. // Doklady Earth Sciences, Vol. 454, Part 1, pp. 89–93, 2014.
[9] Lorenz R.D. // Icarus. V. 156. No. 1. pp. 176-183, 2002.
[10] Mitri G., Showman A. // Icarus. V. 193. pp. 387–396, 2008.

RADIATION HAZARD FOR DIFFERENT SCENARIOS OF SPACE MISSIONS TO JUPITER'S MOONS

M.V. Podzolko, I.V. Getselev, Yu.I. Gubar
D. V. Skobeltsyn Institute of Nuclear Physics, M. V. Lomonosov Moscow State University, Leninskie gory 1(2), GSP-1, Moscow, 119991, Russian Federation.
spacerad@mail.ru

In the next decade world space agencies, including Russian Federal Space Agency (Roscosmos), plan to send the research missions to large satellites of Jupiter. The particular conditions of missions to the system of Jupiter are very high levels of energetic particle fluxes in its magnetosphere and location of the orbits of three large Jupiter's satellites: Io, Europa and Ganymede inside its radiation belts.

Till the present day several flybys of NASA spacecraft near Jupiter have been performed, and the mission of the first and only Jupiter's artificial satellite Galileo, which made 35 high-elliptical circuits in the orbit around Jupiter in 1995–2003. The future missions propose different scenarios: the flight in the elliptical orbit around Jupiter with the flybys near its large satellites ("Juno", "Europa Clipper"), entering the low-altitude orbit around one of Jupiter's large moons and landing to its surface ("JUICE", "Laplace").

In the current study estimates of radiation conditions for different scenarios of missions to Jupiter's moons are given and ways of minimizing the radiation hazard are suggested.

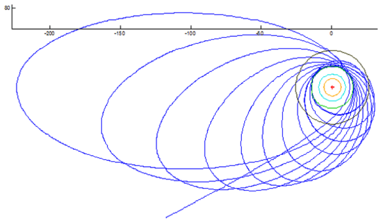

Fig. 1. Trajectory of gravity assists in the system of Jupiter for entering the orbit around Ganymede with relatively low radiation risk: the dose behind 2.2 g/cm^2 Al, equal to the shielding of Galileo spacecraft, for this trajectory is less than 10 kilorad. Orbits of Galilean moons: Io, Europa, Ganymede and Callisto are also shown.

SCIENTIFIC BALLOONING ON JUPITER AND OTHER OUTER PLANETS

V.M. Linkin, A.N. Lipatov, V.S. Makarov, A.P. Ekonomov
Space Research Institute

After the successful experiment with helium balloon on Venus, it is interesting to consider a similar experiment on the outer planets, such as Jupiter. The problem is complicated by low-molecular-weight of the atmosphere, consisting of 80% hydrogen and 20 % helium. The only candidate on the lifting gas is pure hydrogen. Calculation shows that it is possible to implement this balloon for the flight at a height corresponding to a pressure of 10 bar and a temperature of 50 C. So the radius of the spherical envelope shall be more than 2 m when made of 10 micron PBO film. This level corresponds to the undercloud atmosphere. You can also calculate the flight above a cloud layer. In this case, the radius must be more than 10 meters. Usually recommended Montgolfiere has a serious start problem when there is no solid surface. This problem is absent for aèrobot on Titan, but in this case helium balloon are also competitive.

LIFE IN THE SUBGLACIAL ANTARCTIC LAKE VOSTOK: FIRST RESULTS WITH BOREHOLE-FROZEN LAKE WATER

S. Bulat[1], M. Khilchenko[1], D. Karlov[1], M. Doronin[1], D. Marie[2]
[1]Petersburg Nuclear Physics Institute, NRC “Kurchatov Institute”, St. Petersburg-Gatchina, Russia;
[2]Station Biologique de Roscoff, Roscoff Cedex, France.
bulat@omrb.pnpi.spb.ru

The objective was to search for microbial life in the subglacial Lake Vostok (buried beneath 4-km thick East Antarctic ice sheet) by studying the accretion ice (naturally slowly frozen lake water) as well uppermost water layer entered the borehole upon lake entry (February 5, 2012) and then shortly got frozen within. The latest samples included the drillbit water frozen on a drill bit upon lake enter along with re-drilled borehole-frozen water ice.

The comprehensive analyses (constrained by Ancient DNA research criteria) showed that the accretion ice in general contains the very low microbial biomass. The only ice containing mica-clay inclusions (type I) allowed the recovery of few bacterial phylotypes all passing numerous contaminant controls. They included well-known chemolithoautotrophic thermophile *Hydrogenophilus thermoluteolus* (β-*Proteobacteria*), actinobacterium related to *Ilumatobacter fluminis* (95% similarity) along with unidentified unclassified bacterium AF532061 (92% similarity with closest relatives). In contrast, the deeper accretion ice (type II) with no sediments present gave no reliable signals.

As for the first lake water samples all they proved to be contaminated with drill fluid. The drillbit water was heavily polluted with drill fluid (at ratio 1:1) while borehole-frozen water samples were rather cleaner but still contained numerous micro-droplets of drill fluid. The cell concentrations measured by flow cytofluorometry showed 167 cells per ml in the drillbit water sample and 5.5 - 38 cells per ml in borehole-frozen samples.

DNA analyses came up with total 49 bacterial phylotypes discovered by sequencing of different regions of 16S rRNA genes. Of them only 2 phylotypes successfully passed all contamination criteria. The 1st remaining phylotype w123-10 proved to be hitherto-unknown type of bacterium showing less than 86% similarity with known taxa. Its phylogenetic assignment to bacterial divisions was also unsuccessful except it showed reliable clustering with the above mentioned unidentified bacterium detected in accretion ice. The 2nd phylotype is still dubious in terms of contamination. It showed 93% similarity with *Janthinobacterium sp* of *Oxalobacteraceae* (*Beta-Proteobacteria*) – well-known ‘water-loving’ bacteria. No archaea were detected in lake water frozen samples.

Thus, the unidentified unclassified bacterial phylotype w123-10 along with another one (AF532061) might represent ingenious cell populations in the subglacial Lake Vostok. The proof may come with farther analyses of cleanly collected lake water.

STUDIES OF COMETS AND PROBLEMS OF COSMOCHEMISTRY

V.A. Dorofeeva
Vernadsky Institute or Geochemistry and Analytical chemistry,
Russian academy of Science, ul. Kosygina 19, Moscow, 117975, Russia.
dorofeeva@geokhi.ru

Comets are the most primitive bodies of the Solar System available for studies at the present time. Therefore their component and isotopic composition is the main source of cosmochemical information about the composition of the matter of the early Solar System and the processes of its subsequent differentiation. Comets consist of a mixture of refractory component (rock and CHON) and ices of different gases, mainly H_2O, with mass ratio ~ 50:50. Formation of comets, both long-period and shot-period, is associated with regions distant from the Sun – the trans-Neptunian region and the Kuiper belt, respectively. According to current views, in these regions, temperature was ~ 20K, and $P \sim 10^{-9}$ - 10^{-7} bar, therefore the composition of the matter of comets includes all volatile components of nebula, including N_2, CO and inert gases. The major components of the comet's substance are organic compounds, that have, as a rule, presolar origin. They may have been necessary components for the origin of biological life, on the Earth and not only.

Main cosmochemical problems, which can be solved only with the use of data on composition of comets.

1. The radial transport of the matter from the inner regions of the Solar Nebula to outside. In the matter of some comets (81P/Wild 2, C/1995 O1 Hale–Bopp), specific high-temperature mineral phases - calcium-aluminum-rich inclusions (CAIs) have been found. Their formation is connected with high-temperature processes that took place at the early stage of the evolution of the Solar System in the regions close to the Sun. Therefore, for the standard model of formation of the Solar System, the important cosmochemical conclusion has been made. The conclusion is on the radial transport of the matter from the inner regions of a protoplanetary dust-gas disk to its outer regions at the early stages of the Solar system. Therefore, the important cosmochemical conclusion has been made based on the standard model of the Solar System formation. The conclusion is that - there was the radial transport of the matter from the inner regions of a protoplanetary dust-gas disk into its outer regions at the early stages of the Solar system.
2. The relative fraction of water in the protosolar matter. Water is the main component of all bodies of the Solar System. Its mass fraction is especially large in rock-icy bodies of the outer part of the Solar System – satellites of giant planets, objects of the Kuiper belt and so on. In the inner regions, the water evaporates and transformed into gas. Abundance of vapor of water defined of the redox conditions in nebula, and therefore the composition of the Phases that condensated during at its cooling. Therefore, the initial abundance of water in the protosolar matter, of which the Solar System formed, is the main cosmochemical parameter. Since hydrogen was the main component of the nebula, the fraction of water was defined by fraction of other components that include oxygen, mainly such as CO, CO_2, CH_3OH. The cometary matter is the most informative source of the above information. Nevertheless, as it was shown recently at studies of comet 67P/Churyumov-Gerasimenko, the obtained data, in particular, the ratio CO/CO2, are not clear. It will be shown in the presentation.
3. Accumulation of gas component of the disk into the solid phase and its accretion by space bodies at the stage of its formation. Among all bodies of the Solar System, only giant planets accreted volatile components of the nebula as gas. All other space bodies, including comets, accreted them in the form of solids – ices or clathrate hydrates of type $X \cdot 5.75H_2O$ and $X \cdot 5.66H_2O$. All these forms are in the cometary matter, but their study is possible only in situ, for example, with spacecraft, such as Philae in Rosetta experiment. The conditions of transformation of some forms of volatile components to other forms will be shown in the presentation
4. The radial transport of water and other volatile components from the outer regions of the nebula in the internal zone. In contrast to the objects outer solar system the space bodies situated on radial distances from the Sun r ~ 3 AU and closer could not accumulate volatile components, including

water, in situ, since the temperature in the regions of its formation were higher than the temperature of water ice condensation. But all bodies that are situated in the inner zone of the Solar System, including the Moon and Mercury contain (or contained like Venus) water. The main mechanism to provide these bodies with volatiles was radial transport of matter from the outer zones of the solar disk in the internal as at the stage of gas-dust disk, and at the stage of debris the disc. The main indicator of the value of the radial transport volatiles in the solar disk is D/H in the water molecule. Initially it corresponded to D/H_{H2O} in interstellar molecular clouds, that is 3-5 times greater than D/H of the Earth's water. However, not all comets have kept this value, for example, comets of Jupiter family 103P/Hartley 2 and 45P/Honda-Mrkos-Pajdusakova have water with D/H close to Earth's water. Thus it is difficult to use the comet's data in the analysis of radial transport of water and other volatile components from the outer regions of the nebula in the inner zones because it requires certain assumptions regarding the zones of the formation of long-period and shot-period comets.

5. The composition of subsurface water environments and their role in shaping of Titan's atmosphere and of water plumes of Enceladus. The isotopic composition of N2 molecules in the atmosphere of Saturn's largest moon – Titan, the component composition of the water plumes of Enceladus, and the isotopic composition of water in them, clearly points to the fact that the satellites were created from substance with composition similar in composition of the comet. Models of subsequent conversion CO_2 and NH_3 in CH_4 and N_2 (respectively) in environments of the subsurface water will be shown in the presentation. However, the question of why the D/H in the CH_4 molecule Titan's atmosphere strikingly matches the value of D/H for the Earth remains unresolved. This requires the data of D/H_{CH4} for comet ices first of all.

Such data may be derived in result the implementation of the space experiment Rosetta, which is ongoing now.

These are only some aspects of the use of data of the study of cometary material to solve basic problems of cosmochemistry.

NAVCAM OBSERVATIONS OF THE NUCLEUS OF COMET 67P/CHURYUMOV-GERASIMENKO

A.T. Basilevsky[1,2], U. Mall[2], H.U. Keller[3], Yu.V. Skorov[3], G. Michael[4], N.A. Artemieva[5,6], N.E. Demidov[1], S.S. Krasilnikov[1]
[1]Vernadsky Institute, RAS, Moscow, Russia, atbas@geokhi.ru;
[2]Max-Planck Institut fuer Sonnensystemforschung, Goettingen, Germany;
[3]Institute for Geophysics & Extraterrestrial Physics, TU Braunschweig, Braunschweig, Germany;
[4]Institute of Geological Sciences, Freie Universitaet Berlin, Berlin, Germany;
[5]Institute for Dynamics of Geospheres, RAS, Russia; [6]Planetary Science Institute, Tucson, USA.

This work is based on analysis of images of the 67P/Churyumov-Gerasimenko (S-G) comet nucleus taken by the Navigation Camera (NavCam) of the Rosetta spacecraft at a resolution of 0.7-3 m/px. The nucleus consists of two lobes, Body and Head, and connecting them Neck (Figure 1a). The Body dimensions are 4.1×3.3×1.8 km, the Head - 2.6×2.1×1.8 km, the nucleus volume is equivalent to that of sphere with radius 1.72 km = 21.4 km^3, the nucleus mass is ~10^{13} kg, average gravity acceleration ~0.0002 m/s^2, with strong from place to place variations, mean escape velocity is ~0.9 m/s, bulk density ~0.47 ± 0.05 g/cm^3, that, assuming density of the dust+ice mixture as 1.5-2 g/cm^3, suggests the nucleus material porosity from 70 to 80%, geometric albedo at 0.55 micron is 4.7 to 5.9% (Sierks et al., 2015; Groussin et al., 2015). These characteristics of the nucleus control styles and intensities of geologic processes on it.

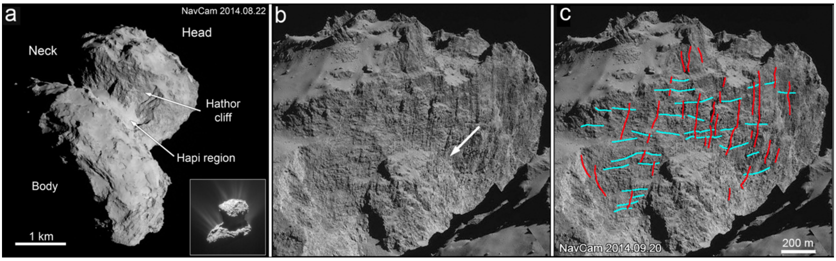

Fig. 1. a) Nucleus of C-G comet; b) NavCam image of the Hathor cliff with the landslide body (arrow); c) The same image with designated downslope (red) and subhorizontal (turquoise) lineaments.

The Head's side of the nucleus Neck is the Hathor cliff, which is very steep, locally with overhangings (Groussin et al., 2015). Its height above the subhorizontal Neck floor (Hapi area), is ~1 km. Figure 1b shows the Hator cliff with prominent bulge ~500 m high and 100-150 m thick, which is probably a body of landslide (Basilevsky et al., 2015). Figure 1c shows subhorizontal lineaments (could be due to layering in the nucleus material (see, e.g., Basilevsky and Keller, 2007, their Figure 8) and the downslope lineaments as well (could be fractures in the nucleus or "scars" from the downslope movements of the disintegrated durable parts of the cliff material (Basilevsky et al, 2015). Figure 2 shows examples of landslides on Earth, the Moon and Phobos.

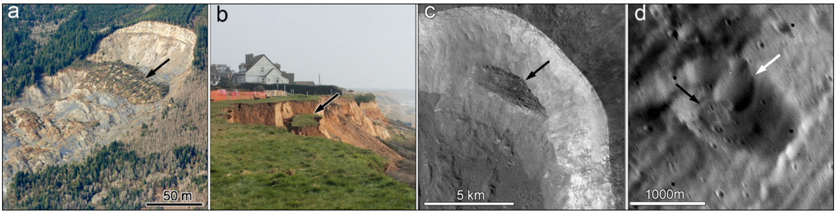

Fig. 2. a) Landslide (arrow) in Oso, Washington, USA, 31.03.2014, http://images.natureworldnews.com/ data/ images/full/5016. b) Landslide (arrow) at Barton-on-the-Sea, South Hampton, Great Britain, 21.06.2008, http:// www.southampton.ac.uk/~imw/barteros.htm; c) Landslide on the inner slope of lunar crater Giordano Bruno, NASA/ASU/LPL and http://planetarygeolog.blogspot.ca/2013/02/the-spectacular-giordano-bruno-crater.html. d) Landslide on Phobos (black arrow) on the floor of a 1.3 km crater, probably provoked by an impact, that formed a 200-m crater (white arrow); portion of VO1 image 243a71 (Basilevsky et al., 2014, their Figure 14e).

Depending on the cohesion strength of the sliding material and the sliding dynamics the landsliding mass could keep its initial form (Figures 2b,c) or be partly or completely destroyed (Figures 2a,d).

Figure3a shows another view of the Hathor cliff and the Hapi area at its foot. Sinuous linear feature here has morphology and orientation suggesting that it is a tension fracture. Estimations by Groussin et al. (2015) based on stability of steep and overhanging slopes show that the tension strength of the Hathor cliff material is 3-15 Pa while the compression strength is 30-150 Pa. These characteristics probably could be considered as typical for consolidated material composing the C-G comet nucleus.

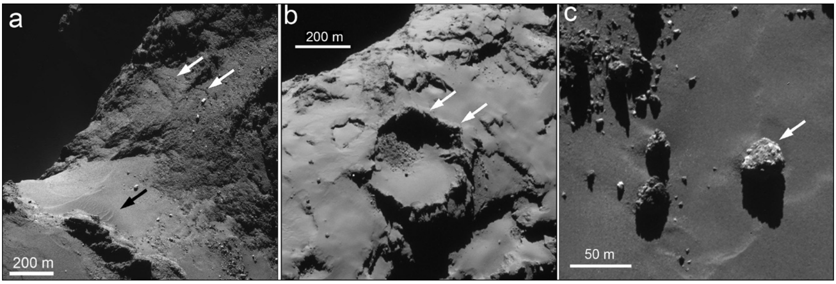

Fig. 3. a) Part of The Hathor cliff with tension fracture (white arrows) and the Hapi area at the cliff foot with ripples (dark arrow), NavCam 20141018T10225; b) The 350 m crater-like feature (white arrows; NavCam 20140921T180854.JPG; c) Boulder Cheops in Imhotep region, NavCam 20141023T182255.

In the lower part of Figure 3a is seen the brighter surface of the Hapi area with ripples (dark arrow) resembling eolian dunes on Earth and Mars. They and the features looking similar to “wind tails” behind the boulders are mentioned in the work of Thomas et al. (2015, their figures S3, S4). If these analogies are correct the “eolian” features could be due to action of horizontal gas jet. Basilevsky et al. (2015) also described in the Hapi area the albedo feature with the fan-like morphology (their Figure 6) that suggests the formation by a kind of flow resembling the downslope movement of pyroclastic flows, snow avalanches or turbidity currents on Earth. Alternatively, this fan-like feature could be formed due to partial deflation by the “subhorizontal” gas jet.

Figure 3b shows a crater-like feature whose morphology resembles that of impact craters. On the C-G nucleus surface there are seen more than 10 features of this sort with diameters from a few hundred meters to ~1 km. Thomas et al. (2015) call them “circular depressions” and find similarity with circular features seen on the nucleus of 81P/Wild 2 comet interpreted by Brownlee et al. (2004) as produced by sublimation or the collapse of internal voids. Basilevsky and Keller (2006) interpreted the Wild-2 features as primarily impact craters changed by the subsequent planation processes. To resolve the enigma of origin of the crater-like features on the 67P/C-G comet nucleus we plan to study details of their topography and to compare with the results of computer modeling of formation of impact craters at different environments (e.g., Artemieva et al., 2013) and to estimate probabilities of the crater-forming impacts in the recent history of the C-G comet as well (e.g., Maquet, 2015).

Figure 3c shows several boulders in Imhotep area with larger boulder Cheops ~50 m in diameter. It is seen that the Cheops boulder has inhomogeneous texture with well seen knobs a few meters in diameter, probably being the boulder components more durable to surface degradation. Textural inhomogeneity is also well seen in the image of ~5 m boulder taken by camera ROLIS during the descent the Rosetta landing module Philae. The textural inhomogeneities are of decimeters scale http://www.esa.int/spaceinimages/Images/ 2014/11/ Comet_from_40_metres. Knobs a few meters to a few tens of meters across are seen in the images of the Hator cliff surface (Figures 1b,c and 3a) and were described by Sierks et al. (2015) as “goose-bumps”. Textural inhomoheneities are typical for the C-G comet material in the finer size scale too: The COSIMA instrument caught and imaged fluffy aggregates of a few hundred microns consisting of particles of a few tens microns across (Schultz et al., 2015). This is certainly not the lower size limit of the particles composing the comet nuclei: The Stardust mission caught in the Wild 2 coma and brought to Earth, particles from 0.1 to 1000 micron in diameter (Price at al., 2010). “Grainy” texture of the comet nuclei material in the scale of sizes of parts of a micron to tens of meters puts constrains on the character of processes forming these bodies.

Concluding:

On the surface of the nucleus of comet 67P/Churyumov-Gerasimenko three kinds of materials are seen: 1) consolidated material outcropped at steep slopes, 2) boulders composed of this consolidated material, and 3) friable “fine” relatively bright material seen on subhorizontal surfaces. The high steep slopes are areas for downward movement of material in the form of landslides, mobilization and falling of individual boulders, as well as the mobilization and down pouring of fine material. The latter in some specific situations seems to be able to move collectively as a kind of flow, producing fan-like features and ripples. The mentioned geological processes seem to be initiated and supported by sublimation of volatile component(s) of the nucleus material and thus should be most active when the comet is close to the Sun. Meteorite impacts can also provoke local geologic activity such as landslides or gas jets.

References:

[1] Artemieva et al., 2013. Meteoritics & Planetary Science. V. 48, 590-627. [2] Basilevsky and Keller, 2006. Planetary & Space Science. V. 54, 808–829. [3] Basilevsky et al., 2014. Planetary & Space Science 102, 95–118. [4] Basilevsky et al., 2015. LPSC-46, abs. 1152. [5] Brownlee et al., 2004. Science 304, 1764–1769. Groussin et al., 2015. Astronomy & Astrophysics (in press). [6] Maquet, 2015. http://dx.doi.org/10.1051/0004-6361/201425461. [7] Price at al., 2010. Meteoritics & Planetary Science 45, 1409–1428. [8] Schultz et al., 2015. Nature. doi:10.1038/nature14159. [8] Sierks et al., 2015. Science. V. 347. No 6220, aaa1044-1-5. [9] Thomas et al., 2015. Science. V. 347. No 6220, aaa0440-1-6.

GEOLOGY IRREGLULARITIES OF THE COMET P67

O.S. Potashko, E.F. Shnyukov
Marine and Ore Sedimentary Formation Division of National Academy of Sciences of Ukraine, 40 Honchara str. Kyiv, Ukraine.
potashko@mail.ru

Comet P67 has several irregularities:

- signs of numerous lava eruptions
- signs of tectonics
- cylinder holes having right forms with diameter from 1 to 200 meters.

All these features may testify on active nature of comet P67.

ON COMPARISON OF THE NUCLEI OF COMETS 67P/CG AND 1P/HALLEY

L.V. Ksanfomality[1], L.M. Zelenyi[1], K.I. Churumov[2]
[1]Space Research Institute of the Russian Academy of Sciences;
[2]T.G.Shevchenko Kiev State University

Exploration of cometary nuclei using space vehicles was begun by the Soviet space missions Vega. On March 6 and 9, 1986, the spacecraft Vega-1 and Vega-2, approached the nucleus of comet Halley, one of the largest short-period comets. The spacecraft converged on comet Halley on a head-on course, at a huge approach velocity of about 75 km s^{-1}. The probes photographed the nucleus and studied in detail the composition of both the dust and the gas ejected by the comet, and also of the magnetic field and plasma surrounding the comet. On March 14, 1986, the space probe Giotto of the European Space Agency (ESA) followed Vega missions. Also, on March 8 Planet-A (Suisei) of the Japanese space agency flew at a greater distance from Halley. 28 years later, on November 14, 2014, the mission ROSETTA – PHILAE returns the properties of 67P/Churyumov-Gerasimenko nuclei. 67P/CG comet is believed to originate from the Kuiper Belt. It currently completes one orbit of the Sun every 6.45 years. Observations of 67P/CG coma taken by the ROSETTA spacecrafts gave the nucleus rotation period of 12.4 hours. Given the irregular shape of the nucleus, about 90% of 67P/CG surface was imaged in detail during the ROSETTA missions. The images revealed a body of an extremely varied topography, with hills, mountains, ridges and depressions, having dimensions of a small part 2.6×2.3×1.8km, and of a large part 4.1×3.3×1.8 km. Its mass is 10^{13} kg and mean density of 0.47 g/cm^3. The Halley's nucleus is larger, barely 15 kilometers long, 8 kilometers wide and about 8 kilometers thick. Its mass is 2.2×10^{14} kg and its average density is about 0.6 g/cm^3, indicating that both nuclei are made of a large number of small pieces, held together very loosely, forming a structure known as a rublle pile. The orbits of the Halley-type comets suggest that they were originally long-period comets whose orbits were perturbed by the gravity of the giant planets and directed into the inner Solar System. If 1P/Halley was once a long-period comet, it is likely to have originated in the Oort Cloud. The report compares the properties of comets 1P/Halley and 67P/Churyumov-Gerasimenko nuclei.

COMETARY DUST WITHIN THE NEAR-NUCLEUS ENVIRONMENT. APPLICATION TO 67P/ CHURYUMOV-GERASIMENKO.

Yu. Skorov[1], P. Lacerda[1], V. Reshetnyk[2],
[1]Max Planck Institute for Solar System Research, Göttingen, Germany, [2]Taras Shevchenko National University of Kyiv, Glushkova ave. 4, Kyiv, Ukraine.
skorov@mps.mpg.de

Introduction:

The Rosetta mission to comet 67P/Churyumov-Gerasimenko is providing unique constraints on the physical and dynamical properties of cometary dust (Rotundi et al. 2015, Schultz et al. 2015), and some of the first results are surprising. Examples include:

- Very large dust grains were detected near the nucleus at heliocentric distances greater than 3.5 AU. Grains from about ten to several hundred micron in size have been detected and collected by GIADA and COSIMA, while the OSIRIS camera revealed tracks of particles up to 2 cm in diameter;
- Dust grains from 67P hit the detectors at speeds 1 to 10 m/s, and grain speed is not strongly correlated with size. Optically detected grains move away from the nucleus at around 3.5 m/s;
- The dust grains appear to be weakly bound, fluffy agglomerates with porosities about 50%.

These results have motivated us to reassess the complex dynamics of cometary dust in the relatively unconstrained near-nucleus region. Here we present models of idealised dust particles and simulate their interactions with gravity from the sun and the nucleus, with solar radiation, and with sublimating gas drag. The dust particles are modelled as porous random aggregates constructed using different algorithms: ballistic particle-cluster aggregation (BPCA, or BA for short), ballistic agglomeration with one migration (BAM1), ballistic agglomeration with two migrations (BAM2), hierarchical aggregates of aggregates (BHAA) and ballistic cluster-cluster aggregates (BCCA).

Model:

Following Shen et al. (2008) we examine aggregates having markedly different filling factor: from 0.15 for the classical ballistic particle cluster aggregate (BPCA) to 0.30 for the aggregates obtained when the growth rule allows projectile sphere to make up to two migrations after collision with target (BAM2). For the first time we thoroughly consider the hierarchical aggregates, i.e. agglomerates of dust aggregates (see Skorov and Blum, 2012). These model aggregates have spatial structure similar to the structure of well-known ballistic cluster cluster aggregates (BCCA), which are also considered in our study. The radiative force is calculated following Kozasa et al. (1992). The optical properties of particles are calculated using a combination of Mie theory and the Maxwell Garnett effective medium theory. The gas drag force is calculated taking into account the non-equilibrium velocity distribution of gas molecules (Skorov and Rickman, 1999) and gas acceleration. A mean momentum transfer from a gas molecule to the aggregate is estimated by Monte-Carlo simulations. Various models of gas flow are examined: 1) a constant velocity gas flow, 2) a free-molecular flow, 3) an Euler flow.

Results:

A quantitative comparison of the forces acting on a dust near the nucleus surface (Fig. 1) clearly shows that the gas drag force is the absolutely dominant force there. For all tested particle sizes, this force in tens of times more than force of cometary gravity and solar radiation force. There is maximum size of particle which can be lifted by gas. This limit is a function of gas production, nucleus parameters (size, mass) and material strength (Gundlach et al, 2015). Due to the rapid reduction in the density of the expanding gas region of effective acceleration of dust is quite small: the speed of the particles adjacent to the terminal speed at a distance of about ten radii. A dust speed is only a few percent of the speed of gas flow, so the gas drag force is decreased mainly due to a decrease in gas density.

Conclusions:

We find that none of the grains structures considered is able to explain at once 1) the high grain porosity, 2) the low speeds and 3) the “flat” velocity curve of dust grains at Rosetta distances from the nucleus. We propose that dust grains must break-up well beyond the gas drag acceleration region, and probably near the spacecraft. Our calculations also showed that the speeds of dust particles measured by the GIADA instrument can not be achieved in a homogeneous model of comet nucleus. The measured dust characteristics indicate that grains are mainly released from the “active spots” where the gas density is highest.

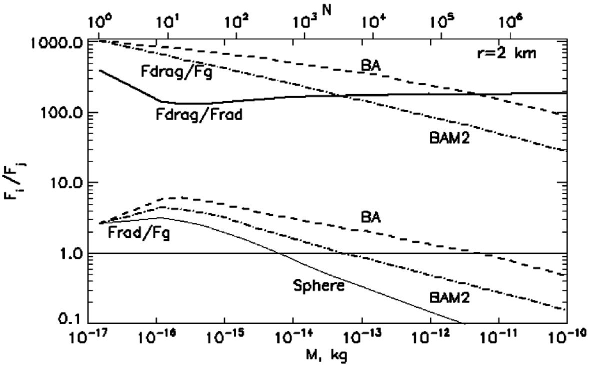

Fig. 1. Ratio of acting forces: F_drag/F_rad, F_drag/F_g and F_rad/F_g as a function of aggregate mass (or number of monomers) on the surface of homogeneous spherical nucleus. Results for BA, BAM2 and solid sphere are shown.

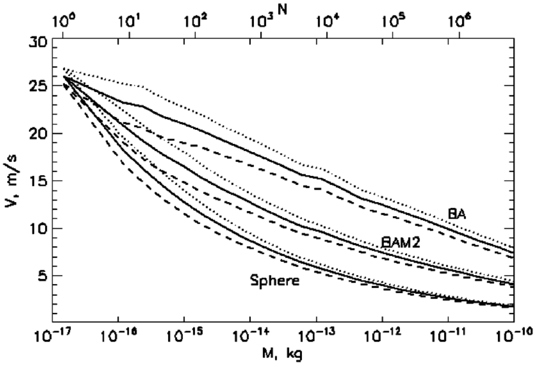

Fig. 2. Velocity of grain as a function of aggregates mass (and monomer number) at 50km from the center of mass. Results for BA, BAM2 and solid sphere are shown. Solid lines correspond to drag acceleration only, dotted curves – anti-solar point, dashed curves – sub-solar point.

References:

1. Kozasa, T., Blum, J., Mukai, T., 1992. Optical properties of dust aggregates. I - Wavelength dependence. Astron. Astrophys. 263, 423-432.
2. Rotundi, A. et al. 2015. Dust measurements in the coma of comet 67P/Churyumov-Gerasimenko inbound to the Sun. Science 347, 6220, id. aaa3905.
3. Schulz, R. Et al. 2015. Comet 67P/Churyumov-Gerasimenko sheds dust coat accumulated over the past four years. Nature 518, 216-218.
4. Shen, Y. et al. 2008. Modeling Porous Dust Grains with Ballistic Aggregates. I. Geometry and Optical Properties. Astroph. J. 689, 260-275.
5. Skorov, Yu.V., Rickman, H., 1999. Gas flow and dust acceleration in a cometary Knudsen layer. Planet. Space Sci. 47, 935-949
6. Skorov, Yu., Blum, J., 2012. Dust release and tensile strength of the non-volatile layer of cometary nuclei. Icarus 221, 1-11.
7. Gundlach et al. 2015. What drives the dust activity of comet 67P/Churyumov-Gerasimenko? (A&A accepted).

VOLATILES IN THE COMA OF COMET CHURYUMOV-GERASIMENKO

P. Wurz[1], K. Altwegg[1], H.R. Balsiger[1], J.J. Berthelier[5], A. Bieler[7], U. Calmonte[1], J. MSJ De Keyser[4], B. Fiethe[3], S. Fuselier[8], S. Gasc[1], T.I. Gombosi[7], A. Jaeckel[1], A. Korth[2], L. Le Roy[1], U.A. Mall[2], O. Mousis[9], H. Rème[6], M. Rubin[1], C.Y. Tzou[1] and ROSINA team
[1]University of Bern, Bern, Switzerland;
[2]Max Planck Institute for Solar System Research, Katlenburg-Lindau, Germany;
[3]Technical University of Braunschweig, Braunschweig, Germany;
[4]Belgian Institute for Space Aeronomy, Brussels, Belgium;
[5]LATMOS Laboratoire Atmosphères, Milieux, Observations Spatiales, Paris Cedex 05, France;
[6]IRAP, Toulouse, France; [7]
Univ of Michigan, Ann Arbor, MI, USA;
[8]Southwest Research Inst., San Antonio, TX, USA;
[9]Aix Marseille Université, CNRS, Laboratoire d'Astrophysique de Marseille, Marseille, France.
peter.wurz@space.unibe.ch

Introduction:

The European Space Agency's Rosetta spacecraft (Glassmeier et al., 2007) has been in orbit of the comet 67P/Churyumov-Gerasimenko (67P/C-G) since August 2014. On board is the Rosetta Orbiter Spectrometer for Ion and Neutral Analysis (ROSINA) instrument suite (Balsiger et al., 2007). ROSINA consists of two mass spectrometers, the Double Focusing Mass Spectrometer (DFMS) and the Reflectron-type Time-Of-Flight (RTOF), as well as the COmet Pressure Sensor (COPS). ROSINA is designed to detect and monitor the neutral gas and thermal plasma environment in the comet's coma by in situ investigation. The two mass spectrometers have high dynamic ranges and complement each other with high mass resolution (DFMS) and high time resolution and large mass range (RTOF). Especially the unprecedented sensitivity and mass resolution of DFMS together with the large mass range of RTOF allow determining precisely light species (e.g. isotopologues) as well as detecting heavy organic species. The pressure sensor COPS measures total gas densities, bulk velocities, and gas temperatures.

ROSINA has been collecting data on the composition of the coma and activity of comet from 3.5 AU until now. The Rosetta mission presents a unique opportunity to directly sample the parent species in the thin cometary atmosphere of a Kuiper-belt object at distances in excess of 2.5 AU from the Sun all the way to the pericentre of the cometary orbit at 1.24 AU. We will report on the first measurements of the volatile inventory obtained from ROSINA observations as Rosetta is following comet 67P/C-G at close distance.

Observations:

One important experimental observation is the isotopic composition of hydrogen of the comet. ROSINA measured the D/H ratio in water early during the mission at a distance of 3.5 AU from the Sun [Altwegg et al., 2015]. The ratio is D/H = $(5.3 \pm 0.7)\cdot 10^{-4}$ (2σ error), which is a factor of about 3 higher than the terrestrial D/H ratio. Thus, the water on Earth more likely was brought by asteroids than by comets.

Molecular nitrogen, N_2, is considered to be the most abundant form of nitrogen in the protosolar nebula. N_2 is also the main N-bearing molecule in the atmospheres of Pluto and Triton, and was probably the main nitrogen reservoir from which the giant planets formed. Yet in comets, often considered as the most primitive bodies in the solar system, N_2 has not been detected. Again early during the Rosetta mission, at 3.4 AU, a determination by the ROSINA instrument of N_2 in the comet 67P/Churyumov-Gerasimenko was made [Rubin et al., 2015]. A N_2/CO ratio of $(2.1\ {-0.7}/{+1.6})\cdot 10^{-3}$ was measured, corresponding to depletion by a factor of about 70 compared to the protosolar value. This depletion suggests that comets formed at low temperature conditions, and that the amount of N_2 delivered by these bodies to the terrestrial planets was limited compared to the other N-bearing species.

The determination of noble gases plays a key role in that volatile inventory of a planetary body. Argon, and its isotope composition is the first noble gas measured in the coma of the comet 67P/Churyumov-Gerasimenko [Balsiger et al.

2015]. Because of the temporal variability and spatial heterogeneity of the coma, see below, only a range of values for the argon to water ratio can be given, $^{36}Ar/H_2O = (0.1–2.3)\cdot10^{-5}$. Because of comparable volatility of Ar and N_2 their abundance ratio is much more stable and is $^{36}Ar/N_2 = (9.1\pm0.3)\cdot10^{-3}$. These gases come from the inside of the comet and are trapped in some form of ice. Also the Argon isotopic composition was measured by ROSINA and the resulting average ratio is $^{36}Ar/^{38}Ar = 5.4\pm1.4$, which is compatible the Earth $^{36}Ar/^{38}Ar = 5.3$ and to the solar wind $^{36}Ar/^{38}Ar = 5.5\pm0.7$ [Weygand et al. 2001].

The determinations of the Ar/CO and N_2/CO ratios in comet 67P/Churyumov-Gerasimenko also allowed comparing the existing scenarios of volatiles trapping in the protosolar nebula. Scenarios proposing the formation of comets from amorphous ices and clathrates match the N_2/CO ratio measured in 67P/Churyumov-Gerasimenko [Rubin et al., 2015]. However, the Ar/CO and N_2/CO ratios in 67P/Churyumov-Gerasimenko can only be simultaneously reproduced by models assuming that this comet agglomerated from clathrates in the ~45–50 K temperature range in the protosolar nebula [Mousis et al., 2015].

Most of the observed species in the coma are volatile material that are released from the comet's surface by sublimation, for example H_2O, CO, CO_2 and many others. The number densities in the coma of the major species H_2O, CO, and CO_2 show independent temporal variations compatible with the solar illumination (diurnal cycle), with seasonal variation (summer and winter hemispheres), and with compositional heterogeneity of the surface [Hässig et al. 2015]. Moreover, the chemical heterogeneity was also observed in some less abundant species, which were HCN, CH_3OH, CH_4, and C_2H_6 [Luspay-Kuti et al. 2015]. The open question is if the observed heterogeneity is restricted to the near surface and evolved over the orbit, because of the seasons of the comet, or if there is true chemical heterogeneity of the nucleus. The combination of the elliptical orbit and the tilt of the rotation axis with respect to the orbit plane leads to long but cool northern summers and hot but short southern summers, which could cause chemical heterogeneity on the surface of the comet. Comparing measurements from before and after the equinox on 5 May 2015 will help to answer this question.

The ROSINA experiment with its three instruments performs local in situ measurements of the total density and the chemical composition. To obtain a total gas production rate of the comet one has to extrapolate these local measurements to the entire comet, which is done by 3D modelling [Bieler et al. 2015]. The result of this modelling shows that the insolation of the cometary surface is the strongest factor for the cometary activity, and with some large scale heterogeneity of neutral gas in the coma, with increasing number densities towards northern latitudes. A constant gas production rate of $Q_{total} = 1\cdot10^{26}\ s^{-1}$ is found to best reproduce the observed ROSINA data up to 1 November 2014.

References:

K. Altwegg, H. Balsiger, A. Bar-Nun, J.J. Berthelier, A. Bieler, P. Bochsler, C. Briois, U. Calmonte, M. Combi, J. De Keyser, P. Eberhardt, B. Fiethe, S. Fuselier, S. Gasc, T.I. Gombosi, K.C. Hansen, M. Hässig, A. Jäckel, E. Kopp, A. Korth, L. LeRoy, U. Mall, B. Marty, O. Mousis, E. Neefs, T. Owen, H. Rème, M. Rubin, T. Sémon, C. Tzou, H. Waite, and P. Wurz, **"Comet 67P/Churyumov-Gerasimenko, a true Kuiper belt comet as judged from its D/H in water,"** Science 347(6220), (2015), article id. 1261952.

H. Balsiger, K. Altwegg, P. Bochsler, P. Eberhardt, J. Fischer, S. Graf, A. Jäckel, E. Kopp, U. Langer, M. Mildner, J. Müller, T. Riesen, M. Rubin, S. Scherer, P. Wurz, S. Wüthrich, E. Arijs, S. Delanoye, J. De Keyser, E. Neefs, D. Nevejans, H. Rème, C. Aoustin, C. Mazelle, J.-L. Médale, J.A. Sauvaud, J.-J. Berthelier, J.-L. Bertaux, L. Duvet, J.-M. Illiano, S.A. Fuselier, A.G. Ghielmetti, T. Magoncelli, E.G. Shelley, A. Korth, K. Heerlein, H. Lauche, S. Livi, A. Loose, U. Mall, B. Wilken, F. Gliem, B. Fiethe, T.I. Gombosi, B. Block, G.R. Carignan, L.A. Fisk, J.H. Waite, D.T. Young, and H. Wollnik, *ROSINA - Rosetta Orbiter Spectrometer for Ion and Neutral Analysis*, Space Science Review 128 (2007), 745-801.

A. Bieler, K. Altwegg, H. Balsiger, J.-J. Berthelier, U. Calmonte, M. Combi, J. De Keyser, B. Fiethe, N. Fougere, S. Fuselier, S. Gasc, T. Gombosi, K. Hansen, M. Hässig, Z. Huang, A. Jäckel, X. Jia, L. Le Roy, U.A. Mall, H. Rème, M. Rubin, V. Tenishev, G. Tóth, C.-Y. Tzou, and P. Wurz, **"Comparison of 3D kinetic and hydrodynamic models to ROSINA-COPS measurements of the neutral Coma of 67P/Churyumov-Gerasimenko,"** Astron. Astrophys. (2015), submitted.

S.A. Fuselier, K. Altwegg, H. Balsiger, J.J. Berthelier, A. Bieler, C. Briois, T.W. Broiles, J.L. Burch, U. Calmonte, G. Cessateur, M. Combi, J. De Keyser, B. Fiethe, M. Galand, S. Gasc, T.I. Gombosi, H. Gunell, K.C. Hansen, M. Hässig, A. Jäckel, A. Korth, L. Le Roy, U. Mall, K.E. Mandt, S.M. Petrinec, S. Raghuram, H. Rème, M. Rinaldi, M. Rubin, T. Sémon, K.J. Trattner, C.-Y. Tzou, E. Vigren, J.H. Waite, and P. Wurz, **"ROSINA/DFMS and IES observations at C-G: Ion-neutral chemistry in the coma of a weakly outgassing comet,"** Astron. Astrophys. (2015) submitted.

K.-H Glassmeier, H. Boehnhardt, D. Koschny, E. Kührt, and I. Richter, *The Rosetta*

Mission: Flying Towards the Origin of the Solar System, Space Science Reviews 128 (2007), 1–21.
M. Hässig, K. Altwegg, H. Balsiger, A. Bar-Nun, J.J. Berthelier, A. Bieler, P. Bochsler, C. Briois, U. Calmonte, M. Combi, J. De Keyser, P. Eberhardt, B. Fiethe, S.A. Fuselier, M. Galand, S. Gasc, T.I. Gombosi, K.C. Hansen, A. Jäckel, H.U. Keller, E. Kopp, A. Korth, E. Kührt, L. Le Roy, U. Mall, B. Marty, O. Mousis, E. Neefs, T. Owen, H. Rème, M. Rubin, T. Sémon, C. Tornov, C.-Y. Tzou, J.H. Waite, and P. Wurz, **"Time variability and heterogeneity in the coma of 67P/Churyumov-Gerasimenko,"** Science 347(6220), (2015), article id. aaa0276.
A. Luspay-Kuti, M. Hässig, S.A. Fuselier, O. Mousis, K.E. Mandt, K. Altwegg, H. Balsiger, J. Berthelier, F. Dhooghe, B. Fiethe, S. Gasc, T.I. Gombosi, A. Jäckel, L. Le Roy, U. Mall, M. Rubin, C.-Y. Tzou, and P. Wurz **"Composition-dependent outgassing of comet 67P/Churyumov-Gerasimenko from ROSINA/DFMS,"** Astron. Astrophys. (2015), in press.
M. Rubin, K. Altwegg, H. Balsiger, A. Bar-Nun, J.-J. Berthelier, A. Bieler, P. Bochsler, C. Briois, U. Calmonte, M. Combi, J. De Keyser, F. Dhooghe, P. Eberhardt, B. Fiethe, S.A. Fuselier, S. Gasc, T.I. Gombosi, K.C. Hansen, M. Hässig, A. Jäckel, E. Kopp, A. Korth, L. Le Roy, U. Mall, B. Marty, O. Mousis, T. Owen, H. Rème, T. Sémon, C.-Y. Tzou, J.H. Waite, and P. Wurz, **"Molecular nitrogen in comet 67P/Churyumov-Gerasimenko as an indicator of its low formation temperature,"** Science 348 (2015), 232-235.
J.M. Weygand, F.M. Ipavich, P. Wurz, J.A. Paquette, and P. Bochsler, **"Determination of the $^{36}Ar/^{38}Ar$ isotopic abundance ratio of the solar wind using SOHO / CELIAS / MTOF,"** Geochim. Cosmochim. Acta 65(24), (2001) 4589-4596.

SPECTRAL SIGNS OF COMETARY ACTIVITY ON PRIMITIVE ASTEROIDS (145) ADEONA, (704) INTERAMNIA, (779) NINA, AND (1474) BEIRA

V.V. Busarev[1,2], S.I. Barabanov[2], V.B. Puzin[2]
[1]Moscow Lomonosov State University, Sternberg Astronomical Institute, Universitetskij Av. 13, 119992 Moscow, Russia, busarev@sai.msu.ru;
[2]Institute of Astronomy of Russian Academy of Science (IA RAS), Pyatnitskaya St. 48, 109017 Moscow, Russia

Introduction:

Using the 2-m telescope with a CCD-spectrometer (working in the range of 0.35-0.97 μm with $R \approx 100$ resolving power) of Terskol Observatory operated by IA RAS, we performed in September 2012 spectrophotometry of (145) Adeona, (704) Interamnia, (779) Nina, and (1474) Beira to specify mineralogy of the asteroid surface matter. According to widely used classifications [1-3], Adeona is of C or Ch type, Interamnia – of F or B, Nina – of M or X, and Beira – of FX or B. Values of their geometric albedos are in the same order: 0.06, 0.08, 0.16, and unknown one from the WISE-data [4]. Despite of previously debuted high-temperature mineralogy of Nina, its radar-observations showed that the body is of a primitive type [5]. Comparing reflectance spectra of the asteroids with their spectra obtained by others, we discovered an unusual shape of Adeona's, Interamnia's, and Nina's spectra manifesting itself in a considerable growth of spectral reflectivity predominantly in the range ~0.4-0.6 μm. Given the lack of such a feature in reflectance spectra of other asteroids observed at the observatory, with the same facility, closely in time and at similar atmospheric conditions, we suspected its belonging to just the bodies.

Reflectance spectra of the asteroids and search for an explanation:

Normalized (at 0.55 μm) reflectance spectra of Adeona, Interamnia, Nina, and Beira together with their spectral data of other authors are shown in Figures 1-4 and shifted arbitrarily along the vertical axis. Our spectra are designated by the number "1" in all pictures. Other data in Fig. 1are: Adeona's reflectance spectrum in inset "A" published by McCord and Chapman (1975) [6], SMASSII – by Bus and Binsel [7], 52-color photometry – by Bell et al. [8]. Other data in Fig. 2 are: SMASS published by Lazzaro et al. [9], SMASSII – by Bus and Binsel [10], and 52-color photometry – by Bell et al. [8]. Other data in Fig. 3 are: SMASS published by Lazzaro et al. [9], SMASSII – by Bus and Binsel [11], and IRTF – by Ockert-Bell et al. [12]. Other data in Fig. 4 are: SMASSII(94) obtained in 1994 and published only in 2002 [13].

As seen from the figures, a considerable growth of spectral reflectivity was observed in the range ~0.4-0.6 μm for the asteroids. However, it took also place at ~0.55-0.75 μm for Beira. One can see that such features are absent in reflectance spectra of the asteroids obtained by other authors (Figs. 1-4). We noted

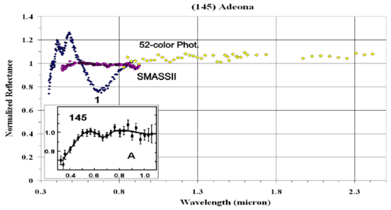

Fig. 1.

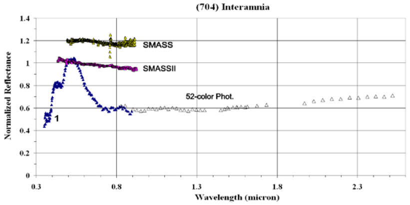

Fig. 2.

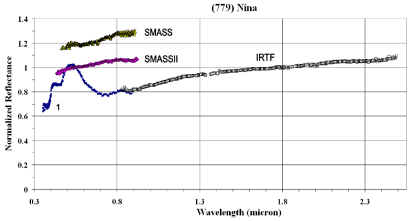

Fig. 3.

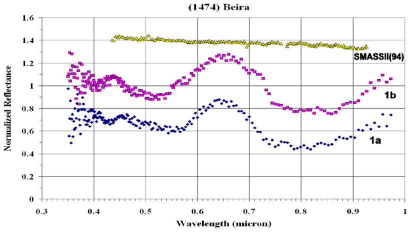

Fig. 4.

that the bodies were at the time of our observations near (or approaching to) of their perihelion distances, when the subsolar temperatures reach maxima. However, mentioned data of others were registered at higher heliocentric distances of the bodies excluding those on Beira obtained near its perihelion about 20 years ago [13]. We suspected that the observed unusual effects in spectral reflectance of Adeona, Interamnia, Nina, and Beira are created by an active process of ice sublimation. As follows from numeric modeling [14], parent bodies of C-type and close asteroids should include an abundant H_2O ice-component because of action of short-lived ^{26}Al in asteroid parent bodies. Another important factor could be changing activity of the young Sun and the corresponding shifting of the "snow line". Accumulated beneath the asteroid surface water ice may be excavated by recent impact events. For an intense sublimation of the fresh water ice, the considered asteroids could acquire a temporary coma of ice dust near their perihelion distances.

Given the Stefan-Boltzmann law for the black-body approximation of thermal radiation of a thin asteroid upper layer, we calculate the subsolar temperature (T_{ss}) on asteroid surface as $T_{ss} = 394K` ((1– p_v) / r^2)^{1/4}$, where p_v is geometric albedo of the asteroid and r – its heliocentric distance (AU). Thus, the subsolar temperatures at the time of our observations were: 236.5 K (Adeona), 238.6 K (Interamnia), and 257.3 K (Nina). However, the value of geometric albedo is unknown for Beira. Taking into account the same taxonomic type of Beira as Interamnia [2], we adopted the same value of p_v = 0.08. Then, the calculated subsolar temperature on Beira averaged over the period of our observations turned out to be 308.3 K exceeding the melting point of water ice by 35 degrees. It is not a surprise, because Beira has a high eccentricity (0.491) and is a Mars-crosser near its perihelion distance. Thus, the subsolar temperatures of all considered asteroids at the time of observations are within several tens of degrees around triple point of water ice, where the sublimation is most intense. Similar calculations show that the subsolar temperatures within a spot of excavated dirty ice will be by ~30 degrees lower then that on the rest of the asteroid surface. Reflection of solar light from such an asteroid and subsequent scattering of light in a "coma" may be an explanation of the observed effects. Interestingly, a "hump" at 0.55-0.75 μm in Beira's reflectance spectra created probably by scattering of reflected light in a hypothetical coma demonstrates a growth with shortening heliocentric distance (Fig. 4): spectra 1a and 1b are averages of data on two consecutive nights.

Our suggestions are in a good agreement with results of a simple model developed to explain unusual shape of reflectance spectra of some distant asteroids with a coma (Fig. 5) [15]. It includes a spherical reflecting light asteroid surrounded by a spherical envelope of water ice (+tholins) particles created by the process of water ice sublimation at concentration 2e+16 particles per cubic meter (Fig. 5). As seen from Fig. 5, the shape of the "total" reflectance spectrum of the system is very similar to those obtained by us for Adeona, Interamnia, and Nina (Figs 1-3). The position of spectral range of the scattering is likely determined by a predominant size of particles in the coma in the case of spectrally neutral refractive index. In the case of Beira, it is shifted to 0.55-0.75 μm and could mean presence of larger particles possibly of silicate content in the coma.

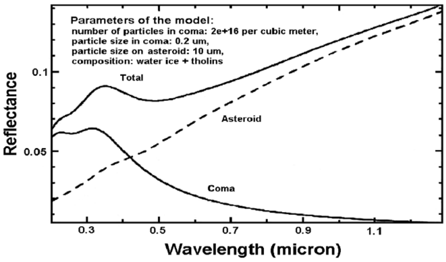

Fig. 5.

Coclusions: Thus, we registered for the first time simultaneous cometary activity on four main-belt asteroids of primitive types, Adeona, Interamnia, Nina, and Beira. Given an abundant ice component on such bodies, the appearance of a temporary coma could repeat by impact events. However, the phenomenon may be mass for primitive asteroids at perihelion distances. To verify our suggestions and results, we need new observations of these and other asteroids at perihelion distances and at different viewing conditions.

References:

[1] Tholen D. J., 1989. In: Asteroids II. Univ. of Arizona Press, 1139-1150. [2] Bus S. J., Binzel R. P., 2002b. Icarus 158, 146–177. [3] DeMeo F. E., et al. 2009. Icarus 202, 160-180. [4] Masiero J. R. et al., 2014. Astrophys. J. 791: 121 (11pp). [5] Shepard M. K. et al., 2010. Icarus 208, 221-237. [6] McCord T. B., Chapman C. R., 1975. Astrophys. J. 197, 781-790. [7] Bus S., Binzel R. P., 2003a. EAR-A-I0028-4-SBN0001/SMASSII-V1.0:145_01_TAB. NASA Planetary Data System. [8] Bell J. F., et al., 1995. EAR-A-RDR-3-52COLOR-V2.1. NASA Planetary Data System. [9] Lazzaro D. et al, 2006. EAR-A-I0052-8-S3OS2-V1.0. NASA Planetary Data System. [10] Bus S., Binzel R. P., 2003b. EAR-A-I0028-4-SBN0001/SMASSII-V1.0:704_01_TAB. NASA Planetary Data System. [11] Bus S. and Binzel R. P., 2003c. EAR-A-I0028-4-SBN0001/SMASSII-V1.0:779_01_TAB. NASA Planetary Data System. [12] Ockert-Bell M. E., 2011. EAR-A-I0046-4-IRTFSPEC-V2.0: NASA Planetary Data System. [13] Bus S. J., Binzel R. P., 2002a. Icarus 158, 106–145. [14] Grimm R. E, McSween H. Y. Jr., 1993. Science 259, 653-655. [15] Carvano J. M., Lorenz-Martins S., 2009. In: Fern´andez J.A. et al. (Eds), Proc. IAU Symp. 263, 223-226.

CHARACTERISTICS OF DUST IN COMET C/1995 O1 (HALE-BOPP) INFERRED WITH POLARIMETRY

E. Zubko[1], G. Videen[2], Yu. Shkuratov[1]
[1]*Institute of Astronomy, V.N. Karazin Kharkov National University, 35 Sumskaya st., Kharkov, 61022, Ukraine;*
[2]*Space Science Institute, 4750 Walnut Street, Suite 205, Boulder, CO 80301, USA.*
evgenij.s.zubko@gmail.com

Introduction:

Polarimetry of comets provides us with clues regarding chemical and physical properties of their dust. The degree of linear polarization significantly varies with the geometry of observation of a comet that is described with the phase angle α, the angle between the lines connecting the Sun and the comet, and the comet and the observer. Note, in planetary science, degree of linear polarization is defined as follows: $P = (I_{\perp} - I_{\parallel}) / (I_{\perp} + I_{\parallel})$, where $I_{\perp}$ and $I_{\parallel}$ are intensities of light polarized perpendicular to and in the scattering plane [e.g., 1], respectively; whereas, scattering plane is determined by the mutual location of the Sun, a comet, and observer. The polarization of a comet often appears to be wavelength-dependent [e.g., 1]. Moreover, at the same phase angle α and wavelength λ, polarization may dramatically change throughout a cometary coma. All these polarimetric features when they are considered simultaneously, place significant constraints on modeling and, thus, can improve the reliability of retrieval characteristics of cometary dust. However, there are only few comets whose polarimetric response was comprehensively studied. One such comet is Comet C/1995 O1 (Hale-Bopp), the object of interest in this short notice.

Observational Facts:

Comet C/1995 O1 (Hale-Bopp) was investigated with imaging polarimetry [2] and aperture-averaged polarimetry [3–5]. Imaging polarimetry revealed at least two types of dust in the Hale-Bopp coma with distinctive polarimetric features. Namely, dust forming the so-called *circumnucleus halo* produces strong negative polarization near backscattering and low positive polarization at side scattering. On the contrary, dust in *jets/arcs* does not reveal negative polarization at small phase angles; whereas, at side scattering their polarization is strongly positive. It is significant that these polarimetric features were detected in two continuum filters. We reproduce observational results [2] in Fig. 1, where data obtained with a green continuum filter are grouped in the left panel and with red continuum filter in right panel. Here, we also demonstrate aperture-averaged polarimetric observations adapted from [3–5]. As one can see, polarimetric responses in whole coma (points), circumnucleus halo (diamonds), and jets/arcs (triangles) dramatically differ one from another. However, it also seems reasonable to suggest that polarization in the whole coma is governed by a mixture of what is in the halo and jets/arcs.

Modeling and Discussion:

We model the polarimetric observations of Comet Hale-Bopp summarized in Fig. 1 using the so-called *agglomerated debris particles*. These particles have highly irregular morphology with packing density of constituent material being consistent with what is detected *in situ* in comets and interplanetary dust particles [6]. It is important to stress that these particles have already revealed success in modeling of photometric and polarimetric observations of Comet C/1975 V1 (West) [6] and in modeling of laboratory optical measurements of a cometary dust analog, forsterite particles [7]. We refer the reader to [e.g., 6] for details of the algorithm for generation of agglomerated debris particles, the technique of computation of their light-scattering response, and some important aspects on modeling polarization in comets.

We study agglomerated debris particles at 31 various refractive indices that are representative for plausible cometary species (see discussion in [6]). At each m, we investigate 24 different radii spanning the range from $r = 0.077$ μm to 2.468 μm. We repeat computations for two wavelength $\lambda = 0.478$ μm and 0.684 μm, that closely match the observational wavelengths. Finally, it is important to emphasize that for each set of m, λ and r, we average the light-scattering response over a minimum 500 particle shapes that yields a statistically reliable computational results.

We start our analysis of Comet Hale-Bopp, modeling separately the polarimetric responses in its halo and jets/arcs. As was previously noticed in [8], the polarization detected in the circumnucleus halo unambiguously suggests the presence of weakly or non-absorbing particles (i.e., Im(m) ≤ 0.02); whereas, fitting angular profiles of polarization also constrains the real part of the refractive index as follows: Re(m) ≈ 1.5. For instance, in Fig. 1, we present the fit of polarization in the circumnucleus halo (dashed lines) obtained with $m = 1.5 + 0i$. This refractive index appears consistent with Mg-rich silicates [9] that are abundant in comets [10]. It is significant that this fit is obtained with polydisperse particle system that obeys a power-law size distribution $r^{-2.5}$. This size distribution is consistent with *in situ* findings in comets [e.g. 11, 12]. We constrain our modeling assuming the same size distribution for particles in the halo and jets/arcs. Under this assumption, the polarimetric response in jets/arcs can be reproduced exclusively with highly absorbing particles, Im(m) ≥ 0.3. Such an imaginary part of refractive index appears, for instance, in organics and amorphous carbon that are known to be present in comets in considerable amounts [10]. In particular, in Fig. 1, we fit polarization in jets/arcs (solid lines) in Comet Hale-Bopp with $m = 2.43 + 0.59i$ that is adapted from measurements of amorphous carbon [13].

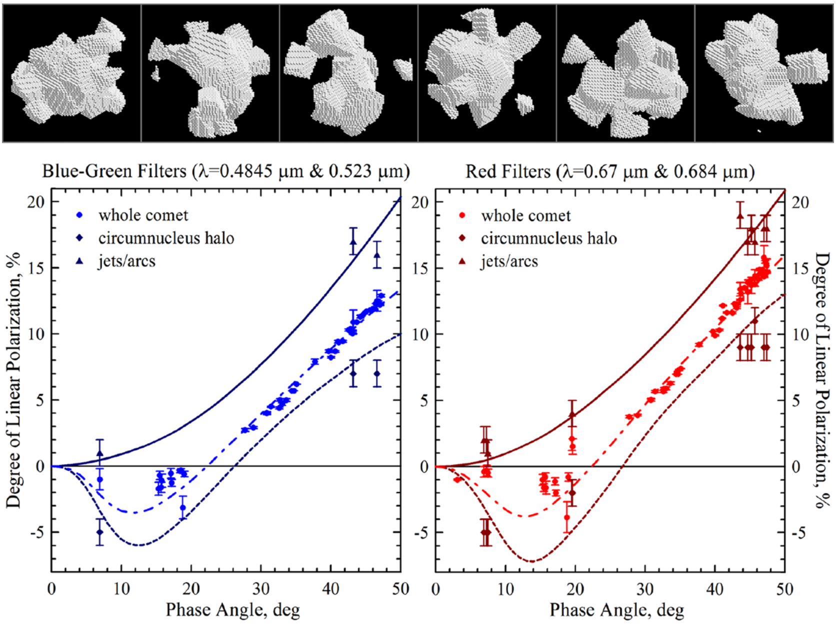

Fig. 1. Six example shapes of the agglomerated debris particles (top) and degree of linear polarization P measured and modeled in Comet C/1995 O1 (Hale-Bopp) as a function of the phase angle α (bottom). Left panel demonstrates measurements (symbols) and modeling results (lines) corresponding to the blue-green continuum filters; whereas, the right panel to the red continuum filters. Polarimetric responses in circumnucleus halo, jets/arcs, and whole comets are discussed in each panel.

Finally, we model the whole-coma polarimetric response by mixing the Mueller matrices [e.g., 14] obtained for agglomerated debris particles in the circumnucleus halo and in the jets/arcs. The fit presented in Fig. 1 with the dash-dot line corresponds to the volume ratio of the halo particles and jets/arcs particles of 1:1. As one can see here, the modeling satisfactorily reproduces observations at $\alpha > 25°$; whereas, at smaller α, it produces the negative polarization systematically exceeding what was observed in Comet Hale-Bopp. This can be explained with the simplicity of our model. Namely, we assume a volume ratio of the halo particles and the jets/arcs particles being constant over a half-year time period of observations. Furthermore, the observations conducted at $\alpha < 25°$ and $\alpha > 25°$ are separated by a 100-day break. Over this time period, the heliocentric distance of the comet decreased from ~2.5 au to ~1.25 au. This suggests different volume ratios at $\alpha < 25°$ and $\alpha > 25°$. We found that the modeling results can be adjusted to observations at $\alpha < 25°$ with a somewhat smaller relative abundance of the halo particles compared to what is retrieved at $\alpha > 25°$. It is important to stress that the best fits presented in Fig. 1 are not unique, various scenarios lead to nearly the same conclusion on chemical composition of the halo and jets/arcs, as well as on their relative abundance at $\alpha < 25°$ and $\alpha > 25°$.

Summary:

Using the agglomerated debris particles we have developed a comprehensive model of dust in Comet C/1995 O1 (Hale-Bopp) that can reproduce multi-wavelength polarimetric measurements of this comet. It is significant that the model reproduces not only the aperture-averaged observations, but also spatial variations of the polarization. Interestingly, chemical composition and size distribution retrieved for dust in Comet Hale-Bopp appear in good quantitative accordance with *in situ* findings in other comets.

References:

[1] Chernova, G.P., et al. 1993, Icarus, 103, 144; [2] Hadamcik, E., & Levasseur-Regourd, A. C. 2003, Astron. Astrophys., 403, 757; [3] Ganesh, S., et al. 1998, Astron. Astrophys. Suppl. Ser., 129, 489; [4] Manset, N., & Bastien, P. 2000, Icarus, 145, 203–219; [5] Kikuchi, S. 2006, J. Quant. Spectrosc. Radiat. Transfer, 100, 179; [6] Zubko, E., et al. 2014, MNRAS, 440, 2928; [7] Zubko, E. 2015, Opt. Lett., 40, 1204; [8] Zubko, E., et al. 2012, Astron. Astrophys., 544, L8; [9] Dorschner, J., et al. 1995, Astron. Astrophys., 300, 503; [10] Fomenkova, M.N., et al. 1992, Science, 258, 266; [11] Mazets, E.P., et al. 1986, Nature, 321, 276; [12] Price, M.C., et al. 2010, Meteoritics Planet. Sci., 45, 1409; [13] Duley, W.W. 1984, Astrophys. J., 287, 694; [14] Bohren, C.F., & Huffman, D.R. 1983, Absorption and Scattering of Light by Small Particles. Wiley, New York

ASTEROIDS NEAR THE SUN

V.V. Emel'yanenko
Institute of Astronomy, RAS, Moscow, Russia.
vvemel@inasan.ru

Near-Earth objects evolve frequently to orbits with small perihelion distances. It is estimated that up to 70% of near-Earth objects collide with the Sun during their orbital evolution. The solar tide, thermal stresses and interaction with the solar atmosphere are expected to be severe for objects passing near the Sun. Asteroids may not maintain their physical integrity during this near-Sun period, producing a number of smaller bodies. Very short cosmic ray exposure (CRE) ages for some meteorites imply their origin from disruption of parent bodies near the Sun. For example, dynamical studies show that there exists a large probability that the Chelyabinsk object was near the Sun in the past. This is consistent with estimates of a cosmic ray exposure age of 1.2 Myr for this meteorite. We have found other observed near-Earth objects that evolve in the same way, reaching small perihelion distances on short timescales in the past. We compare their dynamical features with the orbital evolution of observed sunskirting objects moving now in short-period orbits with perihelion distances q ~ 0.05 AU.

ROTATIONAL DYNAMICS OF COMETARY NUCLEI AND RELATED PHYSICS

V.V. Sidorenko[1], A.I. Neishtadt[2], A.A. Vasiliev [2]
[1]Keldysh Institute of Applied Mathematics, Moscow, RUSSIA;
[2]Space Research Institute, Moscow, RUSSIA.
vvsidorenko@list.ru

Introduction.

It is well known that the orbital motion of the comets depends substantially on the perturbations introduced by reactive forces due to the matter sublimation from their nuclei surface. The rotation of cometary nuclei and the evolution of the rotation are related directly to their physical and structural parameters. So the dynamical studies can provide us with useful information about the properties of the cometary nuclei.

Physical factors that influence a nucleus rotation.

These factors can be divided into two groups: constantly present and sporadically present [1]. The main factors which are constantly present are the reactive torque due to anisotropic sublimation of nucleus matter and energy dissipation at non-stationary nucleus deformations caused by the difference of the rotational state from principal axis rotation. The sporadic factors include possible impacts of various small celestial bodies (as long as they do not result in destruction of the nucleus) and redistribution of nucleus matter at a certain stage of its evolution.

In our studies we were concentrated on theoretical consideration of the rotational excitation and damping of the cometary nuclei.

Excitation.

The influence of the reactive torques due to the sublimation on the nucleus rotation was pointed out in the classical paper by F.L.Whipple [2]. It can cause the nucleus to be in rotational motion which is different from the rotation around the axis with the largest moment of inertia. As an example the non-principal axis rotation of comet 1P/Halley can be mentioned: the long axis of its nucleus is inclined to the total angular momentum vector by 66°[3].

The discussion of 1P/Halley nucleus rotation stimulated the theoretical work to reveal secular effects due to sublimation and to understand what is the “typical” spin state of the nucleus ([4], [5], [6], etc). Most of the investigations were based on the numeric integrations of the motion equations.

In [7], [8] we developed an alternative approach using the averaging procedure. In this way we found the relevant physical parameters that control the evolution of a comet’s rotation state. We demonstrated also that the long-term evolution of a comet’s angular momentum vector varies strongly with the distribution of active regions over its surface.

Damping.

Attempts to evaluate the influence of internal dissipation on a celestial body’s tumbling motion have been made in [9], [10]. The obtained estimation of the damping time scale can be written as

$$T_{damping} \sim \frac{\mu Q}{\rho R_N^2 \Omega^3}$$

where R_N is the nuclear radius, ρ is the bulk density, μ is the rigidity, Q is the following factor, and Ω is the nucleus angular velocity. The formula is given without certain non-dimensional scaling factor since its value is a matter of ongoing discussions.

The internal cracks can make the dissipation more intensive and reduce the dumping scale.

Damping and excitation interplay.

To illustrate the interplay of the damping and excitation factors we would like to consider the dynamics of comet 19P/Borrelly’s nucleus. This comet was observed by the space probe “Deep Space 1” (DS1) during the flyby in September 2001 [11]. The DS1 imaging system revealed a highly elongated nucleus which consists morphologically of two unequal components with a total length of 8 km.

Taking into account that the active zones on Borrelly’s nucleus are placed in the most non-effective way for creation a reactive torque we can assume that the inner dissipation should provide the stability of the rotation about the main inertia axis.

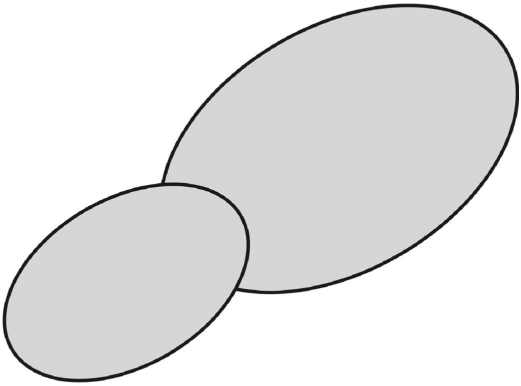

Fig. 1. 19P/Borrelly nucleus: a schematic reconstruction based on DS1 images

Conclusion.

Our results can be used to discriminate between competing theories of cometary matter sublimation using a nucelus' rotation state. They also provide a priori constraints to be placed on a comet's rotation state to aid in the interpretation of its outgassing structure.

References:

[1] Samarasinha N. et al. (2004) in: Festow M.C. et al (eds.) *COMETS-II*, 281-289. [2] Whipple F.L. (1951) *Astrophys. J., 113*, 464-474. [3] Belton M.J.S. et al. (1991) *ICARUS, 93,* 183-193. [4] Samarasinha N., Belton M.J.S. (1995*) ICARUS, 116*, 340-358. [5] Gutierrez P.J. et al. (2003*) Astron. Astrophys., 406,* 1123-1133 [6] Mysen E. (2007) *MNRAS., 372,* 1345-1350 [7] Neishtadt A.I. et al. (2002) *ICARUS, 157,* 205-218. [8] Sidorenko V.V. et al. (2008) *Cel. Mech. Dyn. Astron., 102, 133-147* [9] Burns J.A., Safronov V.(1973) *MNRAS., 165*, 403-411 [10] Efroimsky M., Lazarian A. (2000) *MNRAS, 311*, 269-278. [11] Britt D.T. et al. (2002) *LPI 33*, 1686.

ORIGIN OF ORBITS OF SECONDARIES IN DISCOVERED TRANS-NEPTUNIAN BINARIES

S.I. Ipatov[1,2]
[1]*Vernadsky Institute of Geochemistry and Analytical Chemistry of Russian Academy of Sciences, Kosygina 19, 119991, Moscow, Russia;*
[2]*Space Research Institute of Russian Academy of Sciences, Profsoyuzna-ya st. 84/32, Moscow, Russia.*
siipatov@hotmail.com.

Introduction:

The model of formation of planetesimals as a result of contraction of rarefied condensations was considered by several authors. It was supposed in [1-4] that trans-Neptunian binaries have been formed by contraction of rarefied pre-planetesimals (RPPs). Ipatov [1-3] considered that a considerable fraction of trans-Neptunian satellite systems could get the main fraction of their angular momenta due to collisions of RPPs. Below we study orbital elements of secondaries around objects moving in the trans-Neptunian belt and discuss how such orbits could form in the model of contraction of RPPs.

Prograde and Retrograde Rotation of Discovered Trans-Neptunian Binaries:

In Fig. 1 we present inclinations i_s of orbits of secondaries (or of orbits of the largest satellites) for trans-Neptunian objects. This figure is based on the data presented in http://www.johnstonsarchive.net/astro/astmoons/. Based on new recent observations, the data on the website are upgraded from time to time. Note that i_s is considered relative to the ecliptic and differs from the inclination relative to the plane which is perpendicular to the axis of rotation of a primary. For example, i_s=96^o for Pluto, though Charon is moving in the plane perpendicular to the Pluto's rotational axis. Besides the 32 considered objects with known values of i_s, the above website contains also information about many binaries with unknown i_s. The fraction of objects with i_s>90^o equals 12/32≈0.375 at all values of eccentricity *e* of a heliocentric orbit of a binary, and it is 12/28≈0.43 for *e*<0.3. For all four satellite systems with *e*>0.3, i_s<90^o. The values of i_s are in a wide range, almost from 0 to 180^o (Fig. 1a). It shows that a considerable fraction of the angular momentum of the RPPs, that contracted to form satellite trans-Neptunian systems, was not due to initial rotation of RPPs or to collisions of RPPs with small objects (e.g., boulders and dust), but it was acquired at collisions of the RPPs which masses did not differ much, because else the angular momentum would be positive. Ipatov [1] noted that the angular momentum of collided RPPs could be positive or negative depending on heliocentric orbits of the RPPs. Some excess of the number of discovered binaries with positive angular momentum compared with the number of discovered binaries with negative angular momentum was caused in particular by the contribution of initial positive angular momentum of RPPs and by the contribution of collisions of RPPs with small objects to the angular momentum of the final RPP that produced the binary. There could be also some excess of positive angular momentum at mutual collisions of RPPs of similar sizes.

Inclinations of Orbits of Secondaries at Different Ratios of Diameters of the Secondary to the Primary:

No dependence has been found for the plot of i_s vs. the diameter of the primary. The absence of such dependence can be a result of the evolution of the disk of RPPs, if the height of the disk of collided RPPs is greater than radii of collided RPPs. For the ratio d_s/d_p of diameters of the secondary to the primary greater than 0.7, i_s can take any values, but there are no objects with 130^o<i_s<180^o and d_s/d_p<0.7, and there is only one binary with i_s<50^o and d_s/d_p<0.5 (Fig. 1c). The absence of binaries with i_s>130^o at d_s/d_p<0.7 may be caused by that the contribution of initial positive angular momentum of the RPPs (that collided to form the final RPP) to the final angular momentum of the RPP that contracted to form the considered binary was greater (and the angular momentum acquired at the collision of RPPs of similar masses that produced the final RPP was smaller) at d_s/d_p<0.7 than at d_s/d_p>0.7. The smaller contribution of the angular momentum acquired at the collision at smaller ratio d_s/d_p could be caused by that in this case the masses of collided RPPs differed more than at greater d_s/d_p. The fraction of binaries with d_s/d_p>0.7 is 20/32≈0.625. A considerable (about 0.8) fraction of binaries with d_s/d_p>0.7 was also obtained in the computer models of contraction of RPPs considered by Nesvorny et al. [4].

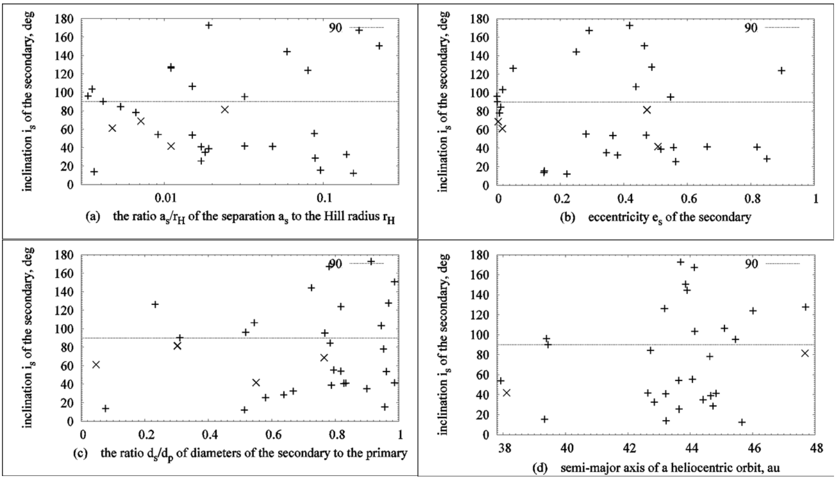

Fig. 1. The inclination i_s of the orbit of the secondary around the primary moving in the trans-Neptunian belt vs. (a) a_s/r_H, (b) e_s, (c) d_s/d_p, (d) a. Data for objects with e<0.3 are marked by plusses '+', and those at e>0.3 are marked by '×'.

Inclinations of Orbits of Secondaries at Different Orbital Elements of Heliocentric Orbits of Binaries:

We found dependencies of i_s on orbital elements (a, e, i) of a heliocentric orbit of a binary object (or an object with several satellites) moving in the trans-Neptunian belt. At 38<a<44 AU, the maximum values of i_s are greater for greater values of a semi-major axis a of a heliocentric orbit of an object (Fig. 1d). The values of i_s exceed 134° only at 44<a<46 AU, and i_s<110° at 38<a<40 AU. Initial semi-major axes of trans-Neptunian objects with e>0.3, probably, were less than 38 AU [5]. Smaller maximum values of i_s at smaller a can be caused by that the maximum values of the contribution of the angular momentum at a collision of two RPPs to the final angular momentum of the formed RPP were smaller (i.e., the role of initial positive angular momentum of RPPs was greater) at smaller a (as maximum values of a separation a_s between the primary and the secondary are smaller at smaller a).

The maximum value of i_s typically is smaller at a greater eccentricity e of a heliocentric orbit. It is close to 180° at e<0.1, is about 128° at e≈0.2, and is less than 90° at e>0.37. For i>13°, e≥0.219 and the values of i_s are in some region around 90° (61°≤i_s≤126°); in particular, 68°<i_s<110° at 13°<i<24°. May be some of the binaries with i>13° originated at a smaller distance from the Sun than most of other considered trans-Neptunian binaries.

Separation Distances at Different Heliocentric Orbits:

For e>0.3 the ratio a_s/r_H of the separation a_s between the primary and the secondary to the Hill radius r_H of the binary was smaller than 0.024, while a_s/r_H can exceed 0.225 at e<0.3 (Fig. 1a). Note that the trans-Neptunian objects with e>0.3 could form in the feeding zone of the giant planets (see, e.g., [5]), i.e., closer to the Sun than the objects with e<0.3. Maximum values of a_s/r_H (and also of a_s) are greater for greater semi-major axis a of a heliocentric orbit of an object at 38<a<46 AU (there is no place in the abstract for all analyzed figures). In our opinion, for smaller distances a from the Sun, the mean sizes of collided RPPs could be smaller, and so the mean values of a_s for the formed binaries could be smaller. The smaller sizes of the collided RPPs at smaller distances from the Sun could be due to their smaller Hill radii (which are proportional to a) at the collisions and, may be, also due to faster contraction.

Orbits of Binaries at Different Separation Distances: For a_s/r_H<0.008, except one object, the values of i_s are between 60° and 105°, i.e., are in some vicinity of 90°. Probably, the origin of such i_s was caused by that for smaller sizes of collided RPPs (that produce binaries with smaller a_s/r_H), the ratio of their sizes to the height of the disk where RPPs moved was smaller, and collided RPPs often moved one above another, but not in almost the same plane as in the case when the sizes of RPPs were about the height.

Fig. 1c shows that i_s is between 60° and 130° for e_s<0.1, but i_s can take any values for greater eccentricities e_s of orbits of secondaries around objects moving in the trans-Neptunian belt. For objects with e_s<0.1, a_s/r_H<0.011; e_s<0.15

at a_s/r_H<0.008. Eccentricities e_s are typically greater than 0.2 at a_s/r_H>0.011. The values of e_s are usually in the range of 0.3-0.7 at 0.009<a_s/r_H<0.035 and are in a wider range (from 0.15 to 0.9) for a_s/r_H>0.035. The greater maximum values of e_s at greater values of a_s/r_H are in accordance with the formation of satellites from a disk of material (e.g., if the disk formed as a result of contraction of a rarefied condensation). Orbits of satellites of planets are also almost circular for small distances from planets.

Conclusions:

The model at which a considerable fraction of the angular momentum of the rarefied condensation that contracted to form a satellite system was acquired at a collision of two condensations is in accordance with observations of trans-Neptunian binaries. For any other theory of formation of trans-Neptunian binaries, it is needed to explain the observations of the binaries, e.g., a considerable fraction of binaries with negative rotation.

Acknowledgements:

This study was supported by the RFBR grant no. 14-02-00319 and by the Program no. 22 of the Presidium of the Russian Academy of Sciences.

References:

[1] Ipatov S.I. (2010) *Mon. Not. R. Astron. Soc.*, *403*, 405-414. [2] Ipatov S.I. (2014) In *Proc. IAU Symp. No. 293* “*Formation, detection, and characterization of extrasolar habitable planets*”, p. 285-288. [3] Ipatov S.I. (2015) In “*Solar System Study: Some Milestones*”, Moscow, Space Research Institute, p. 386-399, in Russian. [4] Nesvorny D., Youdin A.N., Richardson D.C. (2010) *Astron. J.,* 140, 785-793. [5] Ipatov S.I. (1987) *Earth, Moon, & Planets*, 39, 101-128.

CONSTRAINTS ON CERES' INTERNAL STRUCTURE FROM THE DAWN SHAPE AND GRAVITY DATA

A.I. Ermakov[1], M.T. Zuber[1], D.E. Smith[1,2] , R.R. Fu[1], C.A. Raymond[3], C.T. Russell[4]
[1]Massachusetts Institute of Technology, Cambridge, MA, USA;
[2]NASA/Goddard Space Flight Center, Greenbelt, MD, USA;
[3]NASA/Jet Propulsion Laboratory, Pasadena, CA, USA;
[4]University of California Los Angeles, IGPP/EPSS, Los Angeles, CA, USA.
eai@mit.edu

Introduction:

Ceres is the largest body in the asteroid belt with a radius of approximately 470 km. It is large enough to attain a shape much closer to hydrostatic equilibrium than major asteroids. Pre-Dawn shape models of Ceres (e.g. Thomas et al., 2005; Carry et al., 2008) revealed that its shape is consistent with a hydrostatic ellipsoid of revolution. After the arrival of the Dawn spacecraft in Ceres orbit in March 2015, Framing Camera (FC) images were used to construct shape models of Ceres. Meanwhile, radio-tracking data are being used to develop gravity models. We use the Dawn-derived shape and gravity models to constrain Ceres' internal structure. These data for the first time allow estimation of the degree to which degree Ceres is hydrostatic.

Ceres shape and gravity field:

Observed non-hydrostatic effects include a 2.1-km triaxiality (difference between the two equatorial axes) as well as a center-of-mass – center-of-figure (COM–COF) offset. The magnitude of the offset is 660 meters or 0.14% of Ceres' radius. This value is substantially larger than the COM–COF offsets for the terrestrial planets but smaller than for Vesta. This again demonstrates the intermediate nature of dwarf planet Ceres. The Dawn gravity data from the survey orbit shows that Ceres has a central density concentration. Second-degree sectorial gravity coefficients are negatively correlated with topography. Fig. 2 shows the Bouguer anomaly based on the degree-2 gravity field. Negative anomalies are associated with positive topography, which indicates that Ceres' topography is at least partially compensated. Hydrostatic models show that Ceres appears more differentiated based on its gravity than on its shape.

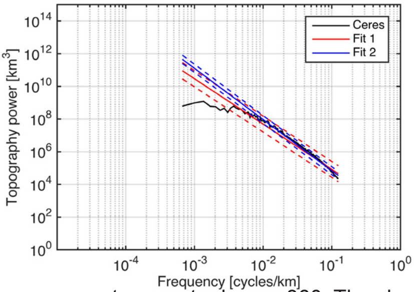

Fig. 1. Ceres' shape power spectrum up to degree 360. The shape model was produced by Ryan Park (JPL) with data from the Dawn Survey orbit. A hydrostatic signal was removed from the spectrum. Fit 1 was performed over all degrees. Fit 2 was performed over degrees higher than 12. The dashed curves indicate the 95% confidence intervals.

Viscous relaxation:

We expand Ceres' shape in spherical harmonics (Fig 1), observing that the power spectrum of topography deviates from a power law fit at low degrees. In order to assess the statistical significance of this deviation, we performed a least-squares linear fit and computed confidence intervals. We removed the hydrostatic signal from the spectrum to avoid biasing the fits. The spectrum deviation from the power law at low degrees is statistically significant, i.e. the spectrum lies outside of the 95% confidence region. We interpret the decrease of power at low degrees to be due to viscous relaxation. We suggest that viscous relaxation has occurred for Ceres but unlike in Bland (2013) it is important only at the lowest degrees that correspond to scales of several hundreds of km. There are only a few features on Ceres of that size and at least one of them (an impact basin provisionally named Kerwan) appears morphologically relaxed. The simplest explanation is that Ceres' outer shell is neither pure ice nor pure rock but an ice-rock mixture that allows some relaxation at the longest wavelengths. We use the finite-element library deal.ii (Bangerth 2007) to compute relaxed topography spectra in spherical geometry. Because relaxation of long wavelengths can be explained by a lower viscosity at depths, in our future work, we plan to model viscous relaxation to constrain the viscosity profile and thermal evolution.

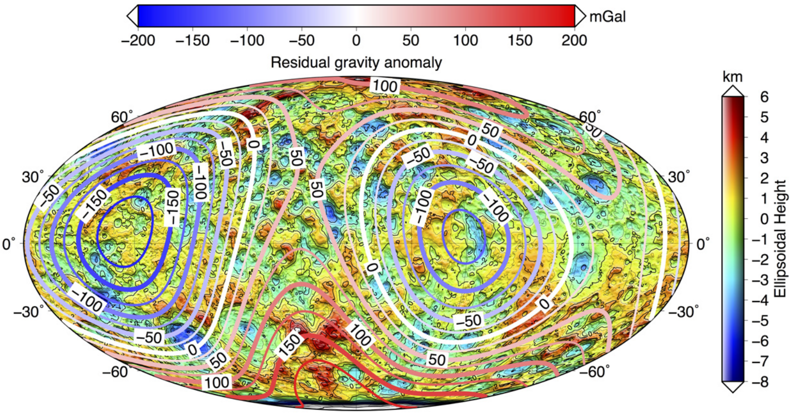

Fig. 2. Ceres' Bouguer anomaly based on a preliminary degree-2 gravity field from Dawn's Survey orbit.

CERES STRUCTURE AND SOME TIPS FOR THE STUDY OF GRAVITATIONAL POTENTIAL BY THE DAWN MISSION

S.A. Voropaev[1]
[1]GEOKHI RAS, Kosygina 19, 119991 Moscow, Russia.
voropaev@geokhi.ru

Introduction:

This study explores the geophysical implications of compositional model recently proposed for Ceres, which assume that the dwarf planet is a differentiated with low-density serpentine (core radius of about 400 km) and outer water ice layer (thickness of about 50 km). The presence of antifreezing material (ammonia) maintaining a liquid layer (thickness of about 20 km) is assumed. A major objective is to predict some of the discoveries that might be made when a spacecraft Dawn visits Ceres, and to offer some tips on the measurement results.

Analytical procedure:

Space mission Dawn targeted asteroid Vesta provides a number of remarkable results concerning as surface coverage as physical parameters of the surviving proto planet. It is currently in orbit about its second target at asteroid belt, the dwarf planet Ceres [1]. One of the obvious measurements to be made are main harmonics of the gravity field. When the value for J_2 is measured and assuming hydrostatic equilibrium, we can estimate value of the moment of inertia. This will put strong constraints on the internal structure of Ceres and allow us to choose among the different scenarios proposed for its thermal evolution [2]-[3].

If the gravitational potential of Ceres is modelled by a spherical harmonic expansion in the body-fixed reference, then the main part in second order is

$$U(r,\theta,\phi) \approx GM/r \{1 + 1/r^2 [(A+B-2C)/2M \, ½(3 \cos(\theta)^2 -1) +$$
$$+ (B-A)/4M \cos(2\phi) \, 3\sin^2(\theta)]\},$$

where A < B < C are principal moments of inertia, M is mass and G is the gravitational constant. The unnormalized coefficents (R is the reference radius of the body) are defined as

$$C – (A+B)/2 = J_2^R MR^2;$$
$$B – A = C_{22}^R \, 4MR^2.$$

Average data from the space and ground-based telescopes observations of Ceres are major axes of the best-fit twoaxial oblate ellipsoid,

a/c/R – 485/455/475 (km); mass, M – 9.43 x 10^{20} (kg); bulk density, ρ_b – 2080 (kg/m3); rotation period,

T - 9.075 (hours) and B = A at second harmonic degree.

In this case, using equatorial axes **a** as the reference radius is more convenient

$$C – A = J_2 Ma^2, \text{ where } J_2 = J_2^R (R/a)^2 .$$

An exact analytical treatment provides for homogeneous twoaxial oblate ellipsoid (with an arbitrary bulk density)

$$J_2^{(0)} = 1/5 \, \varepsilon_1^2 , \text{ where eccentricity } \varepsilon_1^2 = 1 – c_1^2/a_1^2,$$

and if Ceres would be homogenous, $J_2^{(0)} = 0.024$ ($\varepsilon_1 = 0.346$).

In order to explore the implications of the gravity and shape for the interior structure of Ceres, simple two-layer mass-balance model was explored with an assumed core as twoaxial oblate ellipsoid with major axes $a_2 = b_2 > c_2$ and eccentricity $\varepsilon_2^2 = 1 – c_2^2/a_2^2$. In this case,

$$M = M_1 + M_2,$$

where $M_1 = 4\pi/3 \, \rho_1 a_1^2 c_1$, ρ_1 is the outer layer density and $M_2 = 4\pi/3 \, \rho_2 a_2^2 c_2$, where ρ_2 is the difference between the core's and the outer layer density. So, mass-balance provides

$$1 = \rho_1/ \rho_b + \rho_2/\rho_b (a_2/a_1)^2 c_2/c_1 \qquad (1)$$

For two-layer model an exact analytical treatment provides

$$J_2^{(1)} = 1/5\,[\,M_1/M\,\varepsilon_1^2 + M_2/M\,\varepsilon_2^2\,(a_2/a_1)^2\,] \qquad (2)$$

At hydrostatic equilibrium, an exact analytical treatment provides for homogeneous twoaxial oblate ellipsoid with bulk density ρ_b eccentricity $\varepsilon^2 = 1 - c^2/a^2$ and rotation rate ω the following relation

$$\omega^2/2\pi\,\rho_b G = 1/l^3[\mathrm{arctg}(l)(3 + l^2) - 3l] = F(l), \qquad (3)$$

where $l(\varepsilon) = \varepsilon/\sqrt{1 - \varepsilon^2}$ (see Fig. 1). So, for Ceres with the rotation period T = 9.075 h and bulk dencity ρ_b = 2080 (kg/m3)

$$\omega^2/2\pi\,\rho_b G = 0.042$$

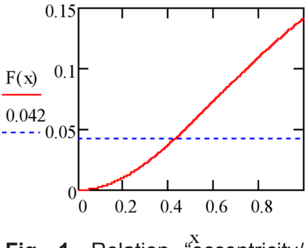

Fig. 1. Relation "eccentricity/ rotation" of a homogenous two-axial oblate ellipsoid

and F(l) provides $\varepsilon^{(0)} = 0.39$ while actual Ceres eccentricity $\varepsilon_1 = 0.346$. *So, $\varepsilon^{(0)} > \varepsilon_1$ is a clear indication of the more dense core relative outer layer.*

Internal structure:

Materials are known to fail under pressure if realistic criterion named for Tresca is met. It states that solids fracture along surfaces halfway between the axes of greatest stress σ_1 and least stress σ_3 whenever the maximum shear stress τ_{max} exceeds some constant S_0 characteristic of the material known as its *shear strength* [4]:

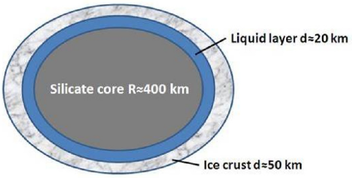

Fig. 2. Estimated internal structure of Ceres

$$\tau_{max} = (\sigma_1 - \sigma_3)/2 > S_0$$

Experimental data for pure ice define an upper limit of shear strength S_0 at 200 K as

$S_0 \approx$ 2.5-3 MPa.

So, we can represent the internal structure of Ceres in the form of a serpentine core (density 2700 kg/m3) and a rigid shell of water ice (density 910 kg/m3) that can withstand gravity loads (see Figure 2). Maximum shear stress attains a peak value $\tau_{max} \approx$ 3 MPa at the crust's lower boundary falling off to the surface.

In this case, analytical treatment like (2) provides for inhomogeneous twoaxial oblate ellipsoid $J_2^{(1)}$ as

$$J_2^{(1)} = 0.02 \qquad (4)$$

This value is very sensitive to the size and shape of the dwarf planet, so direct and accurate data from Dawn is very important for the next consideration.

Conclusions:

The above discussed simple model of the internal structure provides reasonable value for the shear stress and deformation under self-gravity at the ice crust. Serpentine are currently believed to originate from olivine and pyroxene transformation by means of the warm water.

It is known that the thermal evolution of Ceres was a complex process and its initial rocks were probably experienced complex chemistry. Additional investigation of the relation between rotation rate and figure of Ceres given its heterogeneity and compare with some other nearby objects will be very interesting and promising.

References:

[1] Thomas, P.C. et al.: Differentiation of the asteroid Ceres as revealed by its shape, Nature, Vol. 437, pp. 224-226, 2005.
[2] McCord T.B., Sotin, C.: Ceres: Evolution and current state, J. Geophys. Res.,, Vol. 110, E05009, 2005.
[3] Castillo-Rogez, J.C.: Ceres – Neither a porous nor salty ball, Icarus, Vol. 215, pp. 599-602, 2011.
[4] Slyuta E.N., Voropaev S.A.: Gravitational Deformation of Small Bodies of the Solar System: History of the Problem and Its Analytical Solution, Solar System Research, Vol. 49(2), pp. 123–138, 2015.

PRINCIPLES OF THE WAVE PLANETOLOGY MANIFESTING IN THE PLUTO – CHARON SYSTEM, CERES, AND THE MOON

G.G. Kochemasov
IGEM of the Russian Academy of Sciences, 35 Staromonetny, 119017,Moscow, kochem.36@mail.r

“Orbits make structures” – a general principle of the wave planetology [1-5]. In a basis of the statement lie elliptical keplerian orbits meaning that all celestial bodies have periodically changing accelerations. These changes applied to the bodies masses give inertia-gravity forces which inevitably warp the bodies in differing wavelengths aligned in harmonics and in 4 directions. Wave deformed planetary bodies inevitably must rotate to keep in equilibrium angular momenta of wave born tectonic blocks (otherwise, a body will tend to self destruction) [5]. For this purpose a body with a certain speed of rotation regulates angular momenta of tectonic blocks by adjusting their planetary radii and masses. Subsiding blocks with diminishing radii tend to be more massive and, vice versa, uplifting blocks less massive. The most familiar example is Earth with the Western Pacific hemisphere more basaltic and the Eastern continental hemisphere more granitic.

So, the fundamental wave 1 long $2\pi R$ make ubiquitous tectonic (and compositional) dichotomy (tectonic segments or hemispheres). Two-faced appearance of cosmic bodies is well documented. The first overtone wave 2 long πR makes tectonic sectoring superimposed on the hemispheric segmentation. Further harmonics produce superimposing smaller tectonic grains. Naturally polygonal these grains often give an impression of rings, craters, blobs aligned shoulder-to-shoulder in grids and lines.

There is the second well pronounced and also ubiquitous population of tectonic granules size of which depends on orbital frequencies of cosmic bodies [1-2]. The higher frequency the smaller granule size, and, vice versa, the lower frequency the coarser grain. A sequence of well studied tectonic granule sizes is: photosphere $\pi R/60$, Mercury $\pi R/16$, Venus $\pi R/6$, Earth $\pi R/4$, Mars $\pi R/2$, asteroids $\pi R/1$…!Pluto $62\pi R$ (not visible). Granules of Mars and asteroids coincide by size with the above described sectoring and segmentation.

Above regularities were expressed in form of theorems: 1) Celestial bodies are dichotomous; 2) Celestial bodies are sectoral; 3) Celestial bodies are granular; 4) angular momenta of different level blocks tend to be equal.

Pluto-Charon system accentuates these comparative wave planetology theorems. Predicted on March 2015 two-faced (dichotomous) appearance of these bodies now is obvious (Fig.1-3)[4-5]. A sectoral structure is well pronounced in both bodies, especially on surface of Pluto (Fig.5-7). Two large “bull’s-eye” structures in the southern (SE) regions of Pluto and Charon parallel each other (Fig.1). It seems that two-faced dichotomous tectonics concerns also the atmospheric envelope of Pluto judging by an image acquired on 16 July 2015 from ~2 million kms of Pluto (two days after the closest flyby)(Fig. 4). Firstly seen detailed image of the Sputnic area of Pluto discovers bifurcation of sizes of tectonic blocks (Fig. 8-9). The larger distorted (moving ices!) polygons according to the New Horizons scientists are on average 20 km across. The smaller detected spots in lines and grids are seen everywhere. They have 1 km and less in diameter and better seen in seams (troughs) between polygons where they often are black in color (penetration of underlying material?). The larger size calculated with regard of 1/6.4 days orbital frequency and R=1186 km is 16.3 km ($\pi R/228$; the Earth scale is 1/365d. fr and $\pi R/4$ granule size). The 1km and less size is calculated as modulation of the higher fr. 1/6.39 d. by the lower one 1/90465 d.=248 y. (division of the first by the second). It gives the modulated granule size 0.263 km. A fundamental tectonic analogy between such completely different two cosmic bodies as the Moon (R=1738 km) and Ceres (R= 475 km) is their two-faced dichotomous nature (Fig. 10, 11). They are representative of two classes of cosmic bodies: a dwarf planet and a satellite. One is “light” icy, another “heavy” rocky. Nevertheless, they both have along with two faces rather accentuated relief range (12-15 km and ~ 19 km) and some other peculiar features. On place of the SPA basin (Moon) are located two important depressions: Urvara and Yalode (Ceres) (Fig. 1-2). A little smaller but rather pronounced equally sized aligned depressions on the Moon are (Mares) Moscoviense, Freundlich-Sharonov, Dirichlet-Jackson, Hertzsprung, Orientale, on Ceres - Ezinu, Occator (with enigmatic ‘bright spots”), Kirnis, Unnamed (Fig. 10, 11). On subsided hemispheres the Procellarum Basin (Moon) has a highland protrusion from the SE (Fig. 11), on Ceres – comparable highland feature (Fig. 10).

Above examples confirm the only possible main process universally structuring celestial bodies - the wave process.

Fig. 1.

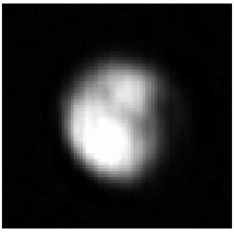

Fig. 2.

Fig. 3.

Fig. 4.

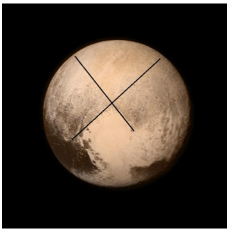

Fig. 5.

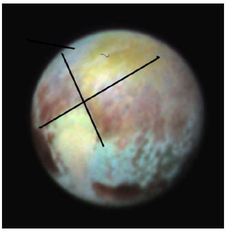

Fig. 6.

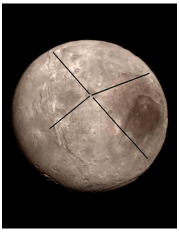

Fig. 7.

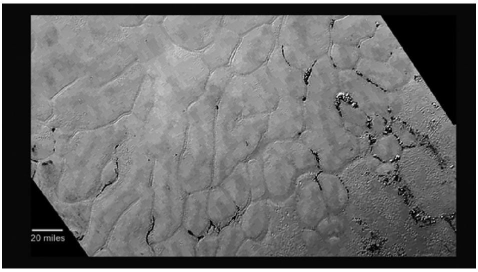

Fig. 8.

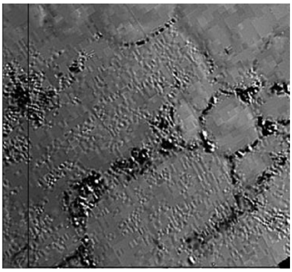

Fig. 9.

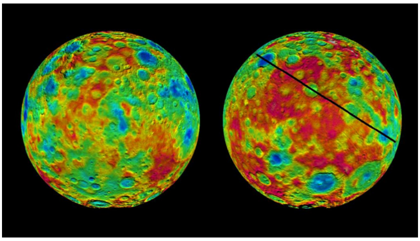

Fig. 10.

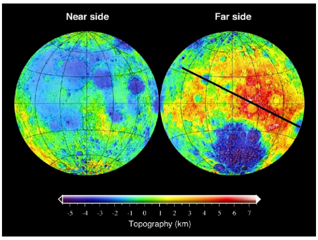

Fig. 11.

Fig. 1. 1-150712-pluto-charon; **Fig. 2**.Enlarged Pluto’ view from 20150609_nh_pluto_charon_4x-20150606-registax on June 6, 2015 from 46 mln. km distance (credit: NASA/JHUAPL/SWRI/Björn Jónsson; **Fig. 3.** Pluto, -July 1, dist. 14.9 mln.km (new-horizonspluto-july-6-2015(2); **Fig. 4.** Atmosphere of Pluto --lor_0299323899_0x630_sci_2; **Fig. 5.** Sectors of Pluto, false color, 1340903185541595237; **Fig. 6.** 150713-Pluto-last-before-flyby-1; **Fig. 7.** Sectors of Charon, nh-charon (1); **Fig. 8.** Pluto, a portion of Sputnic area, 150718174248-pluto-heart-0718-exlarge-169; **Fig. 9.** Enlarged SE portion of Fig. 8, 150714-sputnicplanum_1; **Fig. 10.** Topography of Ceres, Pia19607; **Fig. 11.** Moon. Credit Fig. 1-9: NASA/JHUAPL/SwRI

References:

[1] Kochemasov, G.G. Tectonic dichotomy, sectoring and granulation of Earth and other celestial bodies // Proceedings of the International Symposium on New Concepts in

Global Tectonics, “NCGT-98 TSUKUBA”, Geological Survey of Japan, Tsukuba, Nov 20-23, 1998, p. 144-147. **[2]** Kochemasov, G.G. Theorems of wave planetary tectonics // Geophys. Res. Abstr. 1999. V.1, №3, p. 700. **[3]** Kochemasov, G.G., 2014. From Vesta to Ceres: predicting spectacular dichotomous convexo-concave shape for the largest mini-planet in the main asteroid belt //Vesta in the light of Dawn: first exploration of a protoplanet in the Asteroid Belt, Febr. 3-4, 2014, Houston, Texas, LPI Contribution # 1773, Abstract # 2003. pdf. **[4]** Kochemasov G.G. Ceres’ two-face nature: expressive success of the wave planetology // New Concepts in Global Tectonics Journal, v. 3, # 1, March 2015, 63-64. **[5]** Kochemasov G.G. Celestial bodies: relation between ubiquitous tectonic dichotomy and universal rotation // NCGT Journal, v. 3, # 2, June 2015, 155-157.

GAS-DUST PROTOPLANETARY DISC: MODELING PRIMORDIAL DUSTY CLUSTERS EVOLUTION

M.Ya. Marov, A.V. Rusol
Vernadsky Institute of Geochemistry and Analytical Chemistry RAS, Moscow

Study of the evolutionary processes in the early solar system responsible for planetesimals set up and their subsequent growing is of fundamental importance. Basically, it is rooted in the mathematical modeling, some results being verified by *in situ* study of pristine matter of meteorites (see Marov, 2015; Marov, Kolesnichenko, 2013 for more details). Of the principal interest is the development of primary fluffy clusters formation composed mostly of dust and presumably of fractal internal structure (Kolesnichenko, Marov, 2014) resulted from the original gas-dust disc instability followed by mutual collisions with the different relative velocities in the wide range of spatial-temporal scale. Authors' approach to research of the processes involved is based on the method of permeable particles applicable to computer modeling of both porous dusty structures and rigid bodies (Marov, Rusol, 2011; 2015).

Original matter entering primordial dusty clusters are assumed to form in the molecular nebula from supra-molecular complexes including dozens silicate molecules, as well as interstellar dust. Here we deal with modeling of such supra-molecular complexes giving rise to the formation of spatial structures of progressively larger scale. Their follow up grow results in the formation of dusty clusters of rather complicated configurations.

Investigation of internal structures of fractal dusty clusters requires utilization of powerful computational resources. Basically, the modern technologies of high-speed calculations using graphic accelerators of large capacity such as NVIDIA TESLA GPU accommodate the problem solution. This allows us to address heterogenic processes at the juncture of physics and chemistry and in particular, to consider mechanical properties and internal structure of fractal dusty clusters jointly with physical-chemical evolution of their composed matter in the protoplanetary disc.

Grow of fractal dusty clusters can be qualitatively represented as gluing of dust particles. In reality, properties and composition of such a cluster depends on the conditions influencing the process of grow. Numerical models involving various algorithms of particles motion and interaction in due course of clusters collision allow us to analyze different patterns of growing structures including formation of multifractal configurations. Generally, they correspond to the well known models of fractal clusters grow depending on cluster-particle(s) or cluster-cluster interactions, the mode of clusters/particles motion (either determined or stochastic) and conditions of their integration. Obviously, in the case of Brown motion diffusive particle can just glue to a cluster while clusters collision results in the formation of structure of higher fractal dimension.

Note that process of clusters formation and evolution in the protoplanetary disc consisting of weakly charged particles differs from that in dusty plasma. Indeed, primary clusters are assumed to have characteristic size of about 1-2 nm and only a few silicate molecules can fulfill such a volume. This means that particles are electrically neutral at large distances whereas inhomogeneities of the electric field caused by the spatial charges distribution in molecular objects composing dust particles should be accounted for the region of collision.

A set of the computer experiments was carried out with the following model: diameter of particles 1 nm, density $1.5 \cdot 10^{-21}$ g/nm^3; charge - 1 elementary (positive or negative) charge - the medium is quasi-neutral. A cubic region of 10^6 nm in volume (cube size 100 nm) populated by 10 000 particles was taken. In the volume of such density fluctuations of dust particles may occur due to either eddy motions of the carried flow or influence of inhomogeneous electric fields in the protoplanetary disc. The total time of one computer experiment amounted to $2 \cdot 10^5$ s, continuing computation did not reveal a noticeable change in the derived structure.

The numerical evaluation for the model under consideration showed that in the processes of interaction of supra-molecular silicate complexes clusters of a linear filament structures are formed. The follow on evolution results in the formation of ring-shaped structures, as well as porous (fluffy) objects and larger particles. The rate of change of structures of the forming dusty clusters decreases exponentially as free particles become exhausted and follow up grow occurs mainly due to clusters interaction.

We may conclude that utilization of the modern computer technologies such as NVIDIA TESLA GPU as the basic apparatus and NVIDIA CUDA as the medium of program realization allowed us to progress in the study of key processes of early evolution of the gas-dust protoplanetary discs and to get more insight into fundamental problems of solar and extrasolar systems formation.

References

1. *Marov M.Ya.* The Fundamentals of Modern Astrophysics. A Survey of Cosmos from the Home Planet to Space Frontiers”, SPRINGER, 2015 (350 pp.).
2. Marov M.Ya., Kolesnichenko A.V. Turbulence and Self-Organization. Modeling Astrophysical Objects. SPRINGER ASSL, 2013 (657 pp.)..
3. Kolesnichenko A. V. , Marov M. Ya. Modification of the Jeans Instability Criterion for Fractal Structure Astrophysical Objects in the Framework of Nonextensive Statistics// Solar System Research, 2014, Vol. 48, No. 5, pp. 354-365.
4. Marov, M.Ya., and Rusol, A.V. Model of collisional interaction of bodies in the gas-dust protoplanetary disc. // Dokladi RAS 2011, v. 441 No.4 pp. 464-467.
5. MarovM.Ya., Rusol A.V. Gas-Dust Protoplanetary Disc: Modeling Collisional Interaction of Primordial Bodies //Journal of Modern Physics, Vol.6 No.3 (Gravitation, Astrophysics and Cosmology 2015). http://www.scirp.org/journal/JMP/.

MODELING OF THE INTERSTELLAR DUST PENETRATION INTO THE INTERPLANETARY MEDIUM THROUGH THE HELIOSPHERIC/ ASTROSPHERIC BOUNDARIES

P.S. Akaev[1], V.V. Izmodenov[2], O.A. Katushkina, D.B. Alexashov
[1]Space Research Institute (IKI) Russian Academy of Science, Russia;
[2]Lomonosov Moscow State University, Department of Mechanics and Mathematic, Russia;
[3] Institute for Problems in Mechanics Russian Academy of Sciences, Russia.
izmod@iki.rssi.ru

Dust is an essential component in the interstellar medium and appears as an observable tracer of the different astrophysical phenomena. In particular, the observation of the interstellar dust distribution is one of the possible way to diagnose astrospheres, which are the regions of the stellar wind interactions with surrounding interstellar medium. During last years the interest to the astrospheres increase due to their images obtained by Herschel. Different global shapes of the of astrospheres, which are observed, depend on local interstellar and stellar wind conditions. To analyze the astrospheres correctly, one need to model the dust distribution in the astrospheres. However, these models should be tested somehow. We propose to test the dust distribution models by using interstellar dust data obtained in the most accessible astrosphere – the heliosphere. Interstellar dust has been measured in the interplanetary medium by Ulysses spacecraft. By comparing model result with the Ulysses data we can get information on both the global heliosphere structure and on local interstellar dust distribution.

In this work we present the first results obtained in the frame of kinetic modeling of the interstellar dust particles in the interplanetary medium. The dust particle moves on the action of the several competing forces – solar gravitational force, repulsive solar radiation force and Lorentz force. To compute the distribution of dust particles in the inteplanetary medium we use Osiptsov-Lagrangian method. We compare result of our modeling with Ulysses data and discuss the global distribution including the regions of the interstellar dust accumulation in the interplanetary medium

The work has been done in the frame of Russian Science Foundation project 14-12-01096.

NEGATIVELY CHARGED NANO-GRAINS AT 67P/CHURYUMOV-GERASIMENKO

T.I. Gombosi[1], J.L. Burch[2], M. Horanyi[3]
[1]University of Michigan, Ann Arbor, MI 48109, USA;
[2]Southwest Research Institute, San Antonio, TX 78228, USA;
[3]University of Colorado, Boulder, CO 80303, USA.
tamas@umich.edu

Shortly after the Rosetta mission's rendezvous with 67P/Churyumov-Gerasimenko the RPC/IES instrument intermittently detected negative particles that were identified as singly charged nano-dust grains. These grains were recorded as a nearly mono-energetic beam of particles in the 200–500 eV range arriving from the direction of the comet. Occasionally, another population of particles in the energy range of 1–20 keV were also noticed arriving from the approximate direction of the Sun. We review the processes that can explain the energization and the directionality of the observed nano-dust populations. We show that the observations are consistent with gas-drag acceleration of the outflowing particles with radii of 3–4 nm, and with the returning fragments of bigger particles accelerated by radiation pressure with approximate radii of 30–80 nm. In addition to gas drag and radiation pressure, we also examine the role of the solar wind induced motional electric field, and its possible role in explaining the intermittency of the detection of nano-grain population arriving from the solar direction.

MOLECULAR BANDS IN THE SPECTRA OF THE BENEŠOV BOLIDE

A.A. Berezhnoy[1], J. Borovička[2]
[1]Sternberg Astronomical Institute, Moscow State University, Universitetskij pr., 13, Moscow, 119991 Russia;
[2]Astronomical Institute, Czech Academy of Sciences, Fričova Str., 298, CZ-25165 Ondřejov, Czech Republic.
ber@sai.msu.ru

Introduction:

The Benešov meteoroid entered the Earth's atmosphere on May 7, 1991. Strong bands of diatomic molecules such as MgO, AlO, CaO, and FeO were detected in optical spectra of this bolide by Borovička and Spurn**ý** (1996). After 20 years of unsuccessful searches for Benešov meteorites several small meteorites of different composition (LL3.5, H5, and achondritic clast) were found by Spurn**ý** et al. (2014). Chemical processes during the entrance of Benešov body into the Earth's atmosphere were considered by Berezhnoy and Borovička (2010). In this paper it was found that maximal equilibrium content of metal oxides was reached at 2000 – 2500 K during cooling phase. However, it was assumed that the Benešov meteoroid had elemental composition of carbonaceous chondrites. This incorrect assumption leads to overestimation of carbon-, and hydrogen-containing species in the impact-produced cloud, because Benešov meteoroid belonged to ordinary chondrites with relatively low content of volatile elements in comparison with carbonaceous chondrites.

FeO, CaO, MgO, and AlO Spectral Features and Search for Presence of Other Diatomic Molecules:

Red region of Benešov spectra is dominated by strong broad features of FeO orange system. Weaker CaO broad bands are also present. Unfortunately, electronic transitions, responsible for the origin of FeO and CaO orange systems, are poorly studied. For this reason, it is impossible to perform theoretical modeling of FeO and CaO spectral features and estimate column densities, vibrational and rotational temperature of these species.

AlO and MgO green system bands become prominent at altitudes lower than 40 km. Optical depth increases with decreasing altitude very quickly. We were able to estimate AlO vibrational and rotational temperature and column density only for regions with small optical depth (less than unity) at altitudes of about 40 km. The quality of obtained spectra was not enough for estimation of MgO rotational temperature. For this reason we assume that rotational temperature for MgO and AlO was the same. AlO bands were much stronger than MgO bands and the AlO/MgO ratio is estimated to be about 10. However, Mg is more abundant than Al in about 10 times in LL chondrites (Jarosewich, 1990) and thermochemical calculations also show that MgO is more abundant than AlO during wake phase (Berezhnoy and Borovicka, 2010). The reasons for this disagreement are discussed.

Search for other diatomic molecules such as TiO (α, β, and γ' systems), CO (Asundi, triplet, and Herman systems), CN (red and violet system), C_2 (Swan system) in Benešov spectra was also performed. Molecular constants of these molecules are well known and we were able to estimate theoretical intensities of these transitions as a function of temperature and pressure in the impact-produced cloud. These molecules were not detected neither in bolide head nor in wake spectra at all studied altitudes. Upper limits of column densities of these species and the carbon content in impact-produced cloud were estimated.

We do not confirm presence of Al hydroxides, NiO, and TiO, suggested by Berezhnoy and Borovička (2014), based on preliminary analysis of a Benešov spectrum.

Conclusions and Future Plans:

Study of Benešov spectra confirms stony nature of this meteoroid. Spectroscopy is a powerful tool for study of the chemistry of impact processes in the Earth's atmosphere. It may be used for estimation of the delivery rate of volatile elements to our planet, especially in common cases, when meteorites were not found after the impact. We plan to study CaO electronic transition, responsible for the origin of CaO orange band system in details in the future (see preliminary report of Palma et al. (2015)) in order to estimate CaO column density as a function of altitude.

References:

1. Berezhnoy A.A., Borovička J. Formation of molecules during meteor events, Icarus, 210, 150-157, 2010
2. Berezhnoy A.A., Borovička J. Chemistry of the Benešov meteoroid, Proceedings of the Meteoroids 2013 Conference, p. 125 – 131, Eds. Jopek T.J. et al., Aug. 26-30, 2013, Poznań, Poland, 2014
3. Borovička, J., Spurný, P. Radiation Study of Two Very Bright Terrestrial Bolides and an Application to the Comet S-L 9 Collision with Jupiter, Icarus, 121, 484–510, 1996
4. Jarosewich E. Chemical analysis of meteorites: a compilation of stony and iron meteorite analysis, Meteoritics, 23, 323-337, 1990
5. Palma A., Sandoval L., Rivas-Silva J.F. et al. Franck-Condon factors for CaO, 24th International Materials Research Congress, Cancun, Mexico, August 16-20, 2015, accepted
6. Spurný P., Haloda J., Borovička J. et al. Reanalysis of the Benešov bolide and recovery of polymict breccia meteorites - old mystery solved after 20 years, Astronomy and Astrophysics, 570, id. A39, 14 pp., 2014

STUDY LUNAR SOIL AND DUST WITH CHANG'E-3 MISSION DATA.

Ya. Lu[1], V.V. Shevchenko[2],
[1]Beijing Planetarium, Beijing, China; [2] Sternberg Astronomical Institute, Moscow, Russia.
luyangxiaoyi@gmail.com

Introduction:

Chang'e 3, was launched on 6 December 2013 and made a soft touchdown on 14 December 2013 with a lander and small rover named Yutu. Chang'e 3 was the first soft lander on the surface of the Moon since the Soviet Luna 24 sample-return mission in 1976 . The knowledge of the physical and mechanical properties of the soil is of fundamental importance because it is the basic for engineering activity aimed at construction of lunar bases and for mineral resource exploration. During manned flights the astronauts are operating and walking along the surface and knowledge about surface properties determines considerably the safety of the entire mission. Through Chang'E 3 mission data excavation, we can know physical and mechanical properties of lunar dust and soil at surface of Chang'E 3 landing area.

Analysis of Changes on lunar surface:

From orbiter and descent imaging data analysis, we discover distributed highness of lunar surface over the surface landing area - 34 meters (Figure A.1). After landing process and jet engine reverse thrust stop, there was a rock exposed at the lunar surface under the descent camera(Figure B.2 & D.5).Cause of this landing process, the surface of the rock completely had been exposed under cosmos environment without lunar dust.Lunokhod 1 traveled 11 km and explored the Mare Imbrium. Lunar soil were performed by means of unmanned vehicles Lunokhod-1, particle sizes was less than 1mm, and the physical and mechanical properties of these loose powder materials were same as measurement results from Apollo 16. Figure C.3 shows us :the lunar soil was loose in the local depth, not less than 10cm^{-2} carrying capacity 2 ~ 3kPa. Jet engine reverse thrust caused visible turbulent flow which had been mixed with lunar soil and dust(Figure D.4&6). Dust effected distribution of light and electrostatic field which broke away from lunar surface. Surveyors missions discovered light from a cloud of dust particles with particle size about 5 μm, vertical dimension ~3 - 30 cm, horizontal dimension ~14 m, and about 50 grains on cm^{-2}. The very small size of particle is an important condition of existence of a horizontal levitation of lunar dust.

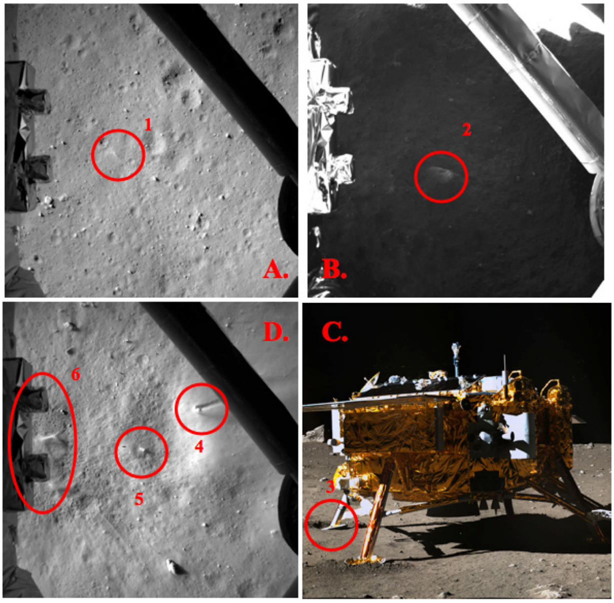

Figure A, B and **D** were taken from descent camera data of Chang'e 3 Lander; **Figure C** were from the imaging camera data of Yutu rover.

Acknowledgments:

We are grateful to the CLEP and CE-3 mission team. This research is supported by joint BJP grant.

References:

[1] Леонович А.К., и др. Основные особености процессов деформации и разрешения лунных грунтов // Космохимия Луны и планет. - М.: Наука, 1975. [2] Rennilson, J. J., Criswell, D. R., 1974. Surveyor observations of lunar horizon-glow. The Moon 10(2), doi:10.1007/BF00655715. [3] Duke M.B. Woo C.C. et. al., Lunar soil: size distribution and mineralogical constituents // Science. - 1970 V167. [4] [6] Apollo 17. Preliminary science report .- Washington, 1972.[5] Sternovsky Z., Chamberlin P., Horanyi M., et. al., Variability of the lunar photoelectron sheath and dust mobility due to solar activity. J. Geophys. Res., Vol. 113, A10104, doi: 10.1029/2008JA013487, 2008. [6] Zook H. A. and McCoy J. E. (1991) GRL, 18, 2117–2120.

ELECTRIC FIELDS AND DUST PARTICLE RISE NEAR THE LUNAR TERMINATOR

S.I. Popel[1], B. Atamaniuk[2], L.M. Zelenyi[1]
[1]Space Research Institute RAS, ul. Profsoyuznaya 84/32, Moscow 117997, Russia;
[2] Space Research Center PAS, ul. Bartycka 18A, Warszawa 02-716, Poland.
popel@iki.rssi.ru

Introduction:

It is now almost universally accepted that the dust over the lunar surface is a component of a plasma-dust system (see, e.g., [1-3]). The first lunar dust observations were made during the Surveyor and Apollo missions. The Surveyor lunar missions revealed that sunlight was scattered in the terminator region, and this led to the generation of the lunar horizon glow and streamers above the lunar surface [4]. Subsequent observations showed that the sunlight was scattered most probably by the charged dust particles originating from the lunar surface [5]. The analysis of the data obtained by the Surveyor landers led to a conclusion that the dust particles with a diameter of about 5 μm might levitate at a height of about 10 cm above the lunar surface.

The description [1-3] makes clear some features of dusty plasma system over the illuminated part of the Moon. However, there are unsolved problems concerning its parameters and manifestations in the terminator region [6]. Here, we consider the terminator region, study dusty plasma properties there, determine the electric fields, and discuss a possibility of the rise of dust particles.

Dusty plasma sheath:

The speed u of the terminator satisfies the conditions $v_{Td} \ll u \ll v_{Ti}$, where $v_{Td(i)}$ is the dust (ion) thermal velocity. The terminator speed does not depend on time. This allows us to look for the plasma parameters in the vicinity of the terminator as functions of the only variable $\xi = x - ut$ which satisfy the hydrodynamics equations for dust and Boltzmann distributions for electrons and ions. Furthermore, we use the orbit-limited probe theory to describe the dust particle charges $q_d = -Z_d e$ and Poisson's equation for the electrostatic potential φ, where $-e$ is the electron charge. We find

$$\left(\frac{d\varphi}{d\xi}\right)^2 = 8\pi\left[n_{e0}T_e\left(\exp\left\{\frac{e\varphi}{T_e}\right\}-1\right)+n_{i0}T_i\left(\exp\left\{-\frac{e\varphi}{T_i}\right\}-1\right)+m_d u^2 n_{d0}\left(\sqrt{1+\frac{2eZ_d\varphi}{m_d u^2}}-1\right)\right], \quad (1)$$

$$Z_d = -\frac{m_d}{e}u^2\frac{n_{d0}^2}{n_d^3}\frac{dn_d}{d\varphi}. \quad (2)$$

where $T_{e(i)}$ is the electron (ion) temperature, m_d is dust particle mass, $n_{e(i,d)0}$ is the unperturbed electron (ion, dust) number density characterizing dusty plasma system at the illuminated part of the Moon far from the region of the lunar terminator (corresponding in our consideration to $\varphi \to 0$), n_d is the dust number density.

The set of equations (1)-(2) has the steady-state solution describing the dusty plasma properties in the terminator region. The necessary condition for the steady-state solution to exist is

$$u^2 \geq \frac{(n_{e0}-n_{i0})|Z_d|}{m_d\left(\frac{n_{e0}}{T_e}+\frac{n_{i0}}{T_i}\right)} \approx |Z_d|\frac{T_e}{m_d}. \quad (3)$$

The condition (3) is easily fulfilled for the parameters of the lunar terminator and the dusty plasma system at the illuminated part of the Moon. This condition is the Bohm criterion for the dusty plasma sheath. The sheath is formed in the region of the lunar terminator. The solutions of Eqs. (1)-(2) are presented in Fig. 1.

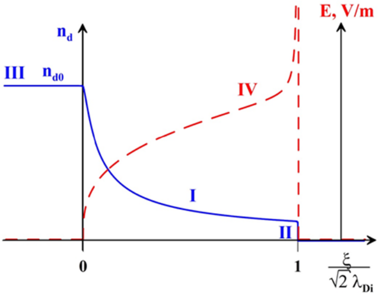

Fig. 1. Dusty plasma sheath in the region of the lunar terminator ($0 < \xi < \sqrt{2}\lambda_{Di}$). The regions $\xi < 0$ and $\xi > \sqrt{2}\lambda_{Di}$ correspond to the illuminated part of the Moon and the dark side of the Moon, respectively. λ_{Di} is the ion Debye length.

Dust number density and electric fields:

The blue curve in Fig. 1 displays the dust number density while the red one shows the electric field E. Almost everywhere in the region of the lunar terminator the dependencies of n_d (curve I) and E are given by the expressions

$$n_d = \frac{n_{d0}}{\sqrt{1+3\left(|Z_d| 2\frac{n_{d0}}{n_{i0}}\frac{\sqrt{3}T_i}{m_d u^2}\left(\frac{\xi}{\sqrt{2}\lambda_{D_i}}\right)^2\right)^{\frac{2}{3}}}} \quad (4)$$

$$E = \sqrt{8\pi n_{i0 T_i}}\left(\frac{Z_d}{3}\frac{n_{d0}^2}{n_{i0}^2}\frac{m_d u^2}{T_i}\frac{\xi}{\sqrt{2}\lambda_{D_i}}\right)^{\frac{1}{3}} \quad (5)$$

In the vicinity of the right boundary of the sheath $\xi = \sqrt{2}\lambda_D$ ($\xi < \sqrt{2}\lambda_D$), we obtain

$$n_d = \frac{n_{d0}}{\sqrt{1-\frac{4T_i|Z_d|}{m_d u^2}\ln\left(1-\frac{\xi}{\sqrt{2}\lambda_{D_i}}\right)}} \quad (6)$$

$$E = \frac{\sqrt{8\pi n_{i0}T_i}}{1-\frac{\xi}{\sqrt{2}\lambda_{D_i}}} \quad (7)$$

Estimates performed on the basis of Eq. (5) show a possibility of an appearance of the electric fields of the order of 10^2-10^3 V/m in the vicinity of the lunar terminator. Such electric fields can result in the rise of dust particles with the sizes of about several micrometers over the lunar surface. This explains the results obtained within the Surveyor missions showing that micrometer-sized dust particles rising over the lunar surface can lead to the sunlight scattering in the terminator region.

Conclusions:

Thus the lunar terminator region can be represented as a dusty plasma sheath. The Bohm criterion for the dusty plasma sheath is fulfilled for the lunar terminator parameters and the conditions characterizing dusty plasmas at the lunar surface. The electric fields of the order of 10^2-10^3 V/m are excited in the vicinity of the lunar terminator. Such electric fields are enough to explain the rise of dust particles with the sizes of about several micrometers over the lunar surface. This accounts for the results obtained within the Surveyor missions showing that micrometer-sized dust particles, which rise over the lunar surface, lead to the sunlight scattering in the terminator region.

Acknowledgements:

This work was carried out as part of the Russian Academy of Sciences Presidium program no. 9 “Experimental and Theoretical Research of Objects of the Solar System and Planetary Systems of Stars” and was supported by the Russian Foundation for Basic Research (project no. 15-02-05627-a).

References:

[1] Popel, S.I., Kopnin, S.I., Golub’, A.P., Dol’nikov, G.G., Zakharov, A.V., Zelenyi, L.M., and Izvekova, Yu.N.: Dusty plasma at the surface of the Moon, Solar System Research, Vol. 47, pp. 419-429, 2013.

[2] Popel, S.I., Morfill, G.E., Shukla, P.K., and Thomas, H.: Waves in a dusty plasma over the illuminated part of the Moon, J. Plasma Phys., Vol. 79, pp. 1071-1074, 2013.

[3] Popel, S.I., Golub’, A.P., Izvekova, Yu.N., Afonin, V.V., Dol’nikov, G.G., Zakharov, A.V., Zelenyi, L.M., Lisin, E.A., and Petrov, O.F.: On the distributions of photoelectrons over the illuminated part of the Moon, JETP Lett., Vol. 99, pp. 115-120, 2014.

[4] Rennilson, J.J. and Criswell, D.R.: Surveyor observations of lunar horizon-glow, Moon, Vol. 10, pp. 121-142, 1974.

[5] Zook, H. and McCoy, J.: Large scale lunar horizon glow and a high altitude lunar dust exosphere, Geophys. Rev. Lett., Vol. 18, pp. 2117-2120, 1991.

[6] Popel, S.I. and Zelenyi, L.M.: Dusty plasmas over the Moon, J. Plasma Phys., Vol. 80, pp. 885-893, 2014.

METEOROID IMPACTS AND DUST PARTICLE RELEASE FROM THE LUNAR SURFACE

S.I. Popel[1], A.P. Golub'[1], Yu.N. Izvekova[1], B. Atamaniuk[2], G.G. Dolnikov[1], E.A. Lisin[3], A.V. Zakharov [1], L.M. Zelenyi[1]
[1] Space Research Institute RAS, ul. Profsoyuznaya 84/32, Moscow 117997, Russia;
[2] Space Research Center PAS, ul. Bartycka 18A, Warszawa 02-716, Poland;
[3] Joint Institute for High Temperatures RAS, ul. Izhorskaya 13/19, Moscow 125412, Russia.
popel@iki.rssi.ru

Introduction:

It is now almost universally accepted that the dust over the lunar surface is a component of a plasma-dust system (see, e.g., [1-3]). The first lunar dust observations were made during the Surveyor and Apollo missions. The Surveyor lunar missions revealed that sunlight was scattered in the terminator region, and this led to the generation of the lunar horizon glow and streamers above the lunar surface [4]. Subsequent observations showed that the sunlight was scattered most probably by the charged dust particles originating from the lunar surface [5]. The analysis of the data obtained by the Surveyor landers led to a conclusion that the dust particles with a diameter of about 5 μm might levitate at a height of about 10 cm above the lunar surface.

The description [1-3] makes clear some features of dusty plasma system over the Moon. However, there are unsolved problems concerning its parameters and manifestations [6]. In particular, significant uncertainty exists as to the physical mechanism through which dust particles are released from the surface of the Moon. Adhesion has been identified as a significant force in the dust particle launching process which should be considered to understand particle launching methods [7].

The problem of the dust particle release from the lunar surface can be solved, for example, by considering meteoroid impacts onto the surface of the Moon. Here, we consider lunar dust particle launching process due to meteoroid impacts. A significant attention is paid to the importance of the adhesive force.

The force of adhesion:

In [7] dust particles with smooth surfaces have been considered. The effect of surface roughness results in significant attenuation of the effect of adhesion in comparison with the results [7]. Indeed, the calculation of the force of adhesion between a plane with an asperity of the radius *r* and a spherical particle of radius *a* gives

$$F=\frac{AS^2}{24\Omega^2}\left(\frac{ra}{r+a}+\frac{a}{\left(\frac{1+rS}{2\Omega}\right)^2}\right), \qquad (1)$$

where *A* is Hamaker's constant, *S* is the surface cleanliness, and Ω=0.132 nm characterizes the diameter of oxygen ion. For lunar regolith Hamaker's constant is $4.3\cdot10^{-20}$ J; surface cleanliness varies in the range of 1 to 0 and for lunar dayside is calculated as *S*=0.88[8]. Calculations based on Eq. (1) show that the effect of roughness results in two-three orders of magnitude attenuation of the effect of adhesion in comparison with the case of a smooth particle (see Fig. 1). Nevertheless, even considering the roughness of lunar regolith particles, the electrostatic forces required to launch dust particles from the lunar surface, as a rule, do not exceed the adhesive forces. Dust particle

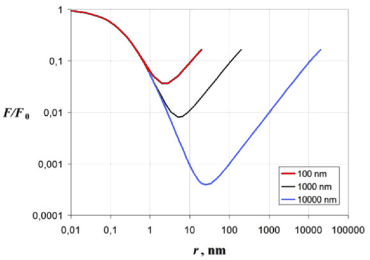

Fig. 1. Dependence of the normalized force of adhesion (to that in the absence of asperity) on asperity size r for the particles with the sizes of 100 nm, 1 μm, and 10 μm under the conditions of the dusty plasma system at the lunar surface.

launching can be explained if the dust particles rise at a height of about dozens of nanometers owing to some processes (e.g., meteoroid impacts, etc.). This is enough for the dust particles to acquire charges sufficient for the dominance of the electrostatic force over the gravitational and adhesive forces, and finally to rise above the lunar surface.

Dust particle release:

When high-speed meteoroid impacts the lunar surface the substances of the impactor and the target are strongly compressed and heated. Under the action of high pressure strong shock wave is formed. The shock propagates and weakens moving away from the impact epicenter. Finally the weakening shock transforms into linear acoustic wave. The zones (around the impact epicenter) of evaporation of the substance, its melting, destruction of particles constituting lunar regolith, their irreversible deformations are formed due to the propagation of the weakening wave. Beyond the zone of irreversible deformations the zone of elastic deformation is created which is characterized by the magnitudes of the pressure in acoustic wave less than dynamic limit of elasticity.

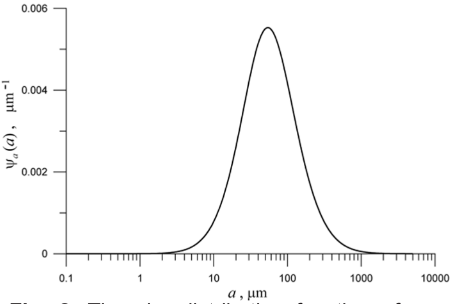

Fig. 2. The size-distribution function of particles released from the lunar surface due to meteoroid impacts.

Considering the balance between the maximum force of pressure in the blast wave and the sum of the adhesive, electrostatic, and gravitational forces we determine the radius of the zone around the impact epicenter which restricts the region where dust particles are released from the surface of the Moon due to meteoroid impacts. Furthermore, we estimate the speeds of the released particles, find their size-distribution (Fig. 2), and evaluate maximum heights of dust particle rise.

Conclusions:

Thus to consider dust particle release from the lunar surface one has to take into account (among other effects) both the adhesion and meteoroid impacts. A possibility of the rise of micrometer-sized dust particles above the lunar surface is shown. In particular, dust particles with a diameter of about 5 μm can be present at a height of about 10 cm above the lunar surface that explains the data obtained by the Surveyor landers.

Acknowledgements:

This work was carried out as part of the Russian Academy of Sciences Presidium program no. 9 "Experimental and Theoretical Research of Objects of the Solar System and Planetary Systems of Stars" and was supported by the Russian Foundation for Basic Research (projects no. 15-02-05627-a, 15-32-21159-мол_а_вед) and the Russian Federation Presidential Program for State Support of Young Scientists (project no. МК-6935.2015.2).

References:

[1] Popel, S.I., Kopnin, S.I., Golub', A.P., Dol'nikov, G.G., Zakharov, A.V., Zelenyi, L.M., and Izvekova, Yu.N.: Dusty plasma at the surface of the Moon, Solar System Research, Vol. 47, pp. 419-429, 2013.
[2] Popel, S.I., Morfill, G.E., Shukla, P.K., and Thomas, H.: Waves in a dusty plasma over the illuminated part of the Moon, J. Plasma Phys., Vol. 79, pp. 1071-1074, 2013.
[3] Popel, S.I., Golub', A.P., Izvekova, Yu.N., Afonin, V.V., Dol'nikov, G.G., Zakharov, A.V., Zelenyi, L.M., Lisin, E.A., and Petrov, O.F.: On the distributions of photoelectrons over the illuminated part of the Moon, JETP Lett., Vol. 99, pp. 115-120, 2014.
[4] Rennilson, J.J. and Criswell, D.R.: Surveyor observations of lunar horizon-glow, Moon, Vol. 10, pp. 121-142, 1974.
[5] Zook, H. and McCoy, J.: Large scale lunar horizon glow and a high altitude lunar dust exosphere, Geophys. Rev. Lett., Vol. 18, pp. 2117-2120, 1991.
[6] Popel, S.I. and Zelenyi, L.M.: Dusty plasmas over the Moon, J. Plasma Phys., Vol. 80, pp. 885-893, 2014.
[7] Hartzell, C.M. and Scheeres, D.J.: The role of cohesive forces in particle launching on the Moon and asteroids, Planet. Space Sci., Vol. 59, pp. 1758-1768, 2011.
[8] Perko, H.A., Nelson, J.D., and Sadeh, W.Z.: Surface cleanliness effect on lunar soil shear strength, Journal of Geotechnical and Geoenvironmental Engineering, vol. 127, pp. 371–383, 2001.

EIGHT AND A HALF YEARS AT VENUS — THE SUCCESSES OF VENUS EXPRESS

H. Svedhem
ESA/ESTEC

Venus Express, Europe's first mission to Venus, was launched from Baikonur, Kazakhstan, on 9 November 2005 and arrived at Venus 11 April 2006. After having orbited our sister planet for more than eight Earth years, before running out of fuel in November 2014, Venus Express has collected a very large set of data allowing a great number of fundamental scientific questions to be addressed and answered. Most of the questions formulated as a part of the mission's science requirement, as formulated in the mission proposal have been answered. These include topics in atmospheric dynamics, structure and chemistry, clouds and hazes, surface and interior, radiation balance and greenhouse effect, induced magnetosphere and plasma environment, and planetary evolution. Solid results have been achieved in all these fields. Naturally, due to the limited scope and budget of the Venus Express mission a number of important questions had to be left unaddressed and to be taken up by future missions. This talk will summarise the Venus Express mission and discuss a number of scientific highlights, and put the results into a perspective of comparative planetology, a higher goal of solar system research. How does the solar system work, and why is Venus so different from the Earth today?

MODELING OF CHEMICAL COMPOSITION IN THE VENUS LOWER AND MIDDLE ATMOSPHERES

V.A. Krasnopolsky
Catholic University of America, Washington, DC, USA; PhysTech, Moscow, Russia.
vlad.krasn@verizon.net

Introduction:

To respond to the current progress in the observational data on the Venus atmosphere, the following models have been developed by the author:

1) Model for excitation of the oxygen nightglow on the terrestrial planets (Krasnopolsky 2011),
2) Photochemical model for the atmosphere at 47 to 112 km (Krasnopolsky 2012),
3) Model for the nighttime photochemistry and nightglow at 80 to 130 km (Krasnopolsky 2013a),
4) Chemical kinetic model for the lower atmosphere up to 47 km (Krasnopolsky 2013b),
5) Model for the H_2O-H_2SO_4 system in the clouds (Krasnopolsky 2015).

The model results will be briefly presented.

Excitation of the oxygen nightglow on the terrestrial planets

The best observational data on the nightglow of the five O_2 band systems and $O(^1S)$ are analyzed along with laboratory data on the excitation, excitation transfer, and quenching of the O_2 metastable states to yield the following scheme of the processes (Table 1).

Table 1. Excitation, excitation transfer, and quenching processes in the O_2 nightglow

State	Bands	τ (s)	α	α_{TE}	α_{TV}	k_O	k_{O2}	k_{N2}	k_{CO2}
$A^3\Sigma_u^+$	HzI	0.14	0.04	0	0	1.3×10^{-11}	4.5×10^{-12}	3×10^{-12}	8×10^{-12}
$A'^3\Delta_u$	Chm	2-4	0.12	0	0	1.3×10^{-11}	3.5×10^{-12}	2.3×10^{-12}	4.5×10^{-13}
$c^1\Sigma_u^-$	HzII	5-7	0.03	0	0	8×10^{-12}	$3\times10^{-14}/1.8\times10^{-1}$	-	1.2×10^{-16}
$b^1\Sigma_g^+$	762 nm	13	0.02	0.09	0.125	8×10^{-14}	4×10^{-17}	2.5×10^{-15}	3.4×10^{-13}
$a^1\Delta_g$	1.27 μm	4460	0.05	0.35	0.65	-	10^{-18}	$<10^{-20}$	10^{-20}

HzI, HzII, and Chm are the Herzberg I, II, and Chamberlain bands; τ is the radiative lifetime; if two values are given, then they refer to high and low vibrational excitation on the Earth and Venus, respectively; α is the direct excitation yield; α_{TE} and α_{TV} are excitation transfer yields for Earth and Venus from the upper states including $^5\Pi_g$ (see details in Krasnopolsky (2011)); and k_X are quenching rate coefficients in $cm^3\ s^{-1}$. Two values of k_{O2} are for $c^1\Sigma_u^+$ (v = 0 and 7-11).

Photochemical model for the atmosphere at 47-112 km

New features of the model are the improved numerical accuracy, the NUV absorption based on the V14 data, the calculated (not fixed) H_2O profile, the NO and OCS chemistries based on the observed abundances, and column rates for all reactions. The calculated vertical profiles of CO, H_2O, HCl, SO_2, SO, OCS and the O_2 dayglow at 1.27 μm generally agree with the observations. Production of CO and O, O_2, O_3 by photolysis of CO_2 is balanced mostly by the ClCO

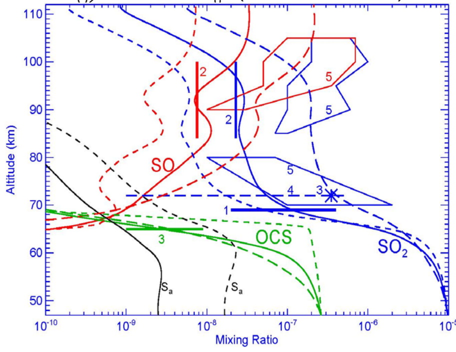

Fig. 1. Variations of sulfur species in Venus' middle atmosphere: Observations and the photochemical model.

cycle; however, the calculated O_2 exceeds the observed upper limit.Formation of sulfuric acid peaks at 66 km and greatly reduces SO_2 and H_2O in the middle atmosphere. Abundances of SO_2 and H_2O in the middle atmosphere are very sensitive to small variations of eddy diffusion near 60 km and the SO_2/H_2O ratio. Therefore the observed variations (Fig. 1) do not require volcanism.

While the production of H by photolyses of H_2O and HCl exceeds the production of Cl, odd chlorine is more abundant than odd hydrogen below 95 km because of the reaction OH + HCl → H_2O + Cl. The chlorine chemistry is very essential in the middle atmosphere. Cycles of the odd nitrogen chemistry are responsible for production of a quarter of O_2, SO_2, and Cl_2 in the atmosphere. A net effect of photochemistry in the middle atmosphere is the consumption of CO_2, SO_2, and HCl from the lower atmosphere and return of CO, H_2SO_4, and SO_2Cl_2.

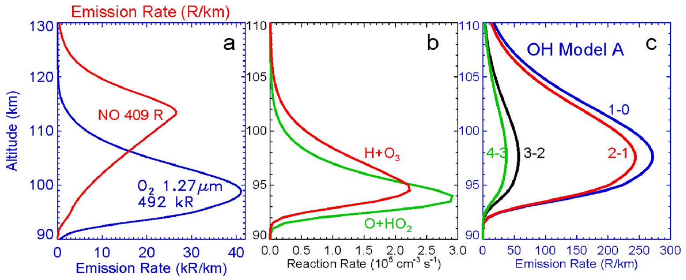

Fig. 2. Calculated vertical profiles of the NO UV nightglow, O_2 nightglow at 1.27 μm, two reactions of the OH formation, and four observed bands of the OH nightglow.

Model for the nighttime chemistry and nightglow at 80-130 km

The Venus Express observations of the NO UV nightglow, the O_2 nightglow at 1.27 μm, four bands of the OH nightglow, and the nighttime ozone require a significant nighttime chemistry. This chemistry is initiated by fluxes of O, N, H, and Cl from the day side with mean hemispheric values of 3×10^{12}, 1.2×10^{9}, 10^{10}, and 10^{10} cm^{-2}, respectively. These fluxes are proportional to column abundances of these species above 90 km. The model includes 86 reactions of 29 species. The calculated nighttime abundances of Cl_2, ClO, and $ClNO_3$ exceed a ppb level at 80-90 km. A scheme for quenching of OH* by CO_2 is developed to fit the observations. Analytic relationships between the nightglow intensities, the ozone layer, and the input fluxes of atomic species are given.

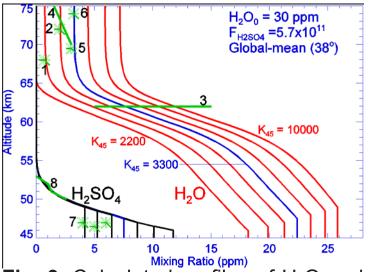

Fig. 3. Calculated profiles of H_2O and H2SO4 vapor for various eddy diffusion are compared with the observa-tions. The preferable profiles are blue.

Model for H_2O-H_2SO_4 system in the clouds

Coupled diffusion of H_2O and H_2SO_4 vapor is calculated in equilibrium with the liquid sulfuric acid. Variations in eddy diffusion near the lower cloud boundary stimulate variability in the cloud properties and abundances of H_2O and H_2SO_4. The preferable global-mean profiles are shown in blue in Fig. 3. Concentration of sulfuric acid varies for those profiles from ~98% near 50 km to ~80% at 60 km and then is almost constant with 79% at 70 km. Latitudinal variations of the H_2SO_4 production, temperature and atmospheric dynamics (simulated by eddy diffusion) induce the observed variations of H_2O and concentration of sulfuric acid.

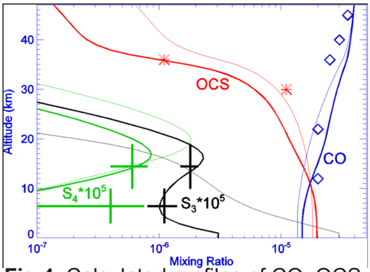

Fig.4. Calculated profiles of CO, OCS, S3, and S4 in the basic model and that without $S_4+h\nu\rightarrow S_3+S$ (solid and thin lines, respectively) are compared with the observed abundances

Chemical kinetic model for the lower atmosphere at 0-47 km

Chemistry of the lower atmosphere is initiated by the fluxes of CO and H_2SO_4 from the middle atmosphere, photolysis of S_3 and S_4, and thermochemistry in the lowest scale height. The chemistry is driven by sulfur that is formed by SO+SO, produces OCS, and makes dramatic changes in abundances of OCS, CO, and S_x. The S_x + OCS mixing ratio is constant at 20 ppm, and the CO + OCS mixing ratio is constant at 35 ppm below 40 km. Free sulfur forms in the lower atmosphere with S_8 = 2.5 ppm above 40 km with condensation into sulfur aerosol near 50 km. Therefore sulfur cannot be the NUV absorber. The model predicts 3.5 ppb of SO_2Cl_2.

References

Krasnopolsky, V.A., 2011. Planet. Space Sci.59, 754-766.
Krasnopolsky, V.A., 2012. Icarus 218, 230-246.
Krasnopolsky, V.A., 2013a. Planet. Space Sci. 85, 78-88.
Krasnopolsky, V.A., 2013b. Icarus 225, 570-580.
Krasnopolsky, V.A., 2015. Icarus 252, 327-333.

CHEMISTRY OF VENUS' MESOSPHERE AS MEASURED BY SPICAV/SOIR ON-BOARD VENUS EXPRESS

D.A. Belyaev[1], A.A. Fedorova[1], F. Montmessin[2], O.I. Korablev[1], A.-C. Vandaele[3], J.-L. Bertaux[2], E. Marcq[2], A. Mahieux[3], D.G. Evdokimova[1]
[1]Space Research Institute (IKI), 84/32 Profsoyuznaya, 117810 Moscow, Russia;
[2]LATMOS - UVSQ/CNRS/IPSL, 11 bd dAlembert, 78280 Guyancourt, France.
[3]Belgian Institute for Space Aeronomy (BIRA), 3 av. Circulaire, B-1180 Brussels, Belgium
bdenya.iki@gmail.com

Introduction

Venus Express (VEx) orbiter made by European Space Agency has finished science operations around the planet; it took time from June 2006 to November 2014. The VEx mission established a new epoch of continuous Venus exploration after a set of probes lunched by USSR and USA in 1970s-1980s. New scientific objectives were devoted to comprehensive study of Venus' atmosphere below, within and above the clouds, ionosphere and plasma environment. A suite of onboard spectrometers SPICAV / SOIR measured chemical content of minor species in the mesosphere (altitudes 65-110 km): such as sulfur and chlorine compounds (SO, SO_2, HCl), water vapor (H_2O), ozone (O_3) and some of their isotopes. These gases play key roles in photochemical processes of Venus atmosphere despite their small content (0.01-1 ppm in volume mixing ratio).

In this paper we make an overview of main results provided by SPICAV / SOIR spectroscopy: UV and IR channels of SPICAV (118-320 nm and 0.6-1.7 μm) and IR spectrometer SOIR (2.2-4.2 μm). Different operation modes allowed probing vertical structure of the mesosphere (solar and stellar occultations) and to track temporal/spatial variations at the level of clouds top using nadir observations (Table 1).

Table 1. List of chemical compounds in Venus mesosphere observed by SPICAV / SOIR spectroscopy in different observation modes. Orange bar points to first detections in specified altitude range.

Gas	λ, μm	Altitudes, km	Instrument	Observation mode	
CO_2	0.17-0.23	~70; 85-150	SPICAV UV	nadir; solar/stellar occultations	
	1.1-1.18	10-20 km	SPICAV IR	nadir (night side)	
	~3.0	70-150	SOIR	solar occultation	
	~4.0	70-150	SOIR	solar occultation	
H_2O	1.37-1.40	58-66 км	SPICAV IR	nadir	
	~2.6	70-90	SOIR	solar occultation	
HDO	~3.67	70-90	SOIR	solar occultation	
SO_2	0.18-0.3	~70; 85-110	SPICAV UV	nadir; solar/stellar occultations	
SO	0.18-0.24	90-100	SPICAV UV	solar occultation	NEW
O_3	0.22-0.28	85-110	SPICAV UV	stellar occultation	
CO	~2.34	70-100	SOIR	solar occultation	
HCl	~3.41	70-90	SOIR	solar occultation	
HF	~2.45	70-90	SOIR	solar occultation	

Results

SOIR was the first high-resolution ($\lambda/\Delta\lambda$ ~ 25000) IR spectrometer working in solar occultation mode near Venus. That made possible to study vertical distribution of the minor gaseous constituents such as H_2O, HDO, HCl and SO_2 on the planet's terminator (morning and evening twilights) in the mesosphere. One of the key results was detection of the HDO/H_2O ratio which occurred to be ~200 times more in Venus mesosphere than on the Earth. That is directly related to the evolution of the water on Venus. Altitude profile of the HCl content was also measured for the first time. HCl is a significant reservoir of hydrogen and the major source of chlorine radicals in the Venus mesosphere. Mixing ratio of hydrogen chloride was ~ 0.1-0.5 ppm in the altitude range of 70-110 km.

Sulfur oxides SO_x are key components associated with aerosols of H_2SO_4 and S_x within and above the clouds. SPICAV-UV nadir observations showed a yearly decline of the SO_2 mixing ratio above the clouds with periodic peaks caused by an unknown source. Pioneer Venus and Venera-15 spacecrafts obtained a similar decennial trend in period 1978-1990. Furthermore, the SOIR and SPICAV-UV spectrometers were capable to obtain vertical profiles of SO_2 and SO density on the planet terminator and to explore SO_2 on the night side using stellar occultation technique in the UV. Two layers of SO_2 absorption were detected in the twilight zone of the mesosphere: a lower layer at altitudes 65-80 km and the upper one at 90-105 km.

An analysis of SPICAV-UV stellar occultation spectra resulted in descovery of ozone layer (the Hartley band at 220-280 nm) at altitudes about 100 km in nighttime mesosphere. A little abundance of O_3 was previously modeled in that region taking into account global subsolar-to-antisolar circulation on Venus at altitudes ~100 km. However, it was not measured so far. Quantity of ozone on Venus occurred to be less than on the Earth by a few order of magnitude.

To resume, SPICAV / SOIR spectroscopy allowed to specify the composition of Venus atmosphere above the clouds, to study in details the vertical structure of minor species and to monitor their long-term variations during over than 8 years of the orbiter's operations.

Acknowledgements

We acknowledge our colleagues from French laboratory LATMOS and Belgian institute BIRA for many years of joint cooperation in SPICAV / SOIR experiment. We also thank to project manager and science coordinator of the VEx H. Swedhem and D. V. Titov from ESTEC in the Netherlands.

REFLECTION OF SURFACE TOPOGRAPHY IN VENUS ATMOSPHERE

L. Zasova, I. Khatuntsev, M. Patsaeva, N. Ignatiev, A. Rodin, A. Turin
Space Research Institute

Introduction

The temperature fields at several levels in the Venus mesosphere (60-95 km) as well as the altitude of the upper boundary of upper and middle clouds retrieved from Venera – 15 (FS-V15) [1], and the zonal wind fields and albedo of the upper clouds, measured by VMC Venus Express [2], and altitude of the upper boundary of clouds VIRTIS-M VEX [3] data are compared with the topographic map, obtained by Magellan [4] . The results show that the isotherms and the altitude isolines of the upper and middle clouds boundary reproduce the extended surface features Ishtar Terra, Beta Regio and Atalanta Planitia. In turn, the shapes of wind isovelocities and albedo at the upper boundary of clouds (VMC) closely follow the details of relief of Terra Aphrodite as well the isolines of altitude of the cloud tops (VIRTIS). In all cases the isolines are shifted with respect to topography by about 30° in the direction of superrotation. Connection between albedo and isovelocities from VMC data and surface topography was studied also in [5]

Data sets and results

We study the traces of influence of the Venus' major topographic features like Ishtar and Aphrodite on the Venus atmosphere.

1. From FS-V15 data the 3-D temperature and clouds fields in mesosphere were retrieved [1]. Earlier it was found that distribution of temperature is described by the Fourier decomposition with 1, 1/2, 1/3, and 1/4days and upper boundary of clouds (1, 1/2 days) harmonics in Solar-fixed coordinates. The amplitudes of the thermal tide harmonics with wavenumbers 1and 2 reach 10 K. We found that in the Sun- fixed frame of reference, both maxima and minima are shifted from noon and from midnight to westwards. The temperature field at 65 km in latitude-longitude coordinates shows a good correspondence between topography (Ishtar, Beta Regio and Atalanta Planitia) and temperature perturbations (coefficient of correlation CC>0.9). In Fig 1 we show the isotherms overlaid the Magellan topography map. We found a good correspondence also between altitude of clouds tops and relief (Fig.2). Based onFS-V15 data we cannot compare separately the solar and topographic longitudes, as we didn't observe Ishtar at different local time. Temperature and clouds maps in comparison of the map of Magellan topography show that the perturbations are shifted by~30° in the direction of superrotation (Fig.1, Fig. 2).
2. The other set of data we consider is the wind speed estimates near the cloud tops, obtained from the UV VMC images [2]. It was found that zonal wind speed correlates with relief (CC > 0.9) in such a way tha tthe extended spot of low wind speed in the region of Terra Aphrodite. A local decrease of the wind speed exceeds 20 m/s. (Fig.1.). The 'image' of the relief on the clouds tops is shifted by 30° to westward direction. Although the observations we used cover the dayside only, the measurements were averaged for many orbits, with local time varying over the day.
3. The altitude of upper boundary of clouds was retrieved from the depth of the CO2 absorption band at 1.5 μm (VIRTIS-M) [3]. The cloud tops altitude isolines are given in Fig 2 with shift of 30 ° to topography. They also show a good correlation. In Fig. 2 we show the albedo map (VMC), also shifted.

Conclusions

We study the different kinds of data, obtained at different time by different methods in the different experiments, with time gap of 30 years (Venera-15 and VEX).We found that Major topographic features as Ishtar and Terra Aphrodite perturb the atmosphere. At altitudes of the upper boundary of clouds the surface "image" is observed in the zonal wind, temperature, altitude of the cloud tops in TIR and NIR and albedo in UV shifted by 30° (this value, initially found for the wind, fits good the other maps).The upper boundary of the clouds may be of several kilometers higher above the mountings, the UV albedo is about 20 % higher above Aphrodite, but wind speed is of 20 m/s lower. (It is worth noting that the variation of thermal zonal wind found from FS-V15 caused by the thermal tides even exceeds this value).

It was found [2] the monotonic increase of the zonal wind velocity in the region of the cloud upper boundary of Venus (from the data of the UV channel). Our study shows that it reflects not a real increase in the wind velocity with time during 8 years observations, but rather is a combined effect of other variable relevent factors such as topography, possibly, local time etc. A strong correlation with the relief features, and similar shifts enables to conclude that in all cases we probably deal with stationary waves, connected to thermal tides linked with the surface topography.

Modeling with non-hydrostatic general circulation model of the Venus atmosphere supports the expected impacts of highlands of Venus surface on dynamic of Venus atmosphere at least up to 100 km altitude [5].

The work is in progress now.

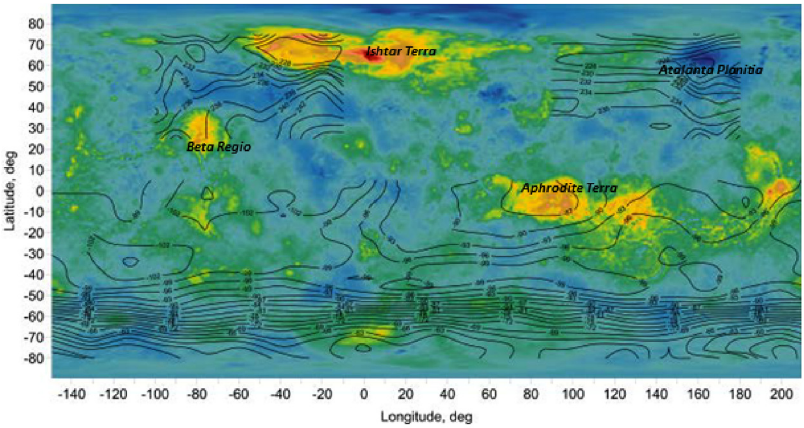

Fig.1. Examples of isolines of temperature (Venera-15, Northern hemisphere) and zonal wind speed VMC Southern hemisphere) at upper boundary of clouds (of 70 km), plotted on theMagellan topography map. One may see that isolines repeat the details of relief. Temperature at upper boundary of clouds decreases with increase of altitude and the wind speed decreases. Correlation with surface details for both cases reaches 90 %.

Acknowledgements

The contriution of AR has been funded by the Russian Ministry of Educaton and Science grant #11.G34.31.0074.

References

[1] Zasova, L.V., et al.: Structure of the Venus atmosphere .Planet. Space Sci. 55, 1712-1728, 2007.
[2] Khatuntsev, I.V., et al.: Cloud level winds from the Venus Express Monitoring Camera imaging, Icarus, 226,140-158, 2013.
[3] Ignatiev, N. I. et al.: Altimetry of the Venus cloud topsfrom the Venus Express observations, J. Geophys. Res. 114, E5, E00B43, 2009.
[4] Berteaux J.-L. et al.
[5] Mingalev, I.V., et al.: Solar System Research, 49, 24-42, 2015

SOME QUESTIONS ABOUT THE VENUS ATMOSPHERE FROM PAST MEASUREMENTS

S.S. Limaye
Space Science and Engineering Center, U. Wisconsin, 1225 W. Dayton St., Madison, WI 53706, USA.
SanjayL@ssec.wisc.edu

Introduction:

The many missions undertaken in the past half a century to explore Venus with fly-by spacecraft, orbiters, descending probes, landers and floating balloons, have provided us with a wealth of data. These data have been supplemented by many ground based observations at reflected solar wavelengths, short and long wave infrared to radio waves. Inter-comparison of the results from such measurements provide a good general idea of the global atmosphere. However, re-visiting these observations also raises some questions about the atmosphere that have not received much attention lately but deserve to be explored and considered for future measurements.

These questions are about the precise atmospheric composition in the deep atmosphere, the atmospheric state in the lower atmosphere, the static stability of the lower atmosphere, the clouds and hazes, the nature of the ultraviolet absorber and wind speed and direction near the surface from equator to the pole. The answers to these questions are important for a better understanding of Venus, its weather and climate. The measurements required to answer these questions require careful and sustained observations within the atmosphere and from surface based stations. Some of these measurements should and can be made by large missions such as Venera-D (Russia), Venus Climate Mission (Visions and Voyages – Planetary Science Decadal Survey 2013-2022 or the Venus Flagship Design Reference Mission (NASA) which have been studied in recent years, but some have not been addressed in such studies. For example, the fact that the two primary constituents of the Venus atmosphere – Carbon Dioxide and Nitrogen are supercritical has not been considered so far. It is only recently that properties of binary supercritical fluids are being studied theoretically and laboratory validation is needed.

With the end of monitoring of Venus by Venus Express orbiter in November 2014 after nearly a decade of observations and the imminent insertion of JAXA's Akatsuki spacecraft into orbit around Venus, it is a good moment to consider the unanswered or unexplored questions about Venus.

UPPER CLOUD HAZE ON THE NIGHT SIDE OF VENUS

N.I. Ignatiev, L. Zasova, D. Gorinov
Space Research Institute of Russian Academy of Sciences, Profsoyuznaya 84/32, 117997 Moscow, Russia.
ignatiev@iki.rssi.ru

Night side limb observations of Venus made by VIRTIS mapping spectrometer onboard Venus Express revealed a thermal emission scattered by the upper haze above the cloud tops. This emission comes from the cloud tops in the spectral range of 4-5 microns and from the hot deep subcloud atmosphere and the surface in several spectral transparency windows between 1 and 2.5 microns. We analyzed the vertical profiles of the scattered emission at 1.18, 1.7 and 2.3 microns to retrieve the upper haze density between 75 and 90 km with the vertical resolution of 3 km. Low sensitivity to particle sizes required an a priori assumption on this parameter to derive the extinction and the equivalent particle number density vertical profiles. As a rule, particle density profiles derived separately from different spectral windows are in agreement between each other. In low latitudes the mean retrieved extinction at 85 km amounts to 10^{-3} km^{-1} at wavelength 1.75 microns and the equivalent mode 1 and 2 densities are equal to 10 and 0.1 cm^{-3}, respectively, with 3σ variability being equal to an order of magnitude. These values are in approximate agreement with both the first analysis of VIRTIS data by deKok et al. (2011, Icarus 211, 51) and the SPICAV/SOIR solar occultation observations (Wilquet et al., 2009, JGR 114, E00B42; Wilquet et al., 2012, Icarus 217, 875; Luginin et al., 2015) obtained for similar conditions. The scale height of the haze density appeared to be about 3 km, which agrees with de Kok et al. (2011), but smaller than 4-5 km obtained from solar and stellar occultation observations with SPICAV/SOIR. At low and middle latitudes limb unit optical depth may be as high as 89 km, while at high latitudes is never exceed 83 km. On the morning side the haze is lower than that on the evening side by about 2 km, which may have an evident explanation: the haze is created during the day from the photochemical production of the sulfuric acid.

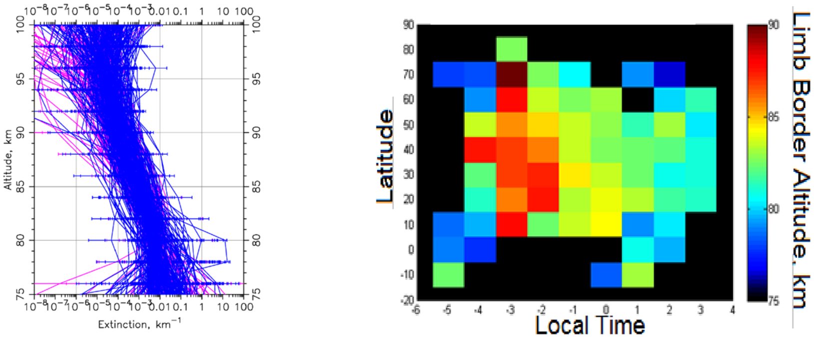

Fig. 1. Vertical profiles of the haze extinctions retrieved from 1.7 and 2.3 μm windows (left) and spatial variability of the upper haze expressed in terms of the unit limb optical depth altitude (right) vs latitude and local time at 1.7 μm.

PAST AND PRESENT VOLCANISM OF VENUS

A.T. Basilevsky[1,2,3], E.V. Shalygin[2], W.J. Markiewicz[2], D.V. Titov[4], N.I. Ignatiev,[5], J.W. Head[3]
[1]Vernadsky Institute, 119991 Moscow, Russian Federation, atbas@geokhi.ru;
[2]Max-Planck-Institut für Sonnensystemforschung, 37077 Göttingen, Germany;
[3]Brown University, Providence, Rhode Island 02912, USA;
[4]ESA-ESTEC, 2200 AG Noordwijk, The Netherlands; [5] Space Research Institute, 117997 Moscow, Russian Federation.

The first reliable information on widespread volcanism on Venus resulted from analysis of side-looking radar images taken by Venera-15-16 (e.g., Barsukov et al., 1986). The morphology of the observed volcanic landforms and the results of geochemical measurements by Venera 8, 9, 10, 13, 14 and Vega 1, 2 landers (Surkov, 1997) showed the essentially basaltic character of venusian volcanism. The results of the radar survey undertaken by the Magellan mission resulted in an improvement in the understanding of venusian volcanism (e.g., Head et al., 1992) and permitted the stratigraphic classification of venusian terrains and landforms, including those related to volcanism (e.g., Basilevsky and Head, 1998). Following this, as a result of the global geologic mapping of Venus, the stratigraphic classification was shown to be reliable (Ivanov & Head, 2011, 2013). The most widespread units are various volcanic plains, but volcanic edifices, mostly shield volcanoes are also common.

The most widespread unit is plains with wrinkle ridges (pwr), also called regional plains (Figure 1, left), occupying ~42% of the surface of Venus (Ivanov & Head, 2011). Their morphology and age relations with impact craters suggest widespread and high-yield volcanic eruptions that occurred during a relatively short time at ~0.5-1 Ga. Shield plains (psh) (Figure 1, right) occupy 18.5% of the venusian surface and represent numerous coalescing volcanic shields typically formed before emplacement of regional plains. Younger than these are smooth plains (ps, ~2%) and lobate plains (pl, ~9%) (Figure 2); the latter form both plains *per se* and gently-sloping shield volcanoes.

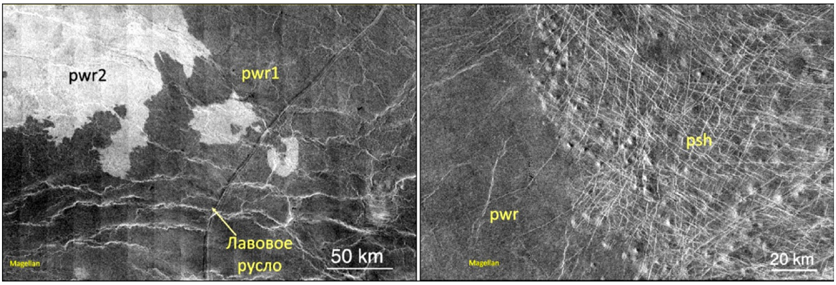

Fig. 1. Left – plains with wrinkle ridges, the older (pwr1) and younger (pwr2) subunits showing the enigmatic channel of Baltis Vallis; Right – shield plains (psh) embayed by plains with wrinkle ridges (pwr).

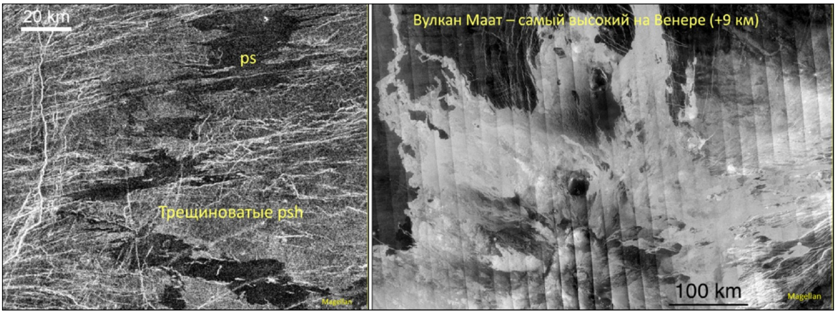

Fig. 2. Left – smooth plains (ps) filling depressions within shield plains (psh); Right – lobate flows forming Maat Mons, the highest volcano on Venus. Radar-bright flows are superposed on the darker regional plains.

Also observed on Venus are steep-sided volcanic domes (Pavri et al., 1992). They could be formed by eruptions of viscous, probably non-basaltic, silicic lavas; alternatively, the high viscosity of these lavas may be due to the presence of numerous gas bubbles. Understanding the nature of these high-viscosity lavas is one of unresolved problems of venusian volcanism. We plan to work on this problem through analysis of 1-micron surface emissivity data taken by Venus Monitoring Camera (VMC) onboard the Venus Express (VEX). First results gained by this approach are given in Basilevsky et al. (2012).

Another intriguing problem of Venusian volcanism is the presence or absence of currently ongoing volcanic activity. Some representatives of the geologically youngest volcanic unit (pl) based on their characteristics, in particular the age relations with dark-parabola impact craters, were dated as formed within the last few tens of million years prior to the present, that is, geologically recently (e.g., Basilevsky, 1993). But the issue of currently ongoing volcanic activity remained unresolved. The work of Bondarenko et al. (2010) and Smrekar et al. (2010) suggested such a possibility, but did not confirm its certainty. More reliable information was recently gained through analysis of the VEX VMC data by Shalygin et al. (2015), who showed that in one of geologically young rift zones, associated with Atla Regio, "hot" spots are observed which appear and disappear at the scale of days to months (Figure 3).

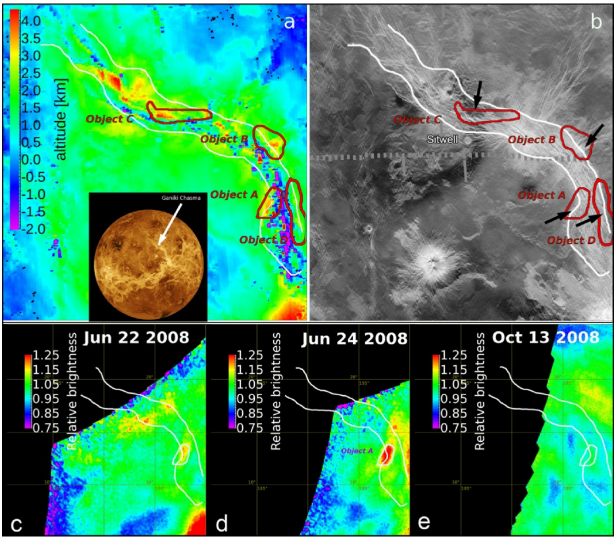

Fig. 3. a) Topographic map of Ganis Chasma area with transient spots (objects A-C), white arrow in the figure inset shows the locality of Ganis Chasma; b) Magellan radar image of this area; c-e) Transient spot A seen/not seen during several observation sessions.

Because the view of the orbital spacecraft is blurred by the clouds, the areas of increased emission appear spread out over large areas of about 100 km across, but the hot regions on the surface below are probably much smaller. Indeed, for the hotspot known as 'Object A', as an option, the real hot area may only be around 1 square kilometre in size, with a temperature of 830 °C, much higher than the global average of 480°C.

So, concluding, Venus was volcanically active at least during the last 0.5-1 Ga and seems to continue to be active now. Venus volcanism is mostly basaltic, but there is some evidence of possible non-basaltic, silicic volcanoes, which we plan to assess in new analyses of the VEX VMC data. Also we plan to continue the search for new evidence of currently ongoing volcanic activity on this Earth-like planet.

References:

[1] Barsukov et al., 1986. J. Geophys. Res. 91. No B4. D378-D398. [2] Basilevsky, 1993. Geophys. Res. Lett. 20(10), 883-886. [3] Basilevsky &. Head. 1998. J. Geophys. Res., 103, 8531-8544. [4] Basilevsky et al., 2012. Icarus. 217. 434-450. [5] Bondarenko et al., 2010. Geophys. Res. Lett. 37, L23202. [6] Head et al., 1992. J. Geophys. Res., 97, 13,153-13,197. [7] Ivanov & Head, 2011. Planet. Space Sci. 59 (13). 1559-1600. [8] Ivanov & Head., 2013. Planet. Space Sci. 84. 66-92. [9] Pavri et al., B., 1992. J. Geophys. Res. 97, 13,479-13,493. [10] Shalygin et al., 2015. Geophys. Res. Lett., 10.1002/2015GL064088. [11] Smrekar et al., 2010. Science, 328 (5978), 605-608, [12] Surkov, 1997. Exploration of Terrestrial Planets from Spacecraft: Instrumentation, Investigation, Interpretation, 2nd ed., John Wiley, Hoboken, N. J. 446 p.

VENUS: MAIN REGIMES OF RESURFACING

M.A. Ivanov[1], J.W. Head [2],
[1]Institute, Address, Country;
[2] Institute, Address, Country.

Introduction: Volcnism and large-scale tectonic deformation on Venus are related to its mantle circulation patterns and represent primary manifestations of the process of global internal heat loss [e.g., 1]. The surface of Venus displays a variety of volcanic and tectonized terrains whose morphologic characteristics are due to either emplacement of volcanic materials or superposition of tectonic structures. Here we describe the temporal distribution of tectonized terrains, their stratigraphic relationships with volcanic units, and how these outline the major episodes in the geological evolution of Venus.

Major volcanic units: Although the surface of Venus displays a variety of volcanic landforms [2-4], three major volcanic units are most important: shield plains, psh, regional plains, rp, and lobate plains, pl. Together they comprise ~96% of all volcanically dominated units and cover ~70% of the surface of Venus. Shield plains (psh, ~18.5% of the surface of Venus): Abundant small (2-10 km across) shield- and cone-like features (volcanic edifices [2,3,5]) characterize shield plains. Shield plains are only mildly deformed by wrinkle ridges and sparse fractures/graben. Regional plains, lower unit (rp1, ~33% of the surface of Venus) are composed of morphologically smooth, homogeneous, sourceless plains. Networks of wrinkle ridges deform the surface of the plains [6]. Regional plains, upper unit (rp2, ~9.8% of the surface of Venus) are characterized by higher radar albedo and deformed by the same families of wrinkle ridges. Lobate plains (~8.8% of the surface of Venus): The surface of lobate plains is occasionally disturbed by graben of rift zones. The most characteristic features of lobate plains are numerous bright and dark flow-like features. The plains are usually associated with the large dome-shaped rises (e.g., Beta, Eistla, Atla Regions, etc.).

Major tectonized units: The following five tectonized units are the most important on Venus and make up ~20% of its surface [7]. (1) Tessera (t, 7.3% of the surface of Venus) displays intersecting sets of contractional and extensional structures [e.g., 8]. (2) Densely lineated plains (pdl, 1.6%) are dissected by numerous densely packed parallel fractures. (3) Ridged plains/Ridge belts (pr/rb, 2.4%) are deformed by broad and long ridges that often form elevated belts. (4) Groove belts (gb, 8.1%) are swarms of extensional structures that completely obscure the characteristics of underlying materials at the scale of the mapping. (5) Rift zones (rz, 5.0%) consist of numerous parallel fissures and troughs that usually completely erase the morphology of underlying terrains.

Age relationships of volcanic and tectonic units: Clear relationships of relative age are often seen among the tectonic and volcanic units at the global scale [7]. Structures of pdl and pr/rb usually cut tessera but in some places they appear to be incorporated into the tessera structural pattern. Graben of gb cut occurrences of tessera, pdl, and pr/rb. Vast expanses of mildly deformed plains units (shield- and regional plains) embay all occurrences of t, pdl, and pr/rb and the majority of groove belts. Structures of rift zones cut the vast plains and are contemporaneous with the younger lobate plains.

Craters embayed by regional and lobate plains: The age relationships between regional plains (rp1) and lobate plains are consistently the same over the entire surface of Venus [9]. In any specific place where these units are in contact, lobate plains embay regional plains and, thus, are younger. The different morphologic characteristics of rp1 and pl and their different ages [10-12] imply that these lava units correspond to different geological epochs with apparently different styles of volcanism [9]. The main characteristic of regional plains is that the majority of their area (slightly over 80%) is concentrated only in three largest occurrences of this unit. The sizes of occurrences of lobate plains are much more evenly dis-tributed within the observable range of areas.

The total number of craters that occur either within or on the boundaries of the areas of rp1 is 582. Out of these, 563 craters appear to be superposed on the plains and the plains embay 19 of the craters. This gives the proportion of craters embayed by regional plains as ~3%. The total number of craters on lobate plains is 79 and the plains embay 27 of them, which gives the proportion of the em-bayed craters in the case of lobate plains as 33%

Discussion: The majority of tectonized terrains (t through gb) are the products of tectonic resurfacing and are embayed by the vast volcanic plains and, thus, are older. There are no units with either mildly- or non-tectonized surfaces that interleave the tectonic terrains, which would be expected if the tectonic resurfacing operated only during specific phases in discrete regions. The major tectonized terrains thus define an earlier, ***tectonically dominated regime of resurfacing*** that occurred at the global-scale near the beginning of the observable geological history of Venus.

This ancient tectonic regime began with formation of the oldest unit, tessera. Both contractional (ridges) and extensional (graben) structures form tessera. There is robust evidence for the relatively old age of the ridges. This suggests that formation of tessera was due to large-scale compression that resulted in regional thickening of the crust [13,14].

The tectonic regime ended by development of pervasive groove belts that mark zones of extension. Branches of groove belts compose the tectonic components of many coronae [15] suggesting that these features are genetically related and that coronae may have punctuated the final stages of the ancient tectonic regime.

This regime was followed by emplacement of the vast volcanic plains, such as shield and regional plains, the surfaces of which are extensively deformed by the global network of wrinkle ridges [6]. Emplacement of the plains has defined the second, ***volcanically dominated regime of resurfacing*** [16], representing a time when surface tectonic deformation related to the mantle convection waned and was changed by massive, catastrophic-like, outpouring of volcanics of regional plains. The small number of embayed craters (3%) suggests that the emplacement of regiona plains was geologically fast.

Rift zones are the stratigraphically youngest manifestations of regional-scale tectonic deformation on Venus. Rifts are spatially and temporarily associated with the youngest lava flows and often cut the crest areas of large, but isolated, dome-shaped rises. Structures of rift zones always cut the surface of the vast plains, which means that rifts are separated in time from the ancient tectonic regime, post-date the regional plains, and represent a new phase of tectonism that was contemporaneous with the late volcanism of lobate plains. Rift zones and lobate plains define the third, ***network rifting-volcanism regime of resurfacing*** that was related to late stages of evolution of the dome-shaped rises. The much larger proportion of craters embayed by lobate plains (33%) suggests a more gradual style of emplacement of volcanic materials during this regime.

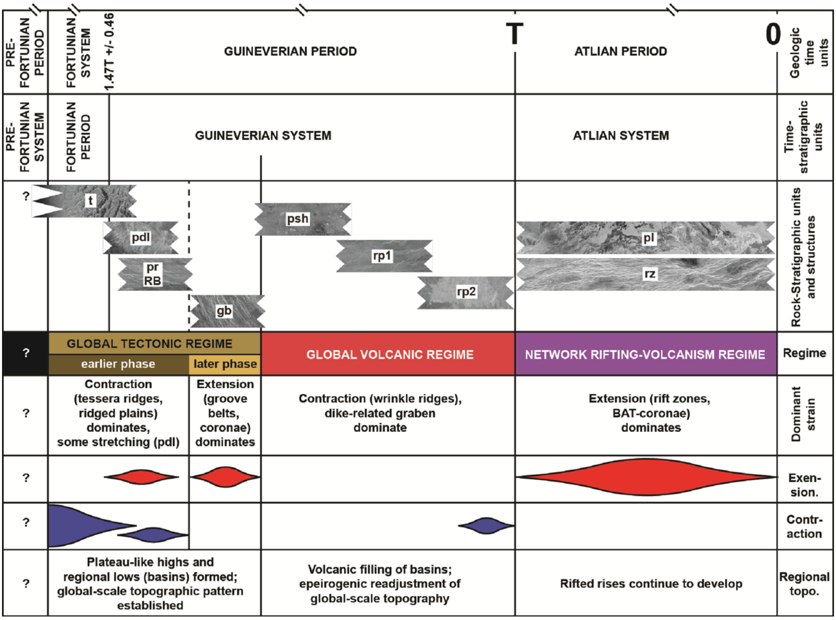

Fig. 1. A global correlation chart that shows the three major regimes of resurfacing on Venus

References:

1. Solomon, S.C. and J.W. Head, JGR, 87, 9236, 1982;
2. Head et al., JGR, 97, 13153, 1992;
3. Guest et al., JGR, 97, 15949, 1992;
4. Crumple and Aubele, in: Encyclopedia of Volcanoes, 727, 2000;
5. Aubele and Slyuta, EMP, 50/51, 493, 1990;
6. Bilotti, F. and J. Suppe, Icarus, 139, 137, 1999;
7. Ivanov, M.A., and J.W. Head, PSS, 59, 1559, 2011;
8. Sukhanov, A.L. In: Venus GGG, Barsukov et al., eds, 82, 1992;
9. Ivanov and Head, PSS, 84, 66, 2013;
10. Namiki and Solomon, Science, 265, 929, 1994;
11. Price et al., JGR, 101, 4657, 1996;
12. Guest and Stofan, Icarus, 139, 56, 1999;
13. Head, J.W., et al., PSS, 42, 803, 1994;
14. Bindschadler, D.L. et al., JGR, 97, 13563, 1992;
15. Stofan, E.R. et al., JGR, 97, 13347, 1992;
16. Ivanov, M.A., and J.W. Head, LPSC 43, #1037, 2012.

THE RIFT ZONES OF VENUS: RIFT VALLEYS AND BELTS OF GRABEN

Guseva E.N.
Vernadsky Institute, Moscow, 11999, Russia.
guseva-evgeniya@ya.ru

Introduction. The spatial distribution of rift zones on Venus is illustrated by the Global geological map of (scale 1:12 M) [1]. The area of rift zones (rz) on the map is ~ 22.6×10^6 km^2, which is about 5% of the surface of Venus [1]. The rift zones concentrated mainly in the equatorial region of the planet [2-4]. They form an extensive system ~ 40,000 km long [5-7]. Rift zones are spatially associated with broad (hundreds of km across) lava plains [8] and large (D>100 km [9]) volcanic constructs [10-11]. The highest concentration of these constructs observed in the regions of triple junction of rift zones [12], mainly in the BAT (Beta-Atla-Themis) region where the large volcanic constructs are often associated with significant positive gravity anomalies [13]. The volcanic features are thought to be mostly basaltic, similar in composition to alkaline [14] and tholeiitic basalts of the Earth [15]. Rift zones are relatively young and characterize a style of the Venus tectonics on the later stages of its geological evolution.

Goals of the study. The spatial distribution, topographic configuration, morphometric parameters, and character of volcanism associated with the morphological varieties of rifts give a possibility to classify varieties of rifts by the types of the rift-forming structures. The results of this study help to classify rift zones into two different facies and give the basis for understanding of the processes of rifting on Venus.

Observations and results. The rifts appear on Venus mostly in the region between ~ 30°N-30°S and ~ 120°-315°E. (Fig. 1). They form broad zones of graben and troughs that cross all structural and material complexes on Venus except for some youngest lava plains. Among rift zones, two the structural facies are identified: the rift valleys and the belts of graben.

Rift valleys. Structures within this facies are collected in long (thousands of km) and wide (hundreds of km) zones [16-17], which are manifested by deep (up to several km) canyons. These zones are spatially associated with domes-shaped rises in the BAT region [5,7-8], which were classified as the rift-related domes [10-11] and interpreted as the areas of rising of the hot mantle material [6,18-20, 10,11]. The canyons are radiating away from the top of the rises and are localized mostly within the BAT region (Fig. 1).

The rift valleys of the Atla Regio propagate from the top of the Atla dome-like rise in the NW, SW, and SE directions for distances up to ~ 3500 km. The Atla dome is ~ 1200-1600 km wide and ~ 2.5 km high [10,17]. The average width of the rift valleys is: ~ 171±66 km for the NW branch, ~ 386±76 km for the SW branch, and ~ 250±75 km for the SE branch. The average depth of the rift valleys is: ~ 2.6±1.4 km for the NW branch, ~ 1.5±0.3 km for the SW branch, and ~ 1.8±0.8 km for the SE branch [17]. In the cross-section, the rift valleys are asymmetric and have a W-shaped profile. The rift valleys of the Atla Region are spatially associated with extensive occurrences of lava plains [8] and with the large volcanoes of Maat and Ozza Montes [10]. The Maat volcano (SW branch of Atla) has the shape of a truncated cone with height of ~ 5.9 km and the base diameter of ~ 341.5 km. The visible volume of the volcano is estimated to be ~ 202×10^3 km^3. Long (up to 600 km) lava flows emanate from the center of the volcano and flow down along its flanks. The Ozza volcano (the triple junction of the Atla rift valleys) has the shape of a truncated cone which is ~ 2.6 km high and which base ~ 347.7 km. The volume of the volcano is estimated to be about 91×10^3 km^3 and the radial flows on the flanks of the volcano can be as long as ~ 800 km. Possible evidence for modern volcanic activity was detected in Atla Regio [21].

The rift valleys of the Beta-Phoebe Regions propagate from the top of the dome-like features, which are up to ~ 2500 km wide [10,20,18] and 2 to 5 km high [10,18]. Three main branches compose the rift valley system in the Beta-Phoebe region: the NW branch, the SW branch, and the S branch that extend southward and merges with Phoebe Regio. The other branches are ~ 2600 km long. The average widths of the rift valleys are: ~ 191±73 km for the NW branch, ~ 182±70 km for the SW branch, and ~ 236±109 km for the S branch. The average depths of the rift valleys are: ~ 2.0±0.9 km for the NW branch, ~ 1.5±0.5 km for the SW branch, and ~ 2.0±1.1 km for the S branch [17]. In the cross section, the rift valleys are asymmetric and have a W-shaped profile. The rift valley of the Beta Regio are spatially associated with the extensive lava fields [8] and a large volcano of Theia Mons [10,20]. The Theia volcano (triple junction of the Beta rift valleys) has an irregular shape which is resulted by complex processes of the dome rising and formation of the rift in this area [10]. The height of the volcano is ~ 3 km and its base is ~ 228 km in diameter; its volume is estimated to be ~ 160×10^3 km^3 [10]. The longest lava flows on the flanks of the volcano can reach ~ 1000 km. Results of geophysical modeling suggest that Beta may be currently rising [22].

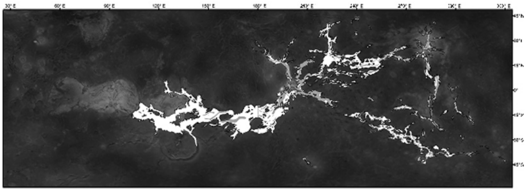

Fig. 1. Map of the distribution of rift valleys (gray) and belts of graben (white) on the surface of Venus. Base – topographic map: http://astrogeology.usgs.gov/missions/magellan, simple cylindrical projection. Boundaries of rift zones are from [1] with modifications.

Belts of graben. These structural facies of the rift zones are localized within long (thousands of km) and wide (hundreds of km) belts. Belts consist of a series of closely spaced graben and manifested by broad swarms of extensional structures. The belts do not show the spatial association with the dome-shaped rises and are more widespread than the rift valley (Fig. 1). The most typical example of the graben belt is in the area to the west of the BAT triangle (Fig. 1). This belt extends from the Atla region toward the Aphrodite Terra through Thetis Regio and ends at the tessera massif in Ovda Regio. The total length of the longest graben belt is ~ 6000 km and its width varies from 500 to 1500 km. The shape of the profile of the graben belts is usually flat, complicated by numerous relatively shallow (many hundred meters) and narrow (km wide) depressions. Occurrences of lobate lava plains are usually associated with the graben belts [23], but the large volcanoes are absent in the belt immediate surroundings.

The belt of grabens of the Thetis Region is a segment of the longest graben belt of Venus. This segment extends for ~ 3500 km from NE to SW; its average width is ~ 510±170 km. The belt consists of a series of closely spaced graben and is manifested by broad swarms of extensional structures. The shape of the profile of the belt is affected by series of topographically shallower, V-shaped depressions. Young lobate lava plains are usually associated with the belt.

Conclusions: 1) The rifts of Venus are classified on two different structural facies: rift valleys and belts of graben. The valleys form the core areas of rift zones. 2) Belts of graben are much longer and wider compared with the rift valleys, 3) The structural facies of the rift zones have different topography: rift valleys represent deep, flat-floored canyons, belts of grabens are swarms of numerous topographically shallower, V-shaped depressions. 4) Rift valleys are associated with dome-like rises and large shield volcanoes (concentrated volcanic sources). No such features occur in association with graben belts. 5) Apparently sourceless lava flows represent the most common type of volcanic features in association with the graben belts.

References:

[1] Ivanov, Head. PSS. 2011. V.59. P.1559-1600; [2] Solomon et al. JGR. 1992. V.97. P.13199-13256; [3] Senske, Schaber, Stofan. JGR. 1992. V.97. P. 3395-13420; [4] Crumpler, Head., Aubele. Science. 1993. V.261. P.591-595; [5] Masursky et al. JGR. 1980. V.85. P.8232-8260; [6] McGil et al. Geophys. Res. Lett. 1981. V.8. P.737-340; [7] Shaber. Geophys. Res. Lett. 1982. V.9. P.499-502; [8] Head et al. JGR. 1992. V.97. P.13.153-13.197; [9] Crumpler et al.//in Venus II, eds. Bougher., Hunten., Phillips. Univ. of Arizona Press. 1997. P. 697-756; [10] Stofan et al. JGR. 1995. V.100. P.23.317-23.327; [11] Smrekar, Stofan, Kiefer.//in Venus II, eds. Bougher., Hunten, Phillips. Univ. of Arizona Press. 1997. P. 845-878; [12] Senske.//Earth Moon Planets. 1990. V.50/51. P.305–327; [13] Smrekar., Phillips. Earth Planet. Sci. Lett. 1991. V.107. P.582–597; [14] Barsukov et al. 17th **LPSC.** Houston. 1986. P.28-29; [15] Surkov et al. XIX meeting of COSPAR. Philadelphia. 1976a; [16] Basilevsky, Head JGR. 2000. V.105. P.24.583-24.611; [17] Guseva. 4th MSSS. 2013. 4MS³-PS-43; [18] Campbell et al. Science. 1984. V.226. P.167-170; [19] Phillips, Hansen. Earth Planet. Sci. 1994. V.22. P.597-654; [20] Basilevsky, Head. Icarus. 2007. V.192. P.167-186; [21] Shalygin et al. Geophys. Res. Lett. 2015. In press; [22] Vezolainen et al. JGR. 2004. V. 109. P.1-8; [23] Guseva, Basilevsky, Head. Solar Syst. Res. 2013. V.47. №3. P.159-169.

ON NON-METEORIC ORIGIN OF LAYERS BELOW V1 IN VENUSIAN IONOSPHERE

M. Bondarenko[1], A. Gavrik[1]
[1]Institute of Radio Engineering (RAN), 1, Academician Vvedensky square, Fryazino, Moscow region, Russian Federation
linuxoid2013@mail.ru

As more data were being collected from radio science occultation experiments on Venus and Mars (PVO, VEX, MGS, MEX), a number of ionospheric electron density (N_e) profiles were produced with additional layers, around 100-120km on Venus, below the smaller Chapman ionization layer V1, and correspondingly below M1 on Mars. Drawing an analogy with studies of Earth ionosphere, these layers were hypothesized to be “meteoric ionization layers” supposedly caused by ablation of meteoric dust, cometary ejecta, meteoric showers and other similar mechanisms in the lower ionosphere of the two planets. Numeric models developed in the early 2000s provided estimates roughly similar to or bracketing the parameters of the observed “layers”.

While the existence of these signal features is indisputable, their interpretation as “meteoric layers”, cautious first, then more and more accepted as a default explanation, needs to be reexamined.

Such reexamination can be started from a little known data set of 8 daytime occultations spanning the range of [-56 ÷ -82] deg latitude, obtained 14÷30 October 1983 in VENERA-15,VENERA-16 joint mission to Venus, as part of its occultation season 1, the strongest of the three in this earlier Soviet study of the planet.

In contrast to the recent publications, we examined signals processed to level 02 rather than completed N_e profiles. All signals in the series up to the V1 altitudes, and possibly higher, feature wavelike variations with growing amplitudes, which exceed uncertainty levels, in one case looking spectacularly like a very well expressed sine with a near-exponential envelope. Using a Morlet wavelet transform combined with subsequent wavelet filtering, the signals were decomposed into the lower frequency component, reflecting the Chapman layers of the ionosphere (and responsible for the N_e profile shape after further processing), and what appeared to be a set of nearly-harmonic components at higher frequencies with bell-shaped envelopes growing to a certain “dissipation altitude”, then subsiding, superimposed on the lower frequency component.

These higher-frequency oscillations with wavelengths approximately between 5km and 15km were further inspected as possible recordings of gravity wave activity at ionospheric altitudes. Knowing background profiles of pressure/density and temperature, it is possible to estimate GW parameters from its dissipation altitude, if it dissipates due to kinetic viscosity and thermal dumping, which affect GWs at ionospheric heights. Profiles determined in other VEX experiments were used for this estimation for both VENERA-15,16 and VEX data. This calculation for the analyzed signal components produced hypothetical GW parameters matching those of real GWs observed on UV daytime photographs of the upper cloud layer of Venus at 66km (Peralta et al, 2008), as well as GWs at 115-135km on images from CO2 non-LTE emissions (Garcia et al, 2009). Additionally, numeric estimates demonstrated that the real GWs identified by Peralta at the upper cloud levels would dissipate at the same altitudes as the components of our signals, if propagating upwards, and moreover that the dissipation altitudes lie at the turbopause heights. The matches conflate these separate observations from two missions into a coherent description of a physical phenomenon, which also seems to be a permanent feature of the Venusian ionosphere (VENERA-15,16 measurements and VEX mission are spaced 23-30 years apart).

A new interpretation of lower ionospheric “layers” below V1 (if the above considerations are correct) immediately follows: what appears on N_e profiles as “additional layers” below V1 may in fact be the last, largest periods of GWs rising from the top of the cloud layer level (65-70km) and being on the verge of disspating at turbopause altitudes, which were registered in high-quality occultation data. Not only of non-meteoric origin, they do not seem to appear as “layers” (which would imply more stability), but according to this interpretation are dynamic and local phenomena.

The overall distribution of N_e profiles with “layers” in the VEX mission, as seen in a recent recalculation of the profiles, falls geographically into higher latitudes (appr. 60-65 degrees poleward for both hemispheres, also noted in various previous works). This also appears to strengthen the GW interpretation, as these are the latitudes of the “cold collar” encircling the polar vortex formations where atmospheric parameters permit propagation of GWs in our range upwards, possibly originating from the top of the cloud layer below.

Is the GW interpretation of “lower ionospheric layers” supported by the VEX VeRa data?

In the more recent Western missions, radio science experiment designers standardized on much shorter wavelengths, in an attempt to emphasize atmospheric studies. The Soviet VENERA-15.16 emitted an S-band signal at 32cm and X-band at 8cm, with most power allocated to the S-band thus producing a signal with a much stronger ionospheric signature. In case of VEX VeRa (S-band = 13cm, X-band = 3.8cm, most power to the X-band) the X-band power (i.e. closed-loop AGC) signal *at ionospheric altitudes* is digital noise.

The Soviet mission experiment design involved comparison between the derivative of the differential Doppler frequency residual (channel one) and accordingly normalized signal power (channel two), which permits separation of signal variations synchronous between the channels and noise. On signals in this form smaller variations are much more obvious. For the VEX VeRa X-band data the lack of meaningful power signal at ionospheric altitudes precludes using the same processing methods.

For the VEX VeRa S-band signal the problem was further compounded by a malfunction: S-band channel power sharply dropped after the first occultation season in 2006, rendering it scientifically useless and for the rest of the mission leaving researchers with data from X-band channels only.

But, even during VEX VeRa Season 1 with a valid S-band channel signal, it has been presented in the archives downsampled to 1Hz, i.e. as points 1 second apart on the time scale, which is too crude to resolve smaller signal variations.

It is also possible that the rest of the occultation measurements, even when sampled at 10Hz in Level 02 processed data, were downsampled to 1Hz for the calculation of N_e profiles, also reducing resolution and possible recognition of GW patterns.

THUS a set of design decisions and an unfortunate technical failure in the VEX mission (combined with a certain tradition in interpreting occultation results) probably prevented researchers from even considering the idea that GWs propagating to ionospheric altitudes may have become registered in the results of occultation experiments and subsequently seeped into N_e profiles as additional “layers” of unknown origin.

HOWEVER, as a result of the above analysis of VENERA-15,16 data it becomes possible to recognize possible GW patterns in VEX VeRa data and use this data in further study of the “low-altitude ionospheric layer” phenomenon i n support of the new GW interpretation.

Relevance of GW interpretation to Mars studies. A preliminary and cautios optimism may be expressed that this interpretation may also account for the appearance of “meteoric layers” on Mars, where, in the absence of atmospheric superrotation, GWs (and therefore additional “layers” on N_e profiles) may be expected to show up less frequently and follow a different pattern. On the other hand, the interpretation leads us to a hypothesis that (rather than Mars orbit comet crossings and similar events, proposed by the “meteoric ion layer” theory) the appearance of “layers” may correlate with GW producing events such as dust storms. And indeed dust opacity is a parameter with which the “meteoric layers” demonstrated the highest positive correlation out of many tested in a review by P.Withers et al, 2008. This hypothesis requires further investigation.

In conclusion, while leaving the possibility of ionization from meteoric ablation at heights below V1, and leaving the question of existence of layers of truly meteoric origin on Venus outside the bounds of this discussion, we propose that the signal features widely reported and branded as “meteoric layers” in recent studies may in fact be traces of GW activity at near-turbopause altitudes.

RESURRECTING THE MARINER 1969 IMAGES OF MARS USING THE MOLA GLOBAL DIGITAL TERRAIN MODEL AND MODERN COMPUTER TECHNIQUES

T.C. Duxbury[1], M.S. Robinson[2], D.E. Smith[3], J.K. Campbell[4], A.H. Culver[5], T.M. Eubanks[6], N.V. Seregina[1,7],
[1]George Mason University, Fairfax, VA, USA;
[2]Arizona State University, Tempe, AZ, USA;
[3]Massachusetts Institute of Technology, Cambridge, MA, USA;
[4]Jet Propulsion Laboratory (retired), Pasadena, CA, USA;
[5]Jet Propulsion Laboratory, Pasadena, CA, USA
[6]Asteroids Initiatives LLC, Clifton, VA, USA;
[7]Moscow State University, Moscow, Russia.
tduxbury@gmu.edu

Introduction:

Mariner 6 and 7 approach and flyby images of Mars [1,2], acquired in August 1969, are the earliest observations that resolved the entire martian surface [2]. Phobos, Deimos and stars were within the fields-of-view of some of the images that might be located using modern computer processing techniques. Phobos was already seen transiting Mars in these images. Sufficient data exists today on the orientation and topography of Mars, the orbits of Phobos and Deimos and modeling of spacecraft attitude and cameras to resurrect these images together with a searchable catalog [3]. Such restored Mariner images would be a valuable resource to the scientific community as the Odyssey, MRO, Mars Express, Opportunity and Curiosity images that are being taken today as they provide a broad scale record of surface albedo and clouds from over 40 years ago. The Mars Observer Laser Altimeter (MOLA) global digital terrain model (DTM) [4,5] provides the means to create synthetic images with the same viewing and lighting geometries to provide the context of each image.These simulated images can also be used as accurate absolute control for the Mariner frames to compute camera pointings, focal lengths and distortions. The reconstructed viewing, lighting, Mars surface coordinates, Phobos, Deimos and star information can be computed and to create a searchable catalog, significantly increasing the utility of the images. The position of Phobos and Deimos relative to Mars and stars would yield precision astrometric data to improve the martian moon orbits even further by extending the spacecraft astrometric data arc by two years.

Example:

Figure 1 (left) shows an original far encounter Mars image taken by the Mariner 7 narrow angle camera.A limb/terminator overlay is included that also shows the location of Phobos in transit across Mars (circle marked “P”).The image on the right was simulated by illuminating the MOLA DTM and projecting it into camera image coordinates using the spacecraft trajectory for viewing geometry, the sun position for lighting geometry, and a camera geometric model.Camera

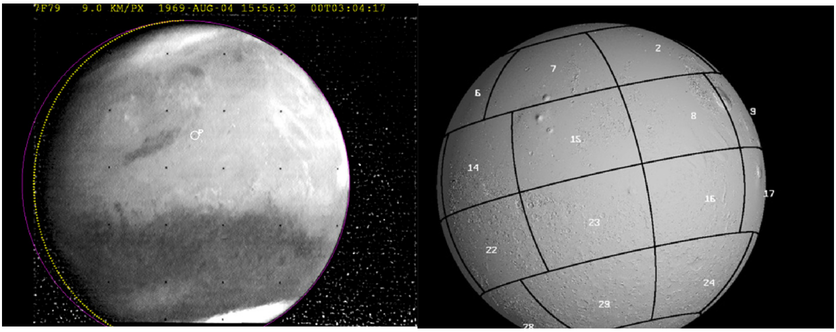

Fig. 1. Original M’7 far encounter image of Mars (left) and simulated Mars image from a MOLA-derived digital image model with the locations of Phobos and Mars’ limb, terminator and quads.

pointing was adjusted to align the limb / terminator and MOLA DIM to the actual image. This type of processing can be used to reconstruct the oldest of the historic spacecraft images into modern PDS4 formats and create precision NAIF SPICE kernels as well as a searchable catalog of Mars surface features, including landing sites, Phobos, Deimos and stars.

References:

[1] Collins, S. *The Mariner 6 and 7 Pictures of Mars,* NASA SP-263, 1971.
[2] NSSDC, *Mariner 6 and 7 Photographic Data,* NSSDC 71-09, March 1971.
[3] Edmonds, K., M.S. Robinson, New Mariner 6 and 7 mosaics of Mars: Clues about time variable surface features, abstract in LPSC XXXIV, #1436, 2003.
[4] Neumann, G., F. Lemoine, D. Rowlands, D.E. Smith, and M.T. Zuber, (2001), Crossover analysis in MOLA data processing, J. Geophys. Res., 106, No. E10, pp. 23753–23768.
[5] Smith, D. E., M. T. Zuber, H. V. Frey, J. B. Garvin, J. W. Head, D. O. Muhleman, G. H. Pettengill, R. J. Phillips, S. C. Solomon, H. J, Zwally, B. Banerdt, T. C. Duxbury, M. P. Golombek, F. G. Lemoine, G. A. Neumann, D. D. Rowlands, O. Aharonson, P. G. Ford, A. B. Ivanov, C. L. Johnson, P. J. McGovern, J. B. Abshire, R. S. Afzal, and X. Sun (2001), Mars orbiter laser altimeter: experiment summary after the first year of global mapping of Mars, J. Geophys. Res., 106, El0, 23,689-23,722.

LYOT CRATER, MARS: MAJOR AMAZONIAN-AGE IMPACT AND THE NATURE OF EJECTA EMPLACEMENT, EJECTA DEPOSIT CHARACTERISTICS AND MODIFICATION

J.W. Head
Department of Earth, Environmental and Planetary Sciences, Brown University, Providence, RI 02912 USA.
james_head@brown.edu.

Introduction:

The ~222 km diameter peak-ring Lyot Crater (Fig. 1) is located in the Northern Lowlands of Mars (50.5°N; 29.3°E), just north of the dichotomy boundary. The lowest point on its floor lies at ~4 km below the rim crest, ~7.3 km below the Mars datum and is the lowest point in the northern hemisphere (1).Lyot and its deposits are very well-preserved and its age has been estimated to be Middle Amazonian [see Dickson et al. (2); ~1.6 in the Hartmann (3) timescale; 3.3 Ga in the Neukum timescale (described in Ivanov (4), or ~3.4 Ga in the Hartmann and Neukum timescale (5,6)].

In this analysis, we build on previous work and new analyses and set the stage to address the following questions: What is the relationship between the formation of Lyot crater and the global and regional climate at the time of the event? How did the formation of Lyot affect the regional/global surface and atmospheric environment? What is the evidence for long-lasting climatic influence and effects from the Lyot crater-forming event?

Lyot Crater Geology and Previous Interpretations:

Lyot has historically been of interest due to its large size, relatively young age, location in the northern hemisphere, and the possible role of such a large, young impact event in the evolution of the climate and atmosphere (7-9), in its potential for sampling the structure of the hydrological system and deep groundwater (10-11), and the suggestion that regional channeled scablands surrounding parts of Lyot could be related to the emplacement of Lyot ejecta (12).

The location of Lyot in the Northern Lowlands (Fig. 1) leads to the prediction (10) that at several kilometers below the surface in this region, the global geothermal gradient should permit melting of ground ice.At this location and depth, if significant groundwater were present, it should be under hydrostatic head, and a drill hole to these depths should produce artesian outflow.Russell and Head (11) pointed out that Lyot crater formation represents a transient 'drill-hole' into the martian hydrosphere/cryosphere system and that cratering mechanics predict that the event should have penetrated the cryosphere and released groundwater held under artesian conditions. Russell and Head (11) found no evidence for groundwater outflow, however, and suggested that a plausible explanation for the lack of evidence for hydrologic activity within Lyot is an absence of abundant subsurface groundwater in the region at the time of impact.

Harrison et al. (12) used new image data to document the presence of an extensive channeled scabland covering ~300,000 km^2 and extending to the north, west, and east of Lyot. The configuration and morphology of the channels supports a water flow origin, and Harrison et al. (12) propose that the scablands results from impact-induced overland fluid flow.They considered two possible formation mechanisms: 1) mobilization of shallow groundwater by seismic energy from the impact event, and 2) dewatering of the ejecta blanket, with the water derived from excavation of permafrost and sub-permafrost groundwater. Harrison et al (12) cite the following points as lines of evidence against an ejecta blanket dewatering mechanism: 1) the general lack of large channels incising the ejecta deposit, 2) the location and fully-formed nature of the channels near the ejecta deposit margin, and 3) the areal extent of the channels and scour.On the basis of these points, they favor the process of seismic triggering of a shallow unconfined groundwater aquifer by the Lyot event as the primary formation mechanism of the channels.

Dickson et al. (2) mapped fluvial valley networks (regional drainage patterns suggesting liquid water stability at the surface, and typically confined to near the Noachian/Hesperian boundary) within, and thus post-dating Lyot crater.

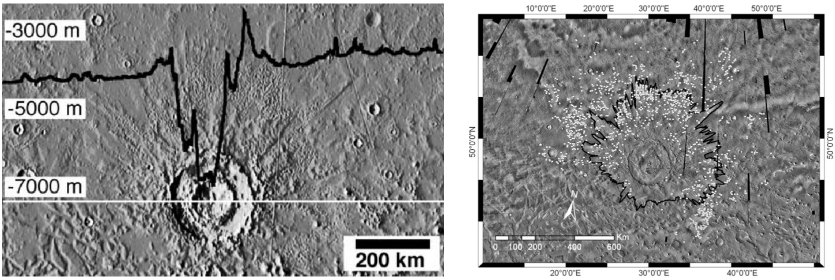

Fig. 1. .Left: Image and altimetric cross-section through Lyot Crater (from 11).Right: Edge of Lyot continuous ejecta deposit (black line) and near-field secondaries (white circles) (from 14).

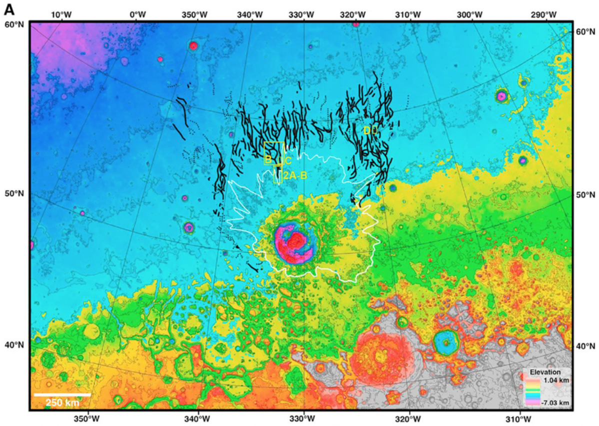

Fig. 2. Lyot and surrounding terrain (MOLA topography) showing mapped channels and areas of scour (black lines) and candidate scour (dotted) (from 12).

These large (tens of km) fluvial systems have the youngest well-constrained ages reported to date (Middle-Late Amazonian) and are linked to melting of near-surface ice-rich units. Following Haberle et al. (13), they point out that the interior of Lyot crater is an optimal micro-environment for melting; its extremely low elevation leads to high surface pressure, and temperature conditions at its location in the northern mid-latitudes are sufficient for melting during periods of high-obliquity. Thus, during the Middle-Late Amazonian, the interior of Lyot was characterized by a microenvironment that included the deposition of regional surface snow and ice deposits, and their melting during periods of high obliquity.

Robbins and Hynek (14) analyzed the distribution of secondary craters surrounding Lyot.They defined *close secondary craters* as those immediately surrounding the continuous ejecta deposit (Fig. 3) and found in long troughs emanating radially from Lyot and its continuous ejecta; they mapped 5341 *distant secondary craters*, found in 143 distinct clusters of 10-300 craters each, with the closest secondary crater clusters occurring at ~700 km (~6 crater radii) and the farthest ~5200 km (~46 crater radii) from the primary impact. The secondary crater clusters are mainly located southeast of Lyot (their Fig. 2). The continuous ejecta blanket has a preferential east-northeast direction (Figure 1). The ejecta deposit distribution (oriented NNE; Fig. 2) conflicts with the southeast dominance of the secondary clusters, but Robbins and Hynek (14) explain this by preferential modification and burial of secondaries towards the south, an interpretation they cite as supported by the geologic mapping of Tanaka et al. (15). Considering this ambiguity, they infer the impactor hit Mars obliquely, generally from the west.

Large impact craters are thought to have had a major influence on the regional and global climate (e.g., 7-9), particularly in the earlier history of Mars when formation of a Lyot-scale event in a denser atmosphere is thought to have caused emplacement of large amounts of water into the atmosphere from the substrate, produced profound heating of the atmosphere from hot ejecta, and resulted in fallout of both hot debris and water vapor (rainfall) to create runoff and to carve valley networks. Later in martian history, however, the atmosphere may not have been thick enough to have produced such effects (9). Analysis of the geology and evidence for climate conditions prior to, during, and following the Lyot event provide an opportunity to test these hypotheses.

The Pre-Lyot Crater Substrate and Climate Setting:

Critical to the understanding of the formation of Lyot, the emplacement of its ejecta, and the interpretation of the resulting landforms and climate effects, is the definition of the baseline climate and surface conditions during the Amazonian.Currently, Mars is a hyperarid, hypothermal polar desert climate (16) with surface water concentrated in the polar caps and near-surface pore water concentrated as ice cement in a global permafrost layer, lying above a kilometers-deep warmer layer capable of holding liquid groundwater.This horizontally-stratified hydrological system (17) is thought to characterize the vast majority of the Amazonian period (10, 18-19).Variations in spin axis/orbital parameters, primarily obliquity (20), cause polar ice to be redistributed to lower latitudes, forming widespread mid-latitude glacial deposits and even tropical mountain glaciers (21) at ~45^{o} obliquity.Laskar et al. (20) have shown that the most likely mean value for obliquity during the Amazonian is ~35^{o}, and Head et al. (22), Madeleine et al. (23) and Fastook et al. (24) have shown that in this obliquity configuration, a significant part of the mid-latitudes is covered with decameters of snow and ice (25), ith a wide variety of glacial landforms developed in a range of sub-environments throughout the mid-latitudes in the Amazonian (26).On the basis of these data and analyses, we conclude that a plausible configuration for the nature of the substrate in the Lyot target point latitude band during the Amazonian is a regional decameters thick snow and ice-covered regolith permafrost surface.We analyze the geology of Lyot crater and assess whether impact into a surface snow/ice substrate offers a plausible alternative to those previously described or if atmospheric effects of the impact are required (7-9).

References:

1) D. Smith et al., 2001, JGR 106, 23689; 2) J. Dickson et al., 2003, GRL 36, L08201; 3) W. Hartmann, 2005, Icarus 174, 294; 4) B. Ivanov, 2001, SSR 96, 87; 5) S. Werner et al., 2004,Icarus 195, 45; 6) S. Werner, 2008, Icarus 195, 45; 7) T. Segura et al., 2002, Science 298, 1977; 8) T. Segura et al., 2008 , JGR 113, E11007; 9) O. Toon et al., 2012, Ann. Rev. 38, 303; 10) S. Clifford, 1993, JGR 98, 10973;11) P. Russell and J. Head, 2002, GRL 29, 1827; 12) T. Harrison et al., 2010, GRL 37, L21201; 13) R. Haberle et al., 2001, JGR 106, 23317; 14) S. Robbins and B. Hynek, 2011, GRL 38, L05201; 15) K. Tanaka et al., 2005, USGS Map I-2888; 16) P. Read and S. Lewis, 2004, The Martian Climate Revisited, Springer; 17) J. Head and D. Marchant, 2014, Ant. Sci. 26, 774; 18) S. Clifford and T. Parker, 2001, Icarus 154, 40; 19) S. Clifford et al., 2010, 10.1029/2009JE003462; 20) J. Laskar et al., 2004, Icarus 170, 343; 21) J. Head and D. Marchant, 2003, Geology 31, 641; 22) J. Head et al., 2010, EPSL 294, 306; 23) J.-B. Madeleine et al., 2009, Icarus 203, 390; 24) J. Fastook et al, 2011, Icarus 216, 23; 25) J. Fastook and J. Head, 2014, PSS 91, 60; 26) C. Fassett et al., 2014; Geology 42, 763).

MAFIC AND FELSIC IGNEOUS AT GALE CRATER: A CHEMCAM STUDY

V. Sautter[1], A. Cousin[2], M.J. Toplis[2], R.C. Wiens[3], C. Fabre[4], O. Forni[2], O. Gasnault[2], N. Mangold[5], S. Maurice[2], P-Y. Meslin[2] and the ChemCam Team
[1]MNHN, Paris, France;
[2]IRAP, Toulouse, France;
[3]LANL, Los Alamos;
[4]G2E, Nancy, France;
[5]LPGN, Nantes, France.
violaine.sautter@mnhn.fr

The Curiosity rover landed at Gale, an early Hesperian age crater formed within Noachian terrains on Mars. The rover encountered a great variety of igneous rocks which are float rocks or clasts in conglomerates. Textural and compositional analyses using MastCam and ChemCam Remote micro Imager (RMI) and Laser Induced Breakdown Spectroscopy (LIBS) lead to the recognition of 53 massive igneous targets [1, 2] both intrusive and effusive, ranging from mafic rocks to felsic samples where feldspar is the dominant mineral. Five different groups have been identified: (1) a basaltic class with shiny aspect, conchoidal fracture, no visible grains (less than 0.2mm) ; (2) a porphyritic trachyandesite class with light-toned, polygonal crystals 1-20mm in length set in a dark gray mesostasis; (3) light toned trachytes with no visible grains sometime vesiculated; (4) microgabbro-norite (grain size < 1mm) and gabbro-norite (grain size >1mm); (5) light-toned diorite/granodiorite showing coarse granular (>4 mm) texture. Overall, these rocks comprise 2 distinct geochemical series [3]: (i) an alkali- suite: basanite, gabbro, trachy-andesite and trachyte including porphyritic and aphyric members; (ii) quartz-normative intrusives close to granodioritic composition. The former looks like felsic clasts recently described in two SNC meteorites (NWA 7034 and 7533), the first Noachian breccia sampling the martian regolith. It is geochemically consistent with differentiation of liquids produced by low degrees of partial melting of the primitive martian mantle. The latter rock-type is unlike anything proposed in the literature for Mars but resembles Archean TTG's encountered on Earth related to the building of continental crust. This work provides thus the first in situ detection of low density leucocratic igneous rocks on Mars in the southern highlands.

References:

[1] Sautter et al. JGR 2014;
[2] Cousin et al. 46thLPSC 2015;
[3] Sautter et al. Nature Geosciences 2015.

DAN CONTINUES ACTIVE NEUTRON SENSING ON MARS: RECENT RESULTS FROM CURIOSITY

M.L. Litvak on behalf of DAN science team
Space Research Institute, Moscow

The most recent results are presented of DAN active neutron sensing of the Martian soil along the traverce of Curiosity.

IMPACT CRATERING AS A CAUSE FOR RAINFALL PRODUCING VALLEY NETWORKS ON MARS: PREDICTIONS AND TESTS OF THE HYPOTHESIS

A.M. Horan[1], J.W. Head[1]
[1]Department of Earth, Environmental and Planetary Sciences, Brown University, Providence, Rhode Island 02912, USA.
ashley_horan@brown.edu

The valley networks on the surface of Mars [Hynek et al., 2010] are fluvial features proving the flow of liquid water on the early martian surface during the Late Noachian and earliest Hesperian [Fassett and Head, 2008].Due to a younger and less luminous Sun, approximately 75% of the present value, the planet was unable to be warmed above the triple point of water solely by incoming solar radiation [Forget et al., 2013; Wordsworth et al., 2013].The formation of the fluvial features observed on Mars does not require continuous warmth throughout the Noachian, leaving two potential candidate end-member climate histories for Mars: “warm and wet” [Craddock et al., 2002] or “cold and icy” [Wordsworth et al., 2013] with periods of warmth to melt and evaporate surface ice.Unable to easily produce a warm and wet early Mars with global climate models [Forget et al., 2013; Wordsworth et al., 2013], the idea of a cold and icy planet with periods of punctuated warmth has been explored through the effects of impact cratering [Segura et al, 2008] and periods of intense volcanism [Halevy and Head, 2014].Major tests for these predictions include the amount of resulting surface water compared to the observed erosion totals ranging 50 – 2500 m [Golombek and Bridges, 2000], the timing of the sulfate deposits observed on the Martian surface, and overall comparison to known terrestrial environments (such as the McMurdo Dry Valleys of Antarctica) where mean annual temperatures are well below 273 K, but peak seasonal and peak daytime temperatures can rise above freezing [Head and Marchant, 2014].

In this analysis, we focus on the mechanism of impact cratering for producing transient warming, rainfall, melting and fluvial erosion, introducing an improved understanding of the processes involved through a series of conceptual diagrams that highlight the important steps.Further, we discuss the geologic implications of an impact-cratering-induced warmth, as implied in the key series of papers, Segura et al. (2002, 2008) and Toon et al. (2012).Including all necessary steps in producing melt-water and rainfall for impact events, as outlined in these papers, we conclude with a series of predictions regarding the validity of the proposed impact cratering mechanism through erosion and rainfall totals, as well as the location, amount, and formation of the valley networks.

References:

Craddock et al. *J. Geophys. Res.* **107**, E11, 5111 (2002).
Fassett, C.I. & Head, J.W.III. *Icarus* **198**, 37-56 (2008).
Forget, F. et al. *Icarus* **222,** 81-99 (2013).
Halevy, I. & Head, J.W.III. *Nature Geosci. Lett.,* DOI:10.1038/NGEO2293 (2014).
Head, J.W. & Marchant, D.R. *Antarctic Science* **26(6)**, 774-800 (2014).
Hynek, B.M., Beach, M. & Hoke, M.R.T. *J. Geophys. Res. Planets***115**, E09008 (2010).
Segura, T. et al., *Science* **298**, 1977-1980 (2002).
Segura, T. et al.. *J. Geophys. Res.***113**, E11007 (2008).
Segura, T. et al., *Icarus* **220**, 144-148 (2012).
Toon, O. et al., *Earth Planet. Sci.* **38**, 303-322 (2010).
Wordsworth, R. et al. *Icarus* **222,** 1-19 (2013).

UNUSUAL SPOT ON THE CRATER GALE: DAN REQUESTS CURIOSITY TO MAKE U-TURN

D.V. Golovin on behalf of DAN science team,
Space Research Institute, Moscow

Very unusual local spot was found by DAN active measurements along the Curiosity traverce. It could have the highest content of ground water ever seen in the crater Gale.

FIELD TESTS FOR MARS EXPLORATION IN YAKUTIA

A.S. Kozyrev on behalf of DAN science team
Space Research Institute, Moscow

Short overview is presented of DAN field tests in the cryigeological sites in Yakutia in comparison with the similar data on Mars.

MAGNETIC ON GROUND SURVEYS ON THE OROGENIC CRUST OF THE PATAGONIAN ANDES. IMPLICATION FOR PLANETARY EXPLORATION

M.D. Michelena [1], R. Kilian[2]
[1]INTA, Ctra. Torrejon – Ajalvir, km 4, 28850 Torrejon de Ardoz, Spain;
[2]University of Trier, Universitätsring 15, 54296 Trier, Germany.
diazma@inta.es

The Patagonian Andes represent a good scenario of study because they have outcrops of diverse plutonic rocks representative of an orogenic crust on Earth and other planets. Furthermore, metamorphic surface rocks provide a window into deeper crustal lithologies. In such remote areas, satellite and aerial magnetic surveys could provide important geological information concerning exposed and not exposed rocks, but they integrate the magnetic anomalies in areas of kilometres. For the southernmost Andes long wavelength satellite data show clear positive magnetic anomalies (> + 100 nT) for the Patagonian Batholith (PB), similar as parts of the older martian crust. This integrated signal covers regions with different ages and cooling histories during magnetic reversals apart from the variability of the rocks.

To investigate the complex interplay of distinct magnetic signatures at short scale, we have analysed local magnetic anomalies across this orogen at representative sites by decimeter-scale magnetic ground surveys. As expected, the investigated sites have positive and negative local anomalies. They are related to surface and subsurface rocks, and their different formation and alternation processes including geomagnetic inversions, distinct Curie depths of the magnetic carriers, intracrustal deformation among other factors. Whole rock chemistry (ranging from 45 to > 80 wt.% SiO_2 and from 1 to 18 wt.% FeOtot.), magnetic characteristics (susceptibilities, magnetic remanence and Königsberger ratios) as well as the composition and texture of the magnetic carriers have been investigated for representative rocks. Rocks of an ultramafic to granodioritic intrusive suite of the western and central PB contain titanomagnetite as major magnetic carrier. Individual magnetic signatures of these plutonic rocks reflect their single versus multidomain status, complex exolution processes with ilmenite lamella formations and the stoichiometric proportions of Cr, Fe and Ti in the oxides. At the eastern margin of the PB the investigated plutons and mafic dykes have been emplaced and equilibrated at 4 - 6 km depth. They do not contain magnetite but include variable amounts of ferrimagnetic monoclinic C4 pyrrhotite, which was formed along fractures zones by a hydrothermal gold-bearing mineralization. The intensity of their positive magnetic anomalies (up to + 220 nT) is well correlated with the amount of pyrrhotite (1 to 4 vol.%). In all cases, high-resolution ground surveys variations of the magnetic signature down to 20 nT could be used to clearly distinguish different rock types on a decimeter scale. In this work we will present scalar and vector magnetic maps and will discuss about the origin of the anomalies in terms of carriers, and the extension and depth of the magnetic sources.

In this study magnetic instrumentation developed for Mars exploration has been used with a double purpose, for comparison of the mars instrumentation with reference instrumentation and because of the importance of these studies prior to the magnetic ground surveys on Mars and the Moon.

Acknowledgements:

This work has been done in the frame of TITANO project under the grant PRI-PIBUS-2011-1150 of the subprogram of international and bilateral projects of the Spanish Ministry of Science and Innovation (MICINN) and MEIGA-MET-NET project under the Grant AYA2011-29967-C05-01 of the Spanish National Space Program (DGI-MEC). We thank Oscar Baeza to performed XRD analyses at Trier and Chuck Stern (Boulder, Colorado) for a review of the geological part of the manuscript.

LESSONS LEARNED IN ANTARCTICA FOR INTERNATIONAL EXPLORATION OF MOON AND MARS

N.E. Demidov[1, 2], V.V. Lukin[3],
[1]Institute of Physicochemical and Biological Problems of Soil Science, RAN, Pushchino, Moscow region, 142290, Russia;
[2] Vernadsky Institute of Geochemistry and Analytical Chemistry, RAN, Kosygin Str.,19, Moscow, 119991, Russia;
[3] Russian Antarctic Expedition, Beringa Str., 39, Sankt Petersburg, Russia.
nikdemidov@mail.ru

Antarctica is the most isolated part of Earth and even in 21century human activity on this continent may represent a good model for developing future research outposts on Moon and Mars. Crew selection, social-psychological behavior in remote and hazardous environments, design of stations, medicine support and many other issues have interesting “Antarctic” solutions which may be useful for planning extraterrestrial human expeditions. Antarctic oases due to presence of permafrost, low temperature, absence of liquid water and soils are recognized as the best analogs of Martian environments (and possibly of polar regions on Moon as well) on Earth and so give an opportunity to test geological and astrobiological scientific instruments. Bases on polar plateau, such as Vostok station at south geomagnetic pole, are better for testing critical technologies necessary for constructing research bases under subzero temperature conditions and for crew behavior simulation during long-duration spaceflights. Mean annual temperature -55.4 º C and absolute minimal temperature -89.2 º C at Vostok station are the same order as this parameters for Martian equator, when maximal temperature on Martian equator >30 º C is well above maximal temperature for Vostok -13.6 º C. History of Antarctic exploration shows how our knowledge about this continent increased when first all year round stations were established and the role of seasonal, wintering, remote sensing, long overland tractors, drilling activities in Antarctic science. Unprecedented positive experience of exploration of Antarctica under principals of peace and cooperation of Antarctic Treaty regardless of changing political situation must also be considered as the main Antarctic practice which is necessary to extrapolate to investigation of Moon and Mars. Such parts of Treaty as absence of territory claims and military measures, free exchange of scientific results, open aces for expectation, environment protocol and other may be taken as basis for Moon and Mars Treaty.

COMBINED VNIR AND RAMAN SPECTROSCOPY OF MARS ANALOGUE SEDIMENTS FROM THE ATACAMA SALT FLATS

J. Flahaut[1], M. Martinot[1], G.R. Davies [1]
[1]Faculty of Earth and Life Science, VU University Amsterdam, De Boelelaan 1085, 1081HV Amsterdam, The Netherlands.
jessica.flahaut@ens-lyon.org

Introduction:

The identification and characterization of hydrated minerals within ancient aqueous environments on Mars are a high priority for determining the past habitability of the red planet. Few studies, however, have focused on characterizing the entire mineral assemblage as it is often difficult to determine from remote sensing data, even though it could aide our understanding of past environments. In this study we use both spaceborne (Landsat, Hyperion) and field/laboratory (VNIR + Raman spectroscopic) analyses to study the mineralogy of various salt flats (salars) of the northern region of Chile as an analogue for Martian evaporites. The aim of the survey is to constrain the salars mineralogy from a combination of field/laboratory techniques (e.g., VNIR + Raman spectroscopy), and provide ground-truth to the remote sensing analyses. In general, there is good agreement between remote sensing, field and laboratory observations on the major classes of minerals in the salars and their spatial distribution. Implications for the upcoming Exomars 2018 rover mission are discussed.

Regional context and study area:

The region of northern Chile/ Central Andes (including the Atacama desert) is characterized by a succession of North-South trending mountainranges and closed basins. The central parts of the basins are filled by evaporate (and older lake) deposits or occupied by saline lagoons, collectively referred to as salars. Receiving minimal precipitation (0-2 mm per year), and being within a volcanic ridge, this region is similar to Martian paleo-environments (Ericksen, 1983; Stoertz and Ericksen, 1974). Mars evaporate rocks appear to have formed under processes similar to the salar rocks and may show common features and mineralogies.

The present study area is located in the Antofagasta region of Chile, North of the Atacama region, south and east of the San Pedro de Atacama village. It includes portions of the pre-Andean depression (salar de Atacama) and of the eastern Andean highlands (located between the Paso Jama and Paso Sico roads). It differs from previous Mars analogues studies that were focused in the Atacama desert itself, between the coast range and Domyeko range, an area that is extremely dry but where the evaporite formation might be influenced by marine aerosols.

Datasets:

High-resolution remote sensing data from hyperspectral (Hyperion) and multispectral (ALI, Landsat) imaging instruments were used to characterize, and map, the mineralogy of the Atacama salars from space. Landsat 8 reflectance data provide full coverage of the area, whereas Hyperion data are only available at selected locations, including the Cordillera de la Sal (Fig. 1a). Landsat imagery has previously been demonstrated to be efficient at mapping salar heterogeneities (Houston, 2006) and was, therefore, used to select field sites within a diverse range of terrains. A field campaign was carried out in February 2015. VNIR reflectance values were measured in the field at selected sites (squares on Fig. 1b) with an ASDinc Fieldspec 4 spectrometer (0.35-2.5 µm), and samples were collected to be further analyzed by Raman spectroscopy (with a 532 nm laser beam) and XRD at the VU University Amsterdam.

Results:

Core (grey tones) and marginal (orange to white) zones within the salars are easily distinguished on the Landsat 8 7-6-5 band colour composite (Fig.1a). Each coloured zone was visited in the field. Outcrops were classified into multiple types based on their morphology, which was found to be strongly related to their compositions (see Flahaut et al., EPSC 2015).

Both VNIR and Raman spectroscopic investigations indicate that distinct mineral assemblages are observed within specific zones of an individual a salar but between the various salars (e.g., Figure 1c,d). The lower elevation Salar de

Atacama (*1* on fig. 1b), located in the Andean pre-depression, is characterized by a unique thick halite crust at its centre, whereas various assemblages of calcium (gypsum, anhydrite) and sodium (mirabilite) sulfates and clays were found at its margin. Sulfates form the main crust of the Andean salars to the east, although various compositions are observed. These compositions seem to be controlled by the type of brine (Ca- (Salar de Quisquiro (*5*)), SO_4- (Laguna Tuyajto (*3*) and Salar de Laco (*2*)), or mixed- (Salar de Aguas Calientes 3 (*4*))).

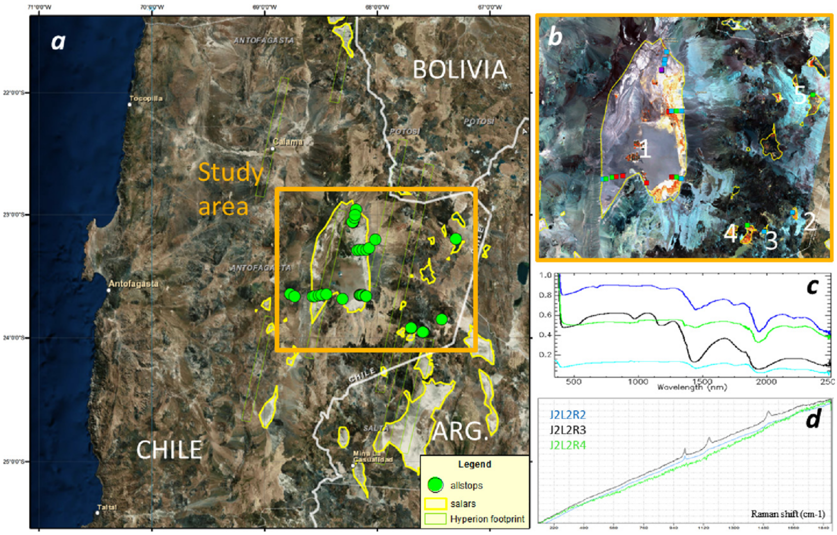

Figure 1: a) Loca-tion of the study area and sampling sites; b) Landsat 8 colour composite (bands 7-6-5) of the study area. Coloured squares correspond to the morphological classification es-tablished from field observations; c) VNIR reflec-tance spectra of 4 different outcrops within Laguna Tuyajto (n°3 on b); d) Associated Raman spectra

Sulfate crusts where found to be generally thin (<5 cm) with a sharp transition to underlying more clay, silt or sand-rich alluvial deposits, of distinct composition,. The only exception lies within the Salar de Atacama where the lower limit of the hard (halite) crust could not be observed, but is estimated to be at least a few meters (Stoertz and Ericksen, 1974). A former, 1 cm-thick calcite-rich crust was observed at 20cm depth in the Salar de Laco, confirming the previous assumptions made on airborne images that this salar must have been occupied by a (more alkaline) lake in the past (Stoertz and Ericksen, 1974).

Discussion, Further Work, and Implications for Exomars

Mineral zonation is observed within the salars on a scale of dozen of metres and appears to be a function of the distance to the (ground)water sources. Variations are observed with depth, as the salt crust only represent the top centimetres of the salt flat. Only major, lateral variations can be observed and mapped from space.

VNIR spectroscopy (from space or field) appear to easily discriminate between clay-dominated and salt-dominated sediments in Atacama, however, it was found to be sometimes incapable of discriminating between sulfates of the same family. Used together, VNIR and Raman spectroscopy, and morphologic analyses provided a powerful tool to distinguish between different types of salt crusts. Ongoing XRD analysis will quantify the various mineral assemblages. We found that the Atacama's unique arid and volcanic environment, coupled with the transition from alkaline, lake waters to more acidic salar brines, has a strong Mars analogue potential. Consequently, we also performed a complementary astrobiological survey (an ongoing joint project with the University of Leiden, the Netherlands) to determine the diversity of micro-organisms that survive in such extreme arid and saline environments.

The goal of the study is to bridge the gap between remote sensing and ground observations of Martian-like sediments but also to test the complementary of diverse spectroscopic techniques to identify sulfate and clay-rich assemblages. This study is particularly relevant in to context of the Exomars 2018 rover mission, which will carry a suite of instruments aimed at identifying organic compounds and characterizing their geological context. The Pasteur payload includes two IR spectrometers (ISEM + MicroOmega), a Raman spectrometer, multiple cameras (CLUPI, PanCam…) and a drill that will allow a morphological and mineralogical characterization of the outcrops laterally and vertically (at depths <2m) in a similar approach to that used in our study of the Chilean desert. Determining how best to coordinate and integrate analytical strategies of the entire instrument suite in order to unambiguously characterise the environment in which the rover is measuring is expected to pose a major challenge. The northern Chile salars appear to represent an excellent field test for the calibration of such instruments and to optimise integrated analytical strategies.

Acknowledgements:

The field VNIR spectra were collected with an ASDinc FieldSpec 4 which was generously loaned though the Goetz Instrument Support Program. We are grateful to all of our sponsors and partners for the field trip, especially our local guide Mathilde Monseu, Bernard Foing at ESA and Andreas Kaufer at ESO and the entire staff at APEX, who provided us with logistic support. The campaign was funded by a Netherlands Organisation for Scientific Research (N.W.O.) VENI Innovational Research grant attributed to J. Flahaut.

FORMATION OF GULLIES ON MARS BY WATER AT HIGH OBLIQUITY: QUANTITATIVE INTEGRATION OF GLOBAL CLIMATE MODELS AND GULLY DISTRIBUTION

J.L. Dickson[1], L. Kerber[2], C. I. Fassett[3], J.W. Head[1], F. Forget[4], J-B. Madeleine[4]
[1]Dep. Earth, Env. & Planet. Sci., Brown U., Providence, RI, 02906, USA, jdickson@brown.edu;
[2]Jet Propulsion Laboratory;
[3]Mt. Holyoke College;
[4]Laboratoire de Meteorologie Dynamique.

Introduction:

The latitude-dependent distribution [1-4] and orientation [5-9] of gullies on Mars indicate that their formation is controlled by climate conditions at the surface within the last million years [10-11], while their morphology [12-13] show direct associations with the ice-rich Latitude Dependent Mantle (LDM), a potential source for melting. Activity in gullies occurs at times that are consistent with the removal of CO_2 frost, leading to destabilization of loose material on steep slopes [14-17].While this activity is capable of mobilizing fines within existing gully channels, the potential for this to form new gullies is unclear. In particular, this activity may not explain (1) sinuosity values in excess of what is measured for dry channels on Earth [18], (2) gullies with slopes below 25° [8], and (3) channels that incise through tens of meters of permafrost [19]. These properties suggest that gullies may be initiated by flows that are comprised by some percentage of liquid, the most reasonable candidate for testing being liquid water [12,20-22].

Global Climate Models (GCM) show that regions where liquid water could exist today are poorly correlated with gully locations [23]. Melting of ice within 50 cm of the surface is predicted at ~35° obliquity [20, 22], a which has occurred within the last million years [24].Ice is also predicted to accumulate in the mid-latitudes at 35° obliquity [25]. Further, recently discovered massive CO_2 units presently sequestered in the South Polar Layered Deposits (SPLD) would sublimate at 35° obliquity, yielding average surface pressures > 10 mb [26].

This new information prompted us to quantitatively reassess the potential for liquid water at the surface at gully locations formed within the last million years.

Methods:

Simulations using the Laboratoire de Météorologie Dynamique (LMD) GCM [27] were run for three separate starting conditions thought to have occurred within the last million years [23].

1) Present day (25° obliquity, 6 mb atmosphere);

2) ~380 kyr transitional scenario (30°, 8 mb);

3) ~625 kyr high-obliquity (35°, 10 mb).

Age/obliquity values are from [24] and globally average pressure values are from [26], which calculated pressure using the NASA Ames GCM [23]. The model ran for 4 Mars years before values were obtained for one Mars year, with 8 timesteps recorded per sol (total of 5352 timesteps). GCM outputs (3.75° (lat) x 5.625° (lon) cell size) were imported into a Geographic Information System (GIS) that contained a new detailed map of gullies in the southern hemisphere based upon Context Camera (CTX) data [28] (Fig. 1a). GCM cells were filtered to include only those that overlap with gully locations (Fig. 1b-d). Analysis of model outputs followed the principles of *Haberle et al., 2001* [23] with regard to quantifying GCM timesteps when a given cell achieved conditons above both 273 K and 6.1 mb. Boiling of water was not considered in this analysis, as the focus was on how many instances predicted the onset of melting, not the duration that meltwater remained on the surface. Timesteps at which transient melting was possible were counted (Figure 1). This yielded the first direct quantitative assessment of liquid water potential at mapped gully locations.

Results:

At present (25° obliquity), conditions for melting in the southern hemisphere are constrained primarily by elevation and secondarily by latitude (Fig. 1b).In the southern hemisphere, only the margins and floors of Hellas and Argyre surpass

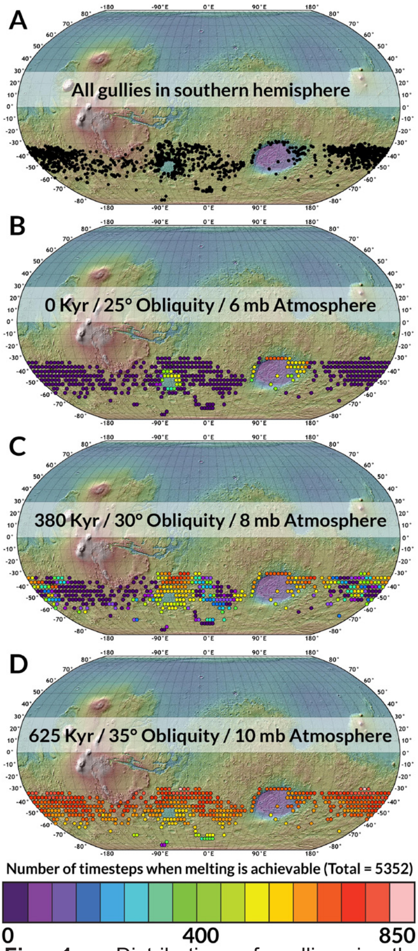

Fig. 1. Distribution of gullies in the southern hemi-sphere and results of three different GCM scenarios. (A) Gullies in the southern hemisphere of Mars as mapped with CTX data through mission phase D06. (B) Conditions for melting under current conditions can only be achieved briefly along the rims and floors of Hellas & Argyre. (C) Melting is still elevation-constrained, with more regional lows (e.g. Newton cra-ter) allowing for summer melting. (D) At high obliquity, melting can be transiently achieved at all locations where gullies have been mapped.

the triple point of H_2O, consistent with the predictions of *Haberle et al., 2001* [23]. Melting conditions are found in the northern hemisphere, though surface pressures are lowest during northern summer, when peak daytime temperatures are at their highest.

During transitional periods (30° obliquity), melting conditions are still constrained by elevation; high-latitude (~70°S) lows experience periods above the triple point; low-latitude highs (e.g. southern Thaumasia) do not (Fig. 1c). Newton crater (43°S, -160°E), a regional low characterized by thick ice deposits and densely concentrated and well-incised gullies [13, 29], frequently surpasses the triple point in this scenario.

At high obliquity (35°), conditions above the triple point are achieved at all locations where gullies are mapped in the southern hemisphere (Fig. 1d).Unlike the first two scenarios, conditions for transient melting are latitude-dependent and exhibit no dependence on elevation.Even gullies that are mapped at polar latitudes experience > 50 timesteps of surface temperatures > 273 K. Previous calculations using the same GCM showed that steep pole-facing slopes in the mid-latitudes, where gullies preferentially occur [5-9], receive greater insolation at 35° obliquity than surrounding surfaces [20], suggesting that temperature calculations reported here may be minimum estimates.

Discussion:

The model results presented here are consistent with the independent model of *Haberle et al., 2001* [23] for present day conditions: meltwater production on the surface of Mars today is unlikely, even if there was a source of volatiles to melt, in all locations, except the major impact basins in the southern hemisphere. This is also consistent with gully activity observed today being related to CO_2 frost [14-17]. However, our results suggest that melting of water ice was considerably more viable as an erosive agent during recent high-obliquity excursions, coincident with periods when ice accumulation is predicted to have occurred at gully locations [4, 25].

GCM results argue for a scenario of gully evolution that is reflected by their detailed morphology [30]: formation by liquid H_2O at high-obliquity followed my modification and erosion by CO_2-related processes at low obliquity.This process is predicted to be cyclical, consistent with morphologic evidence for episodic gully activity [30-31].

References:

[1] Malin and Edgett, 2000, *Science*, 288, 2330. [2] Milliken et al., 2003, *JGR*, 108, 10.1029/2002JE002005. [3] Harrison et al., 2014, *8th Mars*, 1030. [4] Head et al., 2003, *Nature*, 426, 797. [5] Heldmann and Mellon, 2004, *Icarus*, 168, 285. [6] Balme et al., *JGR*, 111, E05001. [7] Bridgesand Lackner, 2006, *JGR*, 111, E09014. [8] Dickson et al., 2007, *Icarus*, 188, 315. [9] Kneissl et al., 2010, EPSL, 294, 357. [10] Reiss et al., 2004, *JGR*, 10.1029/2004JE002251. [11] Schon et al., 2009, *Geology*, 37, 207. [12] Christensen,

2003, *Nature*, 422, 45 [13] Head et al., 2008, *PNAS*, 105, 13258. [14] Dundas et al., 2010, *GRL*, 10.1029/2009GL041351. [15] Diniega et al., 2010, *Geology*, 38, 1047. [16] Dundas et al., 2014, *Icarus*, 10.1016/j.icarus.2014.05.013. [17] Raack et al., 2014, *Icarus*, 10.1016/ j.icarus.2014.03.040.[18] Mangold et al., 2010, *JGR*, 10.1029/2009JE003540. [19] Hobbs et al., *Geomorphology*, 226, 261. [20] Costard F. et al., *Science*, 295, 110. [21] Hecht, M., 2002, *Icarus*, 156, 373. [22] Williams et al., 2009, *Icarus*, 196, 565. [23] Haberle et al., 2001, *JGR*, 106, 23317. [24] Laskar et al., 2004, *Icarus*, 170, 343. [25] Madeleine et al., 2014, *GRL*, 41, 4873. [26] Phillips et al., 2011, *Science*, 332, 838. [27] Forget et al., 1999, *JGR*, 104, 24155. [28] Malin et al., 2007, *JGR*, 112, 10.1029/2006JE002808. [29] Berman et al., 2005, *Icarus*, 178, 465. [30] Dickson and Head, 2009, *Icarus*, 204, 63. [31] Dickson et al., 2015, *Icarus*, 252, 83.

THE FAINT YOUNG SUN PARADOX: WHAT IT MEANS FOR EARTH AND MARS

A.M. Horan[1], J.W. Head[1],
[1]Department of Earth, Environmental and Planetary Sciences, Brown University, Providence, Rhode Island 02912, USA.
ashley_horan@brown.edu

Approximately 4.5 – 2.5 billion years ago, a faint young Sun, nearly 75% as luminous as it is today, was at the center of our solar system, forcing implications for the surrounding planets, including both Earth and Mars. If modern day Earth was put in orbit around a faint and young Sun, the planet would quickly become a barren, frozen world, easily glaciated from pole to pole. By studying the geology, we know Earth had abundant liquid water on the surface billions of years ago, despite the less luminous Sun. With liquid water on the surface, life was permitted to make its earliest appearance, dating back to 3.5 billion years ago. As originally queried by Carl Sagan and George Mullen in 1972, if the Sun was not emitting enough solar radiation to sufficiently warm Earth, what was keeping the young planet warm? Moving just one planet further from the Sun, present day Mars would suffer brutal conditions from the faint young Sun; it would be an extremely cold and dry planet. Similar to Earth, we see geological proof of water flow through the valley networks formed during the Late Noachian period. Arriving at the same paradox, we question how the planet was characterized by liquid water, despite the less luminous Sun.

Despite being 225,300,000 km closer to the Sun, Earth displays important differences from what we know about early Mars, leading researchers to take different precautions when exploring this paradox. Mars, without the ability to recycle itself through plate tectonics and lacking a current ongoing vertically integrated water cycle, shows its history simply on its surface, with features dating back billions of years. In this sense, Mars is easier to study as Earth does not have this quality; we must look through the planet's rock record to find information. While we know Earth had continuous water flow through the Archean period, there is no reason to believe that continuous water flow was necessary to produce the fluvial features on Mars, introducing the possibility of punctuated periods of warmth. In conclusion, we search for a yearly global average of above 273 K for Earth. On Mars, we search for either a yearly average above or close to that of the triple point of water, which could be pushed above 273 K at the peak temperatures during the warm season, or punctuated periods of warmth due to outside forces. Also, we test hypotheses by looking for features we still see today, including the total amount of erosion, distribution of fluvial and lacustrine landforms, and tell-tale mineralogy.

To sufficiently and continuously warm itself, a planet could have a naturally induced greenhouse atmosphere. Through the geological records of both planets, atmospheric scientists obtain constraints on greenhouse gases, which can be used through climate modeling to predict the overall surface temperatures of these planets under such conditions. Two possible causes for periodic surface warmth on early Mars include impact cratering from the period of heavy bombardment or punctuated periods of strong volcanism, for which there is evidence in the geological record.

Questions addressed in our own analysis include: what are the differences in what we are searching for in these very diverse planets, what are the climate history variances, and what are the hypotheses for how the planets supported themselves during the period of a less luminous Sun?

VARIATIONS OF THE HDO/H_2O RATIO IN THE MARTIAN ATMOSPHERE AND LOSS OF WATER FROM MARS

V.A. Krasnopolsky
Department of Physics, Catholic University of America, Washington, DC, USA; PhysTech, Moscow, Russia.
vlad.krasn@verizon.net

Ground-based spatially-resolved high-resolution spectroscopy is currently the only means to observe variations of the HDO/H_2O ratio in the martian atmosphere. These observations are difficult because telluric water exceeds the martian water by two orders of magnitude even at the excellent conditions of NASA IRTF. Our observations of HDO and H_2O at the close wavenumbers of 2722 and 2994 cm^{-1}, respectively, cover six martian seasons in the period from 2007 to 2014. Infrared properties of water ice and dust are rather similar at these wavenumbers, and the HDO and H_2O line equivalent widths are comparable; therefore effects of aerosol absorption and scattering significantly cancel out in the HDO/H_2O ratios. These ratios are rather constant in wide latitude ranges at four observing sessions, in accord with the GCM model by Montmessin et al. (2005). Results of two other sessions demonstrate significant deviations from the model predictions and strong correlation between HDO/H_2O and temperature at ~7 km above the surface with correlation coefficients of 0.9. The observed global-mean HDO/H_2O ratio is 4.6 ± 0.7 times the terrestrial ratio, the ratio in vapor released by the north polar cap is 6.2 ± 1.4, and the ratio in the north polar cap ice is 7.1 ± 1.6. Updating the model of isotope fractionation in hydrogen escape by Krasnopolsky and Feldman (2001), 60 m of the global water layer was lost in the last 4 Byr and more than 1200 m could be lost by hydrodynamic escape of H_2 released in the reaction between water and iron. Variations of telluric D/H above Mauna Kea (Hawaii, elevation 4.2 km) are by-products of our observations; D/H varies from 0.4 to 0.9 in nine observations with a mean D/H = 0.67.

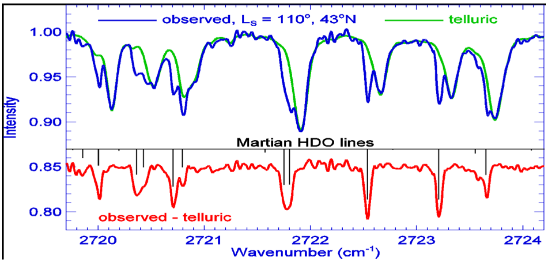

Fig. 1. Processed and adjusted spectrum of HDO is compared with the best fit telluric spectrum. Their difference reveals martian HDO lines; their strengths and Doppler-shifted positions are indicated.

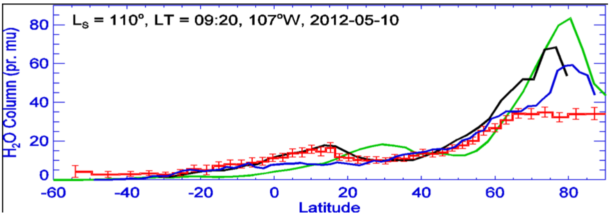

Fig. 2. Observations of H_2O and HDO/H_2O at L_S = 110° (red lines) are compared to the GCM data (green curves), TES (black curve) and SPICAM (blue curve) observations of H_2O. Black curve in the lower panel shows temperatures at the half pressure level.

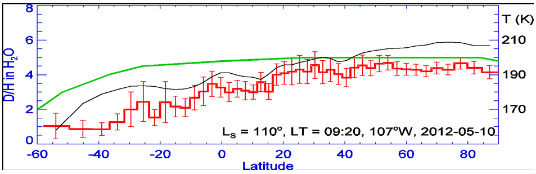

WATER VAPOR IN THE MIDDLE ATMOSPHERE OF MARS DURING THE GLOBAL DUST STORM IN 2007

A. Fedorova[1], J.-L. Bertaux[2], F. Montmessin[2], D. Betsis[1], O. Korablev[1], L. Maltagliati[3], J. Clarke[4],
[1]Space Research Institute(IKI), 84/32, Profsoyuznaya str., Moscow, 117997, Russia;
[2]LATMOS-UVSQ, 11 Bd d'Alembert, F-78280 Guyancourt, France;
[3]AIM/Cea-Saclay, France; [4]Center for Space Physics, Boston University, Boston, USA.
fedorova@iki.rssi.ru

Recent observations of the Martian hydrogen corona in the UV H Ly- emission by Hubble Space Telescope (HST) [Clarke et al., 2014] and the SPICAM UV spectrometer on Mars Express [Chaffin et al., 2014] reported its rapid change an order of magnitude for the short period of a few months in 2007 (MY 28), which is inconsistent with the existing models. One proposed explanation of observed decrease in coronal emission is that during the global dust storm water vapor can be transported to higher altitudes where the rate of photodissociation by the near-UV sunlight increases, providing an additional source of hydrogen for the upper atmosphere.

Since 2004 the SPICAM IR spectrometer on Mars-Express carries out measurements of the vertical distribution of water vapor in the 1.38 m band and aerosol properties in the middle atmosphere of Mars by means of solar occultations. We presents here vertical profiles of water vapor at Ls = 250-310º during the dust storm of MY28. SPICAM observations confirm the increase of the H_2O content at 60 km from Ls=268º to Ls=285º. In the Northern hemisphere (40-60°N) the concentration increases from $<10^{10}$cm^{-3} to 8 10^{10}cm^{-3} at 70 km and from 2 10^{10}cm^{-3} to 2 10^{11}cm^{-3} at 60 km. In the southern hemisphere (40-60°S) the concentration increases from 2 10^{10}cm^{-3} to 6-8 10^{10}cm^{-3} at 70 km and from 0.5-1 10^{11}cm^{-3} to 1.5 10^{11}cm^{-3} at 60 km. Observations in MY32 at the same latitudes and Ls=240-320° don't show any increase of the water content from average seasonal values. Nevertheless, the photochemical modeling is required to estimate a contribution of observed water abundance to the hydrogen corona.

Anna Fedorova acknowledges the RFBR grant 15-02-07812 a for financial support.

References:

[1] Clarke, J. T., Bertaux, J.-L., Chaufray, J.-Y., Gladstone, G. R., Quemerais, E., Wilson, J. K., & Bhattacharyya, D. (2014). A rapid decrease of the hydrogen corona of Mars. *Geophysical Research Letters*, *41*(22), 8013–8020.

[2] Chaffin, M. S., Chaufray, J.-Y., Stewart, I., Montmessin, F., Schneider, N. M., & Bertaux, J.-L. (2014). Unexpected variability of Martian hydrogen escape. *Geophysical Research Letters*, *41*(2), 314–320. http://doi.org/10.1002/2013GL058578

NEUTRAL ESCAPE INDUCED BY THE PRECIPITATION OF HIGH-ENERGY PROTONS AND HYDROGEN ATOMS OF THE SOLAR WIND ORIGIN INTO THE MARTIAN ATMOSPHERE

V. I. Shematovich
Institute of Astronomy RAS,48 Pyatnitskaya str., Moscow 119017, Russian Federation.
shematov@inasan.ru

Solar forcing on the upper atmosphere of Mars via both absorption of the XUV (soft X-rays and extreme ultraviolet) radiation and solar wind plasma results in the formation of an extended neutral corona populated by the suprathermal (hot) H, C, N, and O atoms (see, e.g., Johnson et al., 2008). The hot corona, in turn, is altered by an inflow of the solar wind plasma and local pick-up ions onto the planetary exosphere. Such inflow results in the formation of the superthermal atoms (energetic neutral atoms ENAs) escaping from the Martian neutral atmosphere due to the charge exchange with the high-energy precipitating ions.

One of the first surprises of the NASA MAVEN mission was the observation by the SWIA instrument of a tenuous population of protons with solar wind energies traveling anti-sunward near periapsis, at altitudes of ~150-250 km (Halekas et al., 2015). While the penetration of solar wind protons to low altitude is not completely unexpected given previous Mars Express results, this population maintains exactly the same velocity as the solar wind observed. From previous studies it was known that some fraction of the solar wind can interact with the extended corona of Mars. By charge-exchanging with the neutral particles in this corona, some fraction of the incoming solar wind protons can gain an electron and become an energetic neutral hydrogen atom. Once neutral, these particles penetrate through the Martian magnetosphere with ease, with free access to the collisional atmosphere/ionosphere.

The origin, kinetics and transport of the suprathermal O atoms in the transition region (from thermosphere to exosphere) of the Martian upper atmosphere due to the precipitation of the high-energy protons and hydrogen atoms are discussed. Kinetic energy distribution functions of suprathermal and superthermal (ENA) oxygen atoms formed in the Martian upper atmosphere were calculated using the kinetic Monte Carlo model (Shematovich et al., 2011, 2013; Shematovich, 2013) of the high-energy proton and hydrogen atom precipitation into the atmosphere. These functions allowed us: (a) to estimate the nonthermal escape rates of neutral oxygen from the Martian upper atmosphere, and (b) to compare with available MAVEN measurements.

This work is supported by the RFBR project No. 14-02-00838a and by the Basic Research Program of the Presidium of the Russian Academy of Sciences (Program 09).

References

Johnson et al., Sp. Sci. Rev., 2008, v. 139, 355.
Shematovich, Solar System Res., 2013, v.47, 437.
Shematovich et al., J. Geophys. Res., 2011, v.116, A11320; 2013, v. 118, 1231.
Halekas et al., 2015, 46th Lunar and Planetary Science Conference, 1381.

MARS ATMOSPHERIC LOSSES INDUCED BY THE SOLAR WIND: COMPARISON OF OBSERVATIONS WITH MODELS

O. Vaisberg
Space Research Institute, Russian Academy of Sciences
olegv@iki.rssi.ru

With new results from Mars-Express on plasma environment of Mars and two new Mars satellites the study Martian atmospheric losses receives new attention. Paper summarizes experimental results concentrating on configuration of Martian atmosphere and the measurements of planetary ion escape induced y the solar wind. Several plasma populations constituting solar wind induced mass loss have been identified. Measured ion flux and calculations of the total escape rate including solar cycle variations from the measurements are summarized. Several types of simulation of the solar wind with Mars are considered and results of representative models are given and compared with experimental results. There is significant difference between total loss rates obtained from simulation and from measurements on the spacecraft, latter ones are larger by factor of 2 to 10. Altogether they amount significant flux that considered as important factor of loss during cosmogonic time of the planet. The origin of each solar wind induced loss component and its contribution to total amount are discussed and compared with relevant computer models. The best current estimation of solar wind induced mass rate of $2{,}5 \cdot 10^{19}$ g/s.

RECENT SCIENCE HIGHLIGHTS OF THE MARS EXPRESS MISSION

D. Titov[1], J.-P. Bibring[2], A. Cardesin[3], T. Duxbury[4], F. Forget[5], M. Giuranna[6], M. Holmström[7], R. Jaumann[8], P. Martin[3], F. Montmessin[9], R. Orosei[10], M. Pätzold[11], J. Plaut[12], and MEX SGS Team[3],
[1]ESA-ESTEC, 2200 AG Noordwijk AG, The Netherlands;
[2]IAS-CNRS, Orsay, France;
[3]ESA-ESAC, Madrid, Spain;
[4]George Mason University, Fairfax, VA, USA;
[5]LMD, Paris, France;
[6]IAPS-INAF, Rome, Italy;
[7]IRF, Kiruna, Sweden;
[8]IPF-DLR, Berlin, Germany;
[9]IATMOS-CNRS, Guyancourt, France; [1]
[0]IRA-INAF, Bologna, Italy;
[11]RIU-Uni Cologne, Cologne, Germany;
[12]JPL, Pasadena, CA, USA.
dmitri.titov@esa.int

Mars Express opens its second decade in orbit in excellent health. Several papers that summarized the mission results from 10 years of operations have been recently published. Jaumann et al. (2015) reviewed the use of ***HRSC*** camera in the analysis of geological processes and landforms on Mars on a local-to-regional spatial scale that allowed constraining the Martian geological activity in space and time and conclude about its episodicity. Vincendon et al. (2015) completed a comprehensive study of the surface albedo using six years of observations by the ***OMEGA*** imaging spectrometer. Correction for atmospheric dust resulted in the albedo values on average 17% higher than the previous estimates for bright surfaces while remained almost unchanged for dark regions. The surface albedo changes have been mainly associated with the dust storm seasons.

The ***SPICAM*** UV&IR spectrometer continuously monitored atmospheric water on Mars revealing details and variability of the atmospheric water cycle. Taking into account scattering on the atmospheric dust resulted in ~10% higher water amount in polar regions in summer and up to 60-70% higher values for observations at large solar zenith angles (Trokhimovsky et al., 2015). High spectral resolution and long duration of observations allowed the ***PFS*** spectrometer to search for hydrogen peroxide that is known to play a key role in oxidizing capabilities of the Martian atmosphere. The derived mixing ratios of the specie were found to be close to the detection limits (0-60 ppb) (Aoki et al., 2015).

In 2015 the ***MARSIS*** radar experiment celebrates 10 years of the antenna deployment and beginning of science operations (Orosei et al., 2015). The most remarkable results of the experiment are related to subsurface sounding of various regions on Mars and determination of thickness of the polar caps, as well as sounding of the ionosphere that revealed complex interplay between plasma, crustal magnetic field and solar wind (Withers et al., 2015). The instrument also detected a dense ionized layer in the upper atmosphere of Mars caused by the impact of dust from comet Siding Spring (Gurnett et al., 2015). The structure of the ionosphere and neutral atmosphere is being regularly investigated by the radio-occultation ***MaRS*** experiment. The knowledge of the mass of Phobos was also significantly improved due to radio science measurements during close flybys (Paetzold et al., 2015). ***ASPERA*** continued observations of plasma environment and atmospheric escape emphasizing comparative planetology aspects (Dubinin and Fraenz, 2015). The observations now cover a complete solar cycle, and the flux of escaping ions is seen to follow the solar cycle, with increasing escape for larger solar activity (Lundin et al., 2013). The ***VMC*** (Visual Monitoring Camera) continuously monitors global behavior of the atmospheric dust and annual evolution of the polar caps providing valuable support

The Mars Express extension in 2015-2016 aims at completion of the surface coverage by imaging and spectral imaging instruments, continuing monitoring of the climate parameters and their variability, study of the upper atmosphere and its interaction with the solar wind. In the investigation of the upper atmosphere Mars Express is currently working in collaboration with NASA's MAVEN mission. MEX remote sensing complements in-situ monitoring of trace gases abundance in the lower atmosphere by NASA's Curiosity. MEX is looking forward to arrival in 2016 of the ESA/ROSCOSMOS ExoMars Trace Gas Orbiter to join the efforts in the study of the Red Planet.

References:

1. Jaumann, R. et al. (2015), Planet. Space Sci., doi:10.1016/j.pss.2014.11.029.
2. Vincendon, M. et al. (2015), Icarus, doi:10.1016/j.icarus.2014.10.029.
3. Trokhimovsky, A. et al. (2015), Icarus, doi:10.1016/j.icarus.2014.10.007.
4. Aoki, S., et al. (2015), Icarus, doi:10.1016/j.icarus.2014.09.034.
5. Orosei, R. et al. (2015), Planet. Space Sci., doi:10.1016/j.pss.2014.07.010.
6. Withers, P. et al. (2015), Icarus, doi:10.1016/j.icarus.2014.08.008.
7. Gurnett, D.A. et al. (2015), Geophys. Res. Lett., doi:10.1002/2015GL063726.
8. Paetzold, M. et al. (2014), Planet. Space Sci., doi:10.1016/j.pss.2014.01.004.
9. Dubinin, E. and M. Fraez (2015), Magnetotails in the Solar System, eds A. Keiling, C. M. Jackman and P. A. Delamere), John Wiley & Sons, Inc., Hoboken, NJ. pp 43-59, doi: 10.1002/9781118842324.ch3.
10. Lundin, R. et al. (2013), Geophys. Res. Let., 23(40), 6028–6032, 2013.

IONOSPHERE OF MARS AS SEEN BY MARS EXPRESS

E. Dubinin[1], M. Fraenz[1],
[1]Max-Planck-Institute for Solar System Research, Justus-Von-Liebig Weg,3, Goettingen, Germany.
dubinin@mps.mpg.de

The Martian ionosphere is studied using the local electron number densities and total electron content (TEC) derived from the observations onboard Mars Express. The data are complemented by the ASPERA-3 observations which provide us with the information about upward/downward velocity of the low-energy ions and electron precipitation. We consider 5 years of Mars Express observations at different solar cycle intervals. Different factors which influence the ionosphere dynamics are analyzed. The focus is made on a role of the crustal magnetic field on the Martian ionosphere.

MESOPHERIC CO2 CLOUDS AT MARS: SEVEN MARTIAN YEARS OF CO2 CLOUDS SURVEY BY OMEGA/MEX

B. Gondet, J.-P Bibring,
Institut d'Astrophysique Spatiale, UniverSud, Paris, Orsay France.
Brigitte.gondet@ias.u-psud.fr

Mesospheric clouds have been detected first from Earth (Bell et al 1996 [1]), then from Mars orbit (MGS/TES and MOC, Clancy et al 1998 [2]). Their composition (CO2) was inferred from temperature. Similar detection and temperature-inferred composition was then performed by Spicam and PFS on board Mars Express (Monmessin et al [3], Formisano et al [4]., 2006).

The first direct detection and characterization (altitude, composition, velocity) was performed by OMEGA/ Mars Express (then coupled to HRSC/ Mars Express, and confirmed by CRISM/MRO (Montmessin et al. [5], 2007, Maattanen et al [6]., Scholten et al. [7], 2010, Vincendon et al [8]., 2011).

Omega is a very powerful tool for the study of CO2 clouds as it is able to unambiguously identify the CO2 composition of a cloud based on a near-IR spectral feature located at 4.26 µm [5],. Therefore since the beginning of the Mars Express mission (2004) OMEGA as done a systematic survey of these mesospheric clouds. Thanks to the orbit of Mars Express, we can observe this clouds from different altitudes (from apocenter to pericenter) and at different local times.

We will present the result of 6 Martians years of observations and point out a correlation with the dust activity.

We also observe that their time of appearance/disappearance varies slightly from year to year.

We will mention also the existence of mesospheric H2O clouds.

References

[1] JF Bell. et al. JGR 1996; [2] RT Clancy et al., GRL 1998 [3] F. Montmessin et al. JGR 2006; [4] V. Formisano et al., Icarus 2006; [5] F. Montmessin et al JGR 2007 [6] A. Määttänen et al. Icarus 2010; [7] F. Scholten et al. PSS 2010; [8] M. Viencendon et al. JGR 2011

VARIABILITY OF WATER VAPOR IN THE MARTIAN ATMOSPHERE IN MY26-30 FROM PFS/LW OBSERVATIONS

A. Pankine[1]
[1]*Space Science Institute, Boulder, CO, USA.*
apankine@spacescience.org

Introduction:

Seasonal variations in atmospheric water vapor abundances have been observed by multiple Mars orbiting spacecraft for several Martian years (MY). Observations by Thermal Emission Spectrometer (TES) onboard Mars Global Surveyor (MGS) provided longest continuous almost global coverage of vapor changes in the Martian atmosphere during MY24–27. An uninterrupted observational record is important for establishing possible interannual variability. Several instruments currently in orbit around Mars provide continued observations of the atmospheric water vapor.

Here I present results of the retrievals of water vapor abundances in the Martian atmosphere from spectra collected by Planetary Fourier Spectrometer (PFS) Long Wavelength Channel (LW) instrument onboard the Mars Express (MEX) spacecraft during MY27–30. PFS/LW vapor abundances are retrieved from the same far-IR spectral range as the TES abundances (200-500 cm^{-1}) and thus are well suited for comparison to TES. At the same time different local times of PFS/LW observations present an opportunity to constrain diurnal variability of water vapor from comparison to TES 2 pm observations. The PFS/LW retrievals are also compared to contemporaneous retrievals from Compact Reconnaissance Imaging Spectrometer (CRISM) onboard Mars Reconnaissance Orbiter (MRO) spacecraft and SPICAM IR spectrometer on Mars Express. Seasonal changes in vapor abundances retrieved from the PFS/LW data are qualitatively consistent with the established seasonal cycle of water vapor; however comparison to other datasets reveals some differences that could be due to differences in the retrieval algorithms and/or due to the non-uniform vertical distribution and diurnal variability of water vapor.

LONG-TERM NADIR OBSERVATIONS OF THE O_2 DAYGLOW BY SPICAM IR

S. Guslyakova[1], A. Feforova[1], F. Lefevre[2], O. Korablev[1], F. Montmessin[2], A. Trokhimovsky[1], J.-L. Bertaux[2]
[1]Space Research Institute, 84/32, str. Profsoyuznaya, 117997, Moscow, Russia;
[2]LATMOS – UVSQ/UPMC/CNRS, 11 bd d'Alembert, 78280 Guyancourt, France.
guslyakova@iki.rssi.ru

The $O_2(a1\Delta g)$ dayglow in 1.27 μm band on Mars is produced during ozone photolysis by solar UV radiation. The SPICAM IR instrument on the Mars Express mission observes the O_2 emission in the Martian atmosphere starting from 2004 [1]. We present a continuous set of the $O_2(a1\Delta g)$ dayglow from nadir measurements for 6 Martian years from the end of MY26 to MY32 [2]. Maximal values of the O2 dayglow reaching 31 MR were observed in early northern and southern springs in both hemispheres. Near the equator a spring maximum of 5-8 MR was observed for all years. The emission intensity is minimal in the southern hemisphere in summer with values of 1-2MR. Comparison of data with GCM simulations [3,4] and simultaneous ozone measurements by SPICAM UV allows to derive the quenching rate (k) of excited O_2 molecules by CO_2 gas of 0.73±0.05 × ×10-20 cm3 molecules-1 s-1. The interannual variation of the O_2 emission has been studied after applying correction for the local time. The O_2 seasonal pattern is quite stable with average year-to-year relative variation of about 21%, in line with interannual variations detected from the ground [5]. The most variable region corresponds to northern and southern spring in middle latitudes, coinciding with sublimation of polar cap in the both hemispheres. Southern latitudes also show a high year-to-year variability in summer (Ls=270-330º) relating to the dust activity in this region. The photolysis of water vapor is the source of the odd hydrogen species H, OH and HO_2 (HOx family) that destroy efficiently O_3 [3]. As a result an anti-correlation between water vapor and ozone is generally expected in the atmosphere of Mars. A comparison with simultaneous SPICAM water vapor observations [6] shows that the $O_2(a1\Delta g)$ dayglow depends on the water vapor variations. We present their anti-correlation features as a function of different seasons and latitudes both for all years and separately for different years, as interannual variations of the O_3 induce the corresponding variations of the O_2 dayglow.

Russian authors acknowledge the Program 9 of RAS and RFBR grant 15-02-07812 a for financial support.

References:

[1] Korablev O. et al., 2006, SPICAM IR acousto-optic spectrometer experiment on Mars Express, *J. Geophys. Res., 111, E09S03,* doi:10.1029/2006JE002696.
[2] Fedorova A. et al., 2006, Observation of O_2 1.27 μm dayglow by SPICAM IR: seasonal distribution for first Martian year of Mars-Express, *J. Geophys. Res.,* **111**, E09S07, doi:10.1029/2006JE002694, 2006.
[3] Lefevre F. et al., 2004, Three-dimensional modeling of ozone on Mars. J. Geophys. Res. 109, E07004.
[4] Lefevre, F. et al., 2008. Heterogeneous chemistry in the atmosphere of Mars. Nature 454, 971–975.
[5] Krasnopolsky, V. 2013. Night and day airglow of oxygen at 1.27 μm on Mars, Planet. Space Sci. 85, 243–249.
[6] Trokhimovskiy A. et al., 2015, Mars' water vapor mapping by the SPICAM IR spectrometer: Five martian years of observations, Icarus, Volume 251, p. 50-64.

EXOMARS MISSION

H. Svedhem[1], J. Vago[1], R. de Groot[1], O. Korablev[2], D. Rodionov[2], L. Zelenyi[2]
[1]ESA European Space Research and Technology Center (ESTEC), Noordwijk
[2]Space Research Institute (IKI), Moscow

The ExoMars programme is a joint activity by the European Space Agency (ESA) and ROSCOSMOS. It consists of the ExoMars 2016 mission with the Trace Gas Orbiter, TGO, and the Entry Descent and Landing Demonstrator, Schiaparelli, and the Exomars 2018 mission which carries a lander and a rover.

The TGO scientific payload consists of four instruments. These are: ACS and Nomad, both infrared spectrometers for atmospheric measurements in solar occultation mode and in nadir mode, CASSIS, a multichannel camera with stereo imaging capability, and FREND, a neutron epithermal detector for search of subsurface hydrogen. ESA is providing the TGO spacecraft and the Schiaparelli Lander demonstrator and two of the TGO instruments and ROSCOSMOS is providing the launcher and the other two TGO instruments.

After the arrival of the ExoMars 2018 mission at Mars, the TGO will handle the communication between the Earth and the Rover and lander through its UHF communication system. The 2016 mission will be launched by a Russian Proton rocket from Baikonur in January 2016 and will arrive at Mars in October the same year. This presentation will cover a description of the 2016 mission, including the spacecraft, its payload and science and the related plans for scientific operations and measurements. A separate presentation will cover the 2018 mission.

USING RADIO-NAVIGATION DATA OF ESA'S TRACE GAS ORBITER (TGO) TO IMPROVE THE MARS' GRAVITY SEASONAL VARIATIONS

P. Rosenblatt[1], J.C. Marty[2]
[1]Royal Observatory of Belgium, Avenue circulaire, 3, 1180 Uccle, Belgium;
[2]CNES/GRGS, Toulouse, France.
rosenb@oma.be

Introduction:

The condensation and sublimation of the atmospheric CO_2 at Mars' polar caps yield seasonal mass redistribution at planetary scale. In turn, this global mass redistribution causes seasonal variations of Mars' gravity field. Such variations should be detected on the first zonal harmonics of the gravity field (namely, the even C_{20} and odd C_{30} harmonics), and provide a direct measurement of the seasonal mass budget. However, these gravity variations produce tiny changes in the orbit of the current Martian spacecraft, i.e. at the level of tens of centimeters. The reconstructed orbit of the spacecraft from radio-navigation data (i.e. routine tracking of the orbiting spacecraft) is however at the meter level of precision, thus preventing to precisely determine the expected seasonal gravity changes (i.e. till 40% of error for the even harmonics changes). In turn, the current solutions of Mars' gravity changes cannot be used to well constrain physical modeling of the CO_2 seasonal cycle.

On one hand, the precision on the reconstructed spacecraft orbit is limited by inaccuracies in the dynamical model of the spacecraft motion more than by the precision or the coverage of the radio-navigation tracking data. Therefore, it seems difficult to improve the current gravity changes solutions with the currently available tracking data of Martian spacecraft. On the other hand, the orbital changes due to the seasonal gravity variations have amplitudes strongly related to the main orbital parameters such as the semi-major axis, the inclination and the eccentricity. For instance, the signature of the even harmonics is proportional to the cosine of the inclination. As all the Martian spacecraft used for the gravity changes solutions have polar orbit, the seasonal signal of the even harmonics on their orbital changes is very small (less than ten centimeters).

The new ESA' Martian spacecraft TGO (Trace Gas Orbiter), to be launched in January 2016, will offer for the first time in recent Mars' exploration, the opportunity to have an orbiter put in a near-circular and non-polar orbit (i.e. 73 degrees of inclination). Analytical and numerical calculations show that the TGO orbital perturbations due to the even harmonics seasonal changes are at least 5 times larger than for polar orbiters, given this inclination and the semi-major axis of about 3800 km. The even harmonics seasonal changes are thus expected to produce TGO orbital perturbations at the same level as for orbital perturbations on polar orbiters due to the odd harmonics seasonal changes. Therefore, TGO would provide a C_{20} variation solution with same precision as the current C_{30} solution. The orbit of TGO has however to be determined with a precision at the meter level or even better.

Determination of seasonal gravity changes and CO_2 mass budget:

The most direct measurement of the CO_2 mass budget is given by the determination of the time-variable gravity field obtained from the least squares fit of the spacecraft orbital motion to the radio-tracking data. The seasonal variations of the first zonal harmonics have been obtained from MGS' radio-tracking data (Smith et al., 2001; Yoder et al., 2003). These estimates have, however, too large formal errors (up to 40%) to be used to constrain physical modeling of the CO_2 seasonal mass budget. More recent analyses have updated the tracking dataset of MGS and added Mars Odyssey ones (Konopliv et al., 2006; Marty et al., 2009) as well as Mars Reconnaissance Orbiter (MRO) ones (Konopliv et al., 2011; Marty et al., 2013). These most recent studies confirmed the detection of the seasonal signal on the odd harmonics but were not able to improve its detection on the even harmonics variations. Smith et al. (2009) have estimated mass seasonal budget directly from tracking data, using a simple model of varying size and height of each Northern and Southern polar cap. They obtained however error on mass budget of up to 30% and their model also depends on the atmospheric mass exchange with the polar caps as constrained by a GCM.

The tiny orbital perturbations due to seasonal gravity changes and the inaccuracy of the modeling of the force acting on the spacecraft explain these large errors on seasonal gravity changes estimates. Indeed, the amplitude of the perturbations of spacecraft position of the polar orbiter (like MGS or MRO) is up to 70 cm for odd harmonics but only 10 cm for even harmonics. As the error on the reconstructed orbit is typically at the meter level, only the odd harmonics variations have been detected while the even harmonics variations determination still remain much noisier in spite of adding tracking data of MRO till the end of 2012 (e.g. Marty et al., 2013). Rosenblatt et al. (2004) have proposed to use the Mars Express (MEX) tracking data in addition to those of MGS/Odyssey in order to profit from the more eccentric orbit of MEX. However, the signature of the C_{20} even harmonics variations is only 20 cm while the error on the MEX reconstructed orbit was on average 20 meters, i.e. ten times worse than the error on the MGS/Odyssey/MRO reconstructed orbit. Therefore, MEX tracking data were unable to improve the time-variable gravity solution.

Orbital perturbations of TGO and time-variable gravity field improvment:

The ESA's TGO spacecraft will have an orbit with an inclination of 73 degrees, which is quite different from the usual polar-orbit of Martian spacecraft. In addition, it has an orbital altitude similar to the MGS/Odyssey one (i.e. 400 km). The signature of the even harmonics variations on TGO orbit is expected to be about 5 times larger than on polar orbit, thus rising up to about the same level as for the signature of the odd harmonics variations on MGS/Odyssey orbits. Therefore, the tracking data of TGO will offer the opportunity to determine the seasonal variations of the even harmonics at the same level of error as for the current solution of the odd harmonics seasonal variations.

However, to reach this expected result, the orbit of TGO has to be determined at the meter level like for MGS/Odyssey. The Precise Orbit Determination (POD) method will be used. This method has been successfully tested on the tracking data of previous Martian spacecraft (e.g. Lemoine et al., 2001; Konopliv et al., 2006; Rosenblatt et al., 2008; Marty et al., 2009). It consists of performing a least squares fit of a dynamical model of the motion of the spacecraft to the tracking data. These tracking data are the Doppler effect on the carrier frequency of the radio-link between the spacecraft and Earth's tracking stations (ESTRACK stations for ESA's spacecraft) as well as the round-trip time delay of the radio-signal, measured at the same stations (see Holmes et al., 2009). As a result to this least-squares fit, are adjusted parameters of the dynamical model such as scale factor of non-gravitational forces (atmospheric drag, solar radiation pressure), corrections to accelerations generated by each attitude maneuver, a reconstructed orbit of the spacecraft as well as partial derivatives of the seasonal gravity changes. Such adjusted parameters allows for reducing the effect on the reconstructed orbit of the inaccuracies of the non-gravitational force models (like the atmospheric density model for the drag). It needs, however, a good knowledge of the optical properties (reflectivity, absorptivity and emissivity) as well as surface areas of the faces of the spacecraft (i.e., the bus, the solar arrays and the High Gain antenna) since these non-gravitational forces act on the surface of the spacecraft. The shift between the center of phase of the HGA and the spacecraft center of mass is also required since the tracking data refer to the center of phase while the motion of the center of mass of the spacecraft is reconstructed. The POD fit is usually performed on data-arcs of 4-5 days long and the partial derivatives of each data-arc are stacked together to derive the seasonal variations of the zonal harmonics of the gravity field of Mars.

The accuracy on the time-variable gravity solution will strongly depend on the precision on the reconstructed orbit obtained from the POD process. Further studies will make numerical simulations of the effects of the inaccuracies of the dynamical model in order to assess the precision on the reconstructed TGO orbit and in fine the expected improvement on the determination of the Martian seasonal gravity changes. The effect of the coverage of the navigation tracking data with time will also be assessed. These numerical simulations and the POD computations on the future TGO tracking data will be performed using the dedicated orbitography software, GINS (Géodésie par Intégrations Numériques Simultanées) developed by the space French agency (CNES) (e.g. Marty et al., 2009) and further adapted at Royal Observatory of Belgium (ROB) for planetary applications.

References:

Holmes et al., 2008, Proc. AIAA/AAS Astrodynamics Specialist Conference, 18, 2008-6395; Konopliv et al., 2006, *Icarus*, Vol. 182, p. 23-50; Konopliv et al., 2011, *Icarus*, Vol. 211, p. 401-428; Lemoine et al., 2001, J. Geophys. res., Vol. 106, p. 23359-23376;

Marty et al., 2009, *Planet. Space Sci.*, Vol. 57, p. 350-363; Marty et al., 2013, *AGU fall meeting*, San-Francisco, USA, December 9-13th 2013; Rosenblatt et al., 2004, *AGU Fall meeting*, San-Francisco, USA, December 12-19th 2004; Rosenblatt et al., 2008, *Planet. Space Sci*., Vol. 56, p. 1043-1053; Smith et al., 2001, *Science*, vol. 294, doi:10.1126/science.1066556; Smith et al., 2009, *J. Geophys. Res.*, Vol. 114, doi:10.1029/2008JE003267; Yoder et al., 2003, *Science*, Vol. 300, p. 299-303.

SPECTROSCOPIC AND MASS SPECTROMETRIC STUDIES ON OZONE - IMPLICATIONS FOR OZONE FORMATION AND THE ORIGIN OF THE OXYGEN ISOTOPIC HETEROGENEITY IN THE SOLAR SYSTEM

C. Janssen, C. Boursier, H. Elandaloussi, P. Jeseck, M. Minissale, D. Simone, Y. Té, T. Zanon
LERMA, Observatoire de Paris, PSL Research University, CNRS, UMR 8112, F-75014, Paris, France

Ozone is a major trace compound in the atmospheres of Earth and other solar system planets and the trace gas has also been identified on solar system moons [1,2]. As such, remote sensing of ozone is of major concern for understanding atmospheric change and the climate system (*eg* Global Atmospheric Watch (GAW) / Global Climate Observation System (GCOS) programs of the World Meteorological Organization (WMO)), but it is also part of past and future space missions, such as JUICE/SWI [3].

Ozone remote sensing depends on reliable spectroscopic data. Here we present recent results of ground based atmospheric FTIR (Fourier Transform InfraRed) measurements using the Paris-FTS (Fourier Transform Spectrometer) instrument [4], that illustrate the limitations of spectroscopic data provided by current data bases in the medium infrared region [5].

Interestingly, the isotope kinetics of ozone formation provides the primary example for chemically induced oxygen isotope anomalies [6] which provide one possible scheme for causing the nebular heterogeneity of oxygen isotopes, recorded in the early solar system refractories [7,8]. Several chemical models, involving ozone formation ($O+O_2$) [9] or formation of SiO_2 (O+SiO) [10] on grain surfaces have been proposed. New laser measurements of ozone decomposition and formation in the laboratory provide further insight in as much as these models might bear relevance to the meteoritic record. The results of our laboratory studies might also further help in identifying ozone formation pathways on solar system bodies.

References:

[1] Noll KS, Johnson RE, Lane AL, Domingue DL, Weaver HA. Science 1996;273:341–3.
[2] Noll KS, Roush TL, Cruikshank DP, Johnson RE, Pendleton YJ. Nature 1997;388:45–7.
[3] Hartogh P, Barabash S, Beaudin G, Börner P, Bockelée-Morvan D, Boogaerts W, et al. European Planetary Science Congress, London: 2013.
[4] Té Y, Jeseck P, Payan S, Pepin I, Camy-Peyret C. Rev Sci Instr 2010;81:103102.
[5] Janssen C, Boursier C, Jeseck P, Té Y. submitted to J Mol Spectrosc 2015.
[6] Mauersberger K, Krankowsky D, Janssen C. Space Sci Rev 2003;106:265–79.
[7] Clayton RN, Grossman L, Mayeda TK. Science 1973;182:485–8.
[8] Thiemens MH, Chakraborty S, Dominguez G. Ann. Rev. Phys. Chem. 2012;63:155–77.
[9] Dominguez G. A Heterogeneous Astrophys J Lett 2010;713:L59–63.
[10] Marcus RA. J Chem Phys 2004;121:8201–11.

NANOBIOTECHNOLOGY FOR DETECTION OF EXTRATERRESTRIAL LIFE

D.A. Skladnev, V.V. Sorokin, V.F. Galchenko
Winogradsky Institute of Microbiology, Russian Academy of Sciences, 117312 Russia, Moskow, prosp. 60-Let ktober, h.7, b.2.
skladda@gmail.com

For decades, the humanity is trying in an organized fashion to find live objects outside the Earth. To date, mankind has tried many remote methods. In recent years, we are getting more and more chances for developing research contact methods. These methods require the use of high-speed and compact scientific equipment.

We offer a fundamentally new, simple and universal, approach for detection of low-concentrated biological objects by registration of metal nanoparticles formed *in situ* in the investigated samples. The authors called the method OBNG – Observation Biogenic Nanoparticles Generation. Its use is determined by the relevance of the analytical instrumentation devices, capable to register a combination of such valuable qualities of metal nanoparticles as unique optical properties (due to the phenomenon of surface plasmon resonance), highly developed surface, catalytic activity, high capacity electrical double layer, and many others. Its unique properties allow to apply successfully the bass to amplify the signal of individual organic biomolecules in fluorescence spectroscopy, in Raman spectroscopy, as well as in the spectroscopy of surface-enhanced Raman scatter-ing.

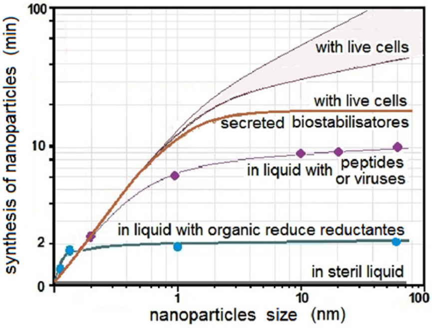

Fig. 1. Schematic illustration for kinetic-controlled and redox-determined forming of nanoparticles.

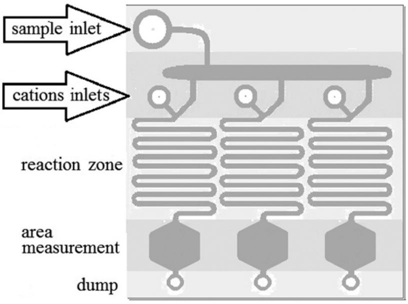

Fig. 2. Basic units Lab-on-Chip for realization OBNG method

Formation of nanoparticles is a kinetic-controlled process favored by relatively slow redox reaction. The controlling factor is determined the dynamic regime of the whole physicochemical process, yet the results also suggested that the redox chemistry could significantly affect the nucleation crystallization and growth process and thus influences the shapes and size of forming nanoparticles. The level of redox activity is directly determined by the fact whether there is in the reaction mixture of organic molecules or biopolymers of living cells surfaces. Thus, the size and shape is determined by the presence of the de-sired object. This is the basis of our proposed funda-mentally new approach.

Terrestrial biological objects formed metal nanoparticles from added sterile solution of cations in the volume of the reaction mixture 20–100 µl for 20–60 minutes (Fig. 1). The proposed approach al-lows using of any analytical methods for recording and research nanoparticles, and gives the opportunity to quickly and accurately detect the presence of bio-genic reducing agents, typical for the cells of micro-organisms and viral particles. In astrobiological stud-ies with the OBNG method, water samples suspected to contain unknown biological objects can be exam-ined.

The authors also propose a schematic diagram of a microfluidic chip (Fig. 2) to produce a miniature automated version of a device based on the OBNG method. The chip device includes an input node of the sample and the test solutions of several cations, capillary plot for the reaction, as well as a concentra-tion chamber for any kind of measurements.

PHAGES AS MARKERS FOR EXTRATERRESTRIAL LIFE

V.V. Sorokin, D.A. Skladnev, A.V. Kusakina, V.F. Galchenko
Winogradsky Institute of Microbiology, Russian Academy of Sciences, 117312 Russia, Moskow, prosp. 60-Let Oktober, h.7, b.2.
vlvlsorokin@gmail.com

The new approach for the search of extraterrestrial life may be focused not on the detecting of only molecular markers, microorganisms and their components, but on the search of phage particles. According to the total number in the biosphere phages are inferior only to the individual molecules of biological compounds, significantly exceeding the number of cellular life forms. The phages as well-known are not independent in their manifestation of the signs of a living object. However many of the properties of phages can certainly contribute to the success in finding them as a marker extraterrestrial cellular life. Indeed, a simple chemical composition of phage particles, the quasicrystalline structure, and morphological features suggests a high probability of their finding even in the conditions of interplanetary space. With the defeat of nucleic components of phages cosmic rays (inactivation abilities of virulent phage), probably should not significantly affect the structural integrity of capsids. This means that even inactive phage particles can be detected and identified.

As the argument for phages searching in Space we want to bring the results of our own studies of natural samples, selected in Yakutia permafrost area. Biota of the permafrost zone of the Earth is considered by many researchers as a model of living conditions beyond our planet. Moreover, in cold area a variety of microorganisms are maintained for a long time. Our experiment was aimed on induction of new phages in original independently selected cultures of isolates containing *a priori* lysogenic phages. Induction by UV irradiation for six bacterial isolates shows the new phages in all six. The share lysogeny clones within each of the isolates ranged from 28 to 90%. It was also noted that one of the isolates contained two types of phage – filamentous and spherical-hexagonal-tailed. The results show presence of different types of phages in the population of bacteria that retain high viability in permafrost. We can say that the absent of nonlysogenic cultures meet expectations – the probability of the existence in Nature of microorganisms, resistant to all phages in a particular ecological niche, almost zero.

.

SPACE FACTORS PROVIDING THE CONDITIONS FOR ABIOTIC ORIGIN OF THE LIVING MATTER

G.G. Managadze[1], M.H. Engel[2], S. Getty[3], P. Wurz[4], W.B. Brinckerhoff[3], A.G. Shokolov[5], G.V. Sholin[6], S.A. Terent'ev[7], A.E. Chumikov[1], A.S. Skalkin[5], V.D. Blank[7], V.M. Prokhorov[7], N.G. Managadze[1],
[1] Space Research Institute, Profsoyuznaya st. 84/32, Moscow, Russi;
[2]School of Geology & Geophysics, The University of Oklahoma, Norman, OK 73019, USA;
[3]NASA Goddard Space Flight Center, Greenbelt, MD 20771, USA;
[4]Physics Institute, University of Bern, 3012 Bern, Switzerland;
[5]Central Research Institute of Machine Building, Moscow, Russia;
[6]NRC "Kurchatov Institute", Moscow, Russia;
[7]Super hard and Novel Carbon Materials Technological Institute, Moscow, Russia.
managa@iki.rssi.ru

Introduction:

Homochirality is generally recognized as the most important structural feature of living matter, and a unique marker of life. Its origin, however, remains unknown, and biochemical replication could not develop, and hence life could not arise, without it [Eigen and Schuster, 1979]. Thus, homochirality must have originated in non-living matter. However, for 130 years, since L. Pasteur [Pasteur,1884] discovered the chiral asymmetry of life, homochirality has remained the main barrier for hypotheses about the genesis of living matter.

The formation of organic compounds from abiogenic precursors was reported for a plasma torch produced by laser irradiation of a target composed of a non-organic substance [Managadze, 2001]. Hence, emulating the impact plasma by high power laser pulses proved to be comfortable and practical at the initial stage of laboratory studies of the properties of impact plasma [Managadze, 2003; Managadze et al., 2003].

Later, a study of the physical fields of a laser-produced plasma torch showed that the generated fields during the plasma expansion have the characteristics of "truly" local chiral physical fields [Managadze, 2005], which may ensure the initial breaking of enantiomers' symmetry.

We present a laboratory reproduction of hypervelocity impacts of a carbon containing meteorite on a mineral substance – representative of planetary surfaces. The properties of the impact plasma torch provide conditions for abiogenic synthesis of protein amino acids: we identified glycine and alanine, and in smaller quantities serine in the impact products. Moreover, we observe breaking of alanine mirror symmetry with L excess, which is identical with the bioorganic world. Therefore the selection of L-amino acids for the formation of proteins for living matter was not random, but was defined by the plasma processes occurring in the impact torch. This indicates that the plasma torch from meteorite impacts could play an important role in the formation of biomolecular homochirality. Thus, meteorite impacts possibly were the initial stage of this process and promoted conditions for the emergence of a living matter.

We realized hypervelocity impact experiments using a ballistic launcher equipped with a light-gas gun. To improve efficiency, the apparatus was adapted to launch a set of 20–50 projectiles at once with diameters ranging from 1.5 to 2.5 mm, at a flat multilayer target. Projectiles of pure ^{13}C synthetic diamond were used, which remained intact during acceleration.

For our experimental conditions, an impact at about 7 km/s and a projectile density of ~3.5 g/cm^3, the initial compression at the impact can reach about 170 GPa, and heating the projectile and part of the target to temperatures of (3–4)x10^4 K.

We analyzed the impact products using three separate analytical techniques with different strengths, limitations, and detection limits: a matrix assisted laser desorption ionization (MALDI) TOF instrument, a laser desorption TOF instrument, and a GC-MS instrument.

The results of our impact experiments can be summarized as follows: the expansion of the impact-produced plasma torch results in:

1. The synthesis of the protein amino acids – glycine and alanine, which were

discovered using GC-MS, and confirmed by laser mass spectrometry and the additional detection of serine by laser mass spectrometry.

2. The synthesis of organic compounds with mass around 1300 a.m.u. containing fragments of protein peptides with mass ~ 300 a.m.u., composed of glycine, alanine and serine.
3. The excess of L-alanine over D-alanine determined in the SIM mode – from 1.15 by amplitudes to 1.68 by integrals of peaks.
4. The "sign" of asymmetry coincides with the bioorganic world.

The analysis of the impact experiments also shows that the samples contain no amino acid contaminants.

Thus, we showed experimentally that the natural plasma mechanisms arising in a plasma torch during hyper velocity impact of meteorites can provide the synthesis of protein amino acids, the moderate break of their mirror symmetry with the "sign" coinciding with bioorganic world and the formation of short peptide molecular structures consisting of the same protein amino acids synthesized in a plasma torch.

Supported by the Presidium of the Russian Academy of Sciences (grant no. 22), and the Swiss National Science Foundation. This work was directed to Journal of Geophysical Research Letters.

The most important result of these researches is presented on Fig. 1 in the form of original chromatograms showing the excess of L-alanine over D – alanine. On Fig.2 – TsNIIMASh multi-purpose ballistic launcher equipment.

References:

1. Eigen M. & Schuster P. *The Hypercycle. A Principle of Natural Self-Organization*. Berlin: Springer-Verlag. (1979).
2. Pasteur L. *Bull, Soc. Chem. France N.S.*, 1215-220. (1884).
3. Managadze G.G. Organic compound synthesis in experiments modeling high-speed meteor impact. Proceedings of 26th General Assembly of the European Geophysical Society. *Geophys. Res. Abstr.*, 3, 7595. (2001).
4. Managadze G.G., The synthesis of organic molecules in laser plasma similar to the plasma that emerges in hypervelocity collisions of matter at the early evolutionary stage of the Earth and in interstellar clouds. *J. Exp. Theor. Phys.*, 97, 49-60. (2003).
5. Managadze G.G., Brinckerhoff W., Chumikov A.E. Molecular synthesis in hypervelocity impact plasmas on the primitive Earth and in interstellar clouds. *Geophys. Res. Lett.*, 30, 1247-1251. (2003).
6. Managadze G.G. *Abiogenous synthesis of chiral organic compounds in the plasma generated under the influence of SHV-Impact*. Preprint. Pr-2107. Moscow: Space Research Institute ofthe Russian Academy of Sciences, 20 pp. (in Russian). (2005)

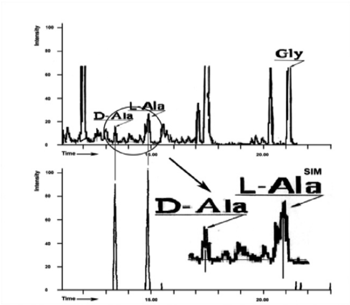

Fig. 1

Fig.2

A NOVEL TECHNIQUE AND MASS-SPECTROMETRIC INSTRUMENT FOR EXTRATERRESTRIAL MICROBIAL LIFE DETECTION VIA ANALYSES OF THE ELEMENTAL COMPOSITION OF MARTIAN REGOLITH AND PERMAFROST/ICE SAMPLES

K.A. Luchnikov[1], G.G. Managadze[1], A.A. Safronova[1], E.A. Vorobyova[1,3], N.S. Duxbury[4, 5], P. Wurz[2], N.G. Managadze[1], A.E. Chumikov[1], R.X. Khamizov[6],

[1]*Space Research Institute, Russian Academy of Sciences, 84/32 Profsoyuznaya Str, Moscow, Russia;*
[2]*University of Bern, Sidlerstrasse 5CH- 3012 Bern, Switzerland;*
[3]*Lomonosov Moscow State University, Soil Science Faculty, Moscow;*
[4]*Lomonosov Moscow State University, Geology Faculty, Moscow;*
[5]*George Mason University, 4400 University Dr., Fairfax, USA;*
[6]*Institute of Geological Chemistry, Russian Academy of Sciences, Moscow.*
luchnikov@iki.rssi.ru

Introduction:

We propose and substantiated a new technique for detection of microorganisms via elemental composition analyses of a sample extracted from the regolith, permafrost and ice of extraterrestrial objects. We also show the design of the laboratory prototype for the on-board time-of-flight laser mass-reflectron (TOF LMR) ABIMAS and the unit for sample preparation and biomass extraction.

This instrument was approved to fly on-board the ExoMars lander 2018 mission. The instrument can be used to analyze the elemental composition of possible extraterrestrial microbial communities and compare it to the elemental composition of terrestrial microorganisms. The microorganisms can be detected by these criteria:

1. the abundance ratios of biogenic markers K/Ca, P/S;
2. the presence and abundance of the matrix biogenic elements: C, N.

Our technique has been tested experimentally in numerous laboratory trials on cultures of microorganisms and on terrestrial polar soils containing microorganisms. These trials included the analysis of polar permafrost samples as a terrestrial analog for Martian polar soils.

We have shown the probable survival of radiation-resistant microorganisms, similar to terrestrial Deinococcus radiodurans in the near-surface Martian regolith layer (at 2-5 cm depth), since the time of their adaptation to radiation on the Martian surface is ~300 yrs versus ~ 3 mln years for acquiring the lethal dose.

In addition, we discuss various methods of microorganism extraction and sample preparation. The developed technique can be used to search for and identify microorganisms in different Martian samples, and also in the subsurface permafrost and ices of other planets, satellites, comets and asteroids, in particular, Europa, Ganymede, Enceladus. Also, this onboard instrument can be used for elemental and isotopic composition analysis of unprocessed Martian regolith and atmospheric dust deposited on the holder.

Article based on these results was submitted to Astrobiology journal.

AEROBIOLOGY RESEARCH ON MARS AND THE POSSIBILITY OF ITS IMPLEMENTATION

G.G. Managadze[1]
[1]Space Research Institute, Russian Academy of Sciences, 84/32 Profsoyuznaya Str, Moscow, Russia;
managa@iki.rssi.ru

Introduction:

Modern state of the life search problem on Mars has entered into the phase in which more and more of the world scientific community who study this problem reasonably believe that microbial life on the Red Planet can't be absent.

Microbiological life on Mars, if it's present, must have a high similarity with one on the Earth.

In this regard, today one of the most interesting field of research may be aerobiological study of the Martian atmosphere.

There is the intercontinental transport of aerosol particles by the wind during dust storms on the Earth's surface. It is known that in such cases the aerosol can contain up to 30% of terrestrial microorganisms.

Studies of migration of terrestrial organisms as a component of atmospheric aerosols have been intensively carried out over the last 10 years. Today the area of knowledge called "aerobiology" examines the distribution of microorganisms in the Earth's atmosphere, studies some important consequences of this natural phenomenon that depend on the characteristics of the wind. Moreover, development of the adaptation processes of microbial communities to new extreme conditions of their life is of high interest too.

For realization of Earth-like aerobiological processes on Mars the following conditions are necessary:

- Martian microorganisms have to be adapted to the extreme conditions on the Martian surface and survive not only in the deep layers of the crust of the planet but also on his surface;
- Microorganisms should be transported during dust storms and tornadoes by the wind together with the sand and dust over long distances reaching in some cases a planetary scale.

Basing on multifactor analysis we can demonstrate that the above conditions with a high probability can be satisfied for virtually all areas of the red planet. This assumption is based on the reliable results obtained in previously conducted experiments in terrestrial laboratories and ones obtained recently from the board of the Martian rovers.

In particular, the microorganisms could colonize Mars before the loss of the planet's atmosphere, however, similarly to terrestrial one they can live in the crust at a depth up to 10 km. Since the process of losing the atmosphere lasted about 100 million years, a part of Martian microorganisms might adapt to the effects of space and UV radiation and turn into extremophiles.

It should be noted that the natural dust ejection to the atmosphere of Mars which is caused by dust storms or meteorite impacts can help to survive adapted microorganisms and to protect the non-adapted ones from direct UV radiation.

Microbiological studies carried out in laboratories indicate the possibility of adaptation and survival of terrestrial microbial communities in extreme conditions.

For example, terrestrial *Deinococcus radiodurans* have radiation resistance providing the ability to restore the genome within 6 hours after the damage. This properties enable it to survive on the surface on the Mars $3x10^6$ years while adaptation of D. radiodurans takes only $3x10^2$ years.

The microorganisms like D. radiodurans also can be easily adapted to UV light. It is important that the resistance to radiation achieved during microorganisms dehydration.

Mass spectrometry studies conducted on Curiosity rover found all elements necessary for the formation of living matter, including nitrogen, in dust deposits. It shows the possibility of the presence of Martian analogs of the terrestrial microorganisms in the wind drifts of dust and sand in Gale crater.

An important feature of aerobiology studies on Mars is that microorganisms can be detected in the dust deposited on the holder, which is a target of laser ablation time-of-flight mass spectrometer. Therefore, such configuration does not require a sample loading device and movement of the device over the surface. This technique is optimal in the case when descent module immobile and hasn't got the sample loading device or manipulator – "hasn't got hands and legs" – and cannot provide clean and correct measurements. It is usually associated with pollution the landing zone by hydrazine and decomposition products during operation of braking engines.

Onboard instrument aimed at this task should have absolute sensitivity not worse than 10^{-15} g, which allows carrying out elemental and isotopic analysis of Martian atmospheric particles. In this case the mass deposited on the 1 cm^2 holder during the exposure does not exceeding 1 sol will be ~$3x10^{-7}$ g.

One such loading will provide 10^3-10^4 single mass spectra with S/N ratio not worse 10^3-10^4.

The instrument allows to work in soft desorption mode allowing measurement of molecular ions.

Before deposited, these micron-size particles of mineral grains and microorganisms of the same size can levitate continuously in undisturbed atmosphere. The process of micron-size atmospheric particles deposition will contribute to the preparation of highly homogenous target that will allow identifying the microorganisms.

It is important that the proposed instrument is aimed at the task of finding microbial life and has no analogues in the arsenal of space instruments.

This instrument is laser ablation time-of-flight mass spectrometer and in the nominal mode has the absolute sensitivity about 10^{-15} g. However, improvement of the instrument tested before in the laboratory can increase its sensitivity up to 10^3 times which corresponds to ~10^{-18} g.

We believe that the appended original technique and unique on-board laser mass spectrometer will find its place in future missions for the realization of the first aerobiology research on Mars.

MARTIAN MAGNETIC FIELD: DESERVE TO BE CONCERNED BEFORE HEADING TO MARS

R.Q. He, W.C. Mo, Y. Liu
State Key Laboratory of Brain and Cognitive Science, Institute of Biophysics, Chinese Academy of Sciences (CAS), 15Datun Road, Chaoyang District, Beijing, China.
rongqiaohe@163.com

Magnetic field is an important factor for the evaluation of the habitability of a planet. All living organisms have been exposed to the geomagnetic field (GMF, ~ 50 μT). However, the Martian magnetic field is much lower than the geomagnetic field (< 5,000 nT), so called a hypomagnetic field (HMF) (Fig. 1). Even though biological effects of the HMF were valued in early studies (1960s), exploration of the space HMF has not rapidly progressed in the following decades. So far, with the development of advanced and standardized HMF experimental systems, significant findings on the effects of the HMF have been reported.

A number of ground-based HMF simulation experiments have made it obvious that the HMF greatly disturbs the functional state of organisms. It has been shown that HMF exposure alters the embryonic development, cell proliferation, oxidative stress state, and the function of immune system. The HMF-exposed animals/human subjects exhibited impaired learning and memory, reduced cognitive ability and working capacity. Recently, we performed a transcriptome profiling assay on the HMF-exposed human neuroblastoma cells and found that HMF exposure significantly affect the transcription of genes related to macromolecule transport, metabolic process, mRNA processing, and to the subsequent pathways involved in the organization of the cytoskeleton, regulation of chromatin condensation, transcription, and brain function. Given the reported adverse impacts of the HMF on many aspects of the life system, especially the brain functions, astronauts are exposed to the HMF and thus to potential health risks during interplanetary navigation or after landing on the Mars. Thus, it is necessary to evaluate and elucidate the mechanism of the HMF effect and to develop effective strategies counteract the HMF for the life support and health care of the astronauts in outer space.

Actually, the microgravity, radiation and HMF similarly act on multiple aspects of an organism including bone formation, brain and cognition, immune sys-

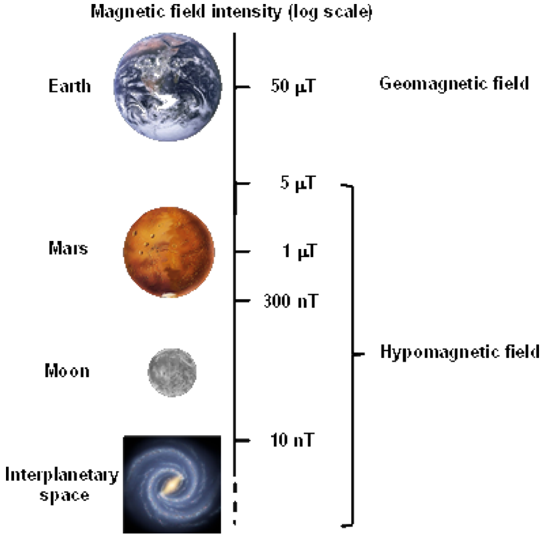

Figure 1 The environmental magnetic field in outer space and the definition of the hypomagnetic field. A weak static magnetic field with |B| < 5 μT is defined as a hypomagnetic field (HMF). Lunar magnetic field range: < 300 nT; Martian magnetic field range: 300 nT ~ 5 μT. The interplanetary magnetic field is lower than 10 nT. The magnetic intensity is plotted in logarithmic scale.

tem, cell growth and embryonic development, cytoskeleton, stability of genetic materials, and oxidative stress responses, which implicates the presence of interactions among the three factors. The design of a feasible, practical and robust experimental set up in the further investigation which can precisely provide the complex combinations of ionizing radiation, microgravity and/or HMF is critical to improve the progress in space life science. The close cooperation between expert biologists and engineers will be greatly valuable and imperative.

This work is supported by the External Cooperation Program of BIC, CAS (GJHZ201302), the project of CAS for the development of major scientific research equipment (YZ201148).

GAS CHROMATOGRAPH FOR ON-SITE ANALYSIS OF ORGANICS ON MARS

Ya. Guan, Zh. Shen, X. Geng, J. Zhang
Dept. of Instrumentation & Analytical Chemistry,Dalian Institute of Chemical Physics, CAS,457 Zhongshan Road, Dalian 116023, CHINA

The aim of the project is to develop a miniaturized analytical instrument that contains a sampling unit for gases in low pressure atmosphere, a thermo-desorption/cracking device for solid samples, a gas chromatograph that contains a capillary column with temperature programming function, and a solid-state thermo-conductivity detector for detection and quantitation. The instrument could separate and detect volatile compounds such as permanent gases and volatile organic vapors in samples. More than 40 organic compounds can be separated and determined quantitatively in one run.

The instrument should tolerate 3D vibration and shock during launching and landing on a planet, and could work at vacuum/low density gas atmospheric conditions.

Research Subject:

1) Gas sampling unit for low density gas atmosphere. A syringe type sampling device is to be developed to suck atmospheric gas molecular into the syringe and compress it to higher pressure, and then inject it onto chromatographic column for separation.
2) Thermo-desorption/cracking unit for solid samples. Temperature up to 750 °C can be reached to realize desorption or cracking, for organics if they exist, and transfer them to a Trap unit by carrier gas.
3) Trap unit. The unit contains a trap column and thermo desorption function. It enriches target compounds, compresses desorption bandwidth and reduce detection limit.
4) Two-channel gas chromatographic system. Chromatographic columns of different properties were employed to separate mixtures of permanent gases and volatile organic vapors up to boiling point of 270 °C.
5) Solid state thermo-conductivity detector that could response to all compounds but carrier gas.
6) Control unit that measures the pressure values of the sample in syringe and carrier gas, control the function of the instrument, collect and covert the chromatographic data into digit, and transmit them to central control unit.
7) Mechanical design and thermal management of the structure of the instrument.

The total power consumption should be no more than 40 W on average, and peak power of ≤ 70 W. The total weight should be ≤ 8 kg.

SCIENTIFIC GOALS AND INSTRUMENTS DESIGN OF THE SOLAR ORBITER PLASMA PACKAGE

A. Fedorov
IRAP, Toulouse, France.
Andrei.Fedorov@irap.omp.eu

Introduction:

Solar Orbiter is a European Space Agency mission dedicated, together with NASA's Solar Probe Plus, to perform short distance in-situ and distant observations of the Solar corona and the Solar wind. This mission will be the first spacecraft since Helios to sample the inner heliosphere inside the orbit of Mercury, at distances as close to the Sun as 60RS. The mission primarily provides an unprecedented opportunity to discover the fundamental connections between the rapidly varying solar atmosphere and the solar wind, revealing the physical links between the outward transport of solar energy, its manifestations in solar convection, the variations of coronal magnetic fields, and the sources and acceleration of solar wind.

The present presentation focus on the Solar Orbiter plasma package named Solar Wind Analyzer (SWA), especially on two ion instruments: Proton Alpha Sensor (PAS) and Heavy Ion Sensor (HIS). Both instruments are designed to provide full 3-D velocity space distribution function of solar wind ions without mass selection (PAS) and with high mass resolution.

The presentation describes in details the instruments design and performance.

Fig. 1. Proton Alpha Sensor onboard of the Solar Orbiter STM

EXOMARS 2018 SURFACE PLATFORM SCIENCE INVESTIGATIONS

D. Rodionov[1], J. Vago[2], H. Svedhem[2], O. Korablev[1]
[1]*Space Research Institute (IKI), Moscow*
[2]*ESA European Space Research and Technology Center (ESTEC), Noordwijk*
rodionov@iki.rssi.ru

ESA and Roscosmos have signed a cooperation agreement to work in partnership to develop and launch two ExoMars missions—in 2016 and 2018. The first mission will study Mars' atmospheric composition in unprecedented detail, and deliver a lander to the surface. The second mission will deliver the ExoMars rover and a Surface Platform to the surface of Mars.

The ExoMars rover will carry a comprehensive suite of instruments dedicated to exobiology and geology research named after Louis Pasteur. The rover will be able to travel several kilometers searching for traces of past and present signs of life. After the rover egress the Surface Platform will serve as long-lived stationary platform (expected lifetime is 1 Earth year) to study surface environment with suite of scientific instruments. The scientific objectives of the Surface Platform are the following:

- Context imaging;
- Long-term climate monitoring and atmospheric investigations.
- Studies of subsurface water distribution at the landing site;
- Atmosphere/surface volatile exchange;
- Monitoring of the radiation environment;
- Geophysical investigations of Mars' internal structure.

To address these objectives scientific payload with maximum mass of 45 kg is proposed.

MAG-TRACE INSTRUMENT FOR EXOMARS'18 FOR EXTENDED CAPABILITIES IN THE PLANETARY MAGNETIC EXPLORATION

M. D. Michelena
INTA, Ctra. Torrejon – Ajalvir, km 4, 28850 Torrejon de Ardoz, Spain.
diazma@inta.es

The understanding of the magnetic sources responsible for the magnetic anomalies is a difficult question, which requires deep study of the magnetic properties of the rocks, of the geologic processes and history and modelling.

This difficulty, which makes magnetic surveys a laborious and very multidisciplinary task, has a magnificent counterpart in the tracing of ancient geological events related to magnetism. This capability has been widely used on Earth and now it could be exploited in other planets and bodies of the Solar System.

To be able to perform magnetic surveys with this potential, it is necessary to count with advanced instrumentation for in situ exploration. Magnetometers are a good choice because they provide contrast between areas corresponding to different compositions and with different geological histories. But one cannot discern about the induced and remanent part of the measured magnetic anomalies, which is a fundamental information to derive properties on the magnetizing field and its history.

Generally complementary characterization to distinguish between induced and remanent contributions of magnetisation is performed in the laboratory with instrumentation that measures the magnetic susceptibility. Thus, for on ground planetary surveys it would be desirable to complement magnetometers with susceptibility-meters i.e. susceptometers.

MAG-TRACE instrument for Exomars'18 combines for the first time these two skills. Furthermore, it measures not only the real part of the susceptibility but also the imaginary part, which gives information on the losses of the matter in the presence of varying magnetic fields related either with the conductivity or with the spin relaxation processes.

In this work we overview the design of MAG-TRACE instrument, present its calibration and discuss on the scientific potential for the planetary exploration.

Acknowledgements:

This work has been done in the frame of TITANO project under the grant PRI-PIBUS-2011-1150 of the subprogram of international and bilateral projects of the Spanish Ministry of Science and Innovation (MICINN) and MEIGA-MET-NET project under the Grant AYA2011-29967-C05-01 of the Spanish National Space Program (DGI-MEC).

MICROMED: A COMPACT DUST DETECTOR FOR MARTIAN AIRBORNE DUST INVESTIGATION

F. Esposito[1], C. Molfese[1], F. Cozzolino[1], F. Cortecchia[2], B. Saggin[3], D. Scaccabarozzi[3], M. Tarabini[3], I. Arruego Rodriguez[4], A. Martin-Ortega[4], V. Apestigue[4]
[1]INAF – Osservatorio Astronomico di Capodimonte, Salita Moiariello 16, 80131 Napoli, Italy;
[2]INAF – Osservatorio Astronomico di Bologna, Via Ranzani 1, 40127 Bologna, Italy;
[3]Politecnico di Milano, 1/c via Previati, 23900, Lecco, Italy;
[4]INTA, Ctra. Ajalvir km 4, Torrejón de Ardoz, Madrid, Spain.
francesca.esposito@na.astro.it

Introduction

Monitoring of airborne dust is very important in planetary climatology. Indeed, dust absorbs and scatter solar and thermal radiation, severely affecting atmospheric thermal structure, balance and dynamics (in terms of circulations). Wind-driven blowing of sand and dust is also responsible for shaping planetary surfaces through the formation of sand dunes and ripples, the erosion of rocks, and the creation and transport of soil particles.

Dust is permanently present in the atmosphere of Mars and its amount varies with seasons. During regional or global dust storms, more than 80% of the incoming sunlight is absorbed by dust causing an intense atmospheric heating. Airborne dust is therefore a crucial climate component on Mars which impacts atmospheric circulations at all scales. Main dust parameters influencing the atmosphere heating are size distribution, abundance, albedo, single scattering phase function, imaginary part of the index of refraction. Moreover, major improvements of Mars climate models require, in addition to the standard meteorological parameters, quantitative information about dust lifting, transport and removal mechanisms. In this context, two major quantities need to be measured for the dust source to be understood: surface flux and granulometry. While many observations have constrained the size distribution of the dust haze seen from the orbit, it is still not known what the primary airborne dust (e.g. the recently lifted dust) is made of, size-wise.

MicroMED has been designed to fill this gap. It will measure the abundance and size distribution of dust, not in the atmospheric column, but close to the surface, where dust is lifted, so to be able to monitor dust injection into the atmosphere. This has never been performed in Mars and other planets exploration.

MicroMED experiment

MicroMED is a miniaturization of the instrument MEDUSA, developed for the Humboldt payload of the ExoMars mission.

It is able to measure the size of single dust grains entering into the instrument from 0.2 to 10 μm radius, giving as products the dust size distribution and abundance. It is an Optical Particle Counter, analyzing light scattered from single dust particles. A pump is used to sample the Martian atmosphere, generating a flux of gas and dust across the instrument trough the inlet. When the dust grains reach the Optical Sensor (OS), they cross a collimated IR laser beam emitted by a laser diode. The light scattered by the grains is detected by a photodiode, which is amplified by the Electronics.

Performances

MicroMED acquires the intensity of the light scattered by single dust grains entering into the instrument. This is related to grain size via scattering models. The run duration has been tuned in order to acquire about 400-2000 particles depending on dust concentration. This will allow to obtain enough statistics to sample the dust size distribution. The system has been designed in order to work up to particle concentrations of several hundreds cm^{-3} before coincidence effects become significant. The estimated fraction of coincidences goes from 0.01% (constant haze) to < 4% (dust devil).

The minimum detectable current from the photodiode is < 5 nA. Using Mie scattering theory evaluation, this implies an expected minimum detectable grain radius of < 0.2 μm (see theoretical curve in Figure 2). The maximum detectable size is related to fluid dynamics constraints inside the instrument and is around

20-30 μm, in the range of expected suspended grain size (radius ~10 μm). Dust abundance will be computed starting from size measurements and sampled volume (fixed by pump flux and run duration). The mentioned performances have been verified with the MicroMED breadboard.

Fig. 1. MicroMED Breadboard.

Monodisperse particles with calibrated size have been injected in the Martian simulation chamber where the MicroMED instrument was placed. Results are shown in Figure 2. MicroMED output current, generated by the photodiode as a response of the detection of light scattered by the grains, perfectly corresponds to the values predicted using Mie's theory.

Performed tests clearly show that the instrument satisfies technical and scientific requirements and perfectly reproduces the results obtained during the simulations that drove its design.

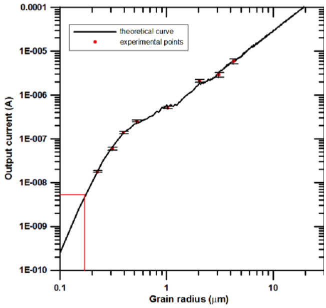

Fig. 2. MicroMED performances.

MicroMED has a mass ~ 500 g and a power consumption of ~2.8 W.

THE WIND SENSOR OF METEOSTATION FOR EXOMARS PROJECT

G.V. Koynash[1], E.N. Evlanov[1], D.S. Rodionov [1], S.N. Podkolzin[1], B.V. Zubkov[1], D.F. Nenarokov[1], A.N. Lipatov[1], K.V. Aleksandrov[1], S.D. Shuvalov[1], A.F. Schlik [1], A.F. Kruchkov [1], P.M. Tyrukanov[2], M.A. Zavyalov[2]
[1]Space Research Institute (IKI),117997, 84/32 Profsoyuznaya Str, Moscow, Russia;
[2]Federal State Unitary Enterprise "All-Russian Electrotechnical Institute Lenin",111250, Krasnokazarmennaya st.12, Moscow, Russia.
greg@iki.rssi.ru

Introduction:

The gas-discharge anemometer is designed to study the dynamics of the gas flow in the experimental and space meteorology and in particular for the measurement of pressure, the magnitude and direction of the velocity vector of gas flows in the boundary layer of the atmosphere of Mars.

The chemical composition of Martian Atmosphere the main component is dioxide of carbon (CO2)-95.3%; nitrogen (N_2) – 2.8 % and less than 1% of impurities; pressure 6-12 torr, range of temperature from - 120ºC to + 20ºC and speed of wind from 0.5 m/s up to 50 m/s. We should provide measurements local distribution of speed and directions of wind (Wind Rose) in landing place. Also we can measurement pressure. The Wind Sensor was included in MeteoStation on Lander platform ExoMars. It's new type of gas discharge anemometer provide better resolution and high speed responsible.

Principle of operation of gas-discharge anemometer based on the phenomenon of deviation low-current low energy ion beam under the influence of the gas flow. To create an ion beam is used glow discharge, which can significantly increase the sensitivity of the gas-discharge anemometer compared to other methods.

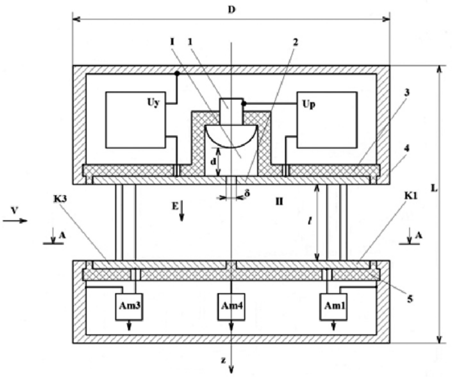

Fig. 1. The Wind Sensor (gas-discharge anemometer).

In addition, we will describe: methods and tools for the calibration of the Wind sensor and will present the results of tests.

ADAPTATION OF TUNABLE DIODE LASER ABSORPTION SPECTROSCOPY FOR *IN SITU* PLANETARY STUDIES. APPLICATION FOR PLANNED MISSIONS TO MOON, MARS AND VENUS

I.I. Vinogradov[1], V.V. Barke[1], V.A. Kazakov[1], Yu.V. Lebedev[1], A.V. Rodin[1,2], O.Z. Roste[1], O.V. Benderov[2], A.Yu. Klimchuk[2], A.A. Pereslavtseva[2], V.M. Semenov[2], A.V. Kalyuzhnyi[3], A.I. Nadezhdinskii[4], Ya.Ya. Ponurovskiy[4], M.V. Spiridonov[4], J. Cousin[5], G. Durry[5], L. Joly[5],
[1]Space Research Institute of the Russian Academy of Sciences (IKI RAS), 117997, 84/32 Profsoyuznaya Str., Moscow, Russia;
[2]Moscow Institute of Physics and Technology (MIPT), Institutsky Dr. 9, Dolgoprudny, Moscow Region, Russia;
[3]Special Design Bureau of Space Device Engineering of IKI RAS, 249100, Tarusa, Kaluga Region, Russia;
[4]Prokhorov General Physics Institute of the Russian Academy of Sciences (GPI RAS), 119991, Vavilov Str., 38, Moscow, Russia;
[5]GSMA, UMR CNRS 7331, Université de Reims, BP 1039, 51687 Reims, Cedex 2, France.
imant@iki.rssi.ru

Tunable Diode Laser Absorption Spectroscopy (TDLAS) is a well-known and powerful tool for studies of gaseous media content, tiny trace gases detection, isotopic ratio measurements, investigation of absorption line contour effects, etc. Miniature size, flexibility of controls, low resource requirements of a TDLAS instrument effectively respond to severe demands on board of an interplanetary orbiter, a balloon or a lander probe.

In a couple of years, researchers of IKI RAS, together with colleagues from MIPT, GPI RAS, and with colleagues of GSMA team (University of Reims, France) are developing TDLAS instruments for carrying out *in situ* measurements for several future space missions to our neighbor planets. Environmental parameters to be encountered with and available space probe resources will radically vary from mission to mission, each time providing another challenge for measurement strategy and instrument realization. In the report, we discuss TDLAS instrument adaptation to actual lander probes, scheduled for research missions to Moon, Mars and Venus.

For the “Luna-Resource”, or “Luna-27” polar lander mission to the Moon, a Diode Laser Spectrometer (DLS) will be used as a proprietary sensor channel, integrated deeply inside Gas Analytical Package (GAP) system, targeted for studies of gaseous components, evolved from Moon soil samples, which will be collected from a close vicinity of the landing point. A system of soil pyrolysis and evolved gas sophisticated controls will provide, by means of a hot background carrier gas He, for slow transport of tiny evolved gas sample through a miniature analytical capillary cell of the DLS sensor, with only one optical pass 20 cm long. During one planned year lifetime of the probe, DLS sensor will be applied for fine measurements of H_2O and CO_2 evolved content and pyrolysis dynamics, and ratio measurements for isotopologues HDO, $H_2{}^{17}O$, $H_2{}^{18}O$, and $^{13}CO_2$, ^{17}OCO, ^{18}OCO.

For the “ExoMars” stationery landing platform, or “ExoMars-2018” mission, a multichannel Martian Diode Laser Spectrometer (M-DLS) will occupy a highest available location on board, as a standing alone instrument of the landing platform scientific payload. During one Martian year lifetime of the landing platform, M-DLS instrument will carry out diurnal and seasonal measurements of atmospheric H_2O, CO_2, CO and CH_4 content near the Martian surface, as well as isotopic ratio measurements of D/H, $^{18}O/^{17}O/^{16}O$, $^{13}C/^{12}C$. To achieve adequate sensitivity for the condition of extremely low pressure of the ambient atmosphere, an unprecedented optical accumulation will be achieved by Integrated Cavity Output Spectroscopy (ICOS) principle realization in a compact multichannel multipass analytical optical cell of the M-DLS, providing for its equivalent optical path to be well above 1 km for measurements of the sampled atmosphere gas. Another effective use of the same set of M-DLS tunable diode lasers will appear in performing direct solar passive heterodyne observations via the full depth of open Martian atmosphere at various zenith angles.

For planned to the next decade “Venera-D” mission, an experiment ISKRA-V

(Investigation of Sulphurous Komponents of Rarefied Atmosphere of Venus) have been proposed for retrieving vertical profiles of sulphurous and minor gases and isotopic ratios at the dense Venusian atmosphere. Active work phase of the ISKRA-V instrument, safely placed inside the highly protected instrumental contour of the “Venera-D” lander, will be started yet in the descent trajectory, at the moment of a heat protection shield removal from the lander under the 65 km altitude and will be continued down to the surface level. Measurements will go on at the descent point up to the lifetime limit of the lander. A multichannel DLS is the core of the ISKRA-V instrument, involving both distributed feedback tunable diode lasers and quantum cascade lasers, operated sequentially. An analytical multichannel multipass optical cell of the instrument will be repeatedly filled in by a sampled portion of the ambient atmosphere, rarefied down to 50 mbar work pressure for achieving of the best DLS efficiency. Operations for safe transport and rapid change of a gas sample, taken from extremely hot and dense environment at low altitudes and on surface are challenging, and will directly affect resulting vertical resolution of atmosphere profiling and scientific value of the data. Preliminary target molecules are: SO_2, CO_2, CO, OCS, H_2O; and isotope ratios: $^{13}C/^{12}C$ for CO_2 and CO, $^{16}O/^{17}O/^{18}O$ for CO_2, D/H and $^{16}O/^{17}O/^{18}O$ for H_2O, $^{34}S/^{33}S/^{32}S$ for OCS.

DEVELOPMENT OF A MAST OR ROBOTIC ARM-MOUNTED INFRARED AOTF SPECTROMETER FOR SURFACE MOON AND MARS PROBES

A. Shapkin[1], O. Korablev[1], A. Ivanov[1], A. Fedorova[1], Y.K. Kalinnikov[2], S. Mantsevich[1,3], N. Viazovetsky[1], N. Evdokimova[1], A.V. Kiselev[1]
[1]Space Research Institute (IKI), 84/32 Profsoyuznaya, 117997 Moscow, Russia;
[2]National Research Institute for Physical-technical and Radiotechnical Measurements (VNIIFTRI), Mendeleevo, Moscow Region, Russia, 141570;
[3]Faculty of Physics, Moscow State University, GSP-2, Leninskiye Gory, 119991 Moscow, Russia

A pencil-beam infrared AOTF spectrometer for context assessment of the surface mineralogy in the vicinity of a planetary probe or a rover analyzing the reflected solar radiation in the near infrared range is discussed. ISEM (Infrared Spectrometer for ExoMars) instrument will be deployed on the mast of ExoMars Rover planned for launch in 2018. A very similar instrument LIS (Lunar Infrared Spectrometer) is going to be flown on Russian Luna-25 (Luna Globe Lander) and Luna-27 (Luna Resource Lander) missions in 2018 and 2021 respectively. On the lunar landers the instrument will be mounted at a robotic arm (Luna-25) or at a dedicated mast (Luna-27). The instrument covers the spectral range of 1.15–3.3 μm with the spectral resolution of ~25 cm^{-1} and is intended to study mineralogical and petrographic composition of the uppermost layer of the regolith. Both the Mars and the Moon instruments target water-bearing minerals, phyllosilicates, sulfates, carbonates in the vicinity of the Mars rover, and H_2O ice and hydroxyl in the vicinity of the lunar lander. The optical scheme includes entry optics, the TeO_2 AOTF, and a Peltier-cooled InAs detector. To cover the extended spectral range the AOTF is equipped with two piezotransducers. At present the qualification prototype of the instrument is being characterized. The requirements, instrument optics, and different aspects of its characterization, including low-temperature survival validation is described.

PLANETARY DATA ARCHIVE: NEW APPROACH TO DATA ACCESS, EXPLORATION AND COLLABORATIVE RESEARCH

A. Garov, E. Matveev, A. Zubarev, V. Patratiy, I. Karachevtseva
Moscow State University of Geodesy and Cartography (MIIGAiK), MIIGAiK Extraterrestrial Laboratory (MExLab), Gorokhovskiy per., 4, 105064, Moscow, Russia.
i_karachevtseva@miigaik.ru

Introduction:

New 3D-web GIS platform for access to planetary data will be presented. The platform is based on previous efforts (Fig. 1a) and is the result of evolution and continuous work (http://cartsrv.mexlab.ru/geoportal/). The current version of Planetary Data Geoportal will be demonstrated as a show case for the platform using lunar data, such as LRO processed images for landing sites [1,2] and archive panoramas [3] (Fig. 1ab).

Development technologies and software:

New Planetary Data Geoportal based on developing 3D-web GIS is a cross-platform application, sharing a single codebase and available for desktop and mobile OS'es and web browser. It was developed entirely in C++, using cross-compilation for web. OpenGL (WebGL in case of a browser application) library is used for graphics. Shaders are actively utilized. Main user UI is modeled i n HTML, based on the various possibilities:

- Solid core web-GIS functionality, such as access to base-maps, vector and raster data, spatial querying and measurements, including various cartographic projections support.
- 3D-mode for visualization of different types of data at various levels, including surface planetary objects, atmospheric data measurements, subsurface radar data, etc. We will use SPICE kernels to present temporal and spatial reconstruction of 3D environment of planetary bodies such as nature satellites or spacecraft on the orbit.
- While basic OGC compatibility module can act as data feed, the new extension will be developed for global data search. The new web-service uses shared spatial and semantic context related to planetary data to search in Internet the new images and data products, modern publications, news, etc.
- Distributed processing mode currently is being developed which will allow utilizing joint processing power without application of complex IaaS stacks.
- Online image data processing is implemented which put the platform closer to professional desktop GIS. It helps to avoid typical usage scenario (when user searches for data, then downloads and process it using locally installed software). The easy online access to planetary data using 3D-web-GIS will facilitate the scientists with visual and interactive spatial instruments, for example, for geology and morphometry analysis (crater counting, profile measurements, etc.)
- A telecom module with ability to broadcast interactive spatial context together with video/audio makes platform for online discussion and presentations of thematic spatial results as a geo-collaboration tool for a distributed scientific community, for example, in peer-reviewing process.

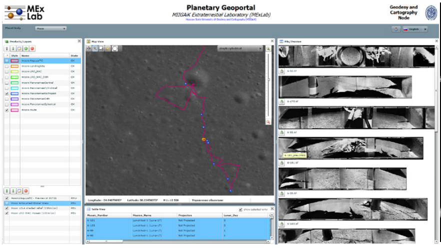

Fig. 1a. Interface of previous version of Planetary data Geoportal

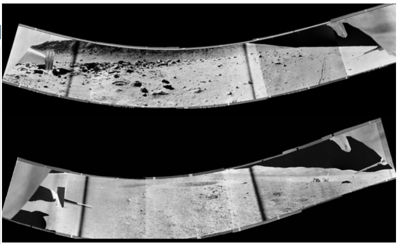

Fig. 1b. Result of modern processing of archive Lunokhod's panoramas

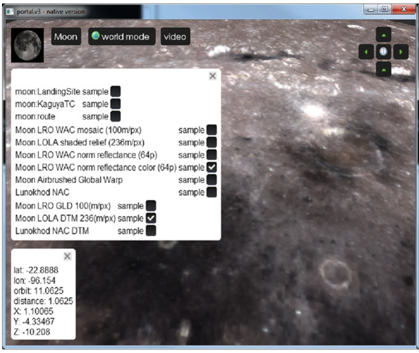

Fig. 2a. Native-version of 3D-web GIS

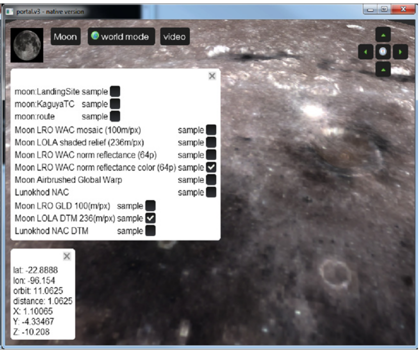

Fig. 2b. HTML-version of 3D-web GIS

Conclusion:

We present the new 3D-web GIS platform which can be used as online map-based interface for access to planetary data archive. It will allow scientists visually and interactively specify objects for measurements and to select new targets on planetary surface for observation and mission planning.

Acknowledgements:

This work was carried out at MIIGAiK and supported by Russian Science Foundation, project 14-22-00197. The image processing of lunar data for landing sites including archive panoramas was supported by the European Community’s Seventh Framework Programme (FP7/2007-2013) under grant agreement n° 312377 PRoViDE.

References:

[1] Zubarev A. E. et al. (2012), [EPSC2012-477]. [2] Karachevtseva et al., (2013), PSS, Vol.85, p. 175-187. http://dx.doi.org/10.1016/j.pss.2013.06.002 [3] Kozlova et al., (2014) ISPRS Archives MTSTC4-2014-103, Volume XL-4, 2014, pp. 121-126

SHORT LIST OF LANDING SITES AT LUNAR POLES

A.B. Sanin, M. Dyachkova, I.G. Mitrofanov

Short list of landing sites at lunar poles is presented, which is based on scientific and engineering criteria for selection.

TESTING FACILITY FOR NUCLEAR PLANETOLOGY IN DUBNA

D.V. Golovin, M.L. Litvak, A.S. Kozyrev, I.G. Mitrofanov

Special testing facility was built in Joint Institute for Nuclear Research for testing and validation of active neutron measurements of celestial bodies, like Mars, Moon and Venus. The first results are presented produced by ADRON lunar neutron and gamma-ray instrument with pulsing neutron generator.

EXAMINING SPECTRAL VARIATIONS IN LOCALIZED LUNAR DARK MANTLE DEPOSITS

E. R. Jawin[1,2], S. Besse[2], L. R. Gaddis[3], J. M. Sunshine[4], J. W. Head[1], S. Mazrouei[5],
[1]Dept. Earth, Environ., Planetary Sci., Brown Univ., Providence, RI 02912 USA;
[2]European Space Res. & Tech. Ctr, Noordwijk, Netherlands;
[3]USGS Astrogeo. Sci. Ctr, Flagstaff, AZ, USA;
[4]Dept. Astronomy, Univ. of Maryland, College Park, MD, USA;
[5]Dept. Earth Sci., Univ. of Toronto, ON, Canada.
Erica_Jawin@brown.edu

Introduction:

Lunar pyroclastic deposits, referred to as dark halo craters or dark mantle deposits (DMDs), are composed of fine-grained, low-albedo volcanic materials [*1*]. Previous studies identified over 100 DMDs on the Moon, ranging from ~10-50,000 km^2 [*2*,*3*]. The largest of these are known as "regional" DMDs, while the smaller are "localized" DMDs [*4*]. DMDs are believed to represent the eruption of gas-rich magmas which originated from mafic parent melts sourced from the deep lunar interior [*5*]. Regional DMDs were found to contain iron- and titanium-rich glass and devitrified beads [*4*,*6*,*7*]. Iron-rich volcanic glass has also been identified in localized DMDs [*8*,*9*]. Volcanic glasses are important in characterizing the lunar interior and understanding the origin and evolution of basaltic magmatism on the Moon. Understanding the mineralogical diversity and variations in crystallinity in localized DMDs can aid in identifying the sources and eruption mechanics of these deposits.

Three localized DMDs in Alphonsus, J. Herschel, and Oppenheimer crater, were analyzed using data from the Moon Mineralogy Mapper (M^3) [*10*] to (a) document DMD mineralogy, (b) characterize the mineralogical variation within and between deposits, and (c) compare the mineralogy of DMDs to nearby mare basalts, in an attempt to constrain mineralogical diversity in localized DMDs.

Data and Targets:

Spectral analyses of the localized DMDs are based on observations from M^3, a visible and near-infrared spectrometer covering the spectral range 0.4-3 µm at a spatial resolution of ~140-280 m/pixel [*10*–*12*]. A continuum-removal was applied to the spectra, approximated by a straight line fit between 0.73-1.62 µm and 1.62-2.58 µm for the 1 and 2 µm bands, respectively [*8*]. Mosaics of context images from the Kaguya (SELENE) Terrain Camera (TC) support the spectroscopic products analyzed here [*13*].

The localized DMDs occur in floor-fractured craters located near a mare unit. Spectral analyses from the DMDs in Alphonsus, J. Herschel, and Oppenheimer craters are compared to spectra of the DMDs in Lavoisier and Walther A craters [*8*,*14*].

Results:

Alphonsus DMD. Spectra were extracted from the three largest sub-deposits in the Alphonsus DMD (Fig. 1). There are variations in albedo within each sub-deposit (inset, Fig. 1A). Spectra of the sub-deposits were taken at various distances from the vent to examine this variation. Unit names (Light, Intermediate, etc.) indicate changes in albedo across the DMD.

Spectra taken close to the vent show 1 µm bands shifted to longer wavelengths and deeper absorption depths (Fig. 1). This suggests that inside the vent and in proximity (Dark unit), spectra are dominated by mafic pyroclastic materials. As distance from the vent increases, spectra become contaminated by noritic crater floor material. This variation is interpreted to represent variable thickness of the deposit. DMD thinning also agrees with the albedo variation.

Spectra were also taken in Mare Nubium (Fig. 1D). The maria show a slightly shorter 1 µm band position, a slightly longer 2 µm band position, and a narrower, symmetric band shape relative to the DMDs. This distinction in spectra signifies a variation in mineralogy or internal structure (crystallinity) between the two units. Previous analyses [*15*] interpreted the wide, asymmetric 1 µm absorption in DMDs such as Alphonsus to indicate olivine. However, olivine does not have a 2 µm absorption feature, and the inclusion of olivine or other mafic minerals would not explain the band center shift to shorter wavelengths at 2 µm. We conclude this spectral signature is indicative of amorphous materials in the form of iron-enriched volcanic glass (e.g., [*8*]).

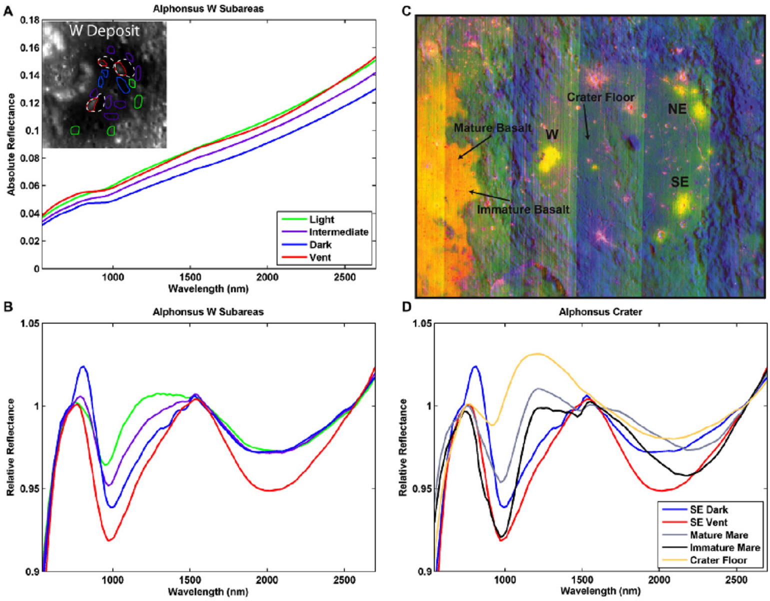

Fig. 1. Alphonsus DMD. (A) Absolute reflectance of DMDs; inset: outlines of each spectral unit in the W sub-deposit. White dashed lines outline the volcanic vents, while areas outlined in red are inso-lated portions used in the analysis. (B) Continuum-removed spectra from A. (C) RGB color composite map of the crater: IBD1000 nm; G: BD1900 nm; B: R1580 nm. (D) Continuum-removed spectra of the DMD, crater floor, and Mare Nubium basalt.

J. Herschel and Oppenheimer DMD. The J. Herschel DMD spectra show similar features to Alphonsus: the shape and location of the 1 and 2 µm bands are distinct from the crater floor and nearby maria, and are consistent with mafic materials containing glass (Fig. 2).

Two of the smallest DMD sub-deposits in Oppenheimer crater (N, SSE) show a similar variation in albedo with distance as in the Alphonsus DMD, which indicates spectral variation and thinning of the deposit. The DMD spectra appear distinct from the surrounding mare deposit, with a similar shift in the 1 and 2 µm bands to longer and shorter wavelengths, respectively, as in Alphonsus and J. Herschel DMDs. This indicates volcanic glass in the Oppenheimer DMDs, although the relative strength of the 1 and 2 µm bands is different than that in the Alphonsus and J. Herschel glassy spectra. In addition, two new DMDs were identified to the northeast of Oppenheimer, in Dryden S and T craters. These DMDs are spectrally similar to the Oppenheimer DMDs.

Discussion:

Assuming the spectral signatures in the DMDs represent the presence of volcanic glass, it is possible to distinguish between glass compositions using a combination of the 1 and 2 µm band positions and 2 µm to 1 µm band depth ratios (not shown here). Based on these two metrics, the spectral signatures of the Alphonsus and J. Herschel DMDs are similar to the green glass returned from the Apollo 15 landing site [*16*], while the Oppenheimer spectra

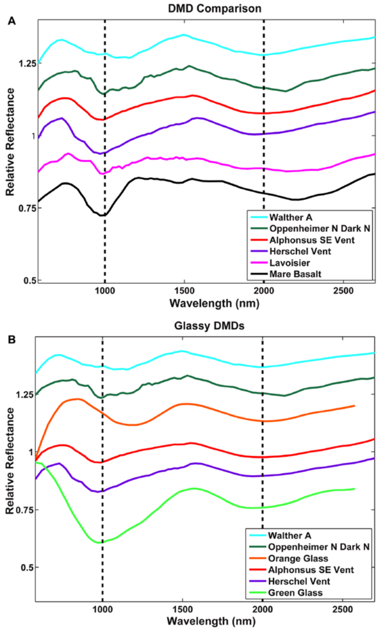

Fig. 2. (A) Continuum-removed spectra of the DMDs, including Wal-ther A and Lavoisier DMDs [11,16], and Mare Frigoris (near J. Herschel). (B) Continuum-removed spectra of the glassy DMDs, relative to lunar pyroclastic orange glass and green glass. Spectra are offset for clarity.

resemble orange glass returned from the Apollo 17 landing site [*7*]. These variations may indicate the presence of olivine (in the case of Alphonsus and J. Herschel DMDs) and/or ilmenite (Oppenheimer DMD).

In addition to a thinning of the DMD, the variation in spectral signatures across the isolated sub-deposits may indicate a variable amount of volcanic glass in the DMDs, with a higher concentration of glass closer to the central vent. This may be evidence of a sporadic, potentially repetitive explosive emplacement style typical of vulcanian eruptions on Earth. In larger, more continuous Hawaiian eruptions, temperatures and optical densities increase towards the center of the eruptive plume, leading to more crystalline material closer to the eruptive vent [*16*]. However, vulcanian eruptions are smaller and sporadic, with eruptive optical densities and temperatures low enough to rapidly quench erupting magma, creating glass [*17*]. Assuming this formation mechanism is representative of most localized DMDs, volcanic glass may be detectable in other similar deposits on the Moon.

References:

1. Wilson and Head, *JGR* **86**, 2971–3001 (1981). **2.** Gaddis *et al.*, *Icarus*. **161**, 262–80 (2003). **3.** Gustafson *et al.*, *JGR* **117** (2012). **4.** Gaddis *et al.*, *Icarus*. **61**, 461–89 (1985). **5.** Delano and Livi, *LPSXII* (1981), 226–8. **6.** Pieters *et al.*, *JGR* **78**, 5867–75 (1973). **7.** Adams *et al.*, *Proc. Lun. Conf. 5th* (1974), 171–86. **8.** Besse *et al.*, *JGR* **119**, (2014).
9. Horgan *et al.*, *Icarus*. **234**, 132–54 (2014). **10.** Pieters *et al.*, *Curr. Sci.* **96**, 500–5 (2009). **11.** Boardman *et al.*, *JGR.* **116** (2011). **12.** Besse *et al.*, *Icarus*. **222**, 229–242 (2013). **13.** Haruyama *et al.*, *EPSL*. **60**, 243 (2008). **14.** Souchon *et al.*, *Icarus*. **225**, 1–14 (2013). **15.** Hawke *et al.*, *LPSC, 19th*, 255–68 (1989). **16**. Delano, *LPSC, 10th*, 275–300 (1979). **17.** Weitz *et al.*, *Meteorit. Planet. Sci.* **34**, 527–40 (1999). **18.** Head and Wilson, *LPSC 10th*, 2861–97 (1979).

YOUNG LUNAR MARE BASALTS: DEFINITION AND ANALYSIS OF THEIR CHARACTERISTICS, DISTRIBUTION, MODE OF EMPLACEMENT AND ORIGIN

L. Qiao[1, 2], J.W. Head[2], L. Wilson[3], L. Xiao[1], J. Dufek[4], C. Pieters[2]
[1]Planet. Sci. Inst., China Univ.Geosci, Wuhan 430074, China;
[2]Dep. Earth, Env. & Planet. Sci., Brown Univ., Providence, RI, 02906, USA;
[3]Lancaster Env. Centre, Lancaster Univ., Lancaster LA1 4YQ, UK;
[4]Sch. Earth & Atmos. Sci., GA Tech, Atlanta, GA,30332,USA.
le.qiao@cug.edu.cn

Introduction: Young lunar basalts are direct products of lunar late-stage volcanism, and provide a window to explore the recent thermal stateof the lunar interior and the processes responsible for mantle melting late in lunar history. These young basalts are also important candidate targets for future *in-situ* robotic missions (e.g., China's Chang'E-4, United States candidate Discovery missions,Russia's Luna missions) and sample-return missions (e.g., China's Chang'E-5). On the basis ofdecades of extensive human and robotic exploration of the Moon, great improvements have been made in our understanding of lunar young basalts in various aspects, e.g., chronology[1-4] and mineralogy [2, 5]. Nonetheless, there are many issues yet to be explored in relation to young lunar basalts. Among these are: (1) What is the definition of "young" lunar basalts in terms of age? (2) What is the distribution of these young mare basalts? (3) What are the mineralogical and physical properties of these young mare basalts? How similar and different are they from each other, and from earlier mare basalts? How many different units can be identified and mapped? (4) What are the associated featurese.g., sinuous rilles, flow fronts, lava tubes, wrinkle ridges, pyroclastics, thickness, etc.? (5) What are the volumes of individual flows and flow units? What are the total volumes? Do they show trends with time? (6) Where are the source vents for the units, and what is their morphology? (7) How do the youngest mare basalts relate to lunar activity thought to be associated with recent gas release or other unusual activity? (8) What do the exploration of the youngest mare basalts in Mare Imbrium by Lunokhod and Chang'E-3 tell us about their nature? (9) What are the modes of emplacement of these youngest lunar mare basalts and what does this imply about their petrogenesis?

Definition of young lunar basalts: Basalt samples collected by Apollo and Luna missions indicate that mare volcanism was active at least between ~4.3 and ~3.1 Ga [6, 7]. Radiometric dating results from a few lunar meteorites further extend the lifetime of lunar mare volcanism, e.g., meteorite NWA 032/479 with acrystallizationage of 2.69–2.85 Ga [8, 9] and NWA 773 with an age of 2.86–2.91 Ga [10, 11]. But the source of lunar meteorites, and their associated geological context, are difficult to track, which limits our interpretation of these samples and theirconstraints and implications on lunar volcanism.

Remote sensing observations, including through both Earth-based telescopes and spacecraft,suggested that returned lunar basalt samples are collected from very limit areas of the Moon, and cannot represent all basalt types of the entire Moon[12, 13]. Fortunately, globalcoverage with imaging, altimetryand spectroscopy data of thelunar surface and associated stratigraphic techniques provide powerful tools to date unsampled basalt deposits. Of these techniques, impact crater size-frequency distribution (CSFD) measurements are the most robust and accepted method [e.g., 14]. Employing this method, extensive mare basalt units on the lunar surface, both on the nearside and farside, have been dated [2-4, 15-18]. The global spatial and age distribution of basalts from previous CSFD measurements [2, 3, 15-17, 19, 20] are cataloged in Fig. 1 and 2, respectively. CSFD investigations indicated thatthe majority of mare basalts erupted in the ImbrianPeriod at ca. 3.3–3.8 Ga, which coincides well with radiometric dating results from returned basalt samples. Mare volcanism since 3.3 Ga shows a sharp decline in mare basalt volume and integrated flux (Fig. 2)[15]. Thus, we can regard these units as products of lunar late-stage volcanism. Despite reduced integrated lava flux, these young lunar basalts displayuniquesignatures in composition and volcanic style. For example, young mare volcanism is characterized by spectrally unique,high-titanium and olivine-rich basalts in the western nearside[5, 21]. These basalts are also characterized by episodic activity and possible association with the PKT. Our suggestionfor the definition of young lunar basalts is also consistent with recent work on various aspects of young lunar mare basalts (e.g., <3.1 Ga[21], <3.0 Ga[4, 5], <2.8 Ga[22]).

Young basalts in Mare Imbrium: Oneof the major occurrences of these "young basalts" isin Mare Imbrium, the basalts filling the interior of the Imbrium impact-basin [23, 24]. Due to its prominence on the nearside, this large basin has attracted extensive research. Previous work generally suggested that the Imbrium basin has experienced three main phases of lava emplacement events [24 and therein]. The basalts in Mare Imbrium show dichotomies in both composition and chronology: younger and higher-Ti basalts are preferentially developed in the western part of the basin. The Imbriumbasin also hosts some of the best-preserved lava flow fronts on the Moon [25], thus providing an opportunity to constrain the rheological properties of the lavas. Through improvements in our understanding of the regional volcanic history of the Imbriumbasin and its volcanism over these years, some newquestions have been raised: (1) What is the detailed nature of the general temporal trend of increasing iron and titanium enrichment of the basalts in time and can this trend be extrapolated to other volcanic provinces on the Moon? What are the implications of the composition-chronologytrends for lunar thermal models? (2) What is the ratio ofFeO and TiO_2 content? (3) Can the composition-chronology trend and FeO-TiO_2 correlation of lunar mare basalts be verified by results from lunar samples?

Analysis Strategy: Work in progress includes an initial focus on young volcanic flows in Mare Imbriumas a target regionin order to explore some basic issues concerningthe young basalts exposed there: (1) Further characterizing and distinguishing the mineralogical and physical properties of these young mare basalts using Moon Mineralogy Mapper (M^3) data. (2) Comprehensive high-resolution mapping and characterizing the associated volcanic feature (e.g., sinuous rilles, flow fronts, lava tubes, wrinkle ridges, pyroclastics, etc.), and seeking possible vent/sources and associated pyroclastic activity. (3) Estimating the volume of flow phases, individual flow sequences, and distinctive flow units, and theirindividual and total volumes, and identifying potential trends with time. (4) Mapping and characterizing the geomorphology of the source vents for these young basalt units and comparing these with other known vents formed previously.(5) Exploring the potential relationship between the youngest mare basalts with recent gas release activity or other unusual recent features such aslunar hollows. (6) Characterizing the nature of the youngest mare basalts investigated by Lunokhod and Chang'e-3 in-site experiments. (7) Constraining the mode of emplacement and petrogenesisof these young lunar basalts.

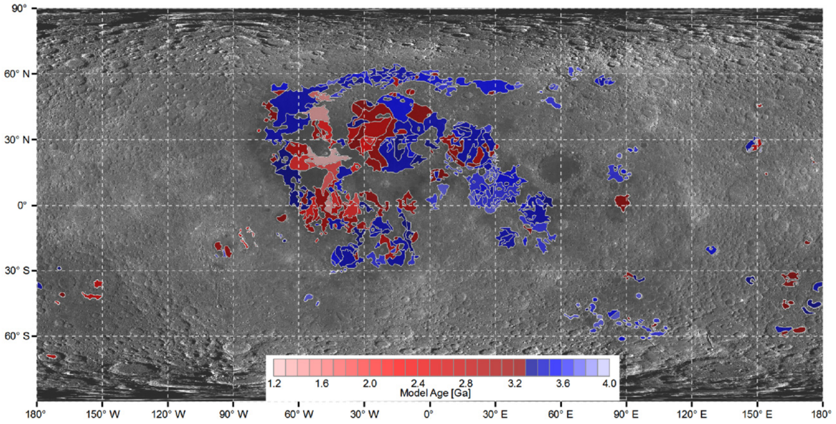

Fig. 1. Globaldistribution of model ages of lunar mare basalts. Red color units are young lunar basalts with absolute model age < 3.3 Ga, and bule color units are older basalts. See text for references of dating results.

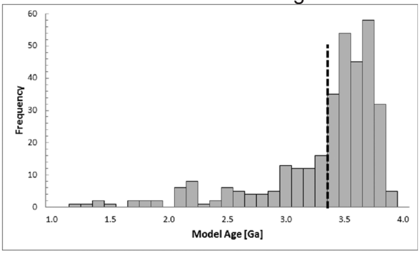

Fig. 2. Histogram of model ages of global mare basalts.

References:

[1] Braden S. E. et al. (2014) NGEO, 7(11), 787-791. [2] Whitten J. et al. (2011) JGR, 116, E6. [3] Haruyama J. et al. (2009) Science, 323(5916), 905-908. [4] Morota T. et al. (2011) EPSL, 302(3–4), 255-266. [5] Staid M. I. et al. (2011) JGR, 116, E6. [6] Head J. W. (1976) Rev Geophys, 14(2), 265-300. [7] Nyquist L. E. and Shih C. Y. (1992) GCA, 56(6), 2213-2234. [8] Borg L. E. et al. (2007) 70th AMSM, abs #5232. [9] Fagan T. J. et al., (2002) MPS, 37, 371-394. [10] Borg L. E. et al. (2004) Nature, 432(7014), 209-211. [11] Fernandes V. A. et al. (2003) MPS, 38(4), 555-564. [12] Pieters C. M. (1978) LPSC IX, 2825-2849. [13] Giguere T. A. et al. (2000) MPS, 35(1), 193-200. [14] Neukum G. et al. (2001) SSR, 96(1-4), 55-86. [15] Hiesinger H. et al. (2011) GSA-SP, 477, 1-51. [16] Morota T. et al. (2009) GRL, 36, 21. [17] Cho Y. et al. (2012) GRL, 39, 11. [18] Pasckert J. H. et al. (2015), Icarus, 257, 336-354. [19] Hiesinger H. et al. (2006) 37th LPSC, abstract #1151. [20] Tyrie A. (1988), EMP, 42(3), 245-264. [22] Varatharajan I. et al. (2014) Icarus, 236, 56-71. [23] Hiesinger et al. (2000) JGR, 105(E12), 29239-29275. [24] Bugiolacchi and Guest (2008) Icarus, 197(1), 1-18. [25] Schaber (1973) LPS IV, 653.

THE EFFECT OF EVOLVING GAS DISTRIBUTION ON SHALLOW LUNAR MAGMATIC INTRUSION DENSITY: IMPLICATIONS FOR GRAVITY ANOMALIES

L.M. Jozwiak[1], J.W. Head[1], G.A. Neumann[2], L. Wilson[3],
[1]Dept. Earth, Environmental and Planetary Sciences, Brown University, Providence, RI 02906;
[2]Solar System Exploration Div., NASA Goddard Space Flight Center, Greenbelt, MD 20768;
[3]Lancaster Environment Centre, Lancaster University, Lancaster LA1 4YQ, UK.
lauren_jozwiak@brown.edu

Introduction:

The GRAIL (Gravity Recovery and Interior Laboratory [1]) mission has enabled unprecedented views of the lunar crust and interior structure. Indeed, the data solutions now resolve gravity anomalies arising from lateral heterogeneities within the crust globally at scales < 10 km [2,3]. Intrusive magmatic features such as dikes and sills are predicted to be prevalent within the lunar crust [4] and gravity data present a unique way of investigating their presence. Recently, GRAIL data were used to interpret the presence of large, ancient dikes within the lunar crust [5]; however, as yet, the detection of smaller scale dikes and sills has proven difficult due to their moderate spatial dimensions and uncertain density contrast.

Recent morphologic studies [6, 7] have supported the hypothesis that members of the class of lunar craters known as floor-fractured craters (FFCs) were formed by the intrusion and evolution of a shallow magmatic body beneath the crater. The presence of a large magmatic intrusion beneath these craters should be easily visible in the observed crater Bouguer gravity anomaly.

Using the FFC Alphonsus as an example, we examine the observed Bouguer anomaly and compare this to idealized predictions of the Bouguer anomaly, which are based on predicted intrusion thickness from crater morphology [6, 7]. We also examine processes within the magmatic intrusion which could alter the intrusion density, and hence affect the Bouguer anomaly. Specifically, we examine how volatiles within the intrusion and intrusion degassing affect the overall intrusion density.

Comparison of Predicted and Observed Gravity Signature:

The crater Alphonsus, D = 119 km, (13.4°S, 2.8°W) is a class 5 FFC [6], possessing a flat floor profile and numerous dark-halo craters [8] identified as pyroclastic deposits [9] located along the crater floor fractures (Fig. 1a).

Using LOLA (Lunar Orbiter Laser Altimeter) data, we measure the crater depth as ~2.7 km, compared with 4.4 km depth suggested by the empirically derived crater depth v. diameter relationships developed by Pike (1980) [10]. We thus infer a maximum intrusion thickness of 1.69 km, ~1.7 km, beneath the crater [6]. We assume a lunar magma density of 3000 kg/m^3 [11] and a lunar crustal density of 2550 kg/m^3 [12]. Assuming the sill morphology can be modeled approximately as a Bouguer plate, an intrusion of constant thickness and large extent will generate a positive Bouguer anomaly of ~30 mGal.

Figure 1b shows the band-filtered Bouguer anomaly for the crater Alphonsus, filtered between orders 100-600, and contoured at 10 mGal intervals. The data were generated using the GRGM900c spherical harmonic solution [2], and band-filtered to strongly attenuate anomaly contributions from regions deeper than ~34 km. The most prominent feature is the broad positive anomaly region in the northeastern quadrant of the crater floor, which has a magnitude of ~10-15 mGal, peaking in places at ~20 mGal. The remaining crater floor area has a positive anomaly of magnitude ~5 mGal. We note the spatial correlation between the large, broad positive anomaly in the NE quadrant and the location of a large number of dark-halo craters and fractures (compare Figure 1a and Figure 1b). Overall, the observed anomaly magnitude within the crater floor region is difficult to distinguish from that in the surrounding region, and is smaller than the magnitude of anomaly predicted from the intrusion morphology.

Given the numerous surficial volcanic features and morphologic evidence supporting the existence of a large magmatic body beneath Alphonsus, we now examine processes inherent to the evolution of magmatic intrusions, which could potentially alter the intrusion density.

Volatile Fraction and Degassing of Magmatic Intrusions: During the formation and evolution of the magmatic intrusion, there are numerous processes which occur, summarized schematically in Figure 2. One of the most important processes is the formation of a magmatic foam at the tip of the dike [13] and corresponding top of the intrusion. The existence of numerous pyroclastic deposits on the floor of Alphonsus [9] provides evidence for volatile build up and explosive venting of the magma. Using the method outlined by Head et al. (2002) [13] and Wilson et al. (2014) [14], and the process described in Wilson and Head (2003) [15] we can infer the volatile mass fraction released during the formation of the pyroclastic deposit. The average velocity of the pyroclasts can be calculated using the radius of the dark halo deposit, *R* [13, 14]:

$$R = v^2/g \qquad (1)$$

Given the average dark halo radius of 3-4 km [8], the inferred eruption velocity is 70-80 m/s. This can be used to calculate the magmatic volatile gas fraction, *n*, from

$$n = [(v^2\, m\, (\gamma - 1)/(2\, Q\, T \gamma)]^{1/2} \qquad (2)$$

which is a compromise between adiabatic gas expansion and gas expansion in the Knudsen regime [14]. Here *m* is the gas molecular weight, 28 kg $kmol^{-1}$, *Q* is the universal gas constant, 8314 J $K^{-1}kmol^{-1}$, *T* is the magmatic temperature, 1500 K, γ is the ratio of gas specific heats, 1.28 (a weighted average of CO and H_2O, the two most common volatile species). We note that CO is the most common volatile species and is produced by oxidation-reduction reactions between graphite and metal oxides at pressures less than ~40 MPa [16], and H_2O is commonly released during exsolution of lunar magmas [17]. For the observed pyroclast ranges, this suggests a gas fraction of 0.0345, i.e. 3.45 mass %. Inverting the method of [14], and using the calculated pyroclast gas fraction, we determine a gas volume fraction of 72.8% within the foam, and a corresponding magma volume fraction of 27.2%. This gas volume fraction is near the theoretical limit of 80% [18] suggesting efficient volatile degassing, consistent with rapid foam formation during the initial formation of the sill. The density of CO gas at intrusion temperatures and pressures is 40 kg/m^3 and magma density is 3000 kg/m^3 [14]. Combined with the gas volume fractions, this equates to a foam layer density of 845 kg/m^3 ((40*0.728)+(3000*0.272)).

It is currently unknown how much of the intrusion volume will be occupied by this magmatic foam, although we are currently working on methods for calculating it. Thus, we present two possible scenarios: 1) foam layer equivalent to 25% of the intrusion volume, and 2) foam layer equivalent to 5% of the intrusion volume. For the conditions of scenario 1, the total intrusion density would be 2461 kg/m^3, which is slightly lower than the average lunar crustal density of 2550 kg/m^3. For the conditions of scenario 2, the total intrusion density would be 2892 kg/m^3, which is closer to, but still below, the commonly assumed fully degassed intrusion density.

Implications for Gravity Anomalies: We have shown that the inclusion of a volatile rich magmatic foam at the top of shallow magmatic intrusions on the Moon has a significant effect on the overall intrusion density. This change in density will significantly alter the observed

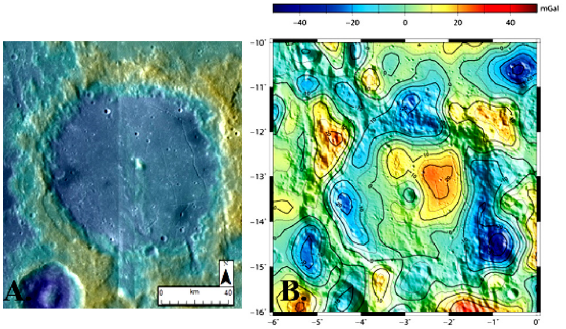

Fig. 1. Floor-fractured crater Alphonsus, D = 119 km, (13.4°S, 2.8°W). **A)** The most prominent features of Alphonsus are the dark-halo craters which lie along the numerous floor fractures. **B)** Contoured band-filtered Bouguer gravity anomaly for the crater Alphonsus, with emphasis drawn to the large positive anomaly region in the NE crater floor quadrant. LOLA topography data (color-coded blue-low, red-high) overlain by LROC-WAC image data (**A**). GRGM 900c Bouguer gravity solution band-filtered between orders 100-600 with 10 mGal contour intervals (**B**).

Bouguer anomaly. For the crater Alphonsus, this process can help explain the difference in predicted Bouguer anomaly (based on a completely degassed intrusion) and the observed Bouguer anomaly (Figure 1b). We also suggest that during intrusion evolution, both passive degassing (such as along fractures) and active degassing (such as pyroclastic deposit formation) can alter the local foam thickness beneath the crater floor, leading to the heterogeneous Bouguer anomalies and the apparent correlation of more positive Bouguer anomalies with surficial volcanic deposits.

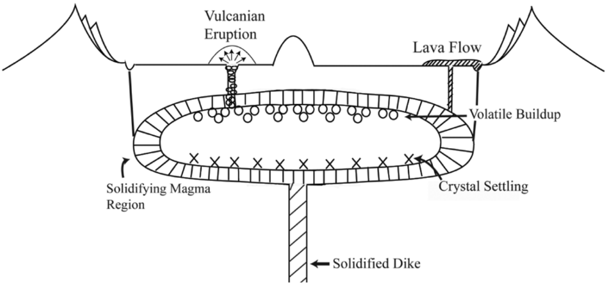

Fig. 2. Schematic diagram illustrating important processes in the physical, thermal and temporal evolution of the floor-fractured crater magmatic intrusions. We specifically focus on the volatile build-up at the top of the intrusion and the relationship of this process to vulcanian eruptions which lead to the production of the dark halo craters.

References:

[1] Zuber, M. T., et al. (2013) *Science, 339,* 668-671. [2] Lemoine, F.G., et al. (2013) *JGR 118*, 1676-1698. [3] Konopliv, A.S., et al. (2013) *JGR 118*, 1415-1434. [4] Head, J. W. and Wilson, L. (1992) *Geochim. et. Cosmochim. Acta, 56,* 2155-2175. [5] Andrews-Hanna, J. C., et al. (2013) *Science, 339,* 675-678. [6] Jozwiak, L. M., et al. (2012) *JGR, 117*, E11. [7] Jozwiak, L. M., et al. (2015) *Icarus, 248,* 424-447. [8] Head, J. W. and Wilson, L. (1979) *Proc. Lunar Planet. Sci. Conf. 10th*, 2861-2897. [9] Gaddis, L. R., et al. (2003) *Icarus, 161*, 262-280. [10] Pike, R. J. (1980) *USGS Prof. Paper 1046-C*. C1-C77. [11] Kiefer, W. S., et al. (2012) *GRL, 39*, L07201. [12] Wieczorek, M. A., et al. (2013) *Science, 339*, 671-675. [13] Head, J. W., et al. (2002) *JGR, 107*, E1, 5001. [14] Wilson, L., et al. (2014) *LPSC XLV*, Abstract #1223. [15] Wilson, L. and Head, J.W. (2003) *GRL 30*, 1605. [16] Rutherford, M. and Papale, P. (2009) *Geology, 37*, 219-222. [17] Saal, A. E., et al. (2008) *Nature, 454*, 192-196. [18] Jaupart, C. and Vergniolle, S. (1989) *J. Fluid Mech., 203*, 347-380.

CONTRIBUTION OF LUNAR BASINS TO MATERIALS IN THE LUNA-GLOB PERSPECTIVE LANDING SITES

M.A. Ivanov[1,2], J.W. Head[2],
[1]Vernadsky Institute, Moscow, Russia;
[2] Brown Univ., Providence RI, USA.
mikhail_ivanov@brown.edu

Introduction:

The region selected for the lander-oriented Luna-Glob mission (0-60E, 70-85S) and crater Boguslawsky, which currently is a primary goal of the mission, are within the ancient cratered terrain near the southern portion of the SPA basin. The large, basin-forming impacts were able to place crustal materials ejected from large depth (tens of kilometers) over a significant portion of the Moon [1-7]. Thus, regolith in both the South Pole Region southward of 60S (SPR) and the Luna-Glob region likely consists of materials ejected from different areas on the planet at different times. The following questions are important for the assessment of the types of materials that will be analyzed at the Luna-Glob landing site: (1) What is the total thickness of the composite layer formed by ejecta from the lunar basins in the SPR/Luna-Glob region? (2) What is the contribution of different lunar basins to this layer? (3) Can the smaller craters excavate materials from beneath the covering of basin-related deposits?

In order to address these questions, we used the models that estimate the thickness of ejecta as a function of the size of an impact structure and the distance from it [8-10], the geological map of the southern portion of the Moon [11] and the new catalogue of the larger impact craters (>20 km) [12,13].

Spatial distribution of materials of different age in the SPR:

The SPA basin [14], which is ~2,000 x 2,500 km [11,15], dominates the SPR. The rim of the basin is highly degraded and its exact position is not obvious. In different reconstructions of the shape of the basin [11,15], the Luna-Glob region either completely or largely occurs outside of the SPA outer rim (Fig. 1); the Boguslawsky crater is within the zone of the SPA ejecta.

The SPA basin is the largest and likely is the oldest (certainly pre-Nectarian) known impact structure on the Moon [16]. In our study, we consider ejecta of the SPA as materials with the lowermost stratigraphic position. The other pre-Nectarian materials occur mostly in the eastern sector of the SPR and along the southernmost portion of the SPA rim. The pre-Nectarian deposits represent the ancient crustal materials related to impact basins and craters [11]. Materials of the Nectarian age are also formed by ejecta from basins and craters and occur in the SPR mostly northward of the Luna-Glob region and around the Schrödinger basin.

Materials of Imbrian age in the SPR are presented by: (1) the ejecta from Orientale (western portion of the SPR), (2) relatively small (a few hundred kilometers across) plains units on the floor of the Australe and Schrödinger and basins, and (3) ejecta blankets around craters Antoniadi and Schomberger. Crater Schomberger (86 km, 76.5S, 25.5E) is near the central portion of the Luna-Glob region and its ejecta overlay a significant portion of this area.

Ejecta from several craters represent materials of the Eratosthenian and Copernican ages in the SPR. A large Eratosthenin crater Moretus (115 km, 70.7S, 5.4W) is near the Luna-Glob region and ejecta from the crater affect the NW potion of this area. Another Eratosthenian crater, Boguslawsky-D (24 km, 72.8S, 47.5E), is on the eastern wall of the Boguslawsky crater. Ejecta from Boguslawsky-D overlay the eastern half of the floor of the main crater [17]. Within the SPR, there are only four craters of the Copernican age [11], the largest of which (60.3S, 50.5W) is ~64 km in diameter. Thus, the contribution of the Copernican craters in the re-distribution of regolith in the SPR is insignificant. However, one of these craters (31 km, 78.6S, 23.5E) is within the Luna-Glob region and its ejecta overlay a portion of the floor of the crater Schomberger.

The nature and spatial distribution of materials within the SPR suggest that they are almost completely related to the impact re-distribution of deposits of various relative ages. The only component of the SPR deposits that may be ascribed to a specific absolute age (the Imbrian-age plains units on the floor of the Australe and Schrödinger basins) make up a few percent of the surface within the SPR. These units occur well away from the Luna-Glob region and, thus, their contribution to the deposits in this area is likely negligible.

Contribution of material deposited in the SPR by impact basins: In order to estimate the thickness of ejecta from the known and possible lunar basins [1], we have used the equations reported in [8-10] that relate the thickness of the ejecta blanket from a basin, the size of the basin, and the distance from it. Diameter of the outermost rim of the lunar basins reported in [1] may overestimate the original size of the impact structure and, thus, give overestimated values of the ejecta thickness. In order to account for this possible bias, we followed the approach described in [8] and considered diameters of the basins reduced by a factor of ~0.84, which is the ratio of the second rim of the Imbrium basin (970 km) to its outer rim (1160 km). Estimates of the thickness of the basin ejecta strongly depend upon the applied model. Specifically, the thickness values derived from the model [8] are 2-2.5 times smaller than those resulted from the model [9,10]. In our study, we used both models and consider their results as likely lower (model [8]) and upper (model [9,10]) limits of the ejecta thickness. Although the models give different values of the absolute thickness, they do not change the estimates of the relative contribution of ejecta from different basins to the composite layer of materials within the SPR.

The catalogue of the larger (>20 km) lunar impact craters [12,13] provide the base to calculate the thickness of ejecta from the basins in the SPR at random points and, thus, to estimate the contribution of materials deposited by each basin. The total thickness of deposits from the lunar basins within the SPR varies from ~900 m (model [8]) and ~2400 m (model [9,10]) to ~4000 m (model [8]) and ~8500 m (model [9,10]) with the mean value of ~1700 m to ~4000 m (models [8] and [9,10], respectively). The largest contribution to the stack of materials within the SPR belongs to the ejecta from the pre-Nectarian baisins SPA, ~78.5%, and Australe, ~8%. The total contribution of the pre-Nectarian, Nectarian, and Imbrian basins is estimated to be ~92.5%, 6.1%, and 1.4%, respectively.

The estimates of the total thickness of ejecta from the lunar basins within the SPR suggest that some of the larger craters (>20 km) can penetrate through the composite layer of the ejecta end bring to the surface materials that underlie (i.e. older) this layer. We have assumed that the excavation depth is 1/10 of the visible crater diameter [18] and compared it with the total thickness of the basin ejecta at the location of each larger craters within the SPR. According to the model [8], out of 228 craters larger than 20 km in the SPR only 17 (~7%) do not penetrate through the layer of the ejecta from all lunar basins. The excavation depth of the vast majority of the other crater exceeds the total thickness of the ejecta. Thus, these craters likely ejected materials that underlie the stratigraphically oldest materials emplaced during formation of the SPA basin. According to the model [9,10], only ~40% of the largest craters were able to excavate materials from beneath the all basin ejecta layer in the SPR.

In order to estimate the thickness of materials from all known and possible basins [1] in the Luna-Glob region, we applied the ejecta thickness formulas [8-10] to the corners of this region. The total thickness of the ejecta varies in the Luna-Glob area from ~1300/3300 m (NW corner) to ~3600/7700 m (SE corner). The total thickness of the ejecta at the locations of the craters Boussingault, Boguslawsky, and Boguslawsky-D is about 1700-1800 m (model [8]) and 4000-4300 m (model [9,10]). In all these places, the fraction of the SPA ejecta varies from~75 -90%. The study of the regional geological settings of the crater Boguslawsky revealed that its floor is overlain by materials ejected from the adjacent craters, most likely from the craters Boussingault (~128. 5 km) and Boguslawsky-D (3.5 km) [17]. According to the model [8], diameters of both craters suggest that these impacts have delivered to the surface materials that are stratigraphically older than the SPA ejecta. Only the crater Boussingault was able to excavate the pre-SPA materials if the model [9,10] is applied.

Conclusions: The SPR represents a region where materials deposited by lunar basins and re-distributed by later/smaller impact craters play a major role. The Imbrian plains of likely volcanic origin occupy small areas within the SPR and their contribution to the composite layer of materials within the SPR appears to be negligible. More than 90% of materials within the SPR is related to ejecta from the pre-Nectarian basins, among which the SPA and Australe basins are the most important. The contribution of the Nectarian (~6%) and Imbrian (~1.5%) basins to materials within the SPR is small. Although the total thickness of the composite layer of ejecta from the lunar basins may reach several kilometers, it is smaller than the excavation depth of some of the craters larger than 20 km. According to different models of the ejecta emplacement, from ~40 to ~90% of these craters were able to excavate materials from beneath the SPA ejecta. Thus, materials that pre-date emplacement of the SPA can be broadly distributed within the SPR. Specifically these materials likely occur within the walls of Boguslawsky crater, the floor of which is overlain by ejecta from the craters Boussingault and Boguslawsky-D.

Acknowledgements:

We acknowledge NASA Lunar Reconnaissance Orbiter (LRO) Mission, Lunar Orbiter Laser Altimeter (LOLA) Experiment Team (Grants NNX11AK29G and NNX13AO77G), and NASA Solar System Exploration Research Virtual Institute (SSERVI) grant for Evolution and Environment of Exploration Destinations under cooperative agreement number NNA14AB01A at Brown University to JWH.

References:

1. Wilhelms, D.E., USGS SP-1348, pp. 302, 1987; 2. Short, N.M., Foreman, M.L. Geology 3, 69-91, 1972; 3. Pike, R.J. EPSL, 23, 265-274, 1974; 4. Arvidson, R. et al., Moon, 13, 67-79, 1975; 5. Head, J.W. et al., PLPSC 6, 2805-2829, 1975; 6. Haskin, L.A., JGR, 103, 1679-1689, 1998; 7. Wieczorek M.A., Phillips R.J., Icarus, 139, 246-259, 1999; 8. McGetchin, T.R. et al., EPSL, 20, 226-236, 1973; 9. Petro, N and C.M. Pieters, JGR, 111, 2006; 10. Petro, N and C.M. Pieters, MPS, 43, 1517-1529, 2008; 11. Wilhelms, D.E. et al., USGS Map I-1192, 1979; 12. Head, J.W. et al., Science, 329, 1504-1507, 2010; 13. Kadish, S. et al., LPSC 42, #1006, 2011; 14. Stuart-Alexander, D.E., USGS Map I-1047, 1978; 15. Garrick-Bethel, I and M.T. Zuber, Icarus, 204, 399-408, 2009; 16. Hiesinger, H. et al., LPSC 43 # 2863, 2012; 17. Ivanov, M.A. et al., PSS, in press, 2015; 18. Melosh, H.J. Impact Cratering: A Geologic Process, pp. 253, 1989.

THREE-DIMENSIONAL SPATIO-TEMPORAL TECHNOLOGY

N.P. Bulatova
Institute of Physics of the Earth RAS, Moscow, B.Gruzinskaya St., 10, Russia.
n.p.bulatova@mail.ru

Introduction:

At the beginning of the 21st century, scholars in Earth sciences started studying our planet as an open system, i.e., as perceiving the influence energy of gravitational, radiation, thermal fields of celestial bodies and space. The periodical and cyclical movements of celestial bodies (sources of gravitational fields, Sun, Moon and etc.), considerably affect on heterogeneity in crust and the Earth's geosphere in general. This influence on active sites of crust by producing tides and related phenomena [1] impacting the Earth's nonhomogeneity (geological, geophysical, etc.) can, working as the trigger, to lead to earthquakes and other catastrophes [2]. In connection with thisit becomes necessary to reveal relationships between Earth's events and the dynamics of celestial bodies. A heuristic approach in this qualitative investigation has been substituted step-by-step bysystematic complex quantitative research.How to learn to distinguish this influence of celestial bodies on Earth?

Three-dimensional spatio-temporal tehnology:

Within Copernicus's theory to describe estimates of the direction and time of such influence of celestial bodies for a surface of Earth possibly, but we will receive decisions bulky since except the celestial motion it is necessary to consider also the movement of the rotating Earth.

Besides, for determination of compliance between location of "a moving source" on the heavenly sphere and these events on Earth it is necessary to define first of all instant coordinates of "a geographical position of a celestial body" on Earth surface which establish according to the direction of the vector connecting the centers of Earth and a celestial body at this moment. As celestial body in the real work the Sun [3] and the Moon [4] were considered.

For the solution of this task the author proposes a system from two modules, each using its own system of coordinates [4]:

- themodule (1) – a model of motionless three-dimensional spherical body of the Earth with the systems of coordinates, one including the location of events that happened on the Earth;
- the module (2) – a compact model constructed on astronomical parameters (vector's angles)of celestial bodies [5] in space and time as vectors that are changing their directions in the set interval of time. Module (2) is known as "Method of moving source" (MDS) [6],and "Three-dimensional spatio-temporal tehnology" modeling [4], developed by the author (Bulatova, 1998-2000).

In common such two modules form the geocentric existential model of relative celestial motion allowing to achieve a goal and to define a geographical place of a source.As a result, on the basis of systematization, joint analysis and aggregation of cosmic data and Earth science databases the cause-and-effect relations between events on Earth and celestial bodies are established [7].

On the movement of the Sun[3]**:**

According to ideas of system of Kepler of the movement of Earth round the Sun with the constant direction of an axis of rotation on a pole of the world it is possible to see that the vector of the Earth -Sun deviates in the vertical plane the equator plane on angular distance ±23° according to a circle of inducement for the Sun in a year.If toassume that Earth doesn't rotate in model Bulatova (1998), movement of this vector round an axis of rotation of Earth looks natural.

As a result the closed conic surfaces with δ=±23°in points of the maximum deviation from the equatorial plane it turns out. It are in points of a winter and summer solstice.Transition between these maximum positions is carried out by the turbinal movement of a vector up and down, in the form of not closed conic surface. Distances in creation of this model are considered in case of need.

On the movement of the Moon[4]:

Similar movements in this model are made also by a vector Earth – the Moon, however time of transition equally to one lunar month (29 day). It describes not closed conic surfaces from the vectors making the periodic movements: 1) circular and 2) in the vertical plane. The maximum changes in different phases of the cyclic movement of the Moon (19,6 years) the maximum deviations change from + 18°– + 28,5° to 18°– -28,5°.

Conclusion:

For influence research Earth – celestial body (the Sun, the Moon) were offered:

1) model of three-dimensional motionless Earth [1] with 3 systems of coordinates (polar and Cartesian) with the center in a point of 0 geospheres [4];
2) 3D systems of coordinates of Earth and space: polar and Cartesian system [3];
3) for representation of the movement for each of couples Earth – a celestial body (for example, the Sun – Earth, the Moon – Earth and so forth) the author was offered system from two modules [4]:
   a) model of three-dimensional geocentric space with coordinates definitely oriented in a space in two systems of coordinates;
   b) models of three-dimensional motion and time of a celestial body concerning systems of coordinates of Earth presented in the form of set of vectors with angles (polar and hour) for each of celestial bodies – the module 2.
4) combination of modules 2 of each of celestial bodies give the chance of simultaneous consideration of the directions of stay (influences) of several bodies in one system of coordinates of Earth.

References:

1. G. H. Darwin. *The Tides and Kindred Phenomena in the Solar System*, edited by J. Murray, Publisher Albemarle Street. London. (1898), 250 p.
2. N. P.Bulatova. *Vulcanology and Seismology*.2, Publisher, MAIK NAUKA, Moscow (2005), pp.57-78 (*rus*.).
3. N. P. Bulatova. On the Solar Neutrino Tomography of The Earth: Scanning Geometry**.** *Izvestiya Physics of the Solid Earth*, *RAS* 35, N2, Publisher, Nauka, (1999) pp.150-160.
4. N. P.Bulatova. Three-dimensional spatio-temporal modeling of geophysical events and the movement of celestial bodies. J. Complex Systems. **2012**, v.20, N3, P. 215-227.
5. V. V. Podobed, V. V. Nesterov. *The general astrometry*. Moscow, Nauka. 552 (1975).(rus.).
6. N. P.Bulatova."Method of a moving source". *Вестник ОГГГГН РАН.* 2, Publisher. ОИФЗ РАН, Moscow (2000), pp.110-125 (*rus*.)
7. The Yearbook of Astronomical Observations, St. Petersburg, Russia: Institute of AppliedAstronomy, Russian Academy of Sciences (1982–2012).

THE CONCEPT IS CONSIDERED IN RELATION TO THE ESTABLISHMENT OF HIGH-PRECISION SELENODETIC COORDINATE SYSTEM DURING THE MISSION “LUNA-GLOB, LUNA-RESOURCE”

A.M. Shirenin
MIIGAiK, 4 Gorokhovskiy pereulok, Moscow, Russia, 105064.
+7- 916-072-52- 55

Introduction.

The concept of constructing a high-precision planetary coordinate system without astronomical points use on the planet’s surface is proved. Instead of astronomical points it is proposed to use optical beacons, and their position relative to the stars to measure with a goniometer placed on board of the planet satellite. The concept is considered in relation to the establishment of high-precision selenodetic coordinate system during the mission “Luna-Glob, Luna-Resource”.

The algorithm of processing the goniometric measurements array on board of the Polar artificial moon satellite (PAMS) captured in images of the moon surface made by beacons and co-ordinate timing of the PAMS for building the reference selenocentric coordinate systems is considered in this paper. The algorithm provides angular positions of point light sources arranged on the Moon surface and the moon landers.

Numerical modeling of the measurement systems operation providing the position-finding and orientation of PAMS during its active phase was held. Recommendations on the use of different measurement types are given: ground radiopath measurements, navigational star sensors using onboard star catalogue, gyroscopic attitude orientation systems and space videos of the moon surface. Calculations were performed using the precision parameters of current measurement systems.

Calculations were performed in the context of measurement systems that are planned to establish during a moon space mission - Luna-Glob, Luna-Resource. The use of photocontours obtained from beacon location survey was provided in compiling the digital catalogue of beacon coordinates, as well as digital images of high resolution, such as The Moon Reconnaissance Orbiter Camera (LROC). Numerical calculations showed that when using the last theories of moon motion [2] the expected precision of the beacon selenodetic coordinates setting may be in the range of 0.5-8 m.

Precision evaluation of PAMS position and orientation was made on the basis of the Kalman filter. In accordance with the space exploration program of the solar system developed in recent years by the Russian Space Agency and Russian Academy of Sciences, one of the priorities is a detailed study of the physical Moon surface, its gravitational field, the influence of the external cosmic radiation on both the Moon surface and the equipment that is installed on in-orbit artificial moon satellites (OAMS), on the moon landers, autonomously moving moonwalkers and moon living bases that are planned in the foreseeable future.

Controlled landing in the place selected from images as well as all the above mentioned moon expeditions require detailed topographic study of the physical Moon surface, namely the presence of large-scale topographic maps presented as digital terrain models of high resolution of about 0.1 m height and from 0.5 to 10 m in plan (challenging terrain).

The creation of such digital terrain models intends precision of high-precision selenodetic coordinate catalogues of moon points which, in turn, must be linked to the digital photocontours of catalogue points location with high resolution, that is within a few meters.

Since the invention of the telescope such catalogues were created by conventional astronomical methods according to the observations of the moon surface points on the star background. Hereafter advanced methods and measurement types [1, 3-11] were developed, namely: trajectory measurements of AMS, photogrammetric, radio and laser moon ranging, position-finding of AMS in the inertial coordinate system using onboard star sensors and highly sensitive gyroscopic systems, etc.

Mathematical formulation.

The most stringent requirements to the board equipment navigation operation are imposed by researchers who carry out the operative and post-flight result processing of the orbital surface survey in order to establish a reference co-ordinate system and to map, definition the external grabitational field parameters, the celestial body's translational-rotational motion study [1, 4, 5, 6, 9-11]. Typically, if these experiments are provided with sufficiently accurate navigation data, then there will be no problems in using them to co-ordinate the timing and process the other experiments results. Therefore,

considering the problem of the PAMS devices navigation provision, first of all we shall proceed from the requirements that are applied to the above mentioned experiments.

The task of coordinate timing is formulated as follows: it is needed to define the position vectors

$\overline{R}_T^T = \left[X_T, Y_T, Z_T \right]$

of the physical moon surface points (light beacons in the coordinates of the images that were measured in the coordinate system of the board device and the two or more corresponding timepoints in the rigidly connected to the Moon coordinate system. The special case of this problem is spherical coordinates determination of devices' principal axes traces on the physical surface of the moon or the celestial vault at the moment of observation. We will use a dynamic selenocentric system as rigidly connected to the Moon coordinate system, as defined in [2]. To compute RT we will apply the algorithm that implements a direct orbital inset based on a search of the hysical point average position on the segment of the minimum distance between the crossing projecting rays that correspond to the images of the point obtained in two timepoints. This algorithm is described by formulae:

$$\begin{gathered}
\overline{R}_{S12} = \overline{R}_{S(i+1)} - \overline{R}_{Si}; \quad \overline{\rho}_1 = M_i \overline{r}_i; \quad \overline{\rho}_2 = M_{i+1} \overline{r}_{i+1}; \\
\rho_1^2 = \overline{\rho}_1^T \overline{\rho}_1; \quad \rho_2^2 = \overline{\rho}_2^T \overline{\rho}_2; \quad \rho_{12}^2 = \overline{\rho}_1^T \overline{\rho}_2; \\
u = \rho_{12}^2 - \rho_1^2 \rho_2^2; \quad a_1 = \overline{\rho}_1 R_{S12}; \quad a_2 = \overline{\rho}_2 R_{S12}; \quad (1) \\
k_1 = 1/u\left(a_2 \rho_{12} - a_1 \rho_2^2\right); \quad k_2 = 1/u\left(a_2 \rho_1 - a_1 \rho_{12}\right); \\
\overline{R}_T = 0.5\left(k_1 \rho_1 + k_2 \rho_2\right),
\end{gathered}$$

where $\overline{R}_{Si}^T = \left[X_{Si}, Y_{Si}, Z_{Si} \right], \overline{R}_{S(i+1)}^T = \left[X_{S(i+1)}, Y_{S(i+1)}, Z_{S(i+1)} \right]$ are AMS position vectors for tht moments t_i, t_{i+1} in a rigidly connected to the Moon coordinate system $\overline{r}_i^T = \left[x_i, y_i, -f \right], \overline{r}_{i+1}^T = \left[x_{i+1}, y_{i+1}, -f \right]$ are vectors of the same physical point (light beacon) location defined in the coordinate system of the video unit with focus f for the moments of time t_i, t_{i+1}; $M_i = \left(\lambda_{1i}, \lambda_{2i}, \lambda_{3i} \right)$, $M_{i+1} = \left(\lambda_{1(i+1)}, \lambda_{2(i+1)}, \lambda_{3(i+1)} \right)$ are transition matrices from the device coordinate system to the rigidly connected to the Moon coordinate system defined for the moments of time t_i, t_{i+1}, and that are the functions of orientation parameters $\overline{\lambda}_i^T = \left[\lambda_{1i}, \lambda_{2i}, \lambda_{3i} \right]$, $\overline{\lambda}_{i+1}^T = \left[\lambda_{1(i+1)}, \lambda_{2(i+1)}, \lambda_{3(i+1)} \right]$.

It follows from (1) that the question point vector $\overline{R}_T$ is a vector function $\overline{R}_T = \overline{F}_R(\overline{P})$ of 17-dimensional parametr $\overline{P}$

$$\overline{P}^T = \left[x_i, y_i, X_i, Y_i, Z_i, \lambda_{1i}, \lambda_{2i}, \lambda_{3i}, x_{i+1}, y_{i+1}, X_{i+1}, Y_{i+1}, Z_{i+1}, \lambda_{1(i+1)}, \lambda_{2(i+1)}, \lambda_{3(i+1)}, f \right] \quad (2)$$

Thus, the components of P (2) vector shall be available for the co-ordinate timing of AMS onboard experiments results for the moment of experiment. They are obtained in the form of estimates with error covariance matrix from the conduction and processing results of navigation measurements containing random errors. Components of the vectors $\overline{r}$ and covariance matrices of their errors K_r are calculated based on measurements of device's physical points images coordinates x, y. Components of the vectors $\overline{R}_S$ their errors are obtained based on the trajectory and covariance measurements, the components of vectors and covariance matrices of errors K_λ are obtained based on measurements K_{RS} of orientation PAMS [6].

Let us assume that $\overline{P}$ is the parameter evaluation vector, K_P is error covariance matrix of the vector $\overline{P}$. The task of co-ordinate timing reduces to calculating estimates of physical points position vectors $\overline{R}_T$ and covariance matrices $\overline{K}_{RT}$

of their mistakes. We have

$$\hat{\overline{R}}_T = \overline{F}_R\left(\hat{\overline{P}}\right); \quad \hat{\overline{K}}_{RT} = G_F^T \hat{K}_P G_F \tag{3}$$

where $G_F = \left[\overline{\nabla}_P \overline{F}_R^T\right]$ is gradient 17×3 matrix of the vector $\overline{F}_R$ of parameters P:

$\overline{\nabla}_P^T = \left[\frac{\partial}{\partial x_i},\ldots,\frac{\partial}{\partial f_i}\right]$ is 17-dimensional vector differential operator on components $\overline{P}$.

Components of the unknown vector and covariance matrices K_{RT} by (1) and (3) depend $\overline{R}_T$ essentially on the programs, content and precision of navigation measurements that are used to determine the vector components of parameters P as well as on processing algorithms for defining the rules for calculating estimates $\overline{P}$ by vector-sample of measurements.

Numerical modeling of measuring systems.

The configuration and programs of navigation measurements were chosen based on the actual conditions of their implementation during the process PC modeling of research results co-ordinate timing and it varied from one experiment to another as follows:

Experiment R+G (radio+gyro). The orbit of PAMS is determined only by ground-based radio measurements once in 12h. The orientation data are received from of the telemetry of the gyro systems at any time of on-board scientific devices operation.

Experiment R+S (radio+stars). The orbit is defined in the same way as in the previous case.

Orientation is conducted by the stars for any time.

Experiment R+T+S (radio+topography+stars). The orbit is determined by ground-based radio measurements once in 2^h and based on survey materials of the Moon surface at every turn (once in 2^h) with the CCD topographic camera. Orientation is determined by the stars for any time.

Software package that was developed by [6] for the navigation referance process PC modeling allows almost any variation of parameters, on which this process is functionally dependent. However, in this case the precision of light beacons reference is of interest, which can be achieved by operation of the existing equipment that is installed in the experiment “Luna-Glob/Luna-Resurs”. As a result of many numerical experiments performed on the PC, it was found that the highest reference precision of one two-hour turn ($\sigma_{RTcp.}$ = 32 meters) can be achieved, if the data of ground-based trajectory measurements and onboard videos are used jointly for the PAMS orbit determination, and the onboard video devices unit data containing images of starry sky areas (experiment ***R***+***T***+***S***) are used for the PAMS actual orientation determination.

There is another possibility of increasing the navigation reference precision using the equipment with the parameters accepted above. As was noted previously, the angle of star camera rotation about the optical axis has the worst precision in determining the orientation. If 2 star cameras will be installed at an angle ~90° on the PAMS board, the precision of determining the actual orientation will increase significantly, resulting in more accurate reference. In order to confirm this position the correspondent calculations were given yielded the following results $\sigma_{RTcp.}$ = 8 meters, $\sigma_{\lambda RTcp.}$ = 7’’ $\sigma_{RTcp.}$ = 7 meters, i.e. the precision increases about three-fold as compared with the method ***R***+***T***+***S*** [12].

Conclusion.

These results show that the navigation reference of the PAMS orbit experiments with proper precision need to have the means to specify the orbit by video images of the moon surface and to determine the actual orientation by the video images of the starry sky areas on board. Depending on the purposes of research elements of the initial orbit and the required precision of navigation reference shall be selected during the PAMS operation. Such data are the starting point for the search of optimal operation programs, configuration and parameters of onboard equipment, which provides the navigation reference with the a given precision. In this case, the algorithms and modeling program systems such as those described in this paper may be useful. The final result of this paper should be submitted as a digital catalogue of the small LED and laser beacons and digital photocontours coordinates of high resolution. Using the methods and algorithms developed in [5, 10, 11] the catalogue of light beacon coordinates can be combined with other selenodetic catalogues that were created before when performing the other moon programs.

References:

[1]. Aleksashin E.P., Timofeev Yu.S., Shirenin A.M. Selenocentric system “Zond-8”. Methods of construction and catalog GCP.//Proceedings. Moscow: Publishing TsNIIGAiK, 1989, 216p.
[2]. Astronomical Yearbook for 2013. Institute of Astronomy practical .St. Petersburg: Nauka, 2012, p. 683.
[3]. Shirenin A.M. Comparison of patterns of physical libration of the Moon in relation to the problem of determining the position of the spacecraft relative to the Moon.//Kinematics and physics of heavenly bodies. 1986, V. 2, issue 5, pp. 68-73.
[4]. Aleksashin E.P., Murunova T.I., Timofeev Yu.S., Shirenin A.M. Using the results in the construction of networks altimetrirovaniya triangulation space images.//Geodesy and Cartography, 1988, Issue 11, pp. 49-51.
[5]. Aleksashin E.P., Shirenin A.M. The method of determining the parameters and algorithms to convert between different coordinate systems applied to problems processing satellite measurements.//Geodesy and Cartography, 2002, Issue 6, pp. 4-26.
[6]. Aleksashin E.P., Timofeev Yu.S., Shirenin A.M. Ensure the requirements of navigation experiments with polar orbit satellite of the moon.//Geodesy and Cartography, 1995, Issue 4, pp. 10-20.
[7]. Aleksashin E.P., Timofeev Yu.S., Shirenin A.M. Zond-8 Selenocentric Coordinate System: Design Concepts and Some Results//12-Soviet-American Microsymposium: Abstracts. - M., 1990. pp. 10-11.
[8]. Shirenin A.M. Comparison of Moon Physical Libration Models Applied to the Problem of Spacecraft Position Relative to the Moon.// The Smithsonian / NASA Astrophysics Data System, 1986, Grant NNX09 AB39G.
[9]. Aleksashin E.P., Timofeev Yu.S., Shirenin A.M. Analysis of Navigational Support recision of Experiments by Moon polar Satellite (LPS)//16-Russian-American Microsymposiym: Abstracts. - M., 1992. pp. 9-10.
[10]. Shirenin A.M. Nonlinear Algorithm of the Parameters Estimation of Transformation Between Two Coordinate Systems of the Planets.//Microsymposiym 36, MS 089, October 14-16, 2002 – Moscow, Russia. Topics in Comparative Planetology. pp. 38-39.
[11]. Shirenin A.M. Some Results by Using of Nonlinear Algorithm for Calculation of Transformation Parameters Between Planet Coordinate systems. p. 31-32.// Microsymposiym 37, MS 087, October 27-28, 2003 - Moscow, Russia. Topics in Comparative Planetology. pp. 47-49.
[12]. Shirenin A.M., Mazurova E.M., Bagrov A.V. Building the global positioning system for uninhabited planets and natural satellites. / Space Colonization Journal. Vol. 15. May, 23, 2014, p. 1-14.

THE WAVE PHENOMENA RESULTED FROM SOLAR WIND-MOON INTERACTION

A.Skalsky[1], A.Sadovski[1], H.Rothkaelh[2]
[1] Space Research Institute of Russian Academy of Sciences (IKI RAS)
[2] Space Research Centre of Polish academy of Science, Warsaw, Poland

The physical processes occurring in lunar plasma environment when the solar wind interacts with the Moon, seem to be complex due to their kinetic nature. It results in variety of wave phenomena occurring over the regions of enhanced crustal magnetic field and in the lunar wake.

The present paper is aimed to review actual observations and different mechanisms of wave generation in plasma environment around the Moon.

PROVIDE: PLANETARY ROBOTICS VISION DATA EXPLOITATION BASED ON LUNAR ARCHIVE PANORAMIC IMAGE PROCESSING

N. Kozlova[1], A. Zubarev[1], A. Garov[1], E. Stovolosov[1], A. Abdrakhimov[1,2], I. Karachevtseva[1] and MExLab team[1]
[1]*Moscow State University of Geodesy and Cartography, (MIIGAiK), MIIGAiK Extraterrestrial Laboratory (MExLab), Russia.*
nataIly.ko@gmail.com
[2]*Vernadsky Institute of Geochemistry and Analytical Chemistry, RAS, GEOKHI, Moscow 119991 Russia.*
albertabd@gmail.com

Introduction:

We present the results of image processing of archive lunar surface panoramas obtained during Soviet lander and rover missions. Our work is a part of PRoViDE project (Planetary Robotics Vision Data Exploitation) Apart from lunar data PROVIDE is focused on different Martian rover missions such as MER-A, B and MSL (www.provide-space.eu). We have collected all imagery data remained since Soviet lunar missions, developed and implemented new techniques for digital processing of archive panoramic images and, additionally, LRO NAC data. It allowed us to obtain new products suitable for modern software and computer use, created a scheme of product levels and structure of lunar data catalogue, carried out geologic assessment of the landing sites and observation points, visualized Lunokhods journeys in video clips to popularize the data.

Main results of lunar surface image processing:

First of all, we have collected images obtained during Soviet Lunar missions (Luna-9, -13, -17, -20, -21) and supplementary data from all available sources (Russian State Archive of Scientific and Technical Documentation, personal archives, old and recent publications, and discussions with participants of the Soviet missions (geologist A.T. Basilevsky and Lunokhods driver V.G. Dovgan). Additionally we have processed LRO NAC data and produced high resolution DEMs for different landing sites based on stereo photogrammetric processing (Zubarev et al., 2013).

Having analyzed the collected data we have developed a structure of **Lunar data catalogue**, described and cataloged all available data. This process revealed mistakes and disagreements among different sources, so they have been checked and corrected where possible.

A new technique for modern **lunar surface image processing** has been developed and implemented by means of modern photogrammetry complex PHOTOMOD, ArcGIS, and specially created software (Fig. 1): 1) to recover panoramic images from archive fragments; 2) to reconstruct some parameters

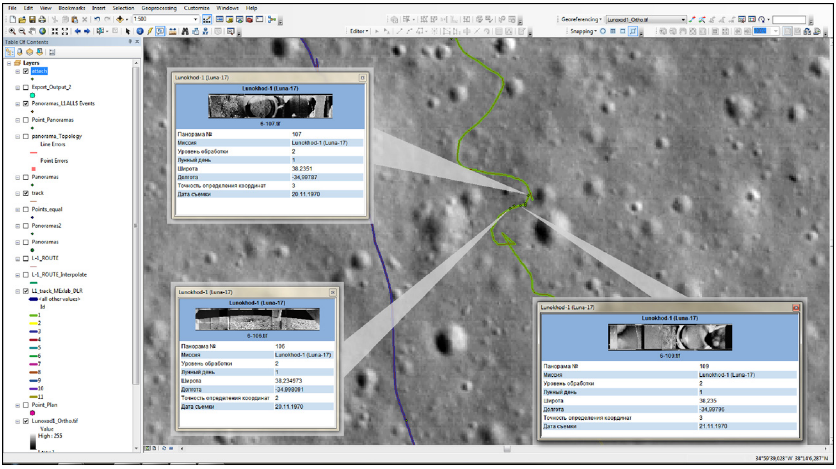

Fig. 1. Identification of observation points and visualization of Lunokhod-1 panoramic images and their metadata using ArcGIS 10.1

of exterior orientation for a substantial part of the Lunokhod-1,-2 panoramas; 3) to produce artificial panoramic images based on DEM. The new techniques allowed us to reconstruct some details of Lunokhod's missions (Kozlova et al., 2014).

Processed panoramas have been used to create a comprehensive **geomorphologic catalogue** including size and structure of various types of objects (craters, blocks, boulders), characteristics of regolith. By combination with LRO orbital data, coordinates and ranges to features of interest seen in the Lunokhod images have been determined. Based on LRO NAC DEMs and mosaics, geologic assessment have been prepared for the areas studied by Lunokhods (Abdrakhimov et al., 2013).

To insert lunar data into the PRoDB a **Lunar data import engine** has been developed including XML-scheme for data loading. Now all obtained results on LRO and Lunokhod image processing are available via Planetary Geoportal (http://cartsrv.mexlab.ru/geoportal/); access to archive lunar panoramas will be organized on special request.

Dissemination. Techniques and programs developed during the study can be used to support navigation of lunar surface vehicles and landing site selection for future Russian missions (Marov et al., 2014). To visualize and popularize the data we have prepared videos of Lunokhod journeys based on new 3D reconstruction of Lunokhod traverses and surrounding territory (http://www.provide-space.eu/new-video-the-journey-of-lunokhod-1/). A lot of students and young scientists from MIIGAiK are involved in this project, they participate in conferences for young scientists and prepare master and PhD theses based on results of the project.

Acknowledgments:

We greatly acknowledge A.T. Basilevsky and V.G. Dovgan for useful discussions and insight view to the Soviet lunar missions. We would like to acknowledge Russian State Archive of Scientific and Technical Documentation which provided image fragments of archive lunar panoramas for our research. The research leading to these results was supported the European Community's Seventh Framework Programme (FP7/2007-2013) under grant agreement № 312377 PRoViDE.

References:

Abdrakhimov A.M., Basilevsky A.T., Karachevtseva I.P. Geological review of Lunokhod 1 area // The Fourth Moscow Solar System Symposium (4M-S3), IKI RAS, Moscow, Russia, 14-18 October 2013. http://ms2013.cosmos.ru/sites/ms2013.cosmos.ru/files/4m-s3_program-10-07.pdf

Kozlova N., Zubarev A., Karachevtseva I. et al. Some aspects of modern photogrammetric image processing of Soviet Lunokhod panoramas and their implementation for new studies of lunar surface. // The International Archives of the Photogrammetry, Remote Sensing and Spatial Information Sciences, Volume XL-4, pp. 121-126, 2014. doi:10.5194/isprsarchives-XL-4-121-2014.

Marov M., Basilevsky A., Dolgopolov V., Head J. Selection and characterization of landing sites for the up-coming Russian robotic missions to the Moon // 40th COSPAR Scientific Assembly, 2014.

Zubarev A., Kozlova N., Nadezhdina I., Kokhanov A., Karachevtseva I. Main Characteristics of Coordinate and Cartographic Support of Luna-Glob Mission // 26th International Cartographic Conference, Dresden, Germany, Abs, 706, p 752, 25-30 August, 2013 http://icaci.org/files/documents/ICC_proceedings/ICC2013/ICC2013_Proceedings.pdf

THE DISTRIBUTION OF EPITHERMAL NEUTRON FLUX IN IMPACT BASINS OVER THE EQUATORIAL LUNAR SURFACE

M.P. Sinitsyn
SAI MSU, 119992, Universitetski pr., 13, Moscow, Russia.
msinitsyn.sai@gmail.com

Introduction:

At present time there are two different neutron spectrometers data (LEND and LPNS) that covered the entire lunar surface including equatorial regions [1,2]. Currently many efforts were devoted to identifying so called neutron suppression regions (NSR) of epithermal neutrons (EN) in the both lunar polar zones [2,3,4]. However, the distribution of epithermal neutrons in the equatorial surface remains still insufficiently explored [5,6]. It is necessary to say, the distribution of EN flux strongly anti-correlated with hydrogen content. This report shows the results of study EN distribution through all large impact basins and marine formation across the equatorial lunar surface.

The distribution of EN suppression factor in longitude:

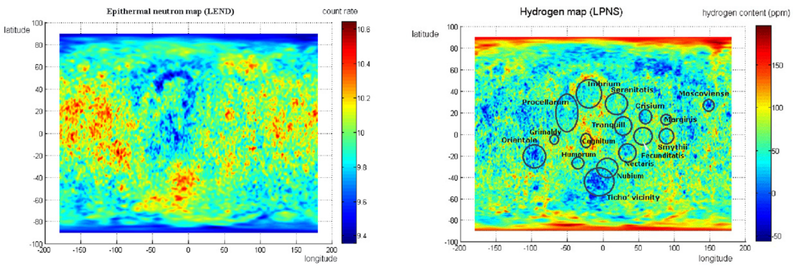

Fig. 1. EN flux distribution around equatorial surface (LEND omnidirectional sensor[7], left) and global map of hydrogen concentration [8] (LPNS, right). These two spectrometers are in a good agreement. The EN fluxes and concentrations of hydrogen are strongly anti-correlated. Some impact basins indicated on the hydrogen map.

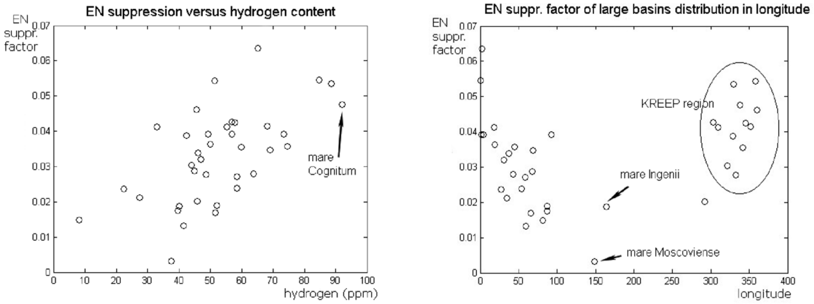

Fig. 2. Relation between EN suppression factor (LPNS) and hydrogen content (left); longitude distribution of EN suppression factor for impact basins and other marine formations (right).

For quantity estimation of EN flux variations through lunar surface the so-called suppression factor has been used [4]. It shows the relative change (suppression) of the neutron flux in the testing zone compared with reference zone (fig.2,left).Each of explored impact basins has been selected as a testing zone. As a reference zone we chose the vicinity of crater Tycho, because it has maximum value of the EN flux. Therefore, zero value of suppression factor corresponds to the maximum neutron flux and, accordingly, the minimum hydrogen content. This is evident from the neutron flux and concentration of hydrogen at the vicinity of crater Tycho (fig.1). Thus, the suppression factors were calculated for impact basins and marine formations around the equatorial surface. It is clearly seen, that neutron suppression δ (LEND) and hydrogen content (LPNS) are good correlated (fig.2, left). Meanwhile, suppression factor has increased values (δ=0.02-0.06) in longitudes correspond to the near side (300°-

60°), especially so called KREEP zone (fig.2, right). In contrast, suppression factors for far side' marine formations like mare Moscoviense and mare Ingenii have significantly lower value (δ=0.003;0.019 respectively). This means, the concentration of hydrogen in average on the near side significantly more. The maximum concentration of hydrogen (92.1ppm) has near side' mare Cognitum (long=337.1°).

Some possible causes for uneven distribution of impact basins' EN suppression factor in longitude:

How can explain this distribution of suppression of EN in longitude? It is believed that in addition to hydrogen, which slows down the neutrons, there are elements that absorb them. It is assumed that such elements include iron, thorium and rare earth elements (samarium and gadolinium). It is supposed also that on the near side of the Moon, wherein the contents of these elements are increased, they have a decisive influence on the suppression of epithermal neutrons [6,9]. However, the evidence that these elements cause EN suppression in general does not exist. As an example we give a plot of EN suppression factor versus the iron content for the same impact basins (fig.3, left). The plot clearly shows there is no noticeable correlation. Therefore, we can conclude that iron content does not affect the EN neutron flux. Thus, it is possible that the hydrogen content is the main cause of variation of EN flux in the equatorial regions.

It should be mentioned another two possible causes of the EN flux variations. The first is the influence of solar wind implanted hydrogen, the concentration of which in this case must necessarily depends on the age (maturity)(fig.3,right). This plot shows, that possible correlation between hydrogen contents and maturity [10] is very complex, but most likely, the correlation is absent, which is also confirmed by Johnson [5].

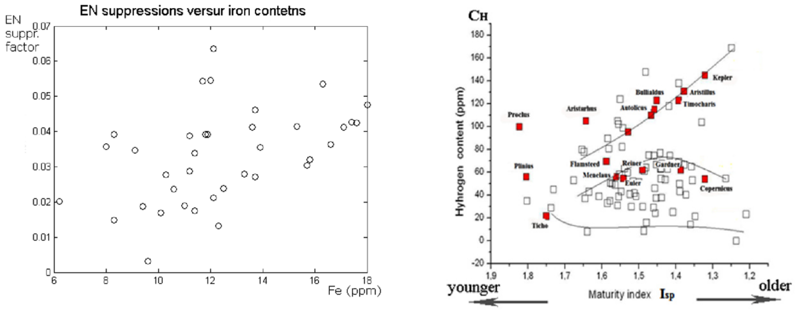

Fig. 3. The plot of EN suppressions versus iron contents [8] (left) and concentration of hydrogen (CH) versus spectropolarimetric maturity index [8,10] (left).

The second possibility the origin of enhanced concentration of equatorial lunar hydrogen is indigenous lunar hydrogen [11]. Currently, there are many studies that prove the presence of hydrogen-containing compounds in the lunar mantle. The recent publication of R. Tartese [12] states about 1500-30000 ppm hydroxyl in apatite from basalt samples with a high content of titanium and 500-15000 ppm OH with the low titanium content. These results indicate that the lunar mantle may contain up to 1800 ppm of hydrogen. Thus, the near side melted basalts can include hydrogen, which is the cause of suppressing the EN neutron flux

References:

[1] Mitrofanov, I.G. et al. Space Sci. Rev. 150(1-4),183-207(2010b)
[2] Feldman, W. C. et al. Science, 281, 5382, 1496-1500(1998)
[3] Feldman, W.C. et al. JGR, 106, 23231-23251(2001)
[4] Boynton, W.V. et al. JGR, 117,E00H33(2012)
[5] Johnson, J.R. et al. JGR, 107, E2, 3-1(2002)
[6] Lawrence, D.J. et al. Icarus, available online, January 2015
[7] Litvak M. L. et al. JGR,117, E00H22(2012)
[8] PDS, Geoscience Node, Lunar Prospector Reduced Spectrometer Data – Spetial Prodacts http://pds-geosciences.wustl.edu/missions/lunarp/reduced_special.html
[9] Elphic. R.C. et al. JGR, vol.105, E8, 20.333-20.345(2000)
[10] Shevchenko,V.V. et al.Solar System Research, 37, 3,178-197(2003)
[11] Saal, A.E. et al. Nature, 454, 170-172(2008)
[12] Tartese, R. et al. Geochimica et Cosmochimica Acta, 22,58-74(2013)

CRATER BOGUSLAWSKY: SLOPE HAZARD ESTIMATION BY SHADOW AREA MEASUREMENT

A.M. Abdrakhimov[1,2], A.T. Basilevsky[1,2,3], M.A. Ivanov[1], A.A. Kohanov[2], I.P. Karachevtseva[2], J.W. Head[3],
[1]Vernadsky Institute, Russian Academy of Sciences, Moscow, 119991, Russia, albertabd@geokhi.ru;
[2] MIIGAIK, Gorokhovskiy per., 4, 105064, Moscow, Russia;
[3] Department of Earth, Environmental and Planetary Studies, Brown University, Providence RI, 02912, USA

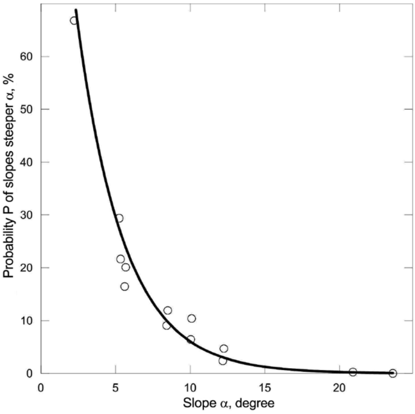

Fig. 1. The dependence of the probability of slopes more than α on the boundary slope angle α for Lunokhod-1 area according DTM of [4].

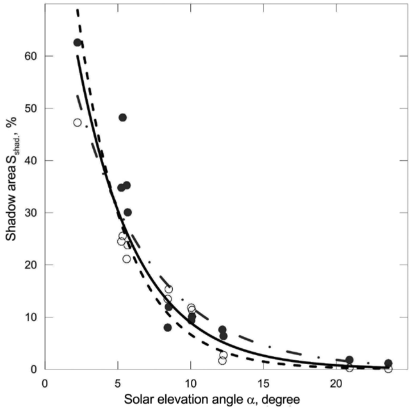

Fig. 2. The dependence of the shadowed area on solar elevation (α) for Lunokhod-1 area. The data were obtained by shadow measuring 13 LRO NAC images (black circles) and by corresponding DTM [4] shadow simulations (white circles). Resulting regression lines: a chain line is regression by NAC shadow measuring (SNAC shad (α) = 79.89exp (– 0.19α)); a dashed line is regression by DTM shadow simulation (SDTM shad (α) =134.49exp (-0.30α)); the continuous line is general regression of both data sets (Sshad (α) = 103.66 exp (-0.25α)).

Introduction:

One of the probable landing sites of future Russian Luna-Glob mission [1,2] is a 15 × 30 km ellipse with center coordinates at 72.9 S, 41.3 E, located on the relatively flat floor of the 95 km crater Boguslawsky in the S lunar polar region. For engineering characterization of the site it is necessary to know the hazard slope distribution on the baseline of the space between the lander feet, ~ 3.5 m. Unfortunately, there are no high-resolution DTMs of this area. But there are more than 50 LRO NAC high-res images (0.5-1 m/px) [3], taken under different heights of the Sun. To solve this task we applied an assessment through the empirical correlation between shading area values of relief and an area occupied by hazard slopes steeper the critical angle.

Method and results:

Since the slopes and, respectively, the visible shadows on a lunar surface are generally associated with craters, possessing a circular symmetry, there is a correlation between the shadowed area obtained at a given illumination angle α and the area occupied by slopes steeper this angle α. However, the shape of craters of different maturity and their slopes is rather complicated. Therefore, we look for the empirical relationship between the proportion of the shadowed area and the area of hazard slopes on the baseline of 3.5 m.

The Lunokhod-1 flat mare area is useful for calibrating this correlation. There are 1) a hi-res DTM (~ 0.5 m/px) [4] and 2) 13 LRO NAC images (~ 0.5-1 m/px) [3], obtained under different illumination angles for the 2 x 4 km Lunokhod-1 working area. This DTM was desensitized up to 3.5 m/px and divided into the sections corresponding to LRO NAC images, which overlapped the studied area. For each of 13 sections we measured the total area of slopes steeper than the boundary angle, corresponded to the NAC image sun height (α) (Fig. 1). According to these data the probability of slopes steeper than α could be de-

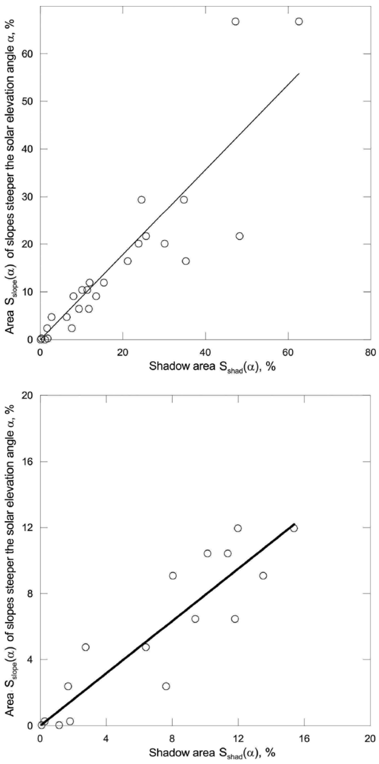

Fig. 3. The dependence of the area, occupied by slopes (baseline 3.5 m) steeper than the critical angle α, on the area, shadowed under solar elevation equal α, for Lunok-hod-1 region and corresponding regressions: a) Data for α = 2-25°. $S_{slope}(\alpha)=0.89S_{shad}(\alpha)$, R2=0.88, $\sigma^2=63.60$. b) The same data for α=7-25°. $S_{slope}(\alpha)=0.79S_{shad}(\alpha)$, $R^2=0.93$, $\sigma^2=3.76$.

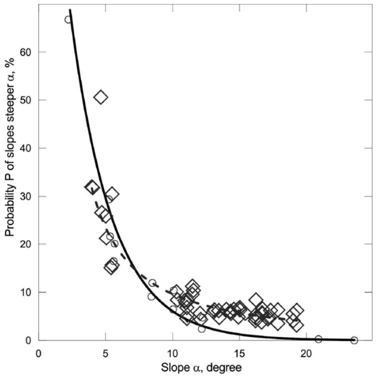

Fig. 4. The resulting relationship between the area occu-pied by slopes steeper than the critical angle α (base 3.5 m) and the angle α for Lunokhod-1 region (circles and a solid regression line $P_{slope}(\alpha) = 144.19\exp(-0.32\alpha)$, $R^2 = 0.97$, $\sigma^2 = 0.13$) and for Boguslawsky floor (diamonds and the dashed line $P_{slope}(\alpha) = 187.07\alpha^{-1.29}$, $R^2 = 0.83$, $\sigma^2 = 0.07$), calculated by shadow measurements under solar elevation angles α.

scribed by the empirical regression $P(\alpha) = 144.19 \exp(-0.32\,\alpha)$, $R^2 = 0.97$, $\sigma^2 = 0.13$.

Next, within each section the area occupied by shadows, S_{shad}, was measured and was calculated basing on the DTM under the corresponding LRO NAC illumination angle α (Fig. 4). The measured shadow area data are close to the calculated data and could be approximated by the general regression $S_{shad}(\alpha) = 103.66 \exp(-0.25\alpha)$ (Fig. 2).

Fig. 1 and Fig. 2 are characterizing the one studied relief. If we combine the data from Fig. 1 and Fig. 2 we obtain the relationship between the shadowed area and the area occupied by slopes steeper than the boundary angle equal to the corresponding solar elevation (Fig. 3a). This is approximated by the regressi on $S_{slope}(\alpha) = 0.89\, S_{shad}(\alpha)$, $R^2 = 0.88$, $\sigma^2 = 63.60$.

Fig. 3a shows that rather steeper slopes, corresponded to small slope area values, have the least variance of the points on the graph. But the variance is significantly increased when the shadow area reaches 20%. According to Fig. 2, that corresponds to the sun height $\alpha \sim 7°$. Apparently, such variance is the combined effect caused by non-crater slopes and the smaller DTM accuracy for small slope measurements.

Fig. 3b was obtained separately for the data set corresponding to areas shadowed less than 20%,. According to Fig. 1 and 2 the area of shadowing less than 20% is related to the areas with slopes steeper than 7°, which should be considered as critical for landing parameters. But the variance σ^2 in Fig. 3b decreases sharply and the sought after slope-shadow dependence could be described by an almost direct regression $S_{slope}(\alpha) = 0.79\, S_{shad}(\alpha)$, $R^2 = 0.93$, $\sigma^2 = 3.76$. The proximity of the coefficient of determination to 1 indicates that when the solar elevation is steeper than 7°, the shadowed area is in direct proportion to the area occupied by slopes steeper than the angle of the sun height on a baseline of 3.5 m.

The derived characteristic regression for the lunar plains allows us to predict the area occupied with slopes steeper than the boundary angle by shadow area measurements. In particular such a prediction is given for the landing ellipse at the Boguslawsky flat crater floor (Fig. 4). The probability of slopes steeper than the critical angle for the Boguslawsky crater landing site could be approximated by the regression $P_{slope}(\alpha) = 187.07\,\alpha^{-1.29}$, $R^2 = 0.83$, $\sigma^2 = 0.07$.

Discussion: The derived data (Fig. 4) show that in the crater Boguslawsky, slopes less than 10° on a baseline of 3.5 m, occupy approximately 90% of the area on the basis of LRO NAC shadow measurements. That is close to the area values of the same slopes at the Lunokhod-1 site area calculated by hi-res DTM [4]. However, for steeper slopes a difference is noticed: >10° - 9.6, >15° - 5.7, >20° - 3.9% for Boguslawsky landing ellipse and >10° - 6.1, >15° -1.3, >20° - 0.3% for Lunokhod-1 area. Obviously, it is connected with differences in a character of a “basic” surface of these two areas. Boguslawsky floor surface is complicated by with mounds and clusters of secondary crater [5] and therefore it is generally rougher than the flat mare plain in the Lunokhod-1 region.

Conclusions:

Thus, the method of slope hazard estimation by shadow area measurements presented here could be recommended for relatively flat lunar areas for which there are no hi-res DTM, but with a sufficient set of hi-res images obtained under different solar elevations.

Acknowledgements:

This work was partly supported by European Community’s 7th Framework Programme (FP7/2007-2013) under grant agreement № 312377 PRoViDE, DAAD grant № 11.9177.2014, NASA grants NNX11AK29G, NNX13AO77G, NNA14AB01A.

References:

[1] Marov M.Ya. et al., 2014. 40th COSPAR Sci. Assembly. 2–10 August, Moscow, Russia. Abstract B0.1-33-14. [2] Zelenyi L.M. et al., 2013. The 4th Moscow Solar System Symp. Abstract 4MS3-OS-02. [3] Robinson M.S. et al., 2010. Space Sci. Rev. V.150. No. 1–4. 81–124. [4] Karachevtseva I. et al., 2013. Planet. and Space Sci.V. 85, 175–187. [5] Ivanov M.A. et al., 2015. Planet. and Space Sci. In Press.

SEARCH FOR IMPACT-PRODUCED OPTICAL FLASHES AT THE MOON ALONG THE TERMINATOR

A. A. Berezhnoy[1], R. Lena[2], M. Iten[3], S. Sposetti[4], Yu. I. Velikodsky[5, 6]
[1]Sternberg Astronomical Institute, Moscow State University, Universitetskij pr., 13, Moscow, 19991 Russia;
[2]Geologic Lunar Research (GLR) Group, Via Cartesio 144, sc. D, 00137 Rome, Italy;
[3]Garden Observatory via Terriciole 15, CH-6596 Gordola, Switzerland;
[4]In Fun I Vign 7, CH-6525 Gnosca, Switzerland;
[5]National Aviation University, Cosmonaut Komarov Ave. 1, Kiev 03680, Ukraine; [6] Institute of Astronomy, Kharkiv National University, 35 Sumskaya Street, Kharkiv, Ukraine. ber@sai.msu.ru

Introduction:

We report the detection of an interesting luminous event probably generated by a meteoroidal impact on the lunar surface occurred at 21h 35m 22.871s ± ± 0.010s UT, on February 26, 2015. The luminous flash was recorded by Marco Iten with a 125 mm refractor equipped with a Watec 902H2 Ultimate videocam from Gordola, Switzerland. The second Swiss observatory was simultaneously filming the Moon but the lunar region, where the flash occurred, was outside its field of view. The third observatory in Rome (equipped with a 130 mm refractor) was not operated due to clouds. A preliminary communication about this unique was reported in [1]. The solar elevation on the impact point was determined to 0.9°, computed using the LTVT software package, developed by Mosher and Bondo [2]. Thus, the flash occurred in the dark side near the terminator.

Analysis:

The position of the flash was along the terminator at selenographic coordinates 25.73°±0.35° S, 7.82°±0.33° W, in Mare Nubium near the crater Lippershey P, located to the south of Birt crater.

We checked for artificial satellites in the field of view using the website http://www.calsky.com. The satellite Molniya 3-40 (21196 1991-022-A) was at an angular distance of 32 arcmin from the Moon center at the time of the detection. Thus, we exclude that this satellite caused the detected flash. Considering that the event was only recorded by one video camera, the possibility of a meteor “head-on” producing the recorded light cannot “a priori” be ruled out. Therefore, we tried to evaluate the post spread of light as being emitted by the ionization of the high altitude gases of our atmosphere. We got the direction of the winds and their speed using the website published by the University of Wyoming [2] from Milan (LIML) and from Payerne (LSMP), the 2 nearest stations from Iten’s observatory at 12h intervals (00h and 12h). The balloons reach about 30 km of height. At that altitude and also some kilometers higher, the direction of the winds during the time interval between Feb 26.5 and Feb 27.0 is around 270 deg and their speed from 30 to 40 knots (LIML data) and from 30 to 99 knots (LSMP data). Projecting the wind speed along the normal direction of the line-of-sight, one gets, with a conservative wind speed of 18 m s^{-1} in the interval of 6.6 s, a drift of about 350 arcsec. This is about 12 times more than the drift in East direction of the “light cloud” in the same interval. The western direction of the winds cannot explain the drift of the “light cloud” in almost a circular shape. Hence, we confidentially exclude that the drift of the “light cloud” was caused by winds at 30 km height.

For the photometry we used the star GSC 13002062 = TYC 130020621 (B 10.97; V 9.54; R 8.88). The star was visible at 20:25:20 UT. The brightness of the flash 0.16 s after the initial detection was +8.0 magV. After the main light drop a successive residual diffuse light lasted for several seconds. This post luminous event and its ever growing dimensions were likely caused by the sunlight reflection on ejected materials, released by the impact. From the very beginning of the event to +0.14 s (the first seven 20 ms field integration time) the intensity of all, or at least some, of the pixels is saturated. The peak brightness of the flash was between +5 and +6 magV, but this is a rough estimation because of the saturated pixels at that instant. The luminosity of the flash at +0.16 s (in the eight field) is +8.0 ± 1.0 magV (Fig. 1). The intensity decreases again for about a half second. From that instant on, we notice an increase in the intensity of light and also an increase of the diameter of the source.

Because of the small activity of the showers at the end of February 2015, we think of a sporadic nature of the meteor shower (V_∞ = 16.9 km s^{-1}). Using the luminous efficiency $\eta = 2 \times 10^3$ (the nominal value determined from Leonid impact flashes [3-4], e.g., the mass of the impactor would be 1.1 kg. The parameters used in the calculation are the projectile density, the target density (2,700 kg m^3), the impact velocity (16.9 km s^{-1}), the peak brightness (5.5 magV), and the flash duration (0.22 s). Based on the above data and assuming a spherical projectile, the diameter of the impactor was inferred to be approximately between 9 and about 20 cm considering a bulk density ranging between 0.3 g cm^3 (soft cometary material) to 3.7 g cm^3 (corresponding to ordinary chondrites). This impactor would strike the target with an impact energy of 1.7×10^8 Joules (4.0×10^{-8} MegaTons).

If the meteoroid is associated as a sporadic source, the impact angle is unknown. We have used the most likely angle of 45° to estimate the size of the crater produced by the impact. Using the Pi-scaled law for transient craters, the final crater would be a simple crater with a rim-to-rim diameter of about 15-20 m.

However, considering that the brightness of the detected flash was saturated and the described presence of a luminous post event, the values inferred for the mass of the probable impactor and the crater size originated by the impact could be considerably higher.

Perspectives of estimation of impact velocities of meteoroids:

One of the methods is to perform observations with interferometric filter, centered on the NaI 5890 Å line. It can be used, because the intensity of the Na line quickly increases with increasing impact velocity [6]. Observations with relatively broad filters (> 0.3 nm) are undesirable, because in this case we will detect also thermal continuum. Another possibility is to perform photometric observations in standard U, B, and V bands, because typical maximal temperature in impact-produced cloud increases with increasing impact velocity. Both proposed observational method must be calibrated during observations of strongest annual meteor showers, when the velocity of impacted meteoroids is the\ same, before performing observations during absence of strong meteor showers.

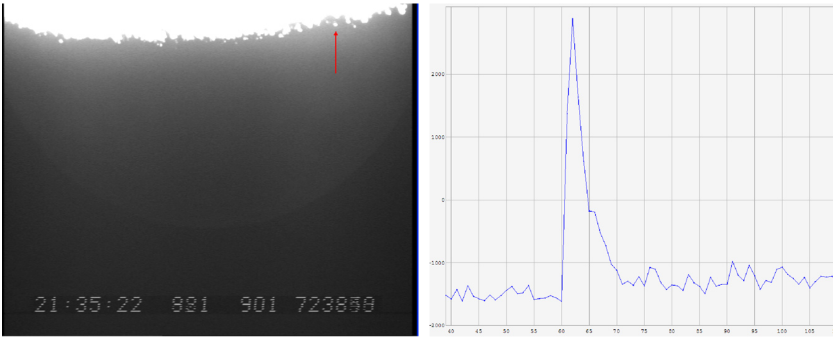

Fig. 1. (Right) Position of the initial flash in the first frame (40 ms). (Left) Lightcurve of the flash. Every dot represents 20 ms (1 field).

References:

[1] Iten M., Lena R., Sposetti S. A very interesting probable meteoroidal impact on the Moon: preliminary report, Selenology Today, Vol. 37, p. 4-11, 2015 http://www.lunar-captures.com//Selenology_Today/ST_preliminary%20report_2015.pdf
[2] Mosher J., Bondo H., 2006. Lunar Terminator Visualization Tool (LTVT). http://inet.uni2.dk/d120588/henrik/jimltvt.html
[3] Ortiz J.L., Sada P.V., Bellot Rubio L.R. et al. Optical detection of meteoroidal impacts on the Moon, Nature Vol. 405, p. 921923, 2000
[4] Ortiz J.L., Quesada J.A., Aceituno J., Aceituno F.J., Bellot Rubio L.R. Observation and interpretation of Leonid impact flashes on the Moon in 2001, Astrophys. J., Vol. 576, p. 567–573, 2002
[5] Melosh H. J., 1989. Impact Cratering: A Geologic Process. Oxford Univ. Press, New York
[6] Sugita S., Schultz P.H., Hasegawa S. Intensities of atomic lines and molecular bands observed in impact-induced luminescence, JGR, Vol. 108, Is. E12, pp. 14-1, CiteID 5140, DOI 10.1029/2003JE002156, 2003

LUNAR MASCONS HIGH RESOLUTION DENSITY STRUCTURE INVESTIGATION USING GRAIL GRAVITY DATA

J. Yan[1], Y. Zhang[1], F. Li[1], M. Ye[1],
[1]State Key Laboratory of Information Engineering in Surveying, Mapping and Remote Sensing, Wuhan University, 430070, China.
jgyan@whu.edu.cn

We proposed an inverse method including geological constraint to obtain high resolution density structure for lunar mascons using recent GRAIL gravity data. The method was implemented in spherical coordinates and validated with simulation test and test region in the Earth. Using this method and high resolution gravity data we obtained high resolution density anomaly structure of lunar nearside maria mascons basins (seven in total) and farside highland mascons (seven in total). The high resolution depth information and density anomalies structure of the lunar mascons are presented for the first time. For both nearside and farside mascon we give the density anomaly and its geometry structure. From the results we can find that the density anomaly depth of nearside maria mascon is shallower than that of the farside mascons. And both of them show smaller density anomaly near subsurface depth. The mascons structure derived from our research is different from current research, and it will provide new constraint information for lunar mascons origination investigation.

NEW FEATURES OF RADIO SCIENCE EXPERIMENTS IN RUSSIAN “LUNA-GLOB” AND “LUNA-RESOURCE” PROGRAMS

A. Kosov and IKI RAS Radio Science Team,
Space Research Institute Russian Academy of Sciences, Moscow, Russia.
akosov@iki.rssi.ru

Introduction:

Russian Luna space exploration program up to 2020 includes three missions to Moon: Luna-Glob lander, scheduled on 2018, Luna-Glob orbiter, scheduled on 2019, Luna-Resource lander, scheduled on 2020.

Currently two different radio science instruments have included into Luna-Glob and Luna-Resource projects: lander’s radio beacon and orbiter’s receiver. By means of lander’s radio beacon and orbiter’s receiver it will be possible to conduct a lot of valuable investigations and celestial mechanics experiments.

Lander’s Radio Beacon

Lander’s radio beacon have one *X* band receiver and two transmitters: *X* band and *Ka* band. The radio beacon has three main modes of operation: autonomic mode of operation, mode of coherent transponder and mode of scientific data transmitter. In autonomic mode the frequency stability of irradiated signal will be determined by the stability of internal reference source. In coherent transponder’s mode the transmitter’s signals will be locked by reference signal sending from Earth. In transmitter scientific data mode the radio beacon can transmit data to Earth’s antenna with data rate up to 0.1 Mbps. This feature is very useful when the lander will powered from nuclear power source and main radio link will be not operative.

The instrument Radio Bacon is a single box with mass about 2 kg and volume about 2 liters. There are three antennas: patch receiver antenna at frequency 7.2 GHz (*X* band), patch transmitter antenna at frequency 8.4 GHz (*X* band) and waveguide transmitter antenna at frequency 32 GHz (*Ka* band). Main beams of *X* band antennas are directed to the Earth, main beam of *Ka* band antenna is directed to zenith. In coherent transponder mode the received reference signal at 7.2 GHz is converted to transmitted signals at 8.4 GHz and 32 GHz without loss of coherency. Such type of conversion is possible by means of PLL circuits with 7/6 and 40/9 ratios for *X* band and *Ka* band frequency translation respectively. As a result frequency fluctuations of internal reference source will not affect to the frequency of transmitted signals. The instrument is capable to irradiate up to 0.5 W in each channel. The antennas gain is 5-7 dB. Polarization is circular right.

The specification of Lunar Radio Beacon is in table 1 below.

Table 1. The specification of Lunar Radio Beacon.

- Transmitted signals frequencies: 8,4 GHz and 32 GHz (coherent);
- •Frequency stability: $1{\cdot}10^{-13}$ (coherent transponder mode);
- Radiating power, W: 0.3 (for each channel);
- Receiver frequency: 7.2 GHz, (ratios 7/6 and 40/9);
- Receiver noise temperature, T_N: 200 K;
- Antennas gain and beam width: 7 dB, 120 deg. (G=0 dB) (each channel);
- Polarization: CR, (each channel);
- Power consumption, W: 7, (each channel);
- Power sources: Solar and nuclear;
- Dimensions and mass, mm and kg: 190 x 150 x 125, 2 kg;
- Autonomic mode frequency stability (OCXO BVA8607 Clock):

Integration time	Allan variance
3-30 sec:	$8{\cdot}10^{-14}$
1-300 sec:	$1{\cdot}10^{-13}$
0.1-10000 sec:	$1{\cdot}10^{-12}$
24 hours:	$5{\cdot}10^{-12}$
1 year:	$2{\cdot}10^{-9}$

- Scientific data transmitter mode:
  - Modulation, data standard: QPSK, CCSDS standard;
  - Speed of data transfer: up to 0.1 Mbps, BER≤10^{-8}, S_{Earth} ~ 1000 m²;
  - Forward Error Correction (FEC): Viterbi ½ or Turbo ½, CCSDS standard.

Luna-Glob orbiter and Ka band receiver

Ka band receiver has been included into scientific payload of the Luna-Glob orbiter. The Ka-band receiver is intended for receiving the signal from Luna's radio beacon or from Earth's transmitter for the precise measurements of Doppler shift and relative acceleration and velocity. The input 32 GHz signal is converted to low frequency, and then digitized for to calculate the frequency shift.

The instrument consists of reference oscillator OCXO BVA8607, two waveguide antennas, low noise amplifier, frequency converters, digital unit and power supply unit.

The specification of the Ka-band receiver is shown below.

- Central frequency: 32 GHz;
- Noise temperature: 150 K, or less;
- Antennas main beam direction: to nadir and to zenith;
- Beam width (G=0 dB): 120 degrees;
- Polarization type: CR;
- Bandwidth: 0.5 MHz;
- Frequency instability of local oscillators (OCXO BVA8607 Clock): like table 1
- S/N (P_{TX} = 0.5 W, ΔF=0.1 Hz, H=500 km) 40 dB
- Accuracy of *dV/dt* measurement, mGal 3

Radio Science Experiments with lander's radio beacons and orbiter's receiver

It is possible to conduct a lot of valuable measurements and radio science experiments with Lander's radio beacon and Orbiter's receiver:

1. By receiving the *X*-band signal by Earth's VLBI network it is possible to measure the Lander's position with accuracy about 10 cm.
2. Orbiter's *Ka*-band receiver can measure acceleration with high accuracy. The acceleration variations could be related to variation of Luna's gravitation field. The accuracy of measurement would be competitive with GRAIL data.
3. If two or more Radio Beacons will be deployed on Moon the SBI (Same Beam Interferometer) experiments will be possible. For SBI experiments several radio beacons on Moon surface should work simultaneously and be synchronized from a single Earth's reference source. SBI experiments allow to measure 3D displacements with accuracy about 0.1 mm. (Gregnanin, 2012). Figure 1 shows the experiments chart.

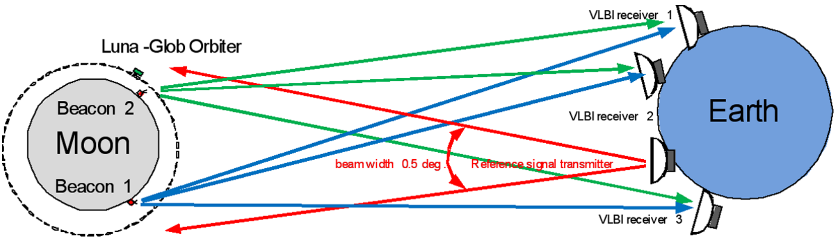

Fig. 1. Chart of celestial mechanics experiments with Luna's radio beacons.

Below there is list of possible scientific objectives for Luna investigation by radio science methods (Dehant, 2012):

- improvement of the reference frames for the Earth;
- better understanding of the Moon's interior, and in particular, through the determination of the moments of inertia of the whole Moon and of its core (inner core and outer core), the core oblateness, the free and forced librations, and the tides and their dissipation, obtain a better determination of the core radius and of the possible presence of an inner core, of the mantle mineralogies, and of the core composition, and there with better constrain the Moon's evolution;
- better determination of the parameters of General Relativity, through the values of the PPN parameters and even tests for the violations of general relativity in the context of other metric theories of gravity;
- better lunar rotation dynamics, lunar orbit, and lunar ephemeris, incorporating the numerous Newtonian perturbations as well as the much more subtle relativistic phenomena, which are all used for spacecraft missions.

References:

[1] Gregnanin, M., at al, (2012). Same beam interferometry as a tool for the investigation of the lunar interior*, Planetary and Space Science, 74,* 194–201*.*
[2] Dehant, V., at al, (2012). Geodesy instrument package on the Moon for improving our knowledge of the Moon and the realization of reference frames, Planetary and Space Science, 68, 94–104.

EVALUATION OF MINIATURIZED BROAD-BAND UV-VIS-NIR SPECTROMETERS FOR IMPLEMENTATION IN A LASER-INDUCED PLASMA SPECTROMETER FOR PLANETARY RESEARCH

S.G. Pavlov[1], S. Schröder[1], P. Thabaut[2], O. Lischtschenko[3], H.-W. Hübers[1,4]
[1]Institute of Optical Sensor Systems, German Aerospace Center (DLR), 12489 Berlin, Germany;
[2]Institute of Planetary Research, German Aerospace Center (DLR), 12489 Berlin, Germany;
[3]Ocean Optics, 6921 EW Duiven, The Netherlands;
[4]Humboldt Universität zu Berlin, 12489 Berlin, Germany.
sergeij.pavlov@dlr.de

Introduction:

Since 2012 the first laser-induced plasma spectrometer (LIBS) on an extraterrestrial platform, the ChemCam instrument, is successfully operating on board of the Martian rover “Curiosity” and delivering mineralogy data on elemental composition from the Gale crater along the rover’s traverse towards Mount Sharp. The ability of ChemCam LIBS for remote detection of targets in distances of up to 7 m has permitted the determination of soil, rock and outcrop chemistry, including the detection of very light elements such as hydrogen [1]. Such excellent data is obtained by a relatively large weight instrument (ChemCam mass ~ 9 kg) as well as the atmospheric pressure of 7-8 mbar at the Martian surface, which is close to ideal for LIBS. Several future space missions to the Moon, to asteroids and, possibly, to remotes satellites of giant planets in the outer solar system will require significant reduction in power and mass budget and the drawback of reduced plasma excitation in atmosphereless environments has to be accounted for. These constrains need to be considered for the development of a new class low-energy low-mass LIBS spectrometer for space research. Low-energy solid state lasers and different commercial and research-grade miniaturized spectrometers have been tested for their suitability to characterize geologic samples relevant for planetary research as well as several standard materials.

Experimental:

The first challenge of the LIBS miniaturization is a powerful and compact laser. In the frame of preparation for ESA’s ExoMars mission a low-energy miniaturized solid-state laser (1053 nm, ~ 3mJ per pulse, ~200 g) has been developed. We have shown previously that this laser can provide the photon irradiance sufficient for the discrimination of elements in geologic samples at low pressure conditions [2]. His twin with a tunable power option (0-3 mJ) has been used in experiments for testing the sensitivity and spectral resolution of two miniaturized grating spectrometers from Ocean Optics (USB4F05779, STSD00838) as well as one high resolution Echelle spectrometer from von Hoerner & Sulger GmbH (vH&S). A few standards, metals, relevant geologic minerals and Mars analog standards have been tested at ambient atmospheric conditions. The laser light was focused on the sample with a lens telescope on a ca. 50 mm spot, part of plasma light was guided with a 600 µm fiber into the spectrometer. The obtained spectra have been compared with those recorded from the same samples by the Aryelle Echelle high resolution spectrometer (LTB). Since no special plasma light collecting optics has been used, only a few major lines have been detected with vH&S Echelle spectrometer. High spectral resolution allows for a clear identification of elements. More compact Ocean Optics grating spectrometers have larger optical throughput and record more plasma emission lines, but closely lying lines, including doublets and triplets of atomic emission transitions, remain unresolved. Since at low pressure conditions LIBS spectra undergo significant reduction of observed lines in the plasma emission spectra, limited spectral resolution of the miniaturized spectrometers from Ocean Optics can be at least partly compensated. Nevertheless, the design of a prototype spectrometer should aim at higher spectral resolution. For low-pressure space environments, the grating spectrometers should provide sufficient spectral resolution and can win with signal throughput, necessary for expected weak intensity plasmas.

Acknowledgements:

We gratefully acknowledge Laser Technik Berlin GmbH (LTB), von Hoerner & Sulger GmbH, Laser Zentrum Hannover e.V., Ocean Optics as well as E. K. Jessberger from the **Institut für Planetologie** der Universität Münster e.V. for the opportunity of testing different optical spectrometers as well as laser systems.

References:

[1] S. Schröder, P.-Y. Meslin, O. Gasnault, S. Maurice, A. Cousin, R. C. Wiens, W. Rapin, M. D. Dyar, N. Mangold, O. Forni, M. Nachon, S. Clegg, J. R. Johnson, J. Lasue, S. Le Mouélic, A. Ollila, P. Pinet, V. Sautter, D. Vaniman "Hydrogen detection with ChemCam at Gale crater**",** Icarus **249**, 43-61 (2015).

[2] S.G. Pavlov, S. Schröder, I. Rauschenbach, E. K. Jessberger, H.-W. Hübers, "Low-energy laser induced breakdown spectroscopy for in-situ space missions to solar system bodies without atmospheres", Planetary and Space Science **71**, 57-63 (2012).

A MINIATURE LASER ABLATION MASS SPECTROMETER FOR QUANTITATIVE IN SITU CHEMICAL COMPOSITION MEASUREMENTS OF ROCKS AND SOIL ON A PLANETARY SURFACE

M.B. Neuland[1], A. Riedo[1], M. Tulej[1], K. Mezger[2], P. Wurz[1]
[1]Physics Institute, University of Bern, Space Research and Planetary Sciences, Sidlerstrasse 5, CH – 3012 Bern, Switzerland;
[2]Institute of Geological Sciences, University of Bern, Baltzerstrasse 1+3, CH – 3012 Bern, Switzerland.
neuland@space.unibe.ch

A miniature laser ablation mass spectrometer (LMS) is presented. The LMS is designed as a flight instrument for planetary and space research and optimised for in situ measurements of the chemical composition of rocks and soil on a planetary surface. By means of measurements of various standard reference materials and a sample of the Allende meteorite we demonstrate that LMS is a suitable instrument for in situ measurements of elemental and isotopic composition with high precision and accuracy. LMS measurements are carried out with high spatial resolution, lateral and vertical, which allows for quantitative analysis of the subsurface. Furthermore, it is shown that LMS data allows deriving of the mineralogy and petrography of rocky samples and the application of in situ age dating methods.

Introduction:

The chemical composition of planetary bodies, moons, comets and asteroids is a key to understand their origin and evolution [Wurz et al., 2009]. Measurements of the elemental and isotopic composition of a rock yield information about the formation of the planetary body, its evolution and processes shaping the planetary surface over time [McSween and Huss, 2010].

From the elemental composition of rocky samples, conclusions about modal mineralogy can be drawn. Isotope ratios are a sensitive indicator for past events on the planetary body and yield information about origin and transformation of the matter, back to events that occurred in the early solar system. Finally, measurements of radiogenic isotopes make it possible to carry out analyses of the age of rocks. All these topics are top priority scientific questions for future space missions to planetary bodies. An instrument for precise measurements of chemical composition will be a key element in scientific payloads of future missions carrying a lander or rover.

Instrument:

The LMS instrument combines a laser ablation/ionisation ion source with a time-of-flight mass analyser. A focused laser beam is pointed on the sample of interest, surface atoms are ablated and ionised. Electric fields guide the produced ions through the ion-optical system on the micro channel plate detector [Tulej et al., 2012]. Measurements in multiple channels with different gain levels assure a high dynamic range allowing the detection of all elements even down to tens of ppb level [Riedo et al., 2013]. Each laser shot results in a full mass spectrum from 0 to 250 amu/q. We are using a fs-laser in the near infrared with a repetition rate of 1 kHz. Together with the custom-made data recording and processing chain, this allows for very fast measurements on spots of less than 10 µm in diameter [Riedo et al., 2013b].

Measurements:

We carried out measurements on four different geological standard samples. Measurements of these samples are used to state the sensitivity coefficients of the instrument and to prove the power of LMS for quantitative elemental analyse. Fig. 1 shows the lower end mass scale of a typical spectrum on one of the standard soils USGS Cody Shale). A few major and minor elements are assigned.

For demonstration of the capability of LMS to measure the chemical composition of extraterrestrial material we use a sample of Allende meteorite. The chemical composition of different regions of interest on the sample surface was measured with high spatial lateral resolution. In total ~4’000 measurements were carried out on the CV3 meteorite with regard to mineralogical analysis of small inclusions and resolution of different regions inside chondrules.

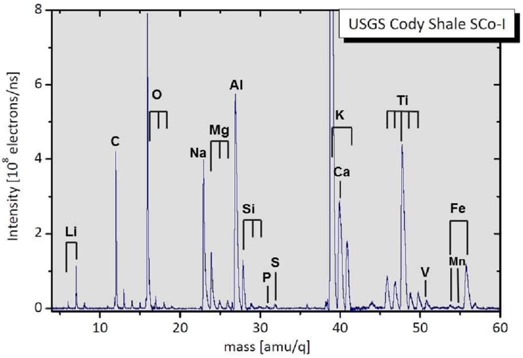

Fig.1. Section of a typical mass spectrum of USGS Sco_I Cody Shale.

Fig. 2 displays the preliminary analysis of one measurement area, where the chemical composition of 680 locations with 50 µm spacing was measured on Allende. Fig. 2a) and b) show the measured relative abundance of Fe and Mg for each single locations. Certain geometrical feature occur in both of the maps, indicated by encompassing lines. Comparing to the optical image of the same region (Fig. 2c), the LMS measurements correctly identifies two different mineral entities separated by the shown contours. Further analysis of such measurements yield detailed information about mineralogy [Neuland et al., 2014]. Investigations of layered samples confirm the high spatial resolution in vertical direction of LMS. It was found that the depth resolution on solid samples is in nm range [Grimaudo et al., 2015], which allows in situ studying of past surface processes on a planetary surface. Measurements on solid NIST samples focused on the analysis of Pb and application of the $^{207}Pb/^{206}Pb$ system for age determination. With the measured correlation between isotope abundance and relative accuracy, an estimate was derived for the uncertainty of the radio-isotope chronology. It results that the statistical uncertainty for the age determination by LMS is about ±100 Myrs, if abundance of ^{206}Pb and ^{207}Pb is 20ppm and 2ppm respectively. For comparison: in lunar KREEP these Pb isotopes have abundances of tens to hundreds of ppm [Riedo et al., 2013c].

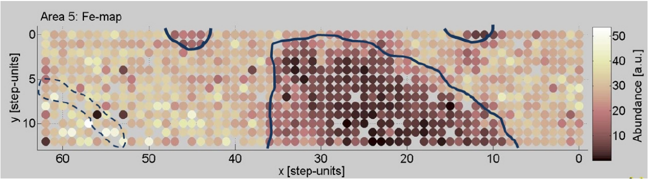

(a) Fe-abundance

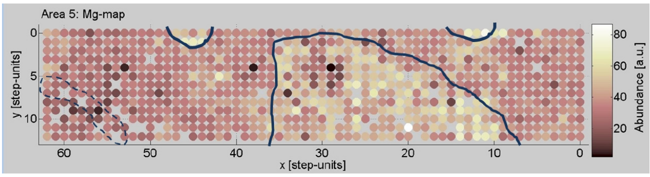

(b) Mg-abundance

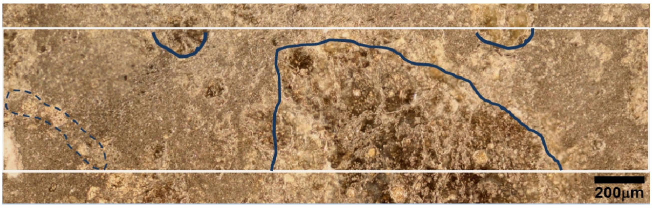

Fig. 2. LMS measurements of Fe (a) and Mg (b) on a sample of Allende mete-orite. The contours found in the element mas agree with a feature also found in the optical image (c) of the same region.

Summary:

We present a miniature laser ablation mass spectrometer for planetary and space research. We established the measurement capabilities of LMS for petrographic and mineralogical analyses, for isotopic studies and dating analyses, which are key topics for future space missions to moons, planets or asteroids. Having the LMS instrument installed on a rover would allow measuring the chemical composition of many rock and soil samples, distributed over a certain area on the planetary surface. LMS measurements would yield valuable conclusions about age and mineralogy.

References:

[Wurz et al., 2009] P. Wurz, J.A. Whitby, G.G. Managadze, *Mass Spectrometry in Planetary Science*, AIP Conf. Proc. CP1144 (2009) 70-75

[McSween and Huss, 2010] H. Y. McSween Jr.Jr., G. R. Huss, *Cosmochemistry*, Cambridge University Press, 2010.

[Tulej et al.,2014] Tulej, A. Riedo, M.B. Neuland, S. Meyer, P. Wurz, N. Thomas, V. Grimaudo, P. Moreno García, P. Broekmann, A. Neubeck, M. Ivarsson, 2014, Geostand. Geonana. Res. 38(4): 441-466.

[Tulej et al.,2012] M. Tulej, A. Riedo, M. Iakovleva, P. Wurz, 2012, Int.J.Spec., Article ID 234949.

[Riedo et al., 2013a] A. Riedo, A. Bieler, M. Neuland, M. Tulej, P. Wurz, 2013, J.Mass Spectrom.48(1):1-15.

[Riedo et al.,2013b] .A. Riedo, M. Neuland, S. Meyer, M. Tulej, P. Wurz, 2013, J.Anal. Atom.Spectrom. 28(8): 1133-1356.

[Riedo et al.,2013c]A. Riedo, S. Meyer, B. Heredia, M.B. Neuland, A. Bieler, M. Tulej, I. Leya, M. Iakovleva, K. Mezger, P. Wurz, 2013, Planet. Space Sci. 87: 1-13.

[Grimaudo et al.,2015] V. Grimaudo, P. Moreno-Garía, A. Riedo, M.B. Neuland, M. Tulej, P. Broekmann, P. Wurz, 2015, Anal.Chem. 87: 2037-2041.

[Neuland et al.,2014] .M.B. Neuland, S. Meyer, K. Mezger, A. Riedo, M. Tulej, P. Wurz, 2014, Planet.Space Sci. 101:196-209.

LUNAR SEISMIC NOISE: NEW ASTROPHYSICS PERIODICITY & NEUTRINOS

O.B. Khavroshkin, V.V. Tsyplakov
Institute of Physics of the Earth, Russian Academy of Sciences.
khavole@mail.ru

Unaddressed existence of extraterrestrial sources of high energy neutrinos was discovered in 2013y. But the most promising addition to supernovae includes objects such as pulsars and closes multiple systems. Relying mainly on its own experience in the search and registration of the seismic response at frequencies of pulsars and close binary stars on Earth and the Moon and using the results to detect solar neutrinos work on the study of modulated neutrino fluxes were continued. The study of the spectra of lunar seismic noise revealed a number of significant spectral peaks that match the frequency to 3-4 significant figures with the frequencies of sending energy pulses from pulsars. At the same time availability of seismic peaks and their characteristics are strongly associated with the shape and depth of the radioactive geological structures of the lithosphere of the Moon. That is the energy of interaction modulated beam of neutrinos from the pulsar radioactive elements Moon differently converted into energy of seismic noise. There have also been recorded seismic peaks well coincides with the period of close binary stars. Some of the peaks previously registered not only as a purely seismic frequency, but as the frequency inherent to radioactive laboratory sources, which further confirms their astrophysical neutrino origin and similarity search became part of high-energy neutrino astronomy.

SOME OBJECTIVES OF THE STUDY AND EXPLORATION OF THE MOON

M.I. Shpekin[1], A.A. Barenbaum[2], Ch.R. Mukhametshin[1]
[1]Kazan Federal University, Russia, Kazan, Kremlevskaya str. 18.
MichaelS1@yandex.ru
[2]Oil and Gas Research Institute RAS, Russia, 119333 Moscow, Gubkin str. 3.
azary@mail.ru

Introduction:

Analysis of the works of recent years shows the revitalization of lunar research which focused on the practical use of the lunar territory. Surprising experiments of Japanese scientists, impressive flights of Chinese and Indian satellites, as well as new American orbital studies dispatch to study the Moon all the power of modern science and technology. Russia is also preparing to send to the Moon orbital and landing spacecrafts. Such a "universal" interest to the Moon research raises the question of priorities. In our report we consider only certain aspects of lunar research which could, according to the authors, contribute to the selection of most perspective goals and tasks.

The first stage of Space Research of the Moon, known as the "Moon Race", brought invaluable experience for researchers. Over the past half century, a considerable part of the results were analyzed by experts. The second stage of Moon studies, in which many countries are participants, occurs today. At this stage the tasks of further planned and scientifically sound study of our natural satellite coming to the fore.

Of course, first of all there is the question of priorities, goals and objectives of the research and expected results. What directions of lunar exploration will bring the greatest results? The decision of what problems associated with the Moon and the Earth-Moon system, the greatest efforts should be directed? What areas of the lunar territory require study in the first place? Finally, what role in study of the Moon should the automatic vehicles and manned spacecrafts play?

All of these questions need serious scientific study and a thorough discussion of relevant specialists. It can safely say that this is a classic example of the broad international cooperation.

Our results:

The authors have already made their proposals on these issues in the reports and speeches and published their findings in domestic and foreign editions. In particular, we presented them to the European Symposium of the Moon in Berlin and at the World Congress MFNA in Greece. These results are also published in international scientific journals "Problems of nonlinear analysis in engineering systems."

Our offers relate to the application of orbital shooting in high resolution, tasks of lunar navigation as well as problems of internal structure of the Moon. Some of them are considered in the report.

Despite the efforts of domestic and foreign experts, the problem of constructing unified selenocentric system of coordinates is still not resolved. If the visible side of the Moon, to some extent is provided by the coordinate system, then the opposite hemisphere as well as Polar Regions are not sufficiently studied.

Another important direction is the study of areas of endogenous activity on the Moon. Today there are at least three such areas and all three were found by Soviet and Russian researchers.

One of these areas was discovered by us in 2009 and thoroughly surveyed in Tsiolkovsky crater on the far side of the Moon. To the north-east of the central peak of the crater, we found a small volcano located on plume foundation. Emissions of the material in the central part of the foundation, in our opinion, caused by the presence under bottom of this young impact crater the magma chamber. In other impact craters previously no one had observed similar formations.

Another important phenomenon is the "glacier's tongue» which coming down, from the south-western slope of the central peak to the crater bottom. We found analogous "tongue" in the Aitken crater. These formations are very similar to mountain glaciers on the Earth, and therefore we can assume that they contain a significant amount of water ice.

Conclusion:

Available data indicates that the surface of bottom craters Tsiolkovsky and Aitken is very young.

Craters Tsiolkovsky and Aitken in our opinion are the most suitable candidates as promising regions of research. This applies to the orbital observations as well as experiments with involving the lander. In addition, the bottom of craters, their central peaks and glacial tongues may be interesting objects not only to accommodate the penetrators, first proposed in the project “Luna-Glob”. But they are the places on the Moon where it would be appropriate to start drilling wells.

It can be expected, that the study of large impact craters will let shed light on the other “global issue” connected with the origin of the craters with a diameter of more than 10 km. The density of such craters on the lunar continents has an exponential distribution of diameters. The same distribution is visible among large craters on Mercury and Mars. In this regard the question arises of the reasons for the similarity in the distribution of large impact craters on different planets, as well as nature cosmic bodies the fallings of which their created.

Thus, studies of young impact craters on the Moon can provide a major breakthrough in the fundamental knowledge about the origin and evolution of the moon and other planets of the solar system. This is the major purpose for which it is necessary to contrive all space experiments.

TWO-WAY LUNAR RADIO RANGING AND PRELIMINARY RESULT FROM CE-3 MISSION

J.S. Ping[1,3,5], Q. Meng[2], G.Y. Wu[3], W.X. Li[1,5], M.Y. Wang[1], C.Y. Chen[2], T.Y. Zhang[2], Z. Wang[1,4]
[1]Key Lab. of Lunar and Deep Space Exploration Research, National Astronomical Observatory of CAS, Datun Rd. 20A, Beijing, China;
[2]Dongnan University, Sipailou, Nanjing, China;
[3]State Key Laboratory of Astronautic Dy-namics, Xi'an, China;
[4]Xinjiang Astronomical Observatory, Urumqi, China; 5Beijing Normal University, Bei-jing China.
jsping@bao.ac.cn

Introduction:

Radio science experiments have been involved in all of the Chinese lunar missions with different research objectives. In Chang'E-3 landing mission, a 2- and 3-way lunar radio total-count-phase ranging and Doppler technique was developed and tested at X-band of 8470MHz by radio science experiment team of Chinese lunar and deep space mission. The technique concept is originally coming from descanso.jpl.nasa.gov/monograph/series1/Descanso1_C03.pdf. Figure 1 shows the structure and antenna config-uration of Chang'E-3 lander. This method, called Lunar Radio-phase Ranging (LRR) can become a new space geodetic technique to measure the station position, earth tide and rotation, lunar orbit, tide and liberation, by means of independent observation, or to work together with Lunar Laser Ranging. Also, it can be used in future planetary lander mission.

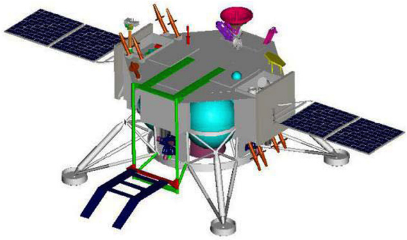

Fig. 1. Configuration of CE-3 lander: the red parabolic high gain antenna works at X-band for up and down link in the radio ranging experiments.

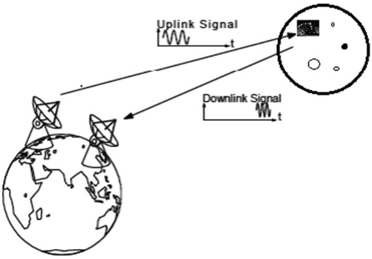

Fig. 2. Open-loop 2- and 3-way radio link concept between the Earth and the Moon.

Experiments:

In the preliminary experiments, an up link deep space tracking station at JIAMUS of northeast of China, for VLBI antenna of Chinese VLBI network joined the observation. Figure 2 shows the open loop 2- and 3-way radio link concept. All stations are equipped with H-maser clock. For the 3-way link, we obtained 1sps continu-ous total-count-phase ranging data on the successful landing day and in the extended mission period, with a reso-

lution of 0.5 millimeter or better. However in the 3-way only range and range-rate measurements, the tiny bias and slow drift between H-masers of uplink station and VLBI stations mixed in the observables terribly, and even till today we are still trying different ways to separate this kind of systematical errors from the geometric infor-mation. The best way is carrying out the 2-way close loop observation at the same period, and comparing the clock bias and drift between two stations using independent way. It will be a very complicated work in this new kind of space geodetic method. Here we only show the first result from a 2-way observation only.

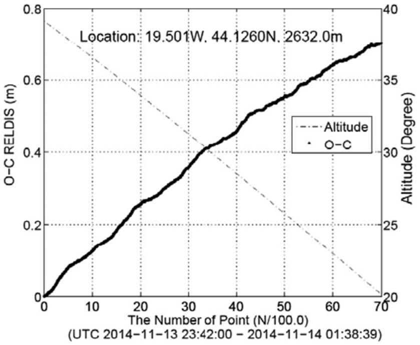

Fig. 3. An example of O-C for 2-way radio phase ranging by JIAMUSI station (thick black solid line) with a coarse coor-dinate for lander. Dash-line is the elevation angle seeing from station.

Figure 3 shows an example of O-C for 2-way radio phase ranging by JIAMUSI station. The observation was carried out from UTC 23:42:00 of Nov. 13 to 02:28:40 of Nov. 14, 2014. A lander position of (19.501°W, 44.126°N) was used to calculated the theoretical ranging with a model resolution or accuracy of 0.5mm. Also, a LE430/DE430 (ftp://ssd.jpl.nasa.gov/pub/eph/planets/ascii/de430) lunar and planetary ephemeris with principal axes for the Moon was adopted to calculate the lunar orbit, physical liberation and lunar lander position using the latest IERS standard.

Data Processing:

When processing the data, we also followed the idea of LLR technique of re-jecting the low elevation angle (<20°) measurement, where the non-linear large atmospheric and ionospheric delay below this truncate angle over the station might destroy the precise estimation. Also we calculated the atmospheric de-lay series by using a Saastamoinen-NMF model based on the metereologi-cal data recorded at the ground station during the tracking period. Additionally, an IONEX GIM global ionospheric TEC product released by IGS-GNSS of IERS was used to calculated the ionospheric delay between the ground station and lander. After carefully removing the media effects, the position of lander was es-timated with some fixed parameters, EOP from IERS products, lunar libera-tion fromLE430/DE430, solid earth tide model of the ground station from IERS stan-dard. The estimated coordi-nates for lander position are read as 19.50456°W and 44.1210°N with a fixed radii of 1734.7680km at landing area. Here, the radii value was calculated from LOLA/LRO DEM model. The radii will be estimated in the fu-ture based on multi epoch data.

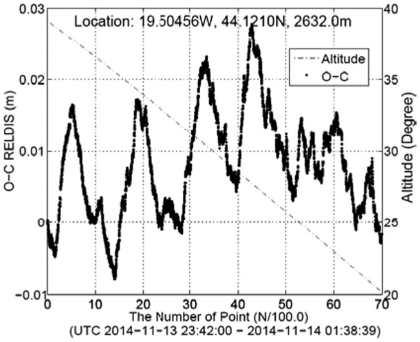

Fig. 4. residual of the 2-way Ranging for Figure 3 after fitting the landing position.

The final fitting residual for the 2-way relative ranging is given in Figure 4. The residual series show wave-like variation with time scale of 5~20 minutes, and amplitude range of 18mm for 2-way or 9mm for 1-way in line-of-sight direc-tion. Similar characteristic also was found at low frequency band. It is mainly come from the atmospheric disturbance, and can be removed by introducing a low pass filter in data analysis. An arc-like drift still appears in the residual figure, which may come from underestimation data analyzing method. This problem will be solved in the near future by processing the multi epoch observation data.

Acknowledgement:

This work is supported by CE-3 lunar lander mission, by the national key basic research and development plan (Grant No. 2015CB857101), and by the State Key Laboratory of Astronautic Dynamics.

HEXAGONAL FIGURES IN SATURNIAN SYSTEM AND ON CERES

G.G. Kochemasov;
IGEM of the Russian Academy of Sciences, 35 Staromonetny, 119017 Moscow.
kochem.36@mail.ru

Introduction:

A significant structural similarity between gaseous giant Saturn and its small icy satellites is observed in respect of very prominent geometric figures on their surfaces. Famous saturnian "hexagon" is repeated on small icy satellite surfaces constantly. A wave origin of observed tectonic similarities in celestial bodies of various sizes and compositions is most probable. Ceres images demonstrate crossing lineaments making hexagons of various sizes.

Results and discussion:

Several examples of well studied cosmic bodies revealed their peculiar tectonic characteristics. The gaseous giant Saturn shows some tectonic and geomorphologic features that repeat themselves at their small companions – satellites. The latter except much smaller sizes normally have differing overall compositions and much smaller inner energy. It implies that certain outer forces act upon these planetary twins. We recognize them as inertia-gravity forces rising in bodies due to their movement in keplerian non-circular orbits with periodically changing accelerations [1]. They produce warping body crossing and interfering waves having a standing character and harmonic lengths. The fundamental wave 1($2\pi R$ long) produces the first Plato's polyhedron (tetrahedron, Fig. 9-10). The first overtone wave 2 long πR produces an octahedron. Structural intersecting lineations of three directions mark orientation of tetrahedron facets. They intersect and make often seen hexagon outlines (Figs. 1-8). Figs 7 and 8 image certain portions of the dwarf planet Ceres clearly showing intersecting fine ripplings reflecting the polyhedron facets and making "hexagons". **Conclusion:** The observation of impressive parallels of important tectonic and morphological features on surfaces of the gaseous planet and its solid satellites (Saturn – icy satellites) proves that for this phenomenon are responsible outer structuring forces. They are recognized as orbital forces due to celestial bodies movement in keplerian orbits. The observations make dubious some planetologic and geologic tectonic hypothesis such as plate tectonics and importance of the earlier giant impacts.

References:

[1] Kochemasov, G.G. 1998. Tectonic dichotomy, sectoring and granulation of Earth and other celestial bodies. Proceedings of the International Symposium on New Concepts in Global Tectonics, "NCGT-98 TSUKUBA", Geological Survey of Japan, Tsukuba, Nov 20-23, 1998, p. 144-147.

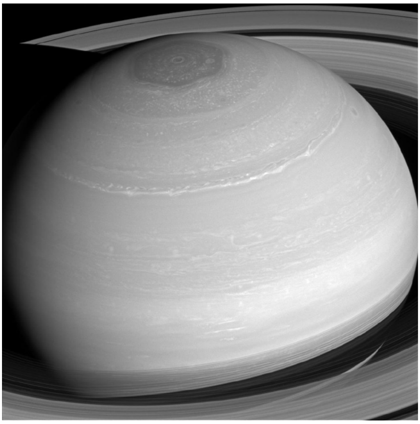

Fig. 1 Saturn, PIA18280, R=60000 km

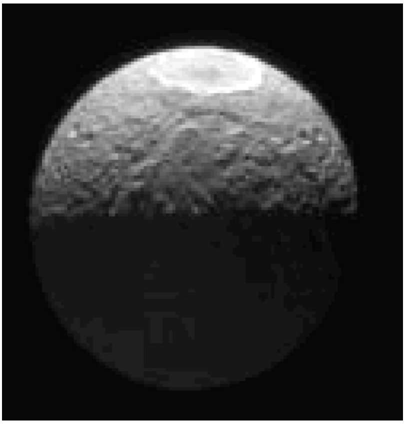

Fig. 2 Mimas, PIA09811, R=197 km

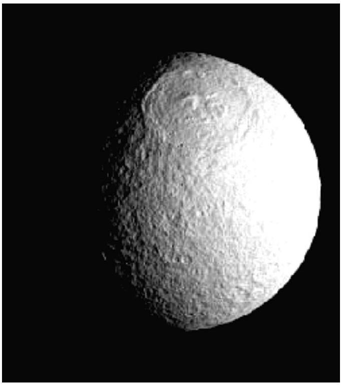

Fig. 3 Tethys, PIA10438, R= 524 km

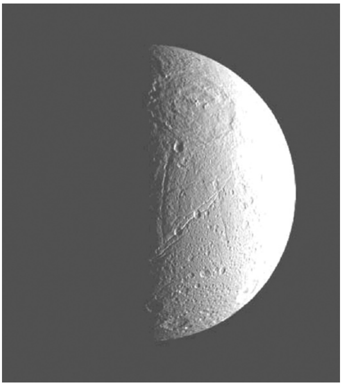

Fig. 4 Dione PIA08938, R= 559 km

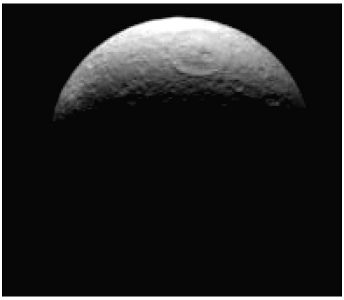

Fig. 5 Rhea, PIA08909, R= 765 km

Fig. 6 Iapetus, PIA08273, R=718 km

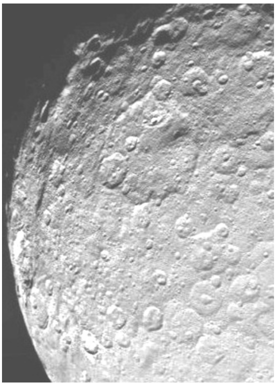

Fig. 7. (left) Ceres. A portion of PIA19542_hires_modified. Intersecting fine ripples and formation of "hexagons".

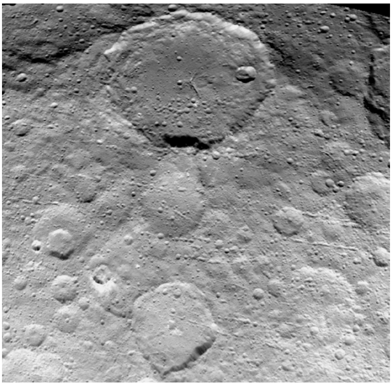

Fig. 8. Ceres from distance 5100 km. May 23, 2015. Coordinates: 13-51˚ N, 182-228˚ E. pia19065-1041. Credit: NASA/JPL-Caltech/UCLA/MPS/DLR/IDA

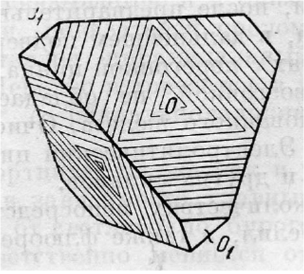

Fig. 9.

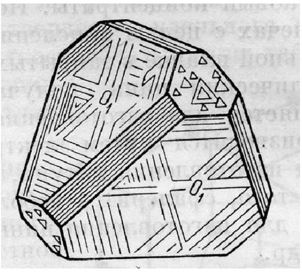

Fig. 10.

Fig. 9, 10. Tetrahedron crystals (sphalerite) with lineations of three directions reflecting orientation of facets (compare with lineations on Ceres' surface).

THE EVIDENCES OF LATITUDINAL ASYMMETRY OF THE AMMONIA ABSORPTION ON SATURN

V.G. Tejfel, A.K. Karimov, N.N. Bondarenko, G.A. Kharitonova, Fessenkov
Astrophysical Institute, Almaty, Kazakhstan, (tejf@mail.ru)

450 zonal CCD-spectrograms, recorded by scanning the disk of Saturn during its equinox at the beginning of 2009, were processed to find the variation of the absorption band of ammonia NH_3 647 nm. This band overlaps with the short-wavelength wing of the absorption band of methane CH_4 667 nm, therefore, to highlight the ammonia absorption spectra were used Uranus and laboratory spectra of methane. It was found that ammonia absorption is enhanced in the northern hemisphere of Saturn, as well as relatively weak bands of methane in contrast with stronger CH_4 bands [1]. It may indicate on the North-South asymmetry in the density of the deeper parts of the ammonia cloud layer of Saturn .

Introduction

The ammonia absorption bands in the visible part of the spectrum of Saturn is much weaker than that in Jovian spectra (Figure 1-Left). They overlap with bands of methane and the selection ammonia absorption so is quite complicated. This research was directed to identify possible latitudinal variations of the NH_3 absorption Saturn in the equinox 2009 period when both hemispheres of the planet are in equal conditions of lighting and visibility.

Observations and processing

In early 2009 the observations of Saturn were carried out with 0.6-m telescope and diffraction spectrograph SGS . For one night 5-6.01.2009 at the Earth saturnocentric declination -0.8 deg there were recorded 5 series of zonal CCD-spectrograms by scanning the Saturn disk from the south pole to the north. Each scan consisted of 70 spectrograms, so that were received and processed 450 spectra corresponding all latitudinal zones of the planet (Figure 1-Right). To extract the absorption band NH_3 647 free of ammonia absorption spectra of Uranus, Saturn's rings were used as well as the calculations based on the laboratory spectra of methane absorption [2]. .As a result of the spectrograms processing and analysis the atlases pf spectral ratios of individual zones of Saturn's disk to the region in the equatorial zone of the planet were prepared. We also calculated the pairwise spectra ratios for symmetric zones of the northern and southern hemispheres.

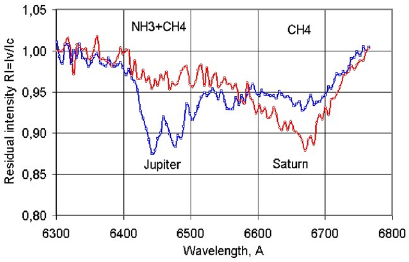

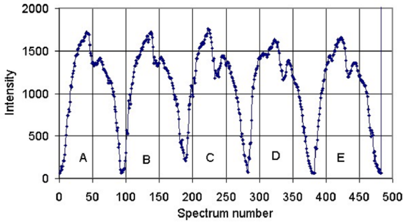

Fig. 1. Left: The absorption NH_3+CH_4 band in the spectra of Jupiter and Saturn. Right: The intensity south-north profiles pf Saturn's spectral scans.

The hemispheric differences of the NH_3 absorption

Analysis of all graphs atlas shows that absorption in the band NH_3 647 nm is enhanced in the northern temperate latitudes in comparison with the southern temperate latitudes (Figure 3-Left). The methane absorption in relatively weak bands is also increased in the northern hemisphere, but the ratio of residual intensities RI647 / RI675 in the northern temperate zone is some smaller than in the southern temperate zone. This means an increasing of the NH_3 absorption in northern hemisphere. The ratio of latitudinally averagedon profiles of the absorption bands for the southern and northern hemispheres (RIn / RIs) shows the same result (Figure 2-Right). Although the depth of the ammonia absorption band is considerably less than the depth of long-wave part of the CH_4 band 2t is seen that this ratio for NH_3 band indicates a greater difference than the ratio in the region of the pure methane absorption.

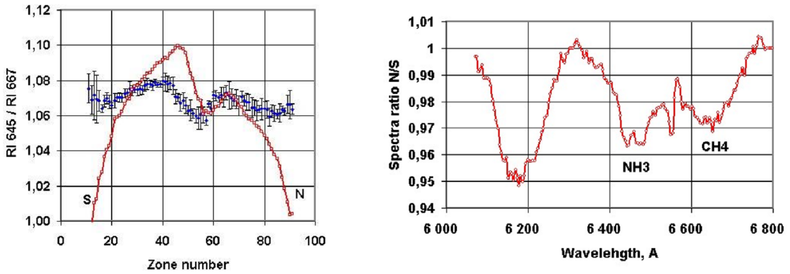

Fig. 2. Left: The S-N zonal variation of the residual intensities at 645 and 667 nm ratio. Right: The ratio N/S for latitudinally averaged band profiles

Conclusion

The results show that the increased NH_3 absorption in Saturn's northern hemisphere coincides with the increase of relatively weak CH_4 absorption bands, observed also in the northern hemisphere. At the same time stronger absorption band of methane, for example, 725 nm band, the similar hemispheric difference is not detected. This may be due to a decrease of the volume density and the aerosol scattering coefficient on the large effective optical depths by raising the temperature. In the upper part of the cloud cover the difference in density of the cloud layer apparently absent or much less pronounced. The temperature measurements in the upper troposphere Saturn at the pressure of about 500 mb [3] shows a even decrease in the northern hemisphere, as compared with the south temperate latitudes.

References

[1]. Tejfel V.G. , Karimov A.M., Kharitonova G.A., Kirienko G.A ,Vdovichenko V.D. The hemispheric differences in the methane and ammonia absorptions on Saturn near last equinox in 2008-2010 .Bulletin AAS,Vol.. 42. - P.1021. , 2010
[2]. Dick, K. A.; Fink, U. Photoelectric absorption spectra of methane CH4, methane and hydrogen H2 mixtures, and ethane C2H6 J. Quant. Spectrosc. Radiat. Transfer, Vol.. 18, P. 433-446 ,1977.
[3]. Fletcher, L.N., Achterberg, R.K., Greathouse, T.K., Orton, G.S et al. Seasonal change on saturn from Cassini/CIRS observations, 2004–2009. Icarus, Vol.208 PP. 337–352, 2010.

THE STUDY OF METHANE-AMMONIA ABSORPTION ON JUPITER IN THE VISIBILITY SEASON OF 2015

V.D. Vdovichenko, G.A. Kirienko, P.G. Lysenko
Fessenkov Astrophysical Institute , Almaty, Kazakhstan.
vdv1942@mail.ru

The problems of selection of the ammonia absorption bands in the near infrared region of the spectrum against the background of the methane absorption bands in the atmosphere of Jupiter are discussed. Special features of the methane and ammonia absorption variations along the equator, STrZ and the central meridian of Jupiter at the time of the Great Red Spot (GRS) passage are given.

Introduction

Methane and ammonia play an important role in the optical and dynamic processes in the atmosphere. The methane absorption bands between 0.6 and 1 μm are widely used to probe Jupiter's atmosphere, because they give an information about different levels (depths) of the atmosphere (from 50-200 mb in the 889 nm band to 10-20 bar in the 619 and 705 nm bands). In [1,2], during a similar research of the GRS and neighboring cloud belts, we have identified for them some basic optical characteristics, and it has been shown that the Red Spot is the highest aerosol formation, located at 10-12 km above the STrZ and at 5-7 km above the equatorial zone EZ. Ammonia in the upper atmosphere (above 0.5 bar) goes into the solid phase, forming some bright crystal clouds below which ammonia's relative concentration is gradually increased up to the 7 bar level, undergoing complicfted spatial variations. In this regard, it is interesting to follow a behavior of ammonia absorption characteristics of the Jovian disc and compare it with a methane one.

Observations

The observations were carried out in 2015, on 5-6-7 of February, during the Jupiter confrontation. The RC-600 telescope with the SGS spectrograph and ST-7XE CCD camera were used. The spectral resolution was 0.43 nm per pixel. The spectra of EZ, NEB, SEB, NTrZ, STrZ and the central meridian, at the time of the GRS passage through it and without GRS on it, were recorded. To identify the methane and ammonia absorption band profiles, all the spectra were related to the reference spectrum containing the telluric bands corresponding to the zenith distance that had been equal to Jupiter's one. The 645 and 790 nm ammonia absorption bands are blended with the methane ones. To isolate them (to show their true forms) we used the technique described in [3,4]. For the 645 nm band we only drew the level of the continuous spectrum between the absorption band wings (Fig. 1a).The band center was averaged within the 643-651 nm interval. We took a ratio of the 790 nm complex (CH_4 + NH_3) absorption band profile to the same band profile for Saturn, where the ammonia band is practically absent because of going into the solid phase almost all the gaseous ammonia. Figure 1c shows that band's profile in the form of residual intensities (B) in the Jupiter disc center and the CH_4's one – in the Saturn disc center; Fig. 1a,b shows the "red" ammonia spectrum derived from their relationship.

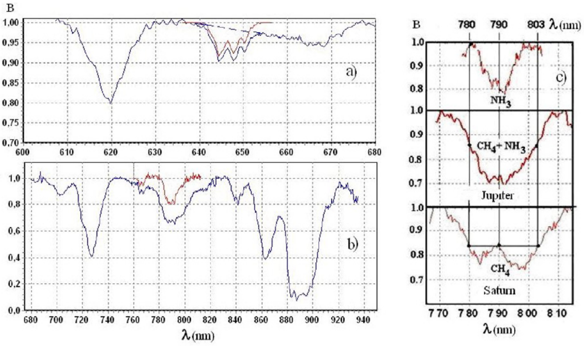

Fig. 1. CH_4 and NH_3 absorption band profiles for Jupiter disc center.

Interpretation

It is difficult to compare together the variations of absorption band depths as well as their equivalent widths with a traditional technique because of large differences in the intensities of the studied absorption bands. In our opinion, a more clear picture there give variations of the absorption band residual intensities (B_υ), which can be represented as $B_\upsilon = I_\upsilon / I_c \sim \exp(-\tau_M)$ for methane or $\sim \exp(-\tau_A)$ for ammonia, where τ_M and τ_A can be considered as some function that is proportional to the product of the absorption coefficient by the number of absorbing gas molecules on the line of sight.

Finding the logarithm of the residual intensity distribution over the disc of the planet, we get variations of τ_M or τ_A course in different absorption bands. The results presented in this way, give more adequate information about the absorbing gas abundance variations over the planet's disc on the line of sight (Fig. 2).

Figure 2 clearly shows that the variation of absorption along the equatorial zone in the 619, 725, 803, 861, 889 nm methane absorption bands are qualitatively well described with the two-layer model consisting of the scattering- absorbing homogeneous cloud layer and a pure gaseous atmosphere above it.

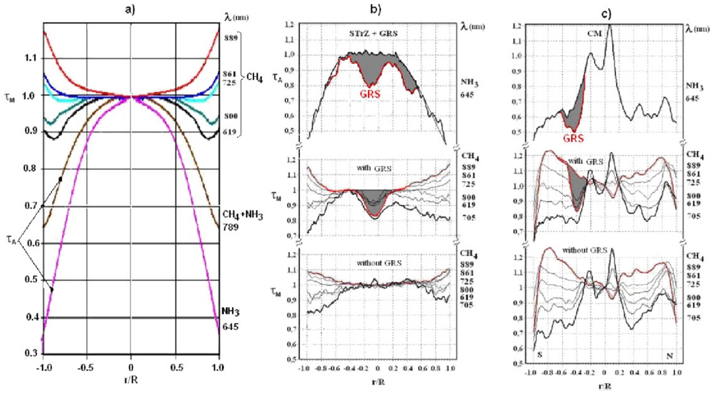

Fig. 2. The cource of τ_M (methane) and τ_A (ammonia), standardized to the center of the disc, on the line of sight along the bright equatorial zone EZ (a), along the STrZ (b) and along the central meridian (c).

In the region of GRS, at the time of its passage through the central meridian, a noticeable decrease of the absorption both in the methane and ammonia bands can be seen (Fig. 2c).

Unlike the methane, absorption course in the 645 nm ammonia band along the equator can not be described with as the two-layer model, or even with as the only scattering-absorbing layer with the scattering function asymmetry parameter g in the range of 0 - 0.75. It is not excluded that the 645 nm ammonia absorption band, because of going into the solid phase almost all the gaseous ammonia in the atmosphere above the clouds and near the upper boundary of the cloud cover, gives an information about the lower part of the cloud layer that can be represented as a diffuse haze having a spherical scattering function.

Conclusion

The research of the course of ammonia absorption over the Jovian disk indicates a complex and changeable structure of the 2nd and 3rd cloud layers, and also confirms the results of [5.6] about a lower ammonia abundance that is observed in the GRS region.

References

[1] Vdovichenko V.D., Kirienko G.A. Atmosphere of the Jupiter. Great Red Spot. LAP LAMBERT Academic Publishing 2014. ISBN: 978-3-659-63264-8. 275 p. (in Russ)
[2] Vdovichenko V.D., Kirienko G.A., Lysenko P.G., Tejfel V.G. The particularities of Jupiter's Great Red Spot in the methane absorption band //Izvestiya NAN RK- 2014.- №4.- p.77-84. (in Russ)
[3] Vdovichenko V.D., Kirienko G.A.,Tejfel V.G., Haritonova G.A. Dramatic events on Jupiter in 2009-2011 // Izvestiya NAN RK- 2012.- №4.- p.58-62. (in Russ)
[4] Tejfel V.G., Vdovichenko V.D., Kirienko G.A, Kharitonova G.A. Spectrophotometric study of the changes on Jupiter in 2009-2011 //44-th Lunar and Planetary Sci. Conf.,

2013, Abstr. No 1205, 2 PP.
[5] West, R.A.; Baines, K.H.; Friedson, A.J. et al (2004). “Jovian Clouds and Haze” In Bagenal, F.; Dowling, T.E.; McKinnon, W.B. Jupiter: The Planet, Satellites and Magnetosphere. Cambridge: Cambridge University Press.
[6] Fletcher L. N., Orton G. S., Mousis O., et al. Thermal Structure and Composition of Jupiter’s Great Red Spot from High-Resolution Thermal Imaging //Icarus 2010. 208. P. 306–328.

CAPTURE OF MATERIAL BY THE CIRCUMPLANETARY DISKS OF JUPITER AND SATURN DUE TO INTERACTION OF THE FALLING PLANETESIMALS WITH THE GASEOUS MEDIUM OF THE DISKS

V. A. Kronrod[1], A. B. Makalkin[2],
[1]Vernadsky Institute of Geochemistry and Analytical Chemistry, RAS;
[2]Schmidt Institute of Physics of the Earth.
va_kronrod@mail.ru

Introduction:

Space missions "Galileo" and "Cassini–Huygens" have enabled substantial refinements of the data on the morphology of the icy moon surfaces, their physical characteristics, data on the gravitational, magnetic and thermal fields. Based on the observational, analytic and numerical information, the models of the internal structure of Ganymede, Callisto and Titan have been constructed [1–3]. There is a good reason for believing that the degree of differentiation of the icy moons depends on the specific features of their formation: the accretion rate and masses of planetesimals falling on the moons, the mass distribution and composition of the planetesimals.

Disk model:

According to the model of a low mass (gas starved) circumplanetary accretion disk, dust particles and small bodies at any given time contain only ~10^{-3}–10^{-2} of the total mass of regular satellites [4–7]. The disk in the model is a species of an accretion gas-dust disk. The model suggests that the mass needed for satellite formation is accumulated gradually through capture of the solid particles and bodies by gravitational field of the central planet and gas drag in the disk.

Problem:

Here we consider the problem of interaction of the circumplanetary disk and solid bodies (planetesimals) falling onto the disk. We surmise that solution of the problem will allow estimation of the masses and composition of bodies that fell on the growing icy moons. This would provide explanation of the differences in the mean density and internal structure of icy moons of Jupiter and Saturn. The multiparameter problem of gas drag, fragmentation and ablation of planetesimals in the gas medium of the circumplanetary disk is solved by a modified approach of the meteor physics. The equations of motion and mass loss due to ablation are written as in [8]. The problem of fragmentation of a planetesimal, passing though the gaseous disk, in response to aerodynamic load is solved in the framework of the known models of fragmentation of a meteorite during atmospheric entry.

Results and discussion:

We simulated passing planetesimals through the circumplanetary disks of Jupiter and Saturn and capture of their material into the disks with consideration of combined processes of aerodynamic braking, fragmentation, and ablation of planetesimals in the disk's gas medium. Below are the results of simulation for the comet material of the planetesimals. We estimated maximum planetesimal size (radius $R_{1,max}$) which the body should have at the entrance to the disk in order to stay in the disk after loosing mass and velocity due to gas drag and ablation. The maximum radius of captured planetesimal $R_{1,max}$ is obtained as a function of distances from the central planet. Ablation coefficient (σ_{abl} =10^{-13} c^{2}cm^{-2}) is taken from [9]. For the planetesimals with radii R> $R_{1,max}$, which were able to escape the disk, the velocities at the exit after crossing the disk should be higher then the escape velocity from the Hill (gravitational) sphere of the planet.

We estimated the ratio (M^o_a=M_a/M_f) of the mass of solid material, lost by the falling bodies through ablation and thus captured by the disk (M_a), to the total mass of the falling bodies (M_f) with R> $R_{1,max}$ (Fig.1). This ratio depends on the maximum value in the mass distribution of falling bodies M_M which is an input parameter of the model. Another input parameter is the exponent q≈1.8 in the power-law mass distribution for planetesimals [10] which move in the vicinity of a giant planet and fall onto its circumplanetary disk: $n(M)dM=cM^{-q}dM$, where $n(M)dM$ is the number of bodies (in the unit volume) with masses in the interval (M, $M+dM$). In the results presented here we adopt for the largest body (with mass M_M) the radius R_M = 1000 m.

We also estimated the ratio $M^o_{ca}=(M_c+M_a)/M_t$ (Fig. 2). Here (M_c+M_a) is the whole mass captured (in the unit volume) in the disk. This value includes the total mass of small bodies with initial $R< R_{1,max}$, which are entirely captured in the disk. The value (M_c+M_a) also includes the mentioned above mass M_a which comes to the disk from the larger bodies through their ablation. The parameter M_t is the total mass containing in all the falling bodies (in unit volume) with power-law mass distribution and with size range from zero to R_{max}. It is seen from Fig. 1 that the ratio $M^o_a=M_a/M_f$ is very small both in disks of Jupiter and Saturn due to small mass loss by ablation M_a (at adopted value of ablation coefficient). At the same time, the parameter M^o_{ca} (in Fig. 2), reaches 27% at the distances of Ganymede and 17% in the region of Callisto. For Titan the value M^0_{ca} is about 11% (Fig. 2). Thus, there is a significant difference in the mass of material captured in the formation regions of Ganymede, Callisto, and Titan. Note that the presented calculations of values M^o_a and M^o_{ca} do not take into account the possible fragmentation of planetesimals. The inclusion of fragmentation would increase the captured masses.

Without regard for fragmentation the bodies with initial radius $R < R_{1,max}$=30 m are captured in the circum-Jovian disk at Callisto distance and $R < R_{1,max}$=100 m at Ganymede distance (Fig. 3). When fragmentation is considered [11, 12], the planetesimals with radius R > 100 m should fragment in the formation region of Callisto (Fig. 4). In the Ganymede region all bodies with R > 0.3 m do fragment. Assuming fragmentation into many small pieces, we obtain that in the region of Callisto formation the bodies with radii R < 0.3 m and R > 100 m are captured. In the region of Ganymede according to the model adopted, the disk captures the planetesimals of any size. In the disk of Saturn at the distance of Titan the bodies with radii $R < R_{1,max}$=12 m and R > 6 km are being captured and fragmented, correspondingly.

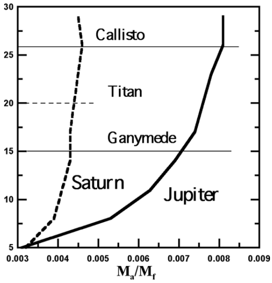

Fig. 1. The ratio of mass lost through ablation and captured in the disk (M_a) to the total mass of the falling bodies (M_f) with $R > R_{1,max}$ and $R < R_M$ at different radial distances r from the central planet (in units of planetary equatorial radius R_p).

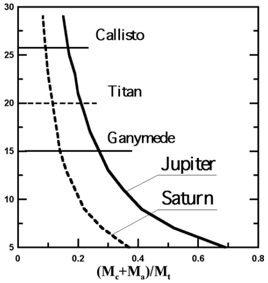

Fig. 2. The ratio of the captured mass (consisting of the mass of small bodies captured in the disk M_c plus the mass of material lost through ablation M_a) to the total mass of the falling bodies M_t at different radial distances r from the central planet.

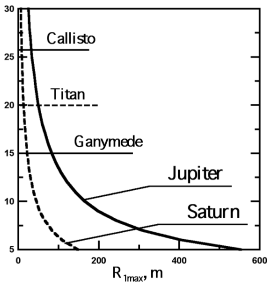

Fig. 3. Dependence of the maximum radius ($R_{1\ max}$) of a planetesimal (at the entrance to the circumplanetary disk), captured by the disk at the first the first pass, on the distance from the central planet r.

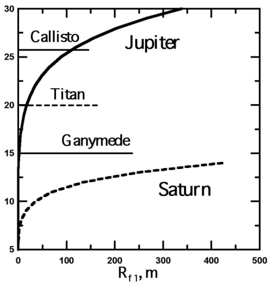

Fig. 4. Dependence of the minimum radius (R_{f1}) of a planetesimal, fragmented in the circumplanetary disk, on the distance from the central planet r. The fragmentation model is taken from [12].

Conclusion:

Our research show that a significant masses of protosatellite material falling on the circumplanetary disks of Jupiter and Saturn are captured in the disks. At the same time the masses captured in the formation region of different moons are very different. Our results also show that the narrow range of sizes of captured bodies, as well as greater duration of satellite formation, due to more remote location could provide a low differentiation of Callisto compared with Ganymede. In the disk of Saturn in the Titan formation region the bodies with radii $R < 12$ m were captured, and fragmentation, apparently, for bodies' capture is irrelevant. This could assist in significant elongation of accretion of Titan and formation of non-differentiated rock–ice mantle.

Acknowledgments:

This research was supported by the RFBR grant 15-05-02572.

References:

[1] Kuskov, O.L., Dorofeeva, V.A., Kronrod, V.A., Makalkin, A.B., Jupiter and Saturn Systems: Formation, Composition, and Internal Structure of Large Satellites), Moscow: Izd. LKI, 2009. [2] Kuskov, O.L., Kronrod V.A. 2001. *Icarus*. Vol. 151. Pp. 204–227. [3] Kuskov, O.L., Kronrod V.A. 2005. *Icarus*. Vol. 177. Pp. 550–569. [4] Makalkin, A.B., Dorofeeva, V.A., Ruskol, E.L. 1999. *Solar Syst. Res.* Vol. 33. No. 6. Pp. 456–463. [5] Makalkin, A.B., Dorofeeva, V.A. 2014. *Solar Syst. Res.* Vol. 48. No. 1. Pp. 62-78.6. [6] Canup, R.M., Ward, W.R. 2002. *Astron. J.* Vol. 124. Pp. 3404–3423. [7] Sasaki, T., Stewart, G.R., Ida, S. 2010. *Astrophys. J.* Vol. 714. Pp. 1052–1064. [8] Gritsevich M., Koschny D. 2011. *Icarus*. Vol. 212. Pp. 877–884. [9] Ceplecha A. Z., Revelle D. O. 2005. *Meteoritics & Planetary Science*. Vol. 40. No. 1. Pp. 35–54. [10] Safronov V.S. 1991. *Icarus*. Vol. 94. No. 2. Pp. 260–271. [11] Ivanov A.G., Ryzhansky V.A. 2004. Doklady Akademii Nauk. Vol. 398. No. 6. Pp. 759-763. [12] Tsvetkov V.I., Skripnik A.Ya. 1991. Astron. vestnik. Vol. 25. No. 3. Pp. 364-370.

DYNAMO ACTION BEYOND THE MAGNETOSPHERES OF QUICKLY SPINNING PLANETS AND HELIOPAUSE

E.S. Belenkaya[1]
[1]Federal State Budget Educational Institution of Higher Education M.V.Lomonosov Moscow State University, Skobeltsyn Institute of Nuclear Physics (SINP MSU), 1(2), Leninskie gory, GSP-1, Moscow 119991, Russian Federation.
elenar@dec1.sinp.msu.ru

Introduction:

For the rapidly rotating planets with strong magnetic field and the Sun, rotation is transferred to the boundary of the magnetosphere/heliosphere and out of it. At this boundary the conductivity is high, but less than out of it. For this reason, the diffusion zone arises, where rotation is smoothly brakes down. The necessary conditions for dynamo action are analyzed in the diffusion zone. It is shown that all these conditions are satisfied and the energy of the damping rotation is enough for magnetic field generation there. For the Solar system this mechanism is relevant to Jupiter.

FORMATION OF PLANETESIMALS: EFFECT OF PARTICLE LAYER INTERACTION WITH SURROUNDING GAS IN THE PROTOPLANETARY DISK AND FRACTIONAL PARTICLE SUBLIMATION ON THE WATER–ICE EVAPORATION FRONT

A.B. Makalkin, I.N. Ziglina, M.E. Artyushkova
Schmidt Institute of Physics of the Earth, B. Gruzinskaya 10, Moscow 123995, Russia.
makalkin@ifz.ru

Introduction:

Formation of self-gravitating pre-planetesimals and initial planetesimals (at least km-sized bodies) in protoplanetary disks, including the solar nebula, is the intermediate stage of planet formation and the least understood theoretical point. One of scenarios of planetesimal formation is gravitational instability (GI) of a dust particle layer in the midplane of the protoplanetary disk [1]. The layer forms due to precipitation of dust particle aggregates to the midplane; it is important that the particle layer though highly enriched in dust phase, also contains gas. This scenario is developing for a long time and is still promising. The global turbulence in the solar nebula as well as the shear-driven turbulence in the layer (which rotates faster then gas in the nebula) stabilizes the layer against GI. The compaction of the layer till GI threshold could occur as particles drift inward due to gas drag and shear stress at the dust layer interface with the outside gas [2–4]. We made new calculations of the particle layer evolution, which explicitly include the drop of solid material mass flux on the water–ice evaporation front. We show that the inclusion of this effect yields substantially new results for planetesimal formation. Turbulent motions of gas in the particle layer exert substantial influence on layer evolution and inhibit GI [3–5]. Turbulent mass diffusion [6] suppresses shortwave perturbations. We show that the diffusion would suppress GI of the layer if interaction of the layer with the surrounding gas of the protoplanetary disk is not taken into account. Masses of pre-planetesimals in the solar nebula regions of terrestrial and giant planet formation are estimated.

Model:

Radial contraction and compaction of the particle layer is considered by solving continuity equation for surface (column) density of the solid (particle) phase of the layer and azimuthal component of the equation of motion to include the transfer of angular momentum from the layer to the gas of the protoplanetary disk. Dividing column density of the layer by layer thickness yields the mean volume density to be compared with the critical one for the onset of GI. The thickness of the layer depends on the turbulence nature and parameters, because of stirring solid particles due to turbulent diffusion. Thus we obtain dependence of density of particle phase ρ_p on the radial coordinate *r* (distance from the sun). The present model, unlike previous works, self-consistently considers sublimation of water ice on the evaporation–condensation front which in the solar nebula is located at the isothermal surface $T \approx 150$ K.. (We do not take into account evaporation fronts for other, less abundant volatiles.)

Solid particles, when moving radially inward, lose water mass fraction (about half mass) on the evaporation front resulting in two-fold decrease of the radial mass flux of solids on the front. The radial dependence of turbulent shear stress causes to about 5–10-fold increase of the radial velocity of particles in the layer. As a result, in order to ensure the conservation of the total mass flax, the surface density of solid phase drops 10 to 20 times.

The present study of GI development includes solution of linearized hydrodynamic equations for small perturbations of both solid (particle) and gas phases in the particle layer with account of interaction between the phases including velocity dispersion and mass diffusion of particles in turbulent gas. We justified the validity of the approximation of incompressible fluid for studying the growth of perturbations in the layer. In this case we come to quadratic equation for dispersion relation, which easily allows the perturbation growth rate to obtain as a function of the wavelength. This makes it possible to estimate the masses of initial dust clumps (pre-planetesimals).

Results and discussion:

Here we consider results of calculations of particle layer evolution for the case, when initial radius of the layer r_p (after precipitation of particles to the midplane) is equal to 50 AU, initial distribution of surface density of the particle layer decreases with heliocentric distance r as $\sigma_p \sim r^{-1}$, the solar nebula at r < 50 AU has radial dependences of surface density and temperature like $\Sigma \sim r^{-0.5}$; $T \sim r^{-0.5}$, the values of Σ and T at r = 1 AU are equal to 2500 g cm^{-2} and 300 K. At these conditions the evaporation–condensation front for water ice with condensation temperature T_w = 150 K is located at the heliocentric distance r = 4 AU. The half-thickness of the particle layer is suggested to be defined by shear-driven turbulence and adopted to be equal to the thickness of the Ekman layer [5]. (This simulation does not include the previous, longer stage the layer evolution, when particles were still precipitating to the midplane.) The results of the modeling are shown in Figure 1. It can be seen that evolution of the already formed particle layer is rather quick (with a timescale about 10^4 years). The density grows in the outer and inner regions of the layer, in the formation regions of giants and terrestrial planets, where it reaches the critical density for GI, about (1–2)ρ^* [1,4,5]; $\rho^*=3M_S/4\pi r^3$, where M_S is mass of the sun. The critical density in the figure is indicated by the grey band. At the same time, the density in the asteroid formation region between 2 to 4 AU practically does not increase and remains about 5 times lower than the critical density. Our calculations show that evolution of the layer depends on the parameters of the nebula (radial dependence of Σ and T) and the initial parameters of the layer. For example, the evolution timescale grows to 7×10^4 yr, if the initial radius of the layer is r_p = 100 AU. The width of the zone of the lowered density varies at various input parameters, it could be wider or narrower than 2.5 AU, but the zone remains with any set of input data.

Our research of GI with account of interaction between solid (particle) and gas phases confirmed the existence of critical density below which GI is impossible. This result is not consistent with the earlier results (e.g. [6]) obtained without taking into account angular momentum transfer from solid (particle) phase to gas. We have got the necessary condition for GI in the layer: ρ_p>(1/3–2/3) ρ^*. Another our result is that GI in the layer is highly improbable without regard for dynamical interaction between the layer and surrounding gaseous solar nebula, because in this case particle r.m.s. velocities prove to be too high. Transfer of angular momentum from the layer to the rest of the gas outside the layer helps GI to occur. A preliminary result for masses of initial pre-planetesimal clumps in the Earth's and Jupiter's formation zones is the following: $m \sim 6\times10^{21}$ g at r = 1 AU, and $m \sim 4\times10^{23}$ g at r = 5 AU.

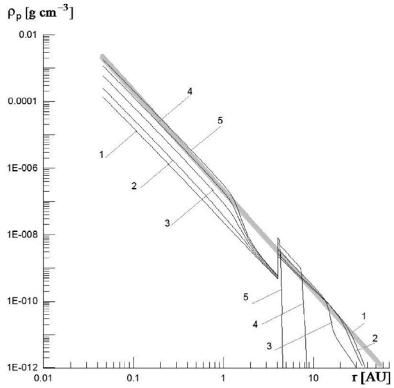

Fig. 1. Evolution of the volume density of the solid (particle) material in the midplane of the particle layer. Curves 1–5 correspond to the following times from the onset layer's evolution (in thousands of years): 1, 2, 5, 10, 16. The gray diagonal band matches the most probable range of values of critical density for GI: (1–2)ρ*.

Conclusion:

The presented results offer the new version for explanation, why there is no planet between orbits of Mars and Jupiter: in this region the critical density necessary for GI of the particle layer and formation of pre-planetesimals never reached. The asteroids of the main asteroid belt may have entered this region at a later stage, possibly, predominantly due to gravitational action of young Jupiter in the late phase of its accretion or after its completion.

References:

[1] Safronov, V.S. 1969. Evolution of the Protoplanetary Cloud and Formation of the Earth and Planets. Nauka Press, Moscow. English Translation: NASA TTF-677. [2] Youdin, A.N., Shu, F.H. 2002. *Astrophys. J.* V. 580. P. 494-505. [3] Youdin, A.N., Chiang, E.I. 2004. *Astrophys. J.* V. 601. P. 1109-1119. [4] Marov, M. Ya., Kolesnichenko, A. V., Makalkin A. B. et al. 2012. From the Protosolar Cloud to the Planetary System. In: Problems of biosphere origin and evolution. Editor: E.M. Galimov, Nova Science Publishers, NY. [5] Weidenschilling S.J. 1980. *Icarus.* V. 44, P.172-189. [6] Youdin A.N. 2011. *Astrophys. J.* V. 731 :99 (18pp).

CHARACTERIZATION OF THE COMPLEX ORGANIC COMPOUNDS SYNTHESIZED BY LASER VAPORIZATION OF SILICATES IN NITROGEN-METHANE ATMOSPHERE: APPLICATION FOR THE IMPACT-INDUCED PREBIOTIC SYNTHESIS

M.A. Zaitsev, M.V. Gerasimov, E.N. Safonova, A.S. Vasiljeva
Space Research Institute of Russian Academy of Sciences (IKI RAS), 84/32 Profsoyuznaya str., 117997 Moscow, Russia.
mzaitsev@iki.rssi.ru

Introduction:

It is well known, that during formation and evolution Solar system bodies are exposed to the asteroid and cometary bombardment. A lot of experimental studies were devoted to resolving the important problem of cosmochemistry and astrobiology – a problem of synthesis, processing, and surviving of organic matter during hypervelocity impacts [1-12].

It should be noted that researchers [10, 12] synthesized the biologically significant organics (amino acids, nucleobases) using a complicated targets, already contains the complex organic precursors.

The aim of our study was the characterization of the wide range of either low- and high-molecular organic compounds (OC) formed during hypervelocity impacts from simple precursors (CH_4 and N_2) in case when colliding bodies don't contain any organics and carbon at all.

We used a laser pulse to simulate impact-induced vaporization of peridotite – a mineral analogue of the rocky asteroids – in nitrogen-methane gas mixture. Model gas mixture was a possible analogue of the early atmospheres of terrestrial planets. CH_4/N_2 ratio of the mixture also corresponded to the CH_4/N_2 ratio for modern Titan's atmosphere. So that, the gas atmosphere was the source of C, N, H, and the silicate target was the source of O for OC formation.

Experiment:

We applied a standard laser pulse (LP) technique [7]. The gas atmosphere in the test chamber contained 4% vol. methane and 96 % vol. of nitrogen (a mixture of 50% vol. CH_4 and 50% vol. N_2 also has been applied). Temperature in the evaporated cloud was about 4000-5000 K, corresponding to hypervelocity impacts of ~10-15 km/s [7].

To characterize OC containing in the solid condensed products of the LP evaporation, we applied two techniques. First one (Pyr-GC/MS) included on-line stepwise pyrolysis (460°C, 15 min → 900°C, 10 min) of condensates (20 mg) under helium flow and GC/MS analysis of the volatiles, accumulated in the cryogenic trap [13-15]. Second technique included repeatable extraction (CH_2Cl_2-MeOH, 9:1 v/v) of condensates (20 mg) on ultrasonic bath and GC/MS analysis of the concentrated extracts [15]. In both cases we investigated the mass-spectrometric data, obtained in the range from 35 to 450 m/z [13-15].

Results:

Solid condensates, obtained in 96:4 v/v N_2-CH_4 atmosphere, produced during pyrolysis (at 460°C) ~ 11,4 µg/g of aliphatic hydrocarbons (saturated and unsaturated, up to C_{19}), ~ 18,3 µg/g of aromatic hydrocarbons (benzene, toluene, naphthalene, alkyl-benzenes up to $C_{19}H_{32}$ etc.), and ~ 9,7 µg/g of nitrogen-bearing compounds (saturated and unsaturated aliphatic and aromatic nitriles and pyrrole). Extraction gave ~ 0,01-0,1 µg/g of individual n-alkanes (C_{14}-C_{19}) and alkyl-benzenes ($C_{17}H_{28}$ - $C_{19}H_{32}$).

It should be noted that these condensates gave the similar products of pyrolysis as a «synthetic» Titan's tholins, formed by spark and plasma discharge in the same nitrogen-methane medium [16]. Moreover, Aerosol Collector and Pyrolyser (ACP) experiment discovered HCN, NH_3 and light hydrocarbons during the pyrolysis of Titan's atmospheric aerosol [17] («natural» tholins).

Solid condensates, obtained in 50:50 v/v N_2-CH_4 atmosphere, produced during pyrolysis (at 460°C) acetonitrile and different polycyclic aromatic hydrocarbons (PAHs): naphthalene, acenaphtylene, acenaphtalene, pyrene etc. in sufficiently (more than 10 times) higher amounts than «96:4» condensates. Extraction gave the wide range of PAHs from naphthalene to acepyrene and oxygen- and nitrogen-bearing OC (fluorenone, phenantrenone, naphtonitriles etc.). Total yield of extracted OC was ~ 18 μg/g.

Clearly that decreasing of methane concentration in the model gas atmosphere leads to decreasing of OC yield during impact-induced synthesis and to changing of their structure. Condensates, obtained in 50:50 v/v N_2–CH_4 atmosphere, produced products of pyrolysis and extraction (mainly PAHs) very similar to the products of pyrolysis of methane itself at 1000°C [18]. Condensates, obtained in 96:4 v/v N_2–CH_4 atmosphere, mainly gave long-chain hydrocarbons and nitrogen-bearing compounds and very small amounts of PAHs. In case of low CH_4 concentration, nitrogen can block the synthesis of polycyclic structures. At the same time, gaseous nitrogen (it is usually very chemical inert) can be involved in the different chemical reactions, passing through the formation of ´CN and other radicals.

Residual pyrolysis of all of the condensates at 900°C gave only carbon dioxide and traces of benzene, toluene, naphthalene and other PAHs. All of these volatiles were the products of the thermal destruction of the high-molecular (kerogen-like) organics.

Conclusion:

Solid condensates obtained from peridotite vaporization in N_2-CH_4 (96:4 v/v) atmosphere contain significant amounts of low- and high-molecular organics. The main volatile products derived from pyrolysis of condensates were long-chain aliphatic hydrocarbons, alkyl-benzenes and nitrogen-bearing compounds (nitriles and pyrrole). The presence of long-chain aliphatic structures indicates that heterogeneous-catalytic reactions, including Fischer-Tropsch reactions, take place during hypervelocity impacts.

Despite of impact-generated cloud has super-high temperature and high oxygen abundance derived from thermal dissociation of colliding silicates [7], nitrogen-methane atmosphere as shown contributes to the impact-driven synthesis of complex OC even when atmosphere contains only small concentration of CH_4, and when colliding bodies not contain C, H, N and other elements essential for OC formation. Presence of N_2, on the one hand, has to provide the synthesis of nitrogen-bearing compounds (important for prebiotic evolution), and, on the other hand, has to provide the saving of the synthesized organics by dilution of an oxidative medium of the impact-induced vapor-cloud.

Actual composition of the early atmospheres of the terrestrial planets is unknown. But in case of nitrogen-methane atmospheres, low- and high-molecular impact-generated organics might be formed at the early stage of planetary formation (during accretion of planetesimals).

Acknowledgements:

This work was supported in part by P-9 Program of the RAS.

References:

[1] Bar-Nun A. et al. (1970) *Science,* **168**, № 3930, 470-472.
[2] Tyburczy J.A. et al. (1986) *Earth & Planet. Sci. Lett.*, **80**, 201-207.
[3] Mukhin L.M. et al. (1989) *Nature*, **340**, № 6228, 46-48.
[4] Sugisaki R. et al. (1994) *Geophys. Res. Lett.*, **21**, № 11, 1031-1034.
[5] Peterson E. et al. (1997) *Geochim. Cosmochim. Acta*, **61**, № 18, 3937-3950.
[6] Korochantsev A.V. and Badjukov D.D. (1998) *Meteoritics & Planet. Sci.*, **33**, A86.
[7] Gerasimov M.V. et al. (1998) *Earth, Moon, and Planets,* **80**, 205-259.
[8] Mimura K. and Toyama S. (2005) *Geochim. Cosmochim. Acta*, **69**, № 1, 201-209.
[9] Nna-Mvondo D. et al. (2008) *Icarus*, **194**, 822-835.
[10] Martins Z. et al. (2013) *Nature Geosci.*, **6**, 1045-1049, doi: 10.1038/ngeo1930.
[11] Burchell M. J. et al. (2014) *Astrobiology*, **14**, № 6, 473-485, doi: 10.1089/ast.2013.1007.
[12] Ferus M. et al. (2015) *PNAS*, **112**, № 3, 657-662, doi: 10.1073/pnas.1412072111.
[13] Zaitsev M.A. et al. (2013) *44th LPSC*, abs. 1905.
[14] Ivanova M.A. et al. (2014) *45th LPSC*, abs. 1014.
[15] Zaitsev M.A. et al. (2015) *SSR*, in print.
[16] Coll P. et al. (1999) *Planet. and Space Sci.*, **47**, 1331–1340.
[17] Israel G. et al. (2005) *Nature,* **438**, 796-799, doi:10.1038/nature04349.
[18] Oró J. and Han J. (1967) *J. of Gas Chromatogr.*, **5**, 480-485.

DEFINITION OF ENVIRONMENT SPECIFICATIONS FOR THE ASTEROID IMPACT MISSION (AIM)

F. Cipriani[1], P. Jiggens[1], A. Galvez[2], I. Carnelli[2], S. Hess[3], E. Daly[1]
[1]ESTEC/TEC-EES, Keplerlaan 1, Noordwijk, The Netherlands;
[2]ESA HQ, 8-10 rue Mario Nikis75738 Paris Cedex 15, France,
[3]ONERA/DESP, BP74025 2 avenue Edouard Belin
FR-31055 TOULOUSE CEDEX 4.
fabric.cipriani@esa.int

The Asteroid Impact and Deflection Assessment mission (AIDA) is a joint European-US technology demonstrator mission including the DART asteroid impactor component (NASA/JHU/APL) and the AIM asteroid rendezvous component (ESA/DLR/OCA). Besides technology demonstration aspects the rendezvous of the AIM platform with Near Earth binary Object 65803 Didymos in October 2022 will allow in situ characterization of the binary asteroid addressing some fundamental science questions. Interestingly, the MASCOT-2 lander will operate in the near surface environment of the binary moonlet, which, together with the potential ability of the Cubesat Opportunity Payloads (COPINS) to sample the dust environment of the binary, will help to better characterize processes of dust charging and transport at airless bodies.

In this context, we provide a preliminary assessment of environmental (namely radiation and charged dusts) related risks for the lander and sensitive elements of the orbiting platforms.

Such assessment is based on :

1) Radiation environment (fluence and dose) specifications for the cruise phase, total mission and surface phase related to the MASCOT-2 lander operation.
2) An estimation of the electrostatic surface potentials distribution of Didymos moonlet, 170m in diameter, resulting from its interaction with solar wind plasma and solar photons, and of the charging levels, mobilization and transport characteristics of regolith grains. In particular, a range of dust density profiles, m/q, and velocities is provided up to 70m above the surface, based on the currently assumed physical properties of the asteroid regolith, solar illumination conditions at Didymos orbit, and the probability of charged dust to be lifted from the surface. A careful assessment is made on dust grains lifetime since radiation pressure forces largely dominates for grain sizes typically below 5 microns.

ON FORMATION OF WATER MOLECULES INCORPORATED IN NEAR-SURFACE LUNAR REGOLITH

A.Yu. Dubinskii, S.I. Popel
Space Research Institute RAS, ul. Profsoyuznaya 84/32, Moscow 117997, Russia.
popel@iki.rssi.ru

Introduction:

Recent studies [1] based on the Lunar Reconnaissance Orbiter data and aimed at detecting the neutron fluxes that passed through the lunar surface regions in the southern hemisphere of the Moon revealed the presence of hydrogen-rich areas in the near-surface lunar region at latitudes exceeding 70°. The emergence of near-surface hydrogen-rich areas may be driven by the solar wind electrons and protons that impact the Moon, are absorbed by (implanted into) its surface, and form neutral atoms and molecules of hydrogen or chemical compounds that contain hydrogen, for example, in the form of hydroxyl groups [2]. This implanted hydrogen may accumulate at the lunar surface according to the following mechanism. The solar wind protons are absorbed by the lunar regolith particles at depths of up to 10^{-5} cm. At the end of the proton path they are chemically bound with atoms of the lunar regolith, in particular with oxygen atoms; as a result, tens of percent of oxygen atoms in the lunar soil regions that interact with the solar wind protons get bound into the OH hydroxyl groups. This implanted hydrogen rises to the lunar surface due to diffusion. The desorption of hydrogen bound in this way progresses very slowly at temperatures lower than 400 K that are typical for the lunar surface. As a result, the surface concentration of hydrogenous materials on the Moon may reach sufficiently large values (up to 10^{17} cm^{-2}) in several thousand years [2]. The hydrogen-rich lunar surface areas are more susceptible to photoemission than the surrounding regions [3], and this influences the process of charging the dust particles, their dynamics, and finally, the properties of the dusty plasma system at the Moon [4-6].

However, the results obtained by Mitrofanov et al. [1] are treated often as those which point at the presence of water ice in the near-surface lunar regions. Justification of such a treatment is important from the viewpoint of future lunar missions and exploration of the Moon, especially with taking into account very low probability of the existence of free water (say, not incorporated in near-surface lunar soil) on the Moon because of strong evaporation into atmosphereless space at day time and impossibility to condense at night time. Here, we present a possible mechanism of the formation of water molecules incorporated in the near-surface lunar soil.

Mechanism:

In accordance with the conception [2], the energy of the solar wind proton is enough to uncouple a molecule of SiO_2 in the crystal lattice of quartz. Then the proton is coupled with an oxygen atom forming hydroxyl (OH-) group. However, the hydroxyl group remains coupled with a silicon atom presenting in the crystal lattice of SiO_2. Such a configuration is not related to the presence of water on the Moon.

The thermal energy is not sufficient to break chemical bonds in quartz. To explain the release of oxygen atoms from the crystal lattice of SiO_2 we consider sulfur compounds (e.g., Ag_2S) containing in the lunar regolith. Sulfur and oxygen atoms have similar structures of outer electron shell, although the size of the sulfur atom is larger than that of the oxygen one. Furthermore, the structure of the molecule Ag_2S is analogous to that of H_2O. This results in a possibility of substitution of oxygen atom in the crystal lattice of SiO_2 by sulfur atom and, correspondingly, in the release of oxygen atom in the regions of lunar near-surface soil where argentum sulphide contacts with silicon oxide. The mechanism of exchange between sulfur and oxygen is the following.

1) When a solar wind proton hits a region of lunar near-surface soil where argentum sulphide contacts with silicon oxide, Si-O bond breakage occurs, while hydrogen forms the hydroxyl group

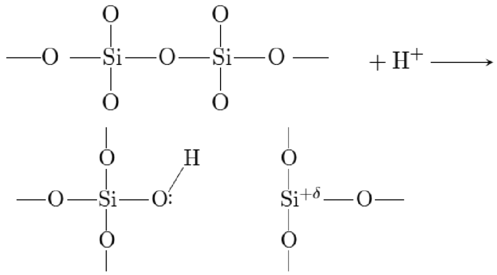

2) Then the interaction of argentum sulphide molecule is accompanied by the approach of sulphide and silicon atoms as well as argentum and oxygen those. The intermediate complex is formed

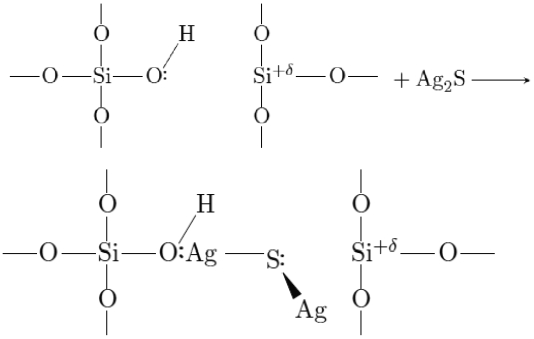

3) The integrated intermediate complex existing due to the covalent-hydrogen bonds is created. Then Ag-S bond breakage occurs

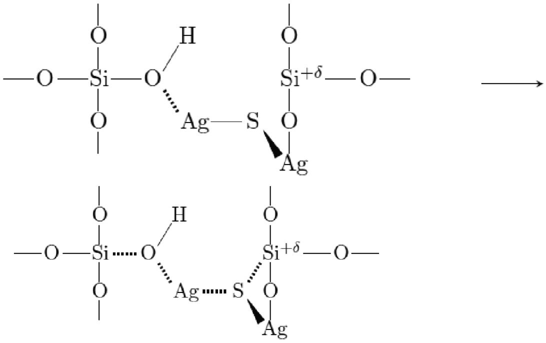

4) As a result, a molecule of argentum hydroxide AgOH is separated from the intermediate complex, and the separation of the argentum atom occurs.

Conclusions:

Thus oxygen atoms are released (as a part of the molecule AgOH) from the crystal lattice of SiO_2. Argentum hydroxide can react relatively easily with hydrogen forming water and silver. This shows a possibility of the formation of water molecules incorporated in the near-surface lunar soil. The presence of water molecules in the near-surface lunar soil influences the photoemission properties of lunar regolith, and finally, the properties of the dusty plasma system at the Moon.

Acknowledgements:

This work was carried out as part of the Russian Academy of Sciences Presidium program no. 9 “Experimental and Theoretical Research of Objects of the Solar System and Planetary Systems of Stars” and was supported by the Russian Foundation for Basic Research (project no. 15-02-05627-a).

References:

[1] Mitrofanov, I.G., Sanin, A.B., Boynton, W.V., et al.: Hydrogen mapping of the lunar south pole using the LRO neutron detector experiment LEND, Science, Vol. 330, pp. 483-486, 2010.
[2] Starukhina, L.: Water detection on atmosphereless celestial bodies: alternative explanations of the observations, J. Geophys. Res., Vol. 106, pp. 14701-14710, 2001.

[3] Kolesnikov, E.K. and Manuilov, A.S.: The way to calculate electrostatic field intensity above lunar surface covered by hydrogen monolayer, Astron. Zh., Vol. 59, pp. 996-998, 1982.
[4] Popel, S.I., Kopnin, S.I., Golub', A.P., Dol'nikov, G.G., Zakharov, A.V., Zelenyi, L.M., and Izvekova, Yu.N.: Dusty plasma at the surface of the Moon, Solar System Research, Vol. 47, pp. 419-429, 2013.
[5] Popel, S.I., Morfill, G.E., Shukla, P.K., and Thomas, H.: Waves in a dusty plasma over the illuminated part of the Moon, J. Plasma Phys., Vol. 79, pp. 1071-1074, 2013.
[6] Popel, S.I., Golub', A.P., Izvekova, Yu.N., Afonin, V.V., Dol'nikov, G.G., Zakharov, A.V., Zelenyi, L.M., Lisin, E.A., and Petrov, O.F.: On the distributions of photoelectrons over the illuminated part of the Moon, JETP Lett., Vol. 99, pp. 115-120, 2014.

LONG-TERM IMPACT OF LOW PRESSURE ON BACTERIAL BIODIVERSITY AND ACTIVITY IN SOIL AND SEDIMENTS

V.S. Cheptsov[1], E.A. Vorobyova[1,2], G.A. Osipov[3], M.V. Gorlenko[1], I.A. Shashkova[2], I.A. Kuznetsov[2] , A.V. Zakharov[2], G.G. Dolnikov[2]
[1]Lomonosov Moscow State University, GSP-1, Leninskie Gory 1-12, Moscow, 119991, Russia;
[2]Space Research Institute of Russian Academy of Sciences, 84/32 Profsoyuznaya Str, Moscow, 117997, Russia;
[3]Academician Yu. Isakov Research Group, Bakulev Scientific Center of Cardiovascular Surgery, 8/7 Leninsky Prospekt, Moscow, 117931, Russia.
cheptcov.vladimir@gmail.com

The present work covers the response of bacterial communities adapted to the earth extreme habitats to the influence of low pressure as potential extra-terrestrial environment-forming factor.

For this study the samples of Antarctic permafrost sediment (Dry Valleys) and gray-brown soils of Moroccan mountain desert were exposed at a pressure of 1.4 Pa for 75 days.

As a result the natural microbial communities in Antarctic permafrost and in arid soil showed high viability to this impact. In spite of slight decrease in the number of proliferating cells, the total content of bacteria in the samples counted by direct microscopic epifluorescence technique remained at the initial level, which indicates the transition of bacterial cells from the active state to hypobiosis. The functional state of microbial communities have changed: metabolic tests testified about activating consumption digestible high energetic substances that may be considered as a response to stress impact. Furthermore, according to gas-chromatography mass-spectrometry of lipids in the soil samples there was a considerable restructuring of microbial communities while maintaining high biodiversity. In the bacterial community of gray-brown soil markedly increased the number of bacteria of the genus *Desulfovibrio* in reducing the number of the dominant groups of bacteria of the genus *Eubacterium* and *Propionibacterium*. Gram negative sulfate-reducing and aerotolerant anaerobic bacteria. *Desulfovibrio* commonly form major community members of extreme oligotrophic habitats. Some species of this genus have in recent years been shown to have bioremediation potential for toxic radionuclides. According to the new data (Amrani et al., 2014) bacteria *Desulfovibrio* use at least three different adaptation mechanisms, according to a hydrostatic pressure threshold that was estimated to be above 10 MPa. Our data prove that these extremophiles are also able to adapt quickly at very low pressure.

In a sample of the Antarctic permafrost a sharp increase in the number of anaerobic bacteria of the genera *Clostridium* and *Methylococcus* was occurred.

The study gives grounds for asserting that very low pressure is not fatal for viable status, biodiversity and potential metabolic activity of putative Earth like aerobic and anaerobic bacteria in extraterrestrial environments.

Acknowledgements:

This work was supported by PRAS №9 and RSF grant № 14-50-00029

References:

Amrani, A., Bergon, A., Holota, H., Tamburini, Ch., Garel, M., Ollivier, B., Imbert, J., Dolla, A. Transcriptomics Reveal Several Gene Expression Patterns in the Piezophile Desulfovibrio hydrothermalis in Response to Hydrostatic Pressure. 2014. PLoS 9(9): e106831. http://journals.plos.org/plosone/article?id=10.1371/journal.pone.0106831

ON THE POSSIBILITY OF PHOTOINDUCED LEVITATION OF DUST PARTICLES UNDER GROUND-BASED LABORATORY CONDITIONS

E.A. Lisin[1], I.A. Kuznetsov[2]
[1]Joint Institute for High Temperatures of the Russian Academy of Sciences
[2]Space Research Institute of the Russian Academy of Sciences

The surface of the Moon, as well as the surface of any space body without an atmosphere, is subjected to the solar wind and ultraviolet radiation. As a result, a charge appears on the surface and electric fields near it are induced. Dust particles from the lunar regolith occurring in the near-surface plasma can levitate over the surface, forming dusty plasma clouds. One of the main problems of future missions to the Moon is associated with lunar dust.

In order to gain a better understanding of mass transfer processes occurring on surfaces of the moon and other atmosphereless celestial bodies it is necessary to conduct physical simulations in a laboratory. Usually, when the UV impact on dust particles is experimentally studied, dust levitation is provided by electric fields of a non-photoemission nature [1], or is not observed at all [2].

In this study, we calculated analytically and numerically the experimental (laboratory) conditions, under which levitation of various samples of dust over the dusty surface (substrate) irradiated with ultraviolet source is possible. Numerical simulation of the double layer was performed by Particle-in-Cell method. Simulation of dust dynamics in the photoelectron layer under UV exposure was carried out by molecular dynamics, and floating potentials of the particle surfaces were calculated analytically.

It was shown that levitation of dust particles over a dusty surface is possible only when directed UV radiation incident at an angle to the surface. The range of permissible angles and the maximum size of levitating particle were determined depending on the UV source power and the composition (wavelengths) of radiation, as well as on the photoemission properties of the particles and the substrate.

Acknowledgements:

This work was supported by the Ministry of Education and Science (MK-7932.2015.8), the Russian Foundation for Basic Research (the grant №15-32-21159) and by the Presidium of the Russian Academy of Sciences.

References:

[1] Sickafoose A.A., Colwell J.E., Horányi M., and Robertson S., J. Geoph. Res., 107, 1408 (2002)
[2] Filippov A.V., Babichev V.N., Fortov V.E., Gavrikov A.V., Petrov O.F., Starostin A.N., and Sarkarov N.E., J. Exp. Theor. Phys.,112, 884 (2011)

RETRIEVAL OF AEROSOL PROPERTIES IN THE UPPER HAZE OF VENUS USING SPICAV-IR DATA

M. Luginin[1,2], A. Fedorova[1], D. Belyaev[1], F. Montmessin[3], V. Wilquet[4], O. Korablev[1], J.-L. Bertaux[3], A.-C.Vandaele[4]
[1]Space Research Institute, Russia;
[2]Moscow Institute of Physics and Technology, Russia;
[3]LATMOS, France;
[4]Belgian Institute for Space Aeronomy, Belgium

The upper haze of Venus located at 70-90 km is composed of submicron aerosol particles of H_2SO_4 (Esposito et al., 1983). Recently, three channels of SPICAV/SOIR instrument onboard the VEX orbiter provided the occultation profiles in three spectral ranges that resulted in discovery of a bimodality in size distribution in the upper haze with a small mode of radius 0.1-0.3 μm, and a large mode of radius 0.4-1.0 μm as well as presence of a detached haze layers (Montmessin et al., 2008; Wilquet et al., 2009). Study of aerosol particles above 90 km could provide a source of sulfur oxides above 90 km (Belyaev et al., 2012).

SPICAV IR is a part of SPICAV/SOIR suit of instruments onboard the Venus Express mission. It can operate in the solar occultation mode in the spectral range of 0.65–1.7 μm. The spectrometer is sensitive to abundance of both submicron (mode 1) and micron (mode 2) particles in the Venus' upper haze. The interpretation of spectral dependence of extinction coefficients using Mie scattering theory with adopted H_2SO_4 refractive indices allows to retrieve particle size and number density profiles assuming bimodal as well as unimodal cases.

In this paper we present vertical profiles of extinction, number density and size distribution from 196 orbits from May 2006 to November 2014. Aerosol scale height is found to be equal to 3-4 km in the upper haze. Aerosol haze top is higher near the equator than near the pole. Bimodaly distributed particles are found to be present on some orbits. Orbit number dependence of effective radius shows grouping of radii within occultation seasons. On the orbits where unimodal distribution is found the particles are bigger in the morning comparing to the evening and at the equator comparing to the poles. Number density profiles for both modes in bimodal case decrease smoothly, from ~1000 cm^{-3} at 75 km to ~100 cm^{-3} at 90 km for mode 1, and from ~1 cm^{-3} at 75 km to ~0.1 cm^{-3} at 90 km for mode 2.

This work is supported by the Program 9 of the RAS Presidium. The authors acknowledge the support provided by ISSI, through the organization of the International Team meeting "Improved understanding of Venus clouds".

VARIATIONS OF WATER VAPOR AND CLOUD TOP ALTITUDE IN THE VENUS' MESOSPHERE FROM SPICAV/VEX OBSERVATIONS

A. Fedorova[1], E. Marcq[2], M. Luginin[3,1], O. Korablev[1], J.-L. Bertaux[2], F. Montmessin[2]
[1]Space Research Institute(IKI), 84/32, Profsoyuznaya str., Moscow, 117997, Russia;
[2]LATMOS-UVSQ, 11 Bd d'Alembert, F-78280 Guyancourt, France;
[3]Moscow Institute of Physics and Technology (MIPT), 9 Institutsky dr., 141700 Dolgoprudny, Moscow Region, Russia.
fedorova@iki.rssi.ru

SPICAV VIS-IR spectrometer on-board the *Venus Express* mission measured the H_2O abundance above Venus' clouds in the 1.38 µm band, and provided an estimation of the cloud top altitude based on CO_2 bands in the range of 1.4-1.6 µm. The H_2O content and the cloud top altitude have been retrieved for the complete *Venus Express* dataset from 2006 to 2014 taking into account multiple scattering in the cloudy atmosphere. The cloud top altitude, corresponding to unit nadir optical depth at 1.48 µm, varies from 68 to 73 km at latitudes from 50ºS to 50ºN with an average of 70.7±1 km assuming an aerosol scale height of 4 km. In the high northern latitudes, the cloud top decreases to 62-66 km. The altitude of formation of water lines ranges from 55 to 70 km. The H_2O mixing ratio at low latitudes (20ºS-20ºN) is equal to 6.2±1.2 ppm with variations from 4 to 11 ppm. Between 30º and 50º of latitude in both hemispheres, a local minimum was observed with a value of 5.3±1 ppm and variations from 3 to 8 ppm. At high latitudes in both hemispheres, the water content varies from 4 to 12 ppm with an average of 7.3±1.5 ppm. The maximum of water at lower latitudes supports a possible convection and injection of water from lower atmospheric layers. The vertical gradient of water vapor inside the clouds explains well the increase of water near the poles correlated with the decrease of the cloud top altitude. On the contrary, the depletion of water in middle latitudes does not correlate with the cloud top altitude and cannot be explained by the vertical gradient of water vapor within the clouds. We obtained H_2O scale heights for exponential vertical abundance profiles of water which varies from 4.5 to 6 km with the altitude of H_2O lost varying from 61 to 66 km which is well consistent with the photochemical modeling [*Krasnopolsky, 2012; 2015*]. Retrieved H_2O mixing ratio is higher than those obtained in 2.56 µm from *VIRTIS-H* data [*Cottini et al., 2015*] at altitudes of 68-70 km. The water vapor latitudinal-longitudinal distribution does not show any direct correlation with the cloud top. Yet a strong asymmetry of H_2O longitudinal distribution has been observed with a maximum of 7-7.5 ppm from -120º to 30º of longitude and shifted to the southern hemisphere (20ºS-10ºN). To the east, the minimum is observed with values not in excess of 6 ppm and over a wide range of longitudes from 30º to 160º. No prominent long-term nor local time variations of water vapor and the cloud top altitude were detected at any latitudes during more than 8 years of *Venus-Express* observations.

References:

[1] Krasnopolsky V.A. (2012) A photochemical model for the Venus atmosphere at 47–112 km. Icarus, 218, 230-246.
[2] Krasnopolsky V.A. (2015) Vertical profiles of H2O, H2SO4, and sulfuric acid concentration at 45–75 km on Venus, Icarus, 252, 327-333
[3] Cottini, V., N. I. Ignatiev, G. Piccioni and P. Drossart (2015) Water vapor near Venus cloud tops from VIRTIS-H/Venus express observations 2006–2011, Planetary and Space Science, 113–114, 219-225

VARIATIONS OF SO_2 CONTENT AT THE NIGHT SIDE OF VENUS' MESOSPHERE

D.G. Evdokimova[1], D.A. Belyaev[1], M.S. Luginin[1], A.A. Fedorova[1], F. Montmessin[2], E. Marcq[2], J.-L. Bertaux[2],
[1] Space Research Institute (IKI), 84/32 Profsoyuznaya, 117810 Moscow, Russia;
[2] LATMOS - UVSQ/CNRS/IPSL, 11 bd dAlembert, 78280 Guyancourt, France.
evd.dar@yandex.ru

Introduction

Venus has a dense CO_2 atmosphere with a thick cloud layer (50-70 km) consisted of sulfuric acid (H_2SO_4) aerosols. Sulfur oxides (SO_x) are directly associated with those aerosols and plays an important role in chemistry of the atmosphere. Any changes of their content within or above the clouds have an influence on photochemical processes in the mesosphere (70-100 km). Recent ground-based observations [1-4] and continuous monitoring from the Venus Express orbiter [5-7] have shown high temporal and spatial variability of SO_2 abundance mostly on the day side: from 20 to 500 ppbv above the clouds. There is a lack in the detailed analysis at the night-time mesosphere where photo dissociation of sulfur dioxide is replaced by interaction with the global subsolar/antisolar circulation and chemical reactions with atoms of Cl, OH, O etc. The night side was observed by the UV channel of SPICAV spectrometer in period 2006-2014.

Results

In this paper we present new results from sulfur dioxide observations made by SPICAV UV spectrometer onboard Venus Express orbiter [8] in regimes of stellar and solar occultation. In the mode of stellar occultation the instrument observes night-side mesosphere while at solar occultation it sounds evening/morning twilights at altitude range 85-100 km. SPICAV UV can register SO_2 absorption bands at 190-220 and 270-300 nm and CO_2 bands at 120-200 nm with spectral resolution 1-2 nm. As a result, vertical distribution of SO_2 mixing ratio was retrieved in observation period from June 2006 to April 2014. On average, the volume mixing ratio increases with altitude from 20 to 200 ppbv (Fig. 1.).

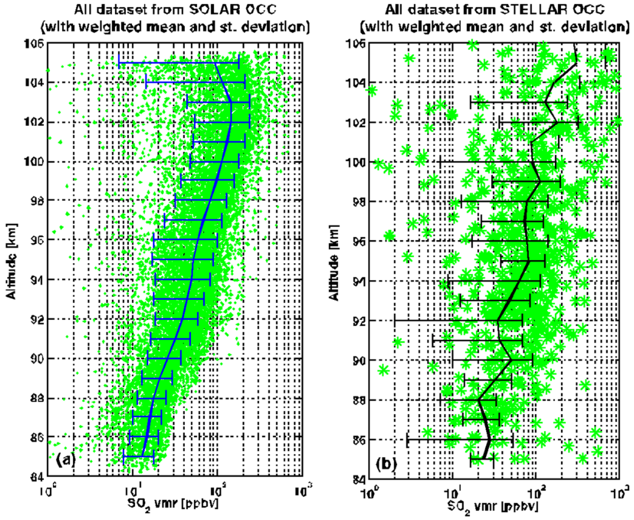

Fig. 1. Altitude distribution of SO_2 mixing ratio from SPICAV UV solar (a) and stellar (b) occultations. Solid lines are weighted mean values with standard deviations.

Annual diagram of SO_2 variations shows a few picks with values >100 ppb from the both regimes of occultation (Fig. 2a). These events are local in time and they are not revealed on the latitude diagram (Fig. 2b). We can also look on the daily diagram where SO_2 content around midnight does not differ from the evening/morning twilights (Fig. 2c). Additional analysis is going on together with properties of aerosol particles [9], in order to establish correlations between SO_2 picks and particles sizes and densities.

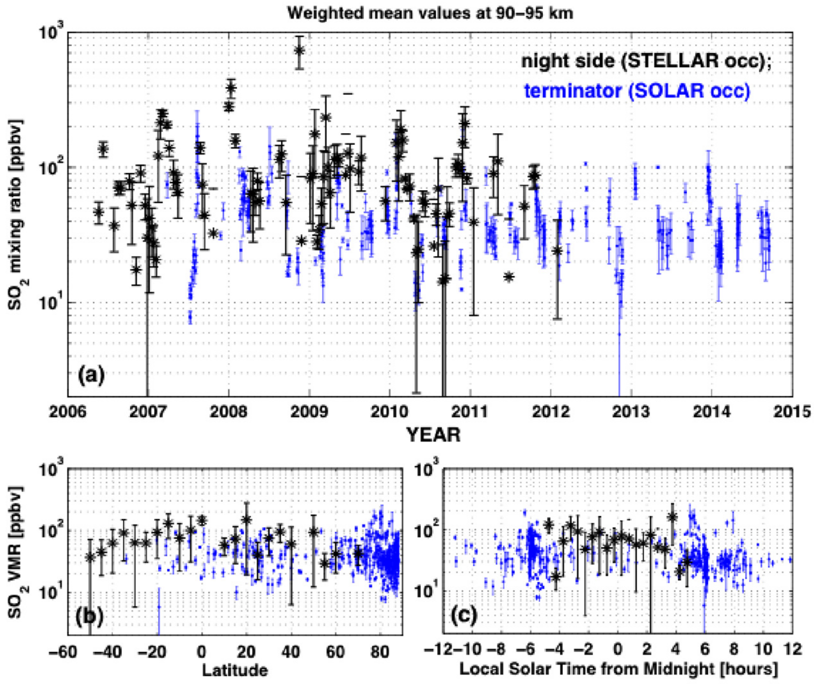

Fig. 2. Time and latitude diagrams of SO_2 variations at altitude level 90-95 km (blue – solar occultations, black – stellar occultations).

Acknowledgements

We acknowledge the program №9 (ex. 22) from the RAS and the support provided by ISSI, through the organization of the International Team meetings "Sulphur dioxide variability in the Venus Atmosphere". D. Belyaev also thanks Embassy of France in Moscow for Metchnikov's stipendium to work in laboratory LATMOS in May-July 2015.

References:

[1] Encrenaz T. et al., 2012. HDO and SO_2 thermal mapping on Venus: evidence for strong SO_2 variability. A&A 543, A153.
[2] Krasnopolsky V.A., 2010. Spatially-resolved high-resolution spectroscopy of Venus. 2. Variations of HDO, OCS, and SO_2 at the cloud tops. Icarus 209, 314-322.
[3] Sandor B.J. et al., 2010. Sulfur chemistry in the Venus mesosphere from SO_2 and SO microwave spectra. Icarus 208, 49–60.
[4] Jessup et al., 2015. Coordinated Hubble Space Telescope and Venus Express observations of Venus' upper cloud deck. Icarus. http://dx.doi.org/10.1016/j.icarus.2015.05.027.
[5] Belyaev D. et al., 2012. Vertical profiling of SO_2 and SO above Venus' clouds by SPICAV/SOIR solar occultations. Icarus 217, 740–751.
[6] Marcq E. et al., 2013. Variations of sulphur dioxide at the cloud top of Venus's dynamic atmosphere. Nature Geoscience, vol. 6, 25-28. DOI: 10.1038/NGEO1650.
[7] Mahieux A. et al., 2015. Venus mesospheric sulfur dioxide measurement retrieved from SOIR on board Venus Express. Planet. Space Sci. v.113-114, p.193–204.
[8] Bertaux et al., 2007. SPICAV on Venus Express: three spectrometers to study the global structure and composition of Venus atmosphere. Planet. Space Sci. 55, 1673–1700.
[9] Luginin et al., 2015. Study of aerosol properties in the upper haze of Venus from SPICAV IR data. Geophysical Research Abstracts. Vol. 17, EGU2015-790.

DEPENDENCE OF LONGITUDINAL DISTRIBUTION OF ZONAL WIND AND UV ALBEDO AT CLOUD TOP LEVEL ON VENUS TOPOGRAPHY FROM VMC CAMERA ONBOARD VENUS EXPRESS

M.V. Patsaeva[1], I.V. Khatuntsev[1], J.-L. Bertaux[2], A.V. Turin[1],
[1]Space Research Institute(IKI), Moscow, Russia;
[2]LATMOS/INSU, UVSQ, Guyancourt, France.
marina@irn.iki.rssi.ru

A set of UV images obtained by the Venus Monitoring Camera (VMC) was used to study the circulation of the mesosphere. The long observation period (from 2006 to 2014) and good longitude-latitude coverage by single measurements allowed us to eliminate short-periodic changes in the velocity component in the zonal flow and to focus on the study of the slow-periodic component. Analyzing the longitude-latitude distribution of the zonal wind for 49,700 (139 orbit) visual and 457,850 (722 orbit) digital individual wind measurements we managed to trace the influence of topography of the underlying surface on the behavior of the mean zonal flow and the average UV albedo for a set of latitude intervals of 10°.

Longitudinal profiles of surface altimetry, average zonal wind speed and average UV albedo were constructed for each latitudinal range. Then correlations between altimetry profiles and profiles of speed and albedo were considered. Shifts between correlated profiles were defined for the maximum correlation coefficient. Dependence was found between the shift and the maximum height difference of the surface relief in a given latitudinal range. The shift between the correlated profiles increases when the maximum height difference decreases (to the south of *Aphrodita Terra*) and therefore the influence of the surface relief is delayed. Due to peculiarities in Venus atmosphere circulation, the influence of the meridional component becomes noticeable at 30 °S. In the middle latitudes, circulation becomes more complex, which is reflected in values of correlation coefficients. The coefficients have low values that don't allow us to track the influence of relief. In the high south latitudes due to bad coverage with data, it is only possible to track the dependence between topography and albedo. The latitudinal interval of 60°S -70°S is a rather stable area of transition between the middle-latitude circulation (jet region) and polar circulation where influence of a polar vortex is significant. There is the some height in this area called *Erzulie Mons*. We observe here the same dependence of correlation shift on height, as in latitudes of *Aphrodita Terra*.

The analysis confirms the influence of the underlying surface topography on the change of speed of the average zonal wind and UV albedo, and also establishes dependence of this influence on the maximum difference of heights in the chosen width interval.

POSSIBLE SIGNS OF FAUNA AND FLORA ON VENUS

L.V. Ksanfomality[1], A.S. Selivanov[2], Yu.M. Gektin[2]
[1]*Space Research Institute, Moscow;*
[2]*OAO Russian Space Systems*

The position of the hypothetical habitability zone in extrasolar planetary system was considered by many authors. Approximately 1/4 of exoplanets orbit their stars at very low orbits, which leads to high temperatures of their surface (if any), up to 800 K or more. Some of them should have the physical conditions close to those of Venus. Is there any possibility that the life forms can exist at quite different environment than "normal", Earth-like physical conditions? Namely the planet Venus could be the natural laboratory for studies of this type, having the dense, hot (735 K) oxygenless CO_2 - atmosphere and high, 9.2 MPa, pressure at the surface. It should be recalled that the only existing data of actual close in TV-observations of Venus' surface are the results of a series of missions of the Russian VENERA landers which took place the 1970s and 80s, working in the atmosphere and on the surface of Venus. No other results of this kind were obtained since. A re-exemination of images of venusian surface obtained from the VENERA landers has been undertaken using a modern processing technique, with a view to detect any possible signs of life under the specific conditions on Venus. This speculative identification rests on two characteristics of these features: (a) their somewhat suggestive morphology and (b) their temporal appearance and behavior (present, than absent on subsequent images of the same area; or changing appearances). The re-exemination has identified previously unreported features [1-4] that may correspond to hypothetical life forms on Venus' surface. Two of them are 'mushroom' and 'amisada' similar to the Australian shingleback lizard. Analysis and comparison of the contents the sequence of panoramas of the venusian surface obtained in the course of the TV-experiments on the VENERA landers (1975-82), allowed the authors to detect some interesting objects displayed on the panoramas. Following the change in their appearance on the sequence of images allowed a suggestion that such changes may be related to the possible habitability of the planet. Some of the objects found were described in about 30 papers of L.Ksanfomality (2012-15). There are also found and listed in the report images of objects with special morphology resembling the shape of some terrestrial fauna. In the absence of new landing missions to Venus, the same study was carried out on the other remaining panoramas. There is a reason to believe that in the panoramas few classis of unusual objects has been found, which will be shown in the report.

References:

[1] Ksanfomality L.V. 2013 Doklady Physics. **58** (5), 204
[2] Ksanfomality L.V. 2013 Doklady Physics. **58** (11), 514
[3] Ksanfomality L.V. 2013 International Journal of Astronomy and Astrophysics, 3, 57-79.
[4] Ksanfomality L.V. 2014 **Acta Astronautica, 105 521–533.**

MULTI-FREQUENCY PHASE-COHERENT SYSTEMS: NEW INSTRUMENT FOR OCCULTATION IN THE PROJECT VENUS-D

A.L. Gavrik, T.F. Kopnina, M.I. Bondarenko, A.A. Smislov
Kotel'nikov Institute of Radio Engineering and Electronics, Fryazino branch, V. A. Vvedensky sq., 1, Fryazino, Russia.
alg248@hotmail.com

Introduction:

Since 1975, Venus-orbiting spacecraft (S/C) have carried out more than 600 two frequency radio occultation measurements of the atmosphere and ionosphere density. Radio science experiments could be accomplished using no more than two coherent downlink signals. The quantities observed during occultation are the phases and powers of radio signals received at a ground station. Such simple systems allow performing the standard radio sounding experiments solely using the well-known and adequately developed techniques. The aim of the report is to present planned non-standard and effective radio science investigations of Venus atmosphere, ionosphere and the solar wind plasma in the project Venera-D.

Multi-frequency phase-coherent system for occultation:

The Cassini Telecommunication System was a pioneer to use two coherent uplinks (X- and Ka-band) and four coherent downlinks (S-, X-, and Ka-band two downlinks). The main scientific objective of such complex Cassini Radio Science System (RSS) was performance of unique gravitational and relativistic investigations and certain radio sounding experiments. Applying a similar multi-frequency phase coherent system on board the S/C Venus-D opens up new opportunities for planetary envelope occultation and space plasma sounding.

The theory of multi-frequency phase-coherent RSS for the deep space exploration considers RSS as a unified system consisting of several coherent uplinks and downlinks. Two coherent uplink signals emitted by the ground transmitter acquire the appropriate phase shifts due to changes in the distance, neutral and ionized components of the space medium propagating between Earth and the S/C. The S/C transponder receives the two signals forming coherently four downlink signals which are received at the ground-station in their passage of the return path S/C-Earth. We make these four signals a measurand $\Psi(t)$ as a linear combination of the signal phases $\Psi(t)=\kappa_1\Phi_1(t)+\kappa_2\Phi_2(t)+\kappa_3\Phi_3(t)+\kappa_4\Phi_4(t)$ using appropriate coefficients κ_1, κ_2, κ_3 and κ_4. For plasma investigation the function $\Psi(t)$ must not depend on neutral component and a distance between Earth and the S/C. It means that the certain conditions for coefficients must be satisfied. We can get three cases which may be realized simultaneously: 1) the time dependence of uplink total electron content variations; 2) the time dependence of downlink total electron content variations; 3) variations of a mean value of a longitudinal component of a magnetic field for ordinary and extraordinary radio waves. The principal requirement of this method is clear now: RSS must provide simultaneous coherent radiation of both two uplinks and four coherent downlink signals in two-way mode. Accordingly ground station must provide coherent simultaneous receiving of four downlink signals and digital processing of the signals allows to realize the phase measurements.

One of the most important sources of the radio occultation experiment errors is total electron content variations in the radio wave path including the Earth ionosphere. We can use multi-frequency phase-coherent RSS for solving the radio occultation inverse problem excluding the unfavorable Earth ionosphere effect. We also offer the new technique of the data analysis that allows us to separate influence of noise, ionosphere and atmosphere on the radio occultation results. Variations of the defocusing attenuation in the occultation experiments are proportional to the velocity of residual frequency changes. Good agreement between frequency data and observed power attenuation has been registered in many occultation events. Coincidence between signal energy and frequency deviations is indicative of the influence of the stratified layers in the atmosphere and ionosphere under investigation. The absence of this correspondence is an indication of the influence of any factors that are not taken into account. This technique considerably increases the sensitivity of the radio probing method to refractive index variations, makes possible to detect wave-like structure in the atmosphere and ionosphere and cleanly separates noise, ionospheric and atmospheric influences during an occultation experiment.

The developed methods provide the ability to obtain high quality information about the Venusian ionosphere and atmosphere. A multi-frequency phase-coherent system in the project Venus-D is capable of carrying out new, non-standard and effective radio science exploration in the field of the space plasma studies: measurements of the total electron content on both the uplink and downlink made simultaneously and/or separately; Venus atmosphere and ionosphere sounding by a new two-way method; location of solar wind plasma clouds and measurement of the plasma cloud magnetic field/

Acknowledgements:

The work is partially supported by the RAS Presidium Program № 9.

FORMATION OF ANALOGOUS GEOLOGICAL STRUCTURES ON TERRESTRIAL PLANETS BY GALAXY'S COMETS (I): THE GALACTIC COMETS AND THEIR MECHANISM INTERACTION WITH PLANETS

A.A. Barenbaum
Oil and Gas Research Institute RAS, Gubkin str. 3, 119333 Moscow, Russia.
azary@mail.ru

Introduction:

The origin of analogous geological structures (continents, seas, volcanoes, mountains, craters, etc.) on terrestrial planets is the question which in planetology has not yet received an explanation. The situation began to change for the better due to discovery of phenomenon of the expiration of gas-dust matter from Galaxy center [1], when the fact fallings of galactic comets on Earth and other planets was firmly established [1–5], and we began to study physical mechanism of interaction these comets with atmosphere and lithosphere of Earth [5–8].

Today it became clear [9-11] that fallings of galactic comets are main reason for formation of leading forms of relief on terrestrial planets. Physical mechanism of comets interaction with planets apparently is versatile, whereas its geological consequences are determined by a combination of four major factors [11]. This: 1) presence and density of gaseous envelope of planet, 2) thickness of lithosphere planet, and 3) degree of heating of lithosphere rocks, and 4) density of cometary fallings.

In first part of this message we give brief information about galactic comets and their interaction mechanism with Earth. A second part will be devoted to discussion action of this mechanism on Moon, Mercury and Mars, as well as to comparison Venus and Earth which have sufficiently dense atmospheres.

Information about Galaxy's comets:

Galactic comets are a class of major space bodies, which move in the galactic plane and cyclically bombard all planets of Solar system exclusively in moments when Sun is located in the jet flows and spiral arms of Galaxy [5]. Those periods are repeated every 20–37 million years and have duration of 1–5 million years old. Therefore fallings of galactic comets have character of relatively short "cometary showers", during of which to Earth may fall of 10^4–10^7 galactic comets. In geochronological Phanerozoic scale all those events are fixed as boundaries stratons. Last bombardment took place at 5.0–0.7 million years ago on border of Neogene and Quaternary and caused a significant heating of asthenosphere which led to a marked lifting of the continents surface. This phenomenon was named "the newest uplift of the crust" [12]. Similar heating of asthenosphere and lifting of continental surface took place also on Mars and Moon [9,10].

Diameter nucleus of galactic comets varies from 100 m to 3.5 km, their mass from 10^{12} to 10^{17} g and kinetic energy from 10^{20} to 10^{25} J. Cometary substance is composed at 80–90% of water ice and at 10–15% of carbon-containing components. Speed of movement comets latest "shower" relative to Sun was close to 450 km/s [5].

Unlike to asteroids and comets of Solar system, galactic comets are characterized by an exponential distribution by diameter, mass and energy, which causes an exponential distribution by sizes of geological structures that were created by their fallings. Another difference is that due to inclination of the ecliptic at angle 62º to Galaxy plane, the last time comets were bombing southern hemispheres of terrestrial planets. Therefore leading landforms of southern and northern hemispheres of planets are differ significantly [10]. And finally we must say that galactic comets cannot be visually detected by means of astronomy currently. Therefore all that is known about them today was obtained by studying of the consequences their falling to the Earth and other terrestrial planets, as well as using the results of their collisions with bodies of the asteroid belt [1,5].

Mechanism interaction of galactic comets with Earth:

We have studied this mechanism as three-step process [8]. In the first stage – in Earth's atmosphere – comet nucleus is transformed into peculiar gas-fluid jet consisting of cometary material, subjected to ablation, and shock-heated air

[6]. In the second stage this jet inelastically collides with a solid surface, creating narrow-directed hypersonic shock wave which penetrates deep into lithosphere of the planet and causes heating of cylindrical column of rocks. The heating is so great that top part of column are vaporized, forming crater, and the material under crater is melted, forming magma chamber. When calculating of heating effects caused shock wave we used the hydrodynamic model of first approximation Lavrentiev [13] designed to study the collisions of bodies with cosmic speeds. In the third stage the heating energy is redistributed in system. The melted rocks which arisen in magma chamber fills crater, while magma's excess can to flow out to surface. If heating energy is not enough, magma crystallizes in upper crust, forming the various compositions of intrusives during cooling.

Heating time the rocks column by shock wave takes split second, and the redistribution time of heat energy in rocks is ~400 thousand years for comets small size and ~2 million years for largest comets. Heat effects created by galactic comets of "small" size – 300 m and a "large" – 3 km are illustrated in Fig. 1. The small comets are able to create craters of deep to ~1 km, whereas large comets – to 7 km and more. At that, magma chambers created by small comets are located at a depth of ~1–3 km from the surface, and at this case the melt that has been formed in magma chamber is not completely fills crater.

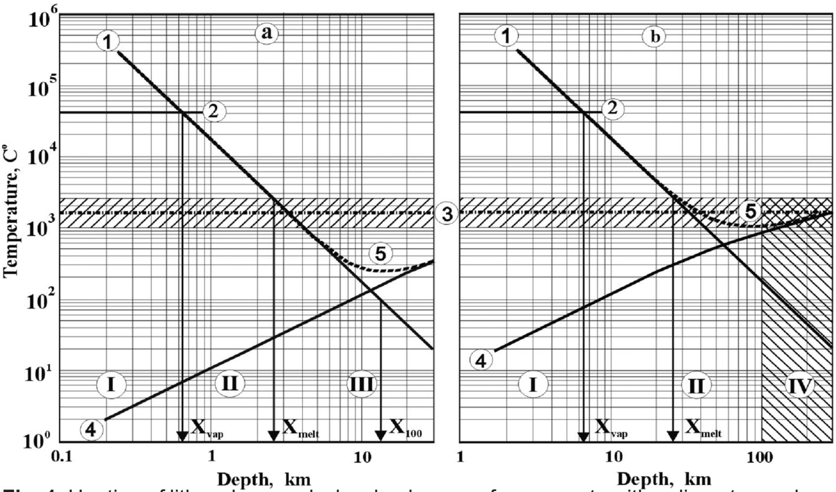

Fig. 1. Heating of lithosphere rocks by shock waves from comets with a diameter nucleus of 300 m (a) and 3000 m (b): 1 – design temperature heating rocks, 2 – evaporation temperature of rocks, 3 – temperature range of melting of rocks (shaded), dotted line – average melting point of 1750 ºC, 4 – natural temperature increase with depth for the continental lithosphere, 5 – cumulative heating of rocks. Heating zones rocks: I – evaporation zone (crater), II – melting zone (magma chamber), III – heating zone, IV – asthenosphere; H_{ev}, H_{melt} and X_{100} – respectively the lower boundaries of the zones of evaporation, melting and heating to a temperature of 100ºC

The large comets may create cameras, which reach of asthenosphere depth ~100–250 km. In result large amount of magma can flow to surface. In both cases crater depth coincides with column diameter of heated rocks. Results of calculations (Fig. 1) are applicable also for comets falling into World Ocean. From energy point of view the energy losses due to evaporation of water at formation of crater are small (~1–10%).

The main difference between falling comets on continents and into World Ocean is that in the former case, when lithosphere is enough "thick" and asthenosphere lies deep, comets are capable create in the column of heated rocks three zones: crater (I), magma chamber (II) and heating zone (III) below the melting point of rocks. In the event of fall comet into World Ocean where asthenosphere is closer to Earth surface, zone (III) may absent. As a result will be created continuous conductive pipe – "plume" through which magma can flow to surface from asthenosphere. At that importantly to note that these plumes may be created not only by large comets but also vast majority of small comets.

References:

[1] Barenbaum A.A. (2002) *Galaxy, Solar system, Earth: Subordinated processes and evolution* (Moscow: GEOS)

[2] Barenbaum A.A., J.B. Gladenkov, N.A. Yasamanov (2002) Geochronological scale and astronomical time (modern condition of problem). *J. Stratigraphy. Geological correlation,* 10(2), 3–14.

[3] Barenbaum A.A., V.E. Khain, N.A. Yasamanov (2004) Large-scale tectonic cycle: an analysis from standpoint of galactic concept. *Vestnik Moscow St. Univ. Ser.4. Geology,* №3, 3–16.
[4] Barenbaum A.A., T.V. Litvinova, V.E. Khain (2009) Geological evidence of the space influence of on the life evolution. Vendian-Cambrian biotic event. Vendian-Cambrian biotic event, *Uralian Geological Journal,* 72(6), 15–39.
[5] Barenbaum A.A. (2010) *Galaxycentric paradigm in geology and astronomy* (Moscow: LIBROKOM)
[6] Barenbaum A.A., V.V. Shuvalov (2007) Modeling interactions of galactic comets with atmosphere. *Physics Extreme States of Matter-2007,* ed. Fortov V.E. *et al.* (Chernogolovka: IPCP RAS), 139–140.
[7] Barenbaum A.A. (2012) On the origin of newest uplifts crust: New formulation of problems global geodynamics. *Uralian Geological Journal,* 90(6), 3–26.
[8] Barenbaum A.A. (2013) A possible mechanism of heating lithosphere rocks galactic comets, *Uralian Geological Journal,* 91(1), 21–39.
[9] Barenbaum A.A., M.I. Shpekin (2011) About age of the lunar surface, *Vestnik Otdelenia nauk o Zemle RAN*, V.3, NZ6011, doi:10.2205/2011NZ000141
[10] Barenbaum A.A. (2012) On the asymmetry of surface of terrestrial planets, caused by falls of galactic comets. *Vestnik Otdelenia nauk o Zemle RAN*, V.4, NZ9001, doi:10.2205/2012NZ_ASEMPG
[11] Barenbaum A.A. (2014) Tectonic-magmatic consequences of fallings galactic comets on terrestrial planets, *Experiment in Geosciences,* 20 (1), 59–63.
[12] Artyushkov E.V. (1994) The newest uplifts of crust on continents as consequences lifting of great hot matter masses from the mantle, *Doklady Akademy Nauk,* 336(5), 680–683.
[13] Lavrentiev M.A. (1959) Problem of penetration at space velocities. *Artificial satellites of Earth,* V.3, 61–65 (Moscow: Academy Sciences USSR)

FORMATION OF ANALOGOUS GEOLOGICAL STRUCTURES ON TERRESTRIAL PLANETS BY GALAXY'S COMETS (II): FACTUAL DATA AND THEIR DISCUSSION

A.A. Barenbaum
Oil and Gas Research Institute RAS, Gubkin str. 3, 119333 Moscow, Russia.
azary@mail.ru

Introduction:

Basing on physical mechanism of interaction of galactic comets with planets, set out in the first part article, below we discuss the features of distribution of craters and mountains on Venus, Earth, Mars, Mercury and Moon depending of two factors [1]: 1) presence of atmosphere and 2) thickness of lithosphere on planet.

Presence and density of atmosphere:

Influence of atmosphere and its density we discuss on the basis of distributions analysis of impact craters of diameters D = 10÷180 km at continental parts of surface Moon, Mercury, Mars, Earth and Venus (Fig. 1).

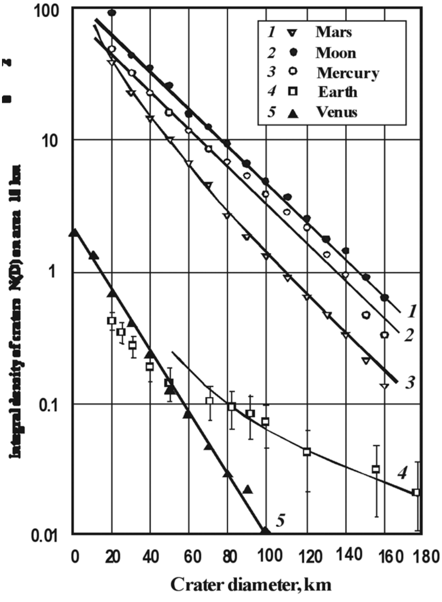

Fig. 1. Integral density of craters on the Moon (1), Mercury (2), Mars (3), Earth (4) and Venus (5). Curve (4) corresponds to inversely-quadratic dependence. Distribution of (1), (2), (3) are based on data [2]; distribution of (4) – on data VI Feldman [3], and distribution of (5) – according to data [1]

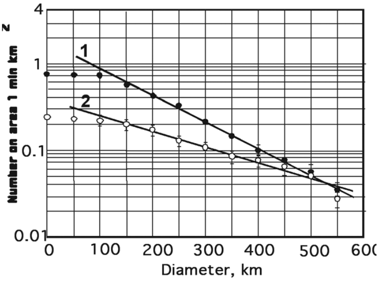

Fig. 2. Integral density on Venus coronae (1) and montes (2) [1]

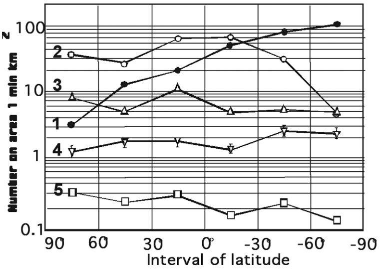

Fig. 3. The density of craters (1, 2, 3), coronae (4) and montes (5) on Mars (1, 2) and on Venus in the latitude belts with step $\Delta\varphi$ = 30°. Craters on Mars have been formed by fallings of galactic comets (1) and of asteroids and comets of Solar system (2)

Unlike Earth vast majority of craters on other planets and Moon were created by fallings of galactic comets. In result on atmosphereless Moon and Mercury the craters distribution N(D) obey by exponential dependence, which reflects the exponential distribution of diameters of cometary nuclei. In rarefied Martian atmosphere the function N(D) is deformed – the number craters of large diameters decreases and small grows. Moreover inasmuch density of cometary fallings in last "cometary shower" is ~5 comets on area 100×100 km^2 [4] continents of Mercury, Moon and Mars are completely saturated craters with D ≥ 10 km. This saturation limit of craters for all planets is identical and equals to ≈100 craters on 10^6 km^2 [3].

In Earth's atmosphere galactic comets are destroyed entirely [3]. Therefore cometary craters with D ≥ 10 km on our planet are absent, and all craters of such size are created asteroids. Their distribution N(D) corresponds to inverse square law which is inherent to large asteroids and comets of Solar system. This dependence for craters on a plot of D < 80 km however is distorted by observational selection.

In more dense gas envelope Venus the galactic comets are destroyed a fortiori. At that the amount of large craters on Venus in ~100 times less than at absence or low density atmosphere. At that their size distribution has the same tilt that for initial portion of function N(D) on Mars.

Thickness lithosphere:

The features of craters Venus indicate their formation in form diatremes [5], which arise in the case of "thick" lithosphere if magma formed is not enough to completely fill the crater cavity. On our planet about 5% such structures contain diamonds. Therefore they are known as the kimberlitic pipes. It is believed that diamond-bearing pipes arise in explosions at depths greater than 100 km [6]. From the standpoint of mechanism heating rocks by shock waves all diatremes can be considered as form of intraplate magmatism [7] which occupies an intermediate position between outpouring of lava on surface and cooling lava in cavity of crater. We attribute the formation of craters on Venus with this type magmatism.

Consequences fallings of galactic comets on "thin" lithospheric plates in particular into World Ocean are of a different nature [8]. In this case is arise much more quantity magma which reach surface where in marine conditions creates seamounts and hotspots and in general takes part in formation of modern ocean crust [9], and in continental conditions produces vast trappean outpourings.

Comparison of analogous geological structures on Venus and Earth:

Lithosphere rocks on Venus and Earth are very similar. Therefore geological structures formed by galactic comets on Venus are almost the same as on Earth. Let us briefly consider their similarities and differences.

Shield volcanoes: Volcanoes of Venus are analogical to seamounts of our planet but smaller in sizes. Most have diameter of 1–20 km and height of several hundred meters. Volcanoes number is of about 10^6 and their size distribution is exponentially [10] as and of seamounts on Earth [11] and cometary craters on atmosphereless planets (Fig. 1). Also it should be noted that the number of volcanoes on Venus is of the same order as Earth's seamounts [11] and cometary craters on planets with no atmosphere. Furthermore, the shield volcanoes on Venus are grouped in fields of ~60–300 km in diameter [12], i.e. of same dimensions that diatreme fields on Earth [6].

Craters: On Venus there are 880 large craters (Fig. 2). The number of craters is about as many as on Earth, but they are distributed according to an exponential law which is not compatible with the hypothesis of their formation as a result of falling asteroid bodies. Craters on Venus are 100 times less than on atmosphereless planets and the slope of their distribution N (D) is steeper. This indicates that Venus atmosphere causes intense fragmentation of cometary nuclei and significantly reduces energy of the gas jet which reaches planet surface.

Coronae and montes: On Venus there are 340 tectonic-magmatic uplifts rounded shapes called coronae and 115 large plateau-like mountains – montes. The size distributions of coronae and montes are shown in Fig. 2, and their latitudinal distributions – in Fig. 3. Distribution of coronae and montes (Fig. 3) excepting area of small diameters distorted by observation selection obeys exponential dependence which is testament to their formation in result falls of galactic comets. This conclusion is confirmed by Fig. 3 where we compare the densities of craters, coronae and montes on Venus with similar latitudinal distribution of craters Mars formed by galactic comets and asteroids [3]. Unlike most of Martian craters which have been formed during the last cometary shower [3], coronae and montes have a much greater age. We consider that coronae and montes are the different stages evolution of objects one nature, which have been created by very high density fallings of galactic comets [1]. At that first formed the montes and subsequently they take form of coronae.

Of course, these considerations about mechanism interaction of galactic comets with planets need further elaboration and justification.

References:

[1] Barenbaum A.A. (2014) Tectonic-magmatic consequences of fallings galactic comets on terrestrial planets, *Experiment in Geosciences,* 20(1), 59–63.
[2] Kazimirov D.A., B.D. Sitnikov, G.A. Poroshkova *et al.* (1980) *Density distribution of craters on the Moon, Mercury and Mars (Preprint)* (Moscow: Geological Institute RAS & Sternberg Astronomical Institute of Moscow State University)
[3] Barenbaum A.A. (2010) *Galaxycentric paradigm in geology and astronomy* (Moscow: LIBROKOM)

[4] Barenbaum A.A. (2012) On the origin of newest uplifts crust: New formulation of problems global geodynamics. *Uralian Geological Journal,* 90(6), 3–26.
[5] Barenbaum A.A. (2013) Lithosphere's reaction on the falls of galactic comets (II): origin of diamond-bearing kimberlitic pipes*, Physical-chemical and petrological researches in the Earth's sciences: Proc. XIV Int. conf. (Moscow, 7–10 October 2013)* (Moscow: Institute of Geology of Ore Deposits, Petrography, Mineralogy and Geochemistry RAS), 35–38.
[6] Milashev V.A. (1984) *Pipes explosion* (Leningrad: Nedra)
[7] Barenbaum A.A. (2013) Lithosphere's reaction on the falls of galactic comets (III): intraplate magmatism and its manifestations, *Physical-chemical and petrophysical researches in Earth's sciences: Proc. XIV Int. conf. (Moscow, 7–10 October 2013)* (Moscow: Institute of Geology of Ore Deposits, Petrography, Mineralogy and Geochemistry RAS), 39–42.
[8] Barenbaum A.A. (2011) Tectonic-magmatic processes in oceans and continents as indicators fallings of galactic comets, *Modern state of Earth Sciences: Proc. Int. conf. commemorating V.E. Khain* (Moscow: Moscow State University), 166–171.
[9] Barenbaum A.A. (2013) Lithosphere's reaction on the falls of galactic comets (I): origin of volcanic-basaltic layer of oceans crust. *Physical-chemical and petrophysical researches in Earth's sciences: Proc. XIV Int. conf. (Moscow, 7–10 October 2013)* (Moscow: Institute of Geology of Ore Deposits, Petrography, Mineralogy and Geochemistry RAS), 31–34.
[10] Aubele J.C., E.N. Slynta (1990) Venus domes: characteristics and origin, *Annu. Meet. Dallas. Texas. Abstr. with programs. V.22, № 04151*. *Geological Society of America,* A 80.
[11] Ilyin A.V. (1996) Changeable face of the deeps. The problems of studying ocean floor (Moscow: Nedra)
[12] Aubele J.C., J.W. Head, L.S. Crumpler *et al.* (1992) Fields of small volcanoes on Venus (shield fields): characteristics and implications, *Lunar & Planet Sci.* 23(1) 47–48.

CONDITIONS AND STRATEGIES FOR DETECTING EPHEMERAL BRINE ACTIVITY AT THE MARS SCIENCE LABORATORY LANDING SITE, GALE CRATER, MARS

J.L. Dickson[1], J.W. Head[1], M. Kulowski[1]
[1]Brown University, Department of Earth and Planetary Sciences, Providence, RI, USA.
jdickson@brown.edu

Introduction:

The Rover Environmental Monitoring Station (REMS) instrument package [1] onboard the Mars Science Laboratory (MSL) [2] provides a suite of fundamental measurements of near-surface atmospheric conditions at a level of detail inaccessible via remote sensing and global circulation models (GCMs). A provocative early finding from this experiment is that diurnal ranges in temperature and relative humidity are such that perchlorate brines could form on contemporary equatorial Mars through deliquescence [3], the absorption of atmospheric H_2O vapor by salts at or within several centimeters of the surface. This discovery coincides with recent field work at multiple sites on Earth that have documented deliquescence as an important process in hyper-arid [4] and particularly polar desert landscapes on Earth [5-6], confirming prescient predictions from earlier investigations [7-8], and showing that this process is capable of supporting ecosystems [4]. Further, this provides a potential mechanism for explaining the contemporary activity of Recurring Slope Lineae (RSL) in both the mid-latitudes [9] and equatorial [10] regions of Mars.

In this contribution we apply lessons from polar desert processes on Earth and laboratory experiments to assess potential indicators of deliquescence occurring at Gale Crater on present Mars or in the past. We further propose observational strategies for MSL that could help document this process without compromising the fundamental goals of the mission.

Deliquescence in polar deserts on Earth:

Present-day surface and near-surface brine generation in polar deserts on Earth, particularly the Mars-like McMurdo Dry Valleys in Antarctica, is challenging due to extremely low weathering rates and limited interaction with marine waters. Brine generation via deliquescence has recently been documented both geochemically [5] and through integrated time-lapse/meteorological observations [6]. Provided a supply of surface or shallow sub-surface salt minerals, deliquescence will occur when the ambient relative humidity surpasses the deliquescent relative humidity (DRH) of that specific salt and the temperature is greater than the eutectic temperature of the generated solution. Once the brine is generated, it favors remaining in a liquid state as its freezing temperature is significantly depressed, making this process an effective engine for producing liquid water in otherwise frozen deserts, and could explain the existence of the perennially-liquid Antarctic Don Juan Pond, the most saline body of water in the world [6-7].

Hyper-arid atmospheric conditions in both the McMurdo Dry Valleys of Antarctica and on the surface of Mars mean that brines that are generated through this process should evaporate. Liquid water on each planet, however, is metastable, in that on slopes it will flow faster than the rate of evaporation [11]. Thus, transient brines can perform geomorphologically observable work (erosion/deposition) on steep slopes before ultimately evaporating back into the atmosphere, as has been proposed for geologically recent gully activity on Mars [11]. This process would be so transient, however, that there is unlikely to be any detectable mineralogical signature of water in depositional aprons formed through this process, making unequivocal confirmation of brine flow a challenge.

Deliquescence in the polar desert of the McMurdo Dry Valleys manifests itself in two primary surface features: water tracks [12] and wet patches [5]. Water tracks transport hyper-saline fluids from surface snowpacks to localized basins, with freshwater from the source snowbank entraining in-situ brine generated via deliquescence. Wet patches are low-sloped units of soil that have elevated salt and water content relative to adjacent soils and hydrate as a function of water vapor concentration in the atmosphere [5].

Deliquescence on contemporary Mars:

H_2O is stable as ice within a meter of the surface of Mars at latitudes > 60° and has been inferred from orbital observations [13-14] and documented by in-situ sampling [15], providing a source for elevated vapor in lower atmosphere above high-latitude terrains. An unexpected discovery from the Mars Phoenix mission was perchlorate salts in the thin regolith layer above the pervasive ice table in the high-latitude northern lowlands [16-17]. Alkaline perchlorates, rare in terrestrial soils, are deliquescent and have a eutectic temperature of ~-70°C [18], providing an attractive candidate for brine generation in polar deserts. Putative evidence has been presented that deliquescence of perchlorate salts occurred during the Mars Phoenix mission [19]. Perchlorate has been documented by MSL at Gale Crater [20-21], suggesting that the well-distributed global layer of martian regolith is perchlorate-rich. Thus, documentation of active deliquescence at the MSL landing site has global implications and could potentially contribute to the explanations of RSL activity [9-10].

Conditions on the floor of Gale Crater achieve the minimum requirements for brine generation only during martian night and the brine would evaporate rapidly after sunrise [1]. This assumes a flat surface, which is appropriate for the terrain upon which the REMS measurements were made. The rover, however, is approaching more rugged terrain as it traverses to Mt. Sharp, outside of the landing ellipse. Outcrops and large boulders provide nanoclimates within fractures and overhangs where conditions for deliquescence may be achieved but evaporation of brines is impeded by topographic shielding from direct insolation. These nanoclimates may also serve as saltation traps, further concentrating perchlorates and increasing the potential volume of brines. By definition these fractures and overhangs will be challenging to observe, but if found on slopes could yield small amounts of flow observable by the rovers imaging suite.

Imaging strategy for transient brines on Mars:

The MSL payload includes sophisticated imaging systems that can be used to monitor localized slopes for transient activity and change detection within the confines of nominal mission objectives. Specifically, both Mastcam and the Mars Hand Lens Imager (MAHLI) [22] provide high-resolution multispectral imagery at a spectrum of scales. Fractured outcrops on steep local slopes will become further abundant through the course of the mission and repeat imaging and quantitative change detection analyses could reveal localized evidence for deliquescence or small flows triggered by brine generation.

Prospective dedicated experiments include nighttime repeat imaging within outcrop fractures using the LED component of MAHLI. Installed on the Robot Arm, this dexterity could permit detailed observations of nanoclimate processes within heavily sheltered regions during times of day when deliquescence is achievable. Finally, dedicated time-lapse imaging of dense regions of fractured outcrops could be used to monitor for change detection during periods of solar conjunction when the rover is immobile. Once synchronized with REMS data, potential surface interaction with atmospheric water vapor can be documented, as has proven successful in the hyper-arid polar desert of the McMurdo Dry Valleys [6, 23].

References:

[1] Gómez-Elvira et al., 2012, *Space Sci. Rev.*, 170, 583. [2] Grotzinger et al., 2012, *Space Sci. Rev.*, 170, 5-56. [3] Martín-Torres et al., 2015, *Nature Geo.*, 8, 357. [4] Davila et al., 2008, *JGR Bio.*, 113, G01028. [5] Levy et al., 2012, *GRL*, 39, L05402. [6] Dickson et al., *Nat. Sci. Rep.*, 3, 1166. [7] Wilson, 1979, *Nature*, 280, 205. [8] Keys, 1980, Ph.D. thesis, Victoria U. of Wellington. [9] McEwen et al., 2011, *Science*, 333, 740. [10] McEwen et al., 2014, *Nature Geo.*, 7, 53. [11] Hecht, 2002, *Icarus*, 156, 373. [12] Levy et al., 2011, *GSA Bull.*, 123, 2295. [13] Boynton et al., 2002, *Science*, 297, 81. [14] Feldman et al., 2002, *Science*, 297, 75. [15] Smith et al., 2009, *Science*, 325, 58. [16] Hecht et al., 2009, *Science*, 325, 64. [17] Cull et al., 2010, *GRL*, 37, 10.1029/2010GL045269. [18] Besley and Bottomley, 1969, *J. Chem. Therm.*, 1, 13. [19] Renno et al., 2009, *JGR*, 114, 10.1029/2009JE003362. [20] Meslin et al., 2013, *Science*, 341, 10.1126/science.1238670. [21] Ming et al., 2013, *Science*, 343, 10.1126/science.1245267. [22] Edgett et al., 2012, *Space Sci. Rev.*, 170, 259. [23] Levy et al., 2013, *Nat. Sci. Rep.*, 3, 2269.

CONCENTRATING ICE IN POLAR DESERTS: LESSONS FOR MARS FROM PUNCTUATED GULLY INCISION IN THE MCMURDO DRY VALLEYS

J.L. Dickson[1], J.W. Head[1], J.S. Levy[2], G.A. Morgan[3].
[1]Dep. Earth, Env. & Planet. Sci., Brown U., Providence, RI, 02906. jdickson@brown.edu;
[2]U. Texas Inst. Geophys., Austin, TX, 78758.
[3]Center for Earth and Planetary Studies, Smithsonian Institution, Washington, D.C., 20013.

Introduction:

The latitude dependent distribution [1-3] and non-uniform orientations [4-8] of young gullies on Mars suggest that their formation and modification are controlled by the activity of volatiles at or near the surface. Given the relative abundance of gullies and Mars' current thermal environment, CO_2 and H_2O are the most likely candidates for contributing to gully evolution. Contemporary modification of gullies in the southern hemisphere is temporally correlated with the removal of CO_2 frost [9-12], but morphologic properties [13-14], slope values [7], depths of incision [15], and thermal modeling [16-18] of gullies indicate that their formation may be controlled by the action of liquid water in recent high-obliquity excursions, when water ice was capable of accumulating in the mid-latitudes [19-21].

If water is a contributor to gully evolution, then understanding fluvial processes in polar desert environments on Earth is essential for formulating hypotheses for fluvial activity on Mars. The McMurdo Dry Valleys (MDV) of Antarctica host a spectrum of water-related landforms [22] that do not form elsewhere on Earth but are morphologically similar to Late Amazonian features on Mars [23].

Here, we outline the geometric and environmental conditions necessary for achieving net erosion of gully channels in the MDV and evaluate whether similar processes may explain their counterparts on Mars.

Erosion of Gullies in the MDV:

Gullies generally form on relatively warm equator-facing slopes in the MDV [23-24] and exhibit similar alcove/channel/fan morphologies to gullies on Mars [1]. In the South Fork of Upper Wright Valley, which represents the most inland area/zone to experience fluvial erosion [23], alcoves are cut into bedrock cliffs while channel incision occurs along the valley walls within the uppermost ~20 cm layer of colluvium. This superposes a pervasive ice-cement layer (which is an aquiclude during gully activity [25]). Alcoves serve as traps for windblown snow in the winter, then as inhibitors to rapid sublimation via topographic shielding in the summer [26]. This, in a region that experiences < 5 cm of snowfall annually [27], provides a method for net accumulation of ice in gully source regions.

Despite mean annual temperatures in Wright Valley of -19.3°C [28], peak surface temperatures in gully alcoves surpass the melting point on cloudless days in austral spring and summer. Due to the narrow geometry of South Fork, melting occurs in gully alcoves first while the floor of the valley ~1 km below is still below 0°C due to shadowing from the Dais, a ~700 m plateau that separates South Fork from North Fork (Fig. 1). Similarly, melting in gully alcoves and on valley walls persists later in the austral summer than it does on the valley floor.

In years when unusually warm late-summer or spring conditions lead to melting in gully alcoves, this meltwater freezes in the shaded gully channel before reaching the fan on the floor of the valley [29]. This generates concentrated in-channel ice reservoirs that provide an abnormally large volatile source once melting conditions are achieved on the valley floor in December/January.

Rapid discharge from melting of these in-channel ice deposits is capable of eroding ~5 m wide, ~80 cm deep channels within gully systems over just 7 days once melting occurs lower in the gully system [29]. This includes mechanical erosion through the ~20 cm colluvium layer followed by subsequent mechanical and thermal erosion of the underlying ice-cement layer, itself another potential source of meltwater. The channel then becomes a trap for windblown snow in the winter [26], providing a feedback process that amplifies activity within existing gullies: once gullies are formed, they become focal points for modification by processes not explicitly related to their initial formation.

Implications for Mars:

Conditions for the accumulation [19-21] and melting [16, 18] of H_2O-ice in the mid-latitudes of Mars were significantly enhanced during recent high-obliquity excursions [30]. Stratigraphic relationships between gullies and the Latitude-Dependent Mantle (LDM) [19], including full inversion of gully channels, indicate that at least 30 m of LDM, which is known to be ice-rich [19], have been removed since many gullies in the southern mid-latitudes were formed [29]. These predictions and observations converge on a scenario in which H_2O-ice played a more significant role in the mid-latitudes during high-obliquity periods than it does today [19].

Gullies on Mars frequently incise mantling material [31], itself ice-rich [19] and broadly comparable to the ice-cement layer that is incised during peak flow events in the MDV. Measurements of neutron flux [32], lander observations [33], and excavations by recent impacts [34] indicate that the weight percent of H_2O in this substrate far exceeds that of ice-cement that is incised by MDV gullies. This provides an additional high-volume source of volatiles within martian gully systems and may help explain why gullies on Mars are more densely concentrated on host slopes than those in the MDV.

The methods by which ice is concentrated in the MDV are all potentially applicable to Mars at high-obliquity. Recent GCM simulations of Mars at 35° obliquity showed that several cm/yr can be accumulated poleward of 30° in each hemisphere, particularly with an active dust cycle [20]. Shaded gully alcoves on pole-facing slopes would be traps for ice and dust, such that a source for gully initiation is available.

In-channel ice-reservoirs similar to those observed in the MDV may form within gullies on Mars but likely due to different geometries. Martian gullies are most common on mid-latitude pole-facing slopes [1-8], such that insolation conditions would rarely be such that an opposing valley wall or crater rim would shield the lower reaches of gully channels and fans, as occurs on equator-facing slopes in the MDV. Due to their azimuth and slope angle, the upper reaches of martian gully systems will receive more direct insolation than their associated channels and fans, particularly early in local spring. This has the potential to generate meltwater early in the season that would refreeze and potentially accumulate in the lower reaches of gully channels. Peak-season insolation across the entire gully system could then rapidly melt this reservoir.

Multiple experimental [17] and modeling [16, 18] studies have predicted that brief melting could occur at gully locations at high-obliquity. Gullies in the MDV provide a more thorough model to be tested with high-resolution GCMs at gully sites on Mars: can ice on Mars be melted, refrozen and concentrated in reservoirs before it is lost to the atmosphere?

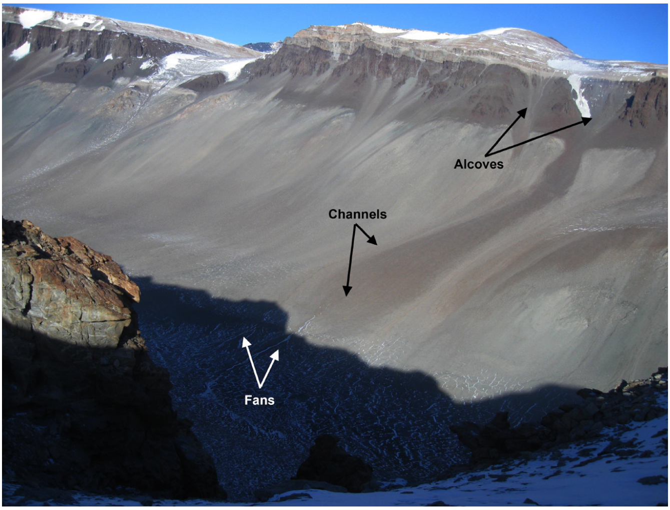

Fig. 1. South Fork of Upper Wright Valley, McMurdo Dry Valleys, Antarctica. Image acquired March 6, 2010. During austral spring and late austral summer, temperatures on valley walls are above freezing while the valley floor is below freezing due to shielding by the opposing valley wall. This creates conditions where meltwater refreezes and concentrates in-channel. Once peak conditions are achieved in austral summer, this reservoir is capable of incising meter-scale channels.

References:

[1] Malin and Edgett, 2000, *Science*, 288, 2330. [2] Milliken et al., 2003, *JGR*, 108, 10.1029/2002JE002005. [3] Harrison et al., 2014, *8th Mars*, 1030. [4] Heldmann and Mellon, 2004, *Icarus*, 168, 285. [5] Balme et al., *JGR*, 111, E05001. [6] Bridges and Lackner, 2006, *JGR*, 111, E09014. [7] Dickson et al., 2007, *Icarus*, 188, 315. [8] Kneissl et al., 2010, EPSL, 294, 357. [9] Dundas et al., 2010, *GRL*, 10.1029/2009GL041351. [10] Diniega et al., 2010, *Geology*, 38, 1047. [11] Dundas et al., 2014, *Icarus*, 10.1016/ j.icarus.2014.05.013. [12] Raack et al., 2014, *Icarus*, 10.1016/ j.icarus.2014.03.040. [13] McEwen et al., 2007, *Science*, 317, 1706. [14] Mangold et al., 2010, *JGR*, 10.1029/2009JE003540. [15] Hobbs et al., *Geomorphology*, 226, 261. [16] Costard F. et al., *Science*, 295, 110. [17] Hecht, M., 2002, *Icarus*, 156, 373.. [18] Williams et al., 2009, *Icarus*, 196, 565. [19] Head et al., 2003, *Nature*, 426, 797. [20] Madeleine et al., 2014, *GRL*, 41, 4873. [21] Mischna et al., 2003, *JGR*, 108, doi: 10.1029/2003JE002051. [22] Levy, 2014, *Geomorphology*, doi: 10.1016/j.geomorph.2014.02.033. [23] Marchant and Head, 2007, *Icarus*, 192, 187. [24] Fountain et al., 1999, *BioScience*, 49, 12. [25] Head and Marchant, 2014, *Ant. Sci.*, 26, 774. [26] Morgan et al., 2010, *LPSC*, 41, 1043. [27] Fountain et al., 2010, *Int. J. Climat.*, doi: 10.1002/joc.1933. [28] Doran et al., 2002, *JGR*, doi: 10.1029/2001JD002045. [29] Dickson et al., 2014, *LPSC*, 45, 1108. [30] Laskar et al., 2004, *Icarus*, 170, 343. [31] Levy et al., 2009, *Icarus*, 201, 113-126. [32] Feldman et al., 2002, *Science*, 297, 75. [33] Smith et al., 2009, *Science*, 325, 58. [34] Byrne et al., 2009, *Science*, 325, 1674.

ICE SHEET LAVA-LOADING ON LATE NOACHIAN MARS: IMPLICATIONS FOR MELTWATER GENERATION, GROUNDWATER RECHARGE, AND GEOMORPHOLOGY

J.P. Cassanelli[1], J.W. Head[1],
[1]Brown University Department of Earth, Environmental, and Planetary Sciences Providence, RI 02912, USA.
James_Cassanelli@Brown.edu

Introduction:

Evidence suggests that cold and dry conditions have persisted on Mars since the mid-to-late Hesperian period [1-3]. While it is likely that the climate conditions of Mars differed during the earlier Noachian period [*e.g.* 2], the exact nature of the martian climate during this earliest period of martian history remains unclear. Geological evidence has been interpreted by some previous investigators to suggest that the early Mars climate may have supported at least episodic "warm and wet" conditions [*e.g.* 4]. However, difficulties in reproducing a "warm and wet" early Mars climate with atmospheric General Circulation Models (GCM) [5], due to a faint young sun [6,7], have led others to propose that the early Mars climate may have instead been predominately "cold and icy" [e.g. 8]. Recent global climate modeling efforts predict generally "cold and icy" conditions, where a Late Noachian (LN) water cycle, combined with slight increases in the atmospheric pressure, results in atmosphere-surface thermal coupling, adiabatically cooling high standing areas [9,10]. As a result, water is transported to high elevation areas where cold temperatures preserve deposited ice, forming regional ice sheets that characterize the Late Noachian "icy highlands" (LNIH) Mars climate scenario [10]. However, the GCM predictions of "cold and icy" conditions give rise to a difficult paradox: How could the abundant features indicating at least transient "warm and wet" conditions for early Mars history have formed if the climate was predominantly "cold and icy"?

Geological evidence unequivocally shows significant LN fluvial and lacustrine activity. Therefore, climate models which predict "cold and icy" early Mars conditions must fail to include some important processes that would allow for melting. Several studies have investigated the possibility for ice sheet basal melting [11,12] to have allowed for liquid water to be generated in spite of "cold and icy" conditions. However, broad-scale ice-sheet basal melting has been shown to occur only at very significant ice thicknesses, geothermal heat fluxes, or through a combination of these factors [11,12]. Additional work has shown that the elevated geothermal heat flux values needed to induce basal melting were likely to have been achieved during the LN on highly localized scales in association with active volcanic features [12]. However, because of the limited scale, the amount of water that can be produced by this "heat-pipe drain pipe" melting is not significant [12].

Are there any other mechanisms for meltwater generation in the context of the LNIH climate scenario? Here we investigate the implications of supraglacial emplacement and loading of lava flows atop LNIH ice sheets for: (1) *top-down* and *bottom-up* ice sheet melting, (2) meltwater generation, transport, and fate (2) *cryosphere* thickness reduction, and *ice-saturated cryosphere* melting, and (3) groundwater aquifer recharge. To assess these processes in the context of the "icy highlands" early Mars climate scenario, we perform a case study on the Hesperia Planum region, an extensive volcanic plains unit in the southern highlands of Mars, where effusive flood basalts may have interacted with regional Late Noachian ice sheets. We divide our assessment to reflect the time-line of lava flow emplacement and loading by considering: (1) Primary supraglacial lava flow emplacement (those lava flows that are emplaced directly atop the ice sheet), and (2) Long-term ice sheet lava-loading.

Ice Sheet Thickness:

We assume the growth of the LNIH regional ice sheets is a supply-limited process (since there is no mechanism to return ice to the lowlands), constrained by a supply 5X the currently observed near-surface/polar water ice budget on Mars (current inventory ~30 m GEL) [13]. Distribution of this water ice reservoir across Mars, above a predicted equilibrium line altitude of +1 km [11], results in average ice sheet thicknesses of ~700 m [11].

Primary and Subsequent Lava Flows:

The short-term thermal interaction between a supraglacial lava flow and the underlying ice is dominated by the transfer of heat from the cooling lava to the ice below. To determine the amount of heat that is transferred to the underlying ice we implement an analytical solution of the 1-D heat equation [*e.g.* 14]. Under nominal LN climate conditions, lava flows that are emplaced across the top of the ice sheets will not encounter a surface comprised of solid ice, but rather snow and firn [15], resulting in more rapid melting. Analysis of the heat transfer from lava flows of varying thickness indicates that thinner lava flows contribute a much higher heat flux to the ice, but over a much shorter period of time, melting less ice (Figure 1).

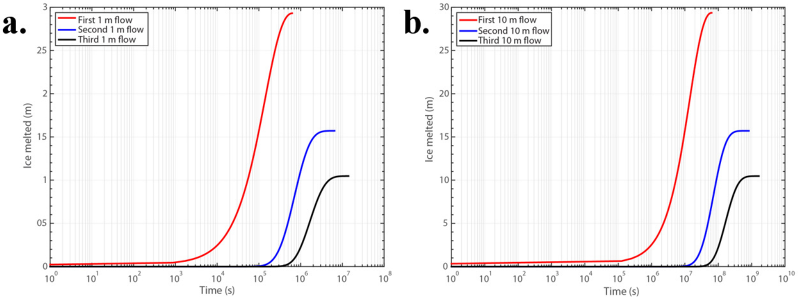

Fig. 1. (a.) Top-down ice melting versus time due to the emplacement of a sequence of 1 m thick supraglacial lava flows. **(b.)** Top-down ice melting versus time due to the emplacement of a sequence of 10 m thick supraglacial lava flows.

After the emplacement of the first flow, subsequent flows will contribute much less heat to the underlying ice sheet because of the intervening solidified lava and will therefore produce less total ice melting (Figure 1). Superposed lava flows will undergo subsidence equal to the total thickness of ice melted, with the potential for fracturing, and degradation of the lava flow morphology. Due to the ability of the firn layer to absorb meltwater, the ultimate result of supraglacial lava flow emplacement will be to simply diminish the firn layer through melting, refreezing, and compaction, leaving an accumulation of degraded lava flows atop the ice sheet.

Lava-loading:

As lava flows accumulate above the ice sheet, heat conducted down into the underlying ice will become significantly reduced such that *top-down* melting will become negligible. At this point, the lava flows will have formed a thermal blanket atop the ice sheets, insulating the ice sheet and acting to raise the ice-melting isotherm. If a sufficient thickness of lava is accumulated, the insulation provided by the lava flows and the ice sheet may allow the melting isotherm to intercept the base of the ice sheet, inducing basal melting.

To model the thermal evolution of the LNIH ice sheet and cryosphere in response to insulation by lava loading, we implement a finite difference technique to numerically solve the 1-D heat equation. We model lava loading of the LNIH ice sheets by assuming that lava flows accumulate in ~10 m increments up to a maximum thickness of 2 km based on measurements of martian flow front thicknesses [16] and partially buried craters throughout the Hesperia Planum region. Previous investigations suggest emplacement of the Hesperian Ridged plains over ~100-200 Myr, with active eruptions occurring for only ~0.01% of this time, giving a total cumulative eruption duration of only ~10 Kyr [17]. Here, we adopt an average emplacement timescale estimate, and model lava accumulation over 100 Kyr. We account for *top-down* melting of the ice sheet from lava flow emplacement with a parameterization derived from the previous analysis.

We find that cryosphere reduction must occur prior to the initiation of ice sheet basal melting (Fig. 1). If the LN cryosphere was porous and saturated in ice, this would result in the melting and release of a significant amount of water to the subsurface. Under the nominal LNIH conditions modeled (surface temperature 225 K [9,10], geothermal heat flux 55 mW/m^2 [18-20]), the cryosphere will extend ~1.5 km below the surface due to the insulation of the 700 m thick LNIH ice sheets. Therefore, if ~1.5 km of lava (with an average thermal conductivity of ~2.25 W/m k; [21]) is loaded atop the ice sheet, the melting isotherm will be raised to the ground surface, thereby removing the underlying cryosphere completely (Fig. 1). Taking a conservative estimate of the martian crustal porosity structure [22], we find that if the cryosphere were *ice-saturated,* complete melting over an area of ~2x10^6 km^2 (approximately the size of the Hesperia Planum region; [23]), would result in the liberation of ~3 m GEL of meltwater to the subsurface.

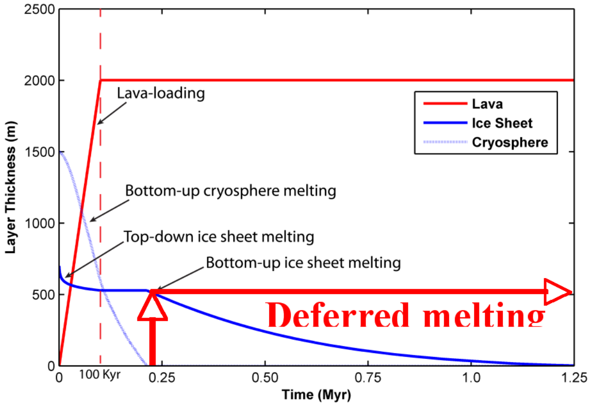

Fig. 2. Model results showing the thermal evolution of the cryosphere and ice sheet in response to accumlating superposed lava.

Under the same LN conditions, accumulation of ~2 km of lava flows will result in complete thermal instability of the LNIH ice sheets and eventual "deferred" melting (Fig. 1). If this occurs over the same area, then a total of ~13 m GEL of meltwater would be produced. Meltwater that is produced from basal melting of the buried LNIH ice sheets will either: (1) infiltrate down into the substrate, since predicted basal melting rates of the ice sheet are significantly below infiltration rates predicted for the martian substrate, or (2) become sequestered beneath the ice due to the presence of an impermeable underlying layer (*e.g.* competent bedrock). If meltwater is able to infiltrate, then the superposed sequence of lava flows will undergo subsidence, leading to fracturing and degradation of the surficial lava flow morphology. If infiltration is prevented, meltwater will pool beneath the ice sheet because the ice sheet margins will remain frozen to the base. Meltwater will then accumulate and become pressurized from the overburden load of ice and lava. If sufficient pressure is built up, the water may fracture through the confining ice at the margins, potentially resulting in large flooding and landslide events.

Potential Implications:

(**1**) *Top-down* melting generated by the emplacement of supraglacial lava flows is limited, but effective at removing the snow and firn layer. **(2)** Sufficient accumulation of lava atop the LNIH ice sheets (~1.5-2 km) can result in cryosphere removal, and ice sheet basal melting, despite "cold and icy" conditions. **(3)** Melting induced by this mechanism over an area the size of Tharsis could liberate up to ~30 m GEL of water from the cryosphere, and ~110 m GEL of water from the ice sheets. **(4)** Ice sheet basal melt is predicted to infiltrate and provide groundwater recharge unless the ice sheets are underlain by an impermeable material. **(5)** Subsidence from melting of subsurface ice will cause fracturing and degradation of the superposed lava flows, and may lead to flooding and landslide events.

References:

[1] Head et al. (2003) *Nature,* 426, 797. [2] Bibring et al. (2006) *Science*, 312, 400. [3] Ehlmann et al. (2001) *Nature* 479, 53. [4] Craddock and Howard (2002) *GRL*, 107, 5111. [5] Haberle (1998) *JGR Planets* 103, 28467. [6] Newman and Rood (1977) *Science*, 198, 1035. [7] Gough (1981) *Physics of Solar Variations*. Springer Netherlands, pp. 21–34. [8] Haberle et al. (1993) *J. Atmospheric Sci.,* 50, 1544. [9] Forget et al. (2013) *Icarus, 222*, 81. [10] Wordsworth et al. (2013) *Icarus, 222*, 1. [11] Fastook and Head (2014) *PSS*, 106, 82-98. [12] Cassanelli et al. (2014) *PSS,* 108, 54-65. [13] Carr and Head (2014) *GRL,* 42, 726-732. [14] Wilson and Head (2007) *Annals of Glaciology*, 45, 83. [15] Cassanelli and Head (2014) *Icarus*, 253, 243-255. [16] Hauber et al. (2009) *J. Volcanology and Geothermal Res.,* 185, 69. [17] Halevy and Head (2014) *Nature Geoscience*, 7, 865-868. [18] Russell and Head (2007) *PSS,* 55, 315. [19] Fastook et al.(2012) *Icarus,* 219, 25. [20] Solomon et al. (2005) *Science*, 307, 1214. [21] Robertson and Peck (1974) *JGR,* 79(32), 4875. [22] Clifford (1993) *JGR Lett.,* 98, 10973. [23] Tanaka et al. (2014) Geologic Map of Mars. US Geol. Surv. Sci. Investig. Map 3292.

DEGRADATION STATE OF NOACHIAN HIGHLAND CRATERS: ASSESSING THE ROLE OF CRATER-RELATED ICE SUBSTRATE MELTING IN A COLD AND ICY MARS

D.K. Weiss[1], J.W. Head[1]
[1]Brown University, Department of Earth, Environmental, and Planetary Sciences, Providence, RI, USA.
david_weiss@brown.edu

Introduction:

The faint young sun [1,2] has led to the supposition that early Mars was cold [3-5]. The presence of valley networks and the degraded state of highland craters, however, has led many investigators to suggest that the martian climate in the Noachian was warm and wet, and that precipitation [6] in the form of rainfall [7] and fluvial activity are the likely causes of crater degradation. Recent climate models, however, have shown that climactic conditions in the Late Noachian may not have been favorable for liquid water precipitation [8,9], and that regional snow and ice deposits, much like those inferred to be present in the Amazonian (Fig. 1) [10], characterized the Late Noachian highlands [11]. These climate models have shown that unlike the Amazonian, slightly increased atmospheric pressures in the Late Noachian could allow the atmosphere to thermally couple to the surface [8], a scenario in which the Noachian southern highlands acts as a cold trap and preferentially accumulates atmospheric snow and ice deposits [8,11-13], the *Late Noachian Icy Highlands (LNIH) scenario*.

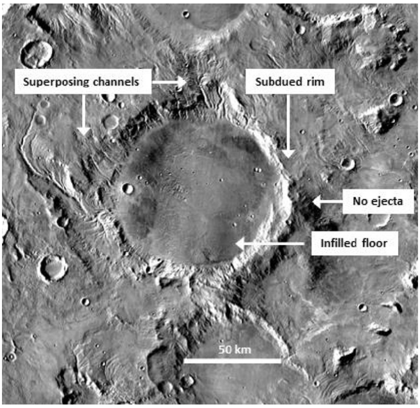

Fig. 1. Noachian highland crater and characteristics.

The degraded martian highland craters are a common feature of the Noachian-aged southern highlands, and may provide insight into the climatic conditions on early Mars. Martian Noachian highland craters (Fig 1) differ from fresh martian craters in that they possess (1) subdued crater rims [7,14,15]; (2) flat/shallow floors [7,14,15]; (3) a paucity of craters <~10-20 km in diameter [14,16-19]; (4) channels superposing crater rims [7,14,15,19]; and (5) a relative absence of ejecta facies [7,14,15]. These characteristics have been variously explained by (1) burial by air fall deposits [20-24]; (2) erosion by groundwater sapping [25]; (3) erosion by rainfall and surface runoff [6,7,15]; (4) impact-induced seismic liquefaction [26]; (5) a complex interweaving of erosion, deposition, and cratering [27]; or (6) erosion from melted snowpack [28].

Based on the suggestion that the Late Noachian southern highlands may have been covered with hectometers-thick snow and ice deposits [8], it has recently been proposed that the degradation state of Noachian highland craters might also be explained in the LNIH model [29]. In this scenario, impacts in the highlands occur in hectometers-thick snow/ice deposits. Investigation of formation of a hypothetical impact crater in such a deposit predicts the following candidate features: (1) structurally-uplifted rims may be partially composed of the surface snow/ice layer, and allow some of the depth of the crater cavity to be accommodated by the surface ice; (2) subsequent removal of the surface ice in a later, different climate could then lower the rim height and produce an apparently smaller crater cavity; (3) following the impact, erosion should modify the crater: backwasting of rim material could contribute to the flat and shallow floors and subdued rims seen in Noachian highland craters [15]; (4) insolation-induced top-down melting, such as proposed for Amazonian gullies [e.g., 30,31], or melting from emplacement of hot ejecta around large craters [28] could generate runoff: such a process could further erode the rim and ejecta, infill the crater, and generate near-rim superposing channels [e.g., 32].

Impact ejecta-induced basal melting?:

In addition to these candidate predicted processes, could basal melting of surface ice [29] contribute to the degradation state of highland craters formed in icy substrates? Highland craters formed on this environment would be unusual in that the snow/ice deposits in which they form would still be present beneath their ejecta facies during modification; snow and ice could also overlie the crater during periods of continuing snow deposition. If basal melting following ejecta emplacement were to occur, fluvial erosion from the melted snow/ice deposits might contribute to rim and ejecta erosion, channel formation, and crater infill. Previous investigators [5,12,33,34] have shown that it may be possible to generate basal melting only in instances of hectometers to kilometers thick ice and snow deposits. The LNIH ice budget above a 1 km equilibrium line altitude may be as low as ~300 m assuming the 34 m GEL Amazonian ice supply limit [35, 36], and thus the Late Noachian regional snow/ice deposits would likely be of insufficient thickness to generate basal melting. Recent work, however, suggests that deposition of low-thermal conductivity ejecta on top of regional snow and ice deposits is sufficient to raise basal temperatures above the melting point of water-ice [29]. In the current analysis, we explore the predicted effects of ice melting below impact crater ejecta on degradation processes and state of Noachian highland craters.

Quantitative assessment of basal melting:

We model the *crater diameters* predicted to exhibit basal-ice melting, *melting timescales*, and *erosional capability of basal ice melting* in the LNIH scenario. Preliminary calculations suggest:

(1) *Crater diameters* above ~40 km have near-rim ejecta thicknesses sufficient to generate basal ice melting (Fig. 2).

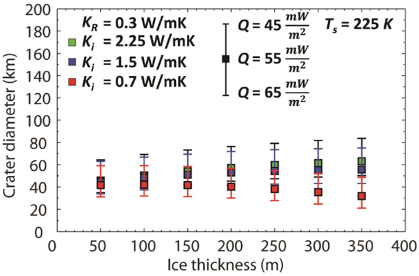

Fig. 2. Minimum crater diameters predicted to ex-hibit basal melting.

(2) *Melting timescales:* The timescale for the ice-melting isotherm to reach the base of the ice sheet (and initiate basal melting) is dependant upon heat flux (*Q)* the initial depth of the ice-melting isotherm (i.e., the thickness of the cryosphere), and the density, heat capacity, and thermal conducitivity (*K*) of the subsurface. We predict that basal melting initiates ~100-200 kyr after impact for craters 40-150 km in diameter. Because the thermal conductivity of ejecta is much lower than that of ice, the entire thickness of ice below the ejecta is generally able to melt. A lower-bound estimate for complete melting of a 300 m ice sheet below the near-rim ejecta is ~53 kyrs, or ~100 kyrs for a 600 m thick ice sheet (Fig. 3a). Basal melting is thus predicted to terminate between ~150-300 kyr following the initial impact.

(3) *Erosion*: The amount of erosion generated by basal melting is dependant upon melt production rates and substrate permeability. We predict the minimum melt production rate from basal melting to be ~4-8 x 10^{-3} m/yr per m^2 (Fig. 3b) for heat flows [37, 12] between 45 and 65 mW/m^2. Substrate permeabilities above ~10^{-16} m^2 allow infiltration rates to exceed melt production rates, favoring minimal erosion (Fig. 3b). Substrate permeabilities below ~10^{-16} m^2 produce infiltration rates below melt production rates, and thus favor erosion. Permeability models [38] show that megaregolith permeability at the surface is much less than 10^{-16} m^2. For basal melting to have an erosive effect, we predict that a low permeability substrate (i.e., bedrock) is required.

Predictions to test the LNIH model:

Basal melting of ice underlying near-rim ejecta of craters is predicted to occur in the LNIH scenario. If an impact occurred in megaregolith, the ice-rich rim should be depressed by melting, but erosion of the ejecta and substrate is predicted to be minimal. If the impact occurred in bedrock, low infiltration rates would favor fluvial erosion, which could contribute to ejecta and rim erosion, channel formation, and crater infill.

The amount of erosion from basal melting is also predicted to be dependant upon the thickness of ice initially beneath the ejecta, which places a supply limit on total melt volume. Because the predicted amount of erosion will be dictated by melt volumes and rates, the validity of the LNIH scenario can be tested and constraints can even be placed on the melting-style in the hypothesized LNIH scenario. For example, if no evidence of basal melting is observed, then the LNIH scenario is not supported. If basal-melt volumes and rates are insufficient to produce the observed erosion, other (warmer) climate scenarios [e.g., 6, 7, 15] or mechanisms to produce melt (e.g., top-down melting of snow [8, 28], and/or volcanically-induced atmospheric warming pulses [39]) would be required. We are currently assessing a representatione population of Noachian highlands craters to test these predictions.

References:

1) Gough, Solar Physics 74, 21, 1981; 2) Newman and Rood, Science 198, 1035, 1977; 3) Kasting, Icarus 94, 1, 1991; 4) Haberle et al., LPI technical report 93, 19, 1993; 5) Carr and Head, GRL 30(24), 2003; 6) Hynek and Phillips, Geology 29, 407, 2001; 7) Craddock and Howard, JGR 107, E11, 2002; 8) Wordsworth et al., Icarus 222, 1, 2013; 9) Scanlon et al., GRL 40, 4182, 2013; 10) Fastook and Head, PSS 91, 60-76, 2014; 11) Head LPSC XXIII, 2137, 2012; 12) Fastook et al., Icarus 219, 25, 2012; 13) Head and Marchant, Antarctic Sci., 26, 2014; 14) Craddock and Maxwell, JGR 98, 3453, 1993; 15) Craddock et al, JGR 102, 13321, 1997; 16) McGill and Wise, JGR 77, 2433, 1972; 17) Jones, JGR 79, 3917, 1974; 18) Craddock and Maxwell, JGR 95, 14265, 1990; 19) Masursky et al., JGR 82, 4016, 1977; 20) Hartmann, Icarus 15(3), 410, 1971; 21) Wilhelms and Baldwin, LPSC XIX, 355, 1989; 22) Grizzaffi and Schultz, Icarus 77, 385, 1989; 23) Grant and Schultz, Icarus 84, 166, 1990; 24) Moore, JGR 95, 14279, 1990; 25) Gurnis, Icarus 48, 62, 1981; 26) Clifford, LPSC XXCIII, 1846, 1997; 27) Malin and Edget, JGR 106, 23429, 2001; 28) Kite et al., JGR 116, 2011; 29) Weiss and Head, LPSC XLV, 1077, 2014; 30) Dickson et al., Icarus 188, 315, 2007; 31) Head et al., PNAS 105 13258 2008; 32) Morgan and Head, Icarus, 202, 2009; 33) Zent, LPSC XXX, 1803, 1999; 34) Cassanelli and Head, LPSC XLV, 1501, 2014; 35) Fastook et al., Icarus 228, 54, 2014; 36) Fastook and Head, LPSC XLV, 1115, 2014; 37) McGovern et al., JGR 109, 2004; 38) Hannah and Phillips, JGR 110, 2005; 39) Halevy and Head, Nature Geosci., 2014.

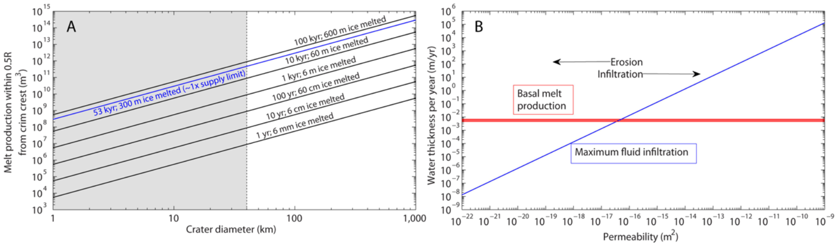

Fig. 3. A) Basal melt volume as a function of crater diameter and time. B) Basal melt production compared with infiltra-tion rates.

THE SECONDARY IMPACT EJECTA SPIKE ON PHOBOS FROM STICKNEY CRATER

K.R. Ramsley[1,2], J.W. Head[1]
[1]Department of Earth, Environmental and Planetary Sciences, Brown University, Providence, RI 02912 USA;
[2]School of Engineering, Brown University, Providence, RI 02912 USA.
Kenneth_Ramsley@brown.edu.

Introduction:

Utilizing two different planetary background flux estimates and counting craters where the Mars Express HRSC camera offers sufficient image resolution, Schmedemann et al. (2014) [1] derive two possible age ranges for the largest impact feature of Phobos, Stickney Crater. Case A derives 2.8–4.2 Ga by assuming that Phobos has orbited Mars during the entire period. Case B derives an age of 38 Ma – 3.4 Ga by assuming that Phobos is a recently captured asteroid that was exposed to Main Belt flux. Our model investigates a third option where we explore the possibility that a young Stickney impact produced a spike in the impact flux in the form of secondary impact projectiles that make its surface look prematurely ancient by forming the vast majority of the counted superposed craters < 0.6 km and a lesser population up to 2 km due to extreme ejecta volume and velocity.

Stickney blocks:

Small boulders on Phobos are degraded and destroyed by meteor impact flux subsequent to their emplacement/exposure at a rate that suggests that these boulders have been exposed for ≤ 0.5 Ga [2]. Consequently, an ancient age for Stickney of 2.8–4.2 Ga is unlikely in view of the work of Thomas (2000) [3] who mapped thousands of blocks that are located proximally to the east of Stickney Crater, and further observes that the quantity and distribution of the blocks is morphologically consistent with ejecta from a large recent impact. Based on their quantity, size, and preferential areal concentration that increases with closer proximity to Stickney Crater, this strongly suggests that Stickney Crater is the source of the blocks [3]. Apart from invoking the substantially uncertain crater-counting age of a recent asteroid capture of Phobos [1], how can one reconcile an age of ≤ 0.5 Ga for Stickney-related boulders [2, 3] and a crater-counting age prediction of 2.8–4.2 Ga [1]? Either the boulders are produced by an alternate source or the craters that are used for counting are produced by an alternate mechanism other than the background impact flux [4]. We investigate the latter case.

Stickney ejecta:

The vast majority of ejecta from Stickney is trapped in orbits around Mars, and because the ejecta is inserted into orbits at a common origin in space, they continue to generally intersect a common origin during subsequent orbits. Eventually, Stickney ejecta fragments and Phobos pass through the same location at the same time [9]. Within dozens to hundreds of years (≤ 200,000 orbits of Phobos) ≥ 95% of Stickney ejecta intersects and impacts onto Phobos. [5–9].

Although ejecta from Stickney returns to Phobos, there is a rule of orbital mechanics that precludes secondary impacts on primary impact sites when the target is a tidally-locked body. Primary impact ejecta on tidally-locked bodies intersects the target body generally on the opposite hemisphere of the primary impact site [9]. Consequently, a primary crater that is produced on a tidally-locked body remains *unexposed* to its own secondary impacts.

Breaking the tidal lock of Phobos:

The rule of celestial mechanics that shields a primary crater on a tidally-locked body from its own secondary impacts is violated when the impact event breaks the tidal lock. If the Stickney impact broke the tidal lock of Phobos, the entire surface of Phobos would be exposed to Stickney ejecta, including Stickney Crater and its proximal regions.

Does the Stickney impact produce an impulse that breaks the tidal lock? First, we assume that the boulder evidence sets an upper limit of 0.5 Ga for the age of Stickney [2, 3]. In view of the increasing orbital decay rate of Phobos, an orbital altitude that is 4,000 km above the present day is selected for our model [10–13]. At this altitude, the Stickney impact increases the rotational rate of Phobos such that it rotates ~6 times for every 5 orbits around Mars. In fact, a Stickney impact at *any* orbital altitude, including the present-day altitude, produces an impulse that is sufficient to break the tidal lock of Phobos.

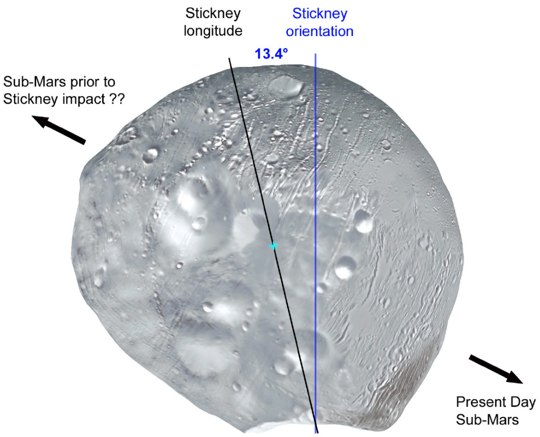

Fig. 1. Stickney Crater is misaligned with the CG of Phobos by 13.4°. Ejecta that is preferentially directed to the west from the tilted crater provides a mechanical advantage to break the tidal lock of Phobos. The pre-impact tidal lock may have been 180° out of phase from the present day or the same as the present.

The Stickney impact is able to break the tidal lock of Phobos because the impact takes place on a western hillside of a high-elevation equatorial region of Phobos. Consequently, a large impulse vector component is directed to the east (Fig. 1). The impulse is analyzed using the Tsiolkovsky rocket equation. The analysis takes into account the inefficiencies of the crater formation process where ~40% of the impact impulse is lost to heating, compression, and the inefficiencies of a cone-shaped "rocket exhaust." By supplying the Stickney impact projectile mass, its velocity, and the impulse inefficiency factor, it is possible to accurately predict the added rotational angular momentum that is produced by the Stickney impact event.

The additional angular momentum breaks the tidal lock if the de-spin time is substantially longer than the time that is required for Phobos to rotate more than ¼ phase from its tidal lock orientation. Beyond this point, Phobos will continue to rotate until it regains its pre-impact tidal lock orientation or is re-locked 180° out of phase from the pre-impact tidal lock orientation. For this reason, the Stickney impact could have taken place in the present-day orientation of Phobos or 180° out of phase from the present day.

If the lock is broken, the duration of the time when Phobos continues to rotate faster than its orbital period must be sufficient to expose the entire global surface of Phobos to returning Stickney ejecta (at least several hundred years). Does Phobos rotate freely for a sufficient period of time? Based on equations from Gladman et al. (1996) [14] and Burns (1977) [15], Phobos de-spins back to a tidal lock after 56,800 years with a lower limit of 14,000 years. Typically, the computation of the de-spin time lacks state information about the initial rotation rate and the orbital altitude of the satellite. However, these variables are supplied by our model. The Love number k_2 and the value of Q also contribute uncertainty. Yet, they may be estimated within factors of ~2X [14], and we are therefore confident in our prediction of a lower limit of 14,000 years for the de-spin time of Phobos after a Stickney impact at 0.5 Ga. 14,000 years is clearly a sufficient length of time to permit Phobos to be globally and uniformly exposed to Stickney secondary impacts.

The Stickney secondary impact spike:

The Stickney impact impulse produces a counterforce. Approximately 10% of the counterforce vaporizes, melts, shocks, and compresses target material. The remaining ~90% of the counterforce is launched as ejecta. During the next several dozen to hundreds of years, approximately 95% of the Stickney ejecta returns to Phobos in the form of secondary impacts that stochastically impact across the entire global surface of Phobos [9]. Based on the mass of the ejecta from Stickney Crater and the kinetic energy of the Stickney ejecta counterforce, it is possible to accurately compute the average secondary impact velocity of returning Stickney ejecta onto Phobos. This works out to an average velocity of 1.1 km/s.

Assuming that ~95% of the Stickney Crater ejecta returns from orbits around Mars, the volume of ejecta projectiles from Stickney that impacts onto Phobos is ~3.7×10^{10} m^3 with a mass of ~6.9×10^{13} kg. Further assuming that Phobos has a surface area of ~1.54×10^9 m^2, the volume of secondary impact flux that is distributed across the geographic surface of Phobos is equal to a projectile material depth of ~24 m.

The spike of ejecta from Stickney returned to Phobos within several dozen to several hundred years in a storm of projectile impacts at an average impact velocity of 1.1 km/s and areal average distribution equal to 3.6 m diameter projectiles impacting onto every square meter of Phobos.

Secondary impact size/frequency:

When we distribute the total volume and average velocity of reimpacting Stickney Crater ejecta on Phobos according to the typical size/frequency curve of a crater population, we predict a sharp spike in the number of craters on Phobos < 0.6 km plus a lesser population up to 2 km due to impact velocities ≤ 4.6 km/s and the extraordinary volume of ejecta that returns. This distribution is entirely consistent with the size/frequency curves of Schmedemann et al. (2014) [1] where the counting area *outside* of Stickney Crater produces a size/frequency curve of large degraded primary craters with a clearly superposed population of younger craters < 0.6 km and a sharp kink in the curve that strongly suggests two separate populations of impact flux.

Furthermore, when Schmedemann et al. (2014) [1] counts craters *inside* Stickney, this reveals no older flux of larger primaries and no sharp kink in the size/frequency curve. Inside Stickney only one population of craters is observed and this population is generally consistent with the population of younger craters that are plotted outside of Stickney. This suggests that the source of the craters inside Stickney is the same flux that produced the superposed population of younger craters outside of Stickney.

Because the crater-counting curve inside Stickney Crater is not exactly smooth, a recent sub-population of primary craters has likely been emplaced inside Stickney since the time of the Stickney impact. Yet, in consideration of the predicted storm of secondary impacts from Stickney and the clearly observed sharp kink in the size/frequency curve in the counting area outside of Stickney, this strongly suggests that most of the craters inside Stickney are secondary impacts from Stickney.

Conclusions:

We conclude that the vast majority of the present-day distribution of craters on Phobos < 0.6 km and a portion of the population ≤ 2.0 km are unrelated to the background meteorite flux of Phobos and are instead consistent with an over-printing of secondary craters from Stickney ejecta that were produced during a brief secondary impact spike within the most recent 0.5 Ga. The emplacement of secondary impacts from Stickney Crater across Phobos severely disrupted the crater-counting clock and produced a crater size/frequency distribution that is consistent with the *apparent* ancient ages that are interpreted by Schmedemann et al. (2014) [1]. Thus, caution must be exercised when determining surface ages by crater-counting in cases where significant ejecta can return to the surface, but may not be recognized as secondary impact craters.

Our analysis suggests that secondary ejecta impacts from a relatively young (≤ 0.5Ga) Stickney Crater can reconcile 1) the observation of Stickney-related boulders by Thomas (2000) [3], 2) the inferred boulder survival lifetimes of Basilevsky et al., (2014) [2] and 3) an apparently ancient age of Stickney of 2.8–4.2 Ga [1].

References:

[1] Schmedemann et al., (2014) *Planet. Space Sci.*, *102*, 152–163. **[2]** Basilevsky et al., (2014) *Planet. Space Sci.*, *102*, 95–118. **[3]** Thomas et al., (2000) *J. Geophys. Res., 105,* 15091–15106. **[4]** Ramsley and Head (2014) *Lunar and Planetary Science Conference,* 1414. **[5]** Dobrovolskis and Burns, (1980) *Icarus 42*, 422–441. **[6]** Juhász et al., (1993) *J. Geophys. Res., 98,* 1205–1212. **[7]** Hamilton and Krivov, (1996) *Icarus 123,* 503–523. **[8]** Krivov et al., (1996) *Celest. Mech. Dyn. Astro. 63,* 313–339. **[9]** Ramsley and Head, (2013) *Planet. Space Sci. 87,* 115-129. **[10]** Burns, (1972) *Rev. Geophys. Space Sci. 10*, 463–483. [**11]** Lambeck, (1979) *J. of Geophys. Res. 84*, 5651–5658. **[12]** Bills et al., (2005) *J. Geophys. Res. 110*, 1–15. **[13]** Jacobson, (2010) *Astro. J. 139*, 668–679. **[14]** Gladman et al., (1996) *Icarus 122*, 166–192. **[15]** Burns (1977) *Orbital Evolution. In Planetary Satellites, (J.A. Burns Ed.)* pp. 113-156.

MORPHOMETRIC CHARACTERISTICS OF POLYGONAL STRUCTURE OF MARS DEPENDING ON SURFACE MORPHOLOGY

S.S. Krasilnikov[1,2]
[1]Vernadsky Institute, RAS, Moscow, Russia; [2]Moscow State University of Geodesy and Cartography, Moscow, Russia.
zergovski@geokhi.ru

Abstract:

Morphology of a thermal contraction crack polygon depends on surface local geomorphology. For study of dependence of polygonal structure from local surface geomorphology we analyzed network of testing sites. It was found that small-scale polygons more distributed on the relatively flat surface, while medium and maximum scale polygons distributed on the more roughness surface.

Introduction:

Thermal contraction crack polygon of Earth are typical for periglacial zones (Tundra, Arctic and Antarctic zones). The presents of H_2O ice in a ground is necessary for formation of this cryogenic forms. The ground ice in Mars spread across Northern and South latitudes and fix up to 30° [1].

The studied region is located in Northern plain of Mars in the West of Olimpia Mensae (74,3°N 93,7°E) and it was analyzed based on the high resolution image HiRISE ESP_018855_2545 (25 cm/pix). For observation of morphometric parameters of the feathers we use testing sites with area of 0,02 km^2. The age of studied area is estimated as Late Amazonian era aged 0,6 – 3,4 Ma and older [2].

Dependence of morphometric parameters of polygons from relief:

The type of polygonal structure on studied region is similar to the High-relief [1] and to S1 type [3] polygons. For this type of polygons a superficial thermal cracks with rare alternation of wide troughs are usual.

In past the studied region could repeatedly overlapped by surge of H_2O ice mass or by viscoplastic CO_2 ice flows [2]. As result the sequence of moraine-like circular ridges was formed in the studied region. Our mapping of studied region shown presence of four main types of surfaces: relatively flat surface, pit-and-knob surface, hill-and-depression surface and moraine-like circular ridges (fig. 1).

All four mapped surface types are located in area between the moraine-like ridges. Roughness of the surface is not more then 1 – 3 m in relatively flat surface, 4 – 10 m for pit-and-knob surface, 20 to 50 m for hill-and-depression surface and 40 – 70 m for moraine-like ridges heights.

Table 1.

Type of surface	Average number of polygons	Average area of polygons, m^2	Average density of polygons in 1 m^2
Relatively flat	793,4	28,82	0,04
Pit-and-knob surface	537,3	41,6	0,027
Hill-and-depression	487,5	47,9	0,024
Moraine-like ridges	417	55,4	0,021

In the studied region where analyzed 7 testing sites for relatively flat surface, 7 testing sites for pit-and-knob surface, 2 testing sites for hill-and-depression surface and 2 testing sites which located on moraine-like ridges. Average number and area of the amount of polygons and their areas is shown in the table 1. Total area of researched testing sites is 0,36 km^2. Average number of polygons for testing (0,02 km^2) is 618. Density of polygons is 0,0281*1 m^2. Average area of polygons for all testing sites is 38,86 m^2.

The more wide variation of polygonal features sizes is located on roughness surface. At that, within relatively flat surface dominance of small-scale polygons is observing at absence polygons bigger than 90 m^2. Amount of the polygonal features on the roughness surface is match less than on the relatively flat surface. Maximum number of polygons shifted in the area range from 10 – 20 m^2 (relatively flat surface) to 20 – 30 m^2 (rough surface).In that case, percent of bigger polygons increase rapidly while number of smaller scale polygons decrease. In moraine-like ridges zone the biggest percent of area is presented by a large-scaled polygons. Polygons alternate between large-scale and small-scale. More concentration of large-scale polygons is typical for north exposed slopes.

Conclusion:

Our study results show that thermal contraction crack polygon formation depends on geomorphological surface types. For relatively flat surface the net of small-scale polygons is typical. The more rough surface type the bigger polygons presented.

Acknowledgment:

Author thanks to Kuzmin R.O., Oshchepkova P.V. and Oshchepkova A.V.

References:

[1] Levy et al., 2009. Journal of Geophysical Research. V. 114, 19. [2] Kreslavsky and Head, 2011. Icarus. V. 216, 111–115. [3] Mangold, 2005. Icarus. V. 174, 336–357.

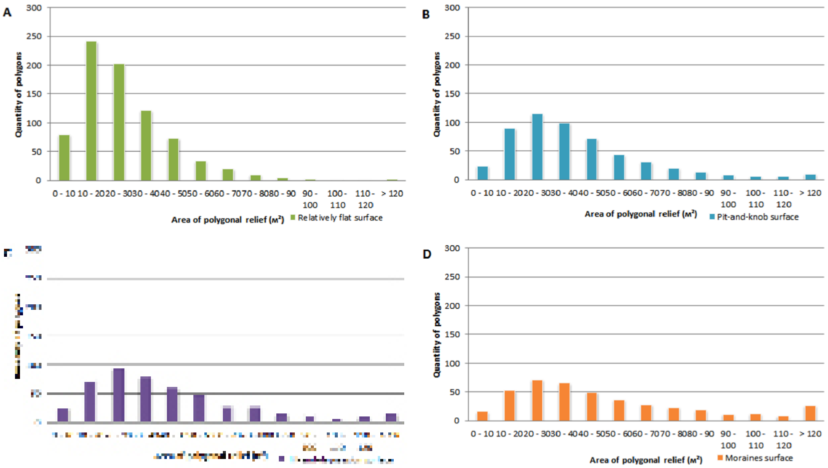

Fig. 2. Dependence numbers of polygons to there areas. A - relatively flat surface. B - pit-and-knob surface. C - hill-and-depression surface. C – moraines surface.

MODELING WATER VAPOR TRANSPORT IN THE MARTIAN SUBSURFACE

E. Gloesener, Ö. Karatekin, V. Dehant
Royal Observatory of Belgium, Brussels, Belgium.
elodie.gloesener@oma.be

Modeling gas transport through Martian subsurface and outgassing processes is essential in the study of atmospheric evolution of Mars. We present a 1D thermal model that includes the diffusion of water vapor through porous Martian regolith. The mass conservation equation takes into account the different phases of water: vapor, ice and adsorbed H_2O. The role of an adsorbing regolith on water transfer, regions of ice stability and the range of parameters that have the largest effect on transport in Martian conditions are investigated. In addition, kinetics of the adsorption process is considered to examine its influence on the water vapor exchange between the subsurface and the atmosphere.

Finally, our model is used locally to model water vapor transport at landing site of several missions like ExoMars 2016 and 2018 and, in particular, at Gale crater in order to reproduce Mars Science Laboratory observations.

STUDY OF THE SEASONAL VARIATIONS OF THE WATER EQUIVALENT OF HYDROGEN AMOUNT IN THE SUBSURFACE REGOLITH ON MARS BASED ON THE HEND DATA ACCUMULATED DURING THE FIVE MARTIAN YEARS

R.O. Kuzmin [1,2], M.L. Litvak[1], I.G. Mitrofanov[1], E.V. Zabalueva[2]
[1]Space Research Institute, RAS, Moscow, 117997, Russia.
rkuzmin@yahoo.com
[2]V. I. Vernadsky Institute for Geochemistry and Analytical Chemistry, RAS, Russia.

Introduction:

Global mapping of the neutrons albedo of Mars by the instrument HEND on board of the orbiter Mars Odyssey has been continued for more than the five Martian years. Such a long period of the observations not only let us study the seasonal variations of the water amount in a surface regolith during seasonal cycle, but also compare a seasonal cycles of different years. The main goal of our work was analysis of the water seasonal variations within the subsurface regolith in the middle latitudes of Mars. For the analysis we used the multiyear HEND observations of the fast and the epithermal neutrons fluxes with different energy ranges (2.5-10 MeV, 1-2.5 MeV, 10 eV-1 MeV, 10 eV-10 keV, and 0.4 eV-1 keV). As the neutrons of each energy range are characterized by definite generation depth, it is possible to estimate the water equivalent of the Hydrogen (WEH) amount at different depths of the surficial regolith.

Methodology:

In our analysis of the seasonal variations we have estimated the WEH amount in subsurface regolith in the latitude belt 30ºN-50ºN which is located outside of seasonal polar cap caver composed from CO2 snow (see fig. 1). To exclude the influence of both Galactic Cosmic Rays (GCR) variations and seasonal variations of the Martian atmosphere thickness, it is necessary to conduct normalization of the measured neutrons fluxes. For the normalization procedure the equatorial belt (0º-10ºN by latitude and 120ºE-240ºE by longitude) has been chosen (fig.1).

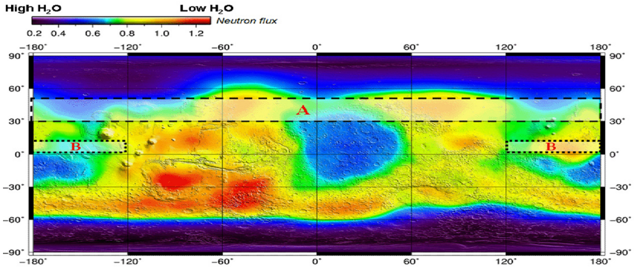

Fig. 1. The studded area of the middle latitudes (A) and the area of equatorial belt (B), used for normalization of the measured neutrons fluxes. Background- the map of the neutron flux measured for summer period of time during 11 Marthian years of orbit observations.

Likely to the studied latitude belt, the equatorial belt is characterized by similar both atmosphere thickness and its relative oscillations from one season to other. The Martian seasonal cycle has been divided on 24 intervals (by length in 15º Ls) and the neutrons flux in each of the intervals has been normalized to the averaged neutrons flux measured in the equatorial belt.

Analysis of seasonal plots of the normalized fast neutrons fluxes (measured in each of the five Martian years) shows that local variations of the neutrons flux may be as large as 10-15%. At that, the plots (averaged over all five years of observations) show systematic deficit of the fast neutrons (~7% and ~10% for neutrons with energy 1-2.5 MeV and 2.5-10 MeV respectively) during autumn-winter period in the northern hemisphere. Such effect is most likely related with redistribution of atmospheric water from the southern hemisphere t o the northern one in the season with succeeding condensation and accumulation of the water in subsurface regolith layer. To estimate the effect's value, we have used data of numeric modeling of instrument HEND and converted related variations of the neutrons flux to relative variations of the WEH amount. For the estimation of the WEH amount absolute value we have used content of water in the equatorial belt region derived from Gamma-Ray-Spectrometer (GRS) measurements on board of the Mars Odyssey orbiter [1]. The value of the water absolute content in the region is equal to ~4.7%. We may collate measured values with numeric calculations and determine the water content in the studied latitude belt using following expression:

***Flux30ºN50ºN/Fluxnorm=Fnum(W%)/Fnum(4.7%)*,**

where *Flux30ºN50ºN* and *Fluxnorm* – measured values in the latitude belt 30ºN-50ºN and the equatorial belt (used for the normalization); *Fnum* is taken from numerical calculations, *W* – is unknown value of the water content. The amounts of the WEH, received by such method, are shown on the fig.2 as the individual plots of a seasonal water contents for each Martian year of observations and averaged one over all five years. For more detailed study of dependence of seasonal variations of the WEH amount in the Martian soil versus depth, we have also analyzed the HEND data gathered by the detectors SD, MD and LD (which are sensitive to the different energy ranges of epithermal neutrons).

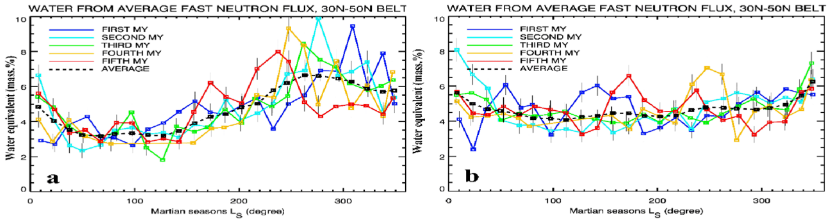

Fig. 2. Plots of seasonal variations of WEH amount in subsurfacel soil layer of Mars for different years of observations estimated based on mapping data of the fast neutrons with the energy 2.5-10 MeV (a) and 1-2.5 MeV (b). Dotted line shows plots averaged over all five the Martian years.

It gives us possibility to study effect of seasonal variations of subsurface water at different depths. The studied latitude belt is characterized by a sufficiently high amount of the physically and chemically bonded water in the subsurface soil layer [1,2] with maximum amount in 10-15 mass.%. Therefore in our analysis we have considered a simple model of two-layer soil – upper dry layer with the water amount 2 mass.% and lower wet layer with water amount 15 mass.%. By using numerical modeling, we have changed the depth location of lower layer and inspected how measured signal has been changed in each of the detectors. It has been found that when the location of the wet layer is close to the surface the neutrons flux decreases essentially. At consecutive increasing of the wet layer depth the neutrons flux is increasing and it approaches the saturation on the depth > 1 m. In the case of the detector LD (detects the neutrons in the energy range 10eV-1MeV) the leakage neutrons flux is close to the saturation level of 95% at depths approaching to the ~50 cm, while in the case of the detectors SD and MD (detect the neutrons with energy < 10keV) it is happen at the depths > 60 cm only.

Results:

As well seen from the fig.2, the average increasing of the WEH amount (averaged over all the five Martian years) for autumn-winter season approaches 3.5 mass.% (in the soil layer with thickness ~20 cm, corresponds to the neutrons measured in the energy range 2.5-10 MeV) and 2 mass.% (in the soil layer with thickness ~40 cm, corresponds to the neutrons measured in the energy range 1-2.5 MeV). Averaging of the WEH amount over all five years (based on the data from the detectors SD and MD) shows that the WEH amount during the seasonal cycle is relatively stable at the depths > 60 cm. Based on the data from the detector LD (fig.3c), the averaged wintertime increasing of the WEH amount approaches up to 0.3 mass.% at the depth of 50 cm. Following to the results of conducted analysis, the most significant seasonal variations of the WEH amount in the studied latitude belt (30ºN-50ºN) are related with subsurface regolith layer with ~20 cm of thickness (see fig.2a). With increasing of a regolith depth the seasonal variations of the WEH amount are becoming weaker (fig.4) and die down completely at the depths > 60 cm.

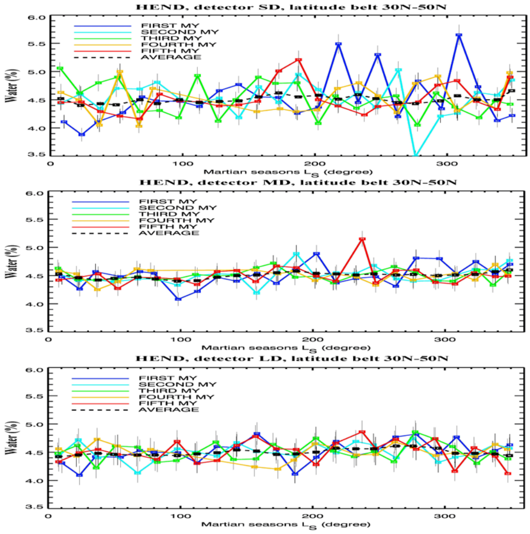

Fig. 3. Plots of seasonal variations of the WEH amount in subsurface soil layer of Mars for different years of observations estimated based on the data from the detectors SD (a), MD (b) and LD (c). Dotted line shows seasonal variations of the WEH amount averaged over all five years of observations.

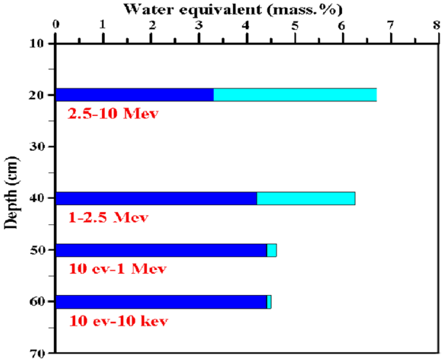

Fig. 4. The values of the WEH amount in summertime (dark blue) and the increasing values of the WEH amount in wintertime (blue) versus the depth. The energy ranges of measured neutrons are shown by red.

References:

[1] Boynton W.V. et al., *J. Geophys. Res.* 2007. V. 112. № E12. [2] Mitrofanov, I. G. et al.,*Solar Syst. Res.* 38, 253–65, 2004.

ANOMALOUS DENSITY WAVES METHOD FOR ESTIMATING THE STRESSES IN THE CRUST AND MANTLE OF MARS

V.N. Zharkov[1], T.V. Gudkova[1], K.I. Marchenkov[2]
[1]Schmidt Institute Physics of the Earth RAS, B.Gruzinskaya, 10, Russia;
[2]Institute of Space Research RAS, Profsouznaya, 84/32, Russia.
zharkov@ifz.ru

Introduction:

Joint analysis of the topography and the non-equilibrium part of the gravitational potencial of a planet provides one of the few available means of remotely probing the distribution of the stresses in the crust and mantle. The recent progress in developing the gravity and topographic models of Mars allowed studing the stress field of the planet. We have used the latest gravity and topographic models: the high resolution MOLA (Mars Orbiter Laser Altimetry) global topography [1] and gravity field MRO110B2 and MRO110C models from Jet Propulsion Laboratory [2].

Method:

The problem is based on a static approach, the planet is being modeled as an elastic, self-gravitational spherical body with density ρ (r), compressional modulus K (r) and shear modulus $\propto$ (r) as functions of radius r. It is assumed, that deformations and stresses which obey Hooke's law are caused by the pressure of relief on the surface of the planet and anomalous density $\delta\rho(r, \theta, \lambda)$, distributed by a certain way in the crust and the mantle. A self-consistent technique of the solutions of this problem (by way of the Green's functions or loading factors technique) has been developed in [3-5], where load factors for deep density anomalies were introduced to interpret the gravity and topography field of Venus and Mars. For the convenience of numerical computations the anomalous density field is represented in the form of weighted thin layers positioned at different characteristic depths. Imposing the anomalous density waves (ADW) on the surface or in the interior leads to the deformation of the planet interior and the distortion of the surface and the boundary interfaces. With the addition of ADW to the planet it goes to a new state of elastic equilibrium, that is, it "adjusts" to the ADW. The density field that is created due to the "adjustment" is of the same order of magnitude as the density field due to ADW itself. Moreover, it is often of opposite sign. Finally, the resulting field may have a sign that does not coincide with that of the ADW. Therefore, positive gravity anomalies may correspond to negative density anomalies and vice versa. So, the problem is reduced to the determination of Green's response function for the case of a single ADW located at some depth level.

Interior Structure Model:

Calculations were carried out based on a model of Mars from [6, 7]. The model comprises four submodels - a model of the outer porous layer, a model of the consolidated crust, a model of the silicate mantle and a core model. The density of the crust is 3000 kg m^{-3}, the density jump at the crust-mantle boundary is 500 kg m^{-3}, the thickeness of the crust is 50-100 km. The choice itself of a specific model for the problem under consideration is not very important: the reological cross section of Mars is of considerably greater importance. Two types of models have been considered. We started with a simple model – an elastic model. Then the models with an elastic lithosphere and weakened layers below it (relaxed values of shear moduli) were calculated: the effective shear modulus (rigidity) of the mantle is reduced in comparison with an elastic one and in extreme case is approaching zero everywhere except the elastic lithosphere. The thickness of the elastic lithosphere was varied from 150 to 300 km.

There is no evidence of plate tectonics on Mars, moreover, the presence of such a huge topographic structure as the Tharsis rise, is evidence of the presence of the thick elastic lithosphere, capable of elastically supporting of nonhydrostatic loading during geological time. The data on the thickness of the elastic lithosphere (300 km, [8]) points at cold state of Martian interiors. Thus, it can be assumed, that if thermal convection takes place under the Martian lithosphere, it is of secondary order, and the stress state is mainly caused by elastic deformations of subsurface layers, that allows us to use a static approach for this study.

The choice of a reference surface:

The definition of the "topography" needs the choice of a reference surface. Usually the "topography" is referenced to the areoid determined from the gravity field. To avoid uncontrollable stresses and deformations in the mantle of the planet due to the significant deviation of Mars from hydrostatic equilibrium state, we do not consider the areoid as the reference surface. An outer surface of a hydrostatical model is taken as a reference surface [9, 10]:

$$r(s_1,\theta)=s_1\{1+s_0(s)+s_2(s)P_2(t)+s_4(s)P_4(t)+...\},$$

where s_1 is the mean radius (the radius of an equivolume sphere) and $P_2(t)$ and $P_4(t)$ are the first even ordinary Legendre polynomials, which depend on even degrees of $t=\cos\theta$, θ is the polar distance.

Results:

Only unequilibrium components of gravity and topography fields have been considered: surface relief (or topography) was referenced to the standard equilibrium spheroid in the first approximation (Fig.1), and the hydrostatically equilibrium field of Martian spheroid was subtracted from the full potential

$$T(r,\varphi,\lambda)=R_{Mars}(r,\varphi,\lambda)-r(R,\theta),$$

$$T_g(r,\varphi,\lambda)=V(r,\varphi,\lambda)-V_0(r,t),$$

$$\varphi+\theta=\pi/2,$$

where $t=\cos\theta$ = sin φ.

Figures 2-4 show maps of the heights of the areoid referred to the standard equilibrium spheroid, the same but for spheroidal harmonics degrees 5-90 and gravity disturbances, respectively. It is seen that the Tharsis uplift makes the main contribution to nonequilibrium field of Mars; besides, a significant positive anomaly noticeable in the equatorial region diametrically opposite to Tharsis.

The model allows one to calculate all stresses (compressional stresses and the maximum shear stresses). In the Tharsis plateau region nonhydrostatic stresses reach their maximum level for different values of lithosphere thickness and the coefficient of astenosphere weakening. It is obvious, that an extrusion of the stresses into the elastic lithosphere occurs with an increasing degree of weakening of the astenopshere and, moreover, this is more intense, the thinner is the lithosphere. The distribution of shear stresses on the surface of Mars reveals a clear correlation with its surface structures. The largest stresses occur in the Tharsis uplift region, which dominates the relief of Mars. The maximum shear stresses at the surface range from 200 to 300 bars (for the elastic model) to 600-800 bars (for the model with a liquid astenosphere). High shear stresses also occur in the regions directly adjacent to Tharsis, for example, in Amazoniz and Arcadia Planitiac. This is evidently connected with the global bending of the lithosphere under the weight of the uplift. From the point of view of seismicity, those regions where high shear stress values are combined with tensile stresses are the most probable sources of Marsquakes.

Acknowledgments:

This work was undertaken during the preparation phase of the SEIS experiment on InSight mission. The work was supported by the Russian Foundation for Basic Research, project no. 15-02-00840.

References

[1] Smith, D.E. et al., 2001. J.Geophys. Res., 106 (E10): 23689-23722; [2] Konopliv et al, 2011. Icarus, 211: 401-428; [3] Marchenkov K.I. et al., 1984. Docklady Acad. Nauk,SSSR,Earth Sci.Sect.279, 14-16; [4] Zharkov V.N. et al., 1986. Sol.Syst.Res. 20,202-211; [5] Zharkov V.N. et al., 1991, Sol.Syst.Res. 25,515-547; [6] Zharkov V.N. et al., 2009.PEPI 172, 324-334; [7] Gudkova T.V., Zharkov V.N. 2015 , 6M-S3; [8] Phillips R.J. et al., 2008. LPSC. XXXIX, 1493.pdf; [9] Zharkov, V.N., Gudkova, T.V., 2000. PEPI, 117: 407-420. [10] Zharkov, V.N., Gudkova, T.V., 2005. Solar System Res., 39: 343-373;

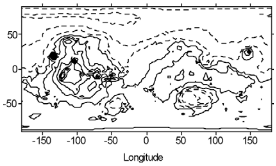

Fig.1. Heights of the surface relief of Mars

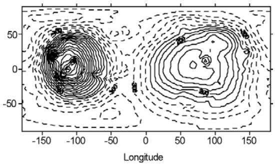

Fig.2. Heights of the areoid

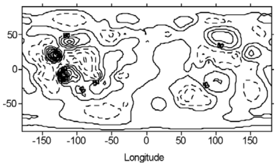

Fig. 3. Heights of areoid for spherical harmonics 5-90.

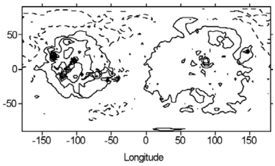

Fig.4. Gravity disturbances.

MARTIAN INTERIOR STRUCTURE MODELS: TRADEOFF BETWEEN THE DENSITY OF THE CRUST AND FE CONTENT IN THE MANTLE

T.V. Gudkova, V.N. Zharkov
Schmidt Institute Physics of the Earth RAS, B.Gruzinskaya, 10, Russia.gudkova@ifz.ru

Introduction:

The construction of current interior structure models of Mars is based on its mass, mean radius, the moment of inertia, the Love numbers characterizing the tidal response of the planet and its chemical composition. Substantial progress has been recently achieved in the gravity data, which are used as the boundary conditions for the interior structure models [1]. At present the density and thickness of the Martian crust is under the discussison. Based on chemistry of Martian meteorites, igneous rocks at Gusev crater and the measurements of the Gamma-Ray Spectrometer on board Mars Odyssey, in [2] it was concluded, that the average crustal thickness is thicker than previously thought (approaching 100 km), with an average density above 3100 kg/m^3 for those materials that are close to the surface.

Set of Interior Structure Models for Mars:

Based on basaltic models of crust determined by numerical thermodynamical modeling [3] and taking into account the DW chemical model [4] and experimental data at high pressure and temperature [5] we present the set of interior structure models with 50- and 100-km thick crust and averaged crustal density varying in the range of 2700-3200 kg/m^3. The model comprises four submodels – a model of the outer porous layer, a model of the crust, a model of the mantle and a model of the core. The first 10- 11 km layer is considered as an averaged transition from regolith to consolidated rock. Since the mean moment of inertia is now known to be smaller and the value of the Love number k_2 is larger [1, 6], we have reconsidered the models of the Martian interior we constructed before. The technique of the modelling is described in detail in [7, 8, 9]. The boundary conditions for models - the mass and the moment inertia can be written as $q=\frac{3}{\bar{\rho}}\int_0^1 \beta^2 \rho(\beta)d\beta$ and $I=\frac{2}{\bar{\rho}}\int_0^1 \beta^4 \rho(\beta)d\beta$, where $\beta=r/R$ is a relative radius of a planet. Dividing both left and right sides of the relations by q and I, respectively, and introducing functions $f_1(\beta)=\beta^2\rho(\beta)/q$ and $f_2(\beta)=\beta^4\rho(\beta)/I$, we have $\int_0^1 f_1(\beta)d\beta=1$ and $\int_0^1 f_2(\beta)d\beta=1$**.** These functions are shown in Fig. 1. The figure shows the influence of different zones of a planet the values of the mass and moment inertia. Figure 2 shows the distribution of density, gravity, temperature, bulk modulus and rigidity along the radius for a trial model of Mars.

Table 1. Parameters of interior structure models of Mars

Model	ρ crust (kg m^{-3})	Fe# mantle	*h* crust	*r* core	P core	Bulk Fe	Fe/Si	I/MR^2	k_2
1	2700	22	50	1773	19.6	27.7	1.75	0.3639	0.1518
2	2800	22	50	1769	19.6	27.5	1.74	0.3643	0.1512
3	2900	22	50	1759	19.7	27.3	1.72	0.3648	0.1499
4	2900	22	50	1784	19.4	27.8	1.76	0.3650	0.1543
5	3100	20	50	1779	19.4	27.0	1.71	0.3647	0.1544
6	3100	20	50	1811	19.0	27.5	1.76	0.3649	0.1604
7	3000	20\	50	1788	19.4	27.2	1.73	0.3642	0.1557
8	3000	20	50	1815	19.0	27.7	1.78	0.3644	0.1608
9	2900	20	50	1821	19.0	27.8	1.8	0.3639	0.1617
10	2800	20	50	1830	18.9	28.0	1.82	0.3634	0.1632
11	3200	18	50	1796	19.2	26.7	1.7	0.3642	0.1596
12	2800	25	100	1776	19.7	28.8	1.82	0.3639	0.1496
13	2900	25	100	1757	19.8	28.4	1.77	0.3649	0.1469
14	3100	20	100	1815	19.0	27.8	1.77	0.3644	0.1611
15	3000	22	100	1796	19.3	28.1	1.78	0.3644	0.1561

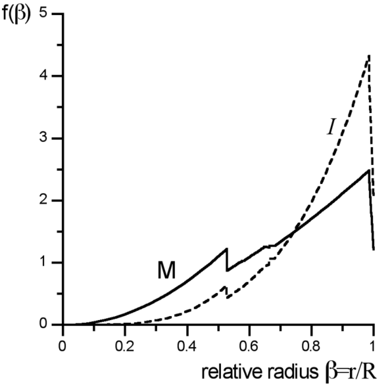

Fig. 1. Functions f_1 (β) and f_2 (β) for the mass and the moment inertia.

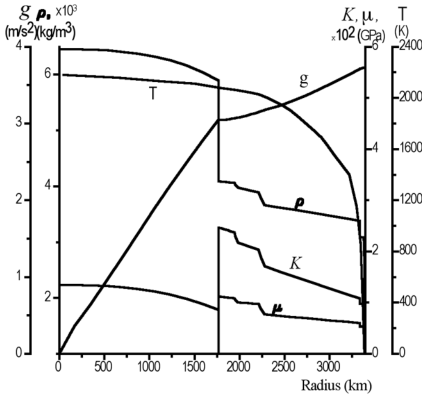

Fig. 2. The distribution of the density, temperature, bulk modulus and rigidity as a function of radius for a trial model.

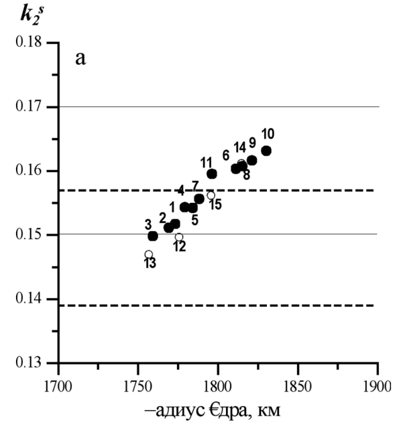

Fig.3. The elastic Love number as a function of the core radius for a set of martian models listed in the Table (• - 50 km crust, o – 100 rm crust). Horizontal lines show the upper and lower bound for k_2^s (solid lines – data from [1], dashed lines – data from [6].

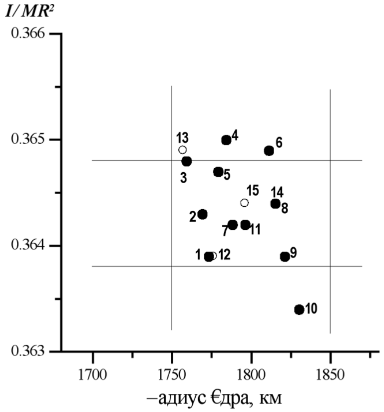

Fig. 4. The moment of inertia I/MR^2 as a function of the core radius. The notations are the same as in Fig.2. Horizontal lines indicate a spread of the admissible values of the moment of inertia [1]. The vertical lines correspond to the inferred core radius of the planet determined using the elastic Love number k_2^s (see Fig.2).

We see that the application of the new data results in the following variation in the parameters of the Martian interior: the mantle ferric number Fe# decreases, both the Fe/Si weight ratio and the core radius increase. The observational data constrain the radius of a liquid core to be within 1700-1850 km (see Fig. 3 and Fig.4). For 50-km thick crust its density is within 3.0-3.2 g/cm^3 (an iron atomic number of mantle silicates $Fe^{2+}/((Fe^{2+}+Mg)$ multiplied by 100: Fe#18), 3.0-3.1 g/cm^3 (Fe#20), 2.7-2.9 g/cm^3 (Fe#22); for 100-km thick crust we have 3.1 g/cm^3 (Fe#20), 3.0 g/cm^3 (Fe#22), 2.8-2.9 g/cm^3 (Fe#25). The models differ in density contrast at the crust-mantle boundary and the core radius that is important for gravity-topography interpretation. As was mentioned in [2], taking into account a porosity would lead to the decrease of the crust density.

Acknowledgments:

This work was undertaken during the preparation phase of the SEIS experiment on InSight mission. The work was supported by the Russian Foundation for Basic Research, project no. 15-02-00840.

References:

[1] Konopliv, A.S. et al. (2011) Icarus, 211, 401-428. [2] Baratoux et al. (2014) J. Geophys. Res., 119, 1707-1727.[3] Babeiko A. et al., Solar System Res.,27,149-165, 1993. [4] Dreibus,G., and Wänke, H. (1985) Meteoritics, 20, 367-381. [5] Bertka, C. and Fei, Y. (1997) J. Geophys. Res. 102, 5251-5264. [6] Konopliv, A.S. et al. (2006) Icarus, 182, 23-50. [7] Zharkov, V.N., Gudkova, T.V., 2000. PEPI, 117: 407-420. [8] Zharkov, V.N., Gudkova, T.V., 2005. Solar System Res., 39: 343-373; [9] Zharkov V.N. et al., 2009.PEPI 172, 324-334

INVESTIGATIONS OF THE SOLAR SYSTEM OBJECTS AT RTT150

I. Khamitov[1,2], R. Gumerov[2,3], I. Bikmaev[2,3], Z. Aslan[4], S. Helhel[5], G. Kahya[1,5], G. Pinigin[6]
[1]TÜBİTAK National Observatory, Akdeniz University Campus, 07058 Antalya, Turkey;
[2]Kazan Federal University, ul. Kremlevskaya 18, 420008 Kazan, Russia;
[3]Academy of Sciences of Tatarstan, Kazan, Russia;
[4]1427. Cd., No:4/24, Balgat, Ankara, Turkey;
[5]Akdeniz University,Faculty of Engineering, 07058 Antalya, Turkey;
[6]Nikolaev Astronomical Observatory Scientific Research Institute, ul. Observatornaya 1, Nikolaev, 54030 Ukraine.
irek_khamitov@hotmail.com

Introduction:

Investigation of Solar System Objects is one of the ongoing scientific programs performed at the 1.5m Russian-Turk telescope RTT150 almost since the observational facilities became operational. Available scientific telescope equipment makes it possible to perform comprehensive studies of these objects including high-precision positional, photometric, and spectroscopic measurements. Following the integration of a polarimeter into the telescope scientific facilities in order to measure the linear polarization of celestial light sources, the polarimetric observations of asteroids have begun at the end of 2014. We report the results of these studies. In the frame of our project of mass determination of selected main-belt asteroids based on dynamical method, positions of 231 asteroids were observed. As a result, more than 14000 precise positions of the objects in ICRF frame and their photometric brightness estimates were obtained. For 10 main-belt asteroids, the accuracy of mass estimation was improved by 30%. The reflecting spectra of NEAs 433 (Eros), 1036 (Ganimed), 1917 (Cuyo), and 8567, with a magnitude range from 10.5 to 16.5 and a proper motion range from 20 to 160 arcsec per hour were obtained. The spectra cover the visible range from 3500 to 9000 Angstroms with the resolution R~600. To compare the quality of spectra of asteroids with known classes (433, 1036 and 1917), the spectral classification in SMASS system were performed. The spectral class of NEA 8567 was estimated for the first time as a class Q. In the frame of an international campaign, in 2007, of photometric observations of the mutual occultations and eclipses of Uranian satellites, the photometric series of two events out of the 27 total events observed were obtained at the RTT150. The processing of all light-curves gave the rms of the O–C residuals with respect to theory as 10 and 20 mas in right ascension and declination, respectively. These observations appear to be the best astrometric data of the Uranian satellites. The RTT150 participated in the international campaign on the observations of the Potentially Hazardous Asteroid (99942) Apophis, which was conducted during the asteroid's latest close approach in the period of December 2012 to May 2013. The new data will help to reduce the orbit uncertainty of Apophis during its close approach in 2029. We present the results of polarimetric and photometric observations of four faint NEAs with high proper motion during their close approaches: 276049, 333578, 163132, and 1999 FN53, using the telescope RTT150. In the near future, we are going to make the albedo estimations of all known NEAs with a diameter more than 1 km, which is important in the study of their population.

THE ELECTROMAGNETIC PHENOMENA AT MARS AND THEIR SURVEY AT LANDING PLATFORM

A. Skalsky[1], S. Klimov[1], I. Dobrovolski[1], N. Rybjeva[1], A. Sadovski[1], S. Savin[1], K. Anufreichik [1], D. Timonin [1], A. Semenov[1], D. Glazkin [1], E. Sokolova[2], I. Popova[2], O. Pokhotelov[2], I. Yegorov[3], I. Kolmasova[4], O. Santolik[4], V. Korepanov[5], V. Pronenko[5], A.N. Skhomenko[6], I.V. Stepanov[6]

(1) Space Research Institute RAS, Moscow, Russia;
(2) The Schmidt Institute of Physics of the Earth RAS, Moscow, Russia;
(3) P.P.Shirshov Institute of Oceanology RAS, Moscow, Russia;
(4) Institute of Atmospheric Physics, Prague, Czech Republic;
(5) Lviv Center of Institute for Space Research, NASU/NSAU, Lviv, Ukraine;
(6) Ramenskoye design company, Ramenskoye, Moscow Region, Russia.

The interaction of incoming solar wind with crustal anomalies at Mars and its ionosphere leads to variety of electromagnetic variations occurring in Martian plasma environment. The dust motion and charging are drivers of waves generated in the atmosphere of Mars.

The present paper is aimed on the review of electromagnetic phenomena at Mars and their implications for monitoring of general state of Martian environment and for investigation of planetary interior with the electromagnetic experiment at landing platform.

NEW CARTOGRAPHY OF MERCURY: MAPS AND GLOBE

A.Yu. Zharkova[1], J.F. Rodionova [1,2], A.A. Kokhanov[1], I.P. Karachevtseva[1], J. Oberst [1,3,4]
[1]Moscow State University of Geodesy and Cartography (MIIGAiK), MIIGAiK Extraterrestrial Laboratory (MexLab), Gorokhovskiy pereulok, 4, Moscow, 105064, Russia;
[2]Sternberg State Astronomical Institute, 119899, Moscow, Russia;
[3]Technical University of Berlin, Berlin, Germany;
[4]German Aerospace Center (DLR), Berlin, Germany.
i_karachevtseva@miigaik.ru

Introduction:

We present first hypsometric maps of the Mercury's hemispheres, which is the basis for the new globe. The development of Mercury globe continues a series of globes of the terrestrial planets, including globes of Venus, Mars and the Moon, created by Sternberg Astronomical Institute with support of Space Research Institute (Rodionova and Brekhovskikh, 2013). In anticipation of Bepi Colombo's mission in 2017 creation of Mercury globe acquires particular relevance.

Study and mapping:

Until recently only part of Mercury's surface was investigated based on Mariner 10 data. The images received by MESSENGER (2011-2015) forced the scientific community to explore Mercury's surface more detail. For example, morphometric analysis of small craters proves that the regolith on Mercury is significantly thicker than on the Moon (Kreslavsky and Head, 2015); study of multi-ring objects shows that the frequency of concentric basins is greater in the western hemisphere (Rodionova and Blue, 2014); study of kilometer-scale topographic roughness of Mercury shows the dichotomy between the smooth northern plains and more heavily cratered terrains (Kreslavsky et al., 2014). Multi-ring basins (Fig.1a) and ray systems (Fig.1b) were identified by global Mercury's mosaic with resolution 220 m/px (http://messenger.jhuapl.edu/the_mission/mosaics.html) produced from MESSENGER'S MDIS (Mercury Dual Imaging System) Wide Angle camera images. Recognizing of smooth plains was based on the results presented in the work (Denevi et al., 2013). MESSENGER's orbit was highly elliptical, therefore digital elevation models (DEMs) have been created for several parts of the planet (http://ode.rsl.wustl.edu/mercury/index.aspx; http://europlanet.dlr.de/node/index.php?id=524). We have analyzed the DEMs, but used for our work global DEM (22000 m/px) derived from limb measurements (Elgner et al., 2014).

Conclusions:

The first time hypsometric maps for Mercury hemispheres were created (Fig. 2, 3). The new maps are cartographic basis for producing of Mercury globe (scale 1: 32 000 000), which continues a series of globes of the terrestrial planets.

Acknowledgments:

We would like to acknowledge the German Aerospace Center (DLR) and personally A. Stark for global DEM of Mercury.
The work was carried out at MIIGAiK and supported by Russian Science Foundation, project 14-22-00197.

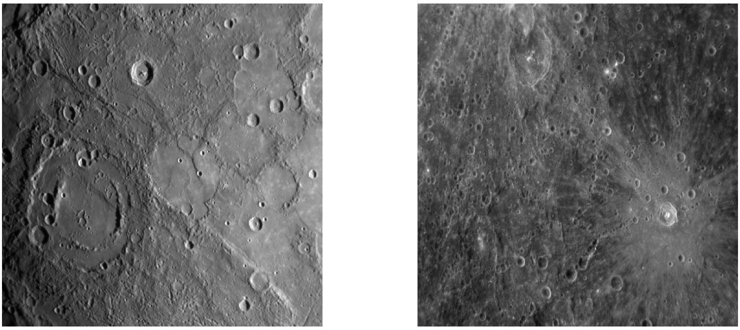

a) b)

Fig. 1. Examples of feature objects on Mercury: a) the large double-ringed crater; b) rayed craters (Photo Credit: NASA/Johns Hopkins University Applied Physics Laboratory/ Carnegie Institution of Washington)

Fig. 2. Layout of hypsometric map for northern hemisphere of Mercury

Fig. 3. Layout of hypsometric map for southern hemisphere of Mercury

References:

1) Elgner S. et al. (2014) Mercury's global shape and topography from MESSENGER limb images // Planetary and Space Science 103, 299–308. 2) Denevi B. W. et al. (2013) The distribution and origin of smooth plains on Mercury // Journal of Geophysical Research 118, 891–907. 3) Kreslavsky M. A., Head J. W. (2015), A thicker regolith on mercury // Abstracts of 46th Lunar and Planetary Science Conference, no1246. 4) Kreslavsky, M.A. et al., (2014) Kilometer-scale topographic roughness on Mercury: Correlation with geologic features and units // Geophys. Res. Lett., 41, 8245-8251. 5) Rodionova J. F., Brekhovskikh J.A. (2013), Hypsometric globe of Mars – 3D model of the planet // Proceedings of the 26th International Cartographic Conference, no 610. 6) Rodionova J. F., Blue J. (2014), Features of Distribution of Mercurian Concentric Basins on the Base of Messenger Data // 40th COSPAR Scientific Assembly, B0.1-93-14. 7) Mariner 10 Digital Terrain Models. URL: http://europlanet.dlr.de/node/index.php?id=524 (accessed: 06.07.2015). 8) PDS Geosciences Node Mercury Orbital Data Explorer. URL: http://ode.rsl.wustl.edu/mercury/index.aspx (accessed: 06.07.2015). 9) MESSENGER Global Mosaics of Mercury. URL: http://messenger.jhuapl.edu/the_mission/mosaics.html (accessed: 06.07.2015)

YUPITER'S MOON EUROPA: PLANETARY GEOELECTRICAL MARKERS AND OREOLS OF THE LIQUID OCEAN UNDER THE ICE ON THE SURFACE OF THE YUPITER'S MOON EUROPE

Yu. Ozorovich[1], A. Fournier-Sicre[2], V. M. Linkin[1] , A.S. Kosov[1], D.P. Skulachev[1], S. Gorbatov[1], S. Potemkin[1] , A. Ivanov[3]
[1]Space Research Institute,Russian Academy of Sciences, 84/32 Profsoyuznaya st.,Moscow, 117810,Russia;
yozorovi@iki.rssi.ru;
[2]FAST-ER, France
[3]Swiss Space Center.

The existence of various forms of the cryolithozone on terrestrial planets and their moons: advanced Martian permafrost zone in the form of existing of the frozen polar caps, subsurface frozen horizons, geological markers and oreols of the martian ancient (relict) ocean, subsurface oceans of Jupiter's and Saturn's moons - Europe and Enceladus, with the advanced form of permafrost freezes planetary caps, it allows to develop a common methodological basis and operational geophysical instruments (tools) for the future space program and planning space missions on these unique objects of the solar system, specialized for specific scientific problems of planetary missions.

Geophysical practices and methodological principles, used in 1985-2015 by author [1-5], respectively, as an example of the comprehensive geophysical experiment MARSES to study of the Martian permafrost zone and the martian ancient (relict) of the ocean, creating the preconditions for complex experimental setting and geophysical monitoring of operational satellites of Jupiter and Saturn - Europe and Enceladus.

This range of different planetary (like) planets with its geological history and prehistory of the common planetology formation processes of the planets formation and to define the role of a liquid ocean under the ice as a climate indicator of such planets, which is extremely important for the future construction of the geological and climatic history of the Earth.

PERIODICITY OF RADIOACTIVITY SOURCE: CHANNELS OF REGISTRATION & PHYSICAL MECHANISM

A.A. Rukhadze[1], O.B. Khavroshkin[2], V.V. Tsyplakov[2]
[1]General Physics Institute, Russian Academy of Sciences,
[2]Institute of Physics of the Earth, Russian Academy of Sciences.
khavole@mail.ru

The existence of periodicities or just perturbation level of radioactivity of different sources found for a long time ago. Thus, the temporal variations β- radiation decay (decay numbers) Cs-137 registered in April 19-23,1994y. (Baurov Y.A.) and other researchers. Temporal variations in the analysis of records of beta - radioactivity have long periods and short hard to stand out and limited to a few days and more. Good stands one-year variation in the distance Sun - Earth. Variations in the analysis of records of gamma - radioactivity have a wide range of periods (from a few minutes to a day or more), all the spectra contain valid periods of the solar oscillations (up 40periodov), long sunny periods are also found in of the Earth and the Moon oscillations. The observed effects of interaction of the neutrino flux from sources of gamma - radiation allow a deeper study of the Sun, Earth seismicity and other related applied research. Study periodicities most effective in monitoring γ-radioactive.

DUST COMPLEX ONBOARD THE EXOMARS-2018 LANDER FOR INVESTIGATIONS OF MARTIAN DUST DYNAMIC

A. Zakharov[1], I. Kuznetsov[1], G. Dolnikov[1], A. Lyash[1], V. Afonin[1], F. Esposito[2], E. Seran[3], V. Gotlib[1]

[1]Space Research Institute (IKI), Russian Academy of Sciences, Moscow, Russia, kia@iki.rssi.ru;

[2]INAF - Osservatorio Astronomico di Capodimonte, NAPLES, Italy

[3]Laboratoire Atmospheres, Milieux, Observations Spatiales, Paris, France

The load of suspended dust in the Martian atmosphere varies dramatically but never drops entirely to zero. Effects of airborne dust contribute to the dynamic and thermodynamic evolution of the atmosphere and its large-scale circulation processes on diurnal, seasonal and annual timescales. Suspended dust plays a key role in determining the present climate of Mars and probably influenced the past climatic conditions and surface evolution. Atmosphere dust and wind-blown dust are responsible for erosion, redistribution of dust on the surface, and surface weathering.

The mechanisms for dust entrainment in the atmosphere are not completely understood, as the current data available so far do not allow us to identify the efficiency of the various processes. Dust-grain transport on the surface of Mars has never been directly measured despite great interest in and high scientific and technological ramifications of the associated phenomena. This paper describes planned, future investigations of the Martian dust environment made possible by the proposed scientific payload Dust Complex" (DC) of the ExoMars-2018 mission's landing platform.

DC is a suite of four sensors devoted to the study of Aeolian processes on Mars with a primary aim of monitoring the diurnal, seasonal, and annual dust-environment cycles by Martian-ground-based measurements of dust flux in situ, i.e., in the near-surface atmosphere of Mars.

This suite includes:

1) Impact Sensor (IS), for the measurement of the sand-grain dynamics,
2) Particle-Counter Sensor (MicroMED), for the measurement of airborne dust size distribution and number density,
3) Electric Field Probe (DEP), for the measurement of the ambient electric field,
4) Radiofrequency Antenna (EMA) for investigation of electromagnetic activity of the Martian atmosphere .

The presentation reviews outlining design and characteristics of DC, various dust effects and dust phenomena that are anticipated to occur in the near-surface environment on Mars and that are possible to observe by DC. Mechanisms associated with the influence of dust in the atmosphere processes are discussed. Scientific outcomes of DC have future meteorological and environmental applications on Mars, for example, for the study of the evolution dynamics of the atmospheric aerosols and near-ground stratification.

The objectives of DC is to provide direct measurements of the atmosphere, Measurement of the daily and seasonally variability and dynamic of the atmosphere dust;

- Detection of the windblown particles and their parameters such as mass distribution and possible charge appearance;
- Measurement of the electrostatic field, electric conductivity of the Martian near surface environment and its correlation with the dust turbidity;

Detection of micro discharges and electric perturbations, any electromagnetic activity in the radiofrequency range.